AN ABSTRACT OF THE DISSERTATION OF

Steven C. Lovejoy for the degree of Doctor of Philosophy in Mechanical Engineering presented on May 30, 2006.

Title: Development of Acoustic Emissions Testing Procedures Applicable to Conventionally Reinforced Concrete Deck Girder Bridges Subjected to Diagonal Tension Cracking.

Abstract approved:

Timothy C. Kennedy

A need exists to develop a non-destructive testing technique that can identify the formation and propagation of diagonal tension cracks in conventionally steel reinforced concrete deck girder (RCDG) highway bridges in the State of Oregon. Such a technique could be included into a structural health monitoring (SHM) system installed on specific bridges to automatically monitor the current state of structural damage in primary load supporting elements and provide notification of recent damage to bridge engineers in nearly real time. This research investigates the practical application of AE used to supplement a conventional SHM on vintage RCDG bridges. Background work presented in the Appendices investigates stress wave propagation in non-reinforced and steel reinforced concrete media. Based on the characterization of stress wave speeds, amplitude attenuation, frequency content and wave forms found in concrete media, testing methods are

developed and applied to 31 full sized RCDG test specimens that include variations in loading, load capacity and structural detailing. Several different AE test procedures are used to characterize the damage states of the test beams as they are progressively loaded to failure. Four previously developed AE parameters that characterize both damage progression and damage state are applied which include the Felicity and Calm Ratios, Severity and the Historic Index. Both Felicity and Calm Ratios were found to respond to the damage state of the test beam as determined from more conventional assessment methods such as crack width and load. For the practical in-service loading ranges of 20 to 80% of ultimate capacity both the Felicity and Calm Ratios were found to respond in a nearly linear manner with increasing damage. Three categories of damage state are defined which are based on the ODOT crack comparator tool which is used for in-service maintenance inspections of these bridges. Felicity and Calm Ratio values are related to these damage states for the specific type of bridge girders being tested and can be used to estimate in-service damage states. The Severity and Historic Index responses were found to be an effective means of identifying the formation and extension of diagonal tension cracks as they developed. Threshold levels for these two parameters are identified for specific AE sensor types when applied to this class of bridge girder.

A preliminary set of AE testing and analysis procedures were developed that were applied to three in-service bridges. These bridge tests used both controlled and ambient loading protocols. The structural response to each load case was quantified by using both crack width motion and reinforcing steel strain range. These structural parameters were correlated with the AE data. The Calm Ratio was found to be of practical importance and that the values recorded were in reasonably good agreement with the laboratory data once the imposed loads and current crack widths were considered. The Severity and Historic Index were also found to be of practical importance to bridge testing and structural health monitoring as they were found to be very sensitive to

increasing damage, yet exhibit good stability provided enough AE activity was present. A recommend set of guidelines and practices for applying AE to vintage RCDG bridges is developed and presented.

Development of Acoustic Emissions Testing Procedures Applicable to Conventionally Reinforced Concrete Deck Girder Bridges Subjected to Diagonal Tension Cracking

by

Steven C. Lovejoy

A DISSERTATION

submitted to

Oregon State University

in partial fulfillment of
the requirements for the
degree of

Doctor of Philosophy

Presented May 30, 2006
Commencement June 2006

Doctor of Philosophy dissertation of Steven C. Lovejoy

Presented on May 30, 2006.

APPROVED:

Major Professor, representing Mechanical Engineering

Head of the Department of Mechanical Engineering

Dean of the Graduate School

I understand that my dissertation will become part of the permanent collection of Oregon State University libraries. My signature below authorizes release of my dissertation to any reader upon request.

Steven C. Lovejoy, Author

ACKNOWLEDGEMENTS

I wish to express my most sincere gratitude to my PhD committee. I hand selected each of you and am honored that you have provided the guidance and support that made this quest most worthwhile. I am also deeply indebted to Chris Higgins for his knowledge, enthusiasm, absolute reliability and most importantly his ability to break very large steel reinforced concrete structures. I must also thank Frank Nelson for his complete support at work and in pursuing this degree. And most importantly I would like to thank my friends and family for enduring this most selfish undertaking.

TABLE OF CONTENTS

TABLE OF CONTENTS (Continued)

TABLE OF CONTENTS (Continued)

Page

TABLE OF CONTENTS (Continued)

Page

TABLE OF CONTENTS (Continued)

Page

TABLE OF CONTENTS (Continued)

Page

TABLE OF CONTENTS (Continued)

Page

TABLE OF CONTENTS (Continued)

Page

TABLE OF CONTENTS (Continued)

Page

TABLE OF CONTENTS (Continued)

Page

TABLE OF CONTENTS (Continued)

Page

LIST OF FIGURES

LIST OF FIGURES (Continued)

Figure | Page

LIST OF FIGURES (Continued)

Figure Page

LIST OF FIGURES (Continued)

Figure Page

LIST OF FIGURES (Continued)

Figure Page

LIST OF FIGURES (Continued)

Figure Page

LIST OF FIGURES (Continued)

Figure | Page

LIST OF FIGURES (Continued)

LIST OF FIGURES (Continued)

Figure Page

LIST OF FIGURES (Continued)

Figure Page

LIST OF FIGURES (Continued)

Figure Page

LIST OF FIGURES (Continued)

Figure Page

LIST OF FIGURES (Continued)

Figure Page

LIST OF FIGURES (Continued)

LIST OF FIGURES (Continued)

LIST OF FIGURES (Continued)

Figure Page

LIST OF FIGURES (Continued)

Figure Page

LIST OF FIGURES (Continued)

Figure Page

LIST OF FIGURES (Continued)

Figure Page

LIST OF FIGURES (Continued)

Figure Page

LIST OF FIGURES (Continued)

Figure Page

LIST OF FIGURES (Continued)

Figure Page

LIST OF FIGURES (Continued)

Figure | Page

LIST OF FIGURES (Continued)

Figure Page

LIST OF FIGURES (Continued)

Figure Page

LIST OF FIGURES (Continued)

Figure Page

.

LIST OF FIGURES (Continued)

Figure Page

LIST OF FIGURES (Continued)

Figure Page

LIST OF FIGURES (Continued)

Figure   Page

LIST OF FIGURES (Continued)

Figure Page

LIST OF FIGURES (Continued)

Figure Page

LIST OF FIGURES (Continued)

LIST OF FIGURES (Continued)

Figure Page

LIST OF FIGURES (Continued)

Figure Page

LIST OF FIGURES (Continued)

Figure Page

LIST OF APPENDIX FIGURES

LIST OF APPENDIX FIGURES (Continued)

LIST OF APPENDIX FIGURES (Continued)

LIST OF APPENDIX FIGURES (Continued)

LIST OF APPENDIX FIGURES (Continued)

Figure | Page

LIST OF APPENDIX FIGURES (Continued)

LIST OF APPENDIX FIGURES (Continued)

Figure | Page

LIST OF APPENDIX FIGURES (Continued)

Figure Page

LIST OF APPENDIX FIGURES (Continued)

LIST OF APPENDIX FIGURES (Continued)

LIST OF APPENDIX FIGURES (Continued)

LIST OF APPENDIX FIGURES (Continued)

Figure | Page

LIST OF APPENDIX FIGURES (Continued)

LIST OF TABLES

LIST OF TABLES (Continued)

LIST OF APPENDIX TABLES

Development of Acoustic Emissions Testing Procedures Applicable to Conventionally Reinforced Concrete Deck Girder Bridges Subjected to Diagonal Tension Cracking

1 Introduction

1.1 Oregon's Bridge Inventory Contains Many Vintage RCDG bridges

The Oregon Department of Transportation (ODOT) owns 2680 bridge structures that are part of the State and Federal Highway system. A particular class of bridge, the reinforced concrete deck girder (RCDG) bridge makes up over 20% of all bridges with 555 such structures as of 2001. These vintage structures were designed and constructed during the big highway expansion of the 1950's and 60's. These structures are typically formed of multiple spans that are structurally continuous over the interior vertical support elements which are called piers or bents depending on their location and design. All of these structures were designed in accordance with the American Association of State Highway and Transportation Officials (AASHTO) design specifications for the years they were built. Many of these structures carry large volumes of vehicle and truck traffic on major routes throughout Oregon.

1.2 Diagonal Tension Cracking is Discovered in 2001

Starting in 2001 biannual bridge inspections started identifying extensive cracking in the girders. It is very common for conventionally reinforced concrete structures to exhibit some cracking in the concrete as a result of shrinkage from the curing of the concrete and to some degree from service loads. However the type of cracking being discovered was believed to be diagonal tension cracking which can occur in the high shear stress zones of the girders, which typically occurs near fixed end supports. This type of cracking can cause concern to bridge engineers in that if the cracks are allowed to develop, a potential for non-ductile failure also develops. The structural load rating method used to assess the in-service capacity of these bridges was the 1994 AASHTO *Manual for Condition Evaluation of Bridges* which recommends a reduction in shear capacity resulting from cracking. New load ratings performed using the measured cracked conditions resulted in load ratings that were not considered adequate for the current loads on many of these bridges. A major inspection effort was under taken to assess the number of bridges with cracking problems. The results showed that of the 555 vintage RCDG structures in service, 178 bridges had randomly dispersed low-density cracking that was not of urgent concern. One hundred and eighty structures had medium-density cracking, mostly occurring near the supports that warranted increased inspection frequencies and would likely require repairs, replacement or load restrictions in the near future. And finally 129 structures exhibited widely dispersed high-density cracking that would result in immediate load restrictions or rapid repair or replacement [51].

1.3 Response to the Cracking Problem

Based on the results of the bridge inspection data, the load rating method in use resulted in unacceptably low ratings for many legal truck configurations and the potential for non-ductile failure modes where diagonal tension cracks were present. ODOT responded by putting load restrictions on many of these bridges. By the end of 2001, 68 bridges had weight restrictions imposed, and by 2003 the number had increased to 140 [51] while ODOT struggled to find practical solutions to this large and complex problem. In addition to load restrictions, some of the more critical bridges were requiring hands on inspection on a weekly basis instead of the normal 2 year cycle.

Running in parallel with the updated load ratings, ODOT initiated a research project with Oregon State University (OSU) Department of Civil and Environmental Engineering to develop more accurate methods for assessing the remaining service life of the vintage bridge structures in question. After extensive public outcry over the effects of the load restrictions on both the trucking industry and local communities suffering from large detours through their towns, the research project was put on the fast track and funded under Strategic Planning and Research (SPR) projects 341 and 350 [50,52]. Oregon also developed and passed one of the largest tax bills in the state's history to replace a large number of these problem bridges through House Bill 2041.

1.3.1 OSU Research Conducts Laboratory and Field Testing to Develop More Accurate Load Rating Methods

The research project headed by Prof. Chris Higgins attacked the problem of diagonal tension cracking in vintage RCDG bridges in a very thorough and well thought out manner. All State owned bridges that fit the description of vintage RCDG design were reviewed by examining design drawings and inspection reports to quantify the diverse structures in terms of span length, girder arrangement, girder detailing, etc. to provide bounds on what should be examined. Three in-service bridges that were of critical importance to ODOT and experiencing heavy cracking were selected for testing with both controlled and ambient loads. An extensive laboratory testing program was also developed to test the effects of various parameters such as loading type, shear stirrup density, poor detailing such as cut-off and under developed reinforcing steel, high and low cycle fatigue and moving loads. A total of 42 full scale laboratory beams were tested up to and including failure, providing a wealth of experimental data to be combined with the field testing and analytical methods applied to predicted girder capacity. This research resulted in developing improved methods for determining the remaining capacity of vintage RCDG bridges specific to those owned by ODOT.

1.3.2 Weight Restrictions Lead to Unacceptable Consequences for the Public

Even with the OSU research under way and on a fast track, the results would not be available for implementation for at least two years and likely longer. The public outcry from the load restrictions was very acute. The trucking lobby quantified the lost revenue caused by the detours and the numbers were very large, being on the order of $40,000 per day of restriction. In addition, large volumes of heavy trucks were being forced to take lengthy detours through small towns that did not have the infrastructure to handle the increased traffic. In 2003 House Bill 2041 was passed allocating 1.3 billion dollars to rapidly replace the most critical bridge structures. In addition the Oregon Transportation Investment Act Part III included 300 million dollars for county and city bridge replacement. This is clearly a very serious response to a very serious problem. Even with the large dollar amounts involved, it will not come close to replacing all of the deficient RCDG bridges in Oregon. A need still exists to deal with the existing structures that are on the replacement list until they can be replaced and to deal with the structures that were not included in the replacement plan.

1.4 What to Do With Bridges That Have Low Load Ratings and Cannot Be Replaced in the Near Future?

Clearly Oregon's cracked bridge problem is very large and serious. It is so large that no matter how much money is thrown at the problem, there will still be many structurally deficient bridges that must remain in-service for 5 to 15 years before a replacement project can be developed and implemented.

1.4.1 Repair and Retrofitting Structurally Deficient Bridges

In many cases repair and retrofitting of the deficient sections is a cost effective and structurally efficient solution. In general there has not been much work focused on designing and implementing repair and retrofit strategies for this class of structure. Several methods including adding extra reinforcing steel or applying fiber reinforced plastic (FRP) to critical sections have been implemented with apparent good success in Oregon. Methods for reassessing the load rating once these repairs have been made are also not common or well developed in general, mostly due to the unknown service life of such repairs and inspection methods of the repaired sections. ODOT has again stepped forward and funded two research contracts with OSU to assess these issues through SPR 619 which focuses on the FRP approach and SPR 636 which looks at other methods. These projects are currently under way with the prospect of implementing the results on real bridges in the next few years.

1.4.2 Structural Health Monitoring

Another practical alternative to imposing load restrictions on structurally deficient bridges is to develop and install a structural health monitoring (SHM) system. Many of the vintage RCDG bridges that do not have an adequate calculated load capacity appear to experienced bridge engineers to be fit for services, at least for the current loading levels. This assessment is typically based on experience with the specific structure type and knowledge that load redistribution will occur as the damage state increases. It also considers that even though a laboratory test beam may fail in a non-ductile manner when combined with 3 or more girders in a structurally continuous manner, sudden and catastrophic failure of the bridge or significant portion of the bridge is very unlikely. Thus for the short term, until repair or replacement, the owner may be comfortable with the current condition and loading of a particular structure even though the load rating indicates a lack of capacity. This is indeed the situation for many of the vintage RCDG bridges in Oregon. Nonetheless federal law requires something be done to assure public safety. One such response is to design and install a structural health monitoring system.

A properly designed and implemented SHM can replace the weekly hands on inspections discussed above with great effectiveness, often with cost savings. By identifying key structural parameters that can be used to assess the performance of the bridge, transducers can be installed on a bridge and monitored continuously. This not only provides a much less subjective set of performance measurements but can take the measurements much more often and thus track historic trends more accurately and conveniently and provide immediate warning to the owner in the event certain thresholds of structural demand have been exceeded. The engineer can monitor the current and historic trends from a central location and does not need to perform any unscheduled on-site inspections unless the data indicates this is necessary. This approach has been applied to dams for several decades and has been developed to such an extent that great reliability in the systems has been realized. Recently ODOT developed and implemented a SHM system to monitor the foundation of a movable bridge in Coos Bay, Oregon. The system has been performing very well since it was installed in 2001.

1.4.2.1 *Structural Health Monitoring for Vintage RCDG Bridges*

It is anticipated that as ODOT's inventory of vintage RCDG bridges continues to age and accumulate damage, there will be a need to keep some of them in-service for several more years until replacement can be afforded and implemented. With or without retrofitting and repair work, a need to monitor both their current condition and in-service performance will be required. ODOT has anticipated this need and is currently implementing a SHM program which focuses on bridge superstructures with vintage RCDG bridges being included. Based on the results and recommendations developed from SPR 341 and 350, pertinent structural response parameters have been identified that could be used as part of the overall SHM system, with shear stirrup strain and diagonal tension crack width being two of the primary parameters to monitor. Stirrup strain is a very sensitive indicator of load on the girders and the crack width is generally a good indicator of damage state. Identifying the formation of new cracks in a girder is not well suited to either of these performance measurements. Another structural health parameter that can be measured and monitored that does have the potential of identifying the formation of new cracks and with a reasonable level of accuracy identifying the location of the new crack is Acoustic Emissions (AE) testing.

1.4.3 Acoustic Emissions Testing is a Relatively New Form of Non-destructive Testing

Acoustic Emissions testing is based on the principal that structural damage releases energy, some of which is converted to stress wave propagation in and on the surface of a structural element. Sensors, typically mounted on the surface of the structure, can detect these disturbances and produce an electrical output that is a function of the disturbance at the site of the sensor. The electrical signals are recorded in either or both of two ways: 1) the full time history wave form from the sensor and 2) a parametric representation of the wave form using a few key parameters that summarize the salient features of the actual wave form. The data can be collected and interpreted by correlating the various AE features with load and / or other structural measurements. Outside of the laboratory AE has been gaining popularity as an effective form of NDT that can solve specific problems nicely or supplement other forms of NDT. In some fields, such as the pressure vessel industry, AE has been developed to the point that the American Society of Testing and Materials (ASTM) has published standards pertaining to its use. Though there are many common practices and analysis methods when applying AE to a particular material or structure, experience with the material and structure of interest is generally required to gain reasonable results. The primary advantage of AE testing when compared to other forms of NDT is that it is very sensitive to the creation of damage as it happens, whereas other methods such as radiography and ultrasonic testing are only sensitive to the accumulation of damage and thus in cyclic loading situations many cycles of damage may need to be imparted before detection can be made.

Previous works as discussed in detail in this paper have shown that applying AE to conventionally steel reinforced bridge structures is plausible, though in its earlier phases of development. This research takes the current state of the art of the practical application of AE testing on concrete structures and develops specific testing, data analysis and interpretation recommendations as they apply to vintage RCDG bridges in Oregon which are subject to diagonal tension cracking. The final product when properly applied with state of the art load rating methods can offer the owner of these types of bridges a reasonable means of assuring adequate structural performance and safety for the remaining service life of the structure.

1.4.3.1 *Implementing AE into a Structural Health Monitoring Program for Vintage RCDG Bridges*

In order to implement AE testing into an effective supplemental monitoring parameter for vintage RCDG bridges, experience with similar or identical structures and materials is required. This project employed three main phases to accomplish these ends. The first phase focuses on understanding how stress waves propagate in plain and steel reinforced concrete. Variations in concrete mix design are considered and tested. The results of this work, which are presented in Appendix A thru E, are used to understand stress wave propagation speed and signal attenuation in real concrete structures. The second phase applies the AE test method to full size laboratory test beams that are subjected to variations in design, loading and structural details. AE damage parameters used in industry are developed for the specific case of vintage RCDG bridges as presented in Chapter 3. The third phase, presented in Chapter 4, applies AE testing to three in-service bridges and is compared to the results of the laboratory testing in Chapter 5. Recommendations for implementation into a structure testing and / or structural health monitoring program are developed from the results and presented in Chapter 6.

1.5 A Brief Explanation of Stress Wave Propagation and Acoustic Emission Signals

Consider a semi-infinite solid as shown in Figure 1.1. If a damage process occurs below the surface, a portion of the energy released will reveal itself as a propagating stress wave which emanates in all directions from the source. As this disturbance travels through the solid medium, it does so in two forms: the dilation (P) wave and the distortion (S) wave. Each of these waves have different particle motions and rates of travel. Once they strike the free surface, a portion of each of the P and S waves reflects back into the semi-infinite solid with mode conversion likely occurring to some degree. The other portion of the P and S waves travels along the surface with a third wave form developing that lags both the P and S waves in time. This third wave called the Rayleigh (R) wave only occurs on free surfaces and has much larger particle motion amplitude components that are normal to the surface than either the P or the S waves.

AE sensors are typically mounted on the surface of a structure and respond to the surface motion. These sensors are extremely sensitive as the peak amplitudes of the surface displacements are on the order of Pico meters. Most commonly used sensors respond primarily to velocity and / or acceleration and are of resonant design. Others respond to displacement and are considered to be a broad band or high-fidelity design. In either case the surface disturbance excites the sensor and an output signal is generated. Figure 1.2 shows a hypothetical transient wave form from an AE sensor subjected to a surface disturbance. The entire wave form can be recorded and / or it can be characterized by using the fundamental parameters for AE testing which are the following: 1) signal duration, 2) peak amplitude, 3) rise time and 4) number of counts or threshold crossings. Each of these parameters is shown in Figure 1.2.

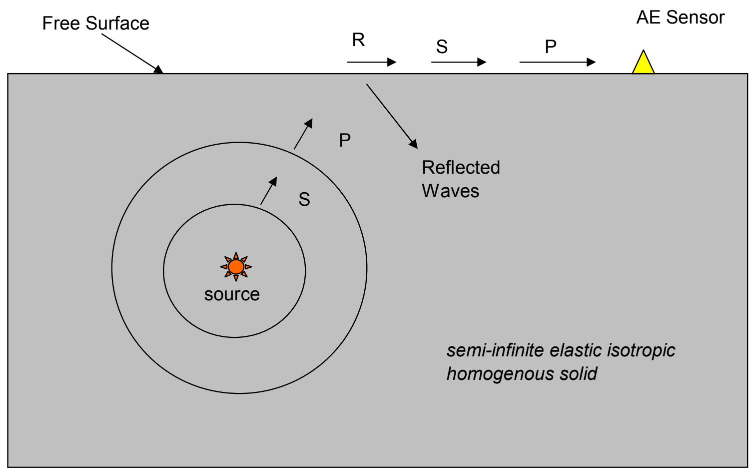

Figure 1.1 Schematic representation of stress wave propagation in a semi-infinite media.

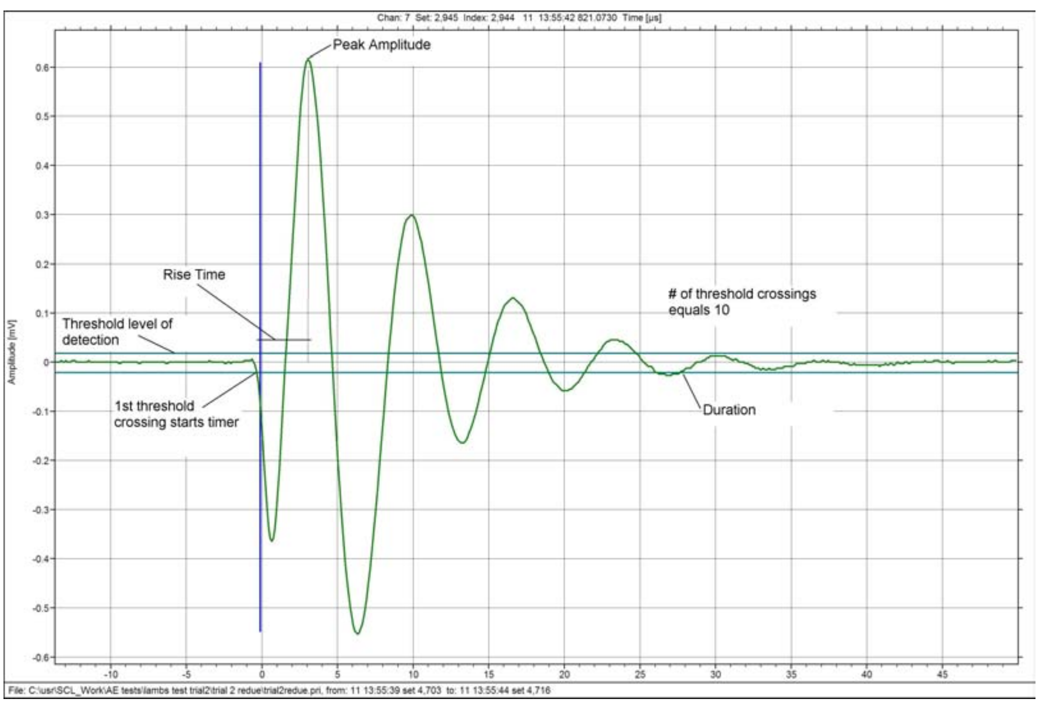

Figure 1.2 Summary of parametric characterization of AE wave form.

2 Literature Review

A literature review was performed to acquire background information into the nature of stress wave propagation in general elastic solids, stress wave propagation in concrete, the current state of the art in damage assessment of concrete using AE, testing of concrete bridges using AE and applications of structural health monitoring systems to bridges.

2.1 Stress Wave propagation in Elastic Solids

Stress waves can propagate on and in elastic solids in a variety ways depending on the type of particle motion of interest and the number and type of boundary conditions present. Of primary importance to this research is the propagation of dilatation, distortion and Rayleigh waves in and on an elastic semi-infinite half space. In such studies a rapid change in stress either inside or on the surface of the half space occurs and propagates throughout the body. This problem was first analyzed by Lord Rayleigh in 1887 [69].This problem was again analyzed by Lamb in 1904 [70] and for the case of surface disturbances is commonly referred to as " Lamb's Problem". Several assumptions concerning the material properties and type of disturbance were made to facilitate a closed form analytic solution. Pekeris [56,57,58] also made contributions to half-space responses from buried and surface sources in the 1940's and presented detailed surface displacement response predictions under the assumption that Poisson's ratio was equal to 0.25 which made closed form solutions more tractable. In 1974 Mooney [55] furthered Lamb's work by considering time varying source functions other then the classic step function with the use of computer solutions for the complex mathematics. Breckenridge [53] performed some experimental work using early forms of AE sensors to validate the responses predicted by the work of Lamb in

1975. And in 1985 Ohtsu [54] developed a generalized theory of AE when applied to a half space which combined elastodynamics and dislocation models.

2.2 Moment Tensor Analysis

Ohtsu [33] first presented the application of seismic moment tensor analysis to AE in 1986. This method considers the P-wave arrivals at several sensor locations mounted on the free surface of a half-space and performs calculations based on the Green's Function of the region of the half space between the AE source and sensors. The source is then characterized in terms of dislocation mechanics resulting in the calculation of a Burger's vector that can identify the type of dislocation, i.e. Mode 1, 2 and 3 displacements. Knowledge of the type of dislocation produced from specific damage sites is useful to gain a fundamental understanding of damage processes in loaded structures. This method of analysis was experimentally applied to steel by Enoki , et. al. [25] in 1988 with good success. Damage source characterization in concrete materials using moment tensor analysis has been successfully applied by Maji ,et. al. [20] in 1990, Ouyang, et. al. [17] in 1992, Landis, et. al. [14] in 1993, Suaris, et. al. [10] in 1995 and again by Ohtsu, et. al. [7] in 1998. The later work developed a computer code called SIGMA (Simplified Green's Functions for Moment Tensor Analysis) to automate the complex calculations required to determine the dislocation deformation patterns. This approach appears to be useful for characterizing structural damage mechanisms in concrete materials but has the disadvantages of requiring good quality source localization which can prove to be challenging in non-homogeneous materials. As P-wave detection methods improve and commercially available applications of the SIGMA code become available this analysis method will likely become practical to apply to in-service bridge structures.

2.3 Stress Wave Propagation and Attenuation in Concrete

In order to practically apply AE to assessing the condition of a structure, the nature of how stress waves propagate in the medium of the structure must be known. Assuming a material is elastic and homogenous is very important to practical applications. The primary features of interest are the stress wave propagation speeds and how they attenuate as they propagate. Landis, et. al. [11] studied the bulk wave speeds and P-wave amplitude attenuation in several different concrete mixes ranging from cement paste to concrete by varying the aggregate size from less then 1 mm to 10 mm. The results showed increasing P and S-wave velocities up to the coarse mortar mix that has 5 mm maximum aggregate size and then slightly decreasing velocities for the 10 mm concrete mix. The maximum variation between mixes was approximately 20% of the average speed. The effect of aggregate size was more pronounced on the peak amplitude attenuation. The mortar mix showed very constant attenuation with respect to frequency over the range of 50 kHz to 1.4 MHz. As larger aggregates were included, the higher frequencies produced more attenuation, and for the 10 mm concrete mix, the effect was considerable for frequencies over 150 kHz. The frequency dependence of the attenuation was attributed primarily to scattering mechanisms.

Surface wave attenuation in concrete mortar was investigated by Owino, et. al. [64]. The frequency dependent material attenuation coefficient was measured over a broad frequency range for several cement mortar mixes. It was shown that most of the surface wave energy is realized at frequencies below 700 kHz. Jacobs, et. al. [4] performed similar experiments but included the effects of aggregate size in the attenuation of surface waves in concrete. Fine aggregates up to 3.5 mm in diameter were tested and found to have little effect on the attenuation of surface waves. It was concluded that scattering losses were negligible compared to absorption losses and that aggregate size does not dominate attenuation. Wu, et. al. [63] used the measured P and R wave speeds in concrete to calculate the apparent elastic constants and corresponding S-wave speed. Typically the elastic constants for concrete are measured using static compression test data. This can lead to serious errors for the elastic constants as they apply to stress wave propagation as concrete material properties can be very strain and strain rate dependent. Compression tests involve large strains at low rates, and stress waves produce low strains at high rates.

Philippidis, et. al. [61] found that the water to cement ratio in paste can have a pronounced effect on the wave speeds and attenuations as can aggregate gradation, but these effects were only significant above 100 kHz. Chang, et. al. [62] studied the effect of concrete age on stress wave speeds and found that they increase rapidly as the concrete aged up to near 30 days, after which they remained nearly constant.

2.4 Damage Assessment in Concrete Using Parametric AE Data

As discussed in Chapter 1, two basic forms of AE data can be utilized to characterize structurally damaging events, wave form and parametric data. For practical applications the later is more tractable as AE testing typically generates very large quantities of data and the later form more easily deals with large data sets. Ohtsu [8] presents a good summary of the history of AE applied to concrete structures which describes the basic parametric variables used in AE and how they apply to characterizing both damage processes and the current state of damage. One of the earlier works found were those of Yoshikawa, et. al. [19] from 1980 where AE is applied to stress estimation in rock using the Kaiser effect. Maji, et. al. [13] investigated the application of AE to concrete focusing on source location and frequency characteristics of AE in 1994. In 1996 Balazs, et. al. [9] focused on damage accumulation at the interface between the concrete and steel reinforcing bars and the corresponding AE responses. Probably one of the most significant contributions to damage assessment in concrete structures using AE was presented by Yuyama, et. al. [5] where the breakdown of the Kaiser effect characterized by the Felicity Ratio and the relative amount of AE activity occurring between the loading and unloading cycles (Calm Ratio) was investigated in 1999. In this paper AE results such as peak amplitudes, number of hits and the Calm Ratio where first correlated to physically observed damage in the form of cracking type and crack mouth displacements. A proposed standard for testing concrete structures with AE was presented. This work lead to a testing standard from the Japanese Society of Non-destructive Inspection (JSNDI) in the form of NDIS-2421 which was presented by Ohtsu, et. al. [2] in 2002. In this standard the loading effects characterized by the Felicity Ratio and the unloading effects characterized by the Calm Ratio are combined into a damage classification chart which, based on AE data, characterizes the current state of damage in the test specimen into three levels: 1) minor damage, 2) intermediate damage and 3) heavy damage. Again the AE damage levels are related to physical damage in the form of maximum crack widths. Landis, et. al. [3] published a paper in 2002 that related AE energy to fracture energy in concrete. Lastly in 2006 Kurz, et. al. [66] presented work that considers stress drop and redistribution in concrete resulting from damage and quantified by the b-value analysis method commonly used in seismic analysis. Colombo, et. al [68] proposed using the " relaxation ratio " for assessing structural damage in concrete bridges which is defined as the ratio of the average AE energy recorded during unloaded divided by the same for loading. This method as presented appears to have some application for flexure damage but did not prove to correlate damage state well for shear dominant failures.

2.5 AE Testing of Concrete Bridges

Very few concrete bridges have been tested using AE compared to conventional testing methods which could employ crack motion, strain and displacement. Recently however, there have been several publications pertaining to in-service testing of conventionally reinforced and pre-stressed concrete highway bridges. Colombo, et. al. [67] summarized some testing procedures and analysis methods performed on a trapezoidal box girder bridge but few results were presented. Then Fowler, et. al. [47] applied Intensity Analysis to pre-stressed concrete girders for the Texas DOT in 2002. This form of AE based damage assessment came out of the fiber reinforced plastic (FRP) pressure vessel industry and appears to be applicable to other composite structures [46]. Such an application was published by Golaski, et. al. [48] where five in-service bridges including conventionally reinforced, pre-stressed and post-tensioned concrete bridges where tested with AE in Poland in 2002. Several analysis methods were presented for the different bridge types. The authors used Intensity analysis on one of the pre-stressed bridges that was newly constructed as a means of establishing base line responses to be used for future condition assessments on the bridge. Adapting this method of damage assessment from the FRP industry to concrete highway bridges appears to be both reasonable and promising. As a result this approach along with the methods developed in the Japanese standard NDIS-2421 are considered for primary investigation in this project.

3 Acoustic Emissions Testing on Full Scale Laboratory Steel Reinforced Concrete Beams

3.1 Background

An extensive research project was conducted at Oregon State University starting in 2001 to estimate the capacity and remaining life of a certain class of bridge superstructures that comprised a significant portion of the Oregon Department of Transportations bridge inventory. The class of bridge studied is called Reinforced Concrete Deck Girders (RCDG) which were constructed during the 1950's as part of the great expansion of the US highway system. Sometime during the late 1990's and early 2000's it was discovered that many bridges in this class were exhibiting extensive diagonal tension or shear cracks in the girders near the supported ends. Conventional load rating methods indicated that many of these bridges were indeed under capacity for the service loads they carried. Because of the large number of these structures in service (approximately 500), repair or replacement would take many years and several billion dollars. In addition to developing a large scale replacement effort, ODOT funded SPR 350 to more accurately estimate the capacity and remaining service life of these structures. As part of this research project, 44 full scale beams were tested in the laboratory for validation of the analytical methods being developed to estimate capacity and compare to field testing of in-service bridges. ODOT funded a separate research project SPR 633 to include the use of Acoustic Emissions (AE) testing of these bridges with the anticipation this form of Non-destructive Testing (NDT) could be used to supplement the fitness-for-purpose evaluations of the remaining cracked bridges in service. Thirty one of the 44 full scale beam tests performed under SPR 350 were included for study with AE under SPR 633.

3.2 Overview of Full Scale Laboratory Beam Testing

3.2.1 Test beam configurations

Forty four (44) full scale beams were designed and fabricated to represent the various configurations, structural details and loading conditions existing in in-service bridges. Two basic configurations of test beam were considered, the T and inverted or IT beam. The T configuration was used to simulate positive flexure where the deck portion of the beam or girder acts as the compression flange as experienced near the mid-span portion of a bridge. The IT configuration was used to simulate the negative flexure portion of the girder where the bottom of the stem acts as the compression flange as experienced near the end supports on multi-span structurally continuous bridges. Both configurations were simply supported and loaded in four point bending. Figure 3.1 shows a schematic of these two configurations with imposed boundary conditions and tractions. Figures 3.2 and 3.3 show the structural details of typical T and IT test beams respectively. The test beams are 26 feet long, 3 feet wide at the deck and 4 feet deep. Variations in shear steel reinforcing (stirrups) and flexural steel anchorages were applied to these basic designs to cover the ranges found in service as discussed below.

3.2.2 Structural detail variations

The primary structural detail variations studied were the density or spacing of shear stirrups and the anchorage condition of the flexural steel. Shear stirrup density was varied from no shear steel to #4 bars (½ inch diameter) spaced every 6 inches. Another variation on shear steel tested was to fabricate the beams such that the stirrups were completely debonded from the concrete with only mechanical anchorage at the top and bottom ends. Flexural steel anchorage was varied from fully developed and well anchored specimens to specimens that had less then minimum embedment and were cut short of the full span. Conditions such as this could occur during construction of real bridges and could significantly affect the shear capacity of the beam if the flexural steel was cut off in the high shear zone of the beam. Vintage concrete mix designs and reinforcing steel were used to fabricate these test beams.

3.2.3 Loading Protocols

A variety of load protocols were employed to characterize the structural response of the test beams. The primary load protocol used was incrementally increasing load amplitudes with unloading before the next increment in load amplitude. These were performed at a slow rate to simulate static responses. A few were tested at service level load rates to quantify the material strength effects that dynamic loading can have on concrete. Figure 3.4 shows a typical loading sequence. Another variation tested with this load protocol was to vary the shear to moment ratio (V/M) on the beam by varying the spacing of the support conditions. All beams were tested to failure. Figure 3.5 shows the static load frame setup.

Both high cycle fatigue (HCF) and low cycle fatigue (LCF) load protocols were used. The test beams were first put through an incrementally increasing load protocol as discussed above to establish damage in the form of shear cracking that was consistent with some of the more severe cases found in service. This is referred to as “ pre-cracking” throughout this report. For HCF tests once the test beam was pre-cracked it was transferred to the fatigue load frame where two loads were imposed. The first load was used to simulate in service dead load and was applied over the high shear zone and held constant through the fatigue test. The second load, applied at mid-span, cycled between a minimum and maximum value for 2 million cycles. The intensity of the fatigue loading was chosen to simulate the most severe conditions measured in the field testing portion of SPR 350. The high cycle fatigue test fixture is shown in Figure 3.6. Once the test beam was fatigued it was transferred back to the static load frame and subject to incrementally increasing loads with unloading between load level increases up to failure.

For LCF tests the beams were pre-cracked and left in the static load frame where cyclic loading of very large amplitude (approximately 95% of ultimate capacity) was applied until failure occurred, which typically took on the order of 10,000 cycles.

3.2.4 Measurements taken during test

A wide variety of physical measurements where taken during during and after each load cycle to capture the structural response of the beam as it was progressed towards failure. These measurements included the following:

1) Mid-span load
2) Mid-span displacement
3) Stirrup strain
4) Shear deformation of the stem
5) Crack width measurements both with a comparator gage and electronic transducer
6) Crack mapping of all cracks as they form and progress
7) Acoustic emissions

All measurements taken with an electronic transducer where recorded continuously during each test. Crack Mouth Opening Displacement (CMOD) transducers were affixed to the test beam as the shear cracks formed. In the course of every load step the cracking patterns were tracked and recorded by hand onto a scale drawing and crack widths were measured using the ODOT crack comparator tool as is practiced on in-service bridge inspections.

The Acoustic Emissions data acquisition system was a Vallen AMSYS 3 with six AE channels and two analog input channels. The AE sensors used where Vallen VS150 and KRN i60 resonant type sensors with a preamplifier gain of 34 and 41 dB respectively. Parametric analog inputs of mid-span load, displacement and CMOD where typically included with the AE data sets. Five different AE sensor arrays were used during these tests with two of them being a planar and three a linear array. The most common array used was the planar array centered on one face of the stem in the high shear zone of the beam as shown in Figure 3.7a (upper schematic). The second planar array used was closely spaced sensors around the main shear crack tip as it progressed into the compression flange which is shown in Figure 3.7c. The most commonly used linear sensor array placed the sensors at mid-depth of the stem evenly spaced over the entire length of the beam as shown in Figure 3.7d. A second linear array used placed all sensor at closer spacing to cover the shear zone at one end of the beam as shown in Figure 3.7e. A third linear array used places all sensors over a single stirrup in the high shear zone as shown in Figure 3.7f. Specific examples of these various sensor deployments at shown in Figure 3.8a-8f.

3.3 Example Static Beam Test with Data Collection and Reduction on Test Beam 2IT12

Before examining the details of the effects of the various beam configurations, details and loading protocols, it will be informative to review a typical static test procedure, look at the structural and AE measurement data as the loading progresses and finally go over the data reduction methods used.

The example test beam uses the inverted T configuration to simulate negative bending. The stirrup spacing was 12 inches which is a very common spacing found in in-service bridges with diagonal tension cracking. No defects such as debonded stirrups or inadequate flexural steel development length were included in this specimen and thus it should behave in a similar manner to a properly constructed in-service beam. A planar array was placed on the West face at the South end of the beam in the high shear zone covering an area of 14” in height and 36 inches in length using the 150 kHz AE sensors with mid-span load and displacement as parametric inputs.

We will first look at basic test data shown over the entire course of the loading sequence to get a feel for the beams general response. Next we will exam each load cycle in more detail and look at detailed measurements of damage as it progresses.

3.3.1 Overall response of beam

The general mid-span load versus displacement for each load cycle sometimes called a hysteresis plot is shown in Figure 3.9. It can be seen that at the lower peak load cycles the beam behaves in a fairly elastic manner with the unload path being very close to the load path. As both flexure and shear cracks form the global stiffness of the beam decreases and more energy is lost to irreversible processes that can be related to damage in the beam. The final load cycle shown, though not the failure load cycle, shows extensive hysteresis and is a strong indication that significant damage has been imparted to the beam.

A general view of the AE response to the loading can be portrayed by plotting the instantaneous AE activity or hit rate over time with the mid-span load variation as shown in Figure 3.10. This particular plot is the response for the sum of all six channels. Individual channel responses are also examined during and after a test. The primary features to gather from this overview plot of the AE activity are the following:

1) At the lower peak load cycles there is very little AE activity and it generally occurs during the loading portion of the load cycle

2) Shear cracks begin to form between 80 and 135 kips (depending on the specific beam) and are accompanied by a very large increase in AE activity

3) From this point forward there is an increasing amount of AE activity during the unloading portion of the load cycle

4) Shear crack propagation occurs after formation up to a load of 200 kips which produces very high hit rates

5) For any given load cycle shown, the AE activity does not significantly increase until the previous peak load is reached.

As will be discussed later feature 3 above can be quantified by using a parameter called the Calm Ratio (CR) and feature 5 , which is more clearly seen in a cumulative instead of instantaneous hit plot can be quantified by a parameter called the Felicity Ratio (FR).

Most of the beams tested failed in a manner which is called Shear-Compression which progresses as follows:

1) From 0 to approximately 70 kips depending on the specific beam tested only the concrete is appreciably contributing to the stiffness until flexural cracks form in the tension zone starting directly below the ram. At this time the flexural steel begins to pick up load and contribute to the overall stiffness.

2) From approximately 80 to 135 kips the flexure cracks continue to initiate and develop driving upward towards the shear zone with more cracks spreading out from the center of the beam towards the ends. These cracks then become heavily influenced by the shear stress field and turn from vertical to diagonal

propagation back toward the center of the beam. At this point the shear stirrups are taking load and participating in the global stiffness of the beam.

3) From approximately 150 kips to over 300 kips (depending on the specific beam) the shear cracks continue to propagate through the shear zone and into the compression zone at the top of the beam on either side of the loading ram. The major diagonal tension or shear cracks (typically 2 to 6 at each of the two shear zones) become much wider at mid-depth of the stem as the strains in the stirrups exceed yield near the stirrup / crack interface. Localized debonding of the stirrup also occurs in the same region.

4) As the shear cracks continue to grow into the compression zone and coalesce into a single shear crack in each of the two shear zones, the compression flange area is reduced up to the point where the compressive strength of the concrete is exceeded by the imposed stress and a compression failure occurs in the top section of the beam on one side or the other of the loading ram.

A more detailed examination of each load step will be shown.

3.3.2 AE sensor installation and calibration

Prior to testing a beam the AE sensors must be physically mounted and acoustically coupled to the surface of the beam. Sensor locations were identified and marked onto the face of the stem considering stirrup locations and predicted shear crack locations. Special fixtures were fabricated that could be glued to the concrete securely and rapidly using a cyanoacrylate glue with activator spray. The surface of the concrete was prepared using course sand paper and a stiff wire brush prior to mounting the fixtures and sensors. Laboratory grade vacuum grease was then applied to the active face or aperture of the AE transducer and mounted into the fixture with a clamping force of approximately 10 lbs.

With the sensors in apparent good mounting condition, acoustic coupling was checked in two manners. The first procedure uses pencil lead breaks on the same surface the sensor is mounted to, two inches away from the center of the aperture. The peak amplitude of each of three pencil lead breaks must exceed 90 dB with a maximum spread of 3 dB. (Refer to ASTM E976). If these criteria are not met, then the sensor is remounted until they are met. This procedure assures that the sensor is in proper acoustic contact with the surface to which it is mounted.

The next procedure checks the acoustic coupling between each sensor in the array. It is conveniently executed automatically by the data acquisition system. Each sensor is sent a series of calibration pulses with peak voltages being adjustable between 50 to 400 volts peak to peak of the sinusoidal cal-pulse wave form. The particular AE sensor the pulses are being sent to is temporarily changed from a receiver to a driver and inputs the strong pulse into the structure to which it is mounted. A precision timer is started and the other sensors wait to receive the signal. (Refer to Appendix C for more details on calibration pulses.) The signals received by the other sensors are used to characterize the attenuation and apparent wave speeds between sensors. These calibration runs can be conducted at anytime during a test to check sensor coupling and sound path degradation in the structure. Figures 3.11 and 3.12 show a photograph of a typical planar array and the measured parameters from an auto-calibration test.

The results of the pretest auto-calibration test are shown in Table 3.1. For the peak amplitude results it can be seen that 29 of the possible 36 paths of sensor communication are functional at the sensor threshold (40 dB) and strength of calibration pulse signal (82 dB). A stronger pulse or lower threshold in a virgin beam such as this would likely establish communication between all sensors as found in later tests. The apparent wave speeds between communicating sensors range from 4 to 116 in/ms. Details on comparing wave speeds between source and sensor using a fixed threshold are discussed in Appendix B and C.

3.3.3 Presentation of AE data

There are a plethora of ways to present the measurements taken from the AE transducers and parametric inputs. Preferences range extensively between industries and specific users but mostly vary only in presentation and not what is being measured. It is very useful to show certain measured parameters in several different perspectives by correlating them other others. The plots chosen for presentation of this test are very brief though widely understood and are suitable for demonstrating the salient features of an AE test applied to a loaded structure. The primary parameters that are investigated in a general structural AE test are peak amplitudes, hit rate , cumulative hits , arrival times and load. Many other very useful parameters are available and commonly used but are excluded from this example for brevity's sake.

3.3.3.1 First load step 0 to 25 to 0 kips P_{max} */ Capacity = 0.07*

The first load step always settled the test beam into its supports and thus was kept to a magnitude just large enough to accomplish this which is measured with displacement sensors at each seat. Little if any cracking occurs in the beam, and it remains almost completely elastic. The first plot to examine is the differential or instantaneous hit rate as shown in Figure 3.13. Spikes in this parameter indicate rapid bursts in AE or high AE activity. Very little activity is seen for this load cycle as expected. Most, if not all of the hits can be attributed to seating noise at the nearby South beam seat. Note the convenience of having load correlated with the AE data.

The next plot of interest is the cumulative hits which is merely the temporal integration of the previous plot. Figure 3.14 shows the cumulative hits for this load cycle. Cumulative hits on individual AE channels as well as the sum of all channels are shown. This plot can show which channels are the most active during various portions of the load cycle.

Figure 3.15 shows the peak amplitudes of each individual hit correlated with load for all six AE channels. This plot is useful for estimating AE activity, hit strength and region of the array based on sensor location. As will be seen at larger loads, the signal strengths for this load cycle are very low compared to AE from actual structural damage of the beam.

Figure 3.16 shows another presentation of cumulative hits and peak amplitudes, both on a per channel basis and the sum of all channels. This presentation is useful for b-value analysis which is discussed later in the chapter. The slope and linearity of the hit versus peak amplitude curve when plotted log – log can be used to differentiate various damage mechanisms.

A fifth plot of interest that can be calculated, if adequate sensor communication and signal strength is present, is event location. Events can be defined when a sufficient number of sensors detect an AE source that appears to be , based on set criteria , coming from the same location and time. These are located in a manner very similar to that used to locate and size the strength of the epicenter of an earthquake. For a linear array at least two sensors must detect the same source, and for a planar array it takes a minimum of three sensors. Thus an AE " event " can be determined from sufficient individual channel hit data. If more then the minimum number of AE channels detect the event the statistical accuracy of the event location can be also determined. For the 25 kip load cycle there were no events located due to the lack of AE activity at the low load level in the virgin beam.

3.3.3.2 Second load step 0 to 50 to 0 kips *P_{max} / Capacity = 0.14*

From visual observation small flexure cracks begin to initiate at the bottom of the test beam near mid-span but do not progress deeper into the section than the flexural bars. An increase in overall AE activity is seen when compared to the first load cycle as shown in the instantaneous hit rate in Figure 3.17, most of which occurs during the loading portion of the cycle. It is also interesting to note that the main body of the AE activity does not start until the previous maximum load of 25 kips is reached revealing a Kaiser effect. The Kaiser effect was first observed by Josef Kaiser in the 1950's in which he found that most materials show low level AE until the previous maximum stress that test component has experienced has been exceeded, at which time the AE increases rapidly. This subject will be addressed in greater detail latter in the chapter. Figure 3.18 shows the cumulative hits with the greatest number of hits at channels 4 and 6 which are closest to the seat and load ram respectively. The total number of hits is still very low indicating little AE activity in the structure. Figure 3.19 shows that the peak amplitudes are still quite low but increasing when compared to the previous load cycle. Figure 3.20 shows the correlation between the number of hits and peak amplitudes. An event was assembled from this load cycle and is shown located relative to the array in Figure 3.21. Its peak amplitude was 61 dB and it was detected by four different channels giving a good indication that it came from an actual source inside the beam as opposed to seat or load ram noise.

3.3.3.3 Third load step 0 to 75 to 0 kips *P_{max} / Capacity = 0.21*

At this load level flexure cracks are beginning to drive deeper into the section at mid-span and initiate outwards toward the high shear zone. No shear cracks have formed yet. Figure 3.22 shows the instantaneous hit rate for this load cycle. Note that again the Kaiser effect is still very clear as the main body of AE activity does not begin until the load reaches the previous maximum value of 50 kips.

Most of the AE activity also occurs on the loading portion of the curve with some present during the load hold and very little during the unloading. Figure 3.23 shows the cumulative hits for this load cycle, which though increasing, is still very low compared to shear cracking. Most of the hits had peak amplitudes less than 75 dB much like the previous load cycle with the exception of a very strong (91 dB) hit from channel 1 during the load hold as shown in Figure 3.24. The number of hits correlated with peak amplitude is shown in Figure 3.25. Three events were located during this load cycle as shown in Figure 3.26.

3.3.3.4 Fourth load step 0 to 100 to 0 kips P_{max} */ Capacity = 0.28*

This is the first load step where flexural cracks have propagated into the high shear zone and are changing direction to become diagonal tension or shear cracks. Figure 3.27 shows the first shear crack outline in black on the beam just to the left of the sensor array. Note how it first propagates upward into the section under the influence of flexure and then turns towards the load ram under the influence of shear. The crack width is visually observed to be hairline using the ODOT crack comparator tool. Figure 3.28 shows the instantaneous hit rate which again is still revealing the Kaiser effect with most of the activity occurring during the load portion of the cycle. Figure 3.29 shows the cumulative hits which shows most of the activity coming from Channels 5 and 6 which are located closest to the shear crack. Because of the high attenuation in concrete the other sensors miss much of this activity. Figure 3.30 shows the peak amplitudes of individual hits, most of which are still below 75 dB. Channel 1 again records a very high amplitude hit at 100 dB which is the saturation level of the sensor. Figure 3.31 presents the hit amplitude correlation. The only event calculated for this load cycle occurred near Channel 1 but was quite strong with a peak amplitude of 99.8 db or saturation and was detected by all 6 channels providing strong evidence, in conjunction with the previous activity in this region, that a significant damage process is occurring in this region. The location plot is shown in Figure 3.32.

3.3.3.5 Fifth load step 0 to 150 to 0 kips P_{max} */ Capacity = 0.42*

The 150 kip peak load cycle produced significant shear cracking in every single beam tested with AE. At this load level the concrete is beginning to fail in tension in the shear zone and transfer load to the stirrups which is guaranteed to produce large numbers of hits at high amplitudes. Three new hairline width shear cracks formed from this load cycle, two of which run through a portion of the array as shown in Figure 3.33. Figure 3.34 shows the instantaneous hits. The maximum hit rate has dramatically increased compared to the previous load cycles. The Kaiser effect is still very clear but a measurable amount of activity is beginning to occur prior to the previous maximum load, which is an indication of damage in the beam. The unload portion of the cycle is also just begging to show an increase in AE activity furthering the evidence of damage in the beam. Figure 3.35 shows the cumulative hits which have increased over a factor of 10 from the last load cycle. Channels 5 and 3 show the greatest activity as they were closest to the developing shear cracks. Also notice that only channel 5 shows significant unloading hits, indicating that the damaged portion of the beam is nearest this location which is where the shear cracks are. The peak amplitudes of each hit can be seen in Figure 3.36. Now there are a significant number of hits above the previous level of 75 dB. There are also a number of energetic hits during the load holding which can be used to assess damage to the structure. Figure 3.37 shows the hit versus peak amplitude correlation. The linearity of the slope indicates one dominate damage mechanism which can be seen to be primarily influenced by hits on channel 5 located in the shear cracking region of the array. Figure 3.38 shows the five located events from this load cycle, the strongest of which are found down in the shear cracking region.

3.3.3.6 Sixth load step 0 to 200 to 0 kips P_{max} */ Capacity = 0.56*

This load step does not initiate anymore visually observable shear cracks but contributes greatly to their extensions in length and opening the widths from hairline to 8 to 16 mils as seen in Figure 3.39. Note that the right most shear crack has propagated directly under channel #3. Figure 3.40 shows the instantaneous hit rate which has again greatly increased compared to the previous load cycle. The Kaiser effect is now clearly beginning to break down as the AE activity begins prior to the maximum previous load of 150 kips. AE activity during the unloading portion is becoming even more evident. The cumulative hits are three times larger than the last load cycle with channels 5 and 3 providing the greatest contributions as would be expected from visual observations of the cracking. Both of the channels show significant unloading AE compared to the others which are not dominated by the shear crack propagation as seen if Figure 3.41. Figure 3.42 shows the peak amplitudes of each hit. Channels 3 and 5 have multiple hits above 80 dB which are considered to be very strong signals compared to background and even moderate damage sources that occur within approximately 12 inches of a sensor. The hit –peak amplitude correlation is again very linear and dominated by the contributions from channels 3 and 5 as seen in Figure 3.43. The propagation of a shear crack directly through a planar array of the dimensions used in the test will generate very large peak amplitudes with which the locations of each event can be located with good accuracy even when using the very simple fixed threshold method of source location. Figure 3.44 is a good example of such, showing the location and strength of each located event superimposed on a photograph of the damaged shear zone. Notice the excellent tracking of the shear crack advancement between channels 5 and 3. Using more sophisticated methods of stress wave onset can produce these results more often and with greater reliability.

3.3.3.7 Seventh load step 0 to 250 to 0 kips *P_{max} / Capacity = 0.69*

This load step produced a very large shear crack that traverses through the middle of the array and in very close proximity to channel 1 as seen in Figure 3.45. At this point there are 6 large shear cracks in the vicinity of the sensor array with widths ranging from 13 to 25 mils. Visually the beam appears to be in a very damaged state. Two sensor calibrations were performed during this load cycle to estimate inter-sensor communication. The first calibration was performed during the load holding portion and the results are shown in Table 3.2. The number of missing communication links in the array has increased from 7, prior to any load cycles, to 12. Of the 24 links still open the peak amplitudes and wave speeds have decreased. Table 3.3 shows the results after the 250 kip load is removed. As the cracks close one link is regained and peak amplitudes and waves speeds slightly increase on average.

Figure 3.46 shows the instantaneous hit rate revealing a large spike in activity near the 220 kip load level which resulted from the formation of the newest shear crack. The Kaiser effect is still identifiable but is continuing to break down. Activity on the unload portion of the load cycle is increasing. The cumulative hits as shown in Figure 3.47 are similar to the last load cycle in magnitude but the activity is better distributed between channels with four of the six channels contributing. Notice that each of the contributing channels are showing unloading activity with channels 3,4 and 5 having more hits during unloading then the loading phase. This provides further evidence of the high state of damage in the shear zone. No hits are recorded during the majority of the load hold because the AE sensors were temporarily disabled while technicians installed CMOD transducers onto the beam. Figure 3.48 shows the peak amplitudes of all hits. There are many hits above the 75 dB level on both the loading and unloading portions of the load cycle. The break down of the Kaiser effect is quit obvious in this plot looking at the activity from channels 3 and 5 prior to reaching the previous maximum load of 200 kips. Large magnitude hits are also shown to occur during the portions of the load hold which were recorded. The hit-peak amplitude correlation shown in Figure 3.49 has become less linear at the high amplitude side of the curve indicating a second damage mechanism may be involved. This other mechanism may be related to damage at the stirrup-concrete interface as the shear cracks widen and pull the stirrup loose of the concrete. Numerous events were located during this load cycle many of which had peak amplitude exceeding 75 dB as shown in Figure 3.50.

3.3.3.8 Eighth load step 0 to 300 to 0 kips P_{max} */ Capacity = 0.83*

The seventh load increase did not appreciably extend any of the six shear cracks in and a around the sensor array as seen in Figure 3.51. However the crack widths increased substantially ranging from 10 to 40 mils. From the plot of instantaneous hit rate shown in Figure 3.52, the peak rate is about one half that of the previous load step. This is consistent with the lack of crack extension, which causes the greatest hit rates. The Kaiser effect has continued to break down and there is nearly as much activity on the unloading as the load side showing a strong indication of very high damage in the beam. The small spike in activity near 1050 seconds was caused by the installation of a CMOD gage on one of the shear cracks as seen in Figure 3.51. The cumulative hits shown in Figure 3.53 reveal a slight increase from the previous load step. The unloading contribution is clearly evident on the most active channels which are again 1,3 and 5. The peak amplitudes shown in Figure 3.54 present the very strong signals generated and also more clearly show the Kaiser effect break down with all of the strong signals occurring early into the loading phase. The peak amplitude – hit correlation is shown in Figure 3.55. Again many events are located with 3 high amplitude events occurring near channel 5 as seen in Figure 3.56.

3.3.3.9 Ninth load step 0 to 350 to 0 kips P_{max} / Capacity = 0.97

This is the last load increment prior to failure. A seventh shear crack has formed in the lower right hand corner of the array and all shear cracks have undergone significant extension as seen in Figure 3.57. Note that the direction of crack propagation is heavily influenced by the strong compression stress field at the top of the beam. Crack widths range from 25 to 80 mils. For reference, shear cracks with widths in the 60 to 80 mils are considered to be critical by highway bridge inspection guidelines. The hit rate can be seen in Figure 3.58 which shows more activity and at a higher rate than the previous load step. The cumulative hit plot shown in Figure 3.59 shows a very large number of hits on all but channel 3, and all have a very significant unloading contribution. The peak amplitudes shown in Figure 3.60 portray a large amount of strong hits with a still discernible but collapsing Kaiser effect on the load side and very strong activity on the unload side. The hit-peak amplitude correlation is seen in Figure 3.61. Channel 2 is much less linear then the other channels. Again many events were assembled and located with activity similar to the previous load cycle as seen in Figure 3.62.

3.3.3.10   Tenth load step 0 to 360 to 0 kips P_{max} / Capacity = 1.00 Failure

The final load step was only slightly larger then the previous with failure occurring in the compression zone on either side of the load ram. This region was significantly out of the sensor array. Little visual change occurred to the shear zone that the sensors were covering as seen in Figure 3.63. The hit rate plot shown in Figure 3.64 depicts some very interesting results. The structural failure is seen in the load signal where the beam rapidly loses stiffness at failure under the displacement controlled loading system. The hit rates during the load and even failure are relatively low compared to previous cycles. This is likely the result of the damage for this load cycle occurring well outside of the array. The unload activity shows very high hit rates which approach that of major shear crack formation. Cumulative hits have dropped from the level seen in the last load cycle as shown in Figure 3.65. The great intensity of activity on the unload portion of the load cycle can also be clearly seen in Figure 3.66 in the peak amplitude plot. Channel 1 appears to be closest to the emitting region. The hit-peak amplitude correlation is shown in Figure 3.67. Fewer events were located during this cycle with only two low amplitude events found near Channel 1 where the hit channel activity was previous seen. This is likely the result of the large cracks causing acoustic isolation between many of the sensors. A sensor calibration was again performed to estimate inter-sensor communication. Table 3.4 shows the results. A total of 18 of the original 29 communication links are gone. Both peak amplitudes and wave speeds have also significantly decreased.

3.4 Damage Assessment Using AE

As was described in detail above the test beam accumulated structural damage from the loading protocol until the remaining strength of the beam was exceeded by the load and failure occurred. The physically observable indications of damage discussed so far were an increase in mid-span load-displacement hysteresis, a decrease in beam stiffness and the formation and growth of cracks in the concrete. The first two parameters are generally only available from laboratory test data and are not collected during routine or even in-depth bridge inspections. Crack formation and growth, however is a very practical and common parameter to observe and record during both routine and in-depth bridge inspections. Qualitatively the more cracks and crack growth experienced indicate more accumulated damage in the beam or bridge member. It is this fact that led to the development of the ODOT crack comparator. A summary of crack formation and growth for test beam 2IT12 is presented in Table 3.5. It is thus desirable to correlate damage accumulation based on AE data to a familiar and easily obtained measure of damage such as crack formation and growth.

Ohtsu et. al.[2] found that the total number of AE hits is proportional to the maximum CMOD in concrete test beams and was in fact a very linear relationship. Figure 3.69 shows the total number of AE hits versus maximum CMOD and load. The CMOD line is plotted at the average value of all shear cracks with the vertical lines indicating the range and extreme spread of the individual cracks at each load step. Both total hits and CMOD appear to increase proportionally as the peak load is increased up to 97% of the ultimate capacity of the beam. The final or failure load step shows a sudden drop in AE hits while the CMOD continues to grow. This can be at least partially explained by the fact that the actual shear / compression failure occurred on the other half of the beam from where the AE sensor array was located and thus many of the failure zone emissions were highly attenuated by the time they had reached the sensor array. The linearity of the hit – CMOD relationship is even more clearly shown if AE hits are plotted against CMOD as seen in Figure 3.70. The load level is also shown for each data point. For reference the crack widths are divided into three ranges as defined on the ODOT crack comparator tool. Level 1 corresponds to crack widths that are visible to the naked eye but are less then 13 mils. These are considered to be hairline cracks, and no particular action on the bridge inspector's part is required for such cracks. Level 2 corresponds to crack widths between 13 and 25 mils and are required to have their extents traced on the beam by the inspector. Level 3 corresponds to cracks with widths greater then 25 mils. These cracks are to have their extents traced and maximum width measured and recorded with the date of the inspection on the beam and on a crack map which is to be included in the bridge inspection report. From this it can be seen that there is a correlation between AE activity and the accumulation of structural damage. More detailed analyses correlating AE activity to damage will now be discussed.

3.4.1 Felicity Ratio

The Felicity Ratio is defined as the load at which AE activity begins in the current load cycle divided by the previous maximum load the beam or structure has experienced as shown in Equation 1. It is one of the most mature AE responses used to characterize damage in structures. A Felicity Ratio of 1.0 or greater indicates that the Kaiser effect is strongly present. As the Felicity Ratio dips below 1.0 enough damage has accumulated such that the Kaiser effect is beginning to break down. Ohtsu et. al. [2] reported that the Kaiser effect disappears when the CMOD of flexure cracks exceed 4 to 8 mils or there are shear cracks present and suggests a critical Felicity Ratio of 0.9. The test beams used were designed to fail in flexure, and the serviceability limit of CMOD was identified to be 4 mils. As will be discussed, selecting the critical Felicity Ratio depends on the expected failure mode and maximum acceptable crack width.

Equation 1

$$\text{Felicity Ratio} = \text{Load at start of AE activity in current load cycle / Maximum previous load}$$

From Equation 1 to calculate the felicity ratio for a particular load cycle, we need to know the maximum previous load the structure has experienced prior to the current load cycle. For laboratory test beams retrieval of this information is usually very straight forward and unambiguous. The load at which AE activity begins during the monotonically increasing load is not as clearly defined. In a strict sense the AE activity begins as soon as the first hit or threshold crossing is reached. As will be shown for concrete beams, this occurs very early in the loading protocol, even on virgin or lightly damaged beams. Typically there is a small amount of AE activity that occurs during the early portion of the loading and, then at some point the AE activity greatly increases. A good example of this observation is shown in the instantaneous hit rate plot shown in Figure 3.34. Using this strict definition the Felicity Ratio would produce values very near zero for all test beams at all but the lowest load cycle. Yet from the previous example testing results it was seen that a Kaiser effect is visually discernible for much of the loading protocol. Thus an alternate definition of the onset of AE activity could prove to be useful to capture and quantify this effect.

3.4.1.1 Defining the onset of AE activity

Four different approaches to defining the onset of AE activity were investigated, 1) strict threshold crossing at various threshold levels, 2) subjective interpretation using the instantaneous and cumulative hit plots, 3) only considering 2 and 3 channel events and 4) defining a percentage of the total loading hits. As discussed above the first definition was found to be too restrictive and of little use for practical damage assessment in concrete beams. The second method was found to be very effective at tracking the changes in the Felicity Ratio over the entire range of loads but had the strong disadvantage of being user dependent. Method 3 proved useful for test beams especially at the higher load levels but did not perform well prior to shear cracking and was too restrictive on the field test data where the overall AE activity is much lower then found in the laboratory tests. Method 4 defines the onset of AE activity based on the accumulation of a straight percentage of the total hits that occur during the loading portion of the load cycle. Thus if a total of 1000 hits accumulate during a particular load cycle from 0 to P_{max} , then the onset of AE is defined to occur once a specified percentage of the total has accumulated. Portions of 1, 5 and 10 percent were investigated and compared to the results of using a subjective interpretation. It was found that using a straight percentage of between 5 and 10 percent produced good results much like Method 2 but was not subjective and thus could be repeated between different users. The results of this investigation will be shown later. The Felicity Ratio can be applied to individual AE sensors or to the entire array. Only the entire array was used during this research project.

3.4.2 Calm Ratio

The Felicity Ratio is focused on the loading portion of the load cycle. Another useful means of assessing structural damage from AE data is to exam the unload portion. As was seen in the previous AE test example, the amount of AE activity produced during the unload portion of the load cycle increases as shear cracks form and develop. This effect can be quantified by using the Calm Ratio as proposed by Ohstu et. al. [2] which is the ratio of the total number of AE hits cumulated during the unloading portion of the load cycle divided by the total number of AE hits cumulated during the load portion as shown in Equation 2.

Equation 2

Calm Ratio = total unloading hits / total loading hits

Thus a low Calm Ratio indicates very little unloading AE activity, and conversely a high Calm Ratio indicates large unloading AE activity. Calculation of this parameter is very straight forward and not subjective as both the numerator and denominator can be quantified directly off of the cumulative hits plot. Also note that both of these values can be easily retrieved from both laboratory and field test data. Again , based on the maximum serviceable CMOD of flexure cracks Ohtsu et. al. [2] proposed a critical Calm Ratio of 0.05. Both the Calm and Felicity Ratios can be combined to produce a damage assessment chart as defined in the Japanese Society for Non-Destructive Inspection (JSNDI) standard NDIS-2421which will be discussed later. The Calm Ratio can be calculated for individual AE sensors or the entire array. For this project only the results from the entire arrays were used.

3.4.3 Application of Felicity and Calm Ratios to Example Test Beam

At this point it will be instructive to go through the calculation of the Felicity Ratio (FR) and the Calm Ratio (CR) for each load cycle of the example test beam. These calculations are shown graphically for all 10 load steps in Figures 3.71 through 3.80. The calculation method is as follows:

1) Determine point of maximum load
2) Determine the total number of AE hits from zero to maximum load
3) Calculate 10% of the total loading portion hits
4) Determine the load at which the first 10% of the total loading hits occurs
5) Calculate the Felicity Ratio from the results of step 4 and knowledge of the previous maximum load
6) Determine the total number of hits from the un-loading portion of the load cycle
7) Calculate the Calm Ratio using the results of step 6 divided by the results from step 2.

A plot of the Felicity Ratios versus peak load is shown in Figure 3.81 for test beam 2IT12. The results from using a subjective interpretation (method 2) of the onset of AE and three different linear proportions of the total load hits (method 4) are shown. A horizontal dotted line is drawn at the critical value from NDIS-2421 as well as a vertical dotted line indicating the load at which the first shear crack forms. Details of shear crack development are left out for clarity. The first two load steps plotted (50 kips and 75 kips) reveal a Felicity Ratio well below the threshold value of 0.9 for all but the subjective definition which would indicate severe damage accumulation. For these two load steps the total number of AE hits during the loading portion of the load cycle are less then 100. Of course at these low loading levels very little damage has occurred in the test beam. The erroneous results are attributed to a lack of AE data and thus a poor signal to noise ratio in the Felicity parameter. By the third load step shown, 100 kips, the total number of loading side hits exceed 200 and most of the Felicity Ratios have peaked near or above 1.0. At this point the signal to noise ratio in the Felicity parameter is adequate to characterize the general state of damage as being low which is consistent with visual observations of the damage state. As the loading protocol continues and damage accumulates the Felicity Ratio generally decreases as expected for all but the subjective method. Both the 5 and 10 percent definitions show a rapid decrease at the failure load step. It will be shown later that many of the test beam data sets show a very linearly decreasing Felicity Ratio with respect to peak load for the load ranges of practical interest when using the definition as described in method 4. The applicability of the threshold value of 0.9 as it applies to the test beams designed to fail in shear will also be addressed.

The response of the Calm Ratio to the loading protocol of the example test beam is shown in Figure 3.82. Salient features of the visually observed damage process are labeled at the various loads. The horizontal dotted line shows the threshold value from NDIS-2421 indicating that all loads indicated a damaged condition. An appropriate value for this threshold as it applies to shear failure will be discussed later. In general the Calm Ratio starts out fairly low and increases with increasing damage accumulation up to over 80% of the beams ultimate capacity, after which it rapidly decreases at 97% of capacity. The failure load cycle shows a slight increase in Calm Ratio from the previous load cycle. In the next section it will be seen that most of the test beams show a very linearly increasing Calm Ratio with respect to increasing load over the practical load range.

Per NDIS-2421 measurement of the Felicity and Calm Ratios allows the development of a damage assessment diagram as shown in Figure 3.83 for the example test beam 2IT12. Four regions are created by the threshold values for each parameter. The threshold values shown are those suggested in the standard and as discussed above were calibrated for flexure cracks with hairline widths (4 to 8 mils). The four regions are identified as being in a state of minor, intermediate and heavy damage as shown. The fit of the test data is marginally well suited as shown but can be greatly improved by adjusting the threshold levels, especially for the Calm Ratio, to conditions found in shear type failures and crack widths acceptable to ODOT. This will be presented in a later section.

3.4.4 Felicity and Calm Ratio Analysis of All Test Beams

Now that an example AE test of a steel reinforced concrete beam has been demonstrated and the definitions and example calculations of the Felicity and Calm Ratios presented it is appropriate to look at the Felicity and Calm Ratio responses for all of the test beams and their respective variations in design, loading and AE sensor arrays. In order to give the greatest clarity in depicting the response of the Felicity and Calm Ratios for these beam tests it is beneficial to first put reasonable limits on the load ranges in which these parameters are calculated and displayed. At the low end of the peak load range, it was shown previously that a minimum of approximately 200 hits are required to stabilize the Felicity Ratio response. This minimum requirement was typically achieved near a load increment that is 20% of ultimate capacity. At the high end of the peak load range, both the Felicity and Calm Ratios tend to diverge from their progression during the main body of the loading protocol. From observation of the test data, this diversion usually occurs between 80 and 95 % of ultimate capacity. If only the test data between 20 and 80% of the ultimate load capacity is viewed, then the responses of the Felicity and Calm Ratios become very clear, repeatable and rather linear. From a practical perspective limiting data below 20% of ultimate is very reasonable considering both the sporadic results caused by an inadequate quantity of AE data and the fact that a real bridge structure operating at such a low loading level would generally not be of concern with respect to serviceability. At the high end of the loading range above 80% , there are certainly some interesting and fairly consistent responses from both the Felicity and Calm ratios, but they are much more complicated. Considering an in-service bridge will not be purposely operated at such a high load level under any legal highway loads, it is also very reasonable to neglect this portion of the response as far as developing in-service testing procedures is concerned.

Using the limited peak load range of 20 to 80% of ultimate capacity, the Felicity and Calm ratio responses are plotted and linear regression curve fits applied for each of the 25 virgin test beams subjected to an increasing , stepped loading protocol that were tested with AE. These plots are shown in Figures 3.84 through 3.109. Table 3.6 provides a useful guide for navigating through the 26 plots of test beam data on the Felicity and Calm Ratios by summarizing the salient features of each test including AE sensor array geometry, sensor type, type of flexure , shear stirrup spacing and unique features of a particular test. More details of each test are labeled on each of the plots such as array dimensions and location relative to the beam, maximum shear crack width at failure, failure load and the mode of failure. In addition a linear regression is applied to each response and the parameters of the curve fit are shown.

3.4.5 Linear Regression Analysis of Felicity and Calm Ratio Data

As can be seen in the majority of the Felicity and Calm ratio plots in Figures 3.84 through 3.109, a rather linear relationship exists between these two parameters and the normalized load. Evidence of this linearity can be seen by examining the curve fit parameter R^2 for all of the test samples as shown in Figure 3.110. The mean value of 0.83 for the Felicity ratio for all test data is shown with the range of +/- 1 standard deviation. A perfect fit would have an R^2 value of 1.0. Figure 3.111 shows the curve fit parameter for the Calm Ratio with a mean value of 0.77. This level of linearity is rather amazing considering the broad range of different variables between the 26 beam tests.

Now that the generally good fit of a linear relationship has been demonstrated it is appropriate to look at the actual slopes and ordinate intercepts for all of the test beams. Figure 3.112 shows the linear slopes calculated for the Felicity ratio response. The mean value is -1.22 showing that the Felicity Ratio drops with increasing load magnitude for virgin beams, as one would expect. The ordinate intercepts for the Felicity Ratio linear fits are shown in Figures 3.113 and 3.114. The slopes for the Calm Ratio linear fits are seen to average +1.19, and thus are increasing with increasing load magnitude as expected. The ordinate intercepts for each test beam are shown in Figure 3.115. Using the mean values for each of these 4 linear fit parameters an average Felicity and Calm ratio response for all of the test beams can be constructed as shown in Figure 3.116. The linear fit equations for each response are shown with the threshold levels specified in NDIS-2421 for the Felicity and Calm Ratios. The Felicity Ratio crosses the specified threshold at a reasonable load level of 50% of ultimate capacity and all calculated Calm Ratios plot exceeding the threshold set under NDIS-2421, suggesting that modifications to the Calm Ratio threshold may be appropriate when testing beams subjected to shear dominant failures and the range of cracks widths that are considered to be serviceable by ODOT.

To make such adjustments it is useful to examine the range of CMOD for the test beams at various load levels and compare them to the three level classification system used on the ODOT crack comparator tool as shown in Figure 3.117(a) and (b). The crack widths measured at each load level for all of the major test variables are plotted. It is clearly seen that when plotted with normalized load, all beams behave in a very similar manner. Measurable shear cracks begin to develop near 40% of ultimate capacity and slowly widen until approximately 70% and then begin to show exponential growth in width with respect to load. The three ranges of crack width defined as ODOT Level 1 , 2 and 3 plot very appropriately with the imposed loads further validating that shear crack width is a good indicator of damage state in these particular class of test beams. The plot in Figure 3.117(b) is normalized with the shear strength contribution from the stirrups only at the critical section and thus takes into better account the variation of stirrup spacing. In Figure 3.117(a) which has load normalized with ultimate capacity of the beam, which included the concrete's contribution to shear strength in addition to the steel, the highly reinforced specimens (6 inch spacing) deviate significantly from the other test beams. Considering that beams with this tight of spacing are not going to present capacity problems in-service, the author chose to use ultimate capacity for normalizing load because it is more tangible to the non-expert in concrete design and appears to work well for the stirrup spacing range of concern in the field. In addition to shear crack width, the number of shear cracks is also important from a qualitative perspective. Figure 3.118 shows the total number of shear cracks measured as a function of load. In general the cracks were symmetrically divided at mid-span with half of the total number of crack occurring in each of the two high shear zones. A maximum of 12 cracks were measured and documented for each beam during these tests. From both of these last two figures it can be seen that generally beams with light shear steel reinforcement (12 inch and greater spacing) develop fewer shear cracks but tend to be wider when compared to the highly reinforced specimens that develop more cracks of less width. This fact was demonstrated in SPR 350.

Now that the relationship between damage state and crack width has been shown for this class of beam, we can go back and revisit the threshold Felicity and Calm

Ratios utilizing this information. Figure 3.119 again shows the average Felicity and Calm Ratio responses to load level for all of the test beams. The load levels at the shear crack width thresholds between Level 1 and 2, and 2 and 3 as found in Figure 3.117(a) have been transferred to the current Figure. Thus Level 1, 2 and 3 loading can be seen relative to the experimentally measured felicity and Calm Ratios. It is proposed to set new thresholds for the felicity and Calm Ratios for this class of concrete beam using the crossing between ODOT Level 1 and Level 2 cracks widths and experimentally determined load levels. These criteria yield a Felicity Ratio threshold of 0.9 which is identical to NDIS-2421 and a Calm Ratio threshold of 0.4 which is nearly an order of magnitude larger then the recommended value on NDIS-2421.

Each of the 3 ODOT crack width levels defined on the ODOT crack comparator card invoke a policy response as discussed above concerning mapping and measuring the in-service cracks. Recall that Level 1 required no action, Level 2 requires tracing the length extent of the crack with a highlighting pen and Level 3 required CMOD measurement and crack mapping into the inspection report. The parallel set of interpretations for the 3 Levels as shown in Figure 3.119 could be as follows:

Level 1 Loading - Light loading with no serviceability concerns

Level 2 Loading – Moderate loading that may justify continued surveillance or refined load capacity calculations when operating near the right end of the range

Level 3 Loading – Heavy loading is implied and will require refined load capacity calculations and possibly a full time structural health monitoring system if the loading is not reduced or capacity increased.

As discussed in the field testing reports in Chapter 4, the Felicity Ratio is often not practically measurable on in-service bridges. Nonetheless it is useful for laboratory testing. Using the proposed thresholds on Felicity and Calm Ratios for this class of concrete beam, a damage assessment plot can be created as shown in Figure 3.120 for test beam 2T12. The various load levels are plotted and the four regions of damage shown. The data generally plots well with each of the progressively larger load cycle indicating an increasing damage state with increasing load.

3.5 Intensity Analysis

Another applicable method for identifying and classifying structural damage using AE parameter data is Intensity analysis as presented by Fowler et. al. [46]. The origins of Intensity Analysis come from the Fiber Reinforced Plastic (FRP) pressure vessel industry and are quit well developed for this class of structure. These methods were first applied to pre-stressed concrete highway girders by Fowler et. al. in 2001 [47]. These methods were again applied to a new bridge constructed with pre-stressed concrete girders in Poland in order to establish a baseline response for future monitoring in [48].

Intensity is a measure of the structural significance of an AE source. Two parameters are needed to determine the Intensity, the Historic Index and the Severity. The Historic Index, H(t) , weighs the average signal strength (peak amplitudes) of the last 20% or 200 hits , which ever is the smallest number, of hits to the average signal strength of all hits for the load protocol. Analytically, it is a method for determining changes in slope in the cumulative amplitude versus number of hits curve discussed in Section (3.3.3) which can identify the arrival of the “ knee “ in the curve . Providing early detection of the “ knee “ in the cumulative amplitude versus hits curve is useful for identifying new damage as it occurs in the loading curve.

Equation 3 defines the Historic Index. It can be seen to be a function of time and is calculated over all peak amplitudes (S_{0i}) from i to N , where N is the total number of hits measured up to and including time *t.* Limits on N-K are imposed to meet the above definition as shown.

Equation 3

$$H(t) = \frac{N}{N-K} \sum_{t=K+1}^{N} S_{0i} / \sum_{i=1}^{N} S_{0i}$$

N= total number of AE hits up to and including time *t*
S_{0i} = Signal Strength of the i^{th} hit
K= empirical parameter

Historic Index does not apply for N<200 hits
K=0.8N for 200 < N < 1000
K=N-200 for N> 1000

The Severity Index, S_r , is defined as the average the average of the 50 largest peak amplitude hits striking a particular sensor. A significant increase in Severity can indicate the onset of more serious structural damage as the loading progresses. It has been found that Severity increases sharply at the “knee” in the cumulative amplitude versus hits curve [46] . The Severity is numerically defined in Equation 4. The parameter J , the number of peak amplitudes to average over , is an empirically derived constant much like N-K in the Historic Index.

$$S_r = \tfrac{1}{J}\sum_{i=1}^{i=J} S_{0i} \qquad \text{Equation 4}$$

S_{0i} = Signal strength of i^{th} hit

J = empirical parameter ranging from 10 to 50 with 50 being the value used in ref. [48]

Severity does not apply until N > 50

Once H and S_r are calculated for each channel over the load protocol they can be correlated by plotting the Historic Index as the abscissa and the Severity Index as the ordinate. Intensity grading curves can be imposed on this plot that are developed from experimental data pertinent to the structure being tested. A schematic example of such a grading chart is shown in Figure 3.121. In general the chart is divided into zones which define the structural significance of the AE depending on where they occur on the plot. Sensors which plot towards the upper right of the chart indicate greatest significance and sensors which plot either at the lower left or below a minimum Severity are considered to be of less or no significance respectively. Recommend actions can be applied to each zone ranging from no action required, through various levels of follow up NDE or analysis, up to taking the structure out of service. Both the grading zones and recommended actions are application specific.

As a late addition to this research, Intensity analysis was applied to the test beams previously analyzed with the Felicity and Calm ratios potentially adding more field adaptable analysis methods using parameter based AE analysis. Since there is very little published work focused on applying Intensity analysis to concrete structures and in particular conventionally reinforced structures, new empirical factors for computing H, S_r and the Intensity grading zones must be established. The subject data base of laboratory and field testing AE data is considerable when considering it comes from a single research project and could potentially help to form the beginnings of new standards for this approach. A few sample test beam data sets were analyzed for Intensity using a range of empirical constants for J and N-K. Though far from extensive, the results indicated that using the values suggested by Fowler et. al. [46,47] are certainly a reasonable start. In general using smaller then suggested values appeared to increase sensitivity at the expense of stability. Using larger then suggested values generally lowered the magnitude of the values as expected but also tended to reduce sensitivity. Thus all laboratory data were analyzed for Intensity using J=50 and N-K=200. The minimum hit requirements were met early in the load cycles, typically by 75 kips, and thus were left constant for all load steps.

To demonstrate these new parameters a sample laboratory beam test will again be stepped through one load step at a time, this time showing the evolution of the Historic Index and Severity. Following this demonstration the peak H and S_r from each load step will be plotted for each beam test.

3.5.1 Test Beam 7T12

Test beam 7T12 is a positive moment loading with 12 inch stirrup spacing, which as previously mentioned is the most common stirrup spacing found in moderately to heavily shear cracked girders in service. Test beam 7T12 is one of the two test beams studied with AE that incorporated debonded stirrups and thus emphasized the effect of shear crack formation in the concrete matrix of the composite structure. The sensors used were 150 kHz resonant type, and they were deployed in a linear array at mid-depth of the stem along the entire length of the test beam. This array geometry was used in the previously cited publications on Intensity applied to concrete beams. Figure 3.122 shows the beam in the test fixture with sensor deployment. AE channel numbers are assigned 1 to 6 starting at the South end of the test beam which is closest to the observer. The 150 kHz resonant sensors are spaced at 43 inches which is near maximum spacing for this sensor if continuous coverage between sensors is desired.

3.5.1.1 First load step 0 to 50 to 0 kips P_{max} */ Capacity = 0.12*

The first load step produces enough AE hits to calculate the History and Severity on the interior sensors where the flexural cracking occurs as shown in Figures 3.123 and 3.124 respectively. The emissions primarily occur during the loading and early load hold phases. The cross correlation of Severity and History, which is used to construct a intensity grading chart, for this load cycle is shown in Figure 3.125.

3.5.1.2 Second load step 0 to 100 to 0 kips P_{max} */ Capacity = 0.24*

The second load step propagates 4 flexure cracks deep into the stem as seen in Figure 3.126. Again the interior channels receive the most AE activity as these cracks propagate. The History and Severity are shown in Figures 3.127 and 3.128

respectively. Note that for the two interior channels (Ch.# 3 and 4) both the History and Severity rapidly increase just after the previous maximum load of 50 kips is reached. As noted by Fowler et. al. [46] the Severity is an effective parameter for determining the onset of AE and thus useful for calculating the Felicity Ratio. The Intensity plot for this load cycle is shown in Figure 3.129 were it can be seen that the interior channels are plotting up and to the right compared to the others, thus indicating the presence of damage from this load cycle in the mid-span portion of the beam where it actually is occurring.

3.5.1.3 Third load step 0 to 150 to 0 kips P_{max} */ Capacity = 0.35*

This load step imparts additional flexural cracks initiating outward from mid-span and causes two prior flexure cracks to turn into the mid-span direction and become diagonal tension cracks as seen in Figure 3.130. All channels are now active on the History plot shown in Figure 3.131 with channels 2 and 5 picking up the shear cracking. The outboard channels are still not registering much Severity unlike the interior channels as seen in Figure 3.132. Again, the channels closest to the shear cracks show the greatest increase, which occurs during the loading phase. The Intensity plot in Figure 3.133 shows that the region around channel 5 incurs the most damage during this load cycle which corresponds with the widest of the two diagonal tension cracks at a CMOD of 0.013”.

3.5.1.4 Fourth load step 0 to 200 to 0 kips P_{max} */ Capacity = 0.47*

The fourth load step causes an addition 10 diagonal tension cracks with two of them extending up to the under side of the top flange or deck section as shown in Figure 3.134. Crack CMOD at load range from 8 to 25 mils. The Historic Index has a very sharp and large magnitude response to the formation of these cracks as seen in Figure 3.135 with an increase of over a factor of 5 from the first load step. Channel 5 indicates activity during the load hold and now on the unload phase. The Severity shows significant activity on all channels with channel 2 showing an order of magnitude increase from the last load cycle. This is an excellent example of how Severity can be used to identify and locate the formation and extension of serious diagonal tension cracks as this is the channel closest to the widest shear crack. The Intensity plot in Figure 3.137 shows this fact with excellent clarity.

3.5.1.5 Fifth load step 0 to 250 to 0 kips P_{max} */ Capacity = 0.59*

This load step generally just widens and slightly extends existing shear cracks. Crack CMOD now ranges from 8 to 40 mils. The two primary shear crack tips are being driven into the high compression zone and thus resist extension as seen in Figure 138. The Historic Index is generally similar to the previous load step but without the single channel extreme as seen in Figure 3.139. The Severity is also lower then the previous load step as seen in Figure 3.140. Notice that several channels are now showing significant Severity on the unload phase. Recall this shows an increasing Calm ratio which implies accumulated damage in the structure. In addition the regions showing the greatest accumulated damage are indeed at the two primary diagonal tension cracks. The Intensity plot is shown in Figure 3.141 where channels 2 and 3 have suffered the most damage from this particular loading. <u>Keep in mind that the Calm ratio is an indication of accumulated damage from all previous loadings and the Intensity, as calculated here per load step, is an indication of current damage specific to the current loading.</u>

3.5.1.6 Sixth load step 0 to 300 to 0 kips P_{max} */ Capacity = 0.71*

Much like the previous load cycle existing cracks are widened and extended slightly. Shear crack CMOD ranges from 8 to 100 mils with the later value applying to the two primary diagonal tension cracks located near channels 2 and

5. The Historic Index is shown in Figure 3.142 and the Severity in Figure 3.143. Notice that only the Severity registers the unload activity. The Intensity is shown in Figure 3.144.

3.5.1.7 Seventh load step 0 to 350 to 0 kips P_{max} */ Capacity = 0.83*

Figure 3.145 shows the test beam after the 350 kip loading. The primary shear cracks are now nearly 150 mils wide which indicate a severe state of damage in the beam. The Historic Index is shown in Figure 3.146 and the Severity in Figure 3.147. All channels are showing significant unloading phase contributions to Severity which is indicative of an increasing Calm Ratio over the entire extent of the beam and thus a high level of accumulated damage. The Intensity is plotted in Figure 3.148.

3.5.1.8 Eighth load step 0 to 400 to 0 kips P_{max} */ Capacity = 0.95*

The primary shear cracks are driven further into the compression zone thus increasing the magnitude of the compressive stress. The primary shear cracks have a CMOD of 171 and 216 mils which is extremely large compared to in-service cracks that are typically less than 50 mils maximum. The Historic Index is shown in Figure 3.149 and the Severity and Intensity are shown in Figures 3.150 and 3.151 respectively. The interior channels which are closest to the primary shear crack tips being driven into the compression zone show the greatest damage from this load step.

3.5.1.9 Ninth load step 0 to 423 to 0 kips P_{max} */ Capacity = 1.0 (failure)*

The final load step drove the southern primary shear crack into the compression zone far enough to cause the classic shear compression failure as seen in Figure 3.152. This Historic Index is shown in Figure 3.153 where channels 2 and 3 have the greatest increase, especially channel 2 which is located on the failing shear crack. The Severity is shown in Figure 3.154. The Intensity plot in Figure 3.155 clearly indicates the failure damage was centered around the Southern primary shear crack at channel 2.

3.5.2 Summary of the Intensity Analysis of Test Beam 7T12

The Historic Index and Severity were intended to be displayed on a per channel or more correctly per coverage zone basis. This point is made clear by the Zone Intensity Processing (ZIP) as presented by Fowler et. al [46] and Golaski et. al [48]. Indeed as shown in the preceding, this approach is applied both considering the AE sensor deployment and Historic Index and Severity analysis. This is clearly a useful approach in identifying the occurrence and general location of damage incurred per load step. Considering that use of these methods is very new to the application to conventionally reinforced concrete highway girders subject to loading conditions that produce diagonal tension cracks that are of concern to serviceability, a basic understanding of the AE responses to damage must first be understood and quantified. To assist in this understanding, the author believes that general structural response trends in AE to the loading protocols must first be shown. Given this paradigm the detailed responses of the Severity and Historic Index can be reduced and characterized as shown in Figure 3.156 which depicts the maximum response of the Severity and Historic Index for all AE channels per load step. As applied to FRP pressure vessels each of these two parameters is calculated per channel and cumulative for the entire loading protocol. This is appropriate for the nature of these structures and their expected service conditions. Given the loading conditions of in-service highway bridges and the loading protocol used for the majority of the subject test beam , i.e. monotonically increasing load steps with unload, each of the two discussed parameters were calculated cumulatively on a per load step basis so as to be comparable to service , proof and potential ambient overloads on real bridge structures in the hopes of identifying new damage as it occurs in nearly real time. This approach should lead to more straight forward implementation into a Structural Health Monitoring (SHM) system. From this figure a measurable and significant increase in both the Severity and Historic Index occurs shortly after the beginning of the formation of diagonal tension cracks. The ODOT loading levels are shown for reference. In this particular plot a polynomial has been fit to each parameter based on the data points shown. The author does not intend to imply these parameters could or do behave in a smooth manner with respect to load as is shown. What is intended is to show the general trends of these parameters more clearly then using discrete data points. In fact these trends are in good agreement with those expressed by Folwer et. al. [46] when applied to FRP pressure vessels. For the Historic Index he states, " The initial value will be close to unity, and it will increase sharply at the " knee " in the (cumulative amplitude versus hits *added*) curve. After the knee, the Historic Index will tend to decline until the onset of failure, at which point it will increase to a maximum." For the Severity he states, " Typically, Severity will increase sharply at the " knee" in the cumulative signal strength versus hits curve. As the damage becomes more serious the Severity will continue to increase, but at a slower rate. At the onset of significant fiber breakage, Severity will again increase sharply." Taking into account the calculations used in his analysis were performed cumulatively over the entire load protocol whereas the data shown in Figure 3.156 are calculated per load step, the trends hold true. As will be seen in the presentation of the other beam test data this effect was repeated in every test.

It is these two parameters that define the Intensity and thus are needed to develop Intensity grading charts for this class of application. Developing such grading criteria will take some more effort before a testing standard can be developed. The data from the test series present in this research can provide a good start if not a basic foundation for developing such criteria. To accomplish this, the overall numeric ranges and basic trends of the Severity and Historic Index as applied to conventionally reinforced concrete deck girder subjected to diagonal tension cracking must first be established.

Figure 3.157 shows the summary intensity plot for test beam 7T12. Again the maximum value from all channels is shown with the corresponding loading level. The load steps that produced major shear cracking and then failure plot out farthest up and to the right, indicating that it was these load steps that produced the most damage, which is consistent with physical observation.

3.5.3 General numeric values and trends in Historic Index and Severity

The results of general numeric values and trends in 23 laboratory test beams will now be presented and discussed. The primary variables investigated are AE sensor type, deployment and loading protocol. The largest factor affecting the magnitude of the Severity and Historic Index was found to the sensor type. The data is presented in three primary groups, a) Beams tested with 150 kHz sensors deployed in a planar array covering one of the two high shear zones, b) 150 kHz sensors deployed in linear arrays either covering a single shear stirrup or the entire stem or web of the beam and c) 60 kHz sensors deployed in a planar array covering one of the two high shear zones. For each test beam the Severity and Historic Index are shown as a function of load increment without an implied curve fit and then the Intensity plot is shown with load increments labeled. Figure 3.156 through 3.177 show the results for Group A, figures 3.178 through 3.191 show the results for Group B and figures 3.192 through 3.205 show the results for Group C.

The general trends discussed above are present in all data sets and in many cases the Severity and Historic Index tract one-another over a good portion of the load range tested. Table 3.7 summarizes the peak values for Severity and Historic Index measured prior to failure for all test beams. Group A results show maximum Severity ranging from 490 to 14,900 with a typical value on the order of 1000. The very high value measured on test beam 7T12 is a result of a large diagonal tension crack propagating directly under on of the 6 AE sensors and thus there was very little attenuation of the event. The maximum Historic Index ranged from 3.0 to 9.1 with a the typical value near 4.0. Again the high value on test beam 7IT12 is attributed to the close proximity of the sensor to a crack. For Group B the maximum Severity ranged from 500 to 9440 with a typical value on the order of 1000. The maximum Historic Index ranged from 4.3 to 10.3 with the typical value being slightly more then 5. For Group C the Severity ranged from 10,000 to 115,00 with the typical value being on the order of 100,000. The maximum Historic Index ranged from 4.7 to 23.2 with a typical value of 13. Discussion of the difference in these parameters between virgin and previously loaded beams will be covered in the next section. Overall Group A and B behave in a similar manner with slightly larger magnitudes found in the linear arrays. Group C has significantly larger magnitudes on both Severity and Historic Index which is a result of the higher sensitivity of the 60 kHz sensors to the AE produced in concrete.

3.5.3.1 Effects of reloading on AE test parameters

Most of the data presented on the laboratory test beams involved monotonically increasing load / unload cycles on virgin beams or beams that had not experienced prior load cycles of greater magnitude. In service bridges however, have been subjected to previous load cycles that are presumably of large magnitude due to the presence of shear cracking in addition to hundreds of thousands if not millions of low to moderate level load cycles. Both low cycle and high cycle fatigue were considered and tested as part of SPR 350 to quantify the effects on the structural capacity. The general conclusion from the cited research was that beams of this particular class when loaded to the maximum strains found in service do not experience a significant loss in ultimate strength as the result of high cycle fatigue loading ,even at the extreme in-service load ranges cycled over 2 million times. The AE test method was applied to 8 different test beams that were subjected to more then one loading sequence and reported here. These load –reload test beams can be separated into 3 main categories , 1) Loading and reloading at varying shear to moment (V/M) ratios , 2) Loading and reloading with identical load sequences and 3) Pre-cracking up to 80% of ultimate capacity followed by 2 million cycles of fatigue loading and concluding with monotonic loading to failure. The AE results from these tests provide very good information on which cycles cause new damage to an already damaged beam and the condition state of the beam.

3.5.3.2 Loading and reloading at varying V/M ratios

Test beams 4IT6-10 and 4IT8-12 were first subjected to a loading sequence with the end supports moved in to increase the V/M ratio of the load. The purpose of this was to impart heavy diagonal tension cracking towards the center of the span and then move the supports back out to the normal 24 foot span length and reload the beam. The affects of this loading on the Felicity and Calm ratios was previously shown in Figures 3.92 and 3.93 for each of these two beams respectively. In both cases the Felicity and Calm Ratios are not greatly affected by the first load cycle which indicates that each load sequence is imparting new damage to previously relatively undamaged regions as was observed visually during the test. It can also be noted that the first load sequence produced cracking more towards the mid-span location on the beam, away from the sensor array whereas the second load sequence formed new cracks within the sensor array.

The Historic Index and Severity as shown in Figures 3.168 and 3.169 also reveal that the first load sequence had little effect on the response of the second due to the location of the damage. The second loading sequence depicts larger magnitude responses as new shear cracks are formed within the sensor array. Thus even in the presence of near by damage all of these AE parameters discussed are able to detect new damage that occurs in closer proximity to the sensor array.

3.5.3.3 Loading and reloading with identical loading sequences

Repeating a loading sequence on a previously damaged beam has a much larger effect on the Felicity and Calm Ratios as shown in Figures 3.206. During the reloading the Felicity Ratio changes slope from negative to positive with respect to load level and starts out at value much less then unity , thus indicating the presence of significant damage from the first load step. The Calm Ratio shows a decrease in slope and starts at a much higher value when compared to the first loading, again a strong indication of damage even at the first load increment. This is an excellent demonstration of the ability of these two AE parameters to characterize the state of damage in a concrete beam.

The Historic index for this test beam is shown in Figure 3.198. Clearly the major damage occurs during the first loading sequence when the cracks are formed with the second loading sequence producing much lower values. The Severity shown in Figure 3.199 demonstrates the same effect. Thus the Calm and Felicity ratios characterize the state of damage and the Historic Index and Severity identify which load cycles produce the most damage.

3.5.3.4 Effects of high cycle fatigue loading

As previously stated high cycle fatigue loading at maximum in-service loading levels does not reduce the ultimate capacity of this class of concrete beam. This fact is also demonstrated in the AE responses. Figure 3.207 shows the responses of the Felicity and Calm Ratios on the virgin test beam 5IT12-B1 (previously shown in Figure 3.95) with the addition of the post high cycle fatigue responses. Much like the previous loading case the response of the Calm and Felicity Ratio change dramatically during the second monotonic loading sequence with the Felicity Ratio changing signs on the slope and starting out at an indicated high level of damage and the Calm Ratio shifting upward also indicating a high level of damage from the first reload increment. It is the reloading responses that are most comparable to in-service bridges that show significant diagonal tension cracking. A summary of the linear regression analysis on four post fatigue test beam responses to Felicity and Calm Ratios is presented in Figures 3.208 through 3.213. These plots are directly comparable to the same plots generated for virgin beams as shown in Figures 3.110 through 3.115 with the exception that only four data points are available and thus the mean and standard deviations have little meaning and thus are not presented. The basic trends discussed above are clearly shown form these data, limited in number as they are.

The response of the Historic Index for this test beam was shown in Figure 3.188 where the post –fatigue loading produces slightly lower magnitudes. The Severity response shown in Figure 3.189 shows much larger differences with the pre-cracking producing large magnitude values and the post fatigue showing smaller magnitudes, thus indicating the damage was imparted during the first loading sequence.

Table 3.1 AE sensor array auto-calibration results on virgin test beam 2IT12.

Amplitude*

Sending channel is in bold italics , results are in units of dB re 1 V / μbar

Ch. #	**1**	**2**	**3**	**4**	**5**	**6**
1	***82 dB***	56	64	49	52	61
2	58	***82 dB***	48	69		
3	65	47	***82 dB***	63	58	52
4	49	69	61	***82 dB***		55
5	53		58		***82 dB***	65
6	62		53		66	***82 dB***

Wave Speed **

Sending channel is in bold italics , results are in units of in/ms.

Ch. #	**1**	**2**	**3**	**4**	**5**	**6**
1	***0 in/ms***	90	115	83	75	115
2	92	***0 in/ms***	64	89		
3	45	68	***0 in/ms***	86	91	82
4	83	89	84	***0 in/ms***		4
5	76		91		***0 in/ms***	113
6	46		82		113	***0 in/ms***

* threshold of detection is set at 40 dB

** dilatation wave speed ranges from 140 to 170 in/ms

Table 3.2 AE sensor array auto-calibration results on test beam 2IT12 during the 250 kip load holding period.

Amplitude*

Sending channel is in bold italics , results are in units of dB re 1 V / µbar

Ch. #	1	2	3	4	5	6
1	***82 dB***	56	48	42		54
2	57	***82 dB***		45		
3	49		***82 dB***	48	44	48
4	43	46	48	***82 dB***		
5			44		***82 dB***	50
6	54		48		50	***82 dB***

Wave Speed **

Sending channel is in bold italics , results are in units of in/ms.

Ch. #	1	2	3	4	5	6
1	***0 in/ms***	65	95	38		74
2	66	***0 in/ms***		47		
3	96		***0 in/ms***	61	46	67
4	38	46	47	***0 in/ms***		
5			44		***0 in/ms***	60
6	102		67		62	***0 in/ms***

* threshold of detection is set at 40 dB
** dilatation wave speed ranges from 140 to 170 in/ms

Table 3.3 AE sensor array auto-calibration results on test beam 2IT12 after releasing the 250 kip load increment.

Amplitude*

Sending channel is in bold italics , results are in units of dB re 1 V / μbar

Ch. #	1	2	3	4	5	6
1	***82 dB***	52	51	41		54
2	51	***82 dB***		45	46	
3	56		***82 dB***	52	51	49
4	42	64	52	***82 dB***		
5			52		***82 dB***	54
6	57		49		55	***82 dB***

Wave Speed **

Sending channel is in bold italics , results are in units of in/ms.

Ch. #	1	2	3	4	5	6
1	***0 in/ms***	67	113	36		80
2	67	***0 in/ms***		54	11	
3	113		***0 in/ms***	75	68	58
4	42	34	78	***0 in/ms***		
5			69		***0 in/ms***	74
6	99		62		74	***0 in/ms***

* threshold of detection is set at 40 dB
** dilatation wave speed ranges from 140 to 170 in/ms

Table 3.4 AE sensor array auto-calibration results on failed test beam 2IT12.

Amplitude*

Sending channel is in bold italics , results are in units of dB re 1 V / μbar

Ch. #	**1**	**2**	**3**	**4**	**5**	**6**
1	***82 dB***	51	49			54
2	52	***82 dB***		44		
3	51		***82 dB***	41	44	
4		45	41	***82 dB***		
5			44		***82 dB***	
6	54					***82 dB***

Wave Speed **

Sending channel is in bold italics , results are in units of in/ms.

Ch. #	**1**	**2**	**3**	**4**	**5**	**6**
1	***0 in/ms***	76	66			70
2	78	***0 in/ms***		49		
3	70		***0 in/ms***	45	43	
4		50	34	***0 in/ms***		
5			42		***0 in/ms***	
6	70					***0 in/ms***

* threshold of detection is set at 40 dB
** dilatation wave speed ranges from 140 to 170 in/ms

Table 3.5 Summary of observable damage to test beam.

Load Step #	**Peak Load (kips)**	**P / P_{ult}**	**# of shear cracks**	**CMOD* @ load (mils) C_L to south end**
1	25	.07	-	
2	50	.14	-	
3	75	.21	-	
4	100	.28	1	Less then 8
5	150	.42	4	Less then 8
6	200	.56	5	13 , 13, 10,16,8
7	250	.69	6	25,16,13,20,(<8),20
8	300	.83	6	20,25,13,40,10,40
9	350	.97	6	30,50,25,60,80,60
10	360	1.0	6	60 and greater

* CMOD measured with ODOT crack comparator tool

Table 3.6 Summary of beam test parameters for felicity and calm ratio study

Test Beam ID #	AE Array type	AE Sensor type	Bending	Stirrup Spacing (inch)	Unique Features
1T18	planar	150 kHz	Positive	18	
1IT18	planar	150 kHz	Negative	18	
2T12	planar	150 kHz	Positive	12	
2IT12	planar	150 kHz	Negative	12	
2IT10	planar	150 kHz	Negative	10	Accidental over load on first load cycle
2T10	planar	150 kHz	Positive	10	
3T12	planar	150 kHz	Positive	12	Precrack for HC fatigue – 10 kip load increments
3IT18	linear	150 kHz	Negative	18	Precrack for HC fatigue
4IT6-10	planar	150 kHz	Negative	6 to 10	Two different V/M ratios used for loading
4IT8-12	planar	150 kHz	Negative	8 to 12	Two different V/M ratios used for loading
4T12-18	planar	150 kHz	Positive	12 to 18	
5IT12-B1	linear	150 kHz	Negative	12	Precrack for HC fatigue
5IT12-B4	linear	150 kHz	Negative	12	
5IT12-B3	linear	150 kHz	Negative	12	Precrack for LC fatigue
6T6	linear	150 kHz	Positive	6	Precrack for LC fatigue
7T12	linear	150 kHz	Positive	12	Debonded stirrups
7T6	linear	150 kHz	Positive	6	Debonded stirrups
7IT6	linear	150 kHz + hifi	Negative	6	Debonded stirrups
8T12-B3	linear	150 kHz + hifi	Positive	12	
8IT12			Negative	12	Flexural bars are cut off short
8T12-B4	planar	150 kHz +hifi	Positive	12	AE sensors deployed after shear crack development
8IT10	planar	60 kHz +hifi	Negative	10	

Continued

9IT12-B4	planar	60 kHz	Negative	12	
9T12-B3	planar	60 kHz	Positive	12	
10T24-B4	planar	60 kHz	Positive	24	
10T24-B3	planar	60 kHz	Positive	24	

Table 3.7 Summary of peak Severity and Historic Index for all test beams.

Group	Test Beam ID	Sensor type	Array type	Maximum Severity prior to failure	Maximum Historic Index prior to failure	Comments
A	7T12	150 kHz	Planar	14,900	9.1	Shear crack formed directly under a sensor
|	2T12	|	|	1580	3.9	
|	2IT12	|	|	8000	5.0	
|	2IT10	|	|	2350	3.1	
|	2T10	|	|	900	3.4	
|	3T12	|	|	520	3.6	
|	4IT6-10	|	|	580	3.0	First of 2 load sequences (high V/M ratio)
|		|	|	1080	5.9	Second of 2 load sequences (normal V/M ratio)
|	4IT8-12	|	|	490	3.0	First of 2 load sequences (high V/M ratio)
|		|	|	1200	3.6	Second of 2 load sequences (normal V/M ratio)
|	4T12-18	|	|	3000	7.8	
B	5IT12-B4	150 kHz	Linear	3090	7.3	
|	5IT12-B3	|	|	900	3.7	
|	6T6	|	|	850	4.3	
|	7T6	|	|	9440	10.3	
|	3IT18	|	|	1440	4.5	
|	5IT12-B1	|	|	880	3.2	Pre-crack for high cycle fatigue
|		|	|	500	2.6	Post high cycle fatigue
C	8IT12	60 kHz	Planar	95,800	16.5	
|	8IT10	|	|	77,800	23.2	
|	9IT12-B1	|	|	101,000	12.9	

Continued

<table>
<tr><td>|</td><td>9IT12-B3</td><td>|</td><td>|</td><td>105,000</td><td>9.8</td><td>First of 2 identical load sequences</td></tr>
<tr><td>|</td><td></td><td>|</td><td>|</td><td>10,000</td><td>4.7</td><td>Second of 2 identical load sequences</td></tr>
<tr><td>|</td><td>10T24-B4</td><td>|</td><td>|</td><td>115,000</td><td>20.1</td><td></td></tr>
<tr><td>|</td><td>10T24-B3</td><td>|</td><td>|</td><td>12,000</td><td>8.5</td><td></td></tr>
</table>

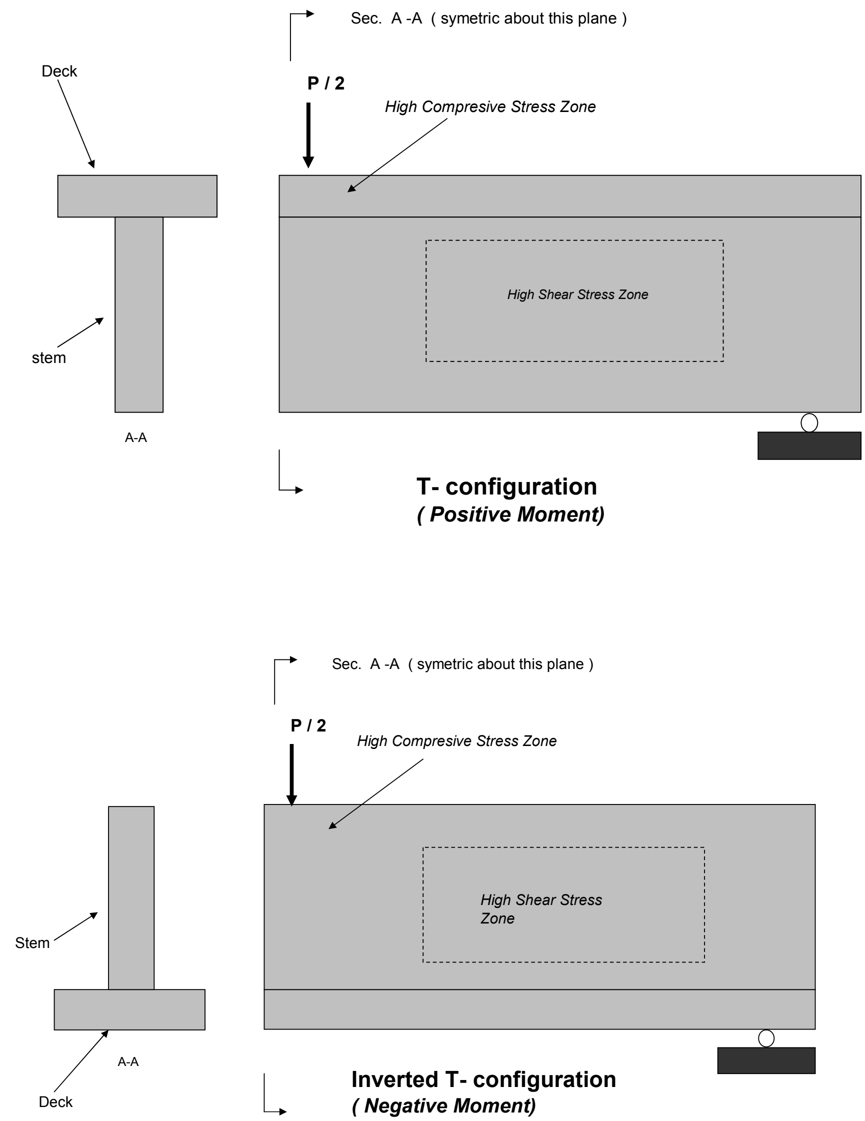

Figure 3.1 Schematic of T and IT test beam configurations with boundary conditions and tractions.

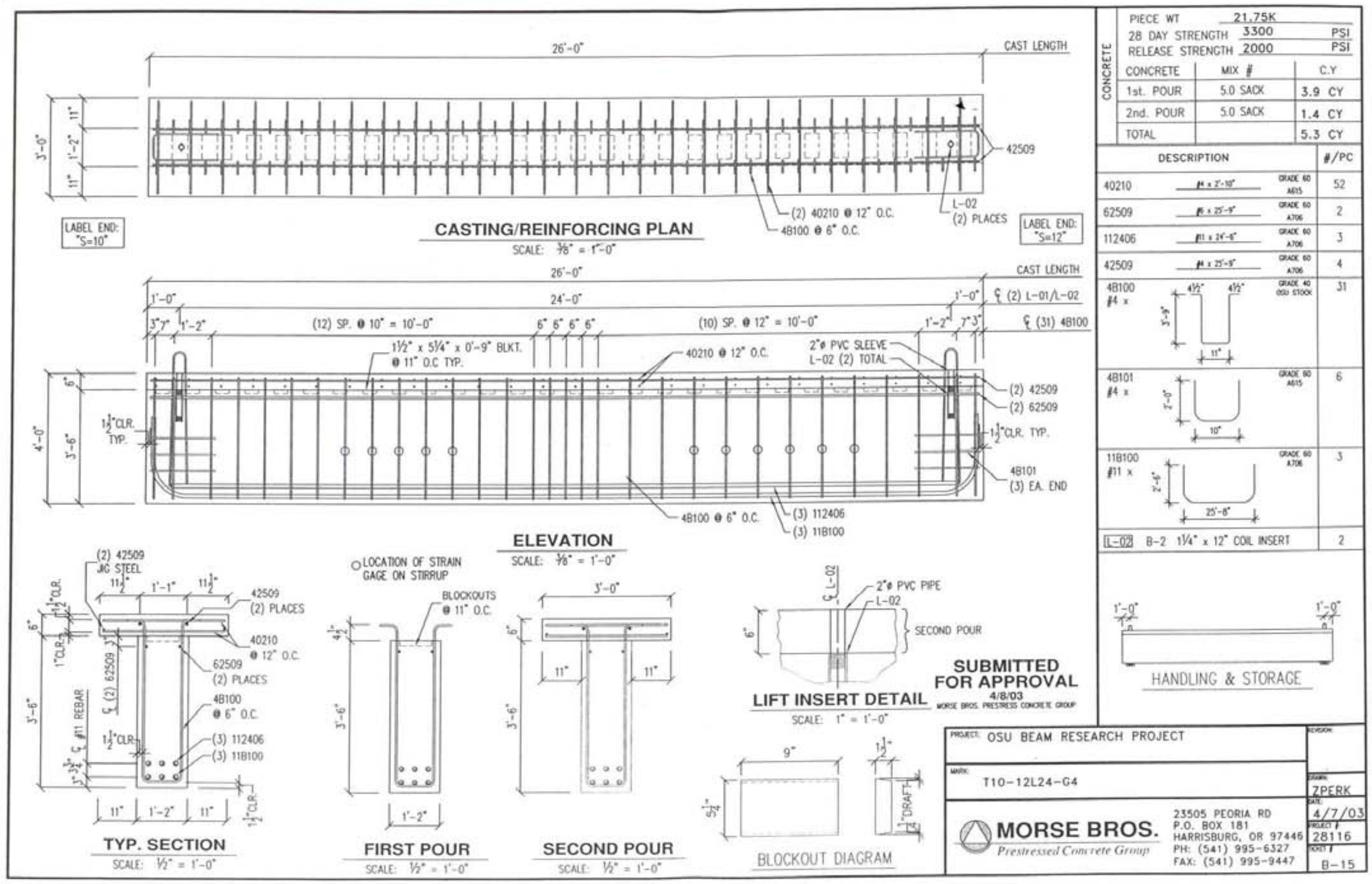

Figure 3.2 Fabrication drawing of typical T-configuration test beam.

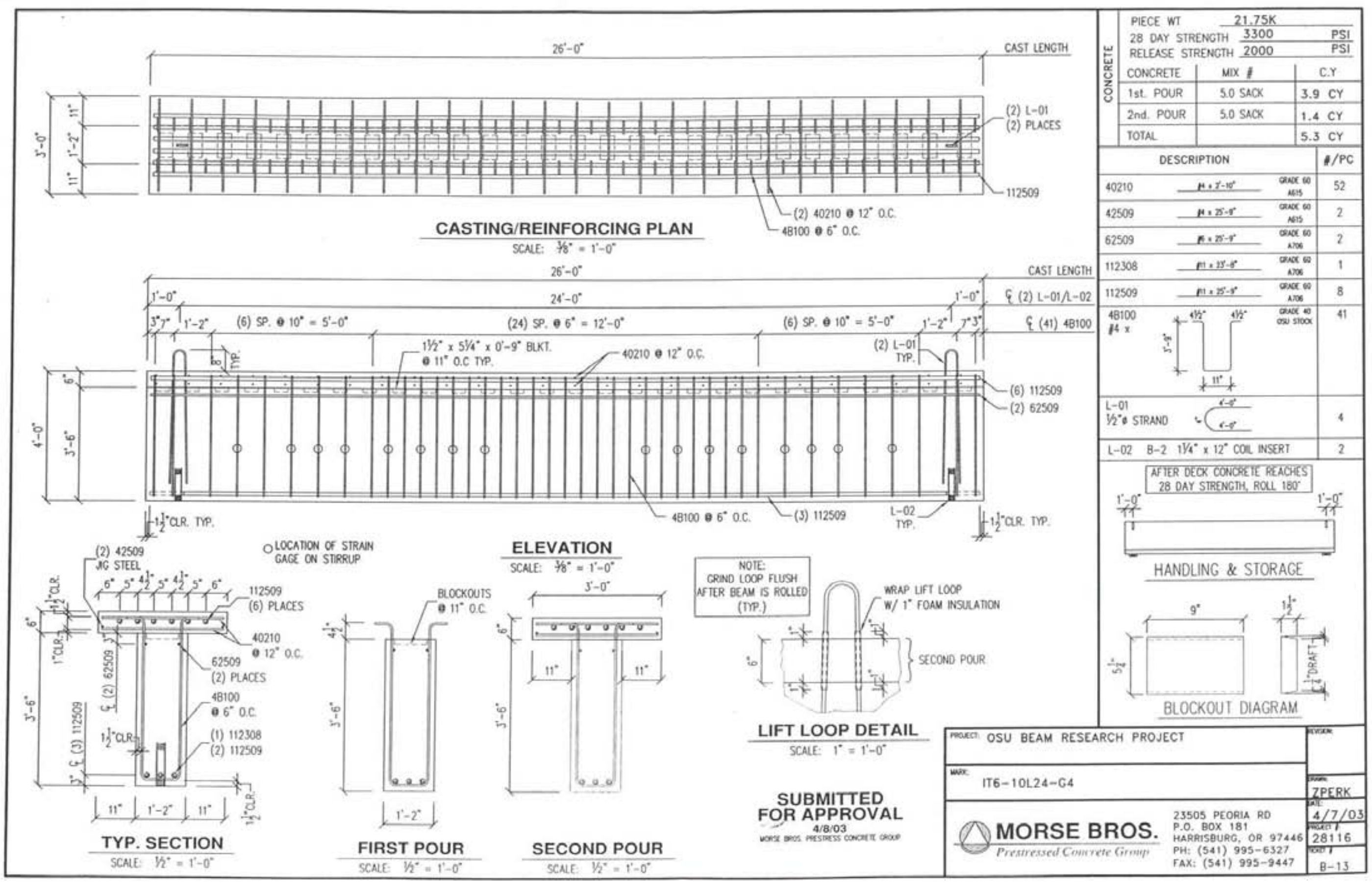

Figure 3.3 Fabrication drawing of typical IT-configuration test beam.

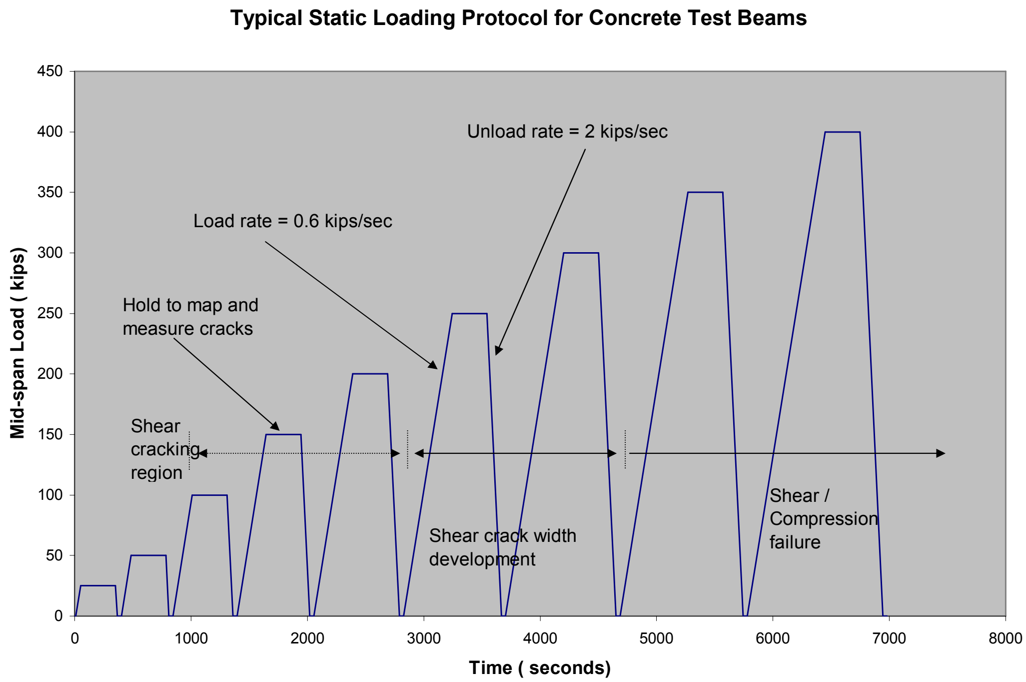

Figure 3.4 Typical static load protocol for test beams.

Figure 3.5 Photograph of static loading system.

Figure 3.6 Photograph of fatigue loading system. Out board cylinder provides dead load and mid-span cylinder provides cyclic loads.

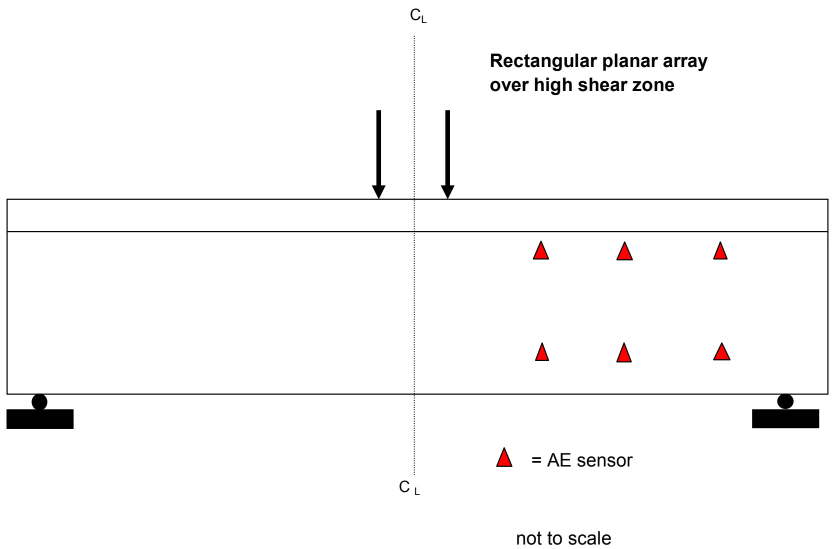

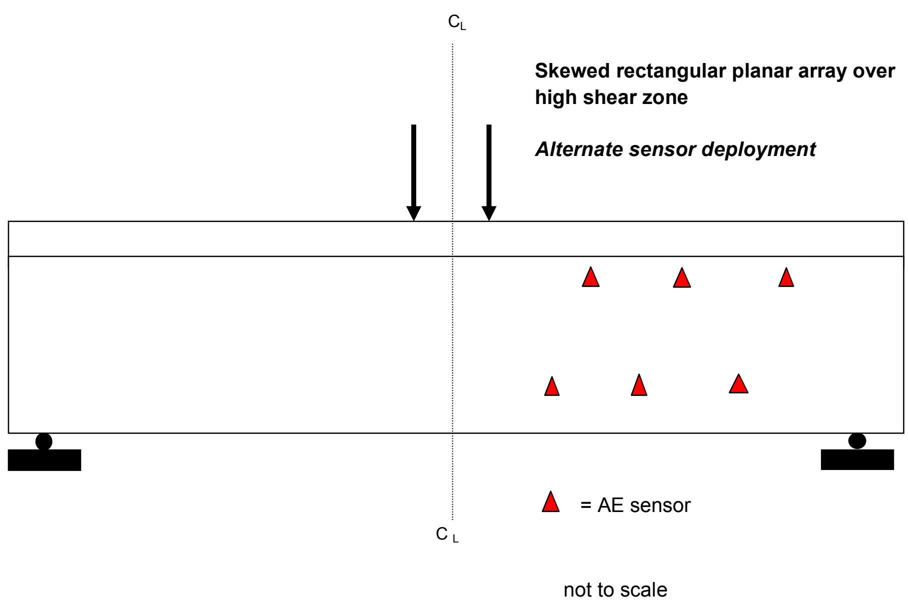

Figure 3.7a (upper frame) and 7b (lower frame) AE sensor arrays.

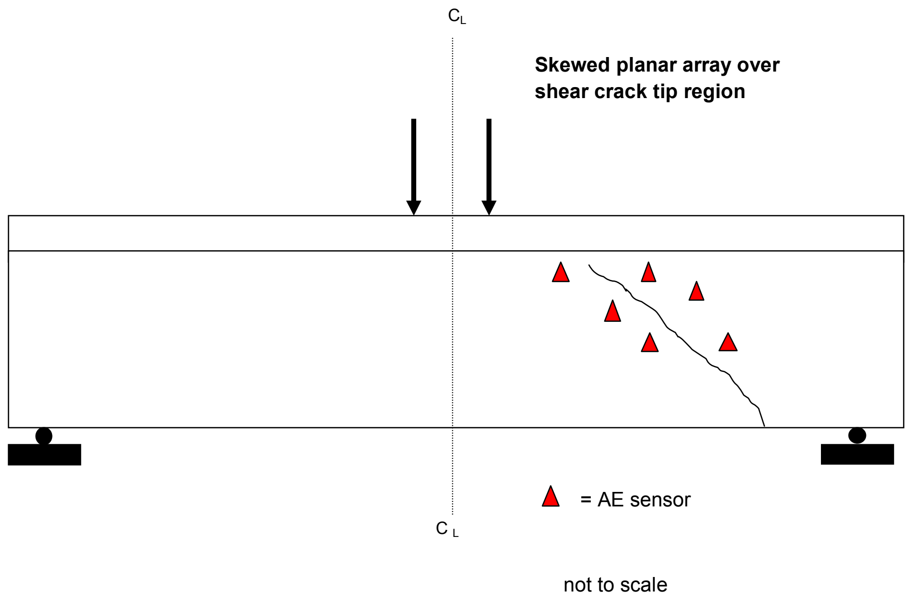

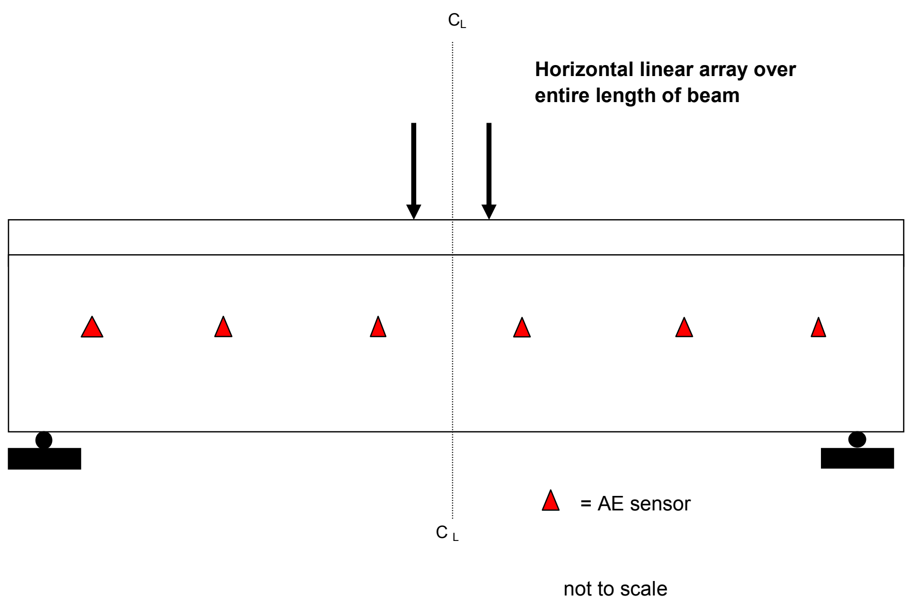

Figure 3.7c (upper frame) and 3.7d (lower frame) AE sensor arrays.

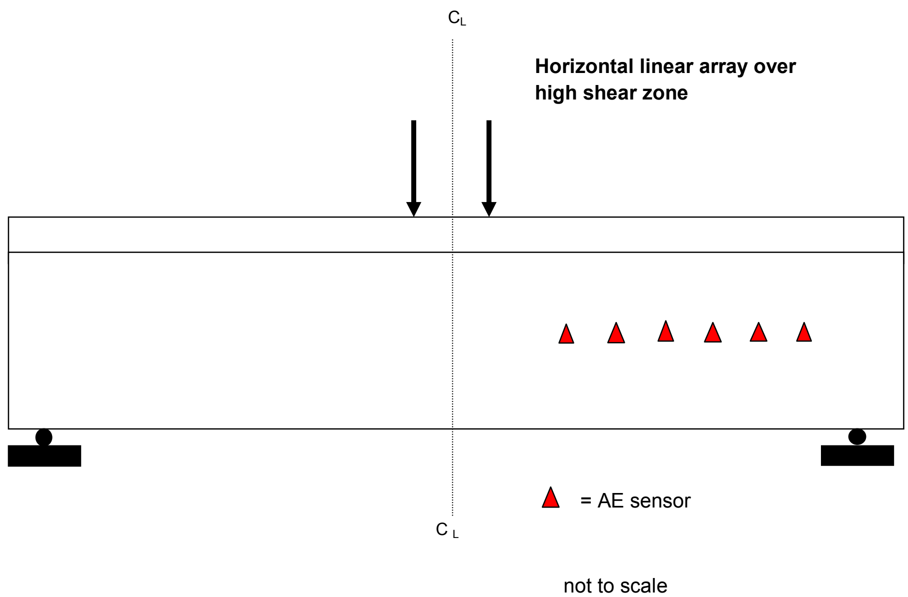

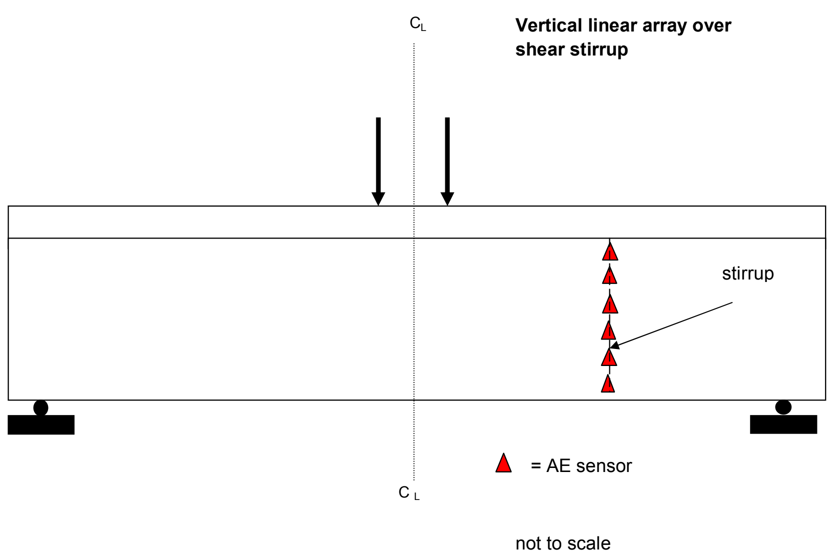

Figure 3.7e (upper frame) and 3.7f (lower frame) AE sensor arrays.

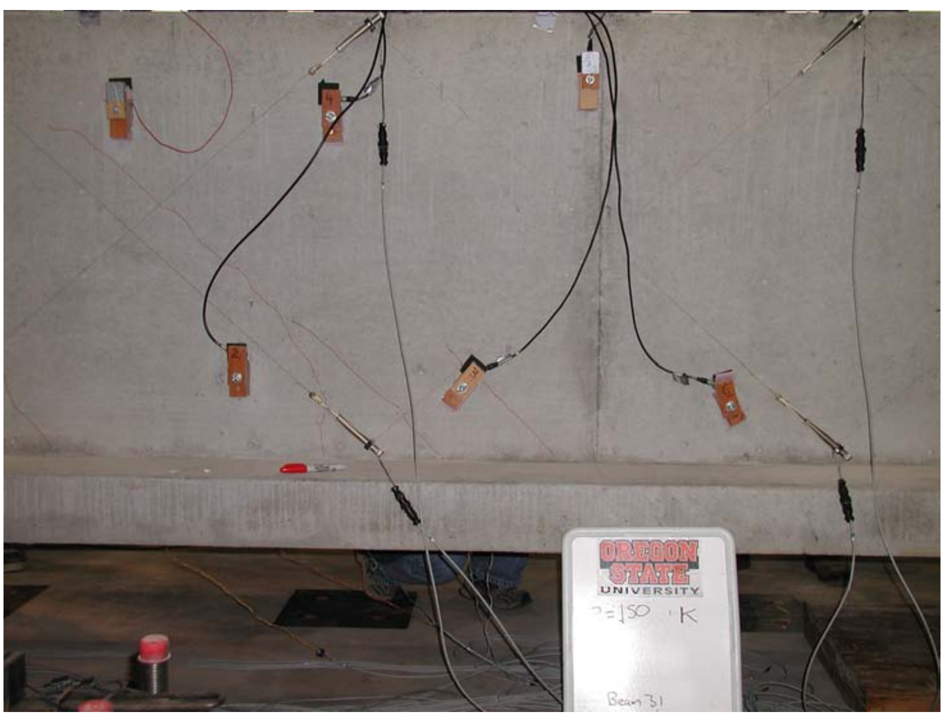

Figure 3.8a (upper frame) and 3.8b (lower frame) AE sensor arrays installed on test beams.

Figure 3.8c (upper frame) and 3.8d (lower frame) AE sensor arrays installed on test beams.

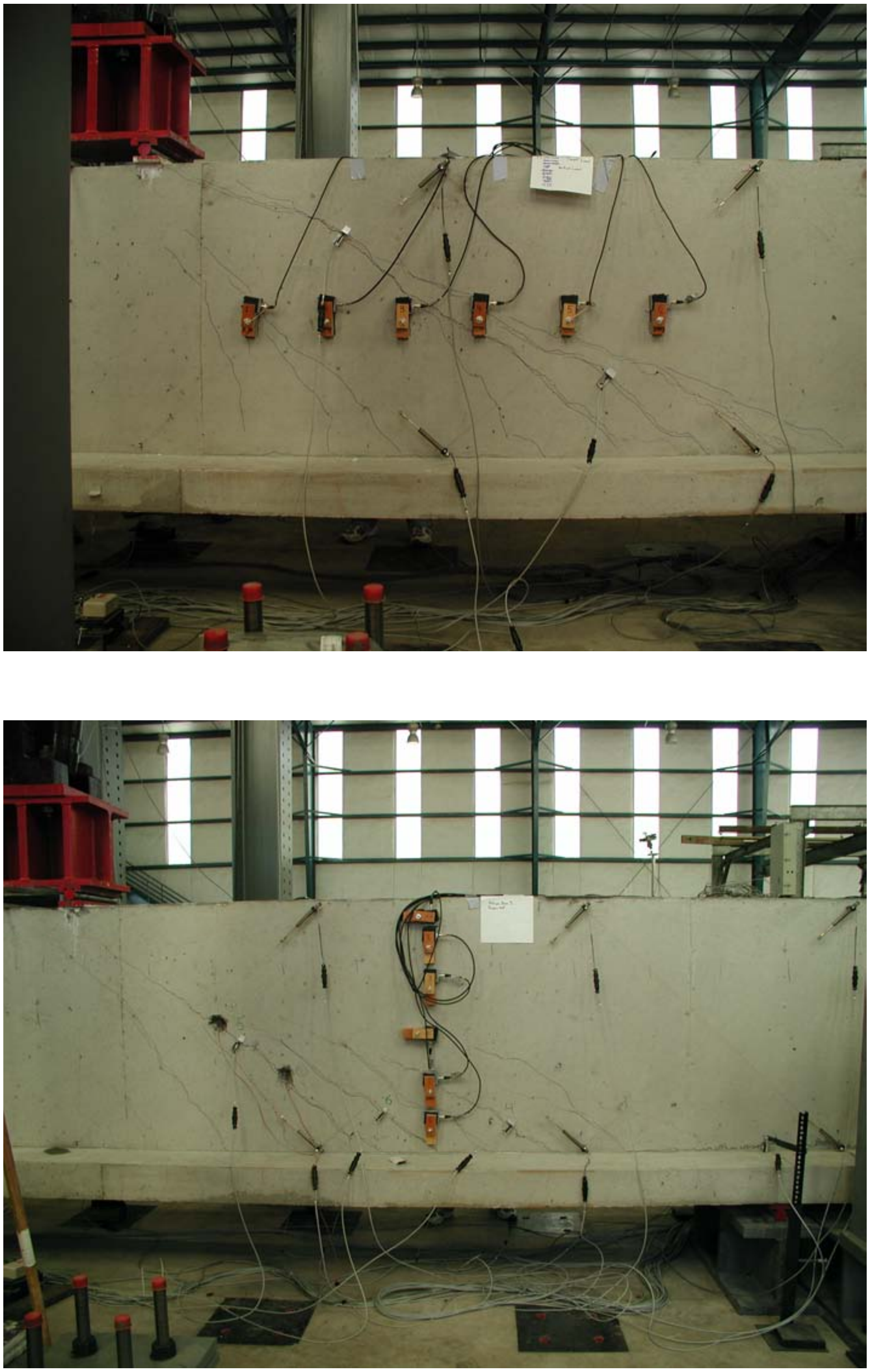

Figure 8e (upper frame) and 8f (lower frame) AE sensor arrays installed on test beams.

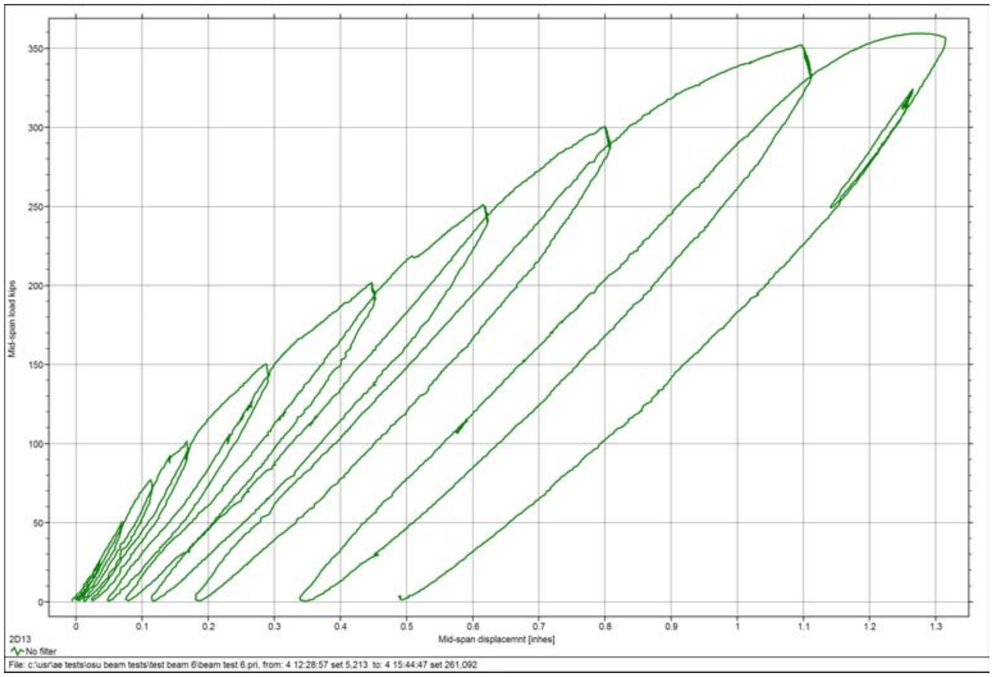

Figure 3.9 Mid-span load versus displacement plot for entire load sequence (example test beam 2IT12).

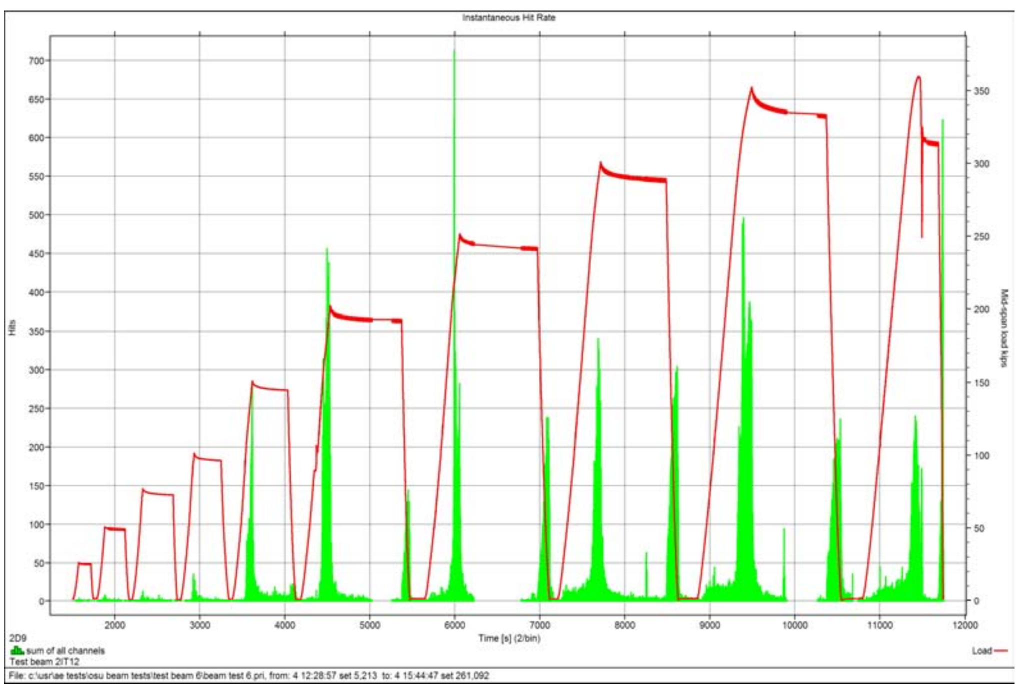

Figure 3.10 Instantaneous hit rate and mid-span load for entire load sequence (example test beam 2IT12).

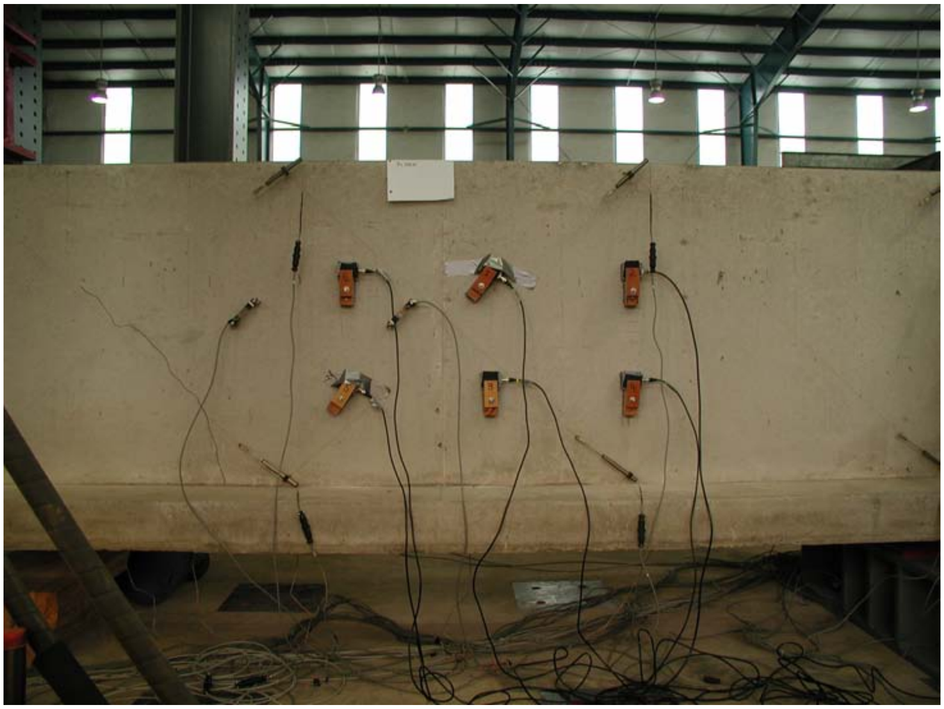

Figure 3.11 AE sensor array used for example AE test.

Ch.# 1 is pulsed at 82 dB

Ch.# 2 thru 6 receive at listed dB

Channel #

	1	**2**	**3**	**4**	**5**	**6**
1	***82***	56	64	49	52	61
2	58	***82***	48	69		
3	65	47	***82***	63	58	52
4	49	69	61	***82***		55
5	53		58		***82***	65
6	62		53		66	***82***

void cells indicate no sensor communication on that particular path

Example Auto-Calibration Table *(peak amplitude option is shown)*

Figure 3.12 Example auto-calibration table for testing the sensor array communication.

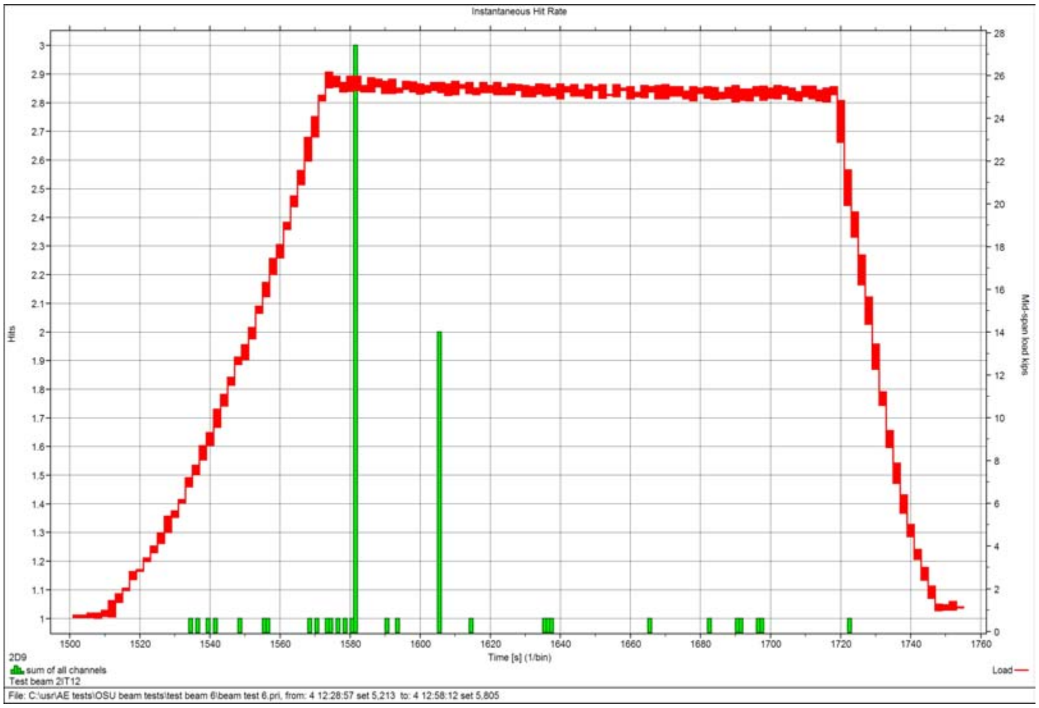

Figure 3.13 Instantaneous hit rate and mid-span load for the first load cycle.

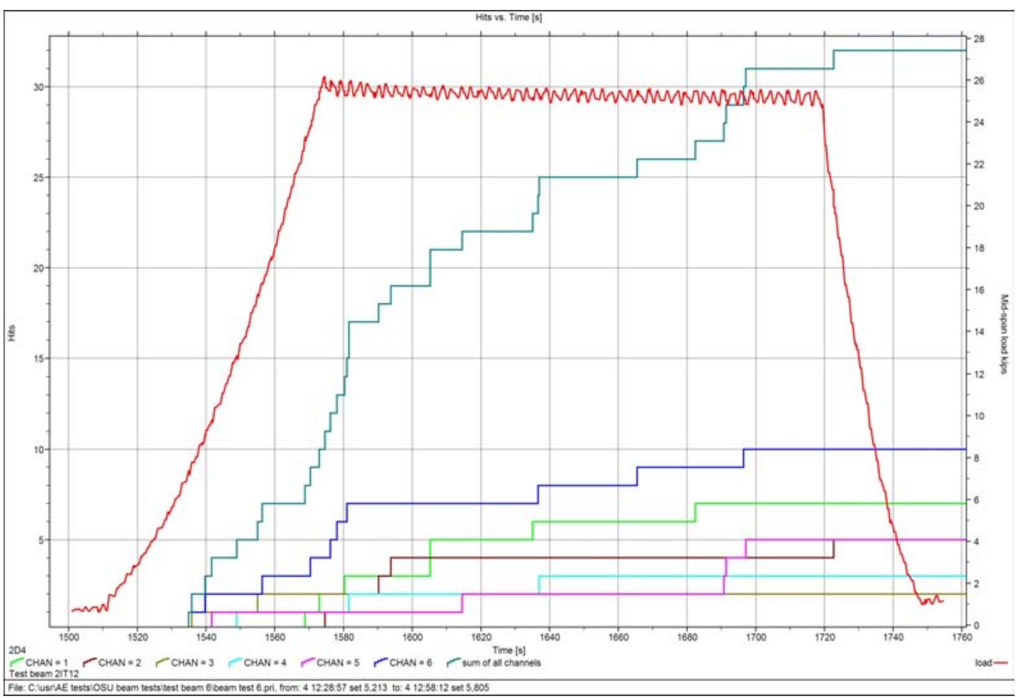

Figure 3.14 Cumulative hits and mid-span load for the first load cycle.

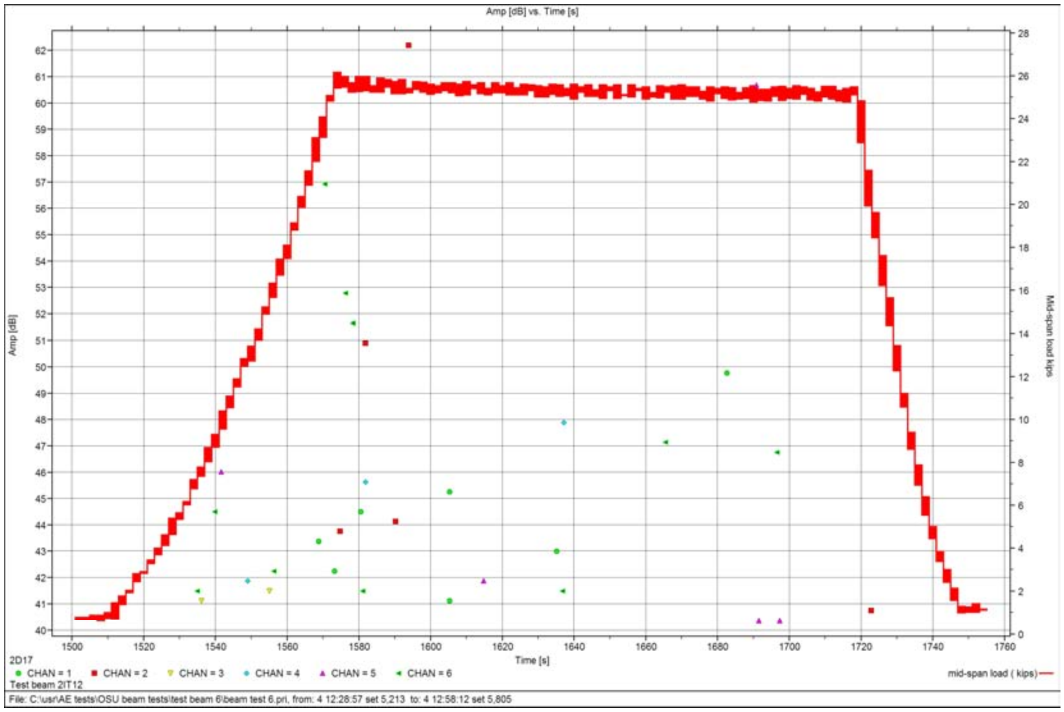

Figure 3.15 Peak amplitudes and mid-span load for the first load cycle.

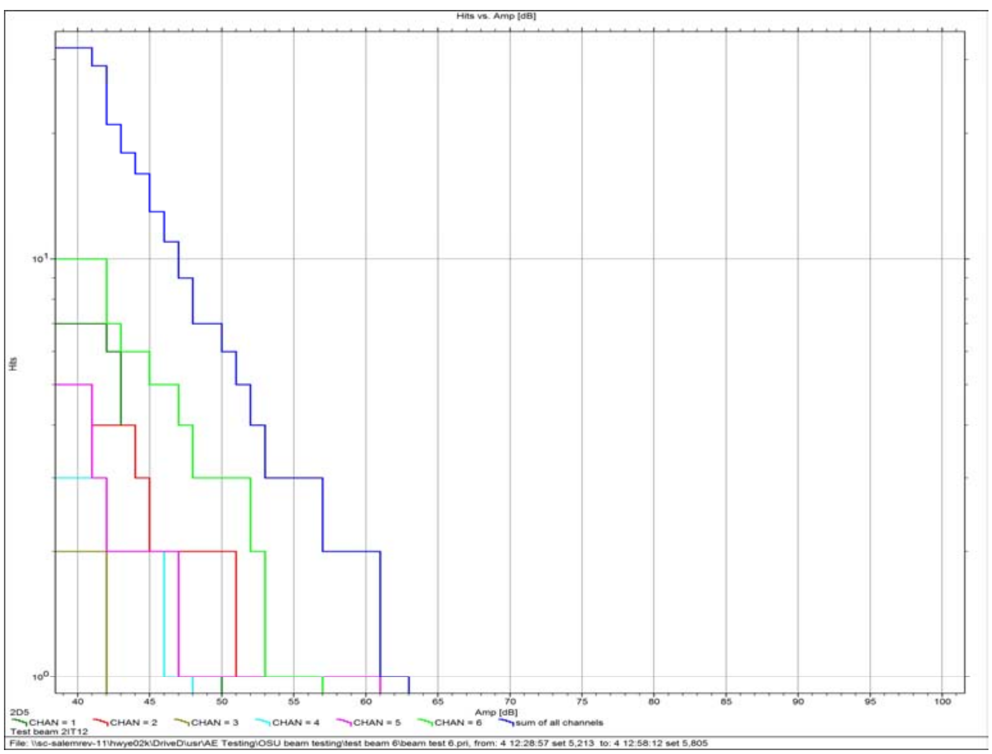

Figure 3.16 Hits versus peak amplitudes for the first load cycle.

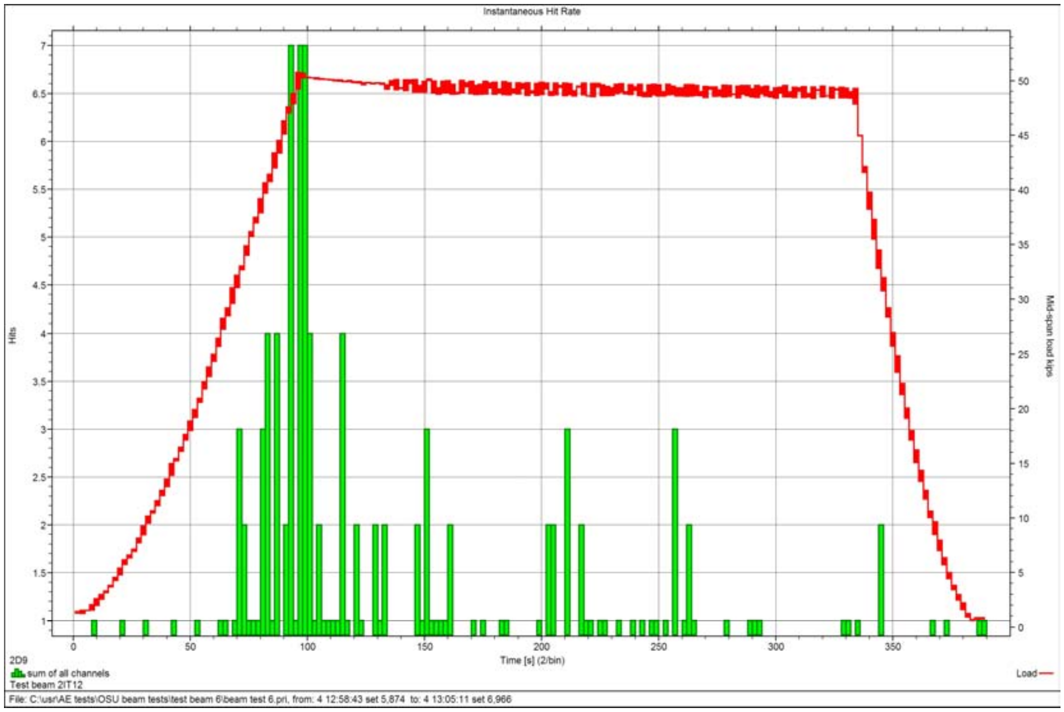

Figure 3.17 Instantaneous hit rate and mid-span load for the second load cycle.

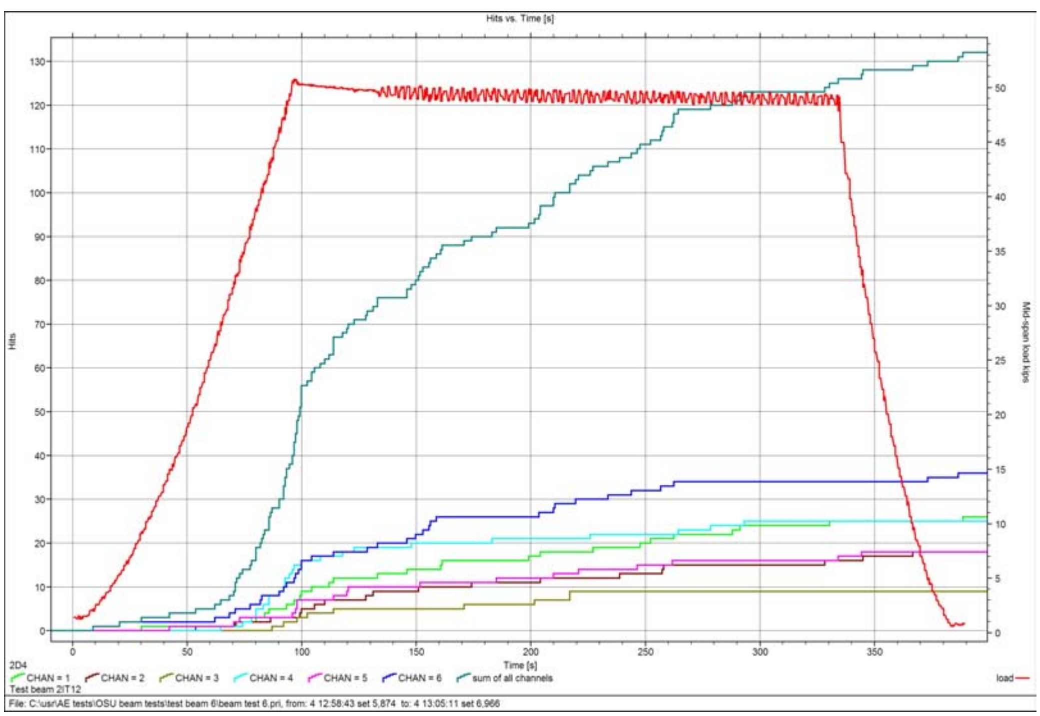

Figure 3.18 Cumulative hits and mid-span load for the second load cycle.

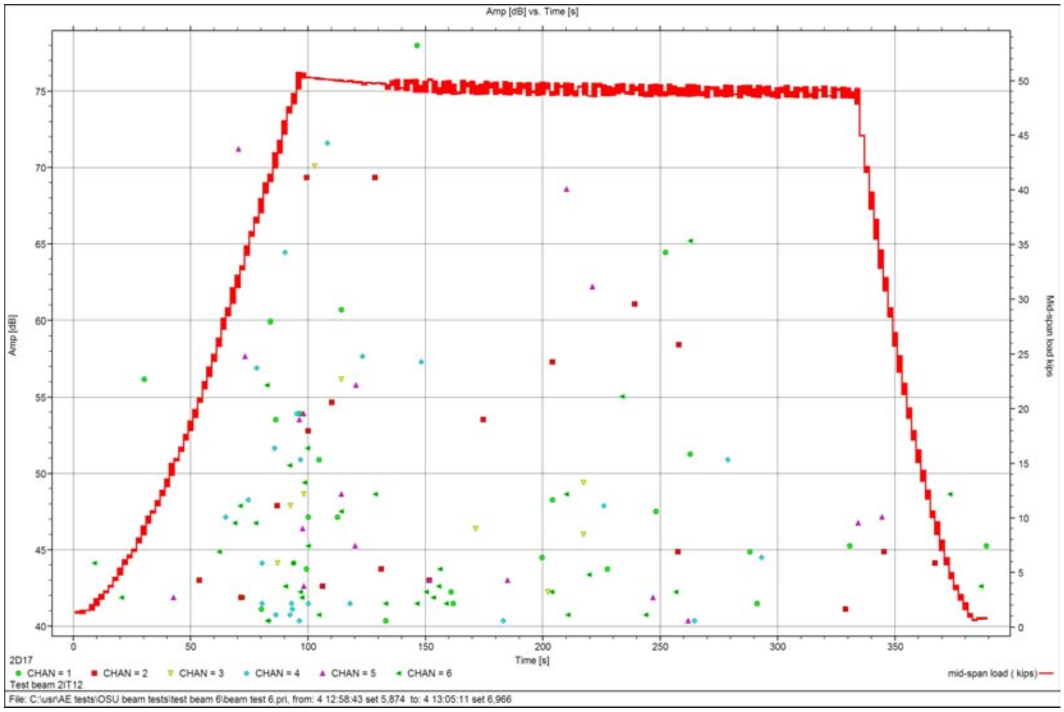

Figure 3.19 Peak amplitudes and mid-span load for the second load cycle.

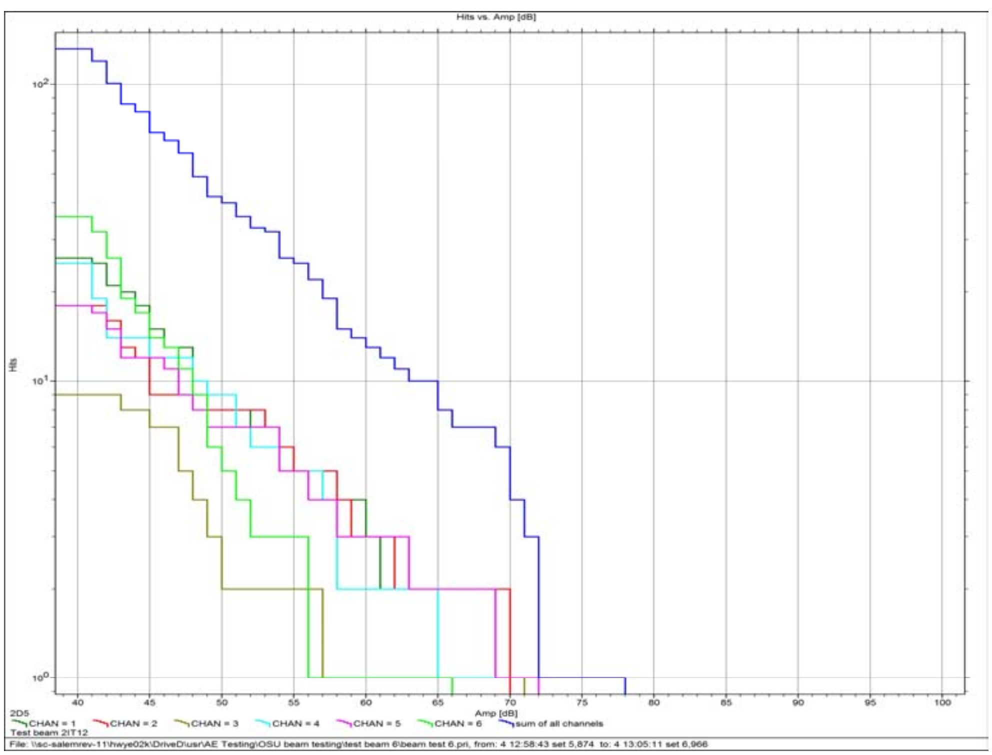

Figure 3.20 Hits versus peak amplitudes for the second load cycle.

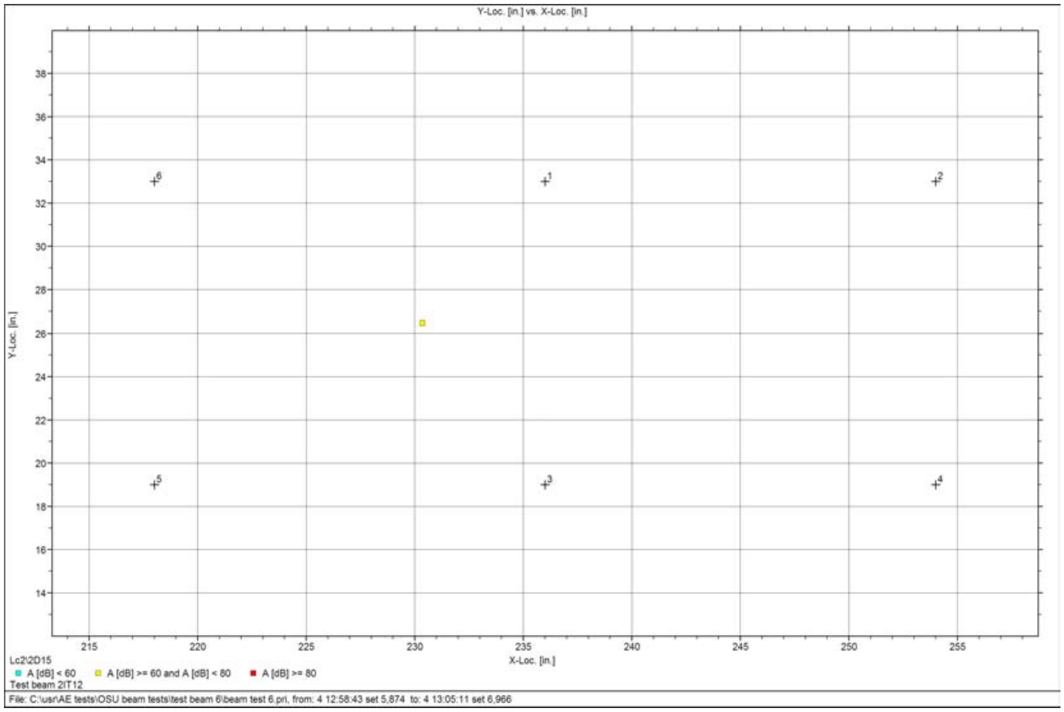

Figure 3.21 Event locations for second load cycle.

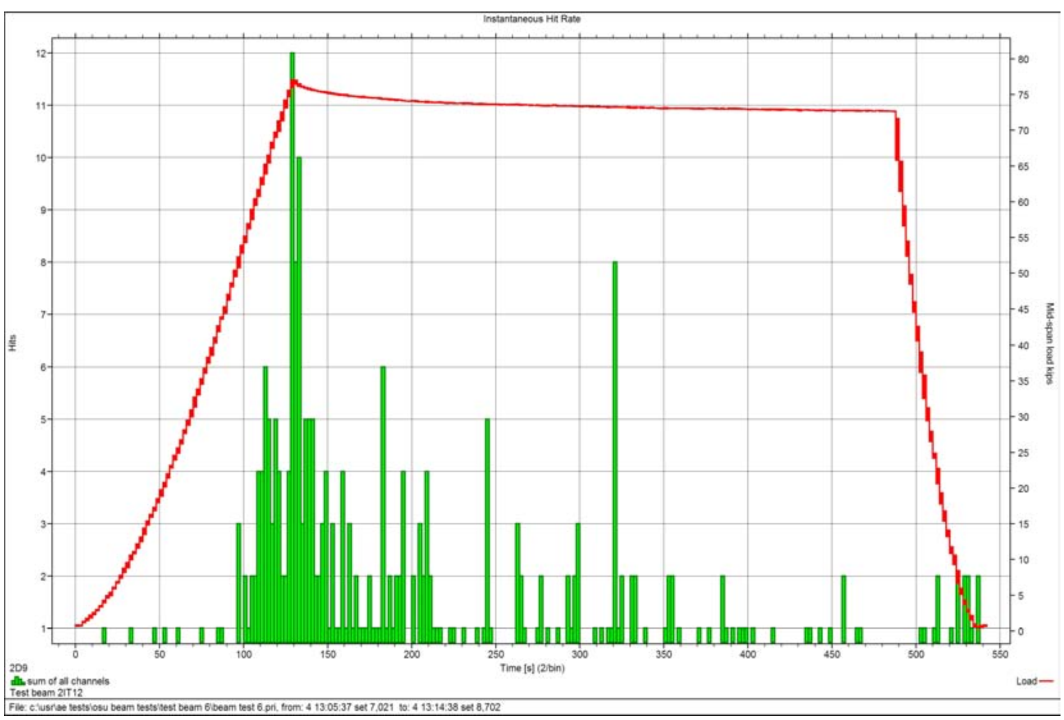

Figure 3.22 Instantaneous hit rate and mid-span load for the third load cycle.

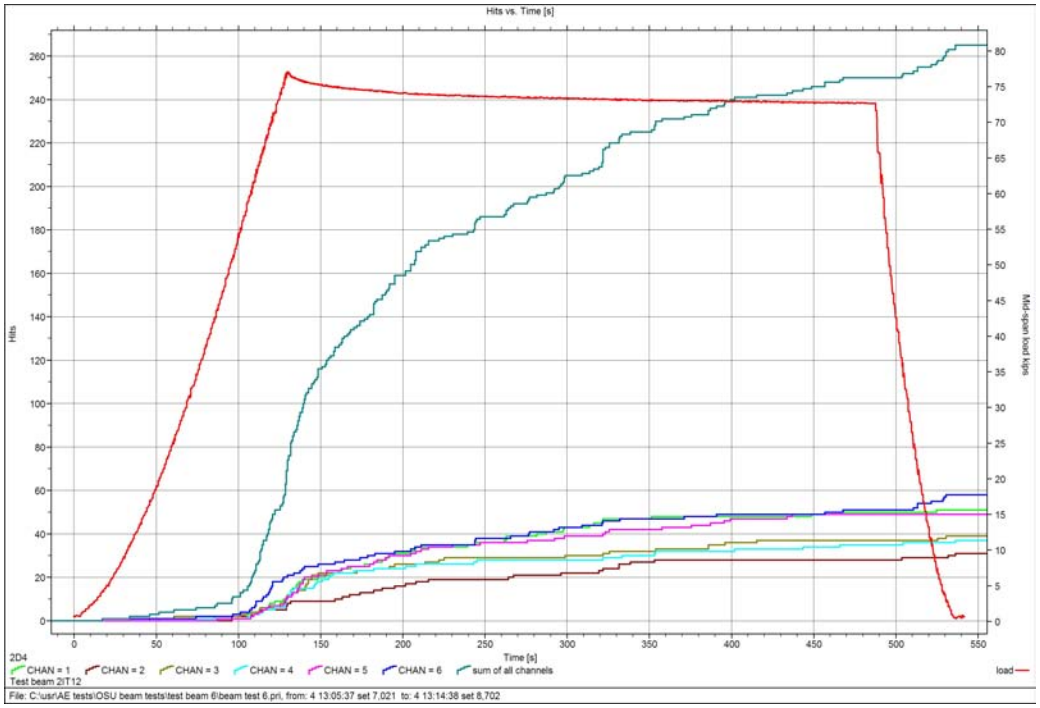

Figure 3.23 Cumulative hits and mid-span load for the third load cycle.

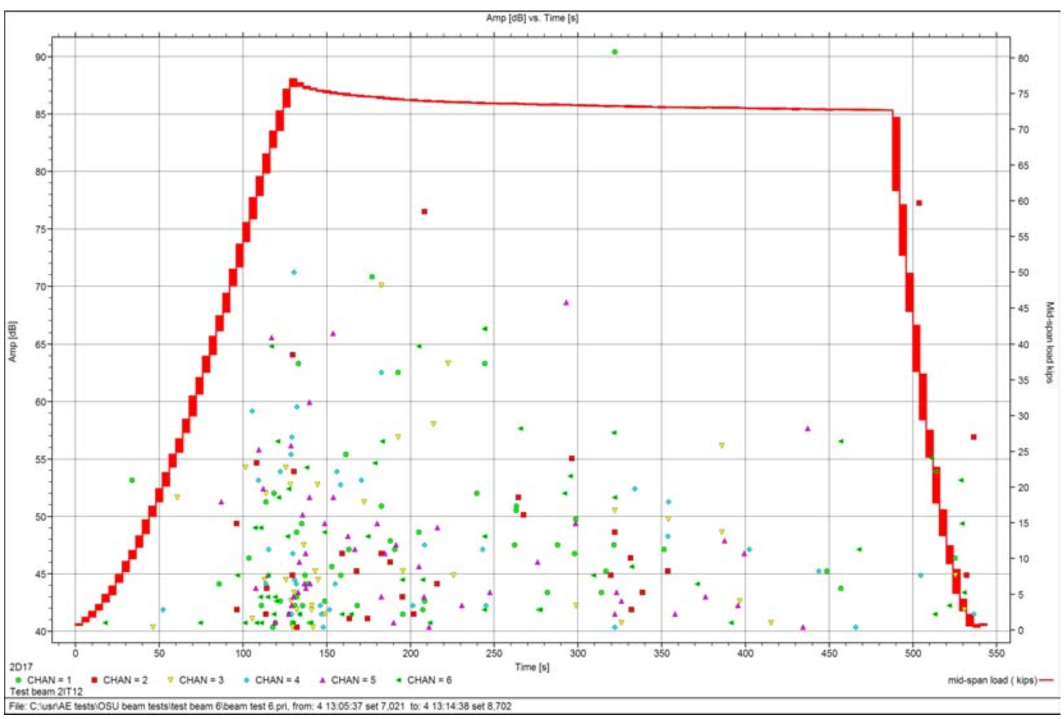

Figure 3.24 Peak amplitudes and mid-span load for the third load cycle.

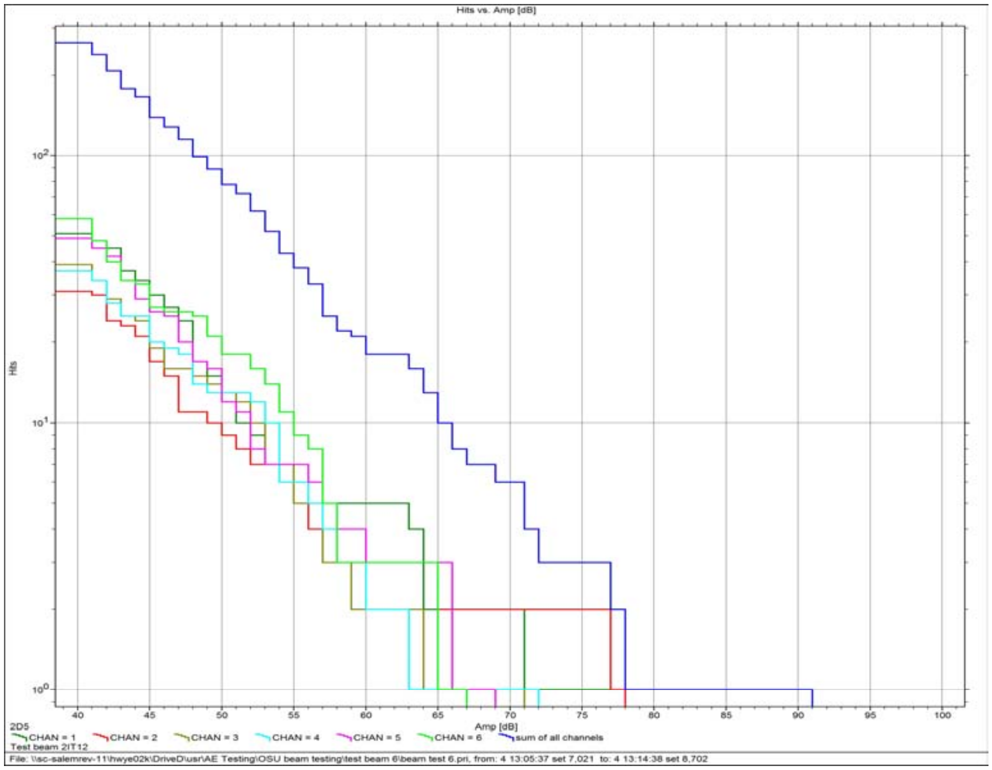

Figure 3.25 Hits versus peak amplitudes for the third load cycle.

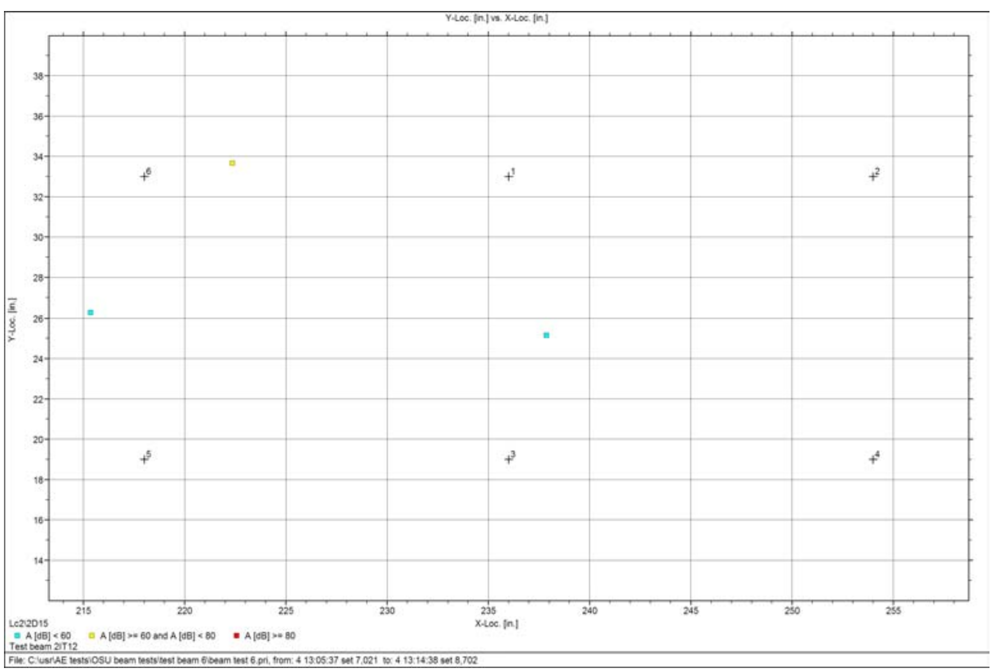

Figure 3.26 Event locations for third load cycle.

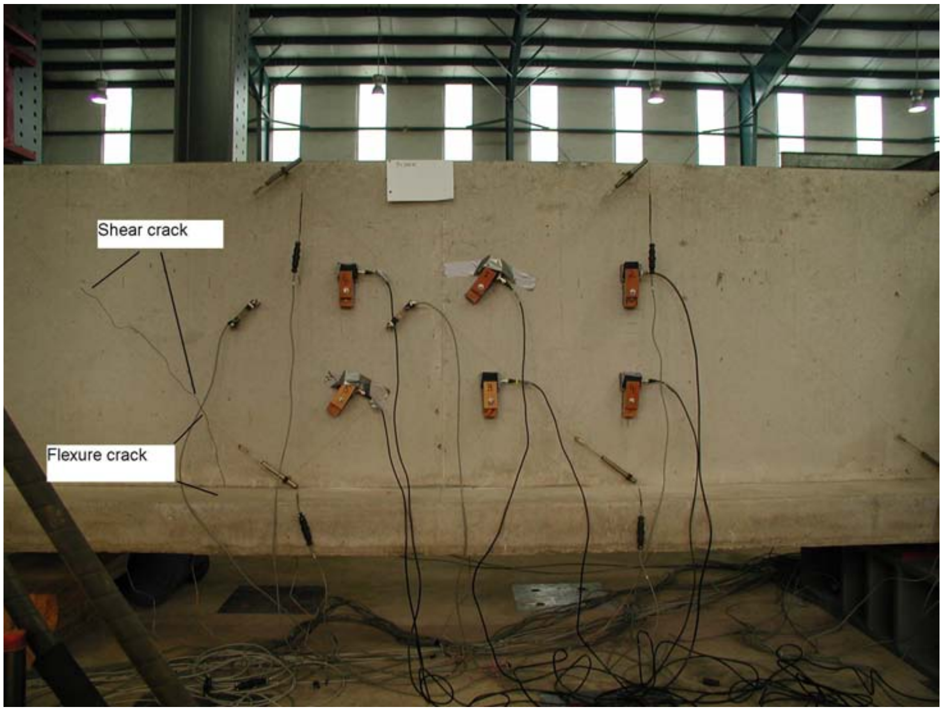

Figure 3.27 Photograph of test beam at fourth load cycle hold period.

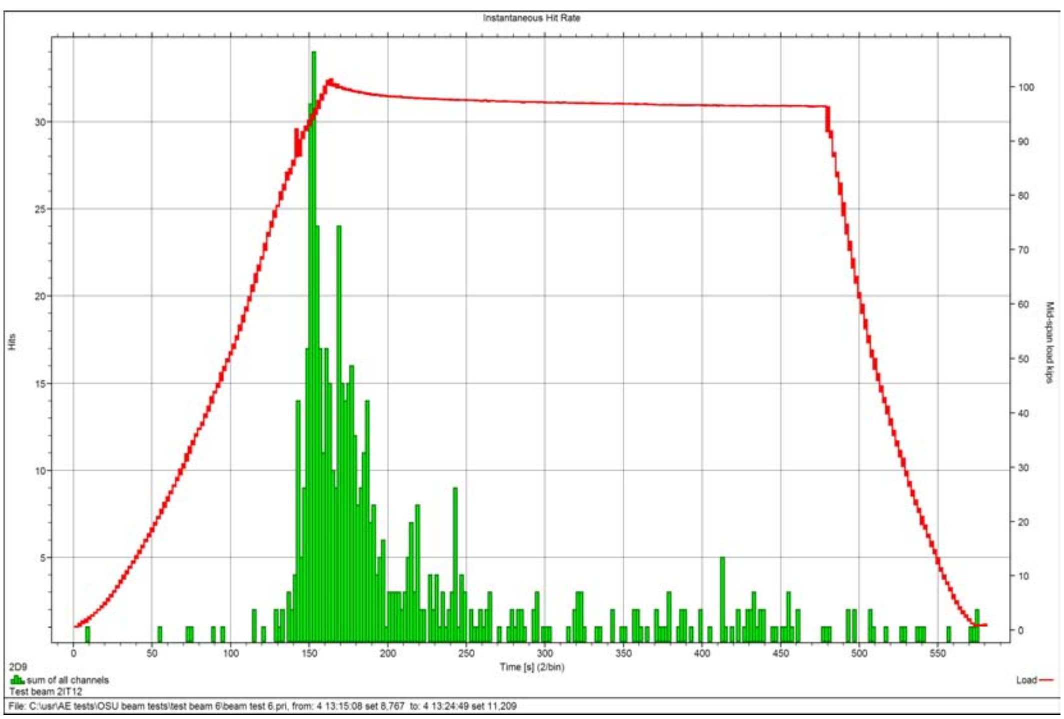

Figure 3.28 Instantaneous hit rate and mid-span load for the fourth load cycle.

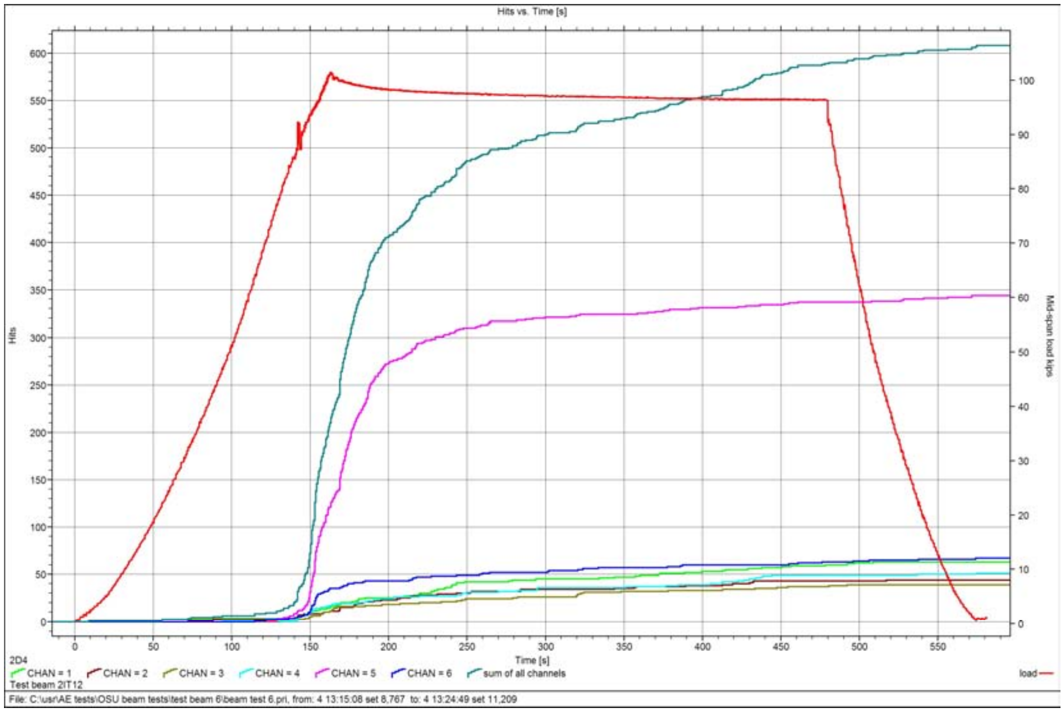

Figure 3.29 Cumulative hits and mid-span load for the fourth load cycle.

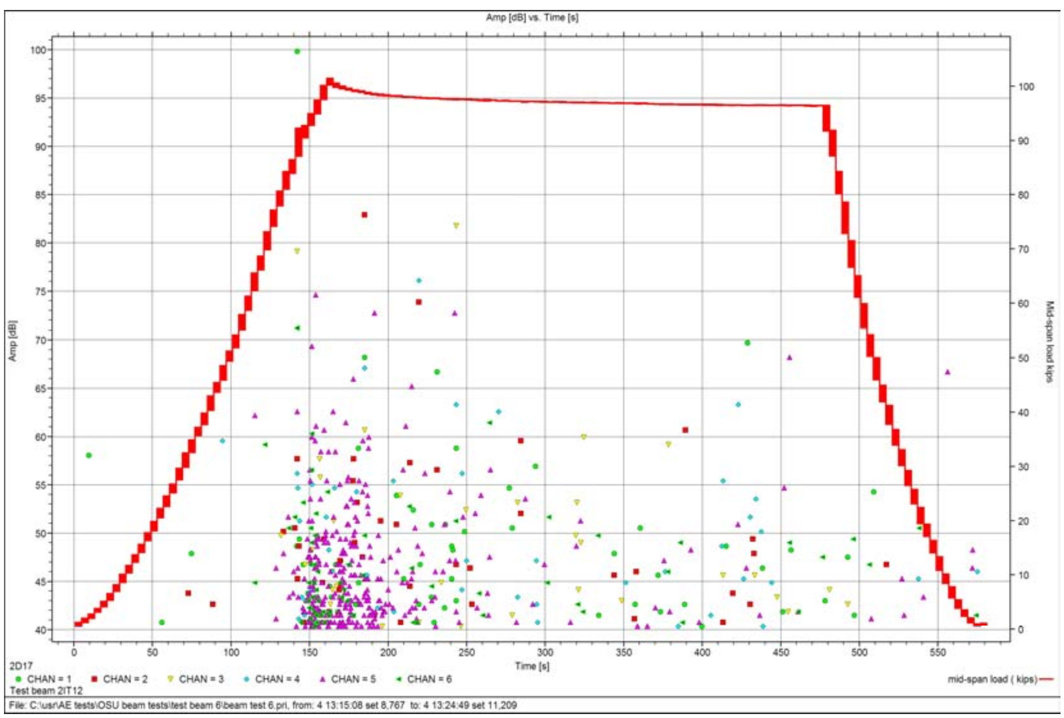

Figure 3.30 Peak amplitudes and mid-span load for the fourth load cycle.

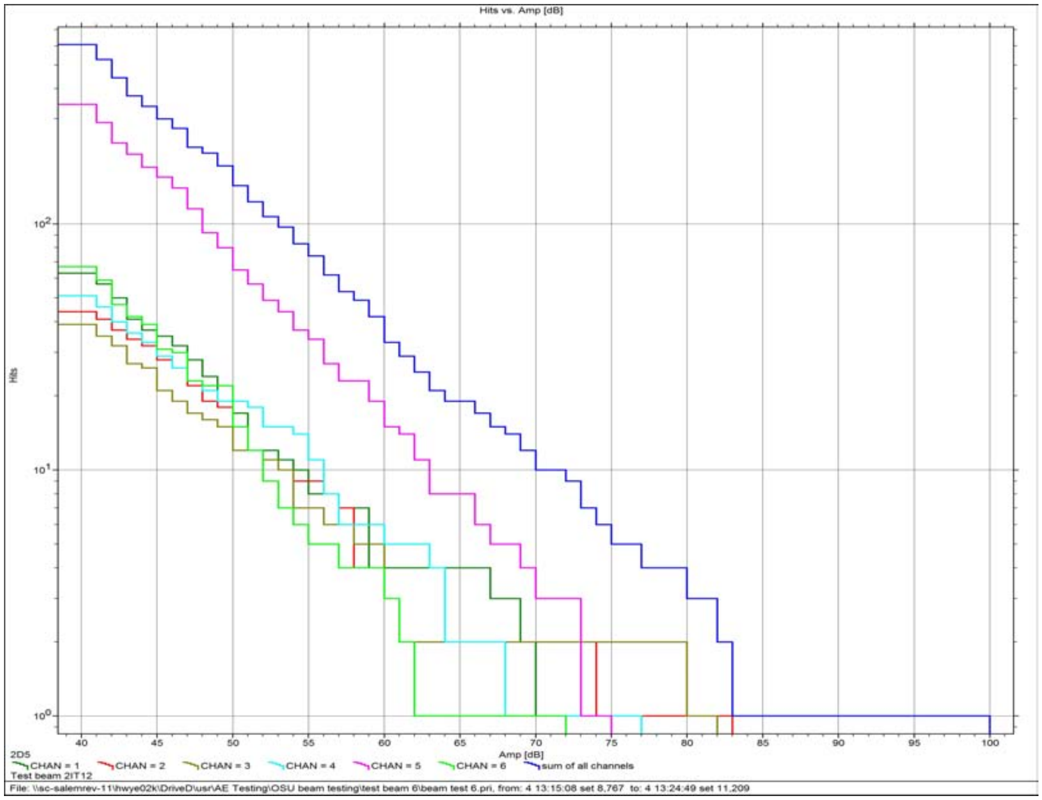

Figure 3.31 Hits versus peak amplitudes for the fourth load cycle.

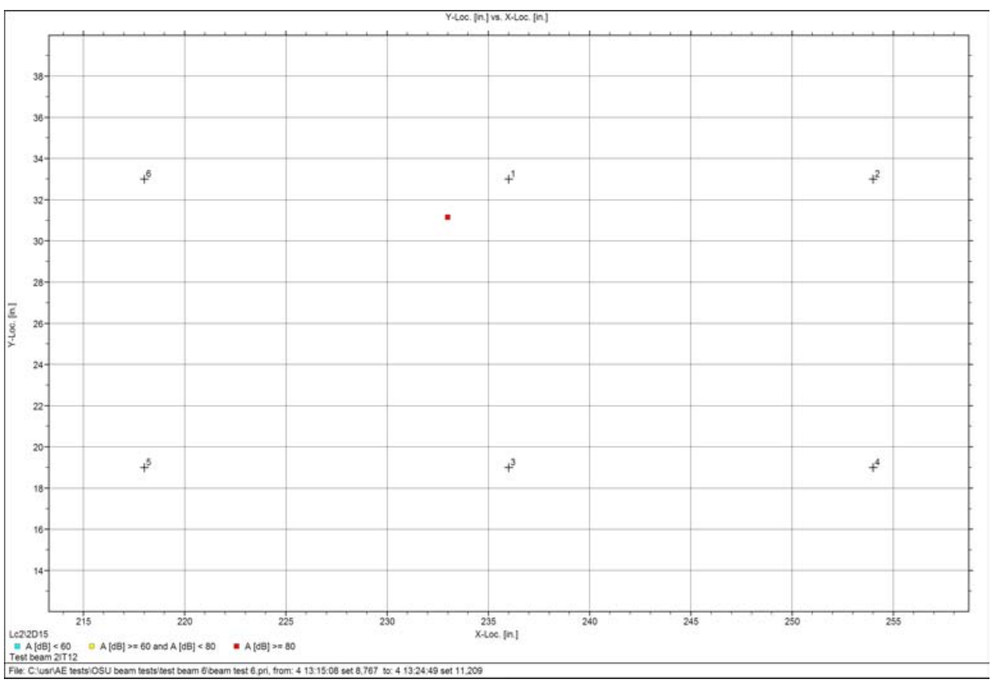

Figure 3.32 Event locations for third fourth cycle.

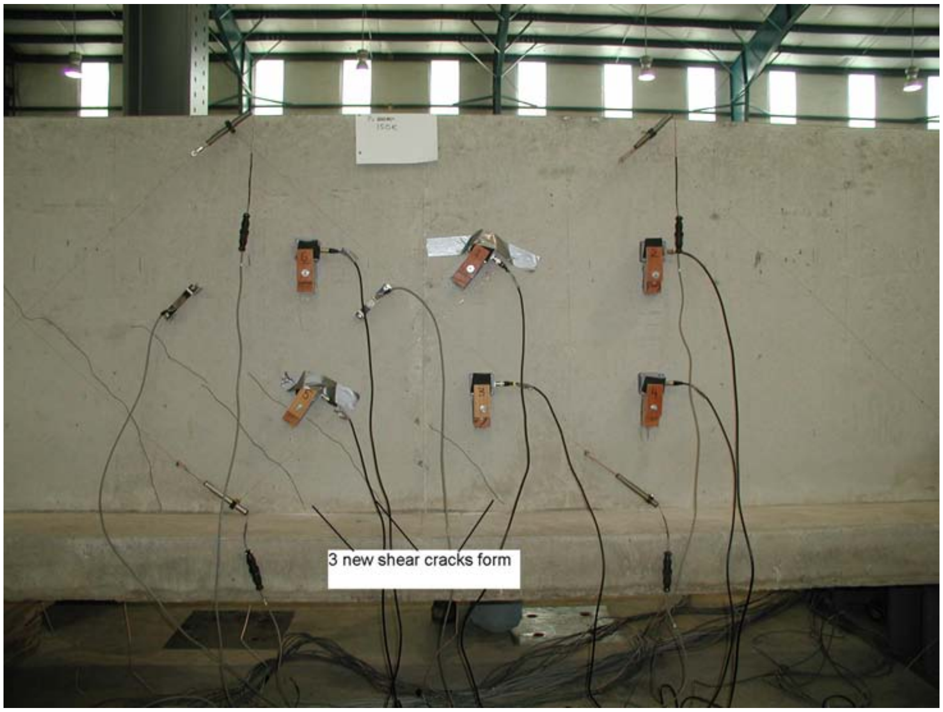

Figure 3.33 Photographs of test beam at fifth load cycle hold period.

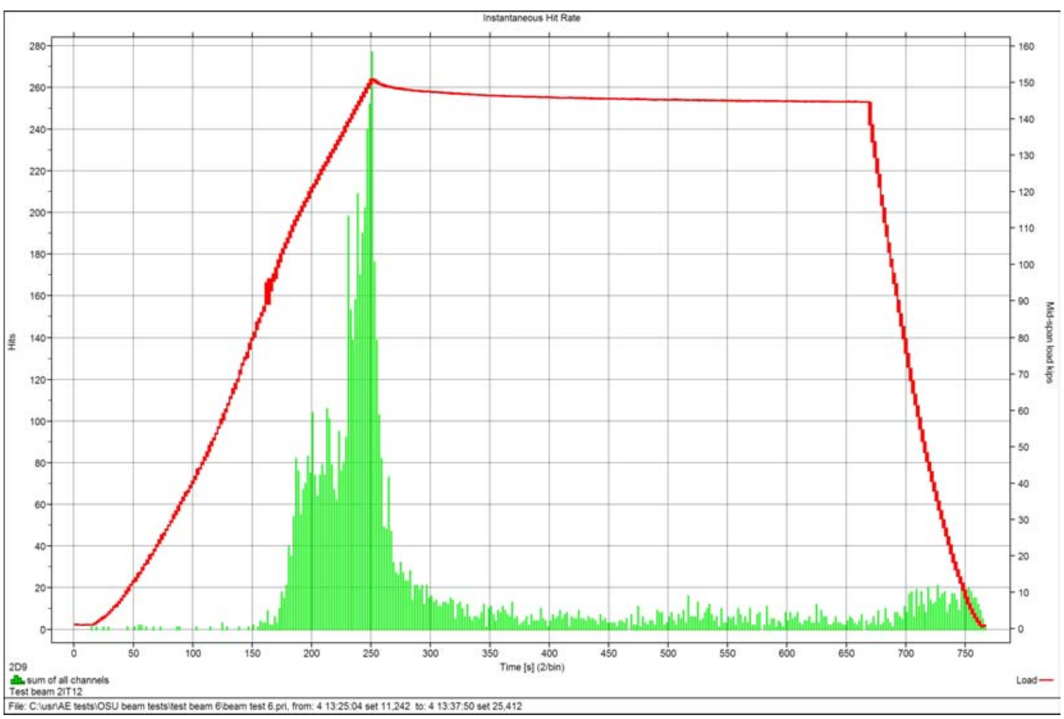

Figure 3.34 Instantaneous hit rate and mid-span load for the fifth load cycle.

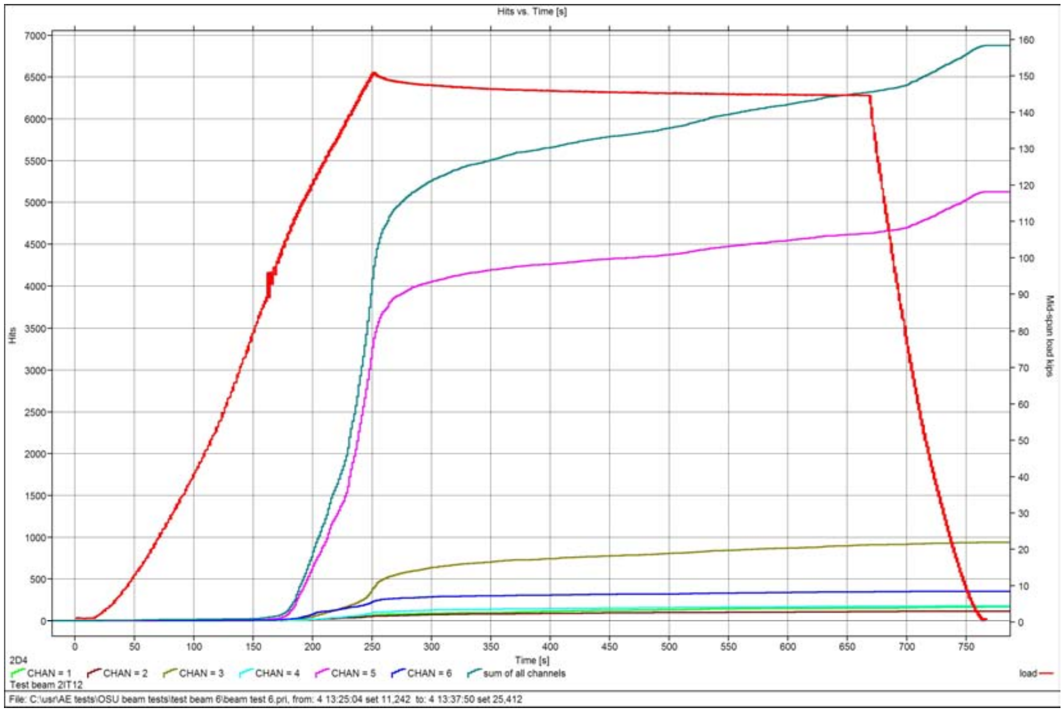

Figure 3.35 Cumulative hits and mid-span load for the fifth load cycle.

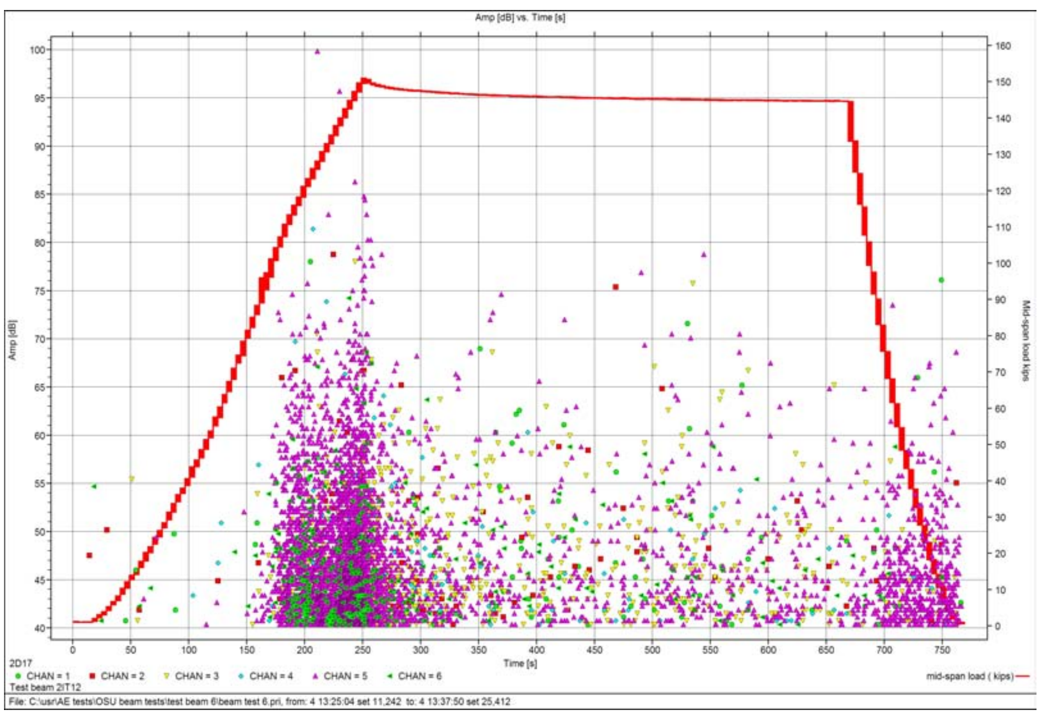

Figure 3.36 Peak amplitudes and mid-span load for the fifth load cycle.

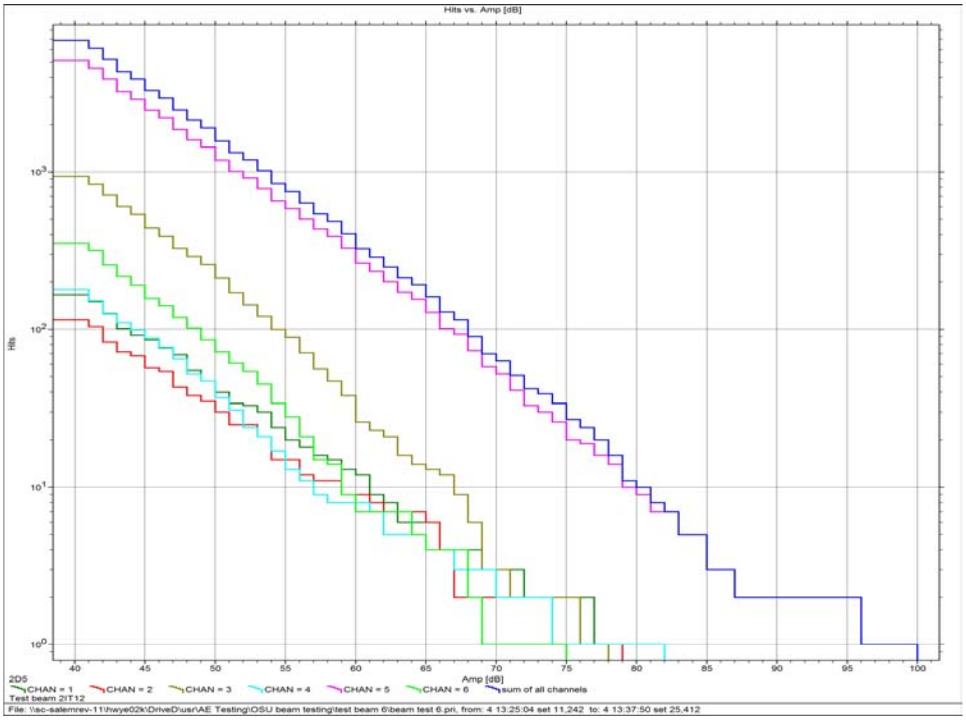

Figure 3.37 Hits versus peak amplitudes for the fifth load cycle.

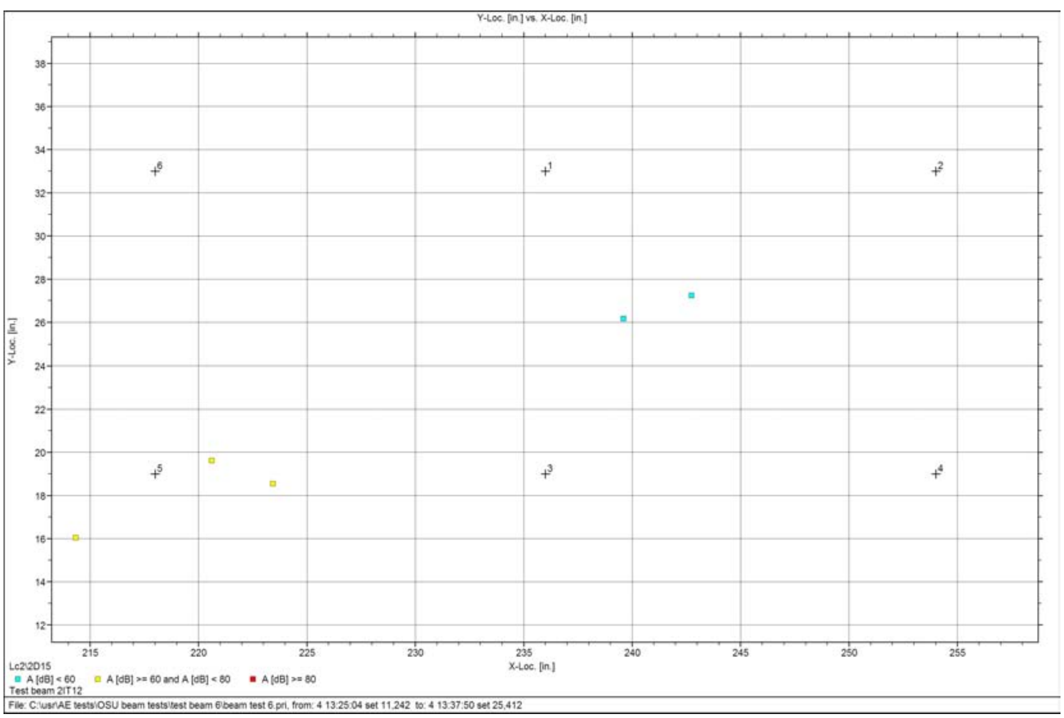

Figure 3.38 Event locations for third fifth cycle.

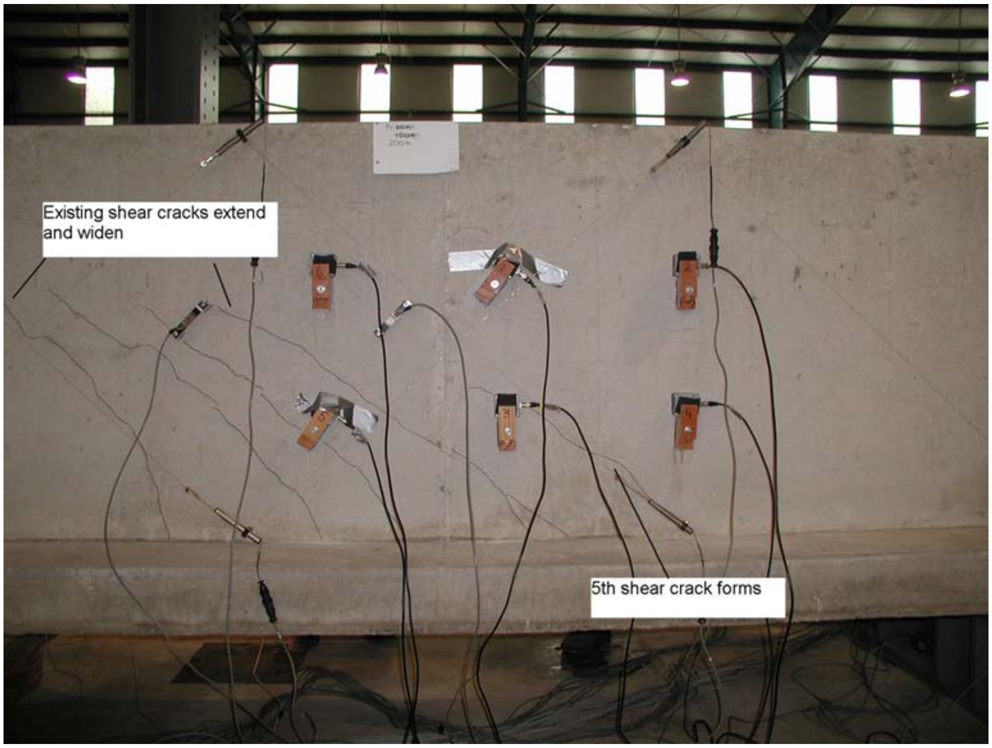

Figure 3.39 Photographs of test beam at sixth load cycle hold period.

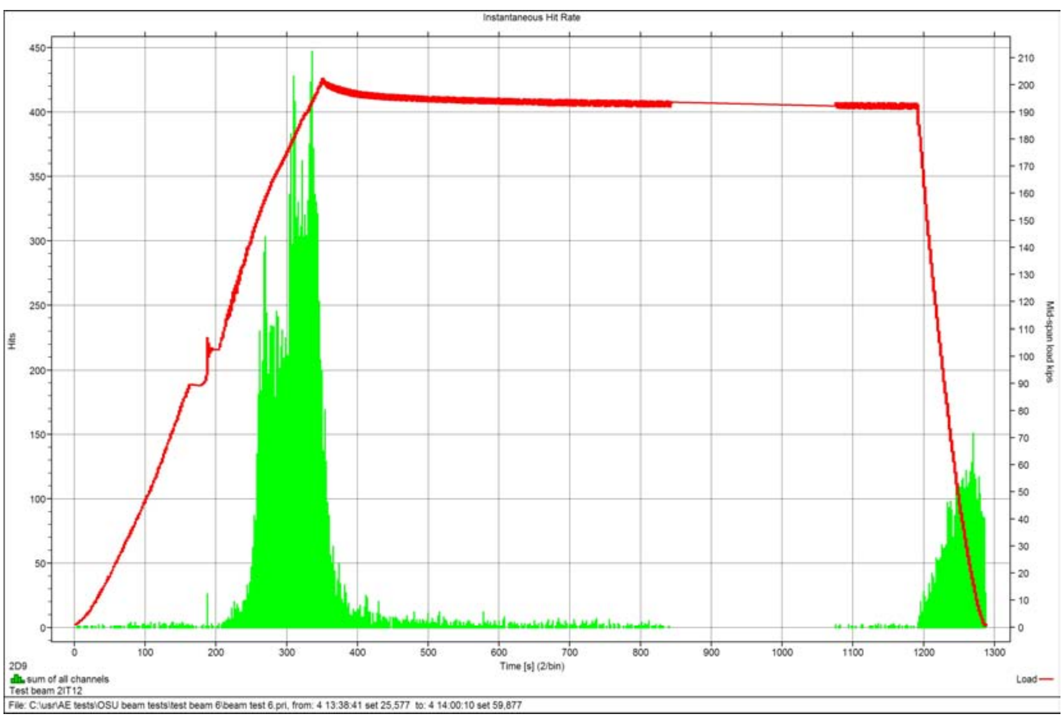

Figure 3.40 Instantaneous hit rate and mid-span load for the sixth load cycle.

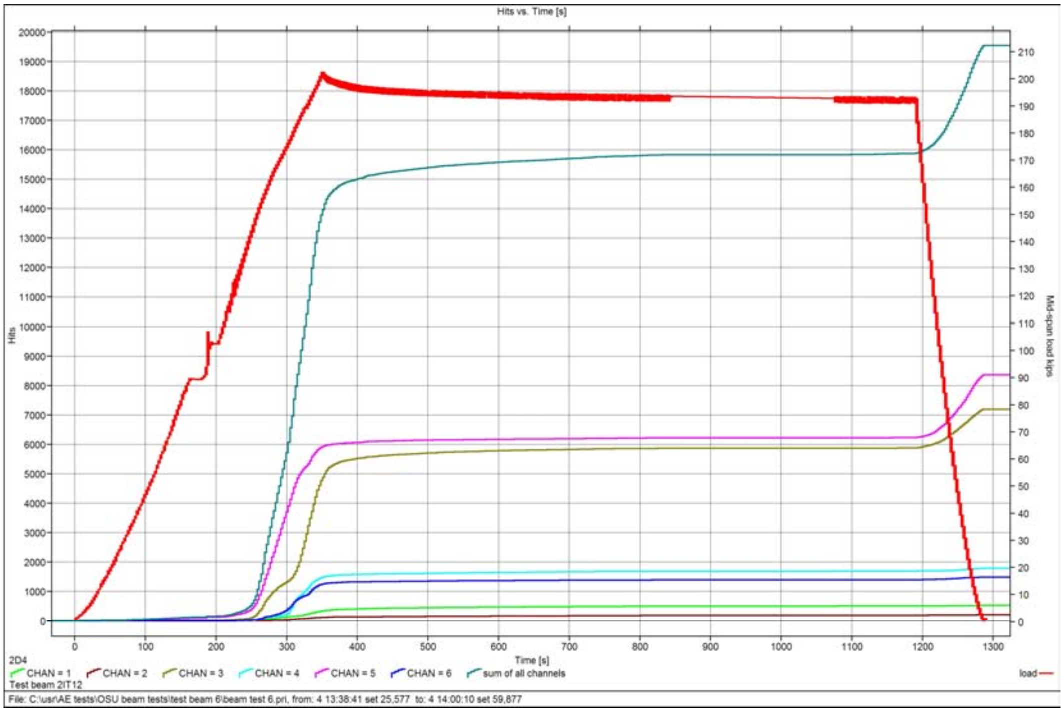

Figure 3.41 Cumulative hits and mid-span load for the sixth load cycle.

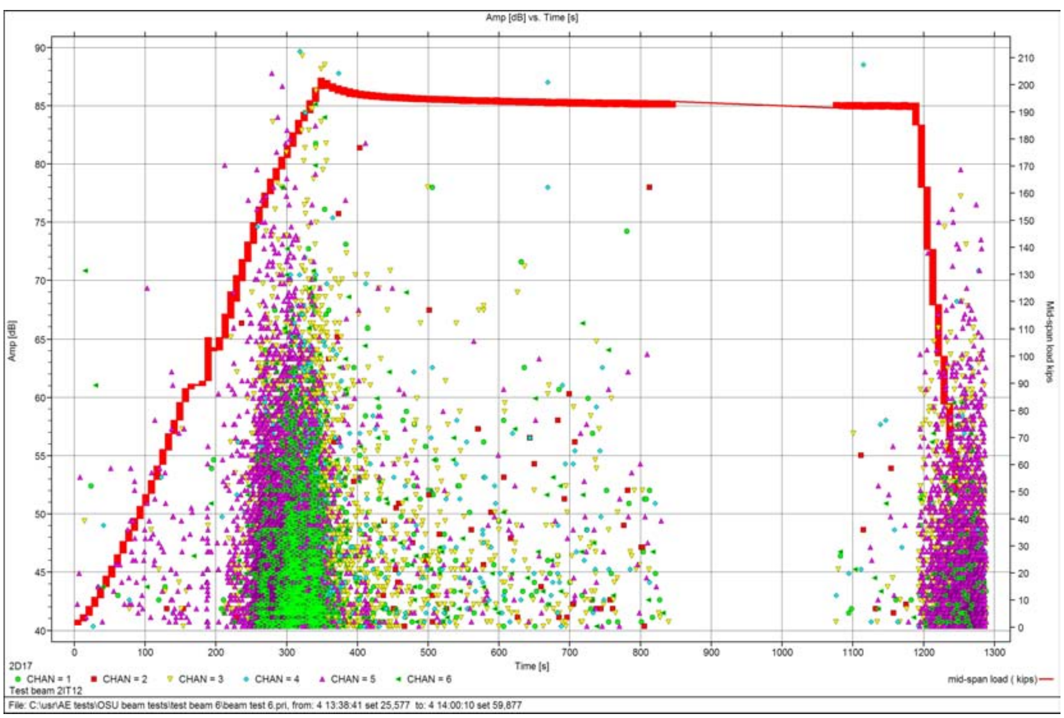

Figure 3.42 Peak amplitudes and mid-span load for the sixth load cycle.

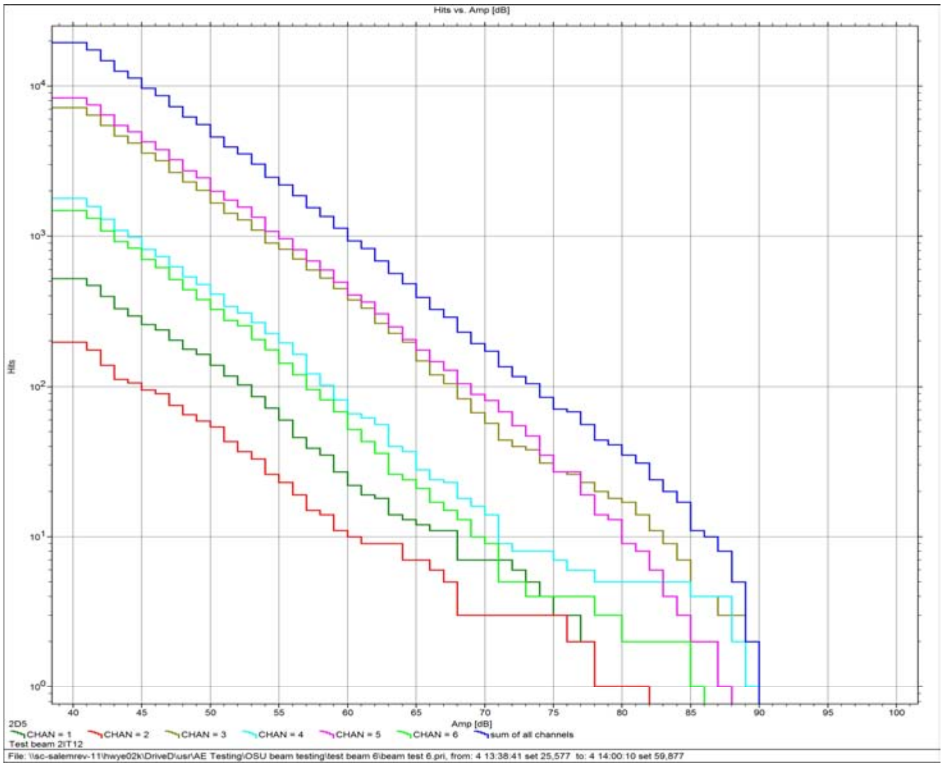

Figure 3.43 Hits versus peak amplitudes for the sixth load cycle.

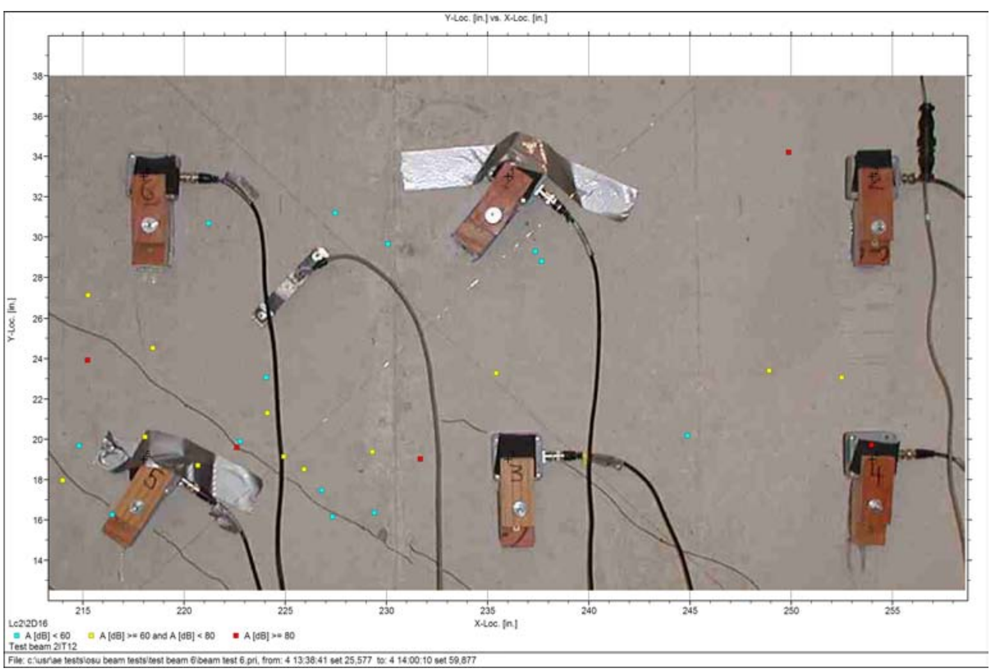

Figure 3.44 Event locations for third sixth cycle.

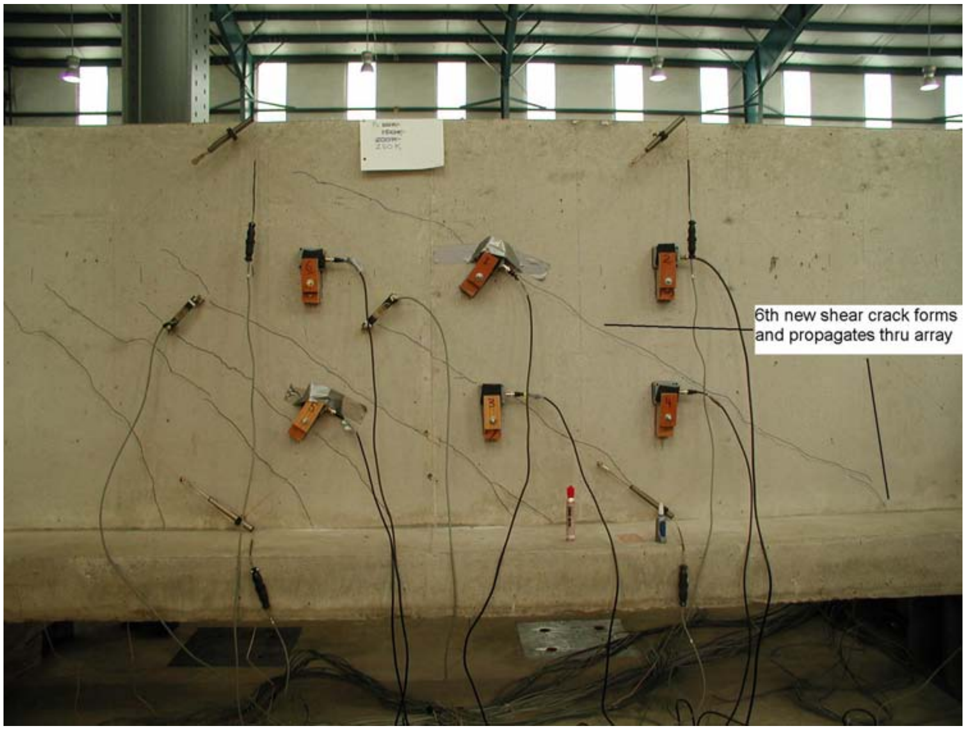

Figure 3.45 Photographs of test beam at seventh load cycle hold period.

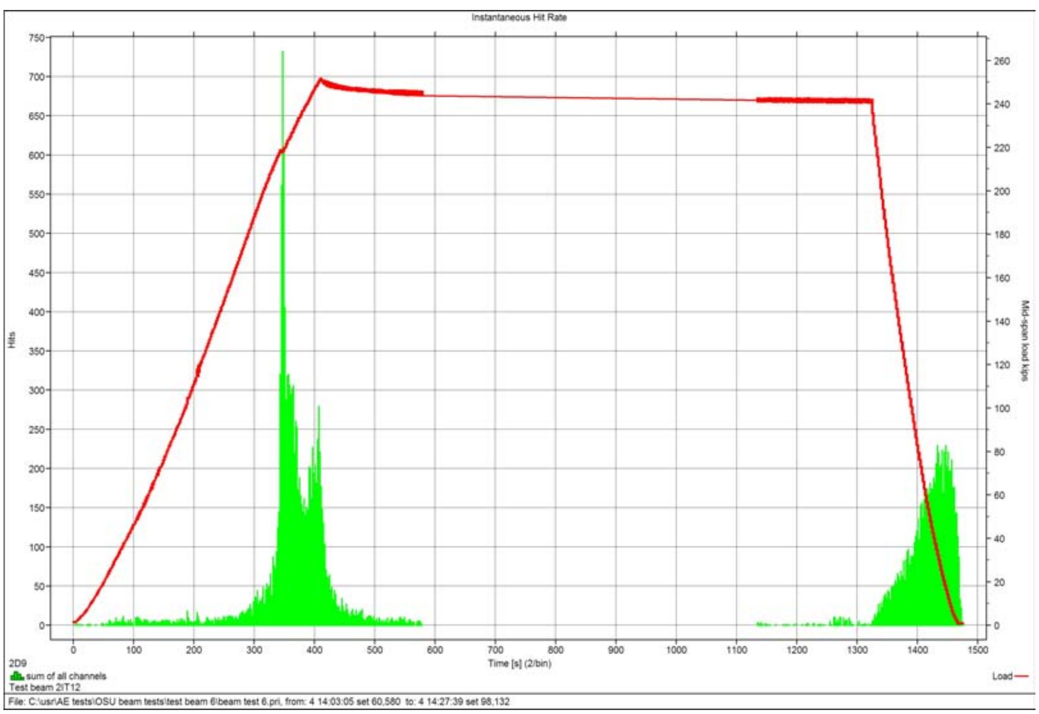

Figure 3.46 Instantaneous hit rate and mid-span load for the seventh load cycle.

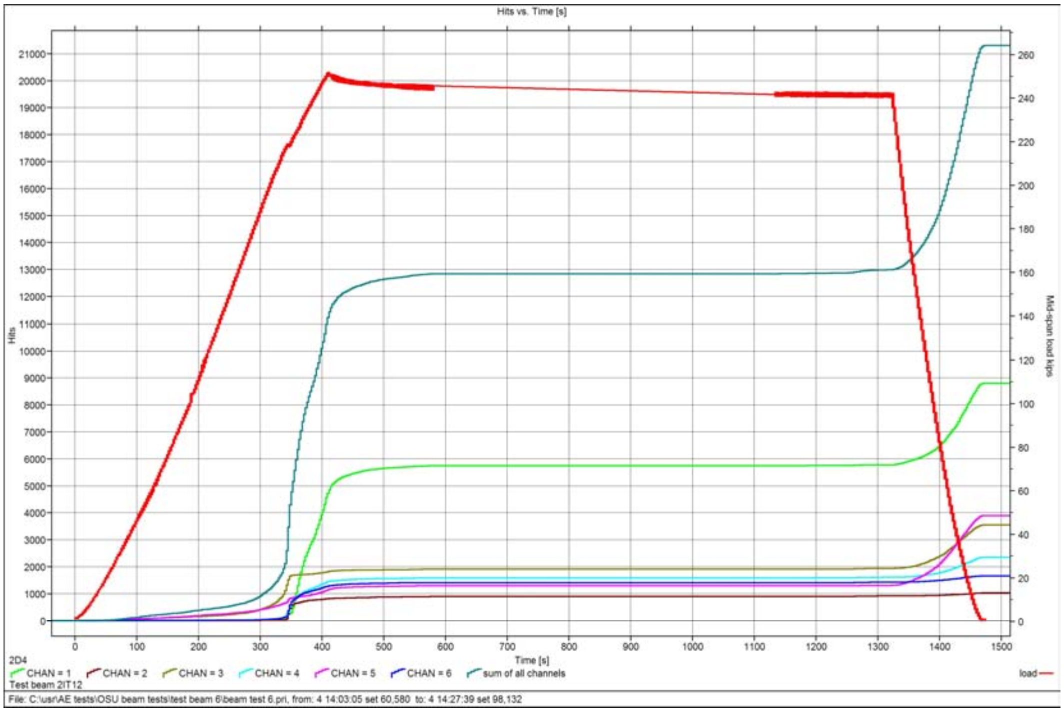

Figure 3.47 Cumulative hits and mid-span load for the seventh load cycle.

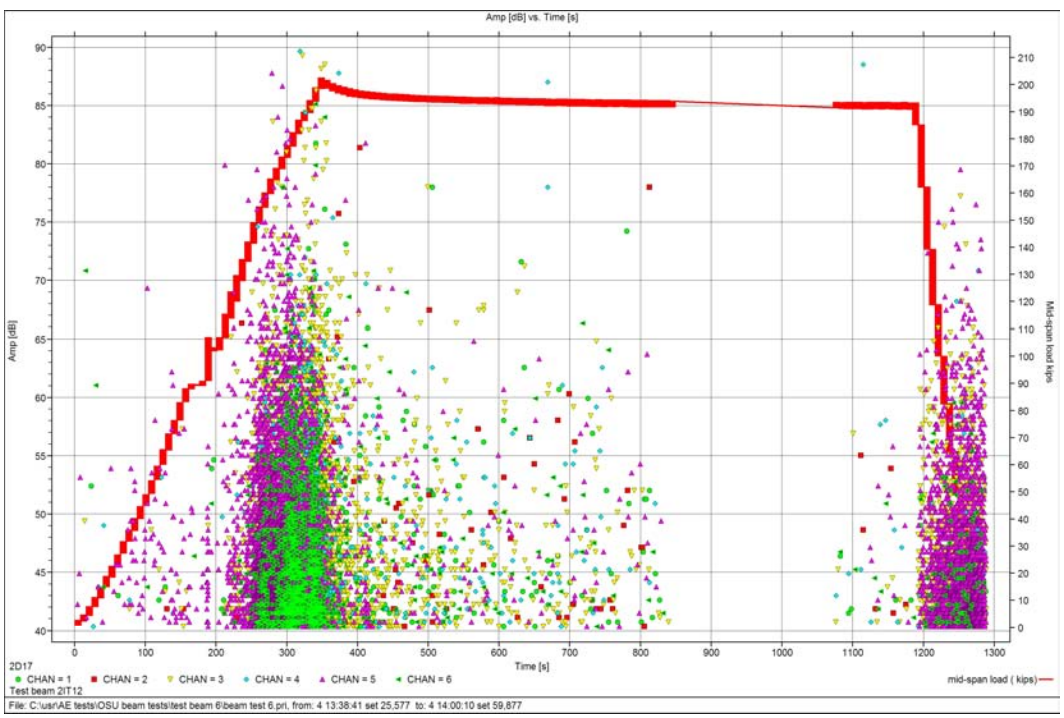

Figure 3.48 Peak amplitudes and mid-span load for the seventh load cycle.

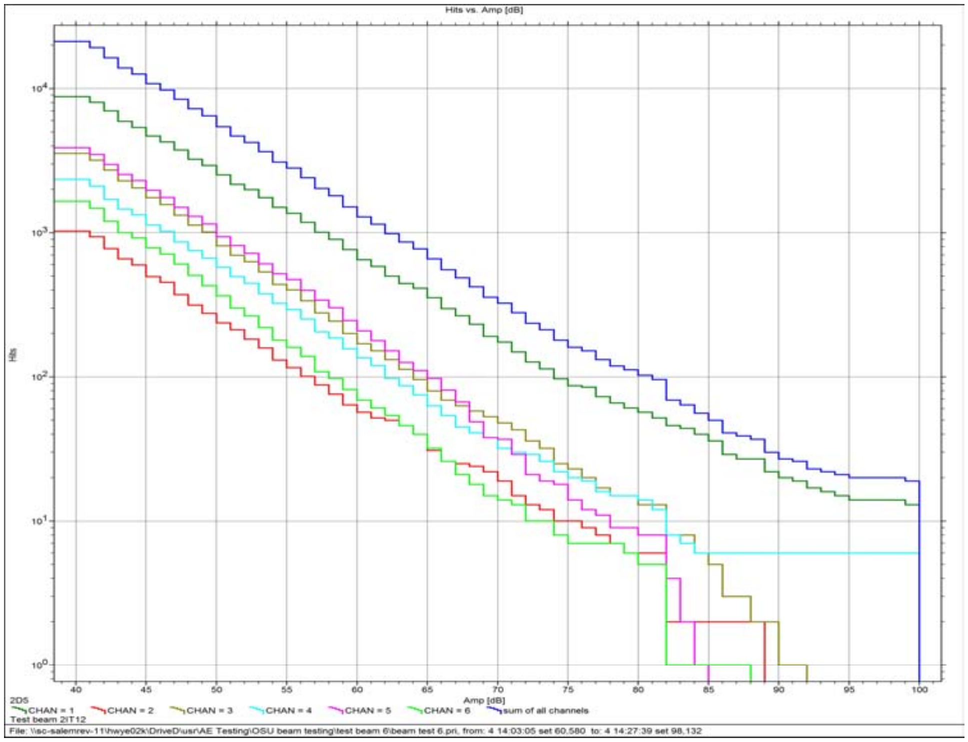

Figure 3.49 Hits versus peak amplitudes for the seventh load cycle.

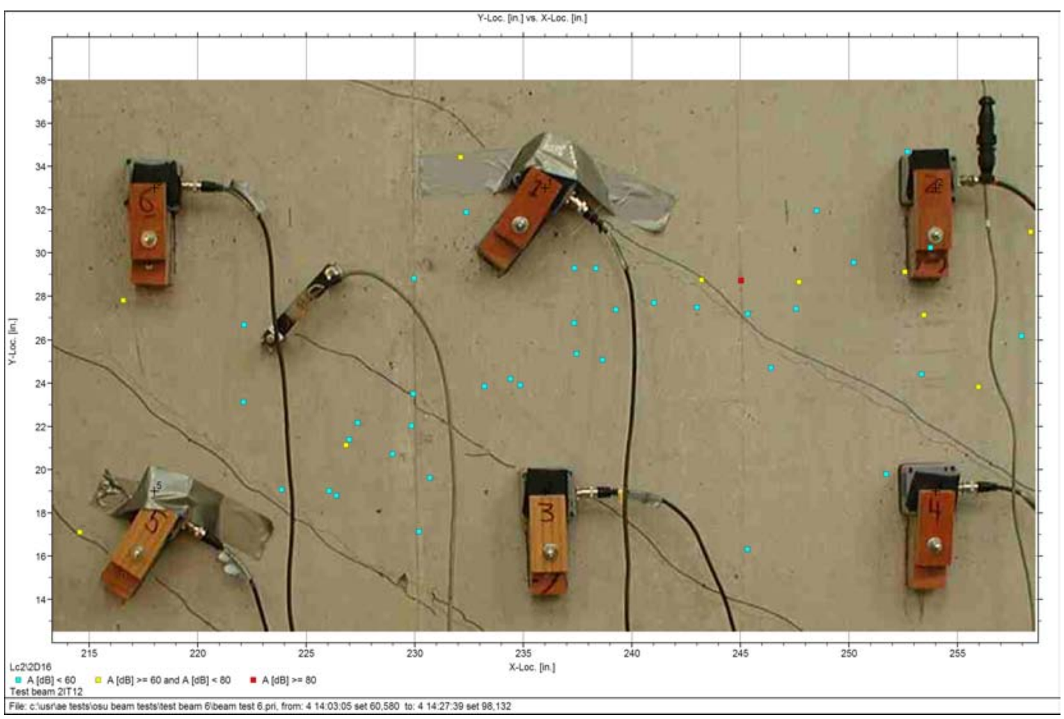

Figure 3.50 Event locations for third seventh load cycle.

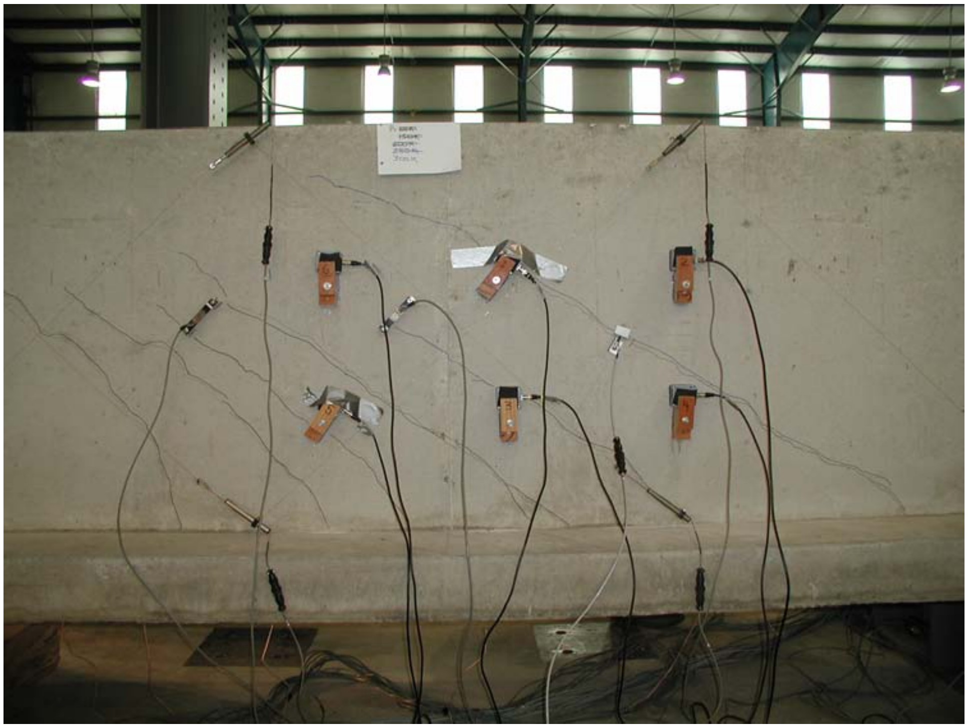

Figure 3.51 Photographs of test beam at eighth load cycle hold period.

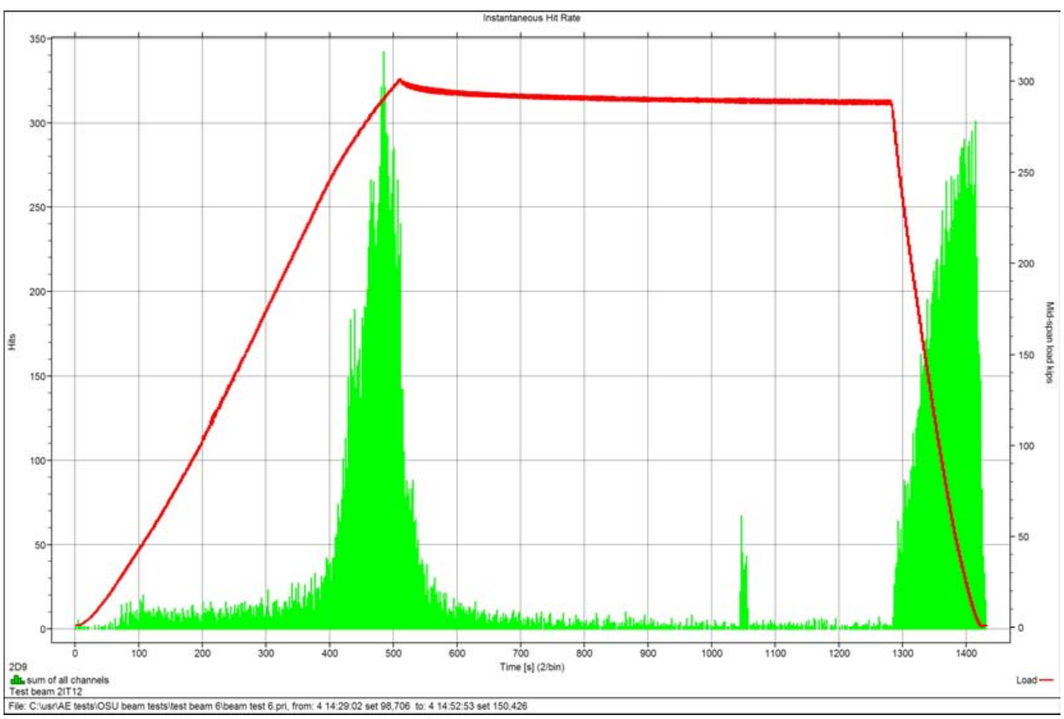

Figure 3.52 Instantaneous hit rate and mid-span load for the eighth load cycle.

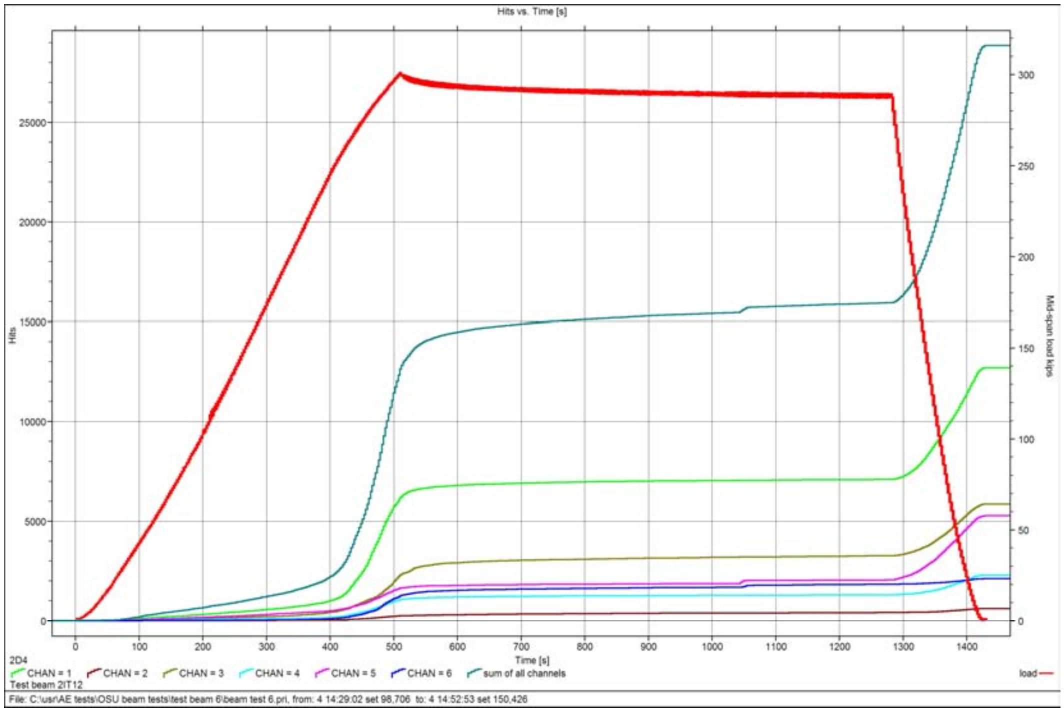

Figure 3.53 Cumulative hits and mid-span load for the eighth load cycle.

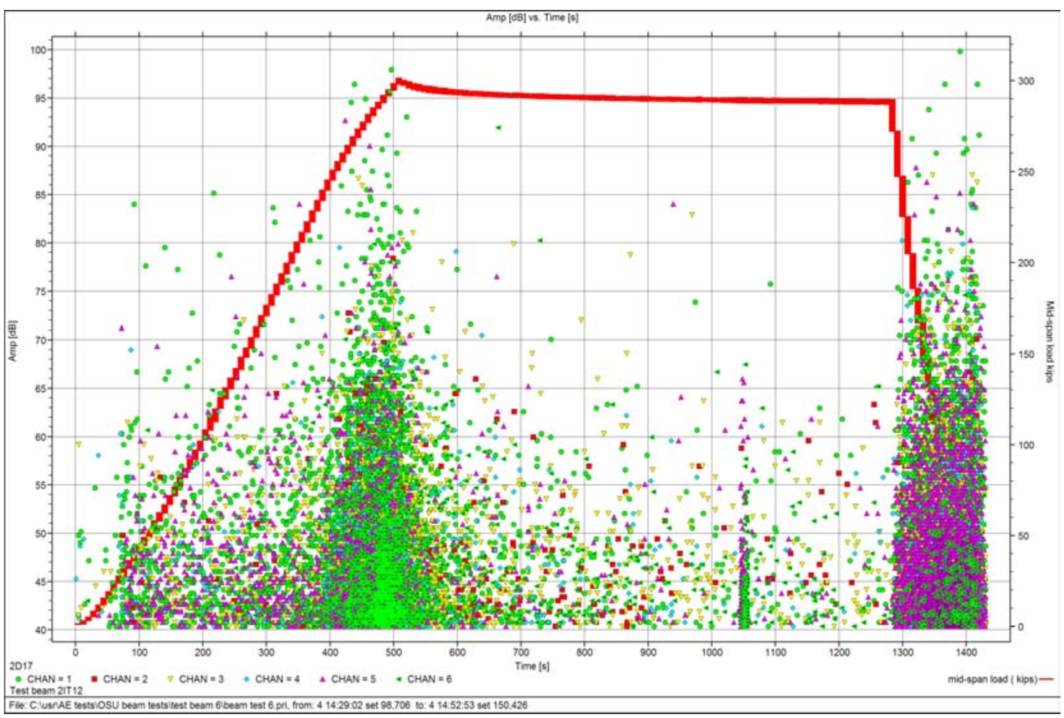

Figure 3.54 Peak amplitudes and mid-span load for the eighth load cycle.

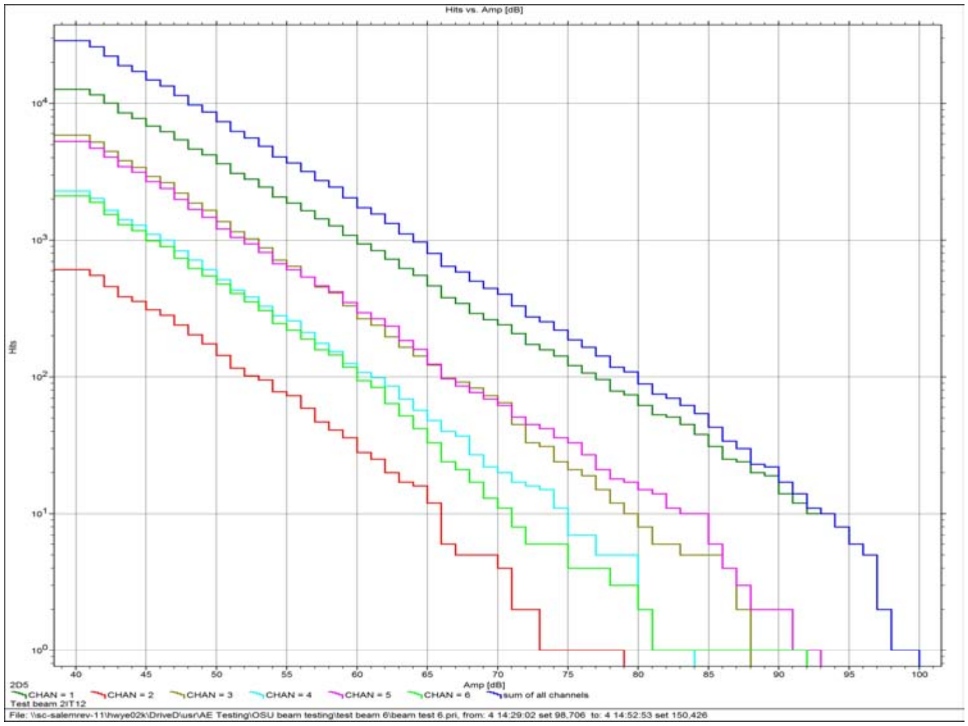

Figure 3.55 Hits versus peak amplitudes for the eighth load cycle.

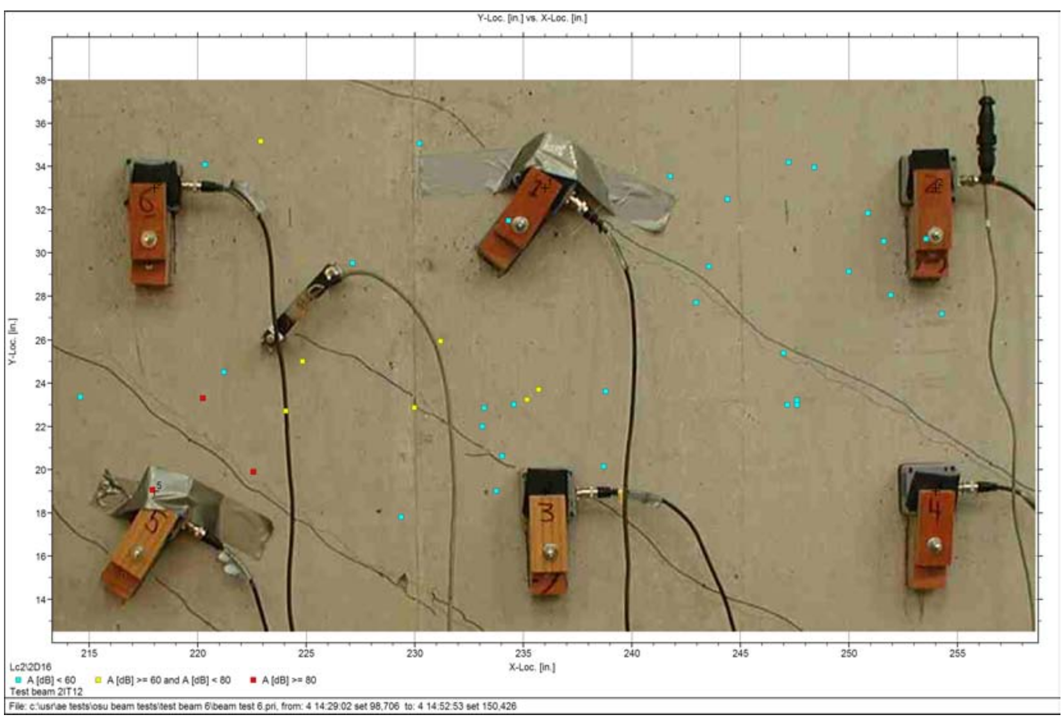

Figure 3.56 Event locations for third eighth load cycle.

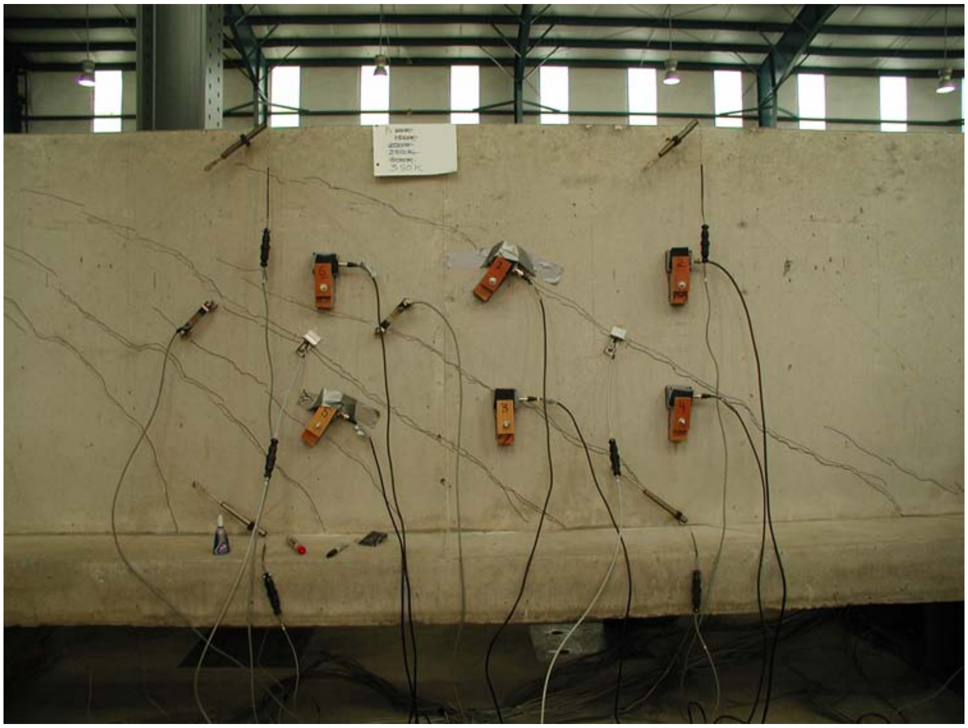

Figure 3.57 Photographs of test beam at ninth load cycle hold period.

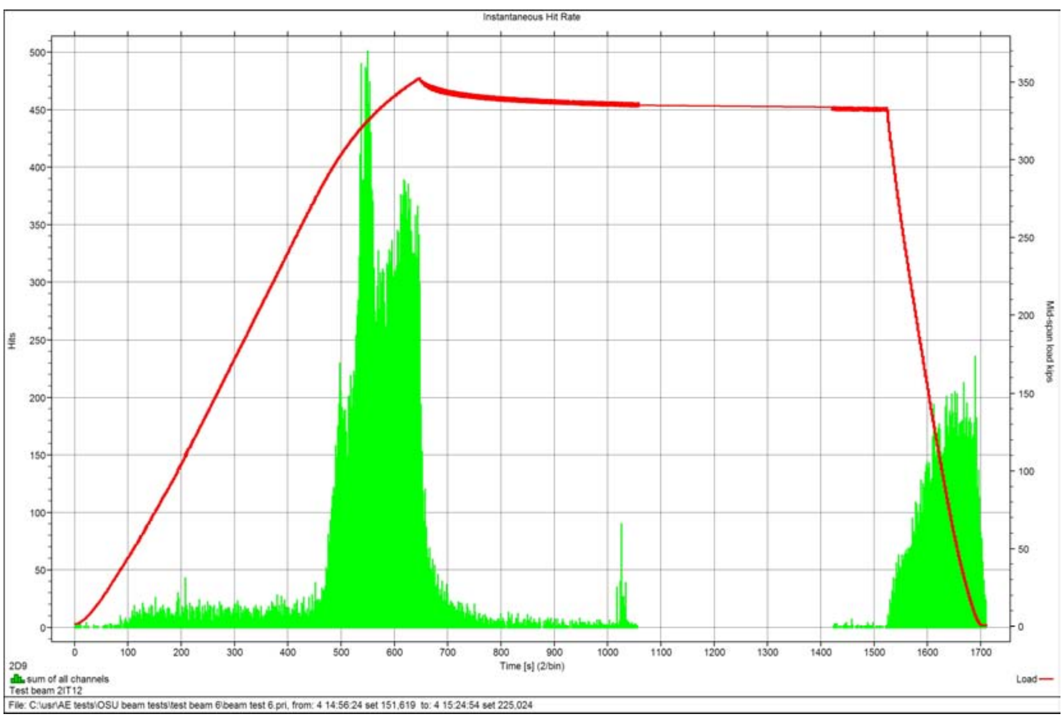

Figure 3.58 Instantaneous hit rate and mid-span load for the ninth load cycle.

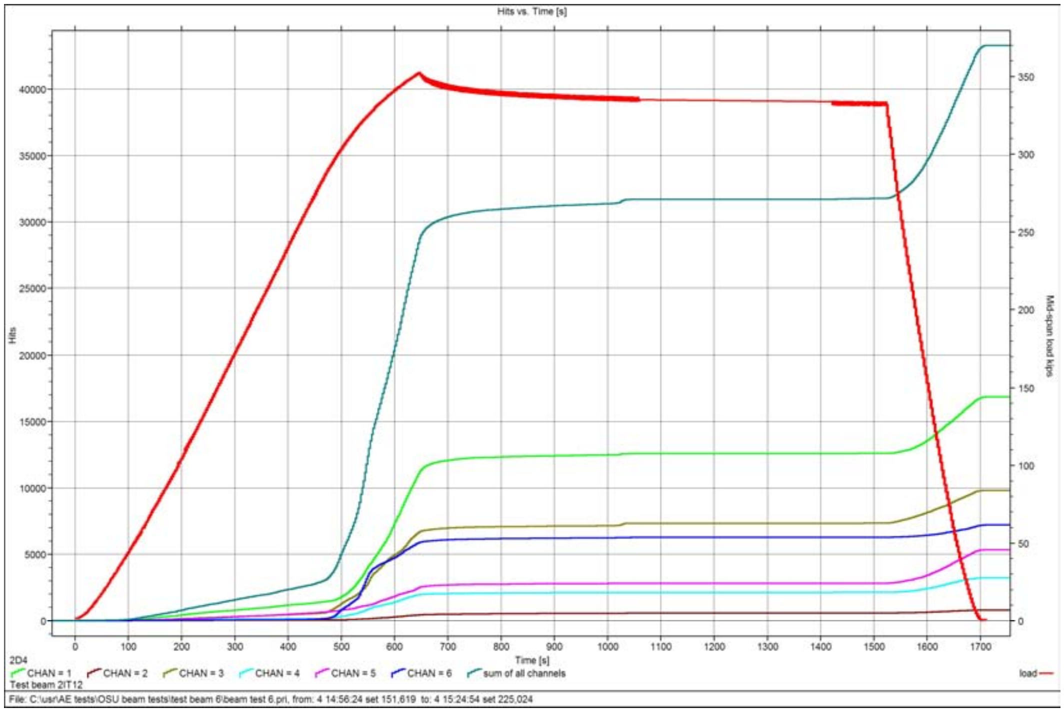

Figure 3.59 Cumulative hits and mid-span load for the ninth load cycle.

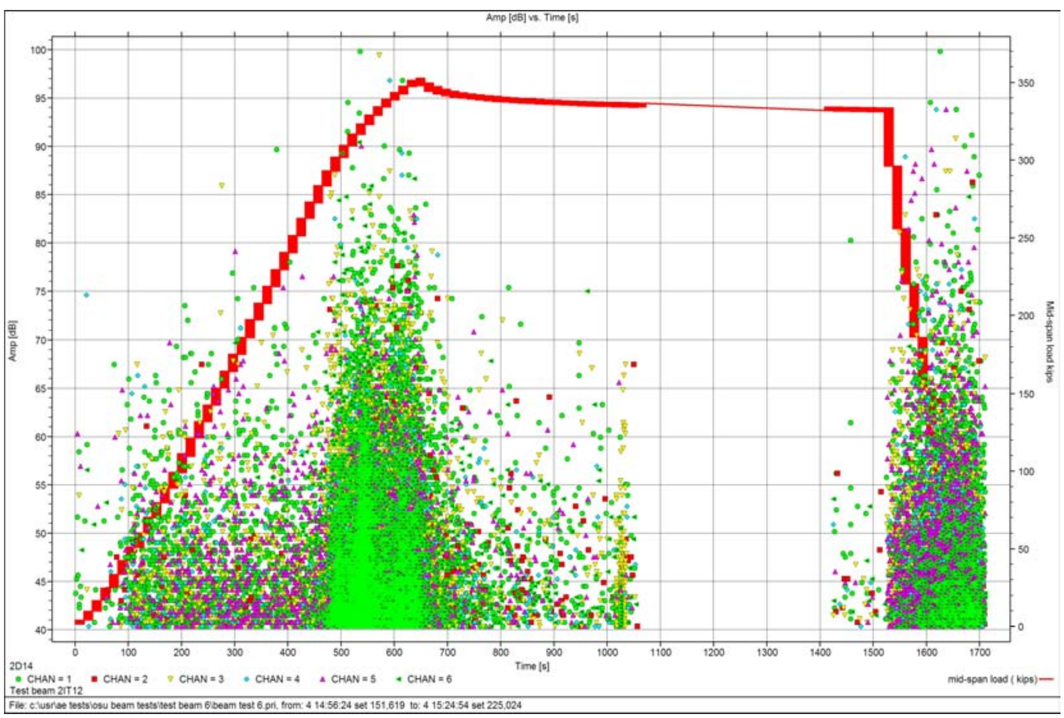

Figure 3.60 Peak amplitudes and mid-span load for the ninth load cycle.

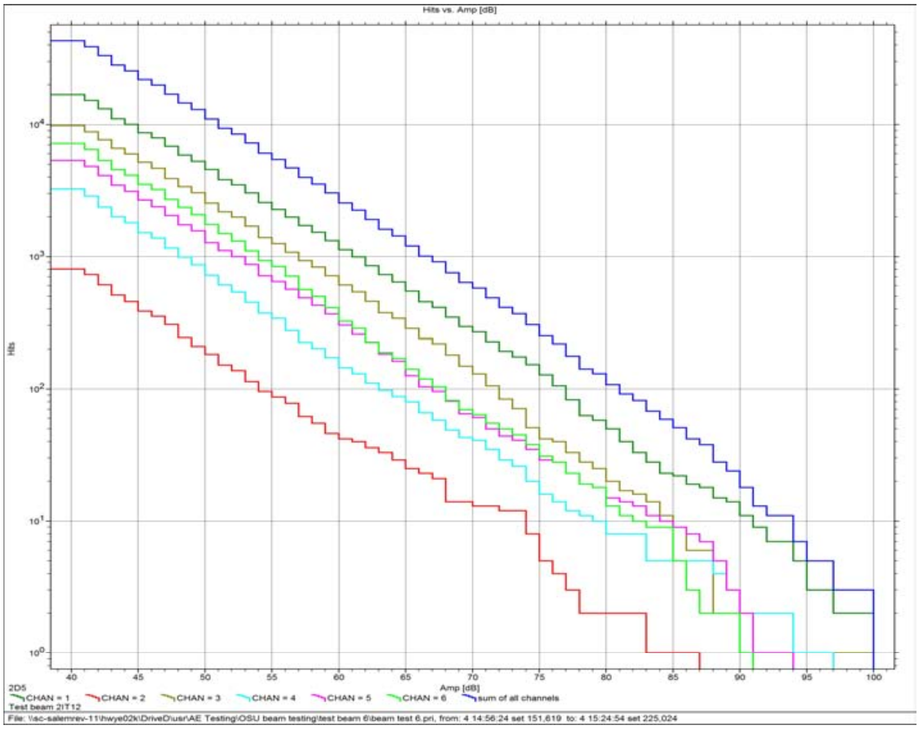

Figure 3.61 Hits versus peak amplitudes for the ninth load cycle.

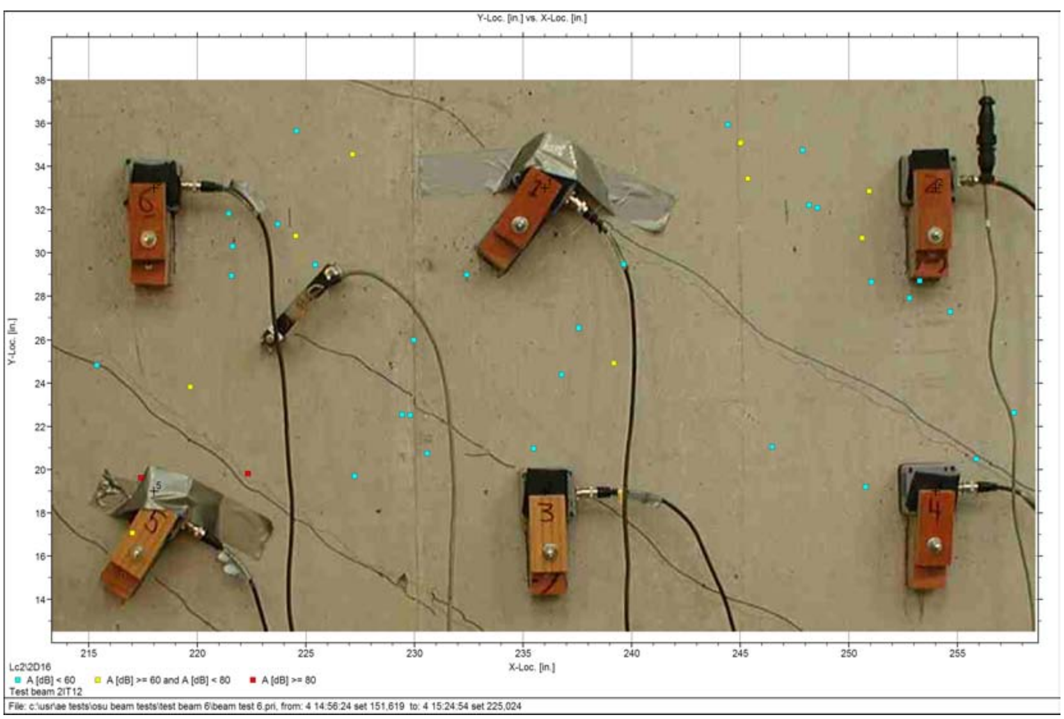

Figure 3.62 Event locations for the ninth load cycle.

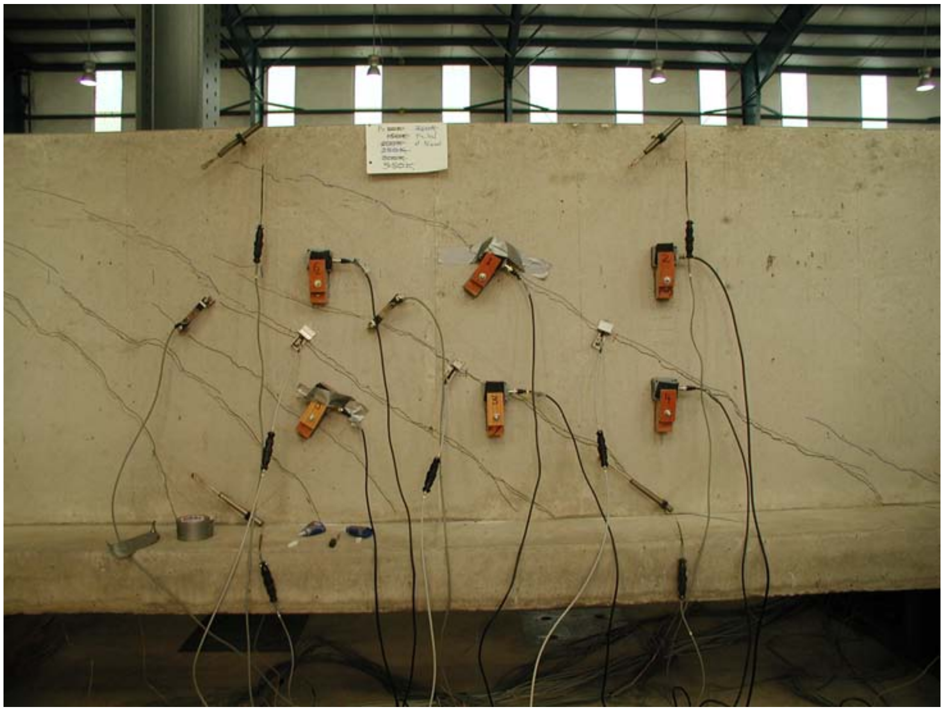

Figure 3.62 Photographs of test beam after failure load cycle.

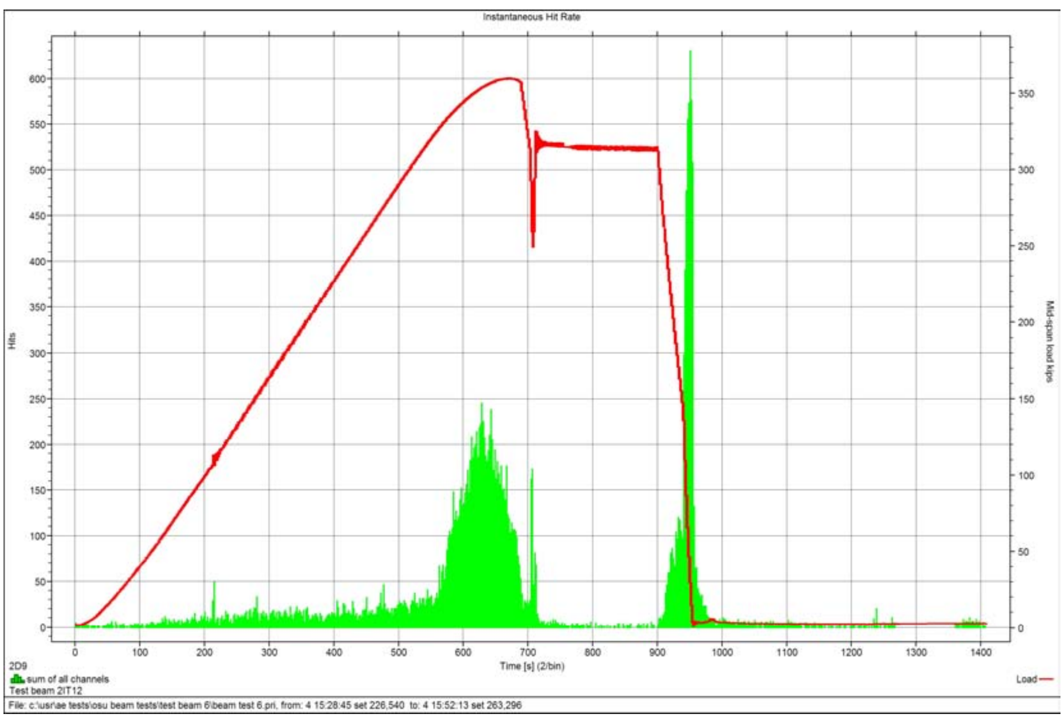

Figure 3.63 Instantaneous hit rate and mid-span load for the failure load cycle.

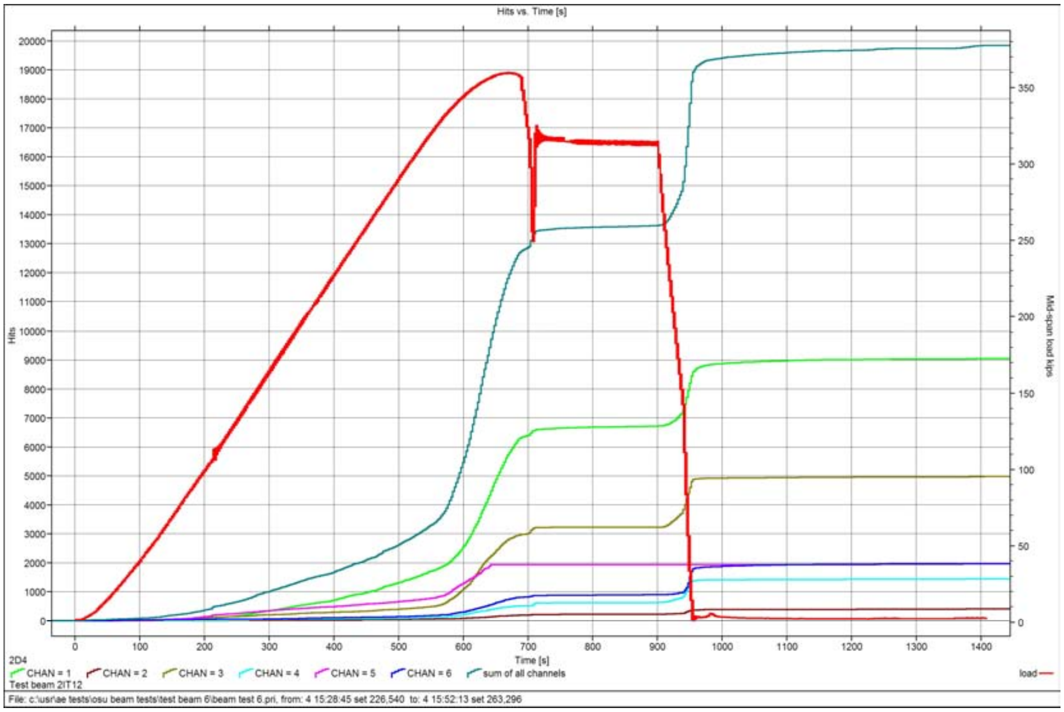

Figure 3.64 Cumulative hits and mid-span load for the failure load cycle.

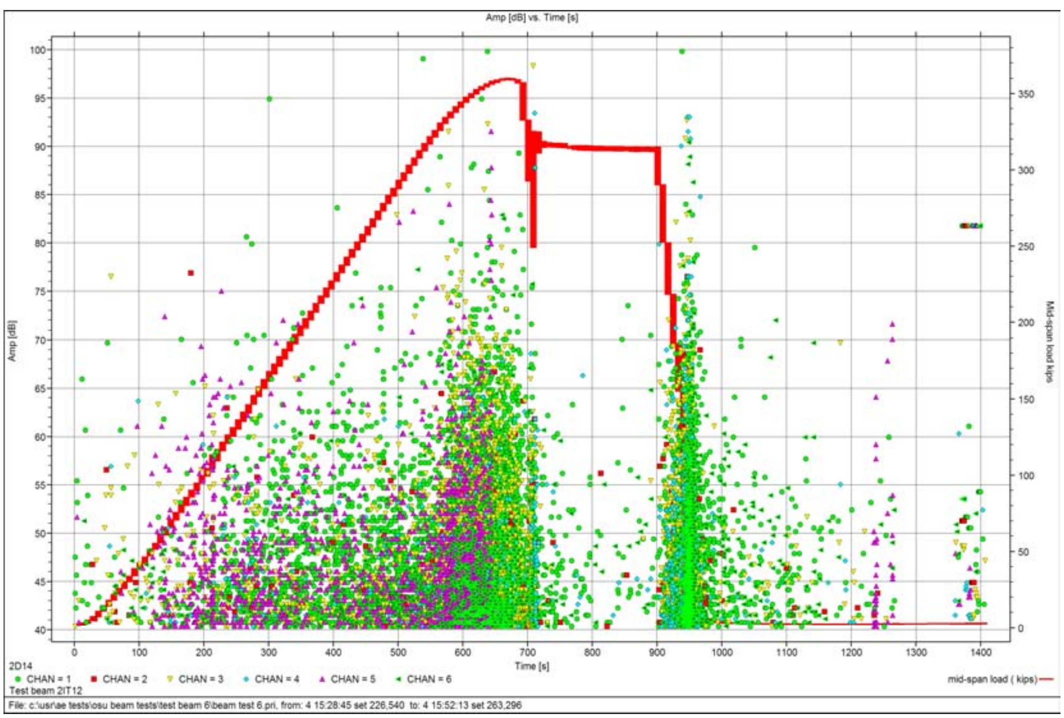

Figure 3.65 Peak amplitudes and mid-span load for the failure load cycle.

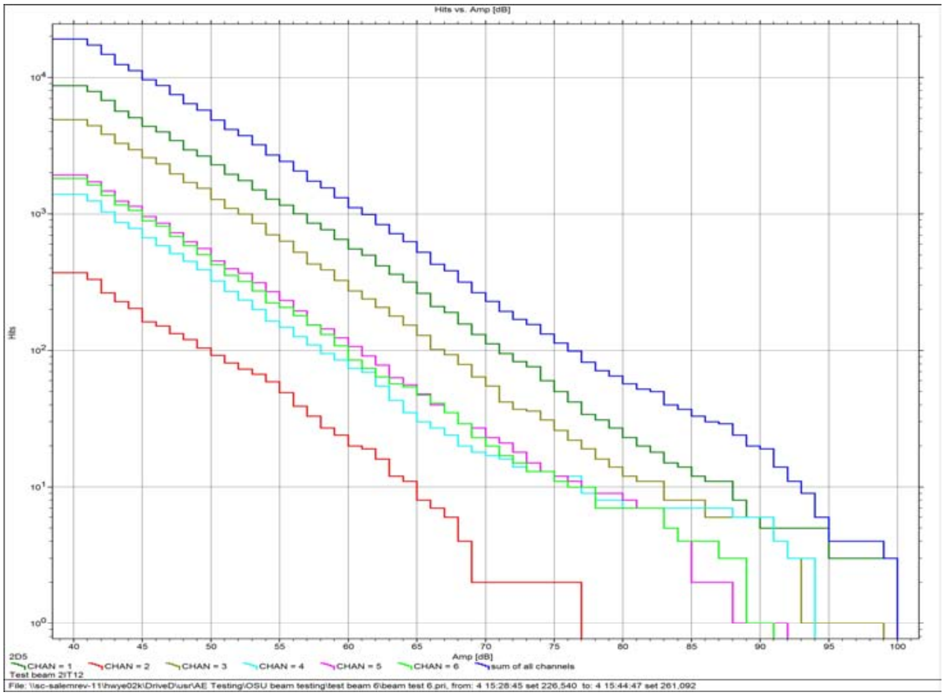

Figure 3.67 Hits versus peak amplitudes for the failure load cycle.

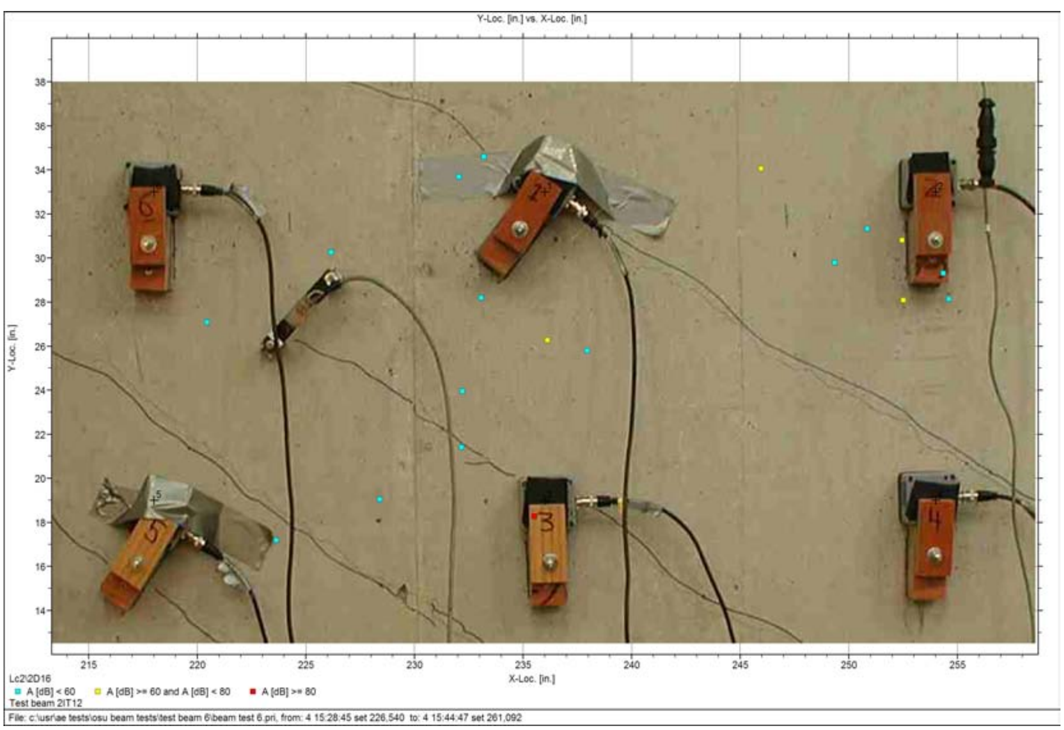

Figure 3.68 Event locations for the failure load cycle.

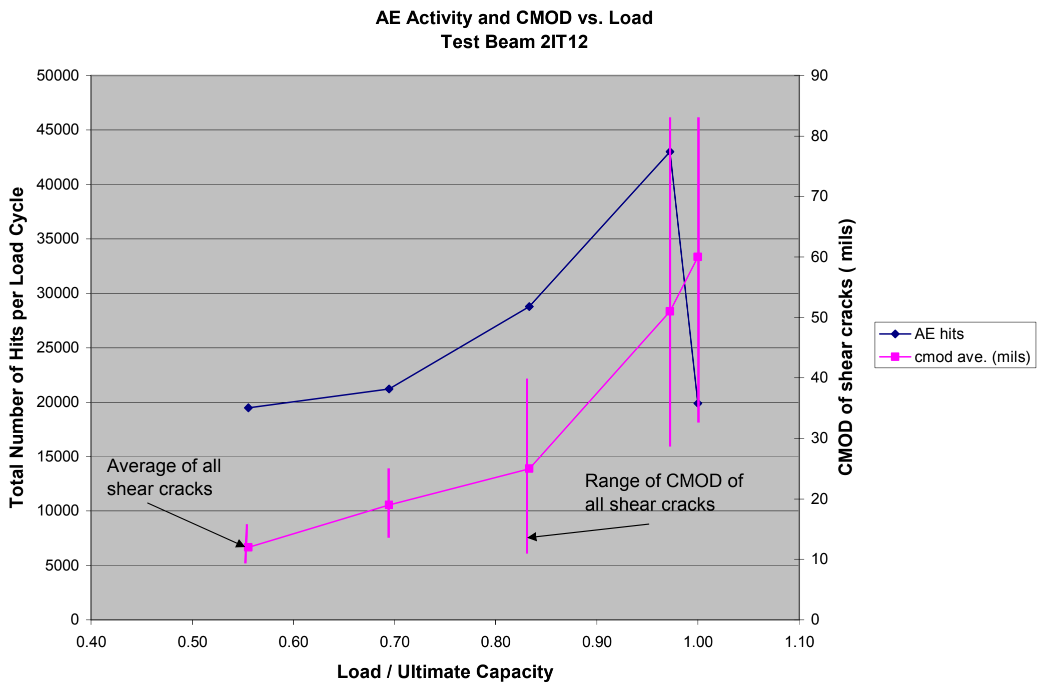

Figure 3.69 AE hits and CMOD of shear cracks versus load for test beam 2IT12.

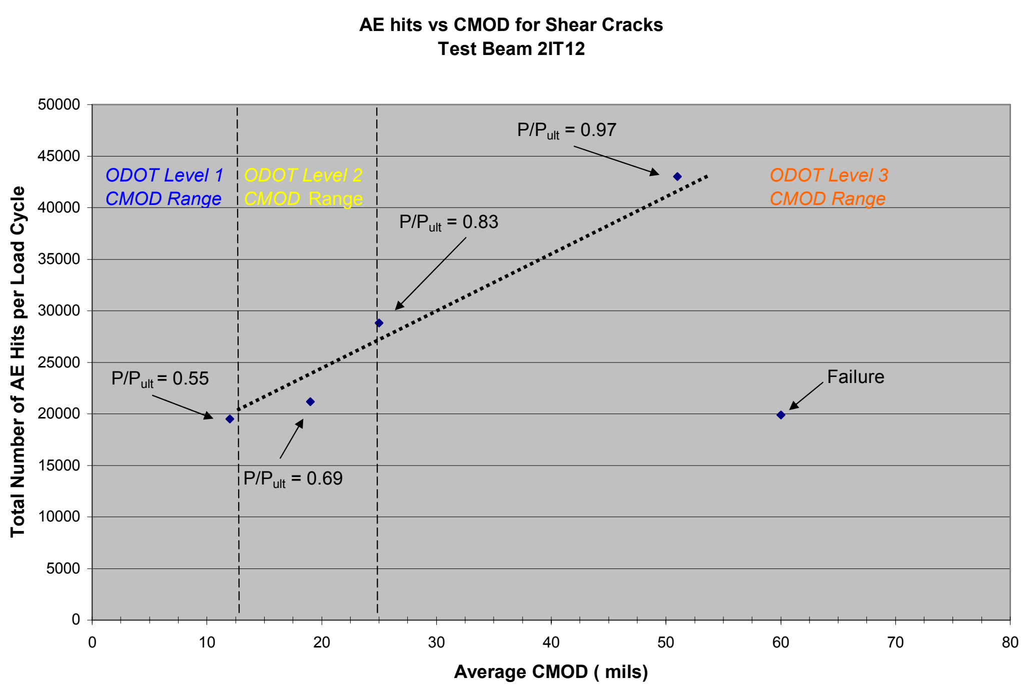

Figure 3.70 AE hits correlated with CMOD of shear cracks for test beam 2IT12.

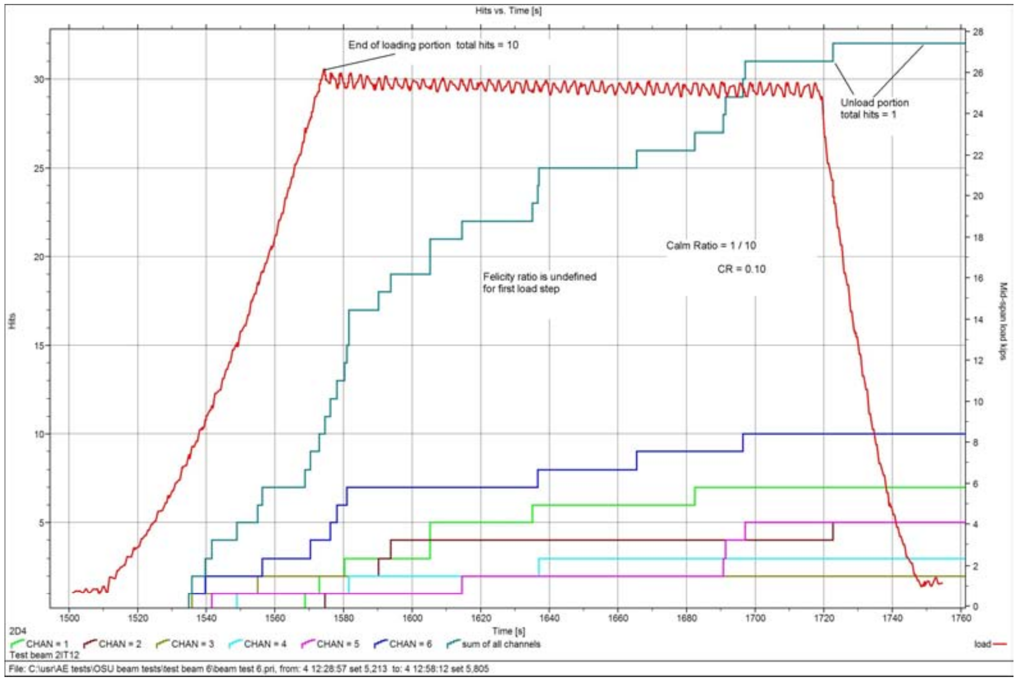

Figure 3.71 Example calculation of felicity and calm ratios for test beam 2IT12 at the first or 25 kip load increment.

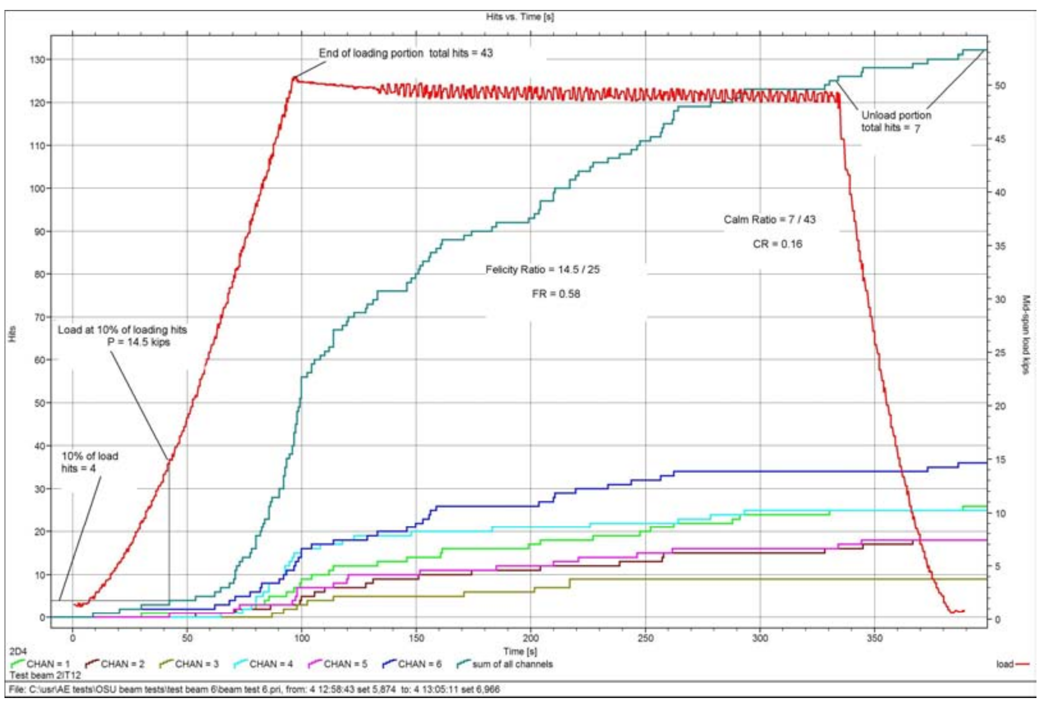

Figure 3.72 Example calculation of felicity and calm ratios for test beam 2IT12 at the second or 50 kip load increment.

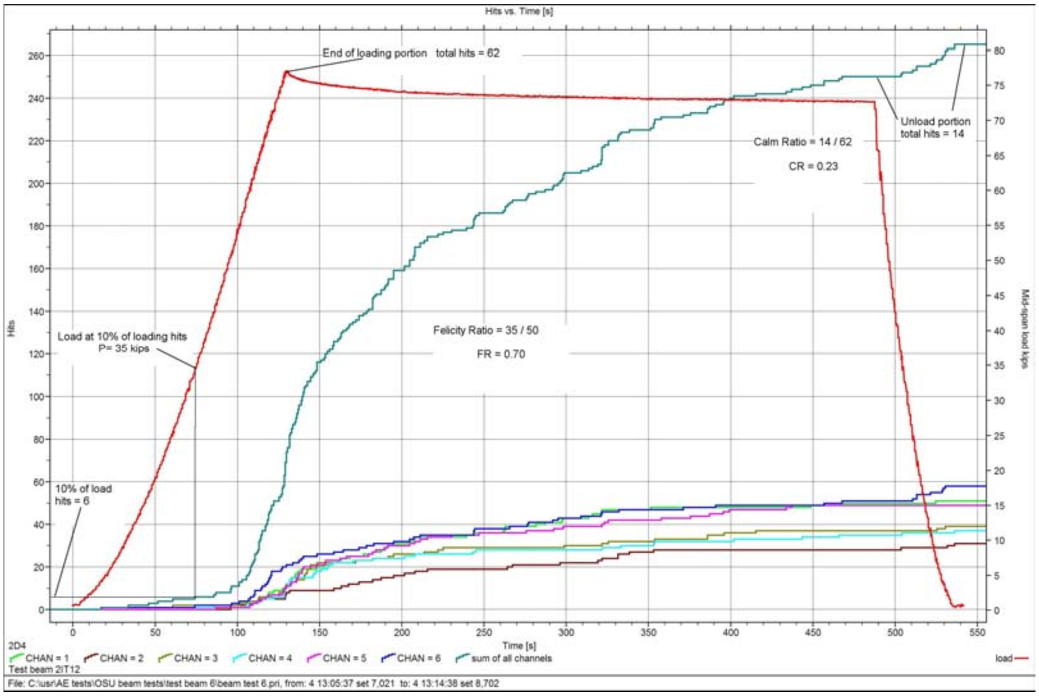

Figure 3.73 Example calculation of felicity and calm ratios for test beam 2IT12 at the third or 75 kip load increment.

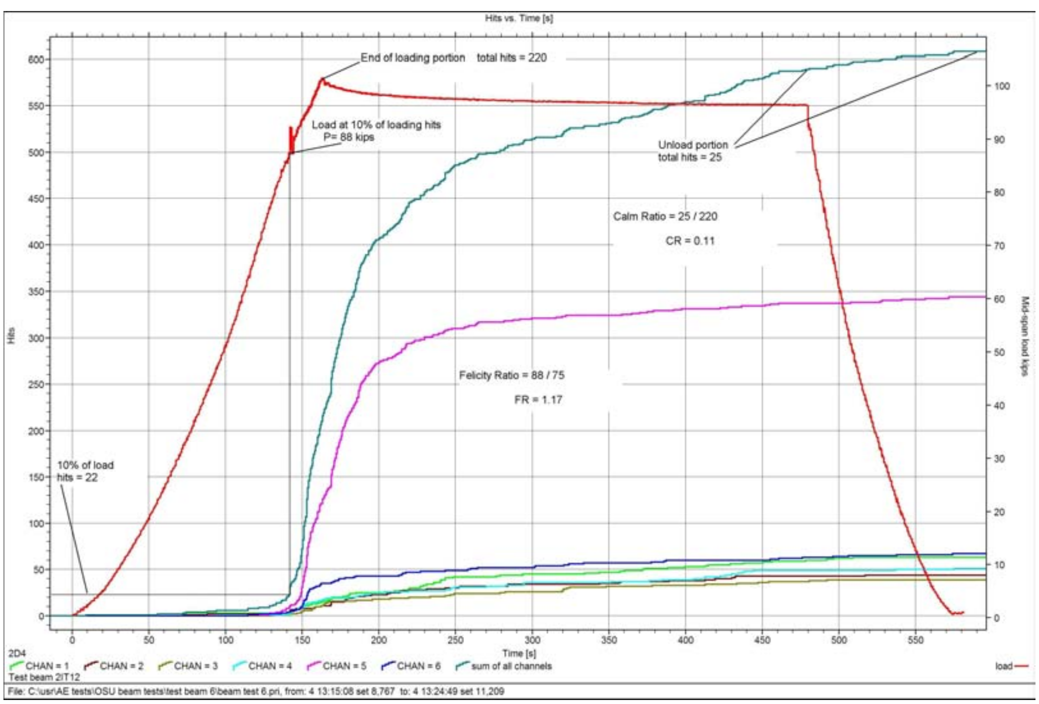

Figure 3.74 Example calculation of felicity and calm ratios for test beam 2IT12 at the fourth or 100 kip load increment.

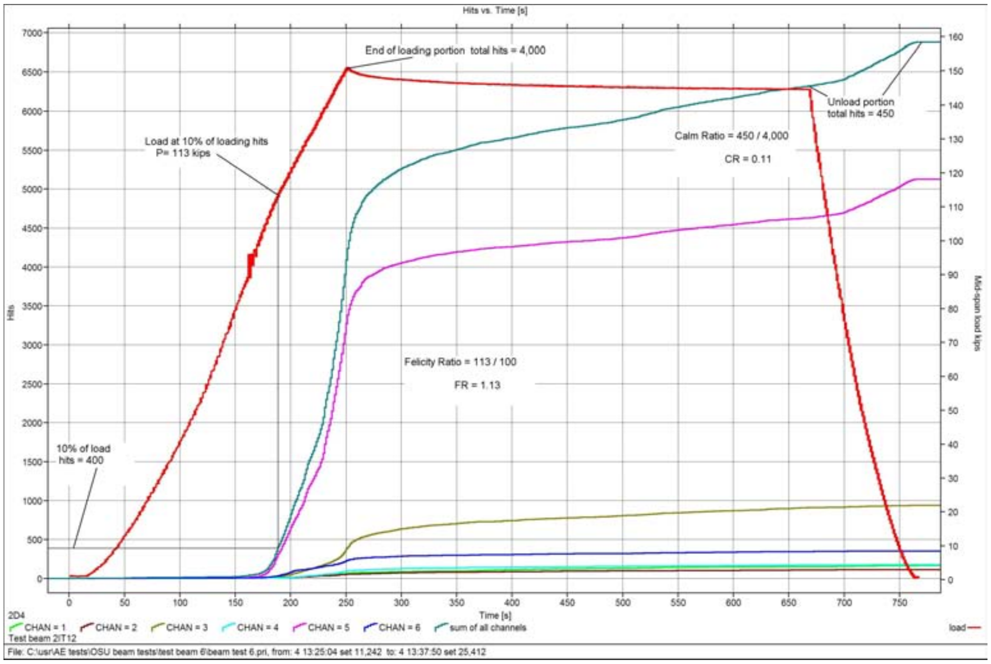

Figure 3.75 Example calculation of felicity and calm ratios for test beam 2IT12 at the fifth or 150 kip load increment.

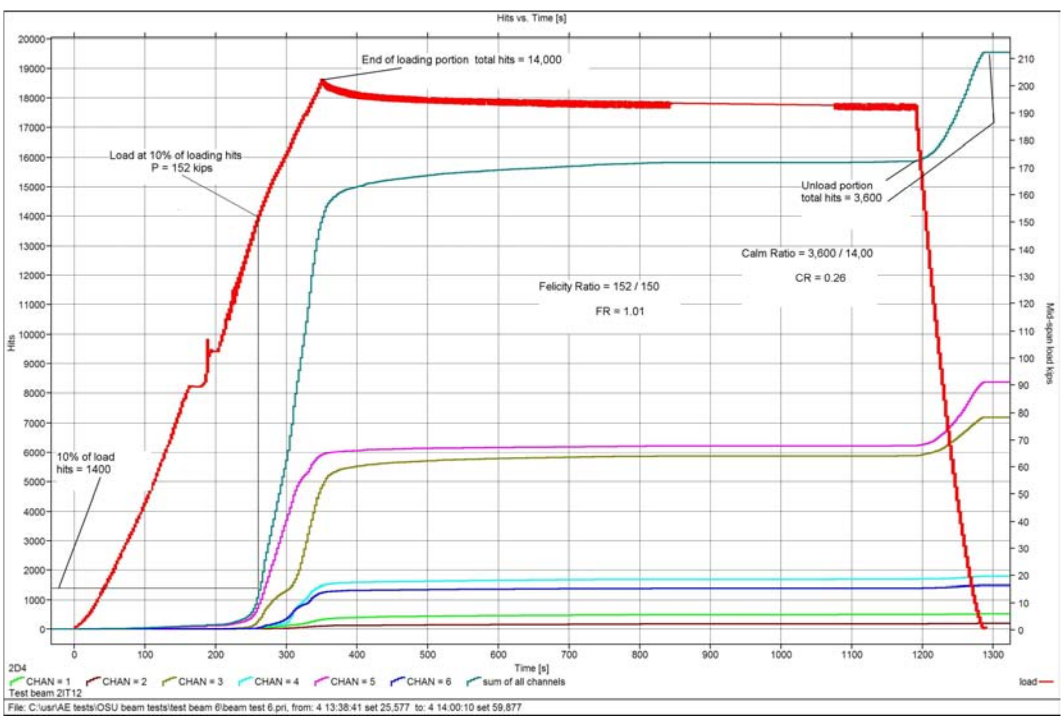

Figure 3.76 Example calculation of felicity and calm ratios for test beam 2IT12 at the sixth or 200 kip load increment.

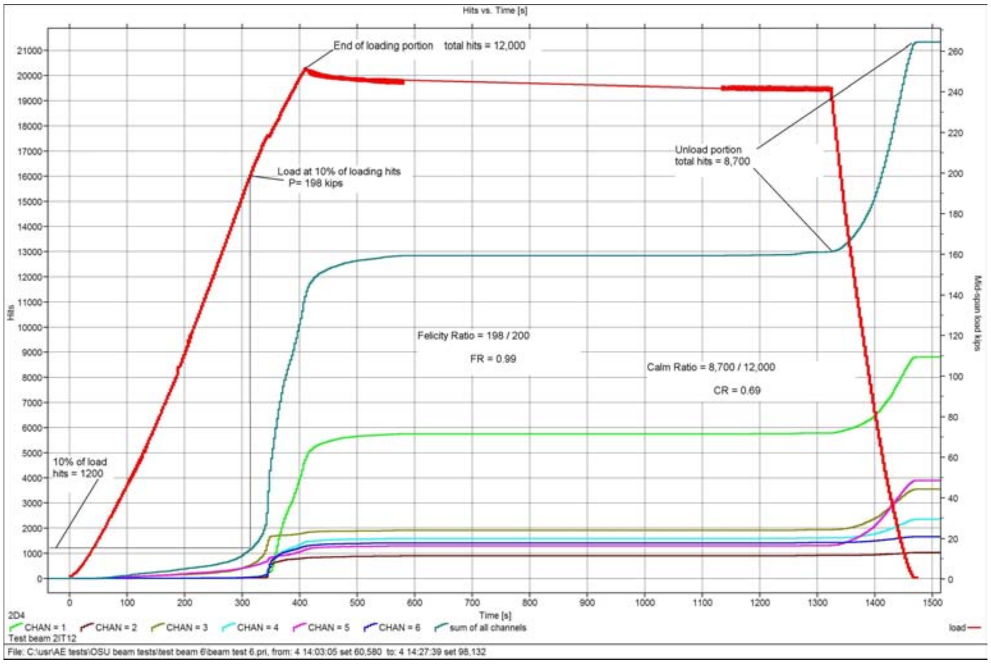

Figure 3.77 Example calculation of felicity and calm ratios for test beam 2IT12 at the seventh or 250 kip load increment.

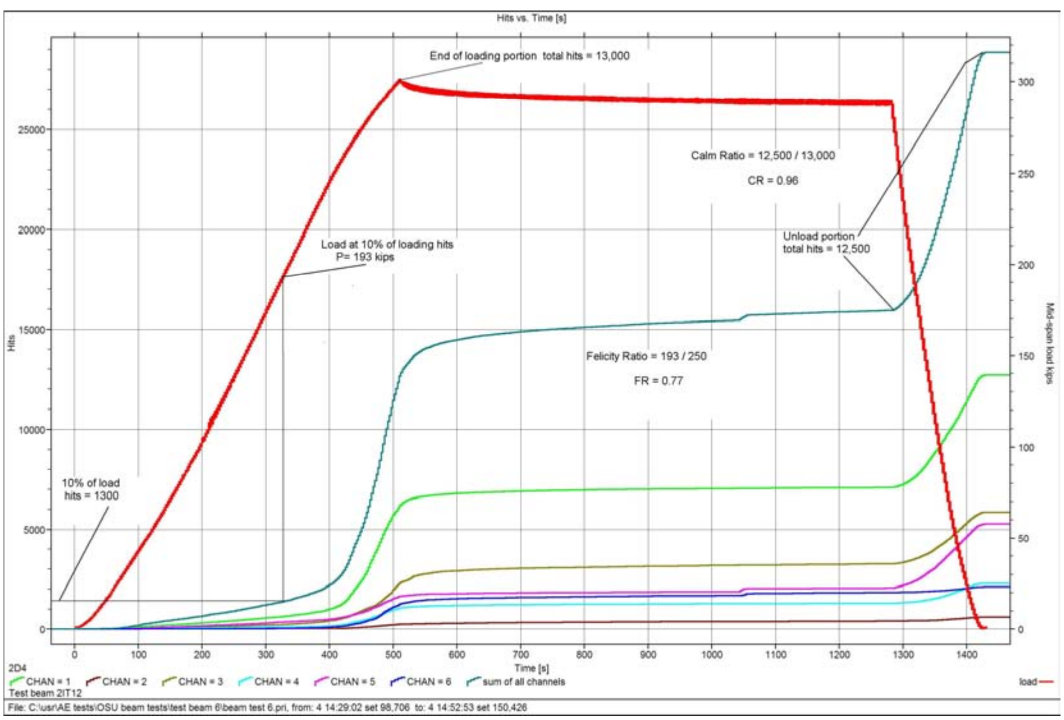

Figure 3.78 Example calculation of felicity and calm ratios for test beam 2IT12 at the eighth or 300 kip load increment.

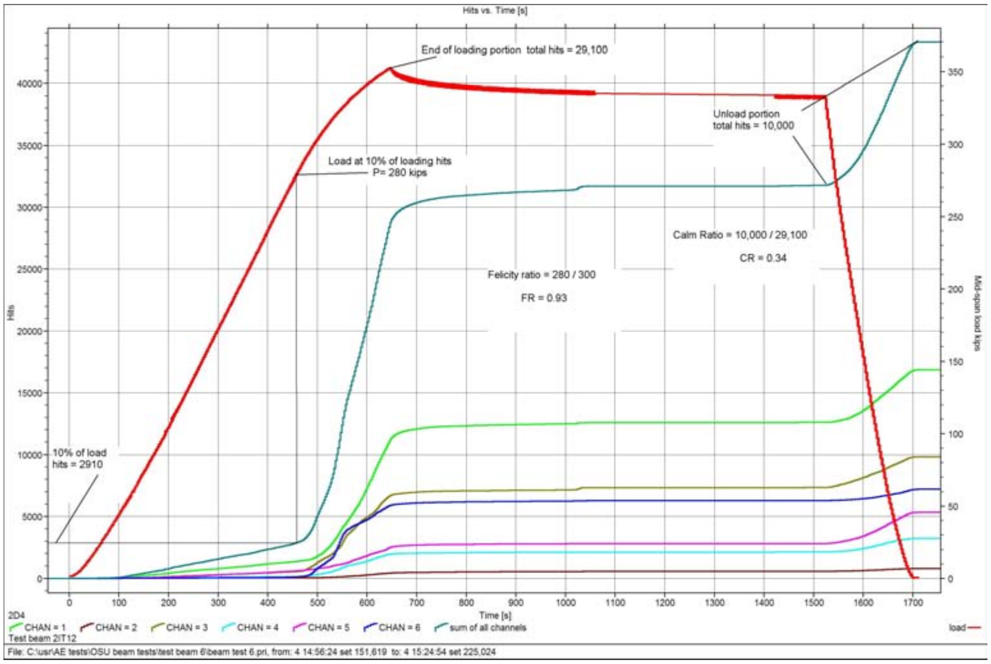

Figure 3.79 Example calculation of felicity and calm ratios for test beam 2IT12 at the ninth or 350 kip load increment.

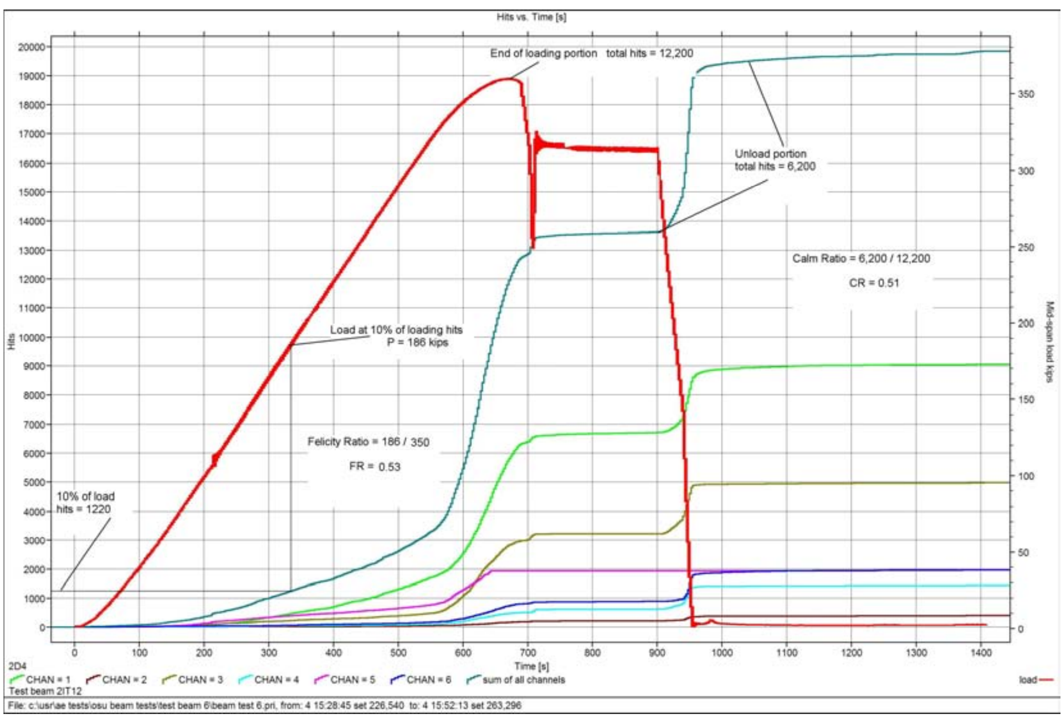

Figure 3.80 Example calculation of felicity and calm ratios for test beam 2IT12 at the tenth or failure load increment.

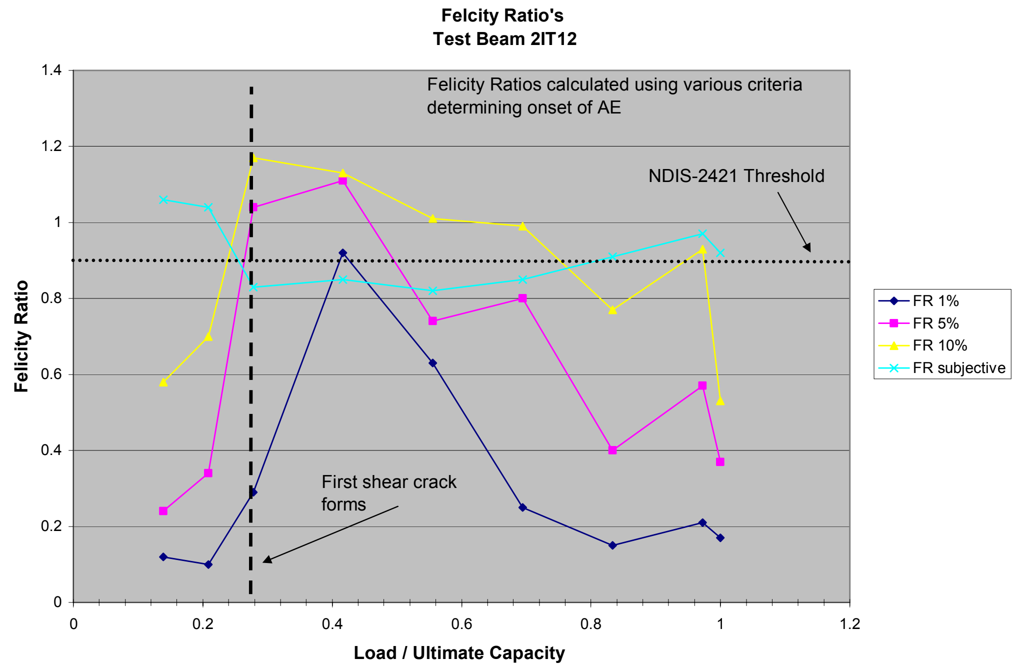

Figure 3.81 Felicity ratios for test beam 2IT12 using various definitions of the onset of AE activity.

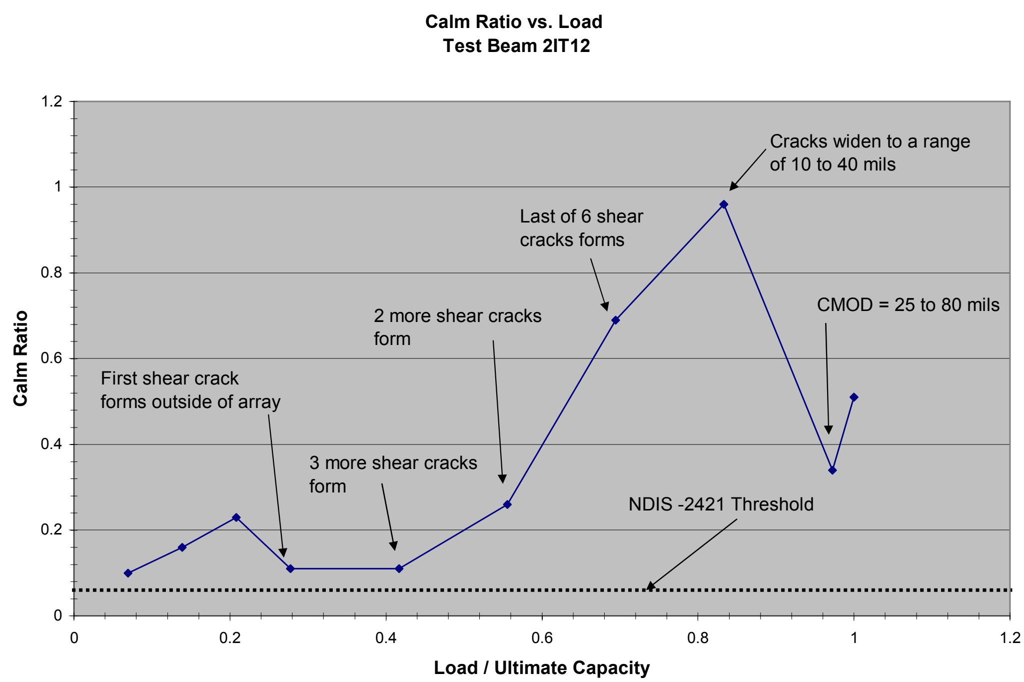

Figure 3.82 Calm ratios for test beam 2IT12.

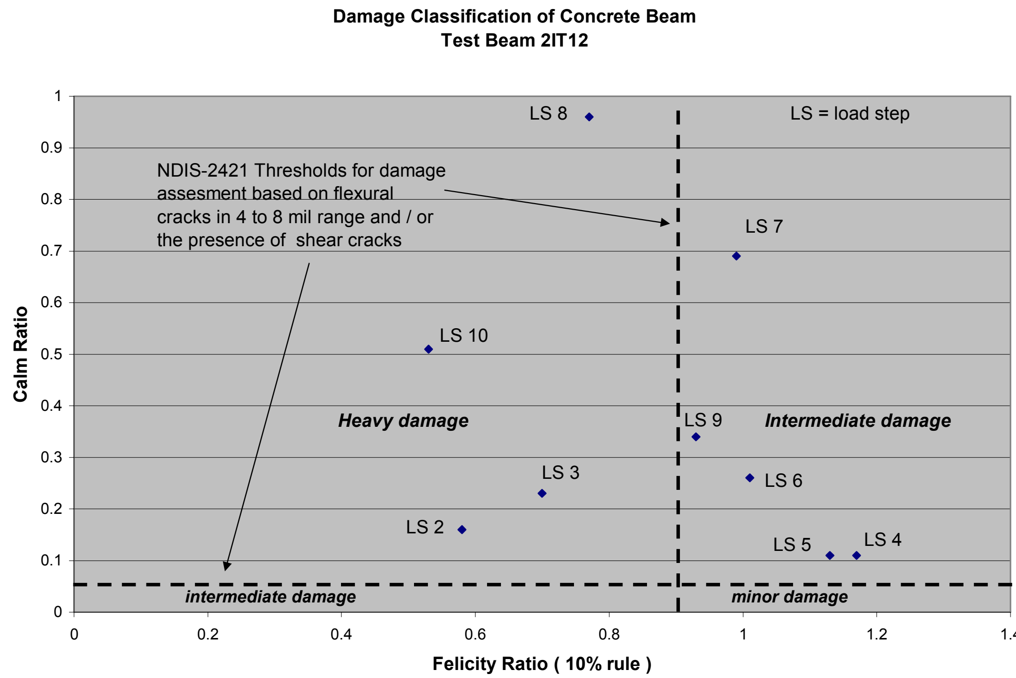

Figure 3.83 Damage assessment chart using the criteria established in NDIS-2421 applied to test beam 2IT12.

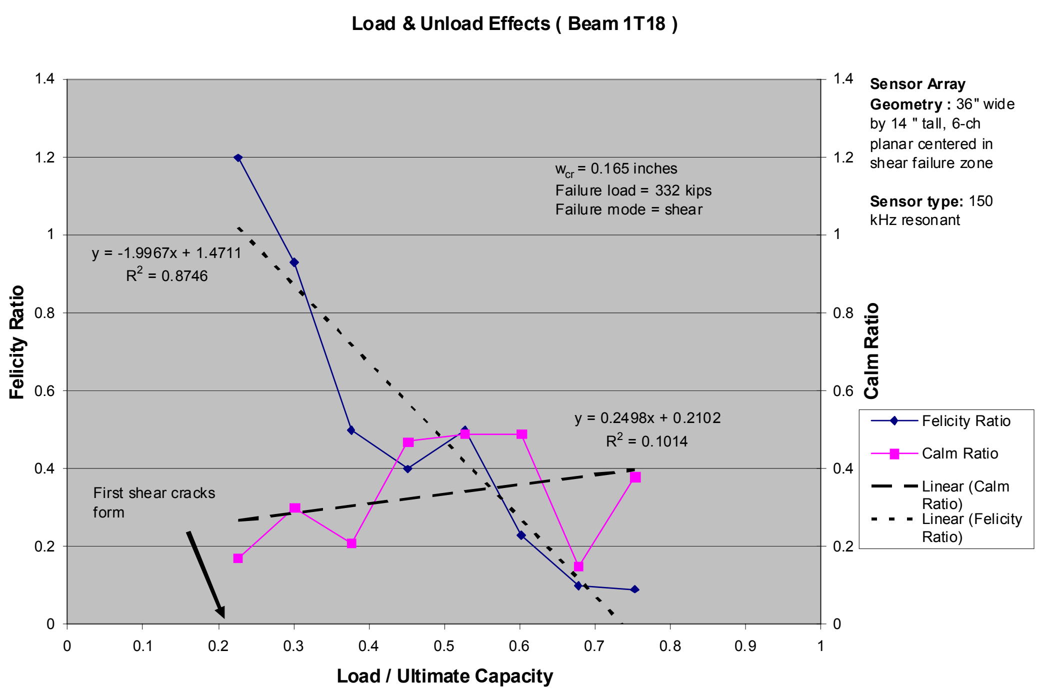

Figure 3.84 Felicity and calm ratios for test beam 1T18.

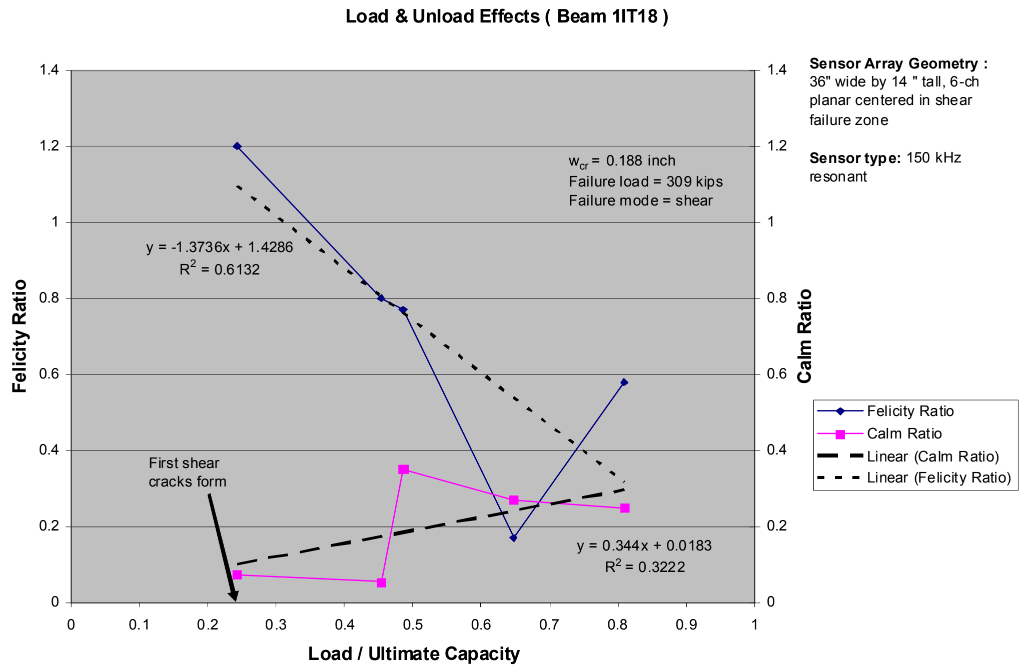

Figure 3.85 Felicity and calm ratios for test beam 1IT18.

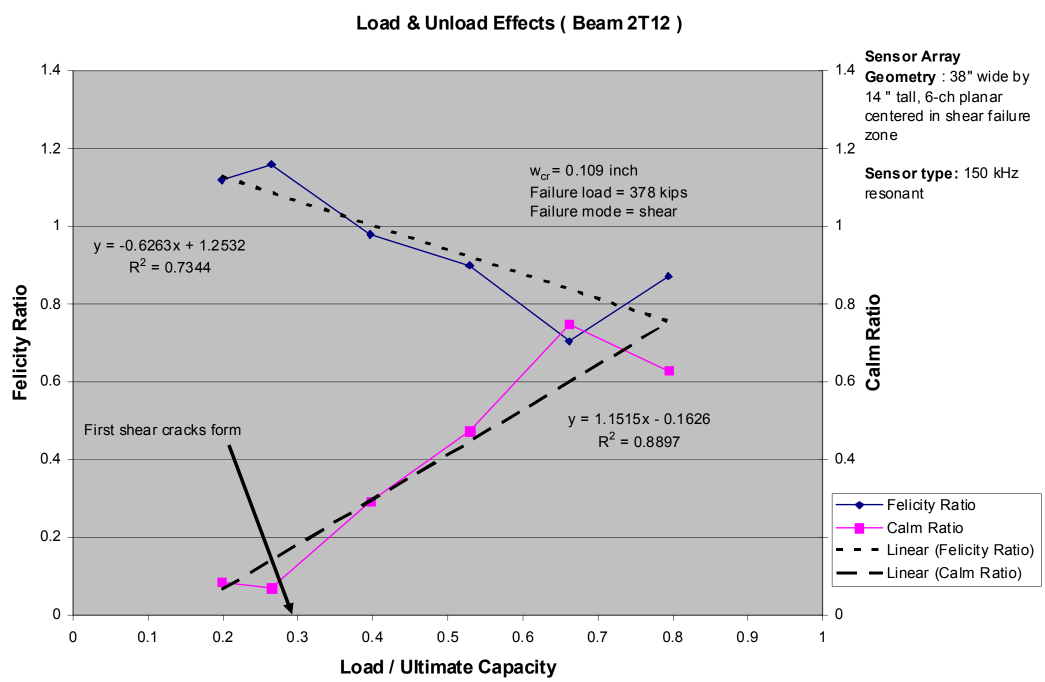

Figure 3.86 Felicity and calm ratios for test beam 2T12.

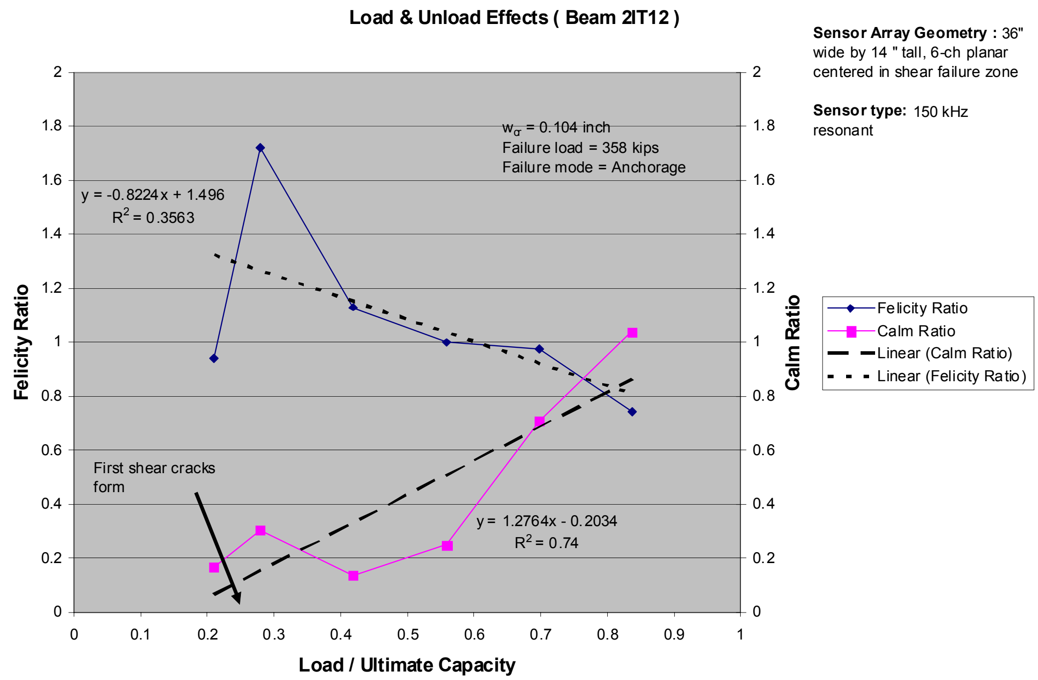

Figure 3.87 Felicity and calm ratios for test beam 2IT12.

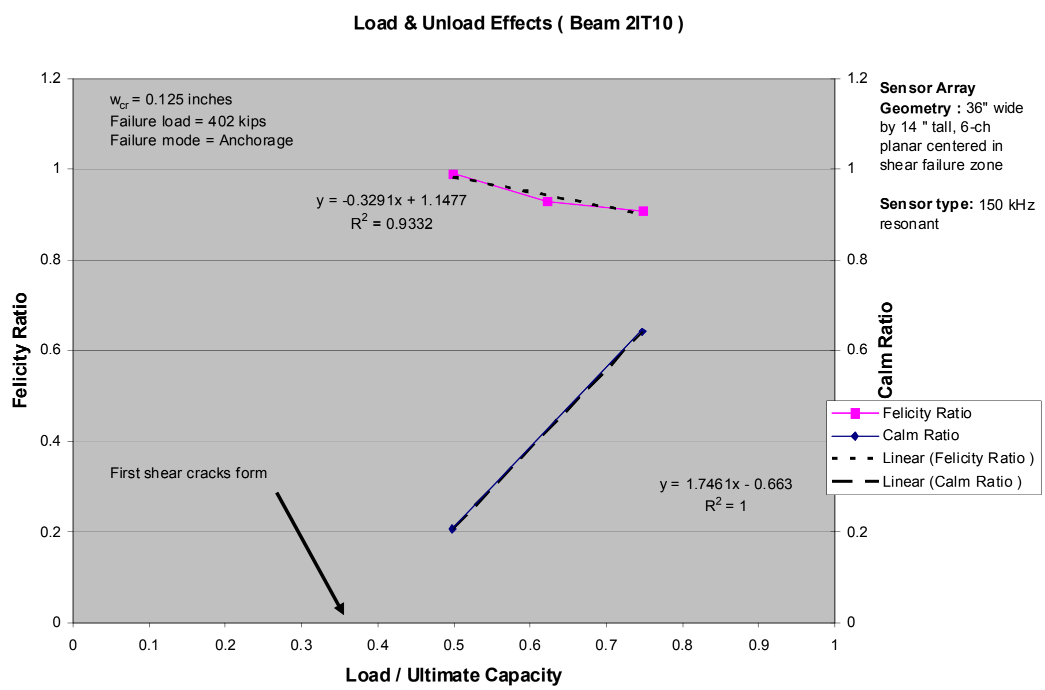

Figure 3.88 Felicity and calm ratios for test beam 2IT10.

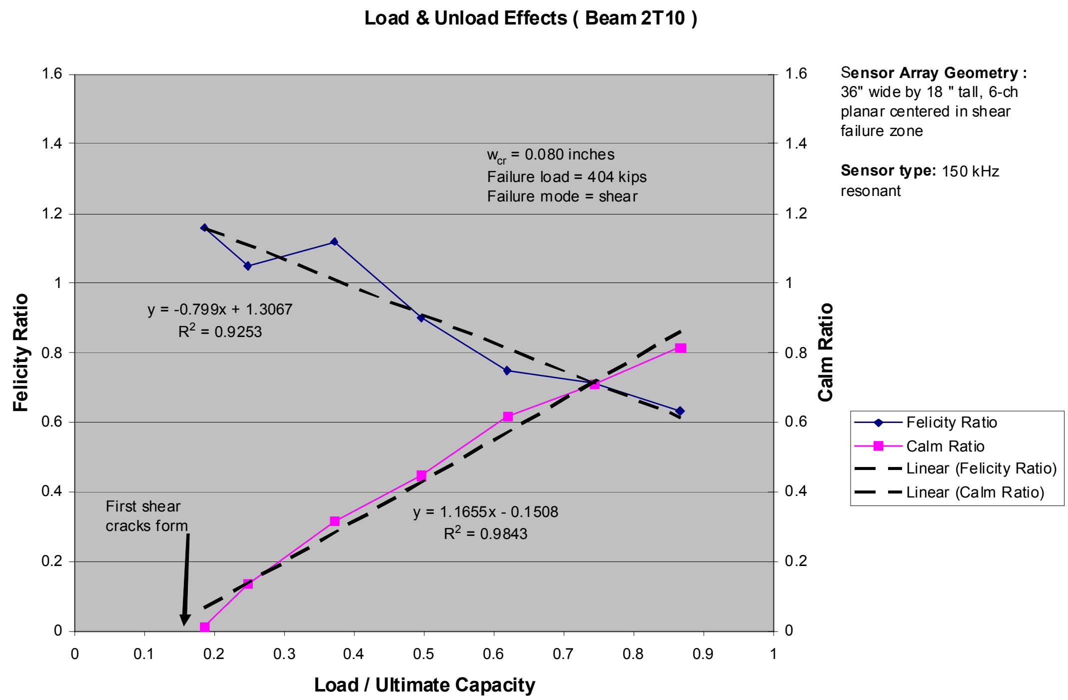

Figure 3.89 Felicity and calm ratios for test beam 2T10.

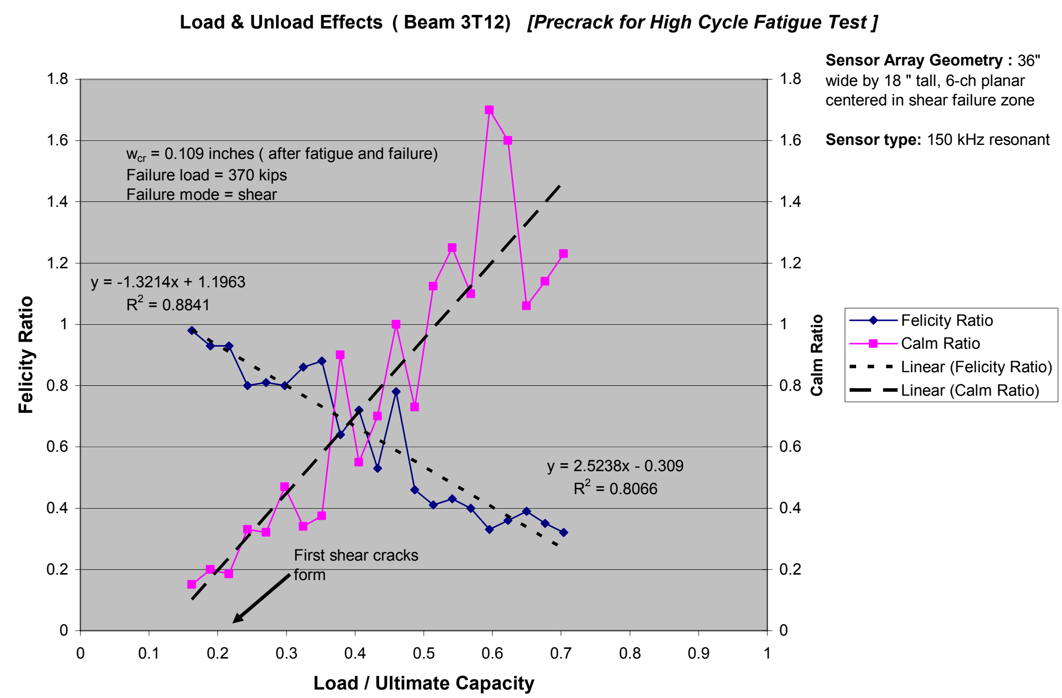

Figure 3.90 Felicity and calm ratios for test beam 3T12-precrack for high cycle fatigue.

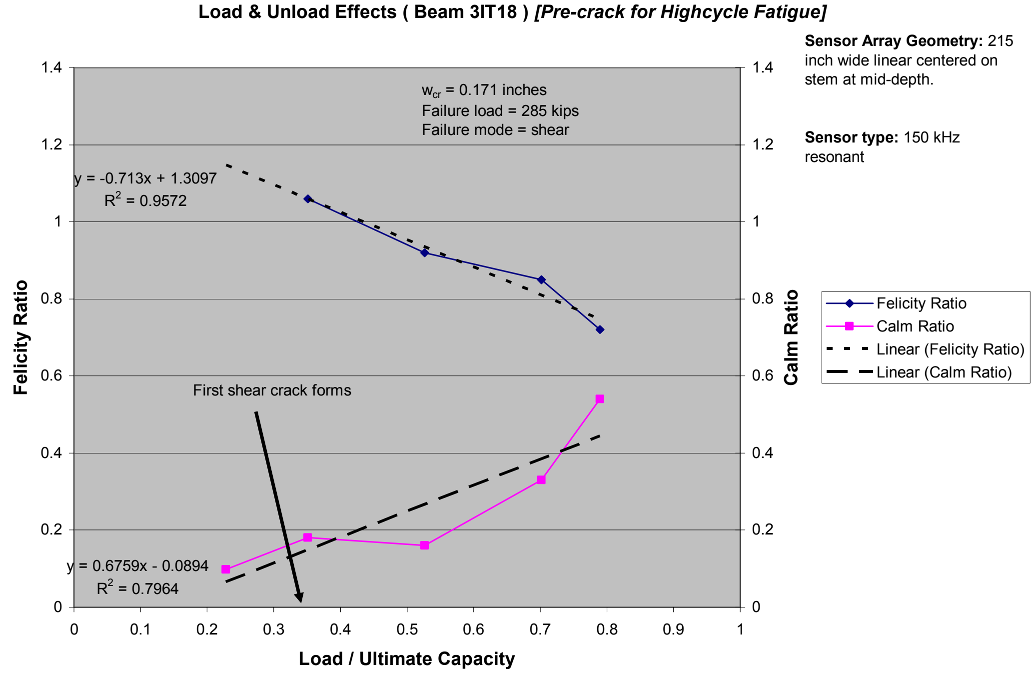

Figure 3.91 Felicity and calm ratios for test beam 3IT18-precrack for high cycle fatigue.

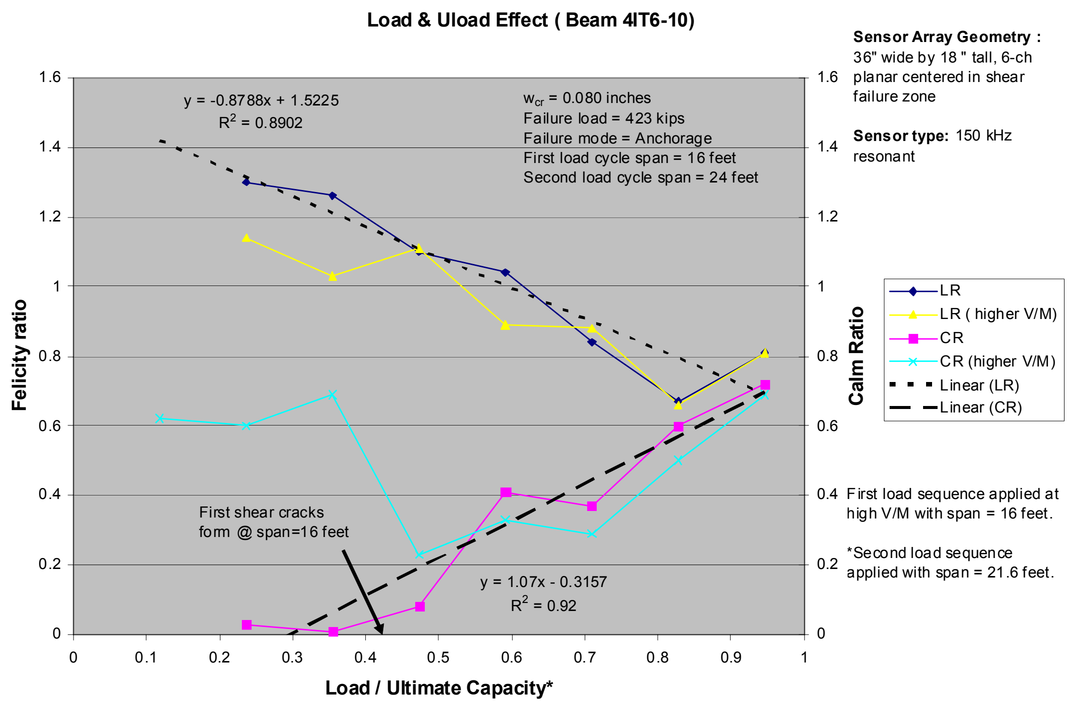

Figure 3.92 Felicity and calm ratios for test beam 4IT6-10.

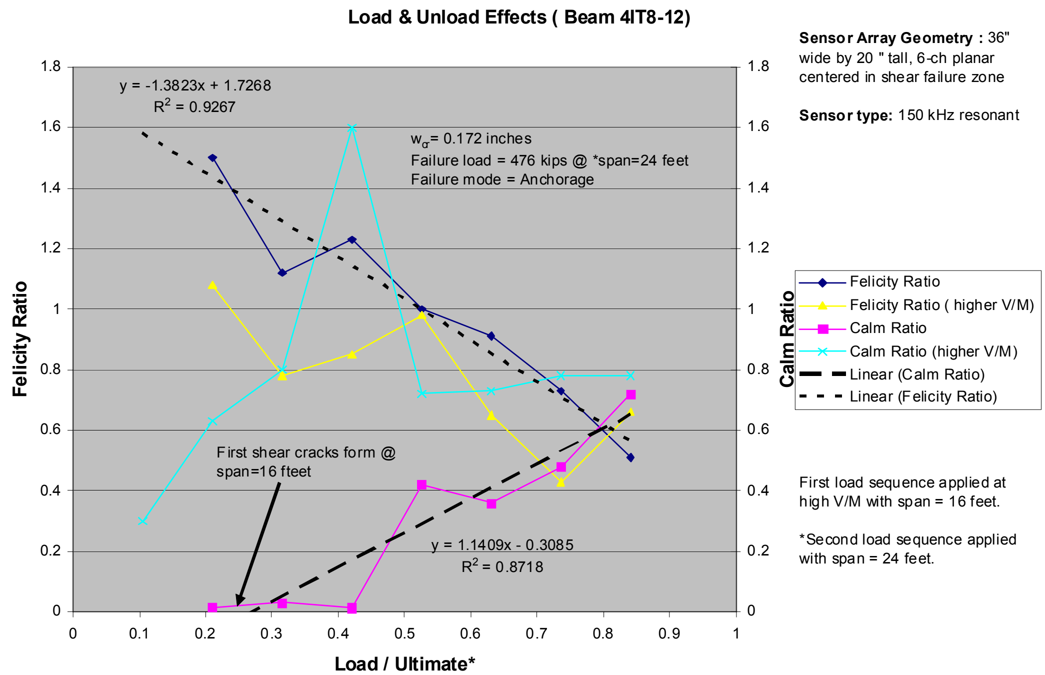

Figure 3.93 Felicity and calm ratios for test beam 4IT8-12.

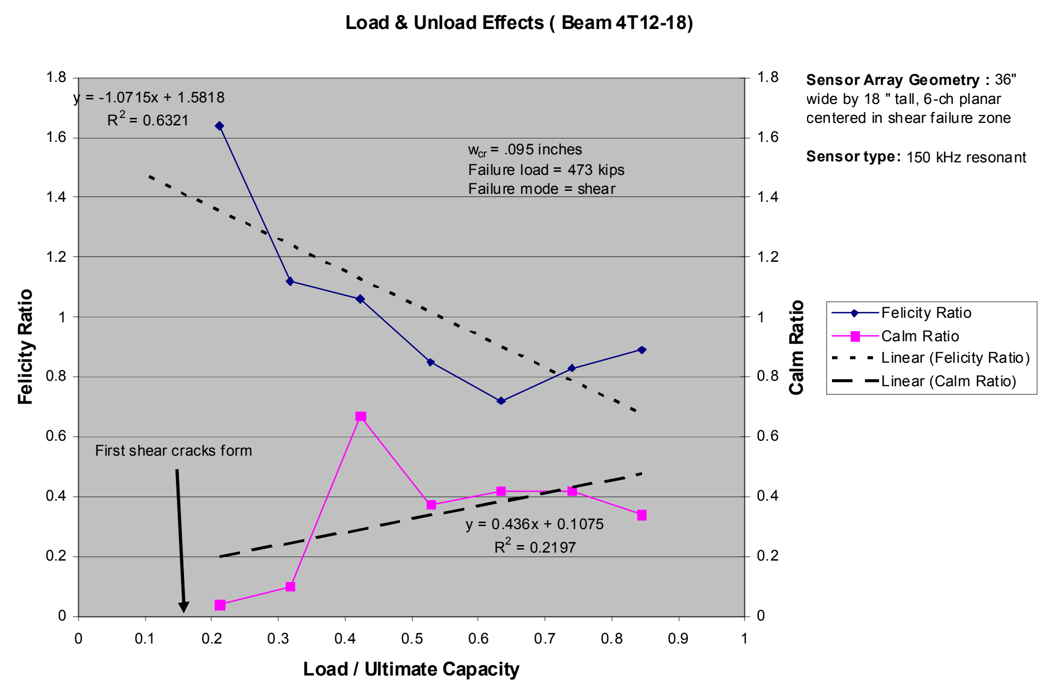

Figure 3.94 Felicity and calm ratios for test beam 4T12-18.

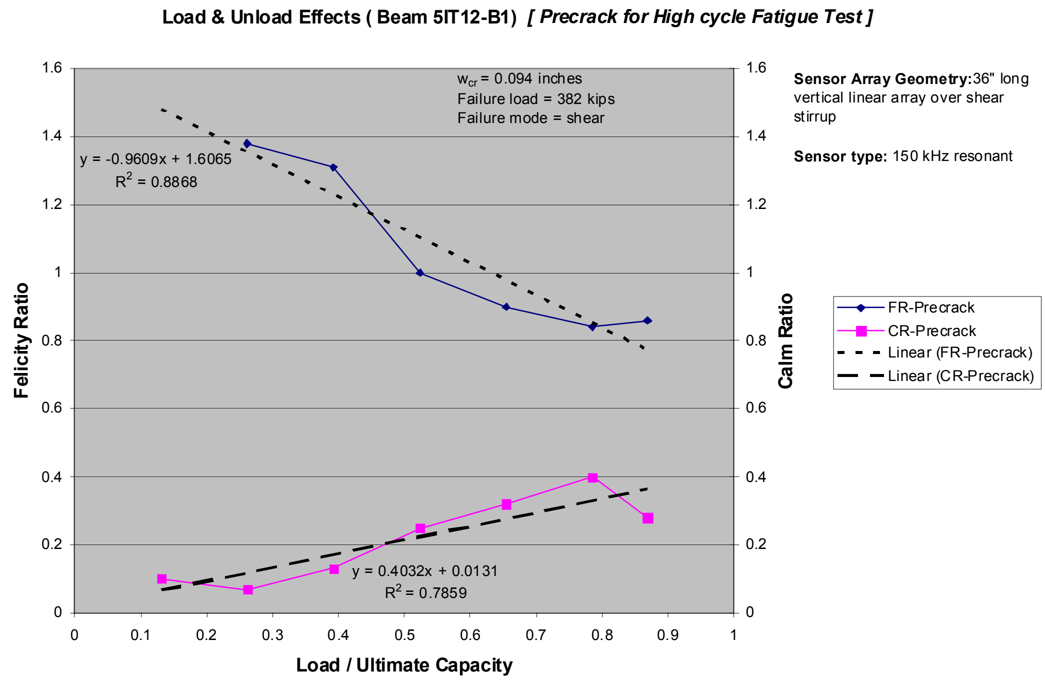

Figure 3.95 Felicity and calm ratios for test beam 5IT12-B1-precrack for high cycle fatigue.

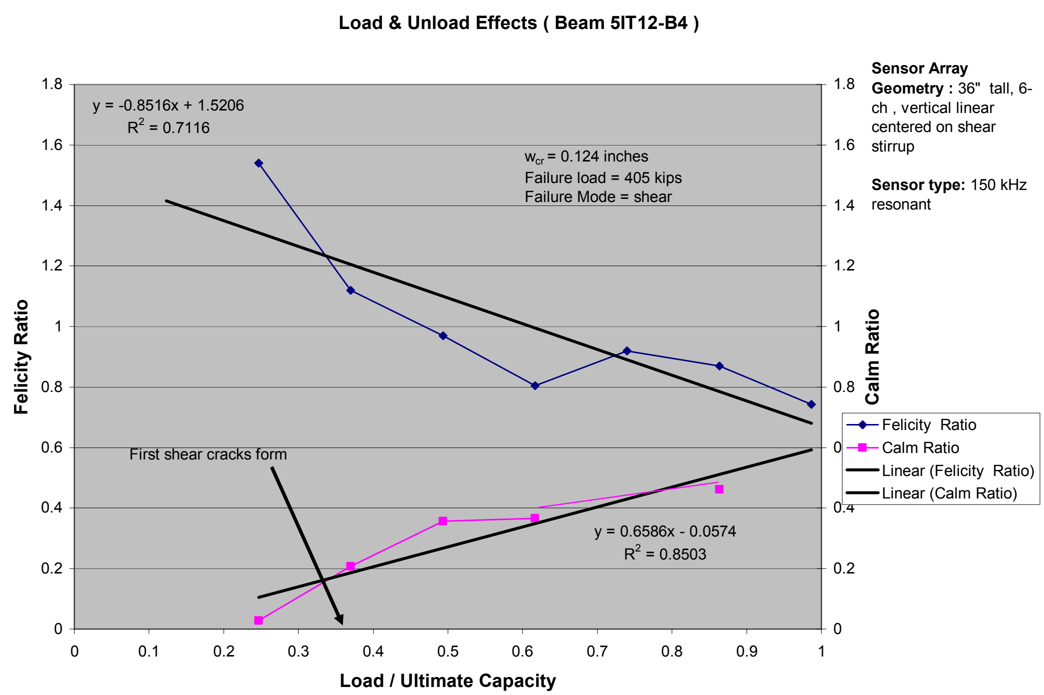

Figure 3.96 Felicity and calm ratios for test beam 5IT12-B4.

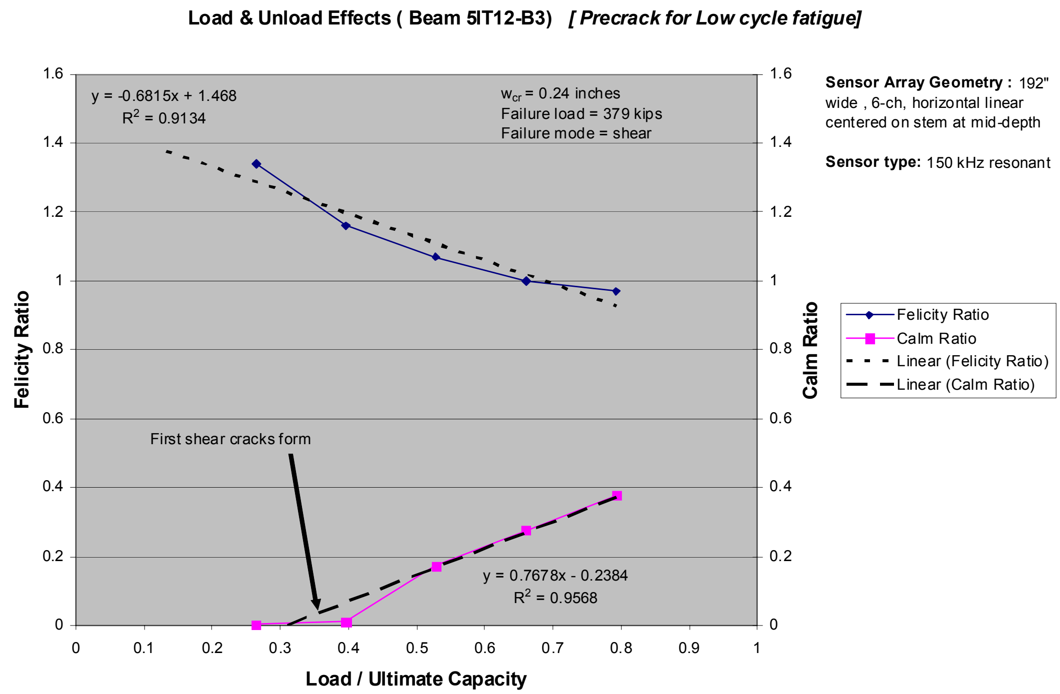

Figure 3.97 Felicity and calm ratios for test beam 5IT12-B3.

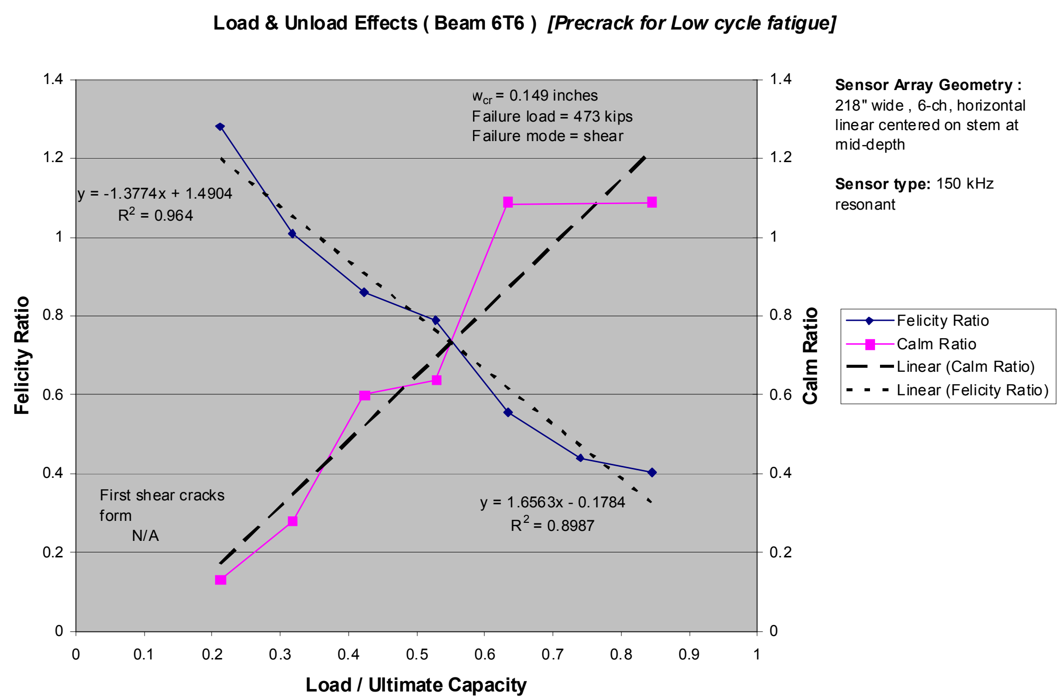

Figure 3.98 Felicity and calm ratios for test beam 6T6.

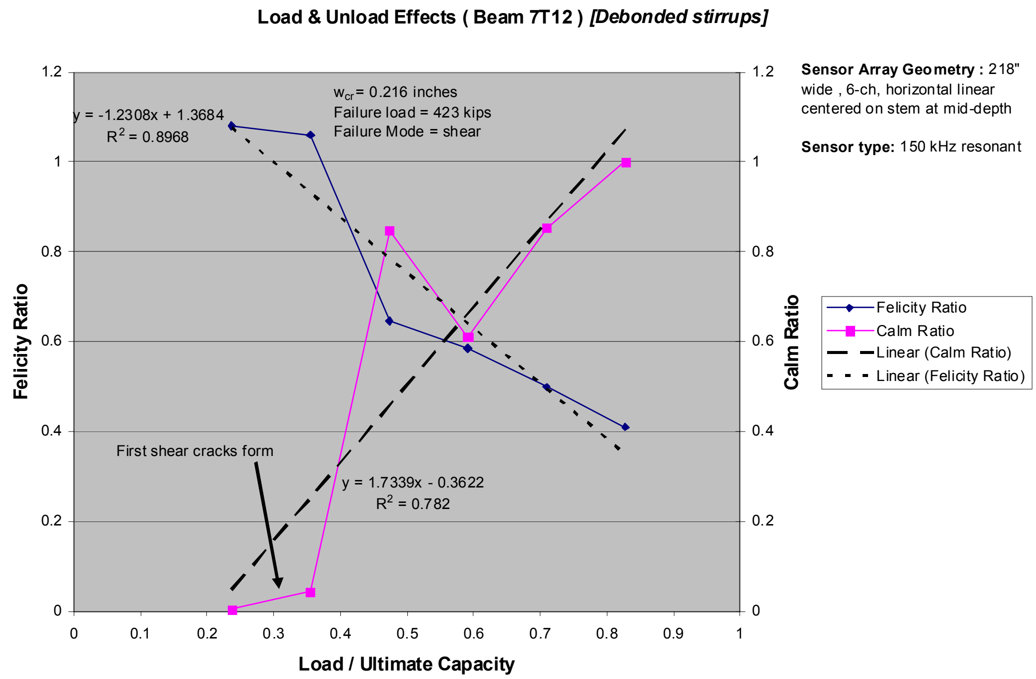

Figure 3.99 Felicity and calm ratios for test beam 7T12.

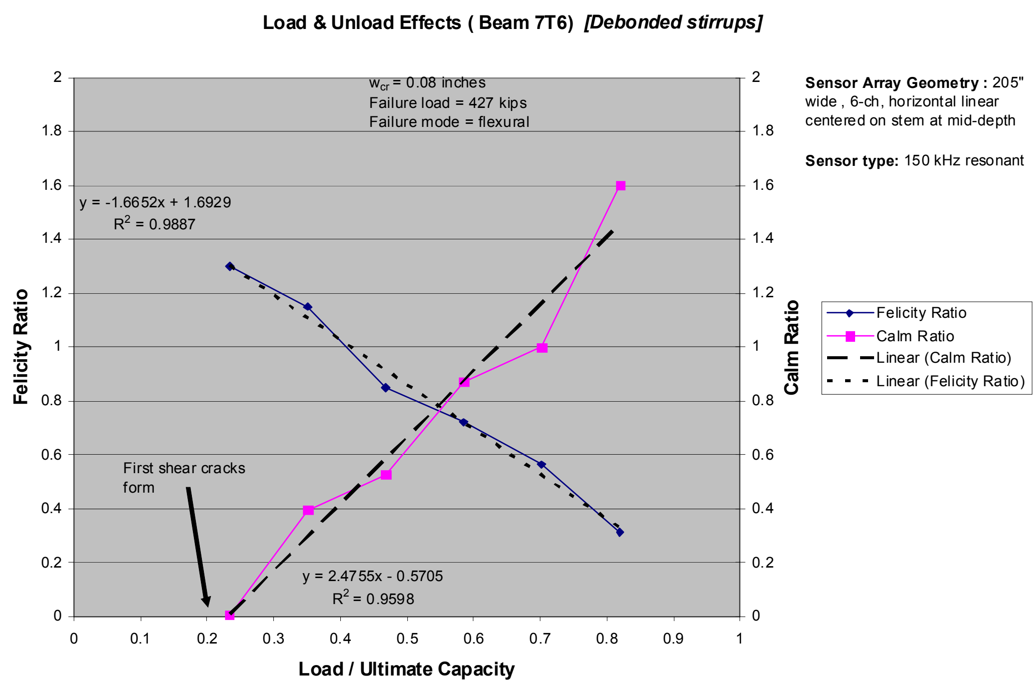

Figure 3.100 Felicity and calm ratios for test beam 7T6.

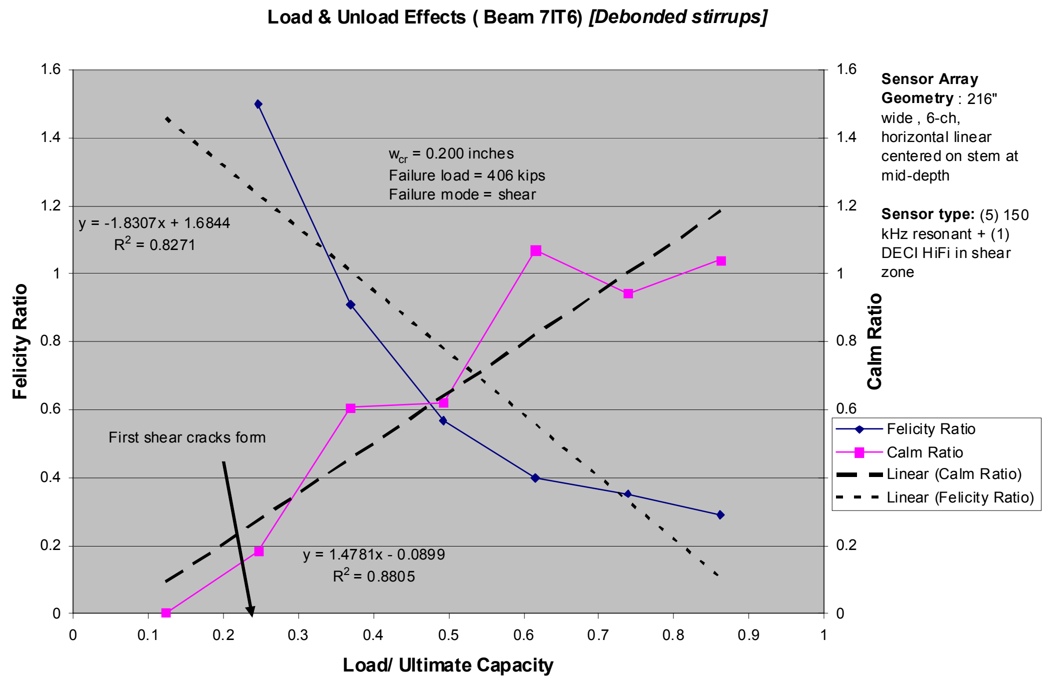

Figure 3.101 Felicity and calm ratios for test beam 7IT6.

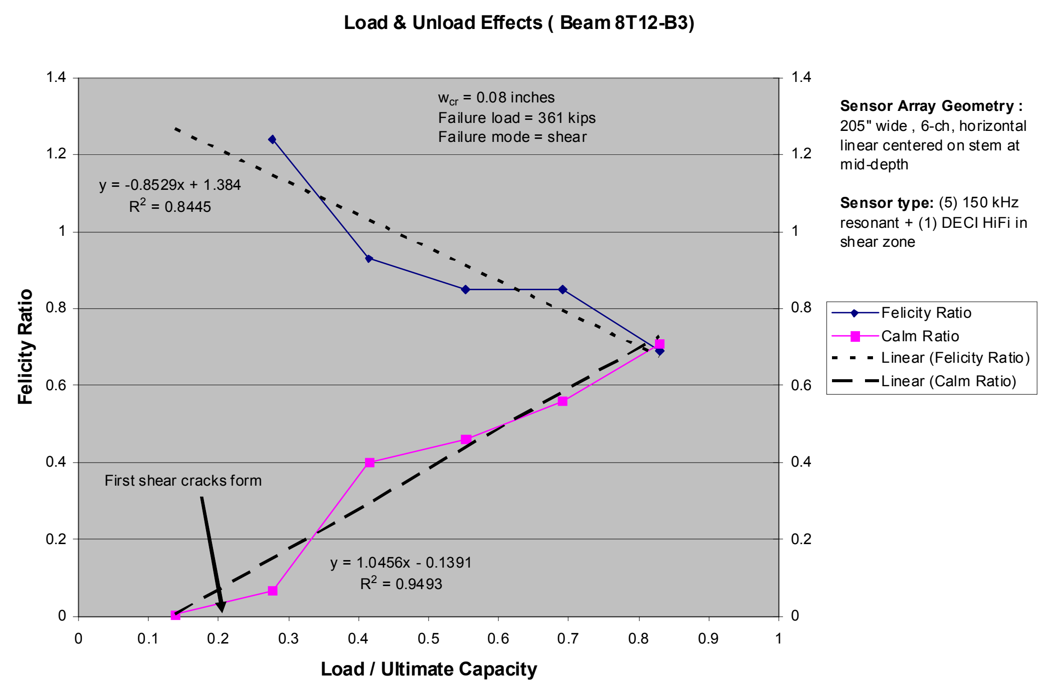

Figure 3.102 Felicity and calm ratios for test beam 8T12-B3.

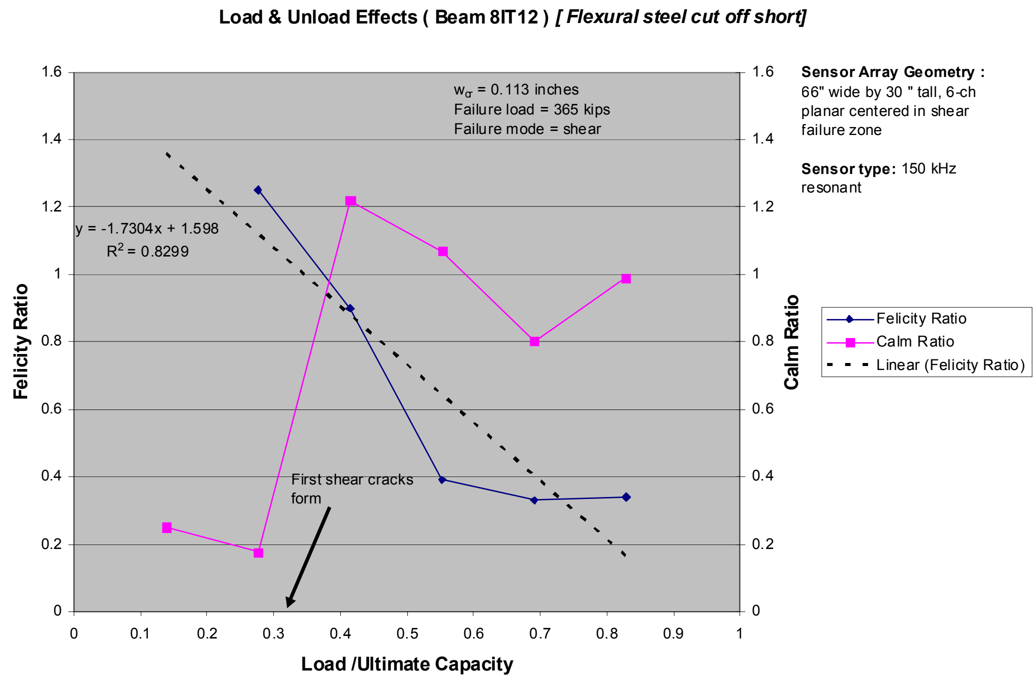

Figure 3.103 Felicity and calm ratios for test beam 8IT12.

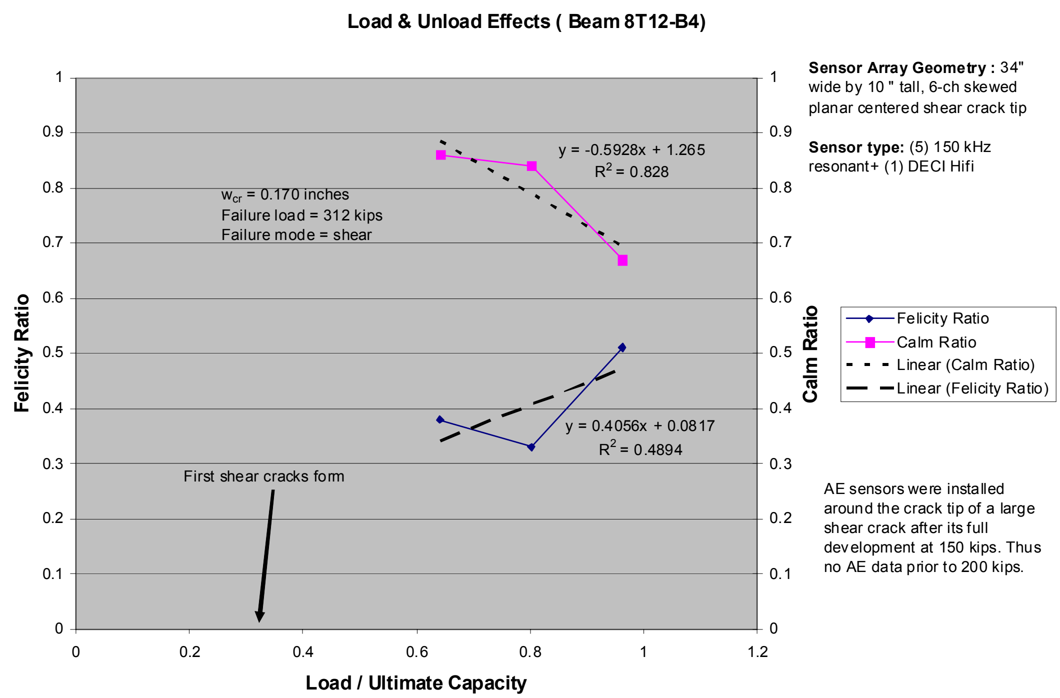

Figure 3.104 Felicity and calm ratios for test beam 8T12-B4.

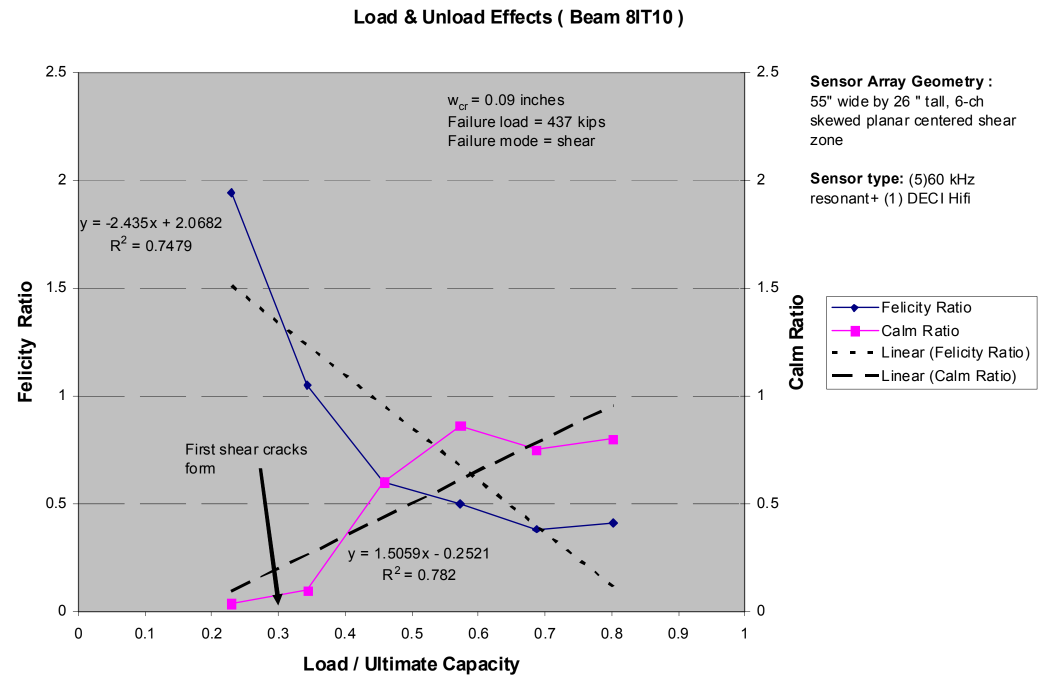

Figure 3.105 Felicity and calm ratios for test beam 8IT10.

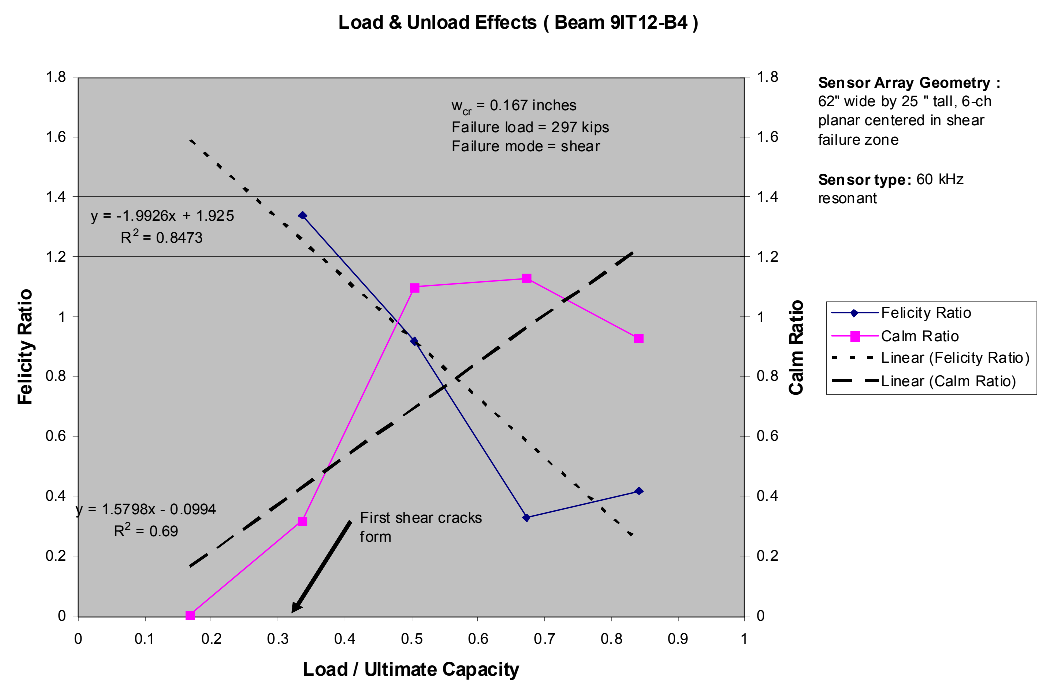

Figure 3.106 Felicity and calm ratios for test beam 9IT12-B4.

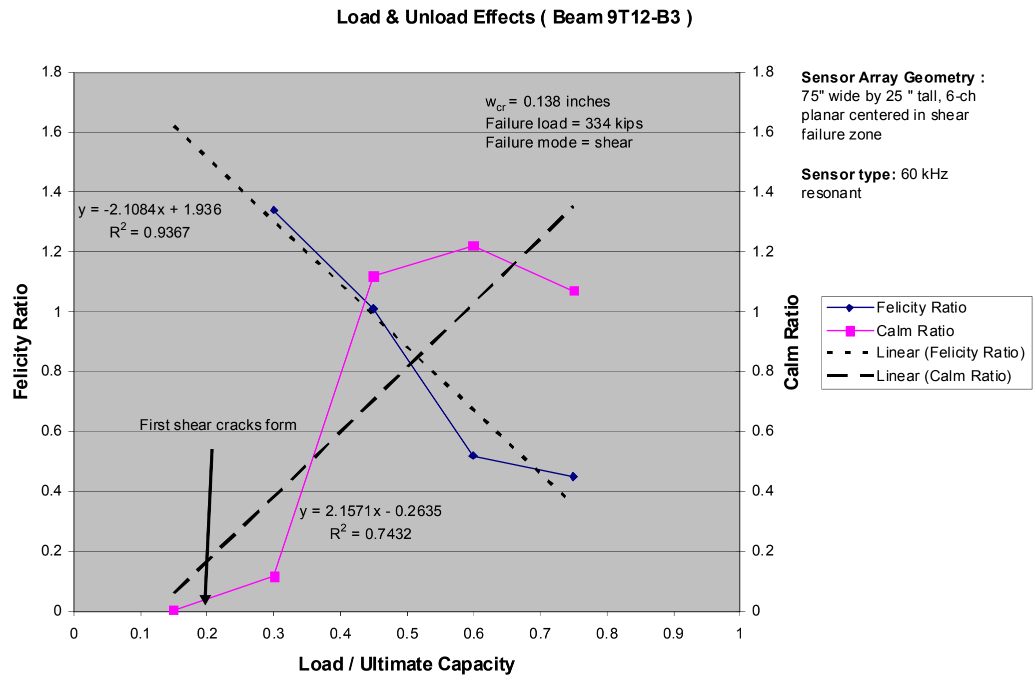

Figure 3.107 Felicity and calm ratios for test beam 9T12-B3.

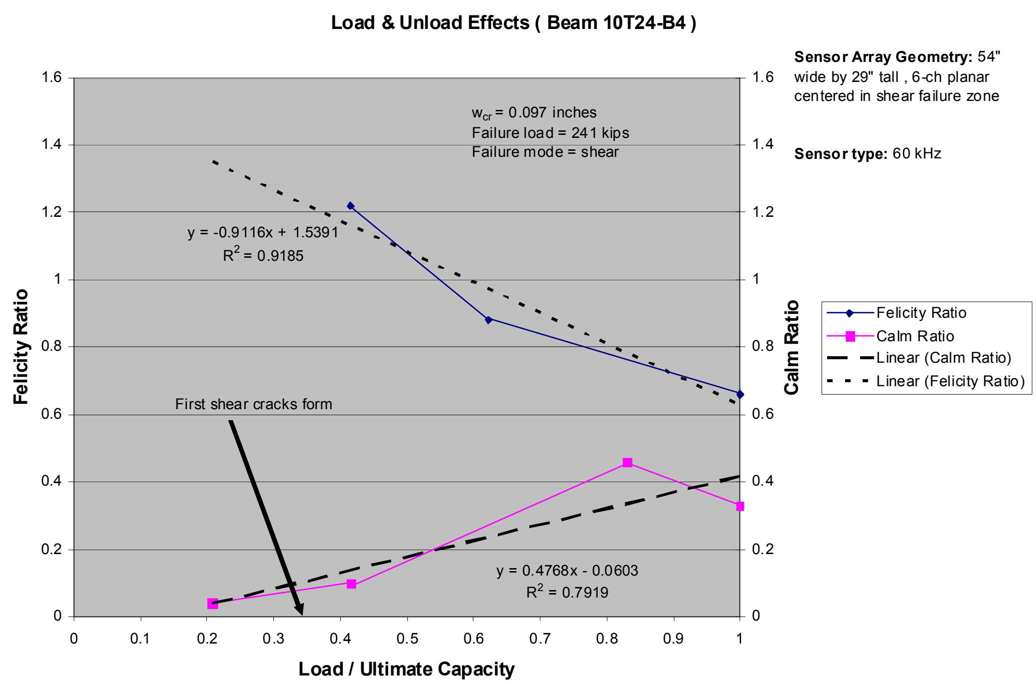

Figure 3.108 Felicity and calm ratios for test beam 10T24-B4.

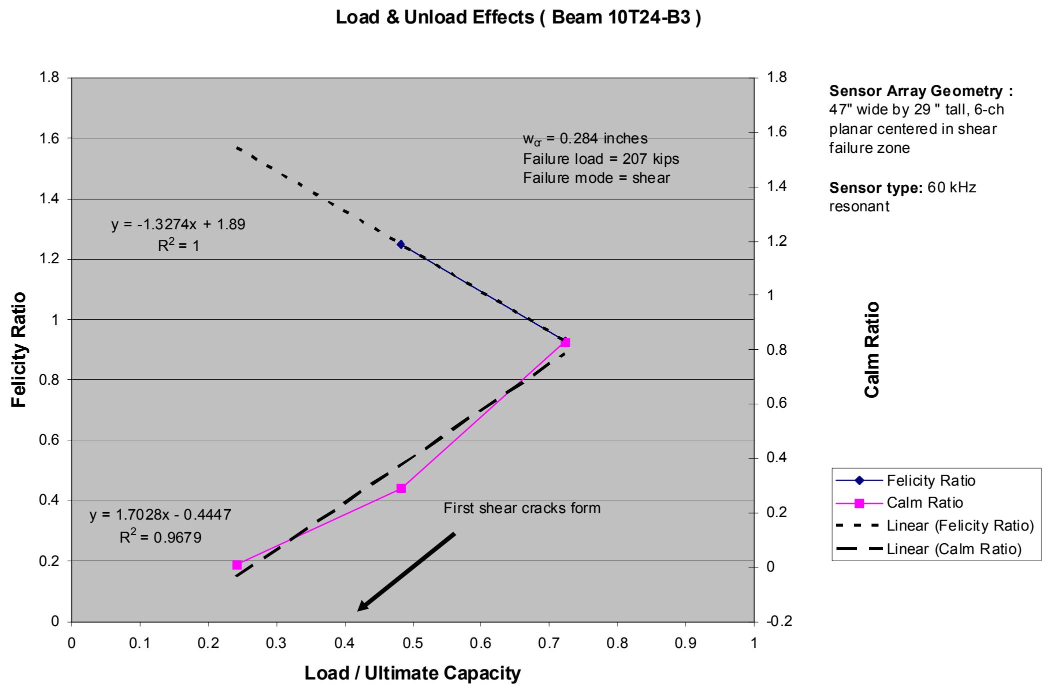

Figure 3.109 Felicity and calm ratios for test beam 10T24-B3.

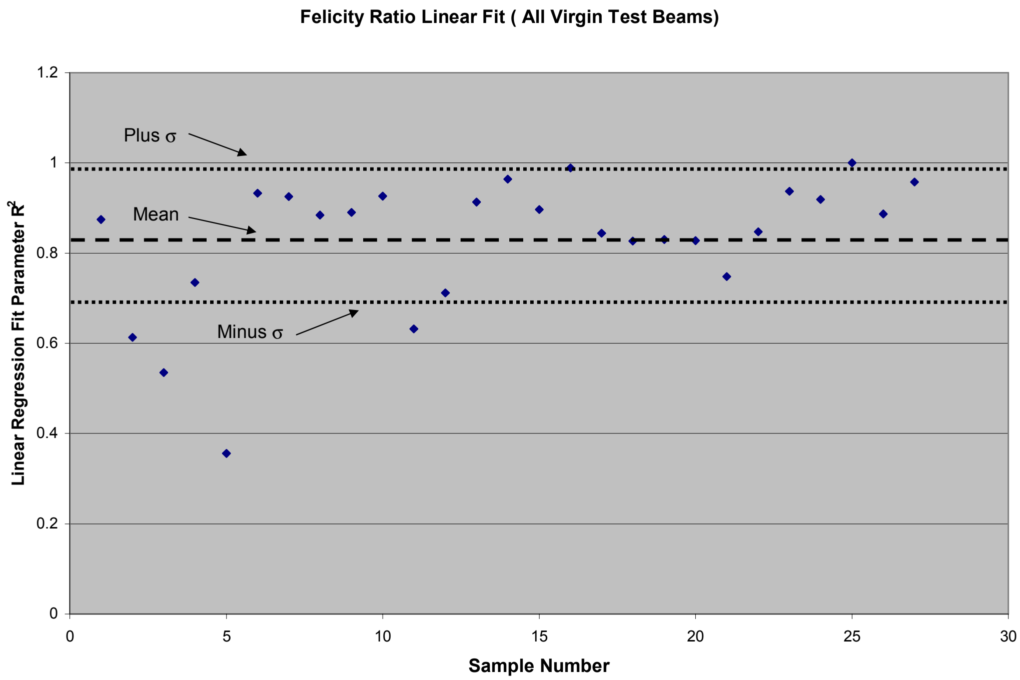

Figure 3.110 Linear regression fit parameter for felicity ratio data on all virgin test beams.

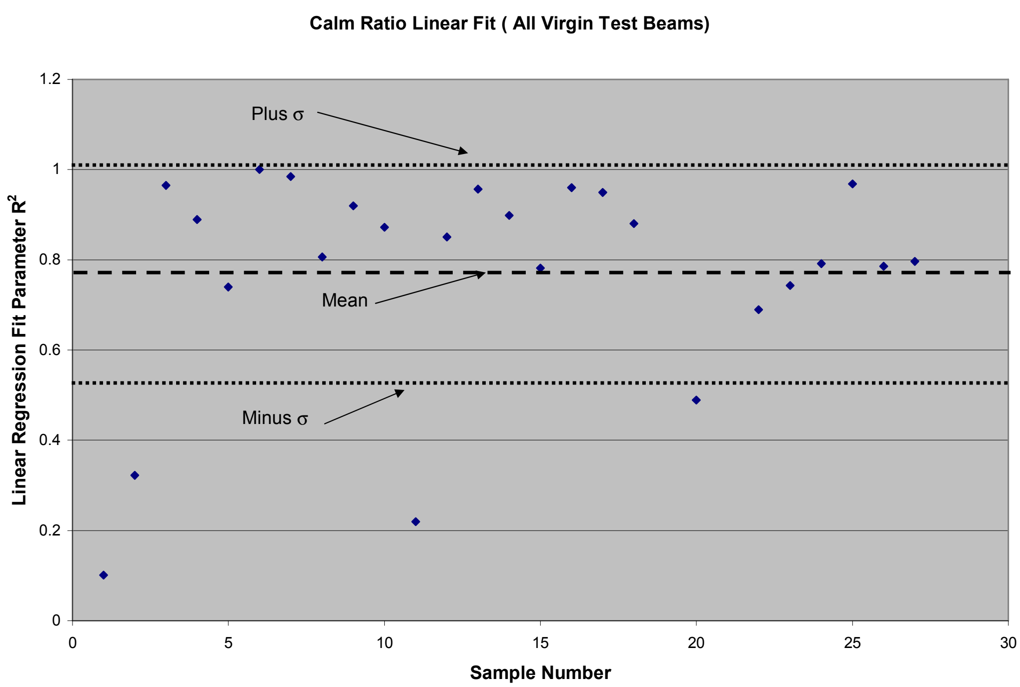

Figure 3.111 Linear regression fit parameter for calm ratio data on all virgin test beams.

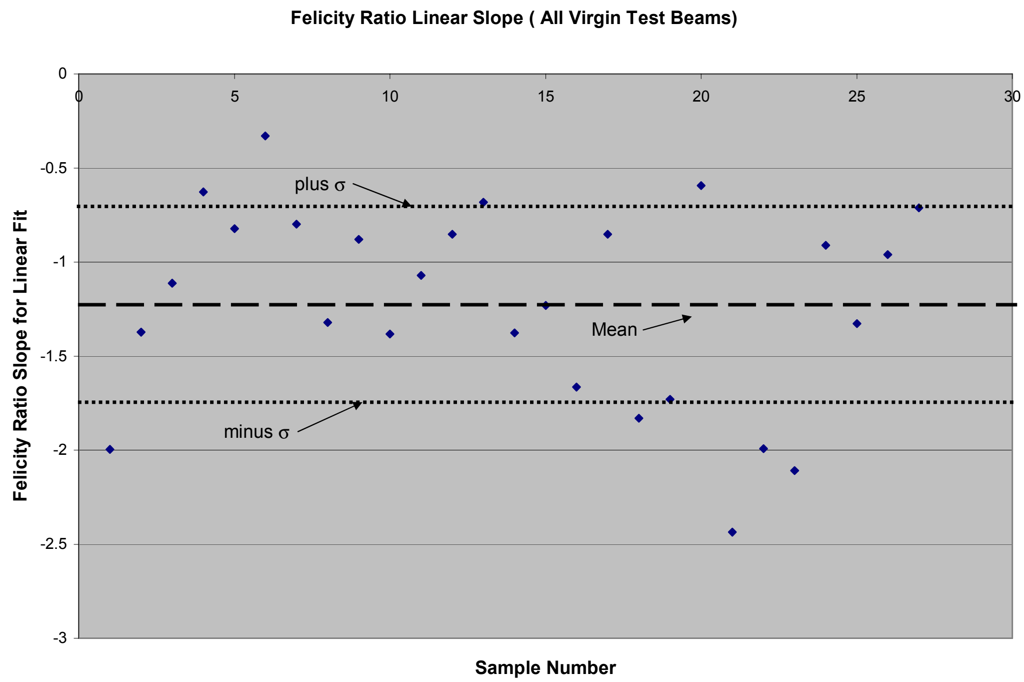

Figure 3.112 Linear regression slope for felicity ratio data on all virgin test beams.

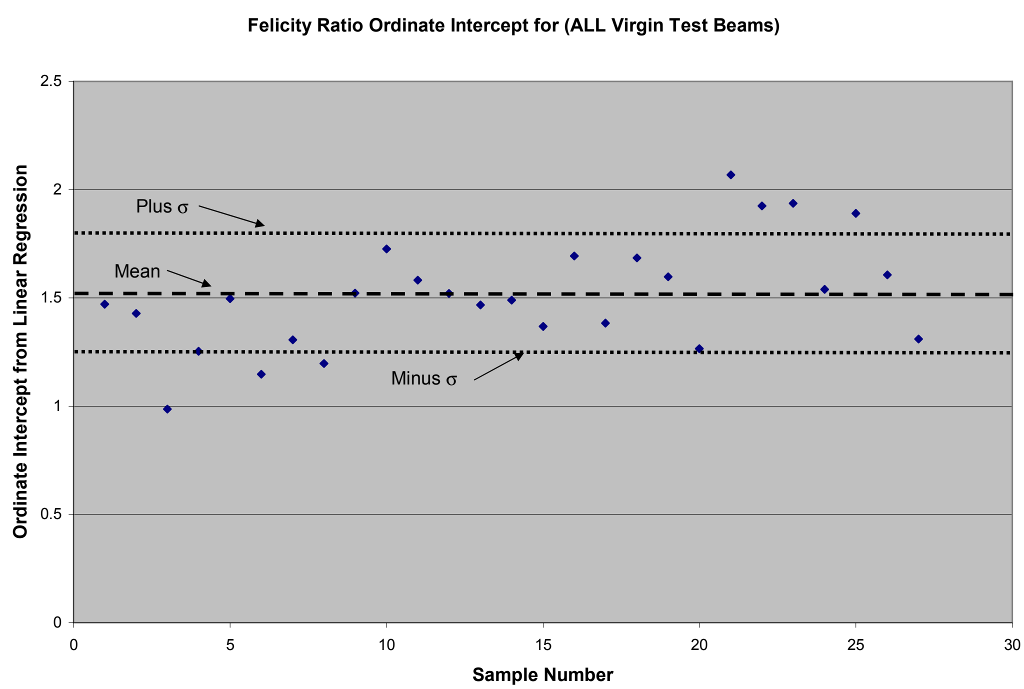

Figure 3.113 Linear regression ordinate intercept for felicity ratio data on all virgin test beams.

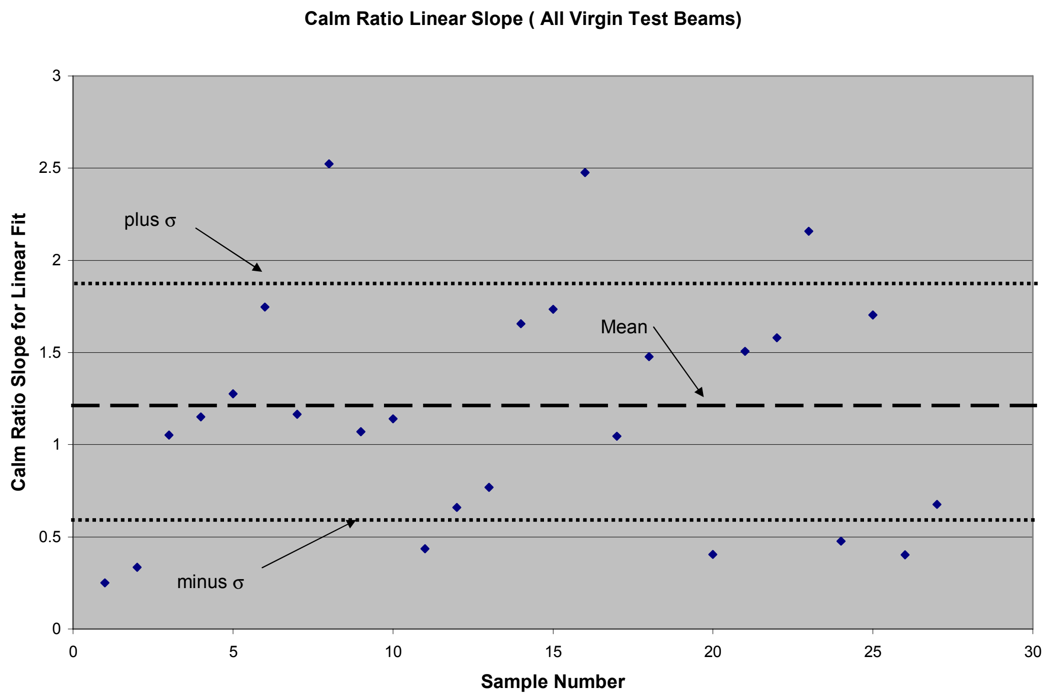

Figure 3.114 Linear regression slope for calm ratio data on all virgin test beams.

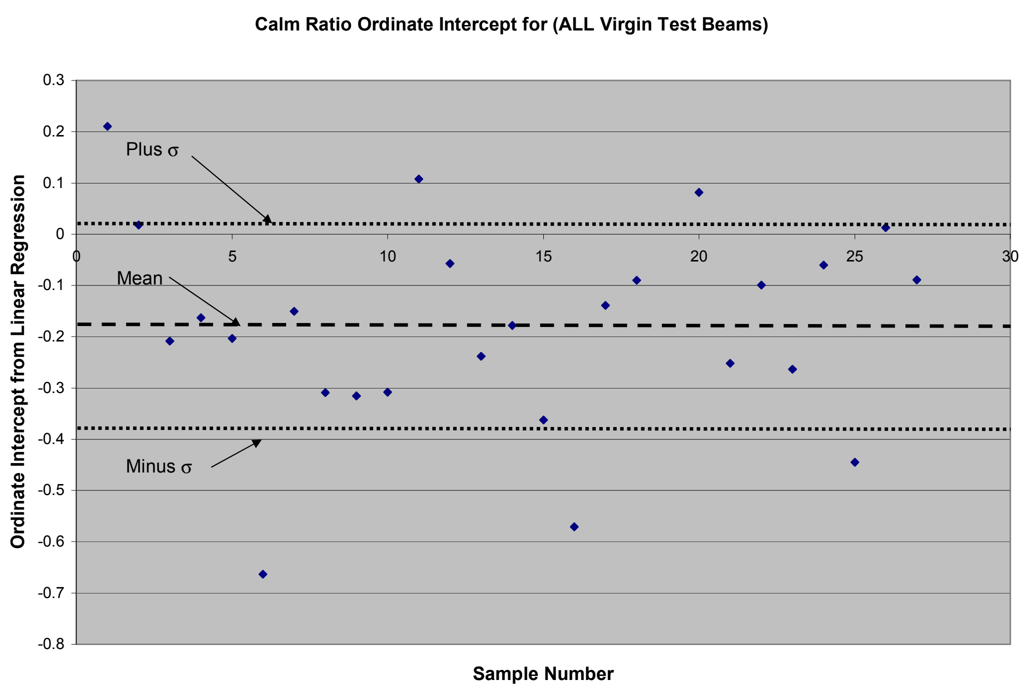

Figure 3.115 Linear regression ordinate intercept for calm ratio data on all virgin test beams.

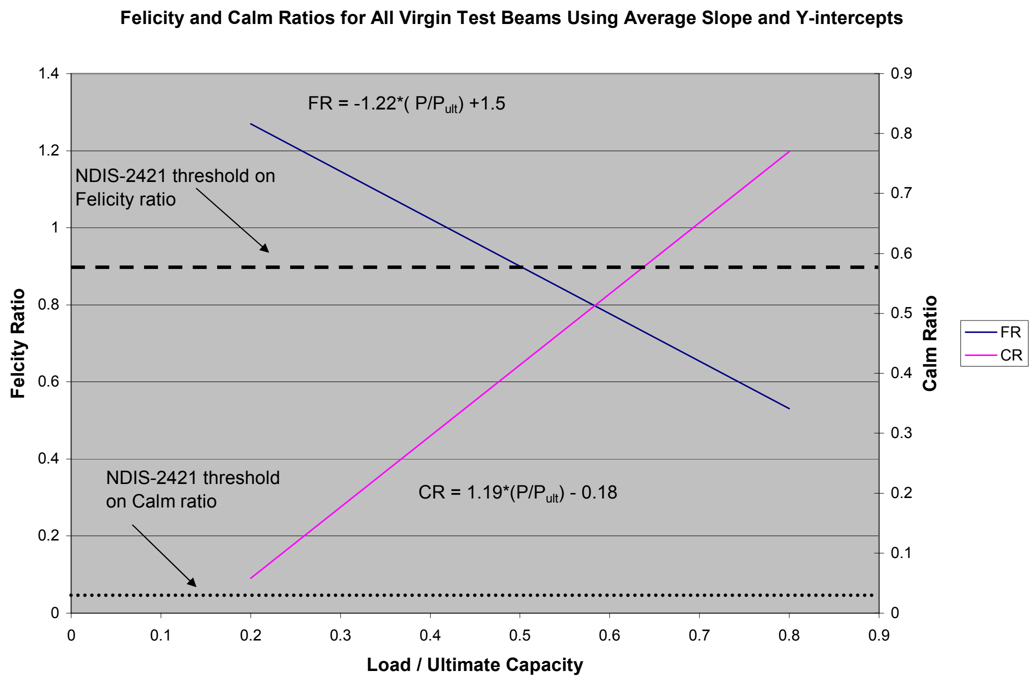

Figure 3.116 Felicity and calm ratio response to loading protocol as represented by the mean slopes and originate intercepts from all virgin test beams.

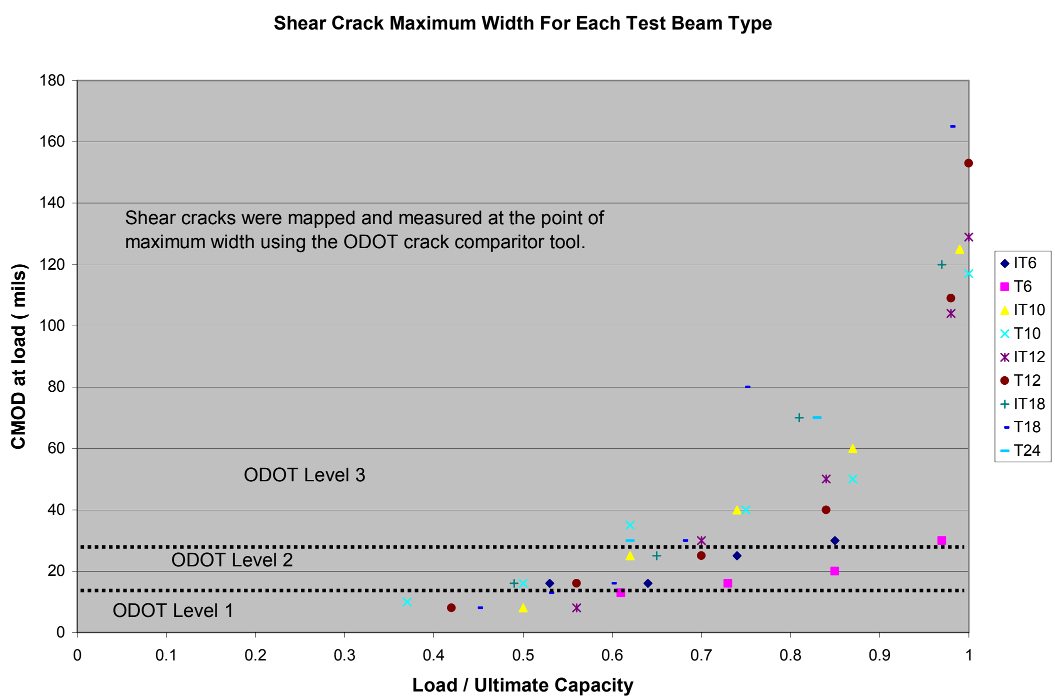

Figure 3.117(a) CMOD versus load normalized with ultimate capacity for each test beam type.

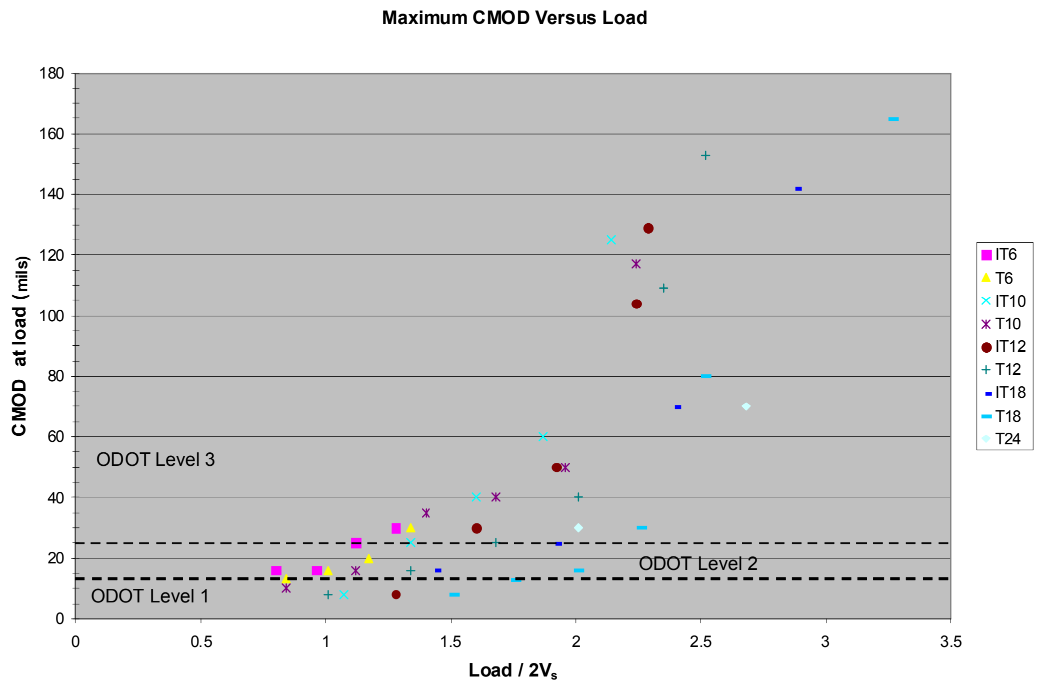

Figure 3.117(b) CMOD versus load normalized with two times the shear strength from rebar (V_s) at critical section for each test beam type.

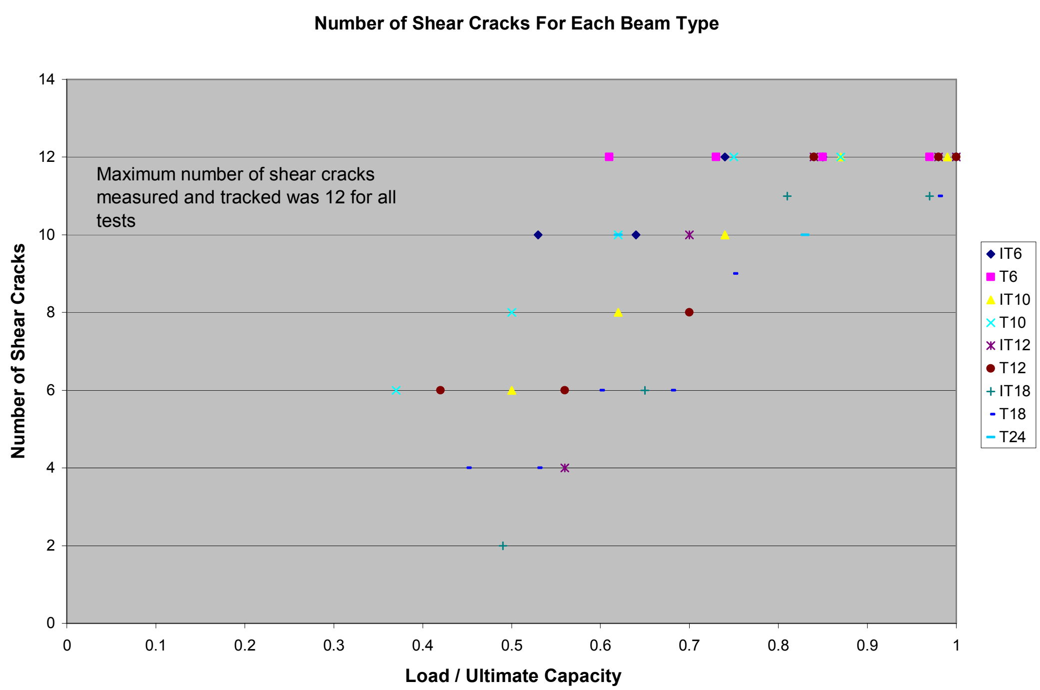

Figure 3.118 Number of shear cracks versus load for each test beam type.

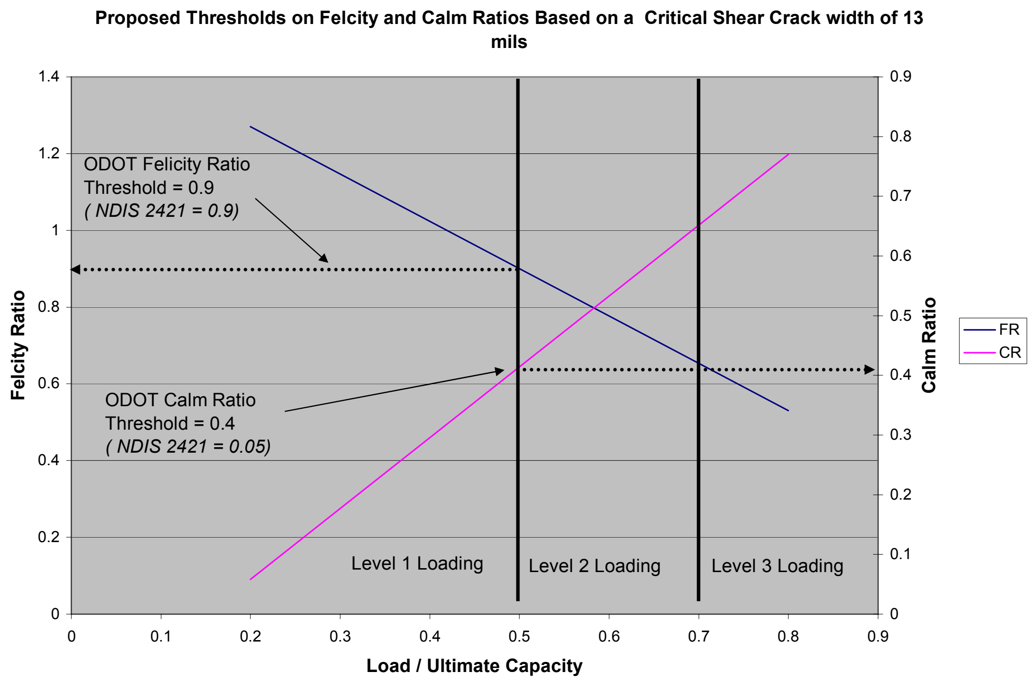

Figure 3.119 Proposed thresholds for felicity and calm ratios based on a critical shear crack width of 13 mils.

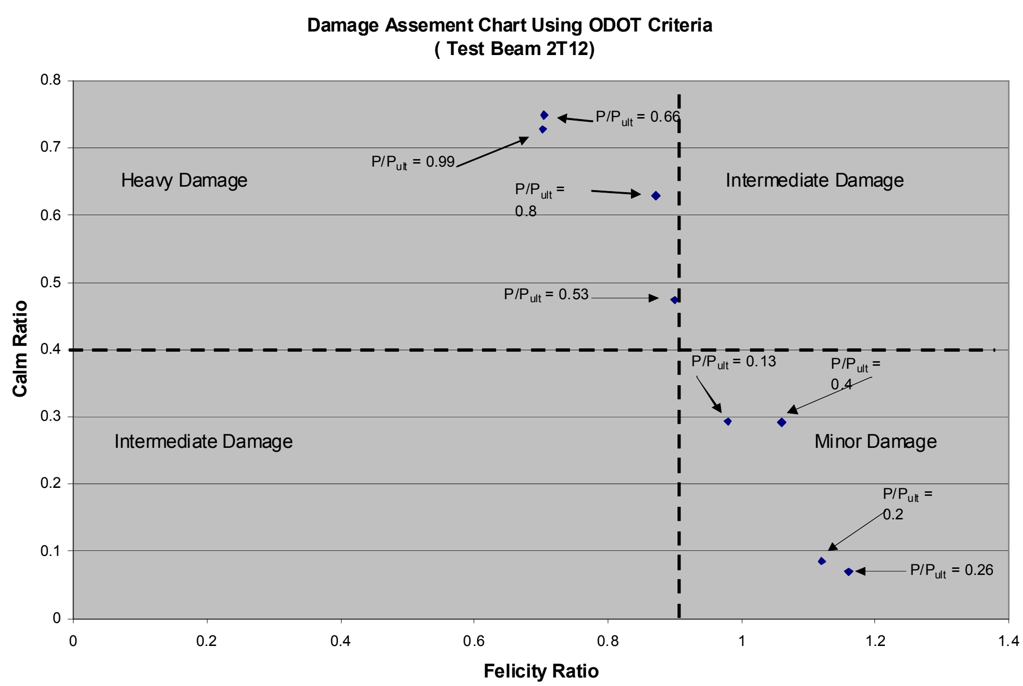

Figure 3.120 Example damage assessment chart for test beam 2T12 using ODOT criteria.

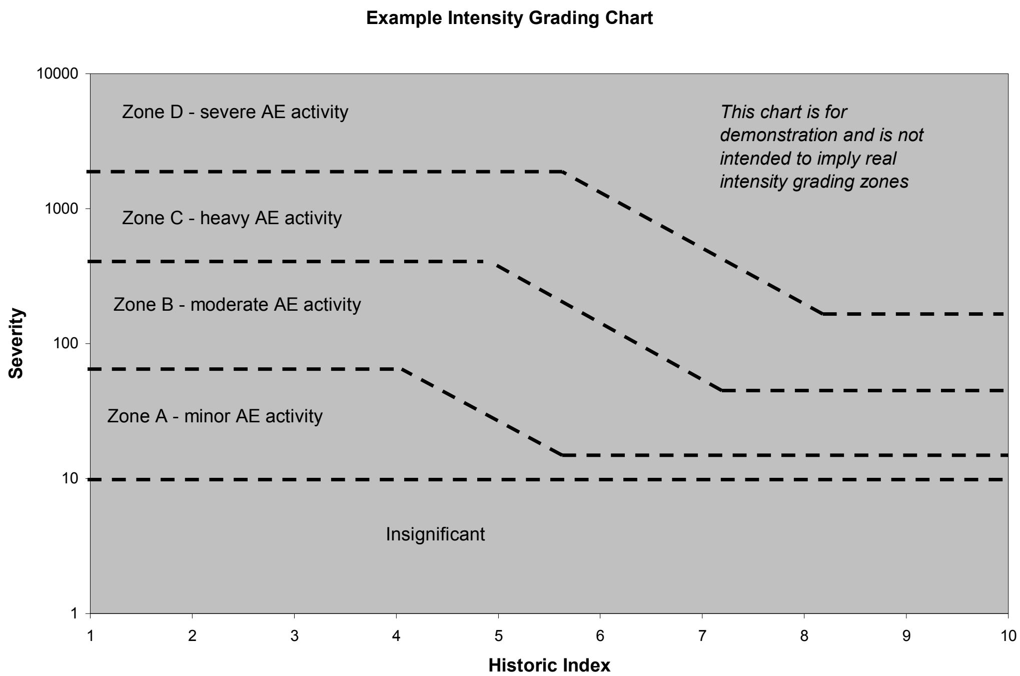

Figure 3.121 Example intensity grading chart (hypothetical).

Figure 3.122 Test beam 7T12 in loading fixture with AE sensor deployment.

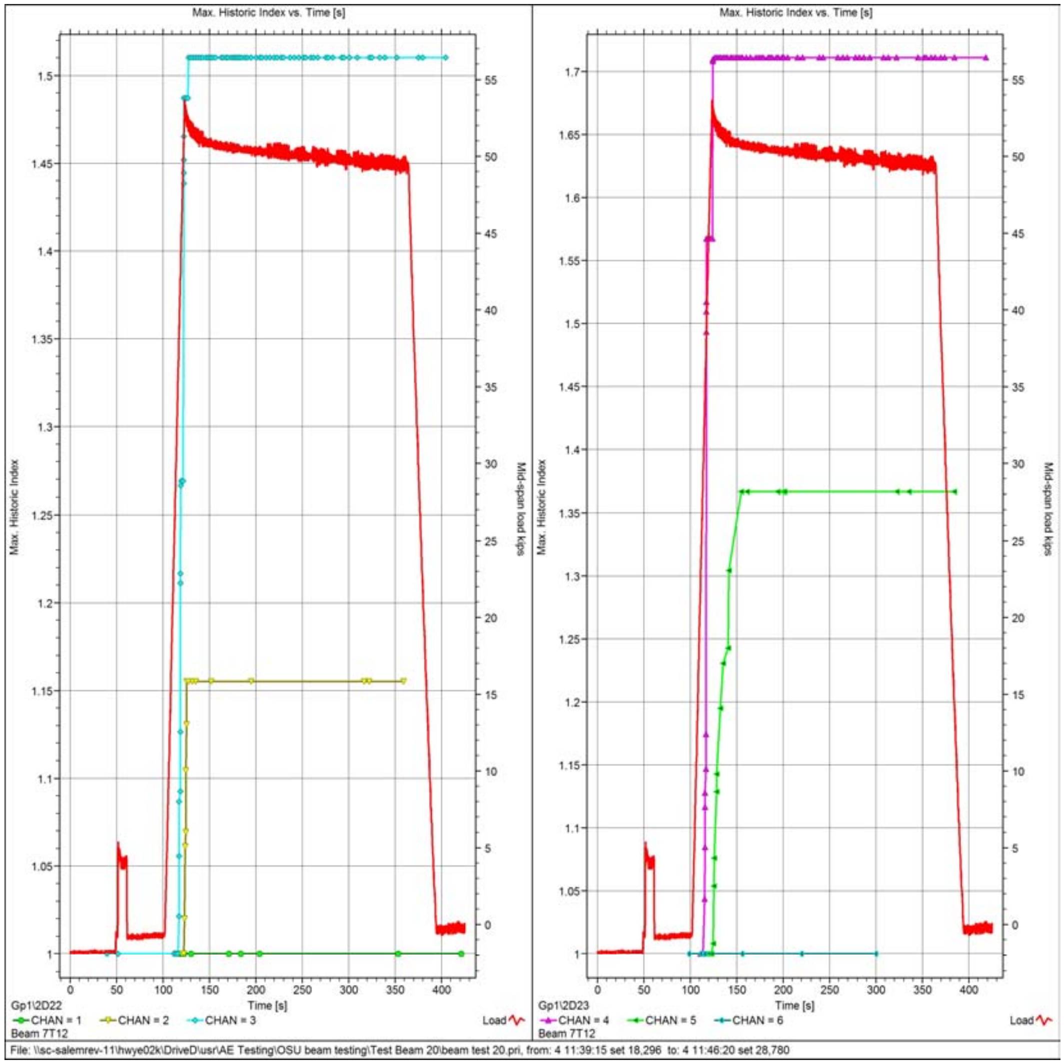

Figure 3.123 Response of the Historic Index during first load cycle.

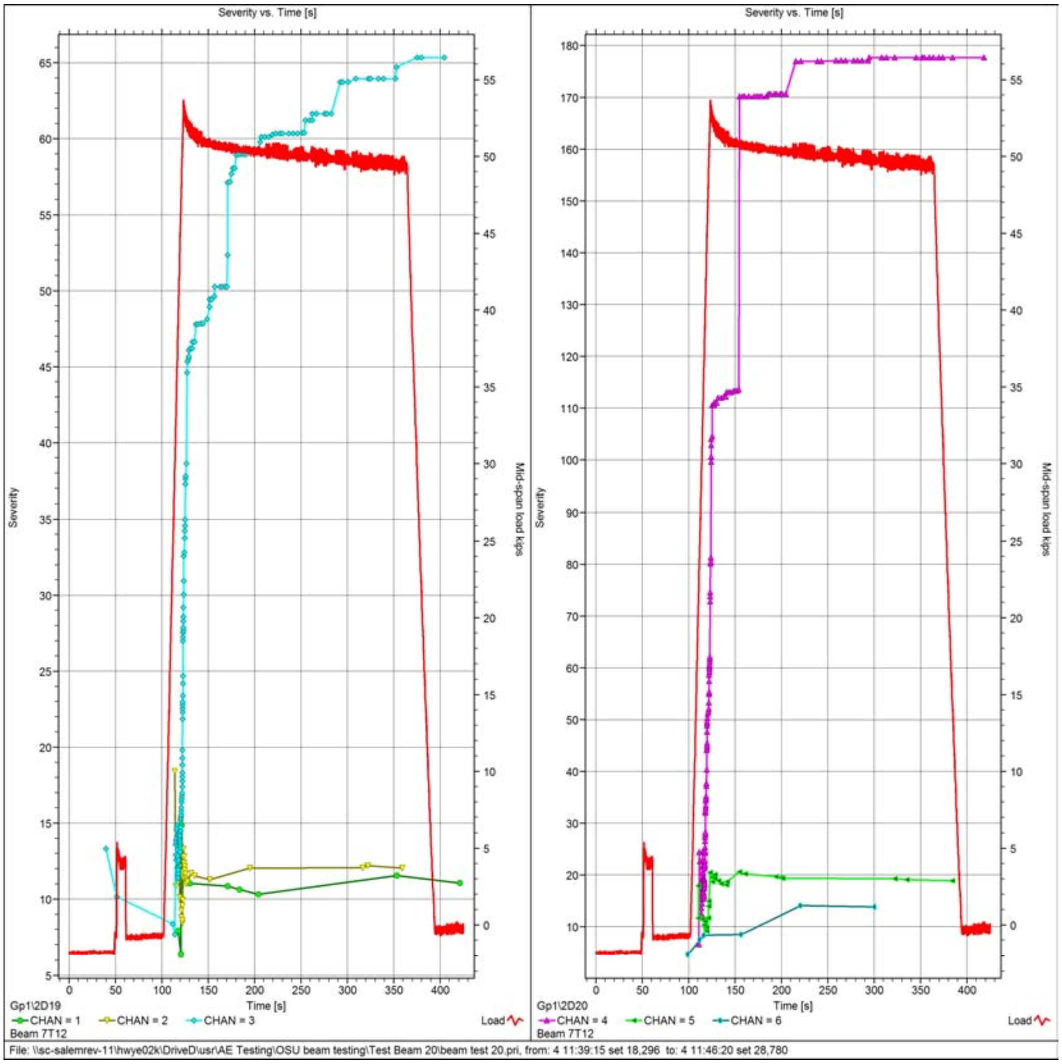

Figure 3.124 Response of the Severity during first load cycle.

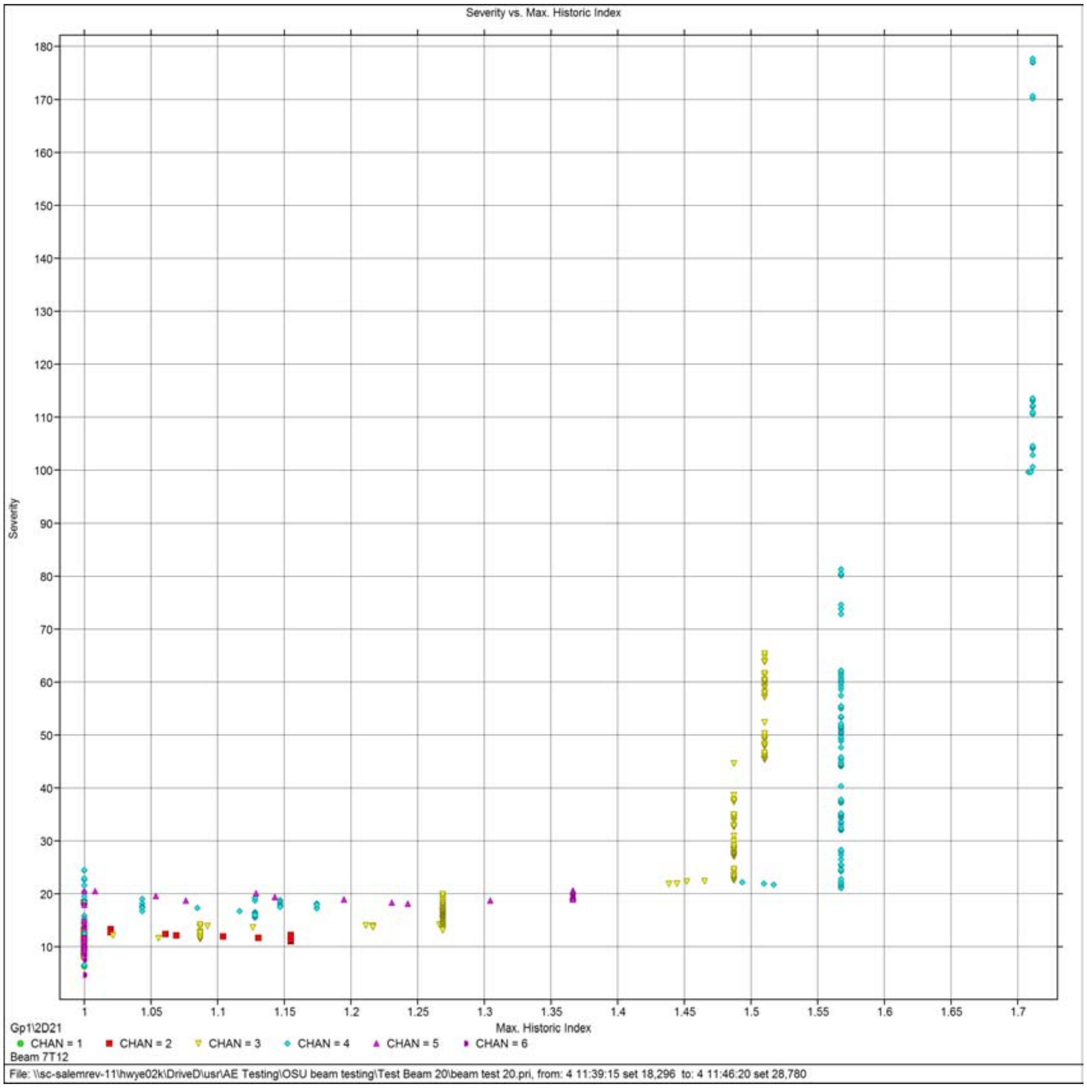

Figure 3.125 Intensity plot of first load cycle.

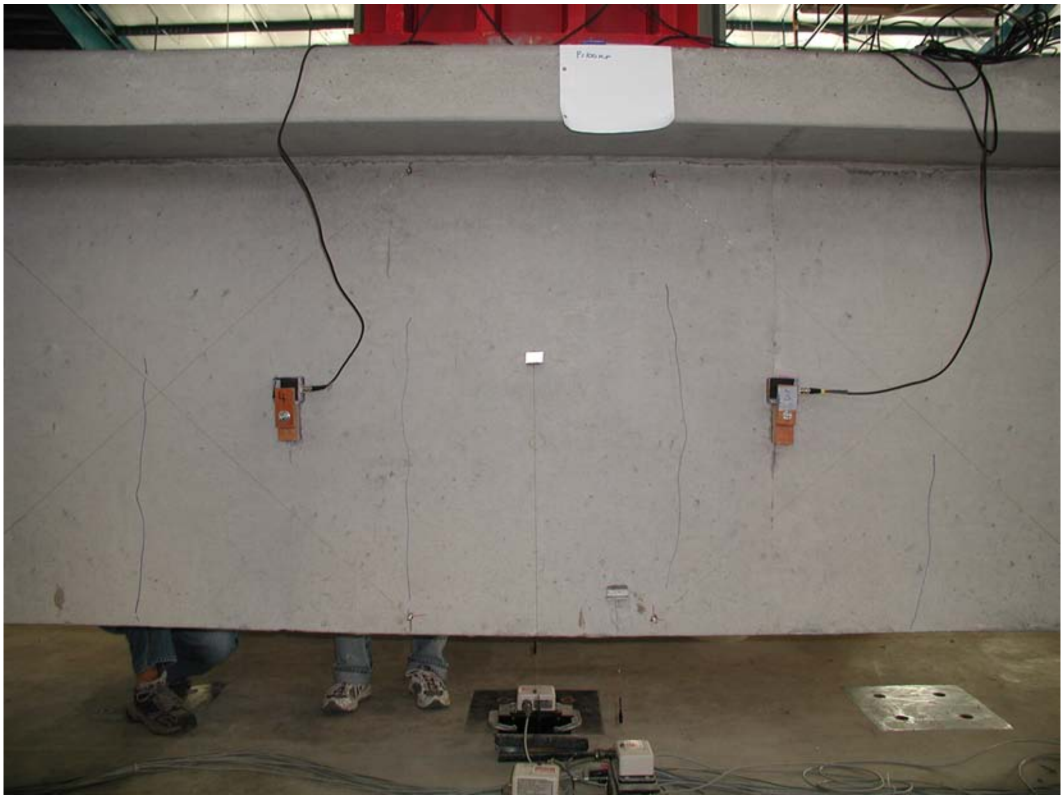

Figure 3.126 Photograph of test beam 7T12 after the second load cycle(P/P_{ult} = 0.24) .

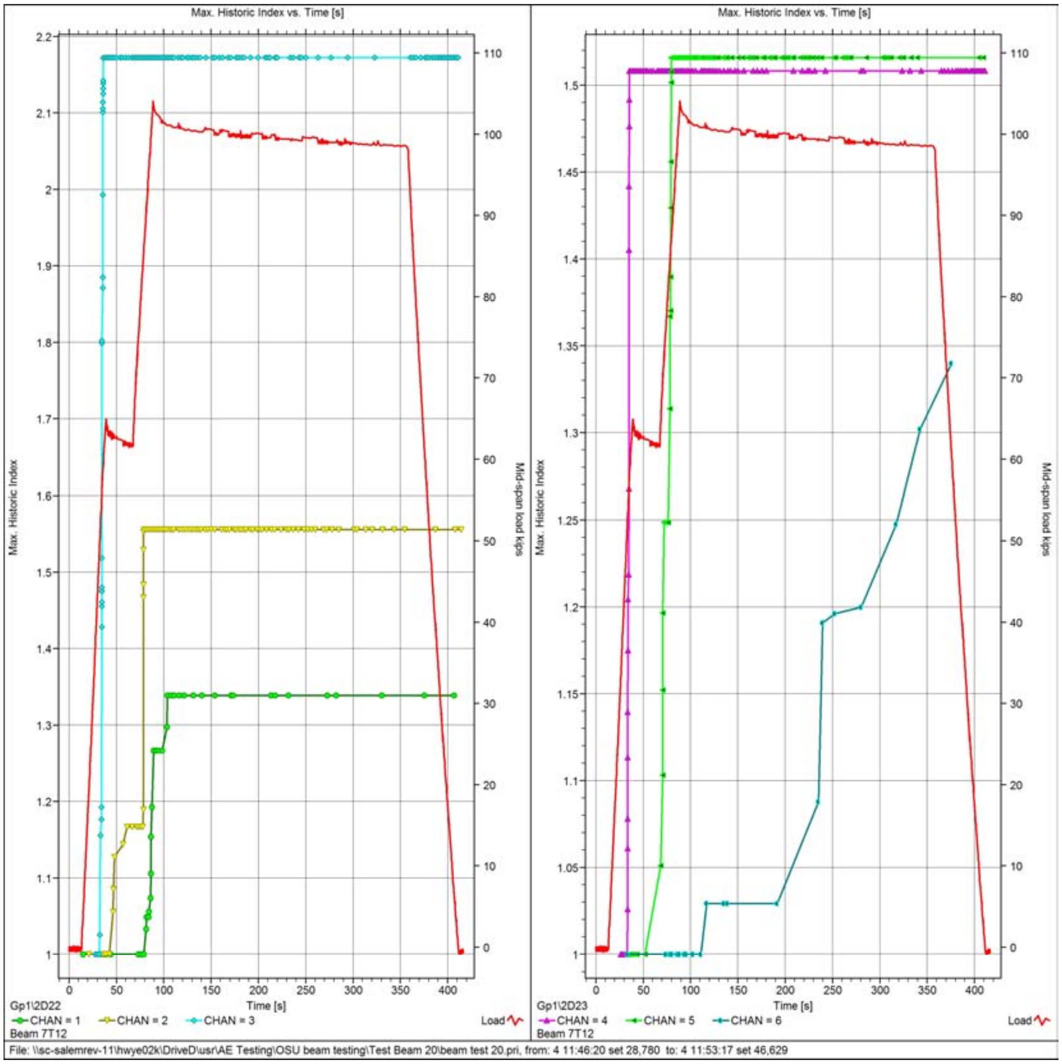

Figure 3.127 Response of the Historic Index during second load cycle.

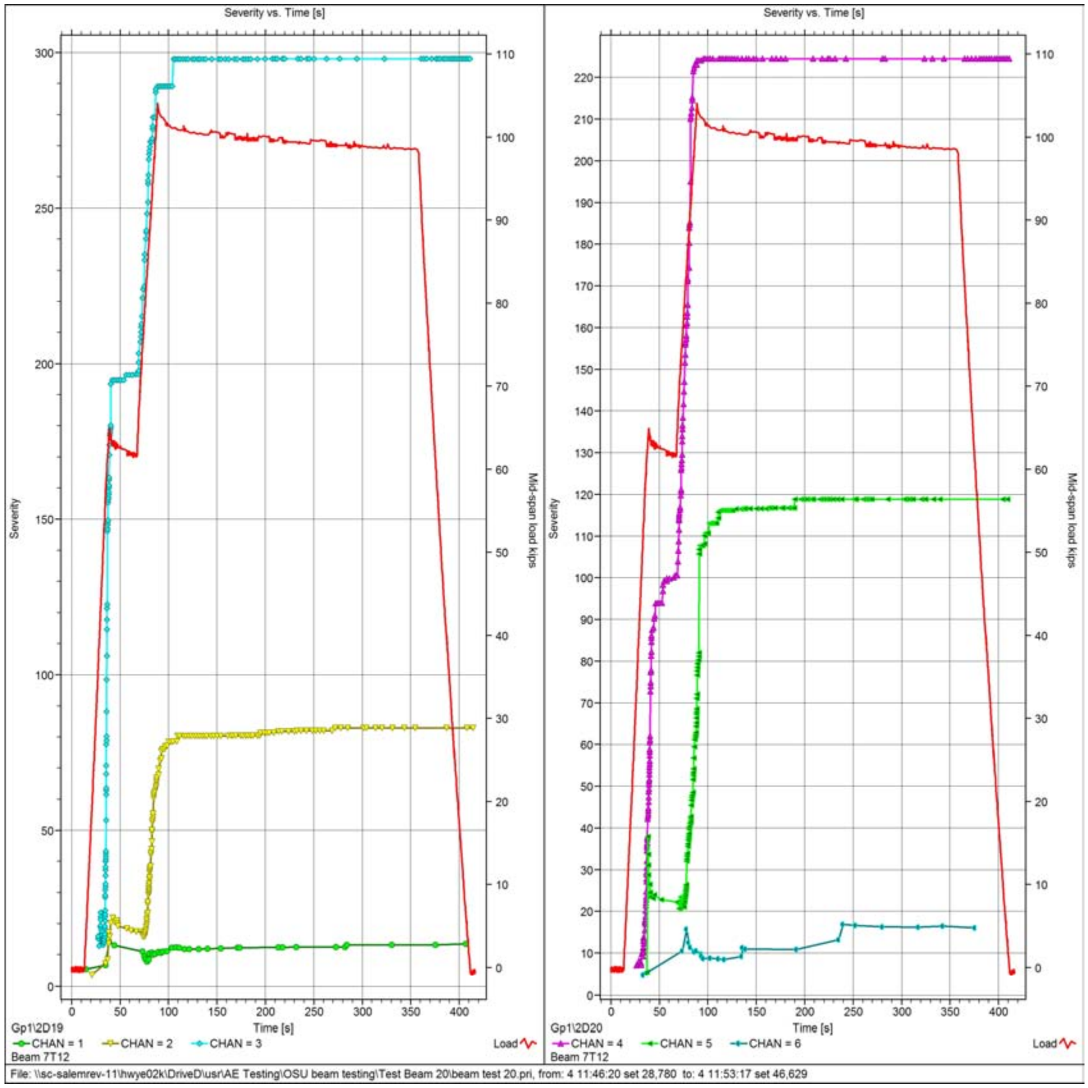

Figure 3.128 Response of the Severity during second load cycle.

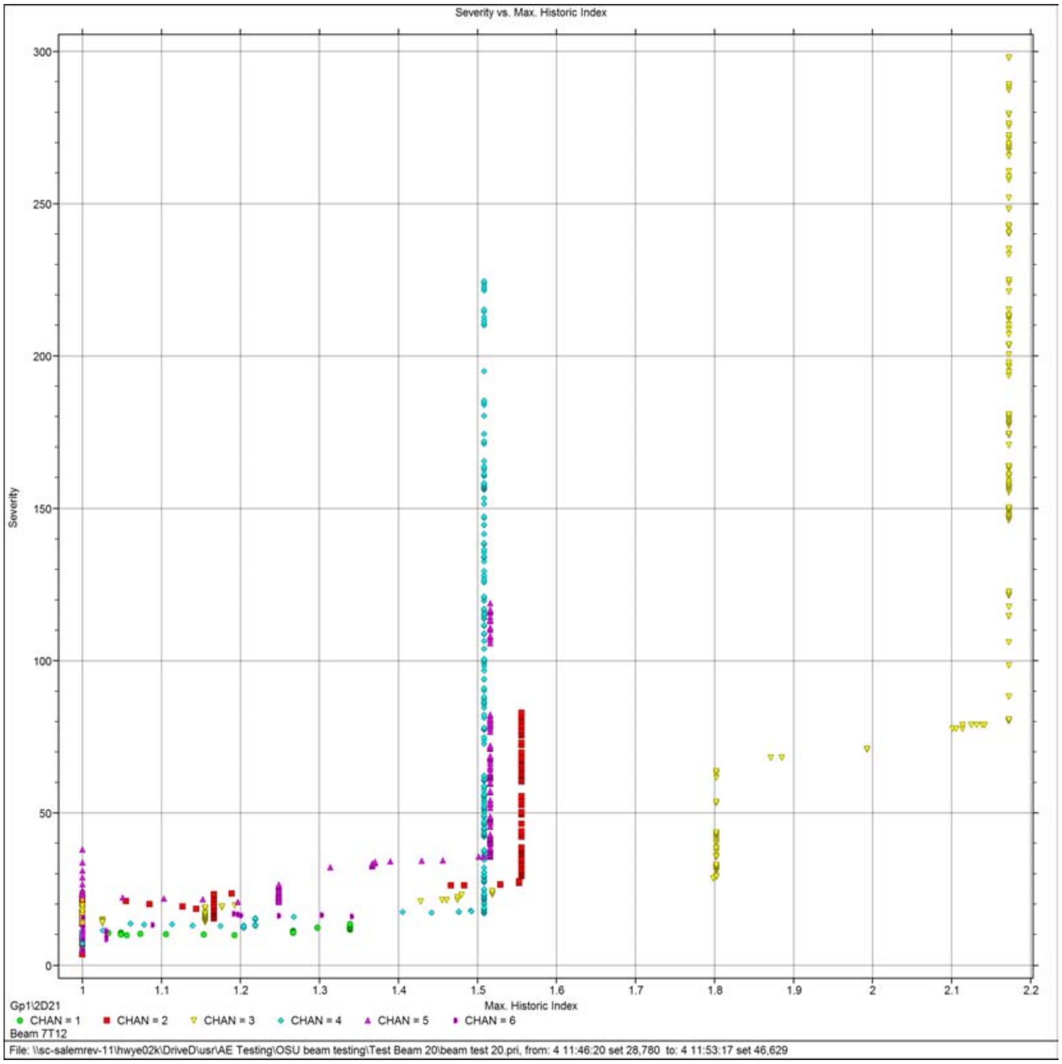

Figure 3.129 Intensity plot of second load cycle.

Figure 3.130 Photograph of test beam 7T12 after the third load cycle (P/P_{ult} = 0.35) .

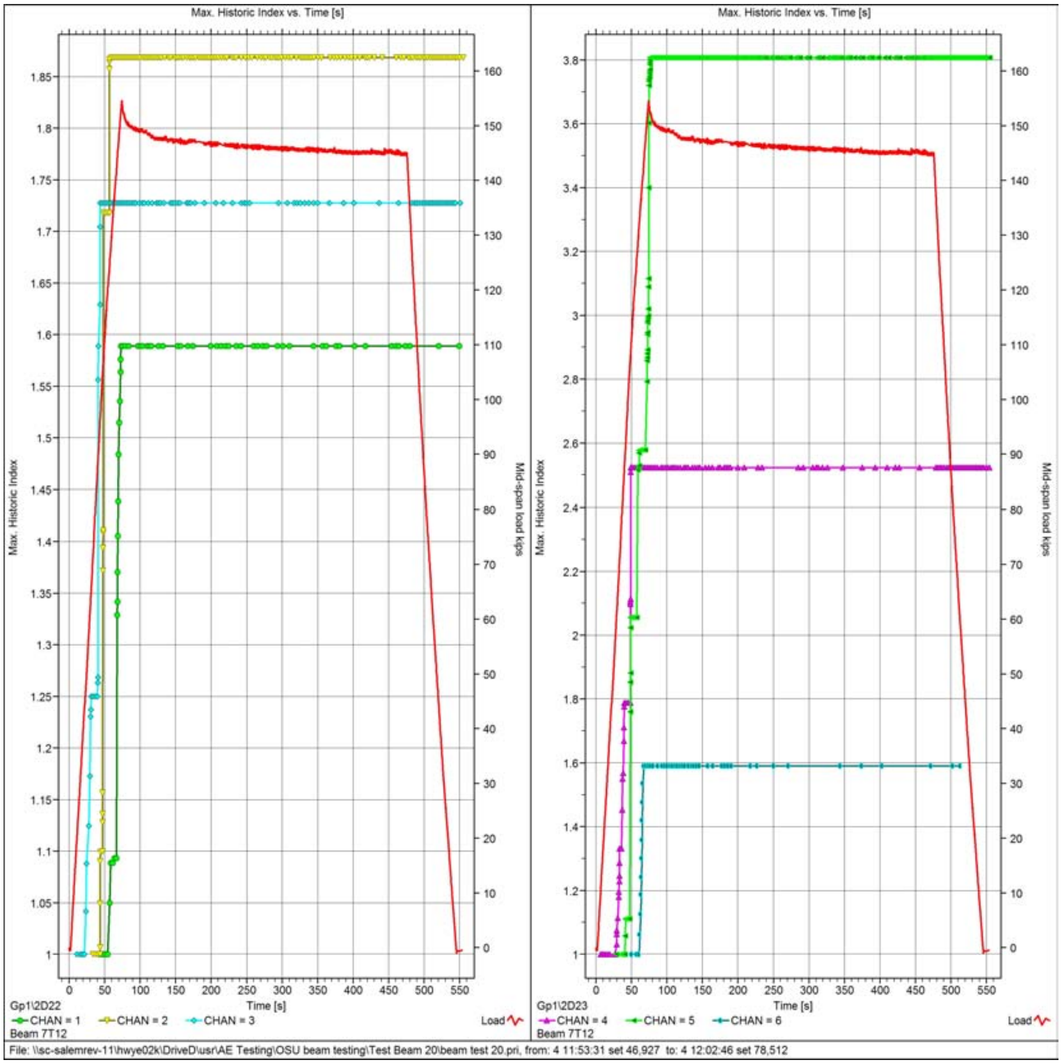

Figure 3.131 Response of the Historic Index during third load cycle.

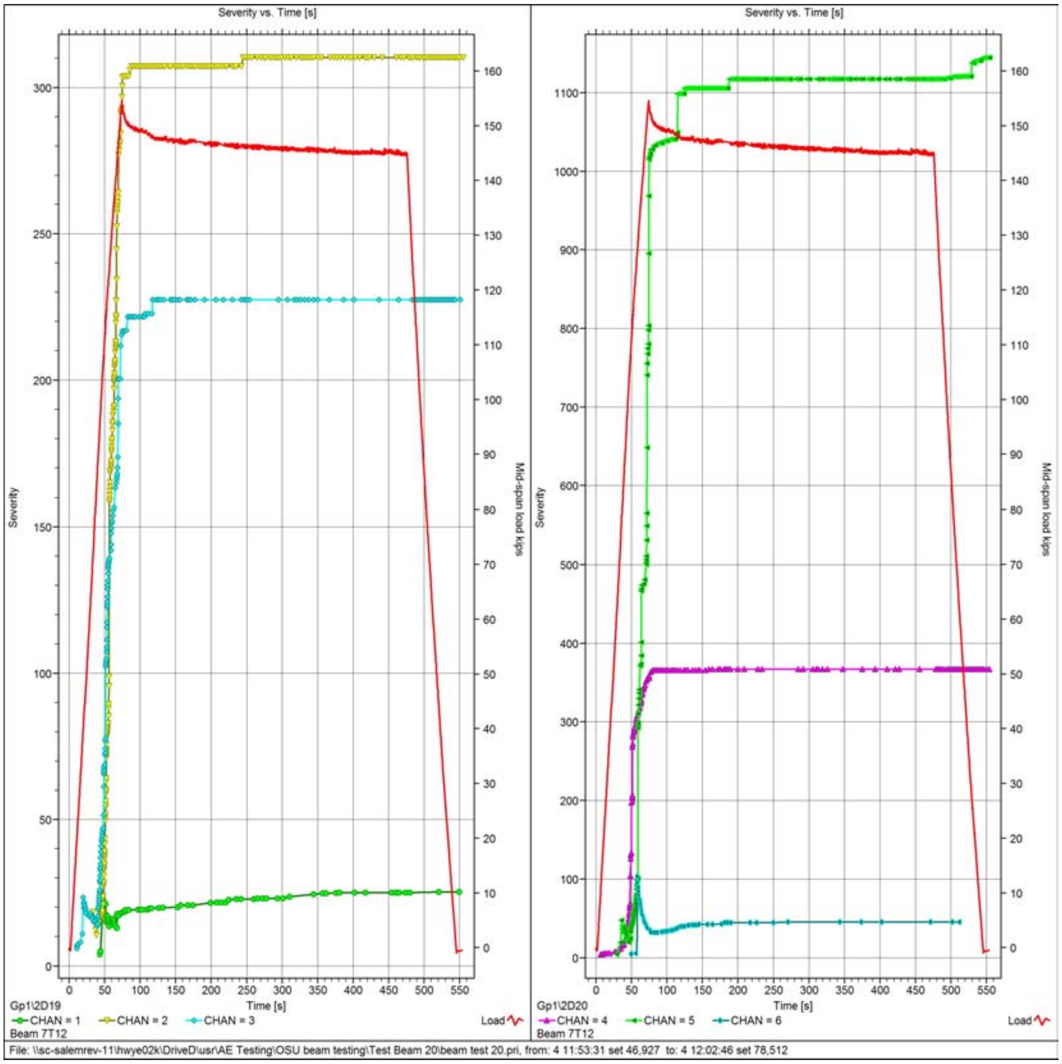

Figure 3.132 Response of the Severity during third load cycle.

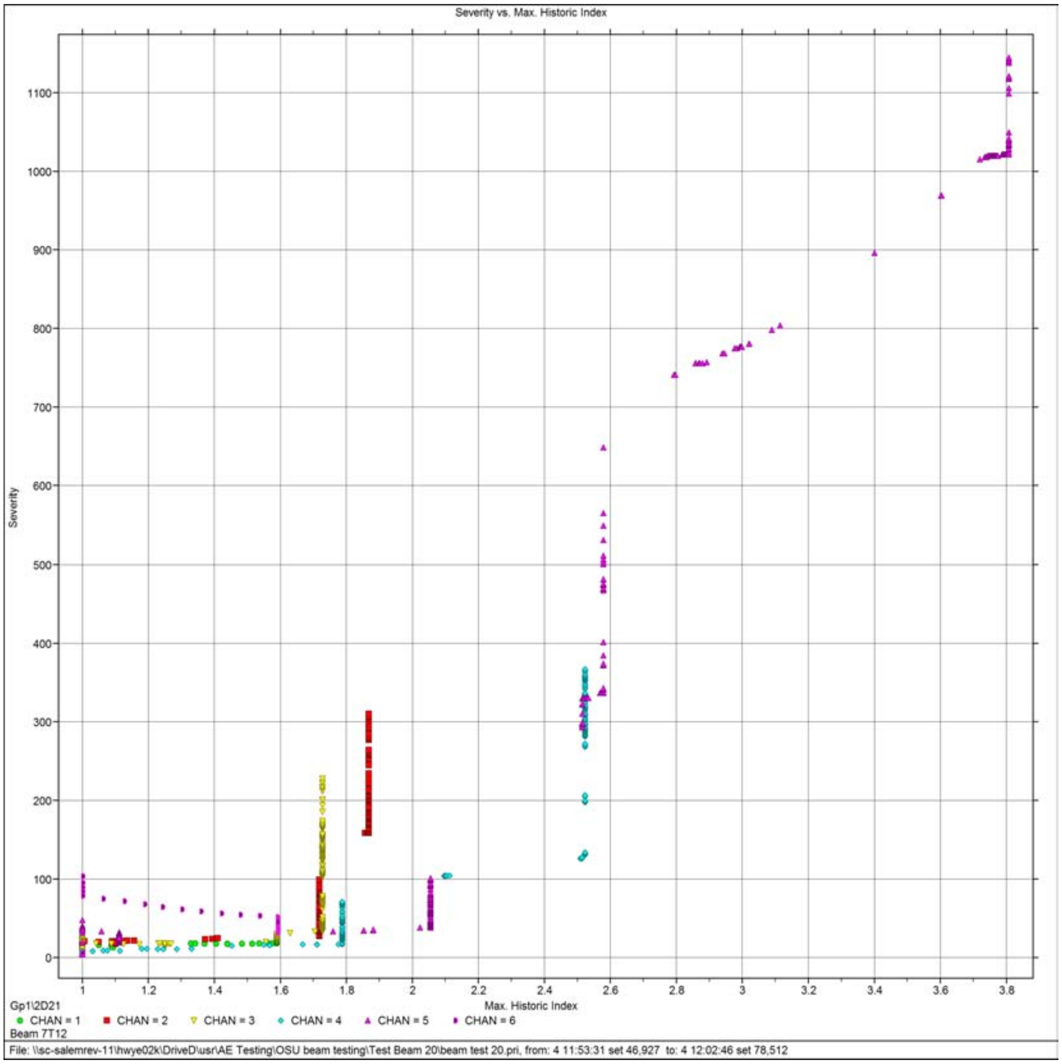

Figure 3.133 Intensity plot of third load cycle.

Figure 3.134 Photograph of test beam 7T12 after the fourth load cycle (P/P_{ult} = 0.47) .

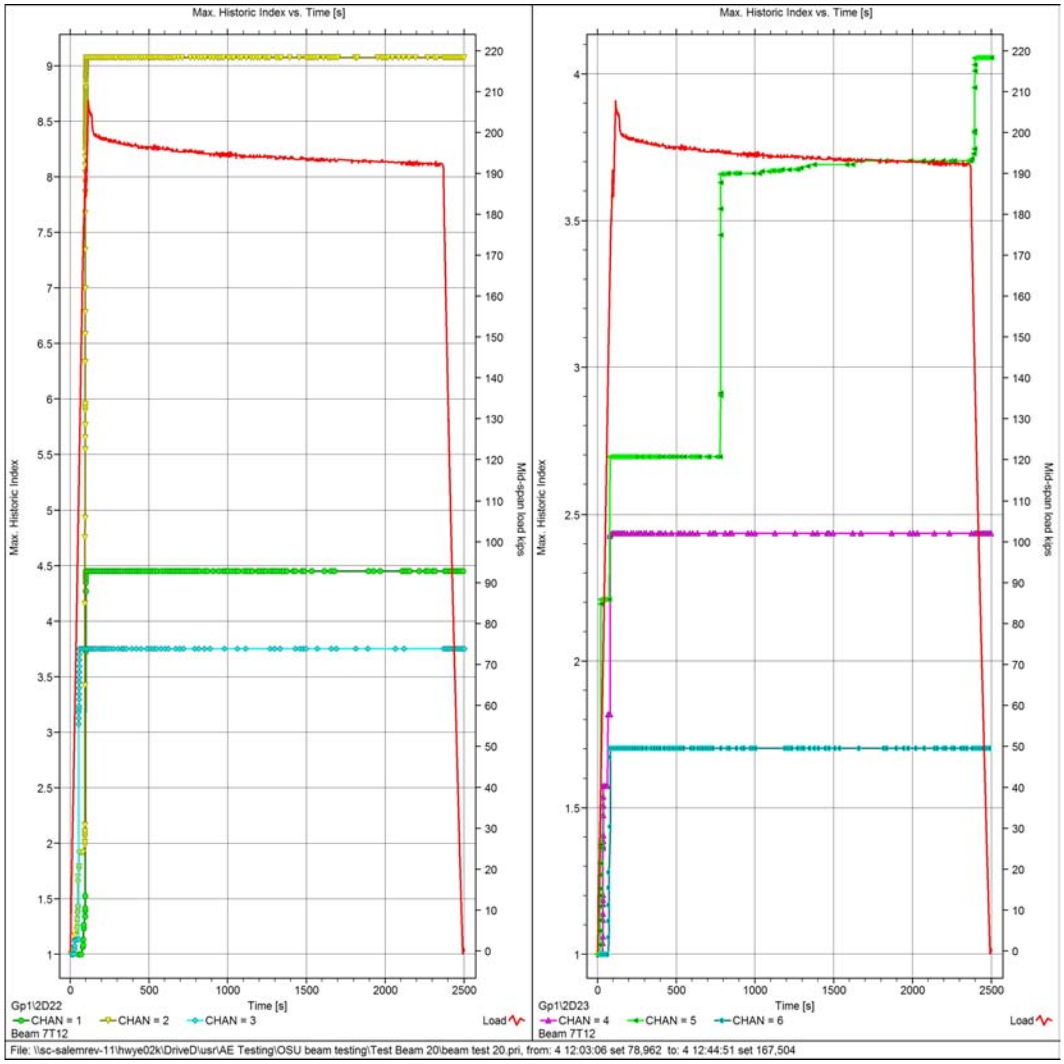

Figure 3.135 Response of the Historic Index during fourth load cycle.

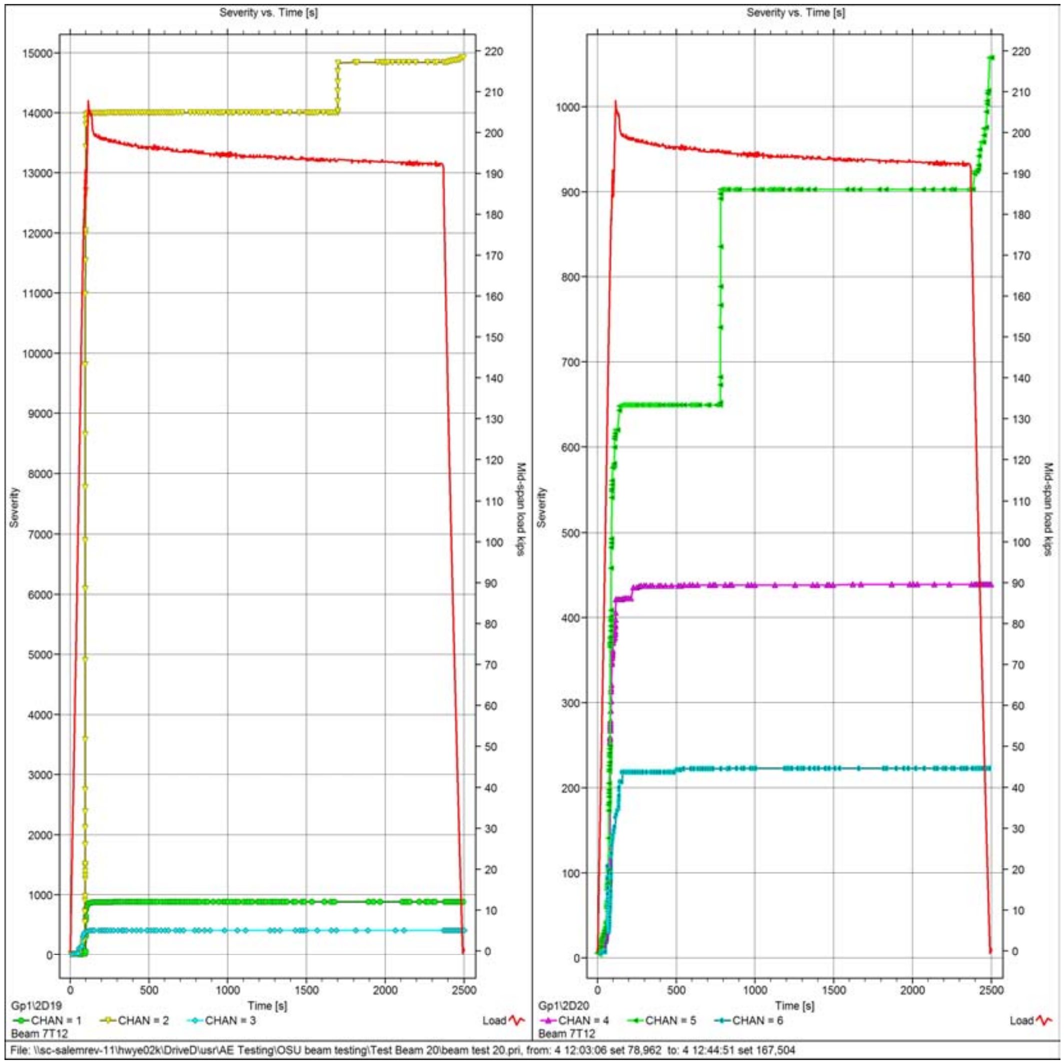

Figure 3.136 Response of the Severity during fourth load cycle.

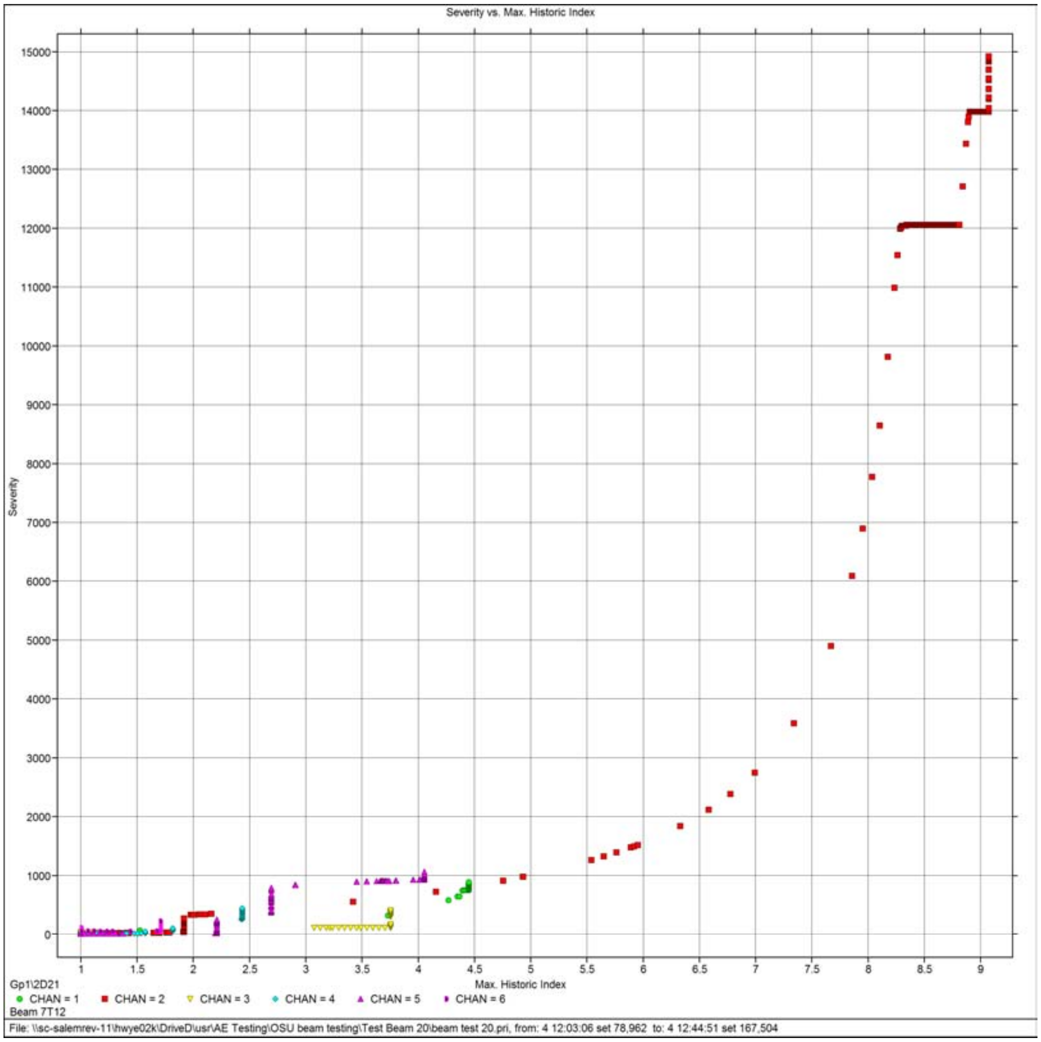

Figure 3.137 Intensity plot of fourth load cycle.

Figure 3.138 Photograph of test beam 7T12 after the fifth load cycle (P/P_{ult} = 0.59) .

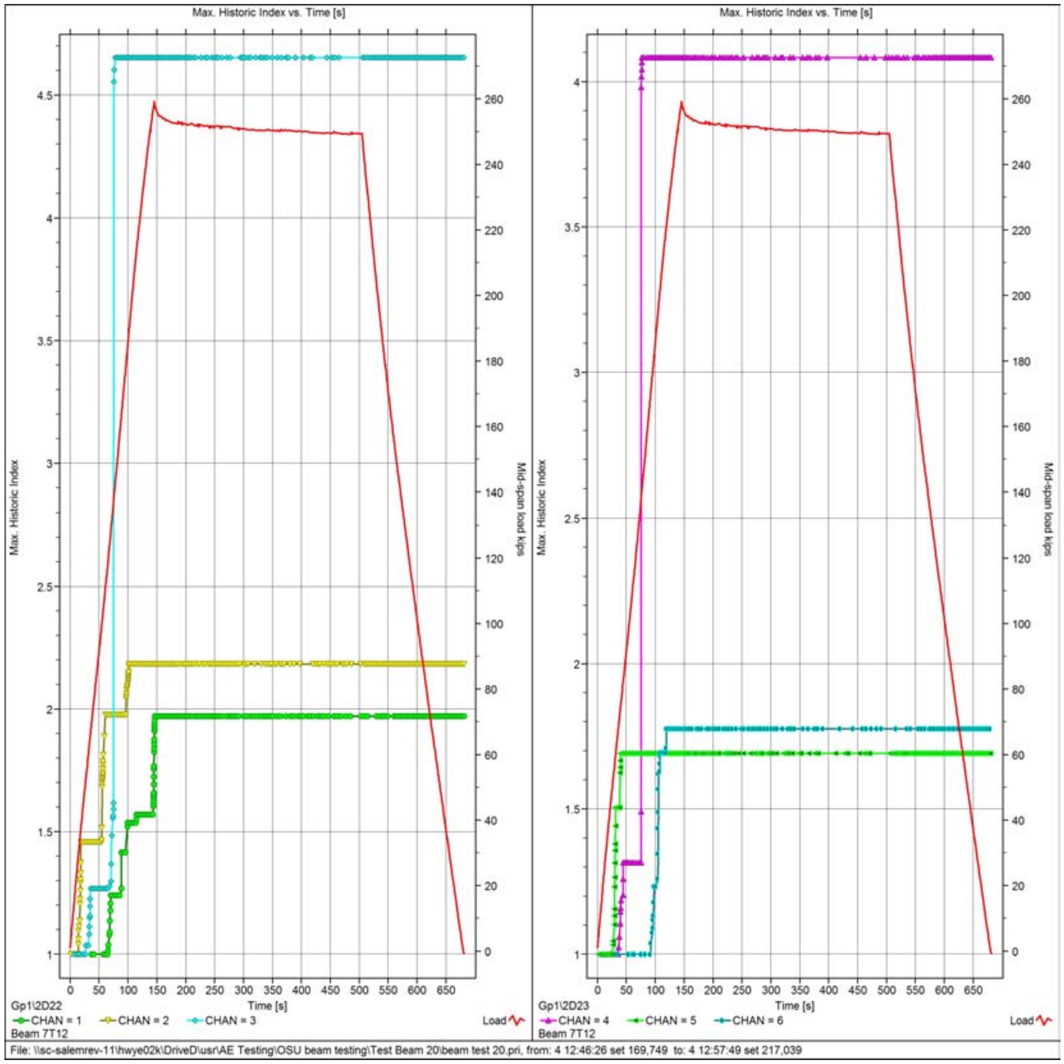

Figure 3.139 Response of the Historic Index during fifth load cycle.

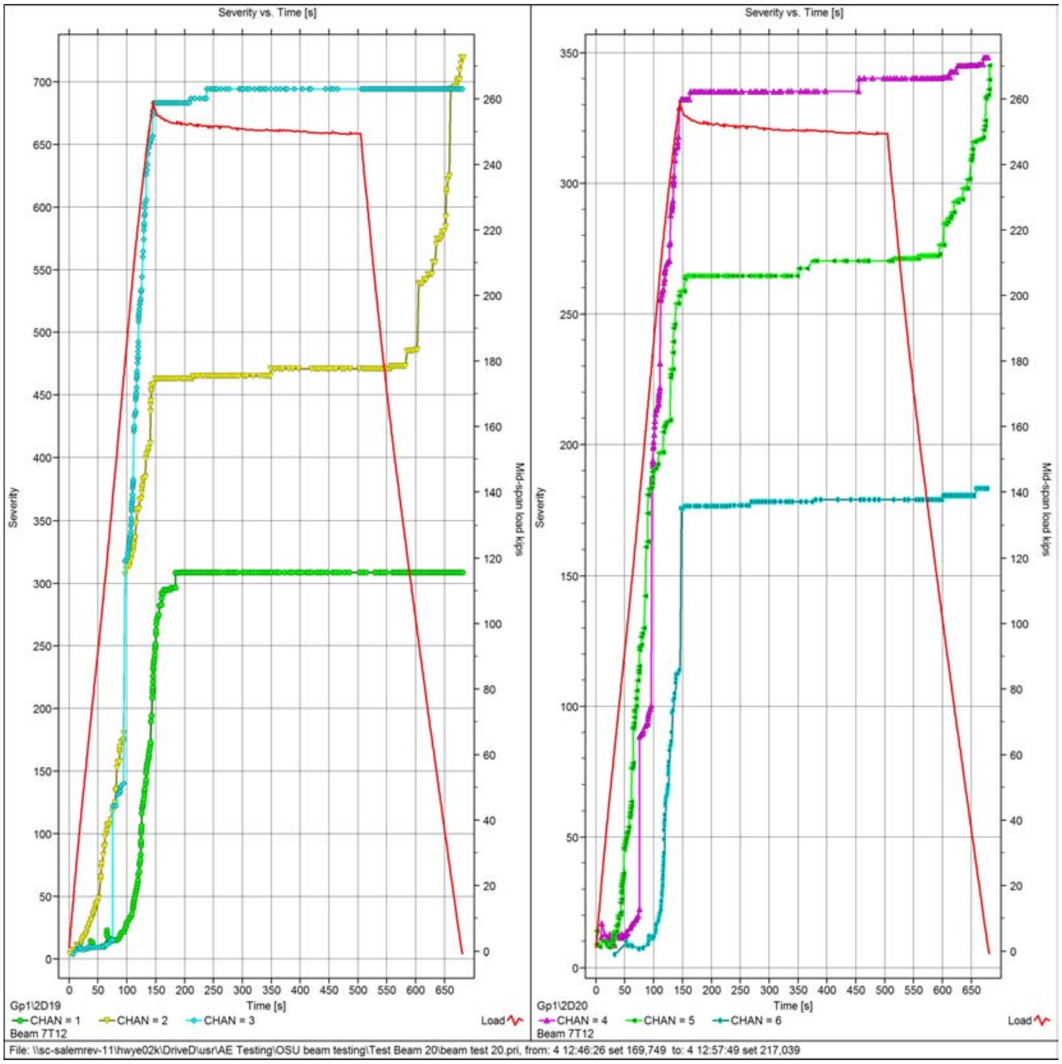

Figure 3.140 Response of the Severity during fifth load cycle.

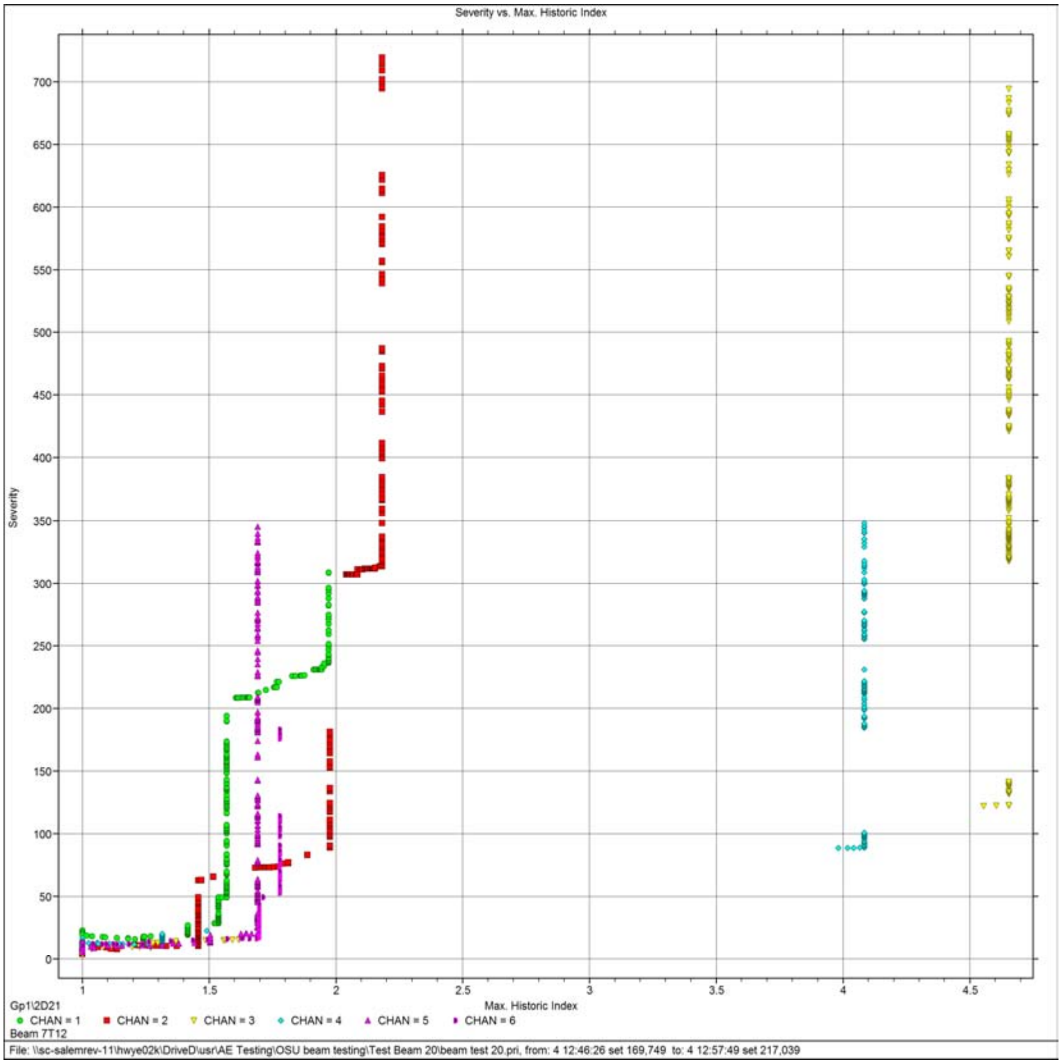

Figure 3.141 Intensity plot of fifth load cycle.

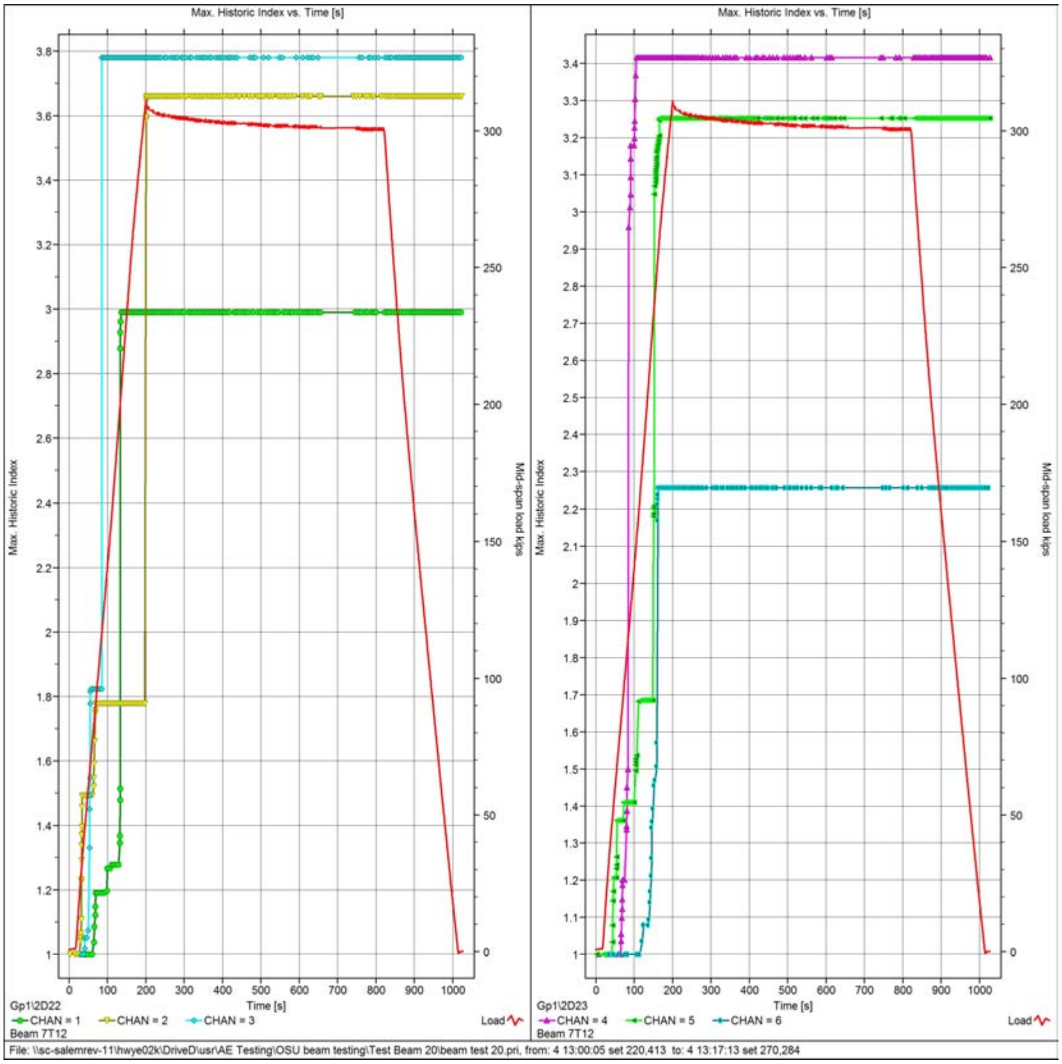

Figure 3.142 Response of the Historic Index during sixth load cycle (P/P_{ult} = 0.71).

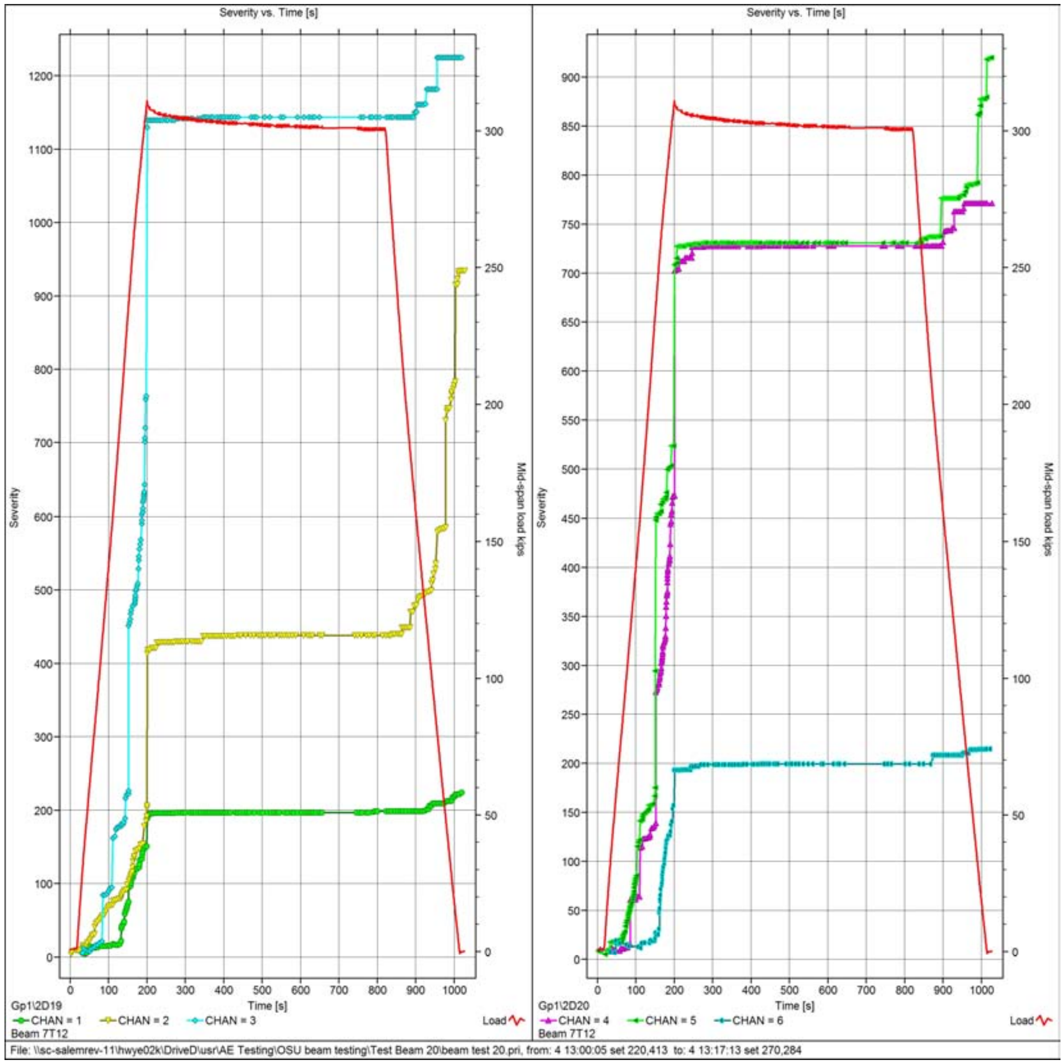

Figure 3.143 Response of the Severity during sixth load cycle.

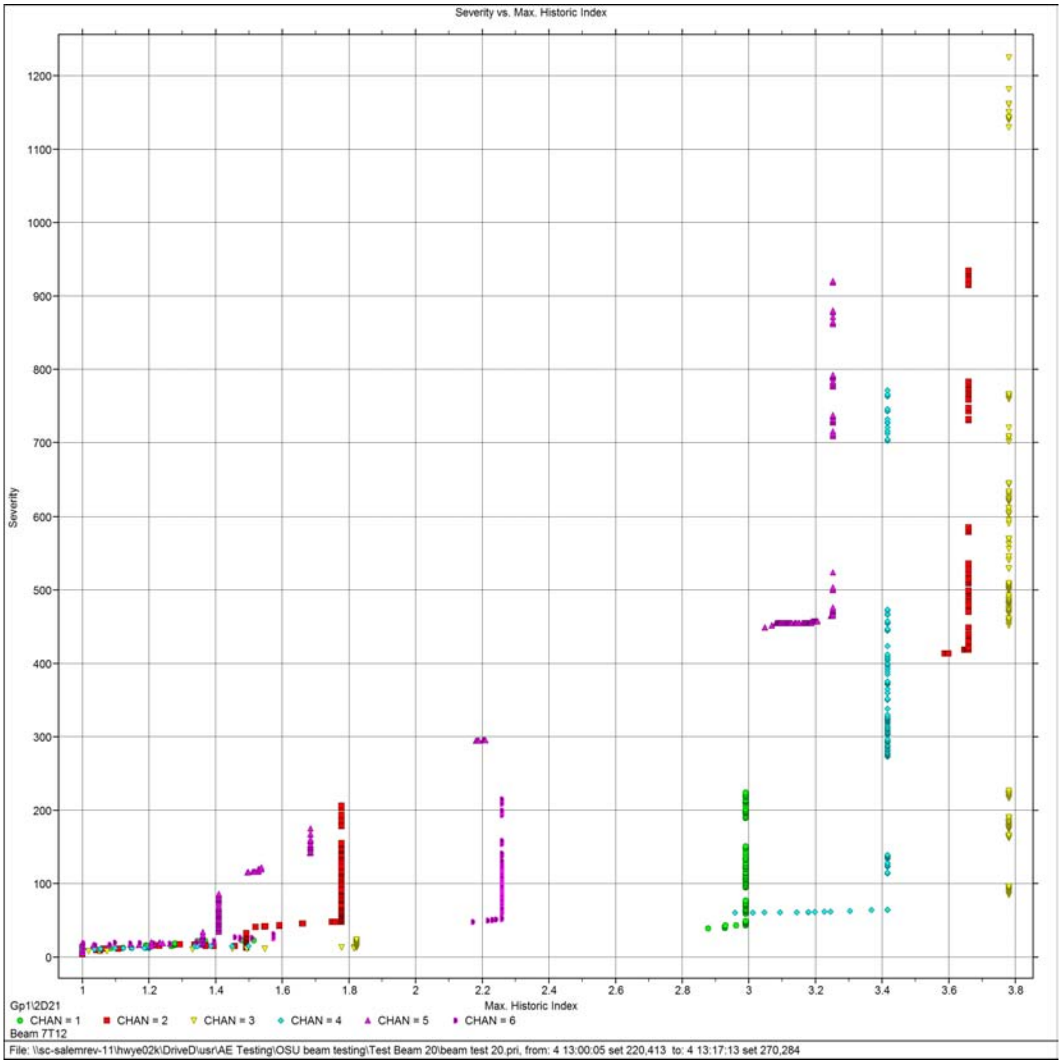

Figure 3.144 Intensity plot of sixth load cycle.

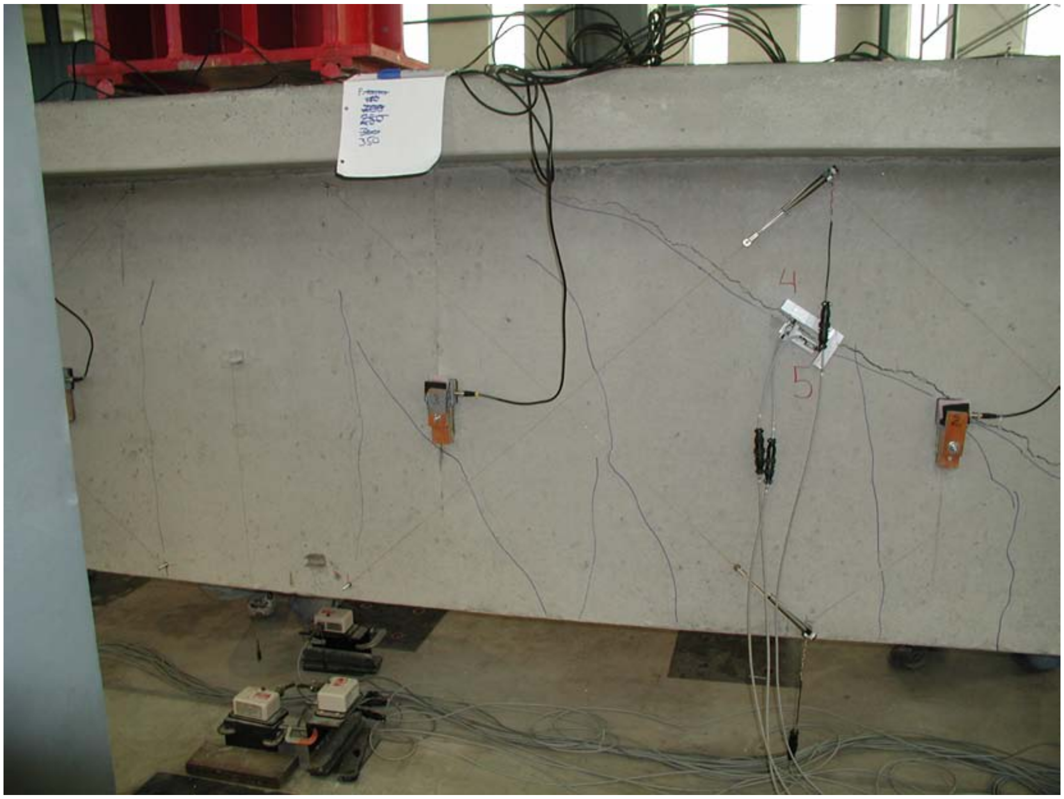

Figure 3.145 Photograph of test beam 7T12 after the seventh load cycle(P/P_{ult} = 0.83) .

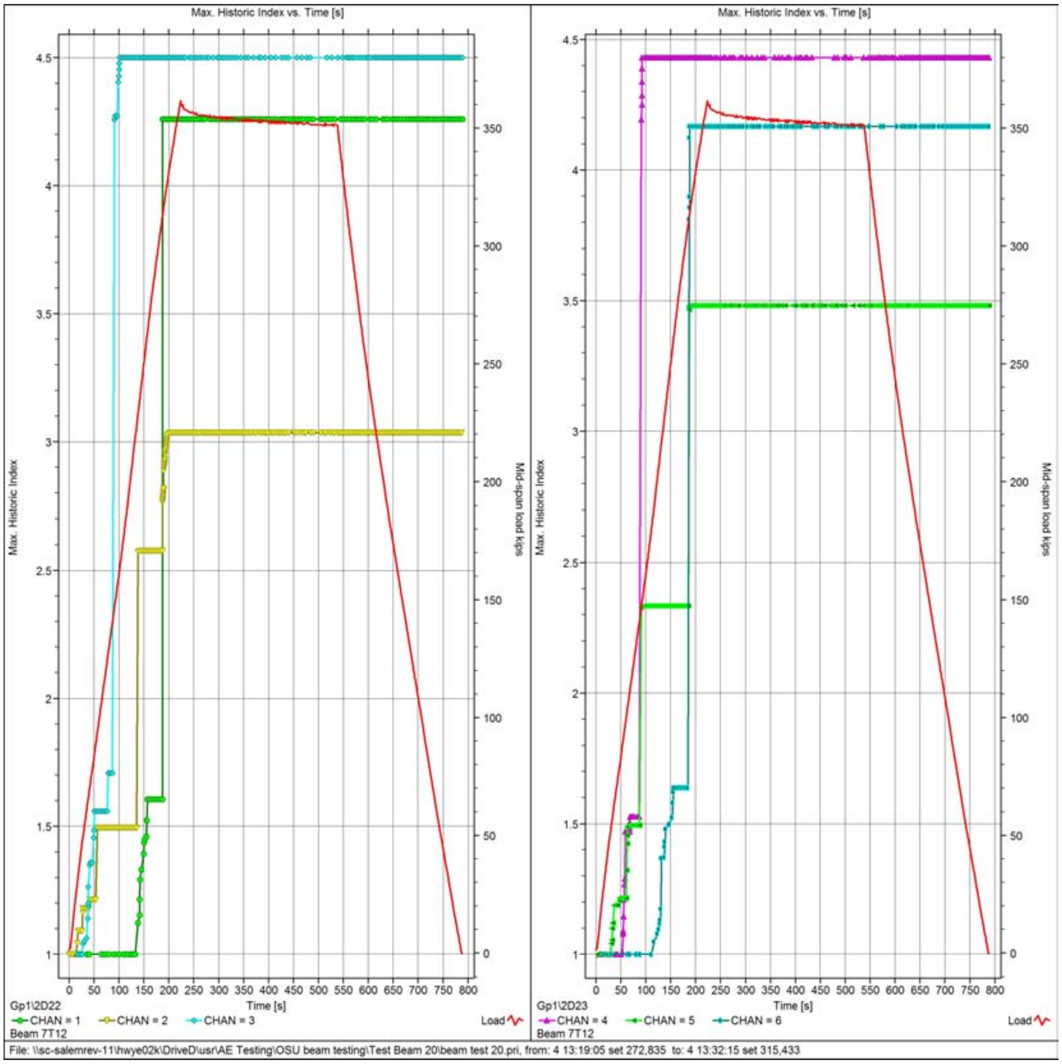

Figure 3.146 Response of the Historic Index during seventh load cycle.

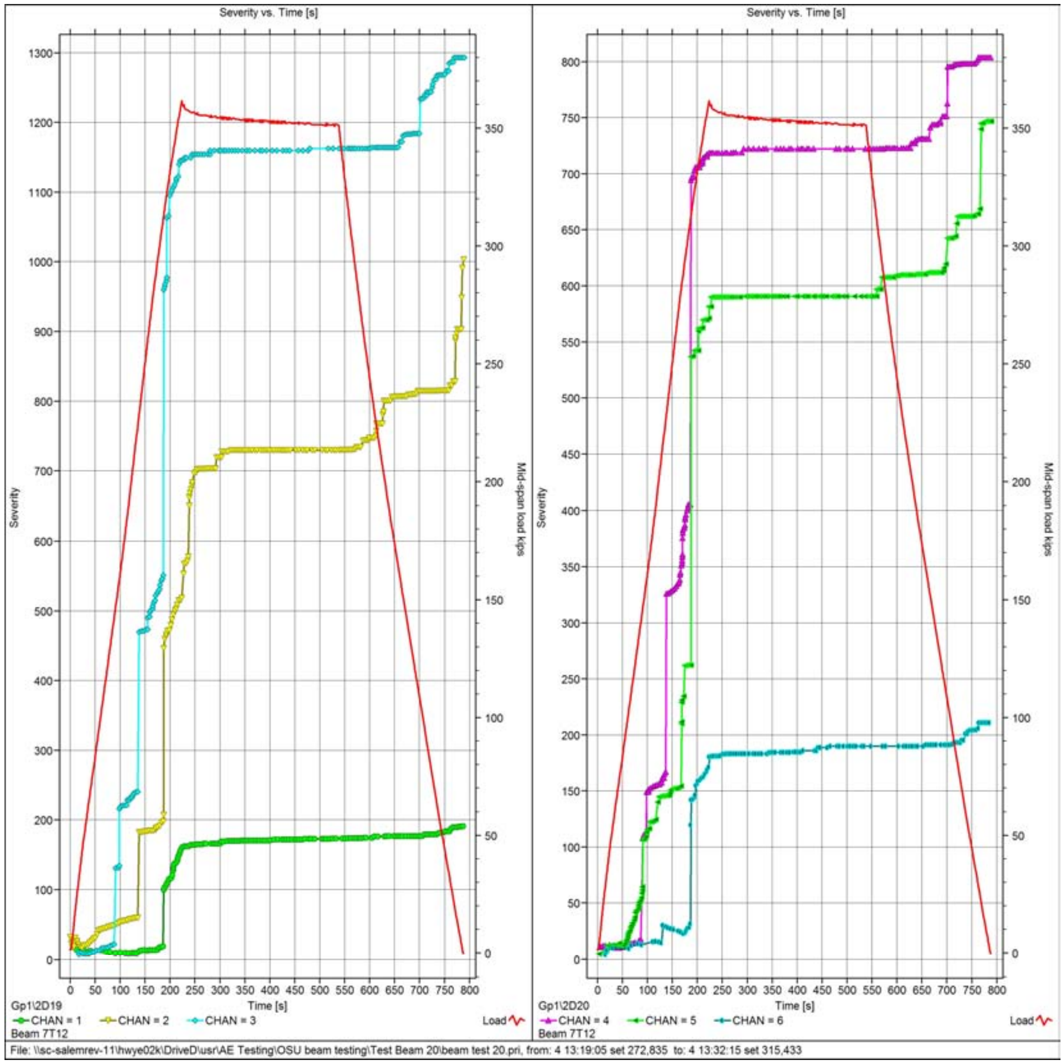

Figure 3.147 Response of the Severity during seventh load cycle.

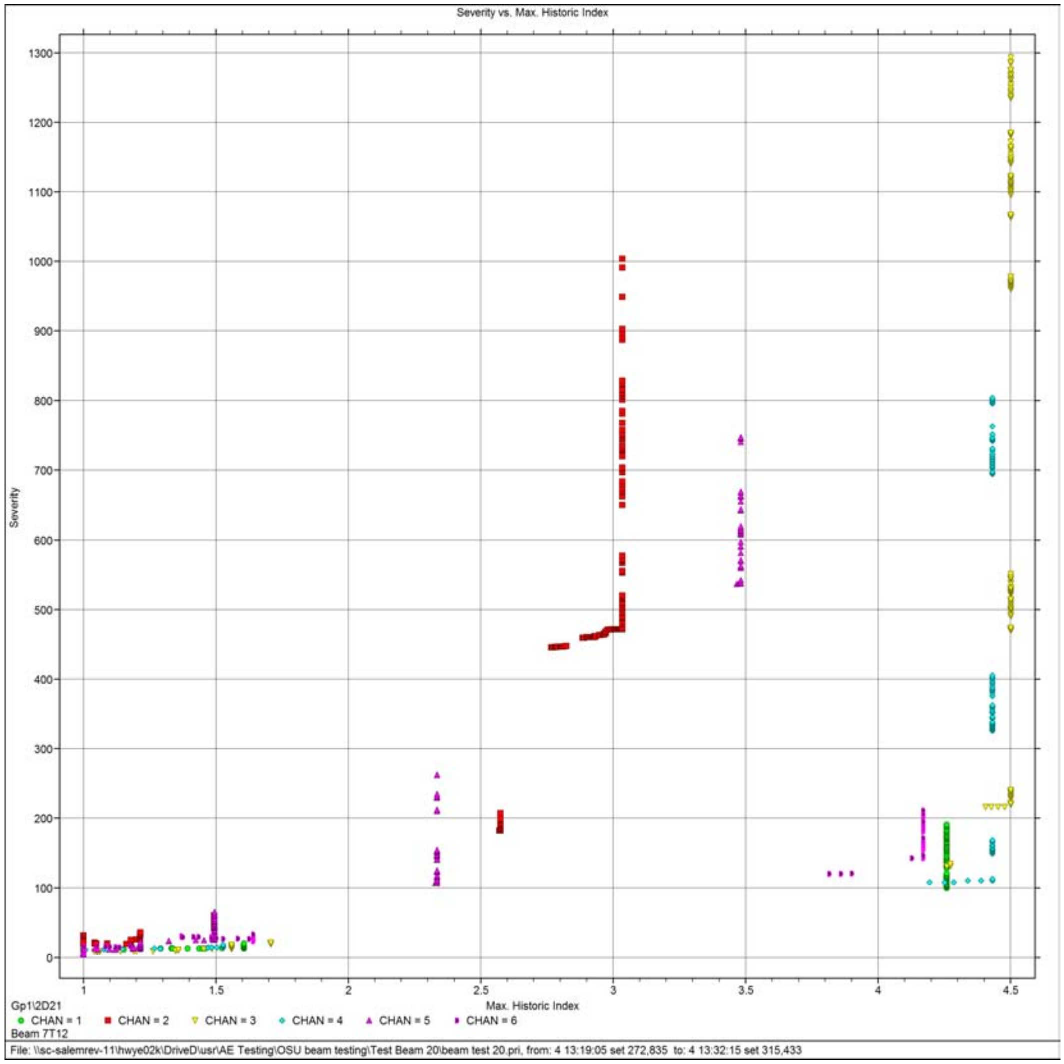

Figure 3.148 Intensity plot of seventh load cycle.

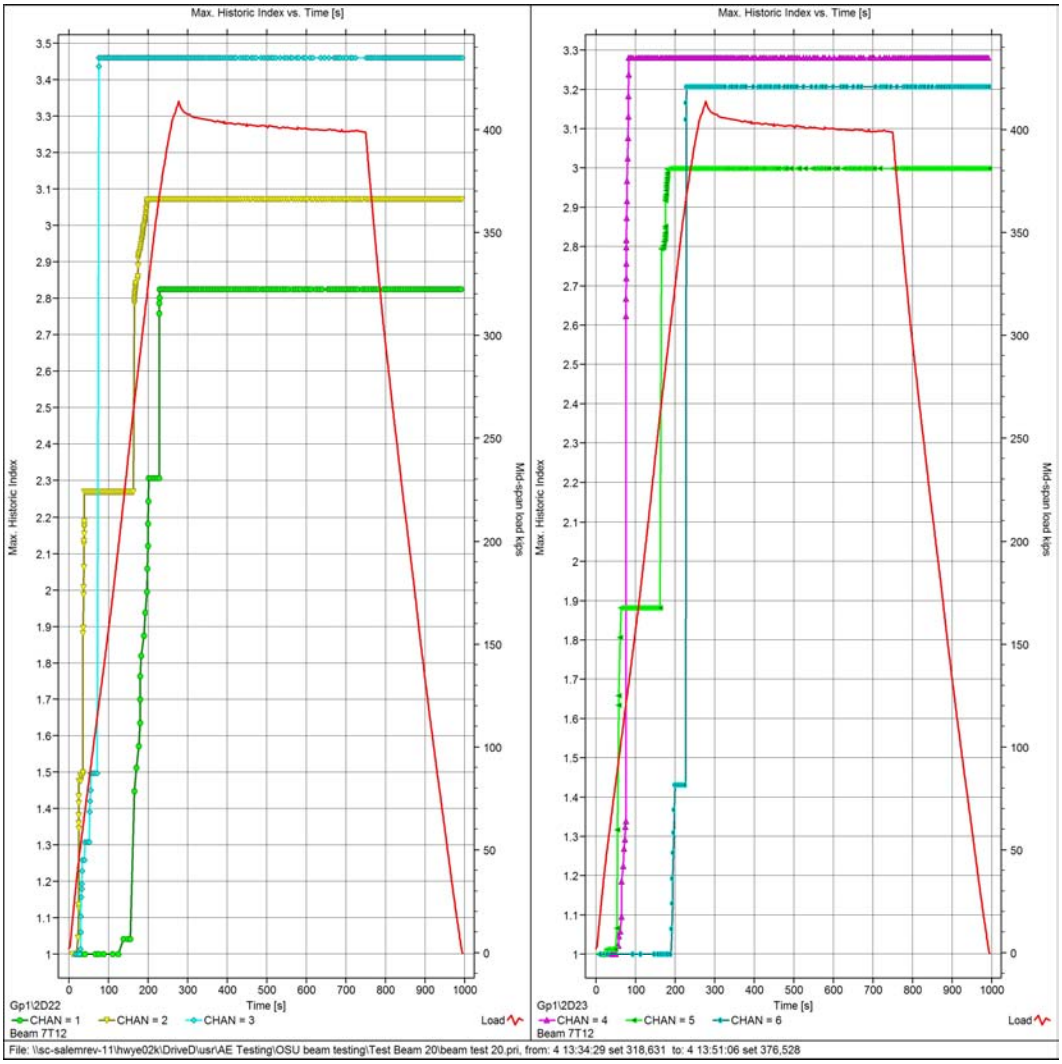

Figure 3.149 Response of the Historic Index during eighth load cycle ($P/P_{ult} = 0.95$).

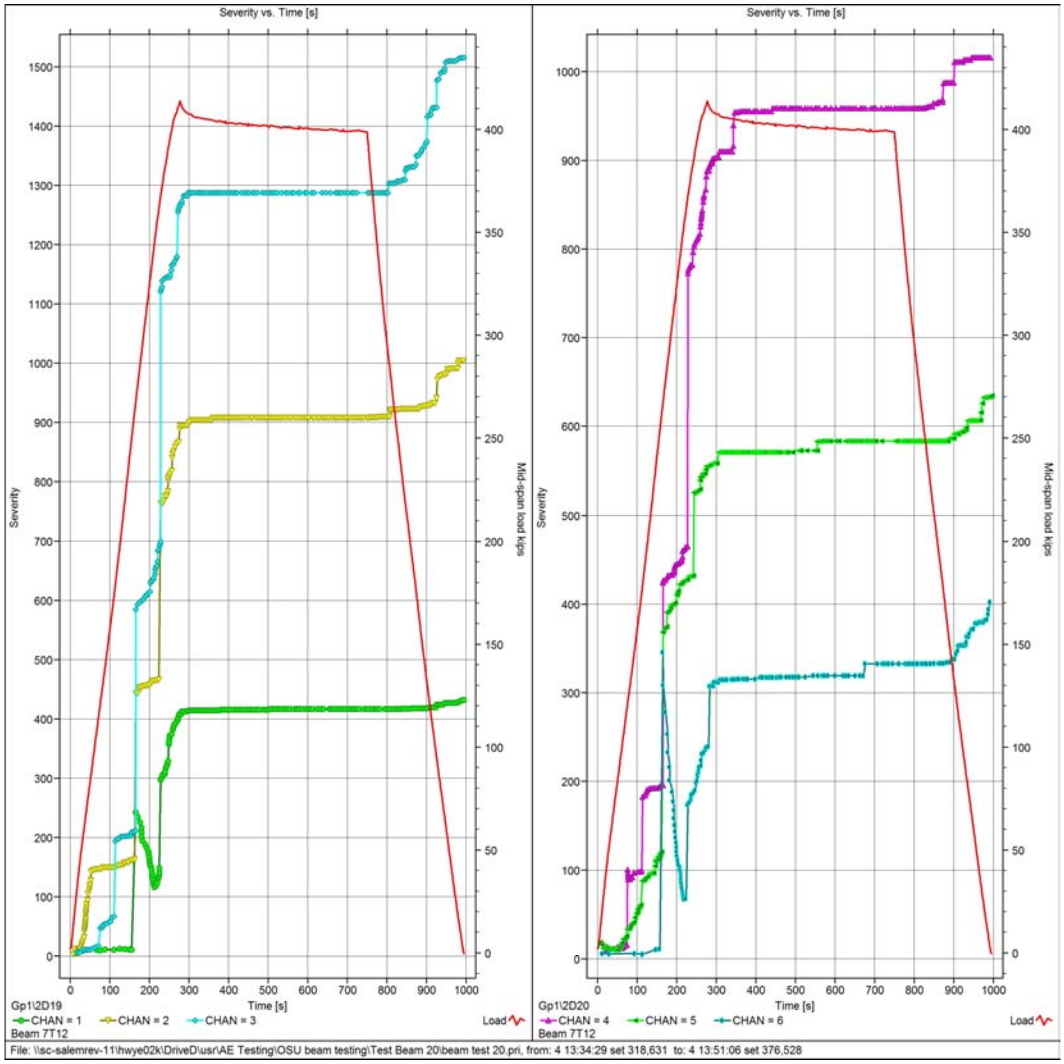

Figure 3.150 Response of the Severity during eighth load cycle.

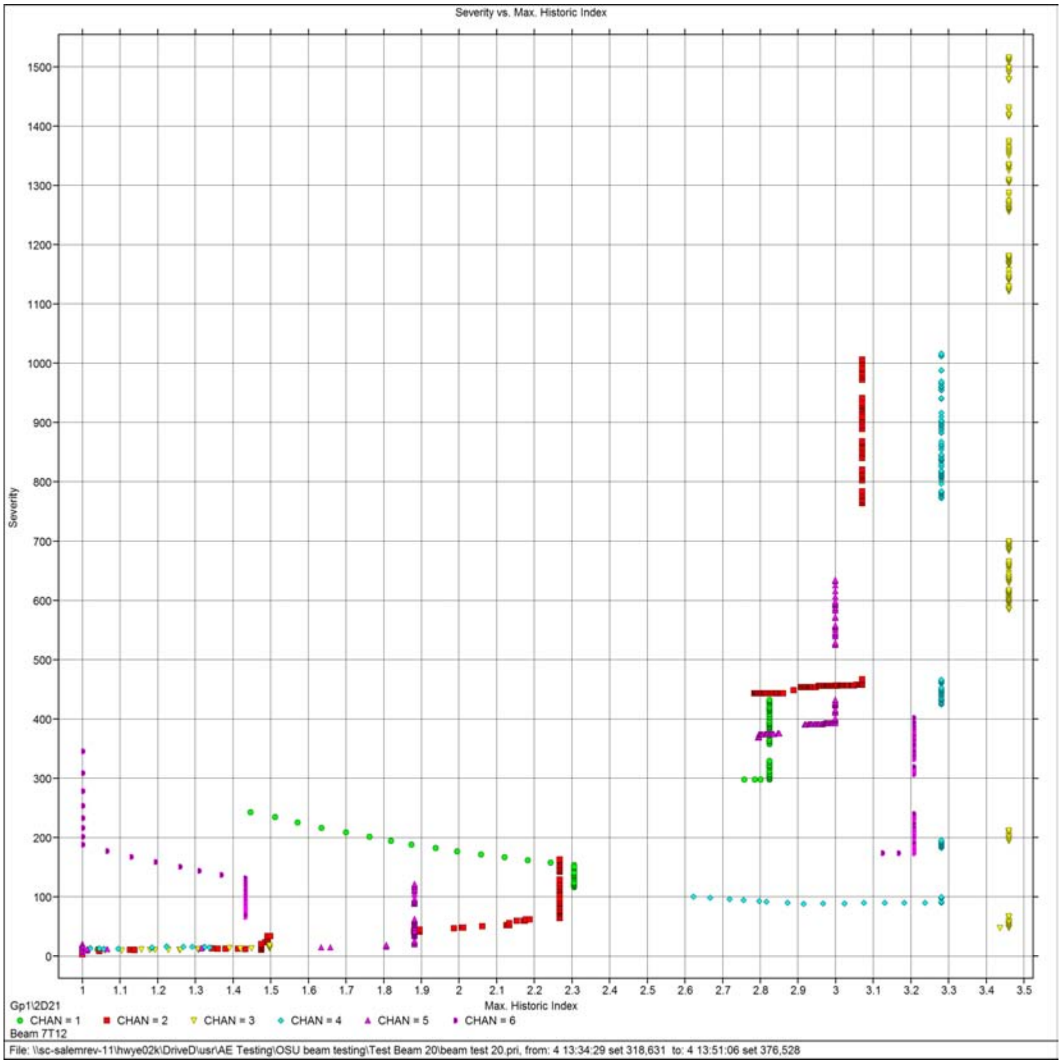

Figure 3.151 Intensity plot of eighth load cycle.

Figure 3.152 Photograph of test beam 7T12 after the ninth and failing load cycle ($P/P_{ult} = 1.0$) .

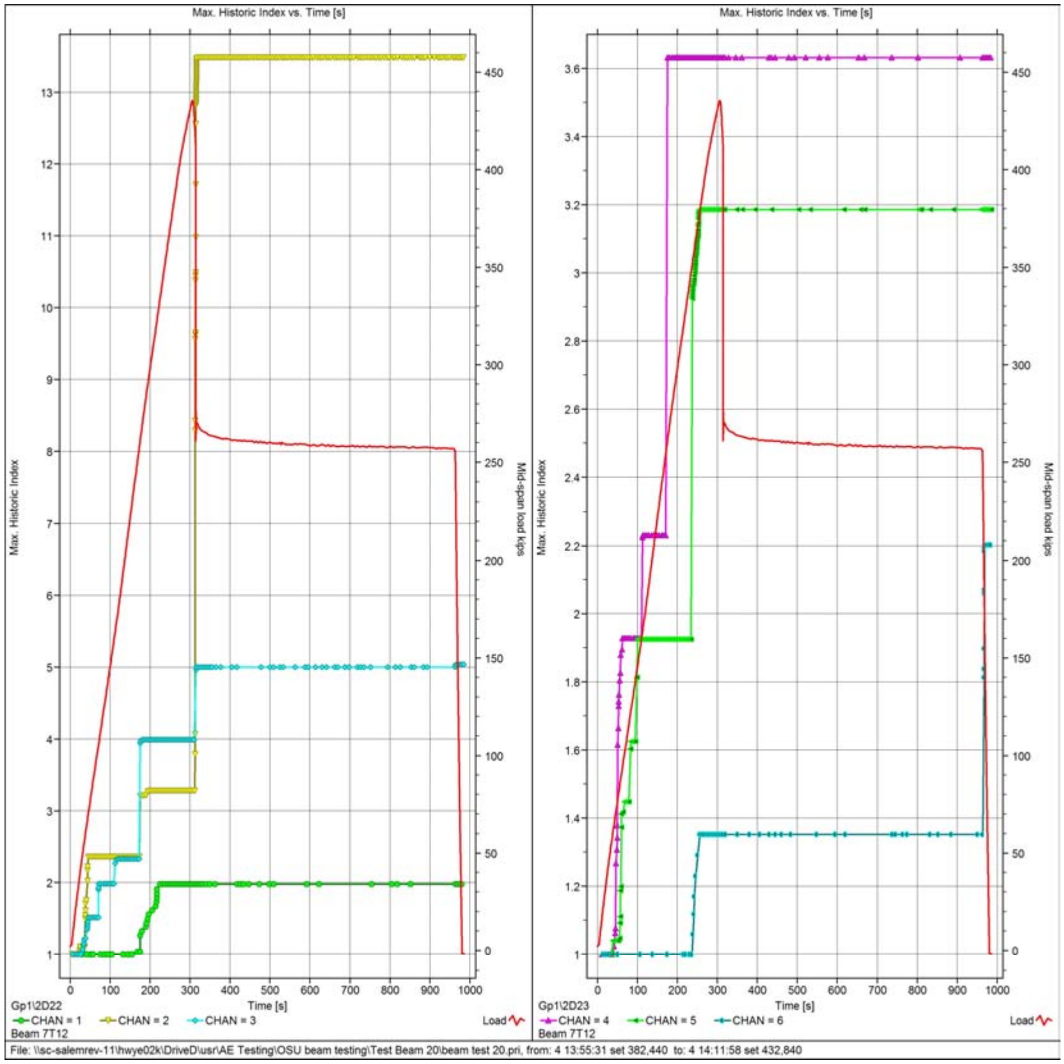

Figure 3.153 Response of the Historic Index during failing load cycle.

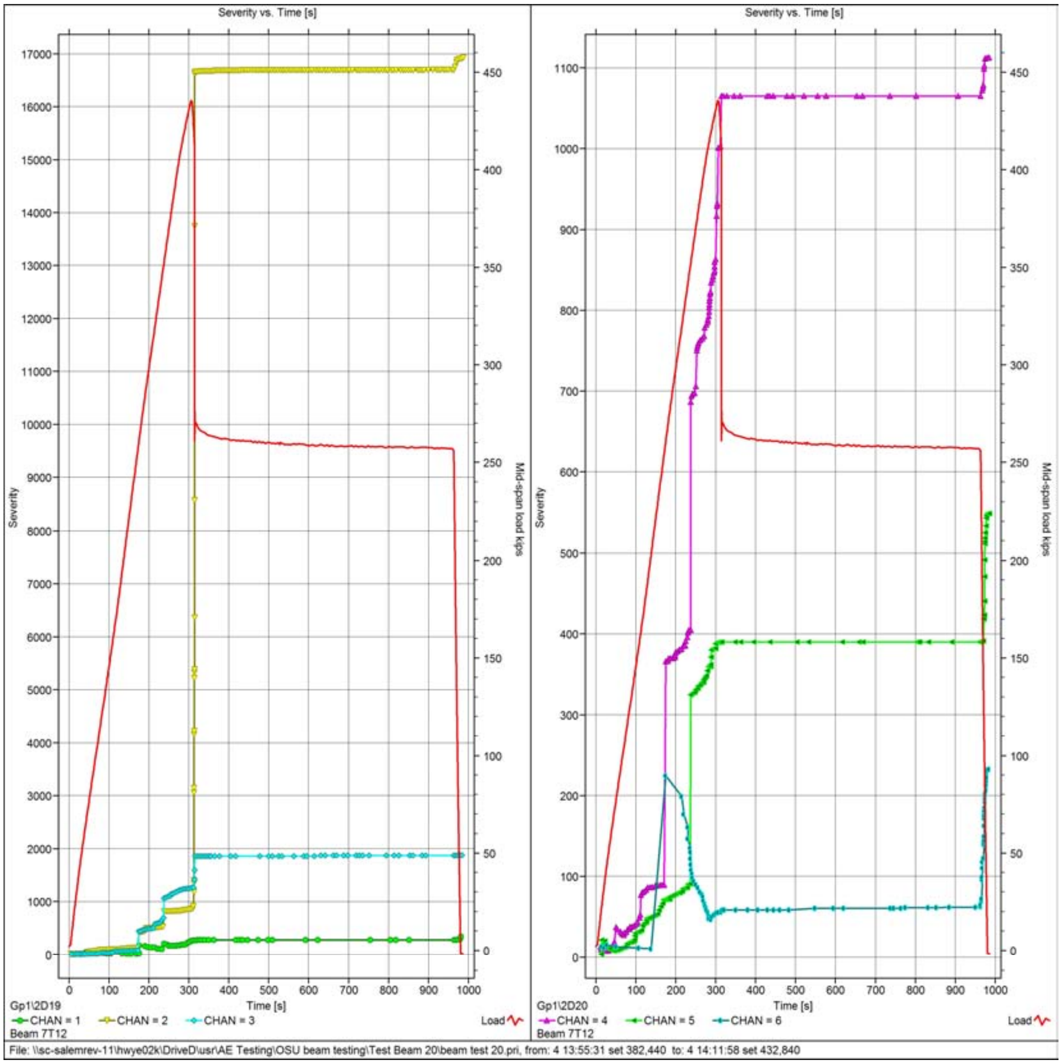

Figure 3.154 Response of the Severity during failing load cycle.

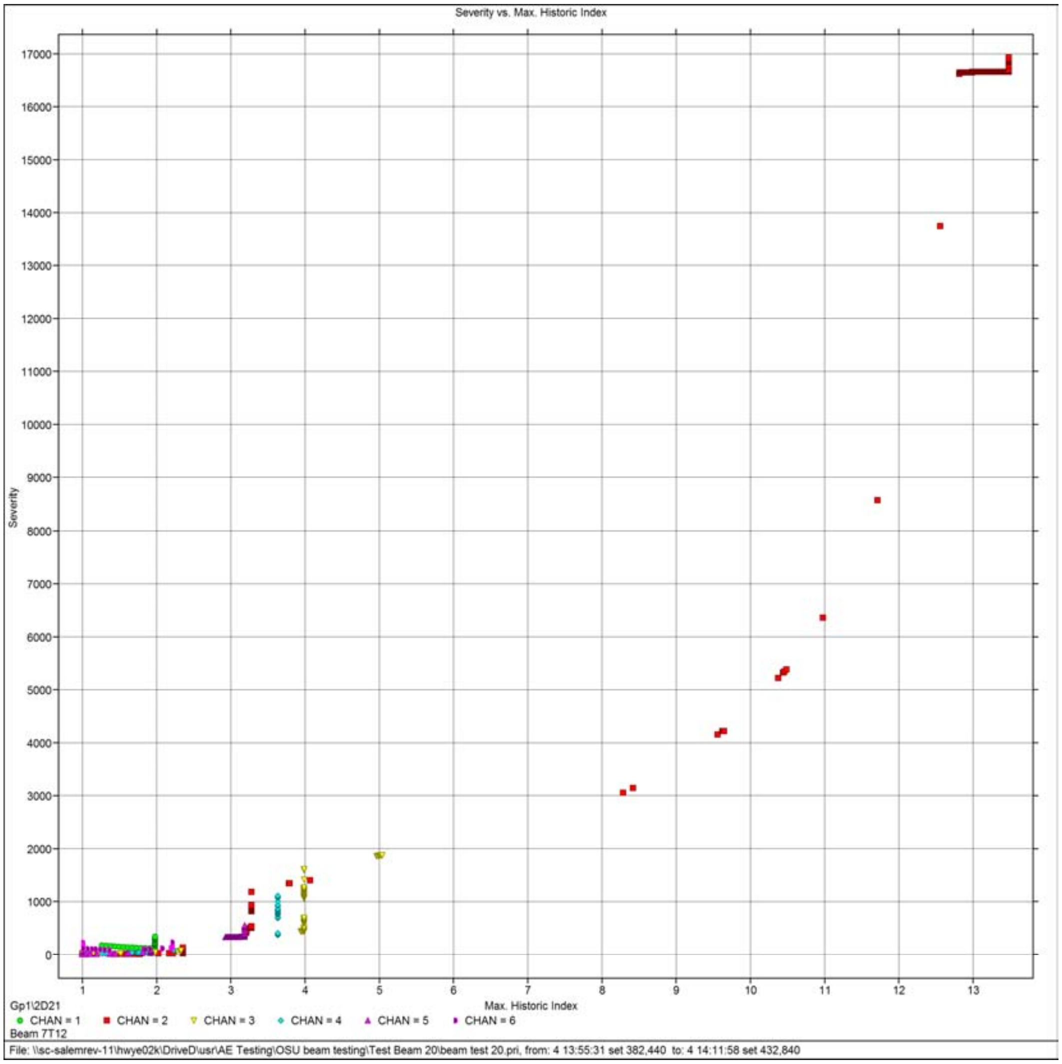

Figure 3.155 Intensity plot of failing load cycle.

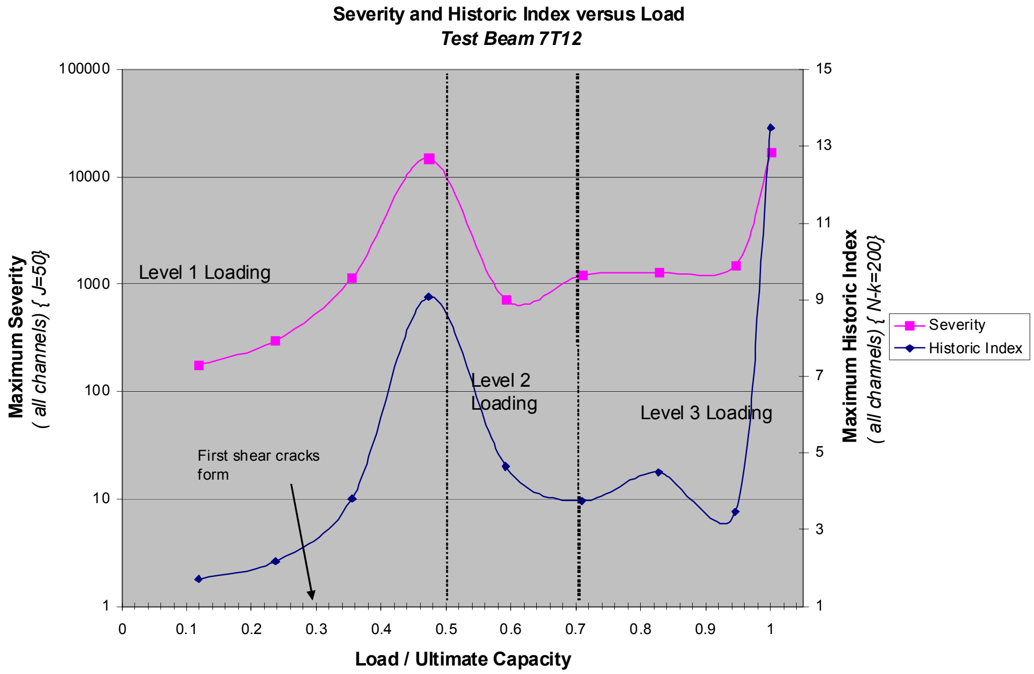

Figure 3.156 Summary of maximum Severity and Historic Index from all channels over the entire load protocol for test beam 7T12.

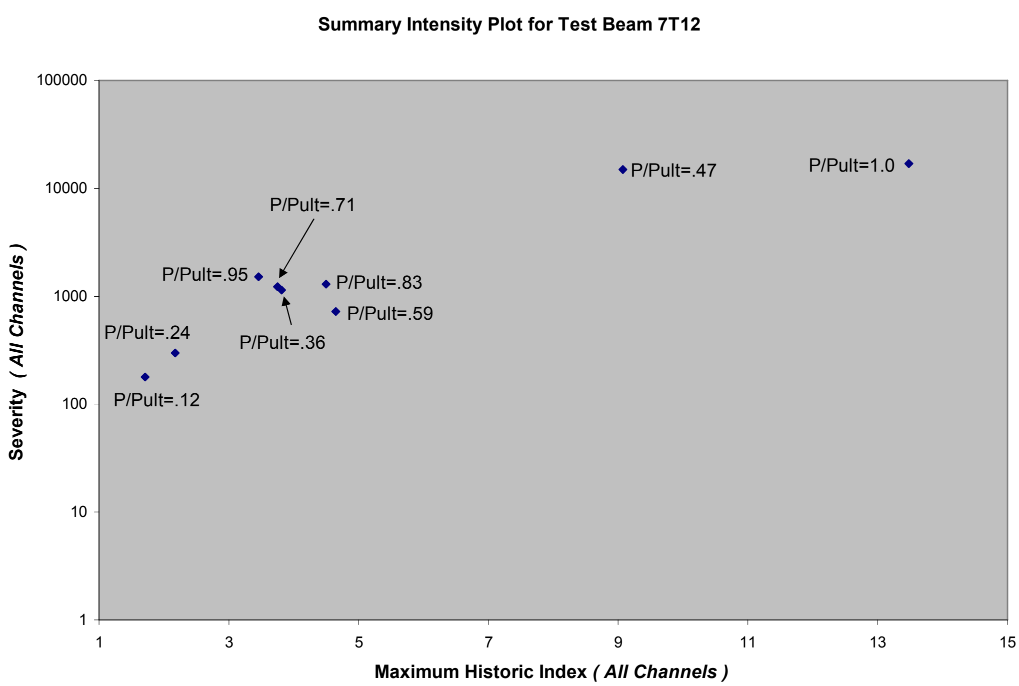

Figure 3.157 Summary of maximum Intensity from all channels over the entire load protocol for test beam 7T12.

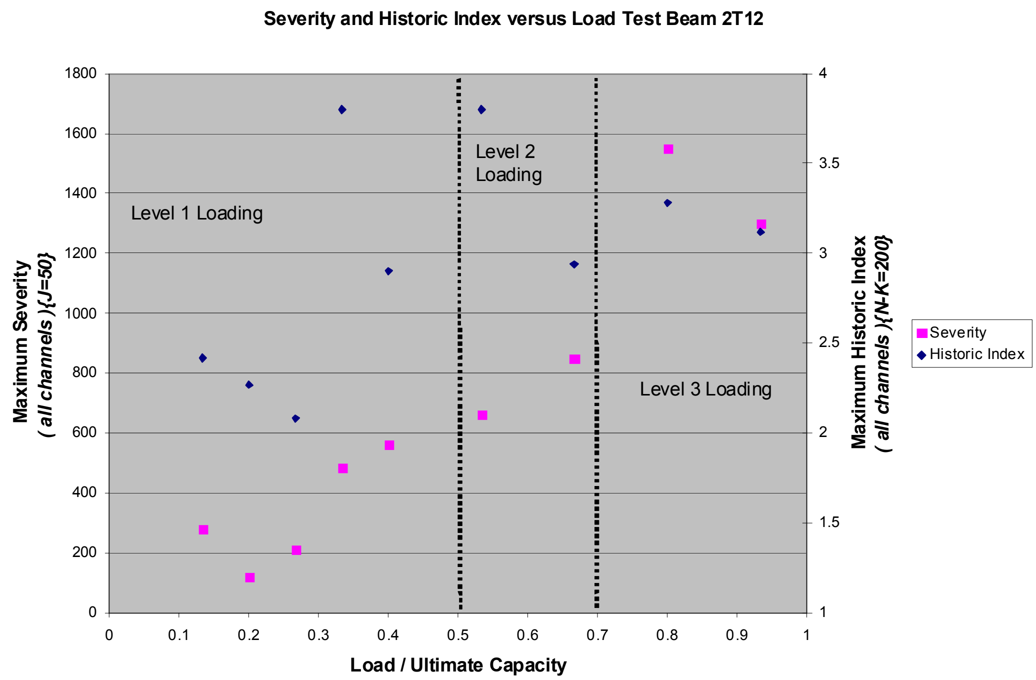

Figure 3.158 Summary of maximum Severity and Historic Index from all channels over the entire load protocol for test beam 2T12.

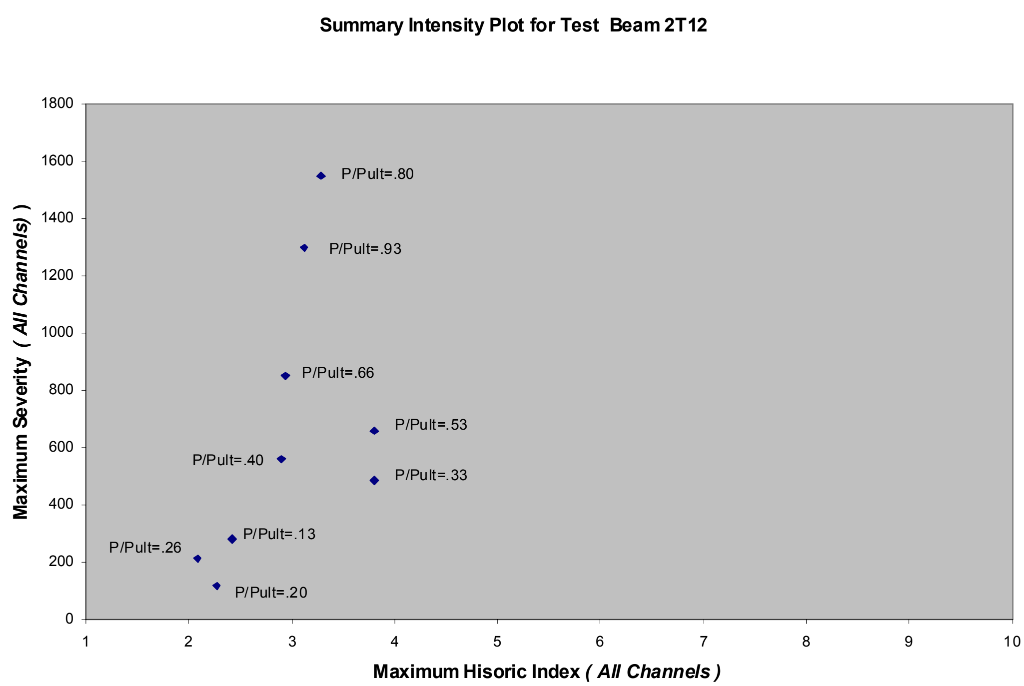

Figure 3.159 Summary of maximum Intensity from all channels over the entire load protocol for test beam 2T12.

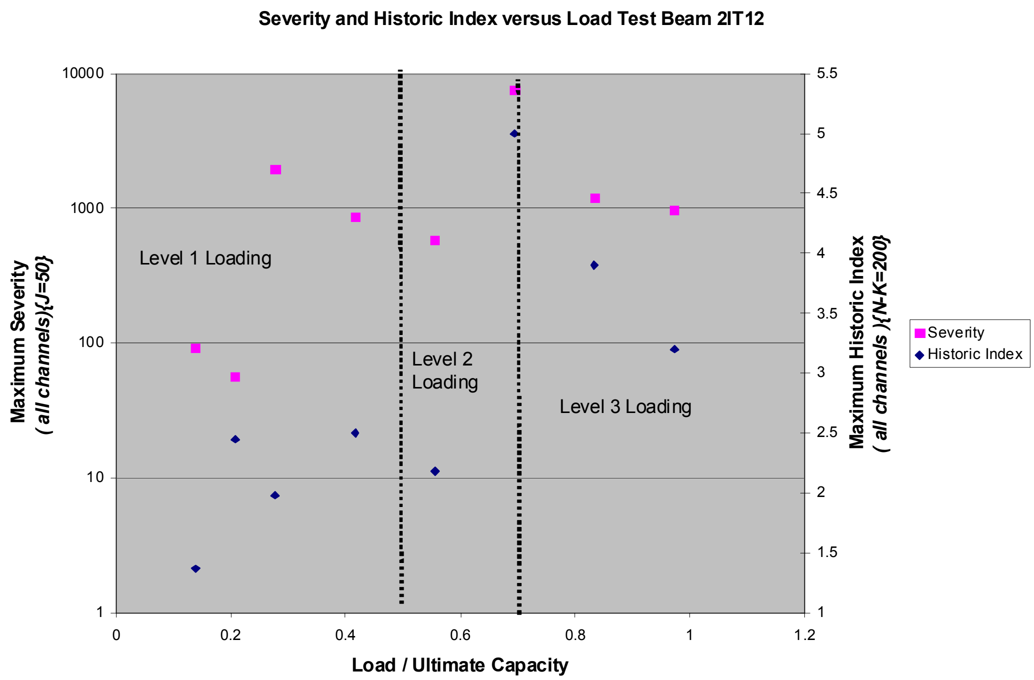

Figure 3.160 Summary of maximum Severity and Historic Index from all channels over the entire load protocol for test beam 2IT12.

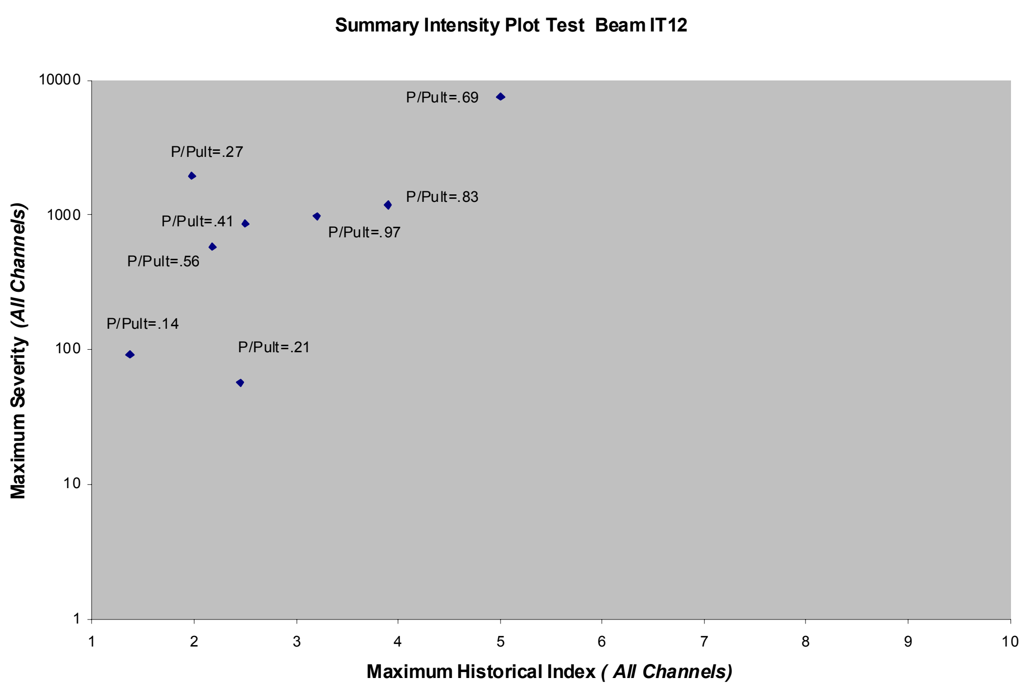

Figure 3.161 Summary of maximum Intensity from all channels over the entire load protocol for test beam 2IT12.

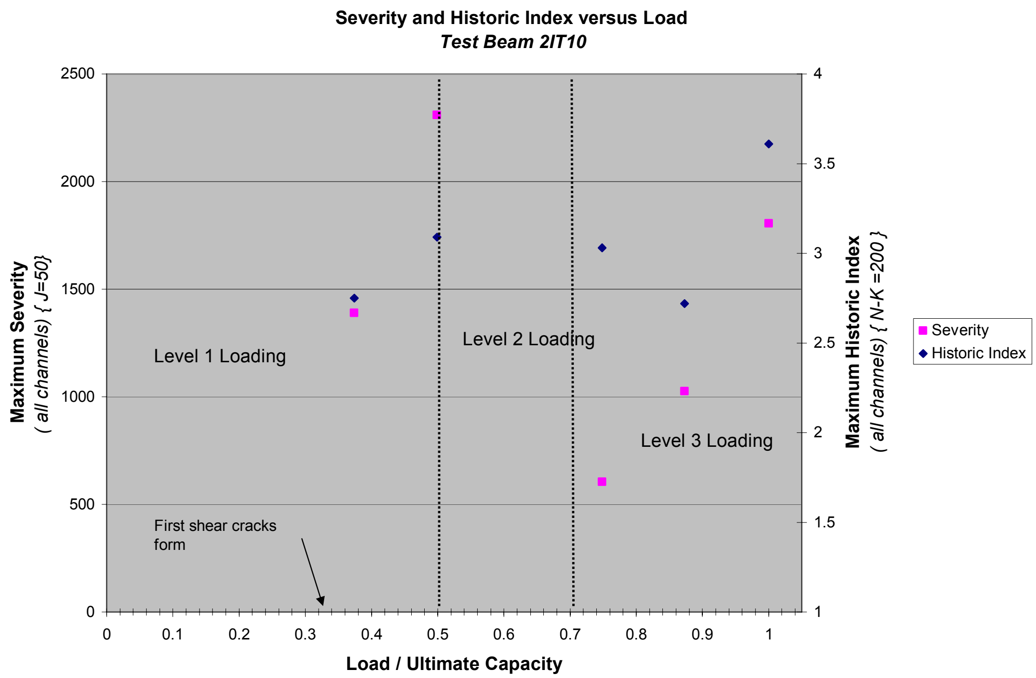

Figure 3.162 Summary of maximum Severity and Historic Index from all channels over the entire load protocol for test beam 2IT10.

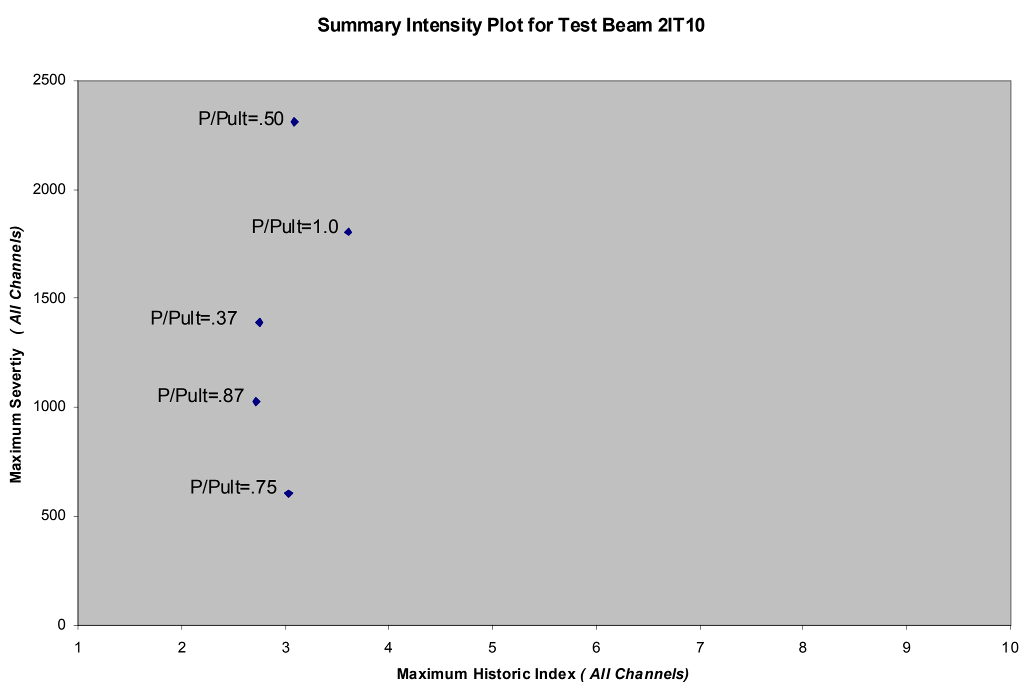

Figure 3.163 Summary of maximum Intensity from all channels over the entire load protocol for test beam 2IT10.

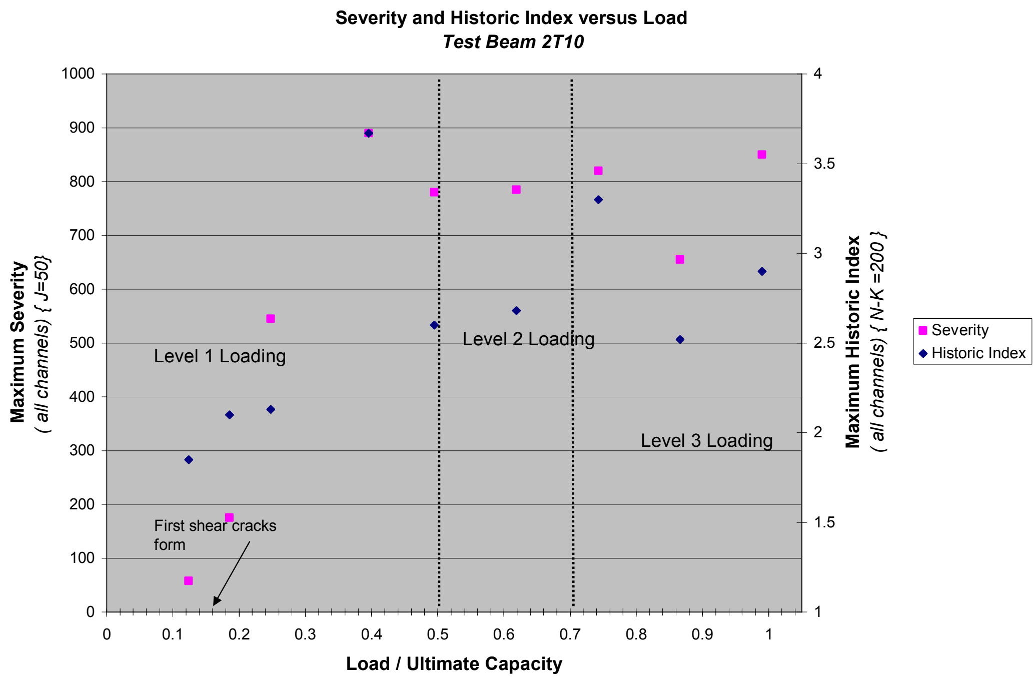

Figure 3.164 Summary of maximum Severity and Historic Index from all channels over the entire load protocol for test beam 2T10.

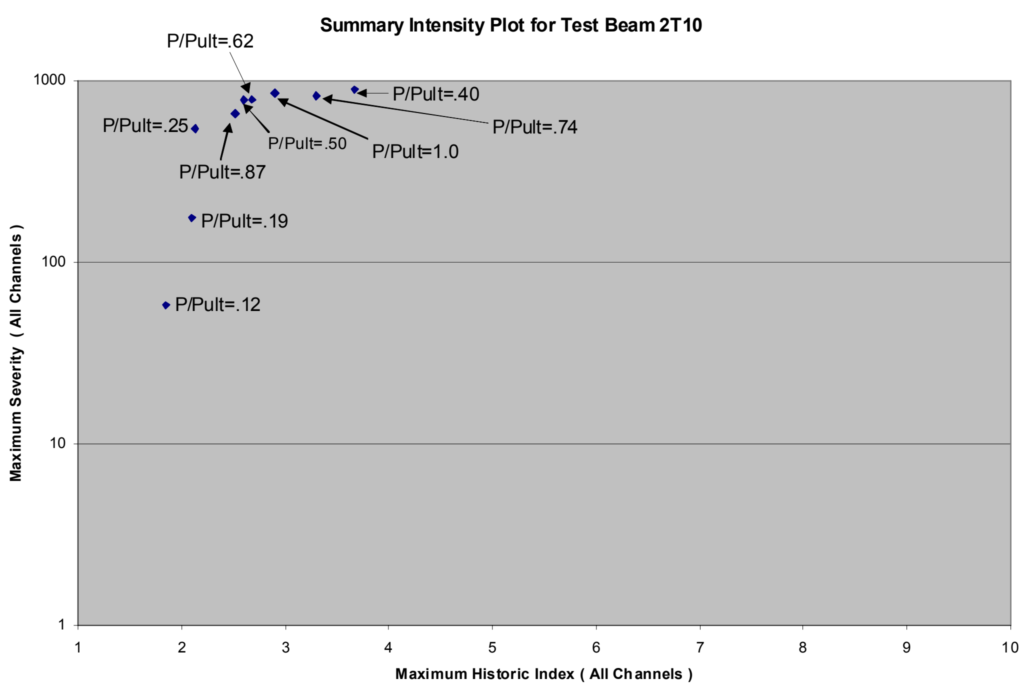

Figure 3.165 Summary of maximum Intensity from all channels over the entire load protocol for test beam 2T10.

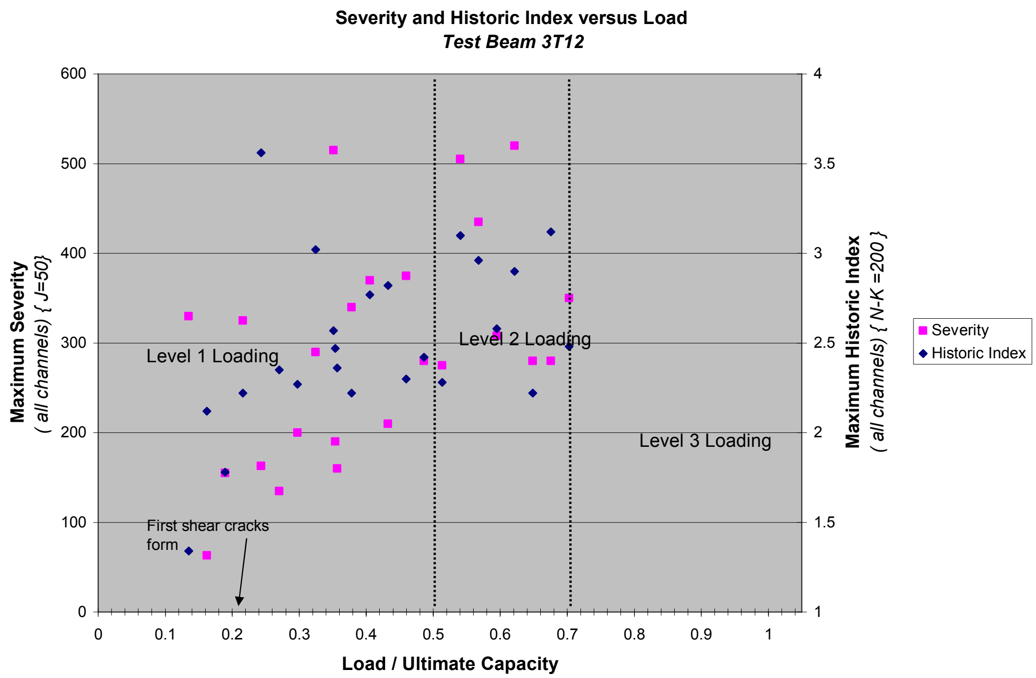

Figure 3.166 Summary of maximum Severity and Historic Index from all channels over the entire load protocol for test beam 3T12.

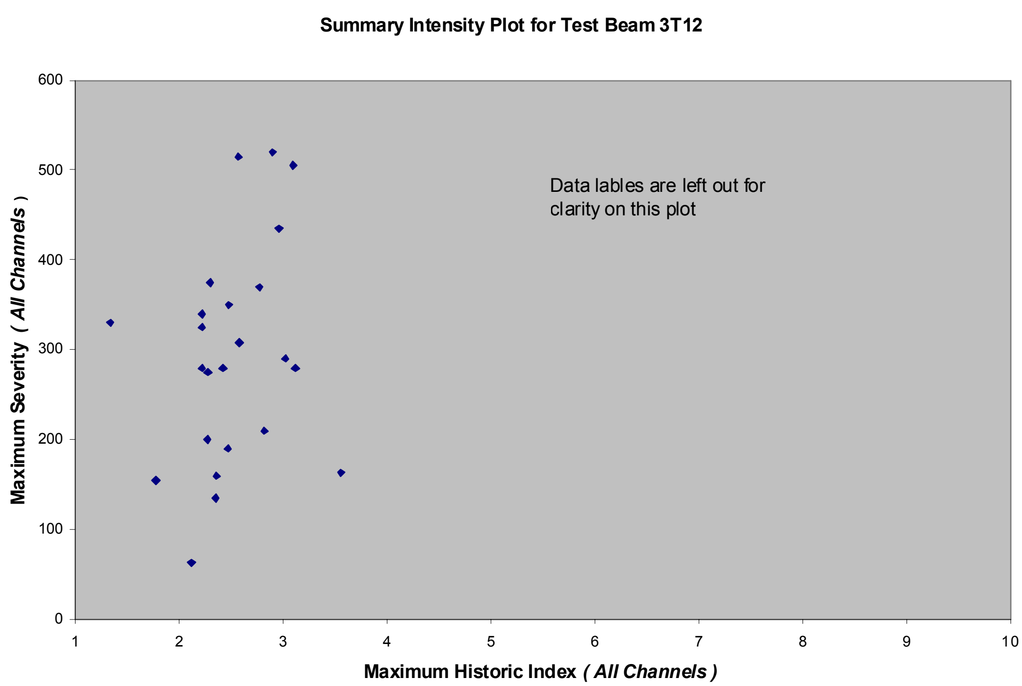

Figure 3.167 Summary of maximum Intensity from all channels over the entire load protocol for test beam 3T12.

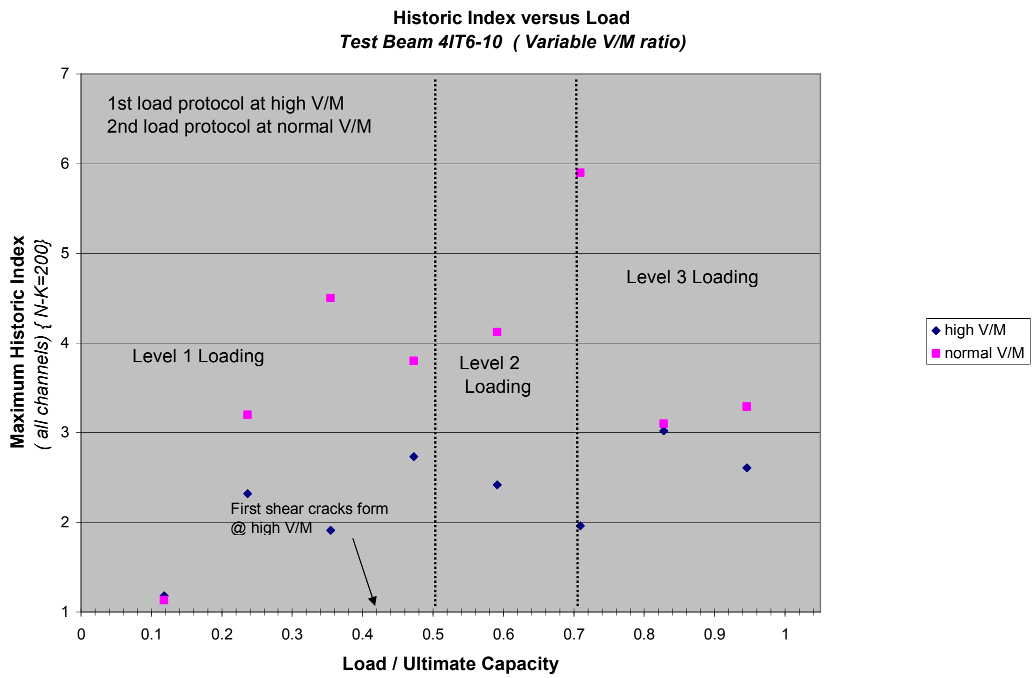

Figure 3.168 Summary of maximum Historic Index from all channels over the entire load protocol for test beam 4IT6-10.

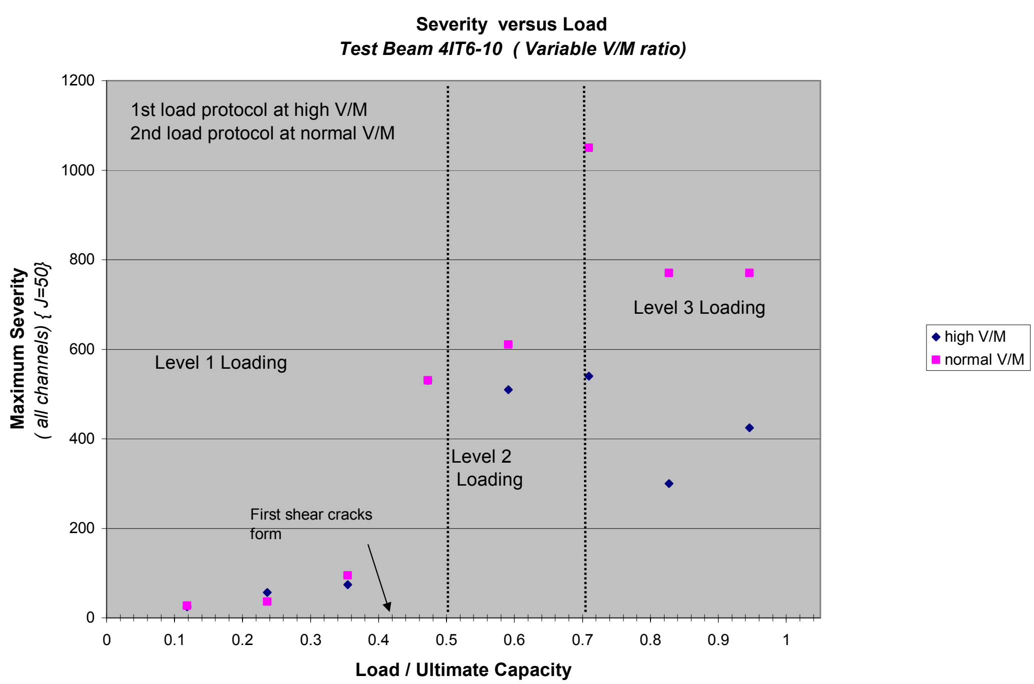

Figure 3.169 Summary of maximum Severity from all channels over the entire load protocol for test beam 4IT6-10.

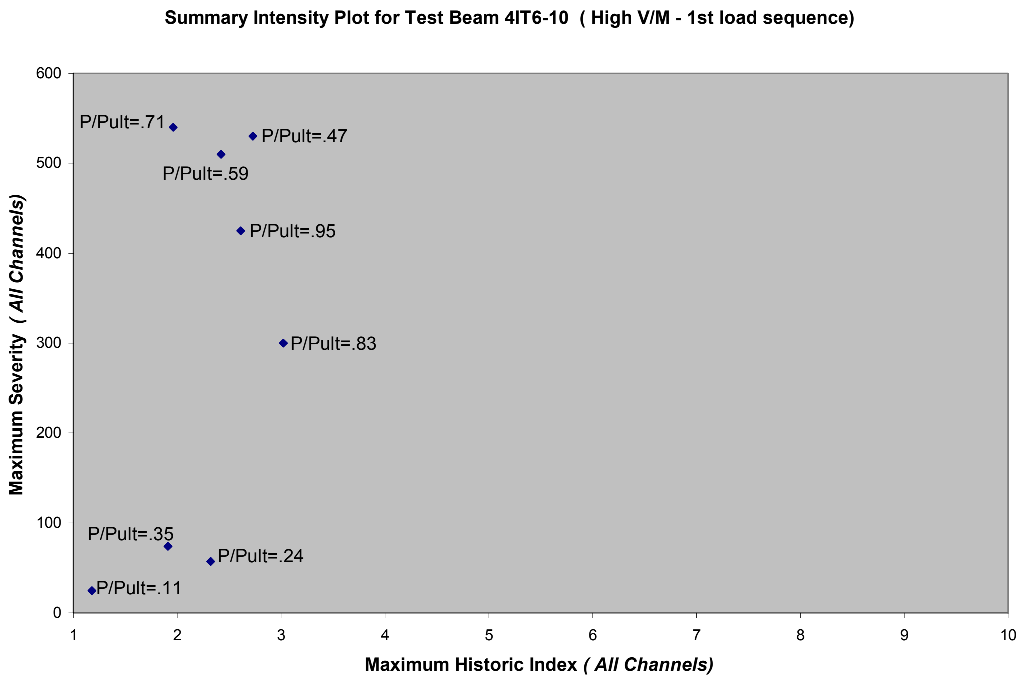

Figure 3.170 Summary of maximum Intensity from all channels over the entire first load protocol for test beam 4IT6-10.

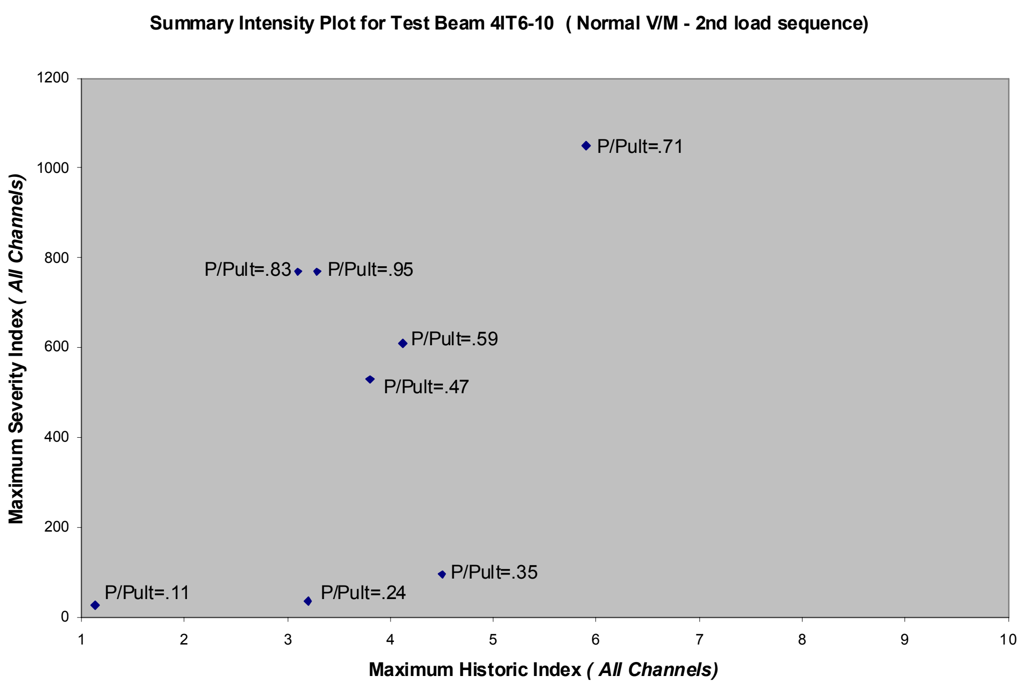

Figure 3.171 Summary of maximum Intensity from all channels over the entire second load protocol for test beam 4IT6-10.

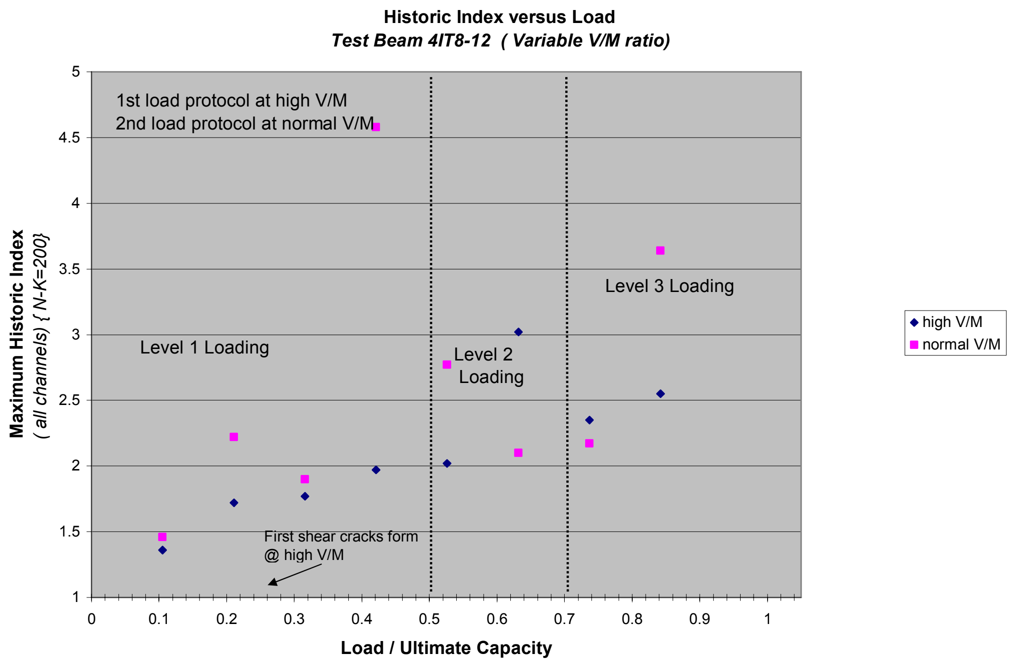

Figure 3.172 Summary of maximum Historic Index from all channels over the entire load protocol for test beam 4IT8-12.

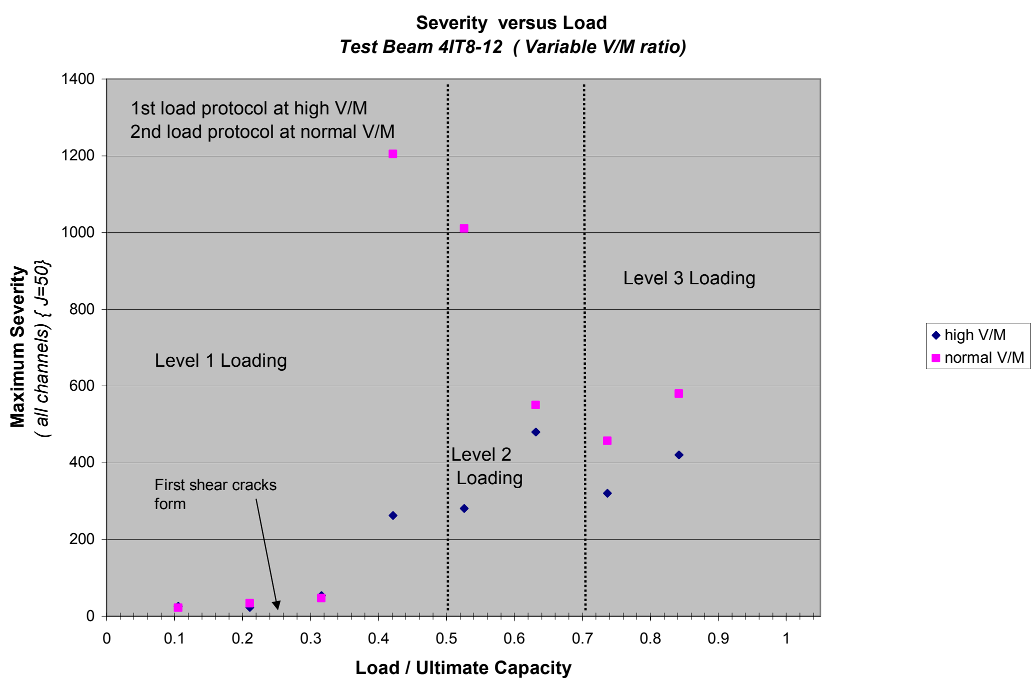

Figure 3.173 Summary of maximum Severity from all channels over the entire load protocol for test beam 4IT8-12.

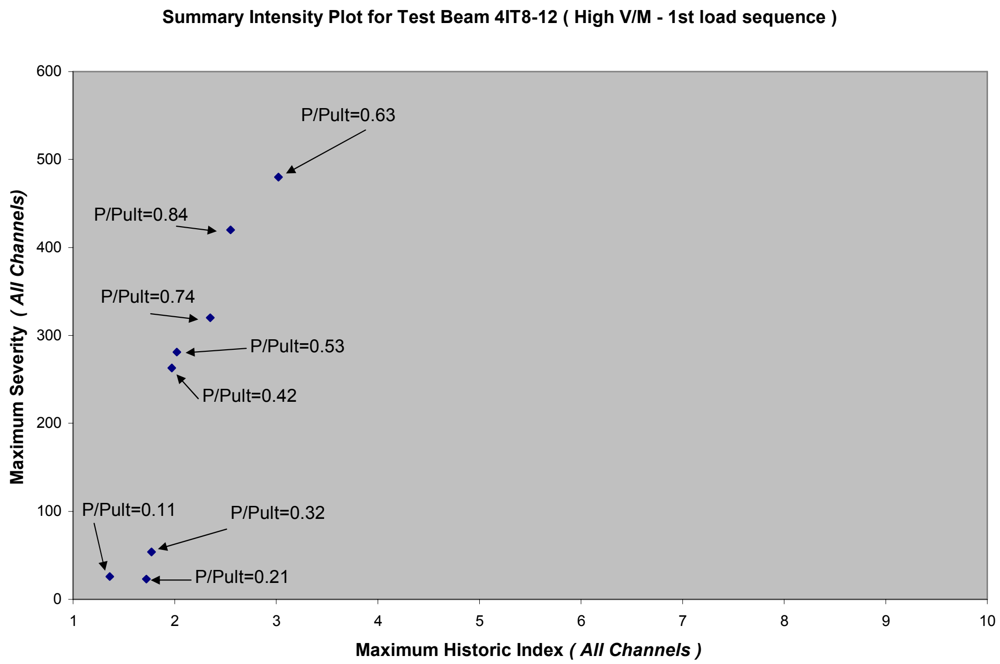

Figure 3.174 Summary of maximum Intensity from all channels over the entire first load protocol for test beam 4IT8-12.

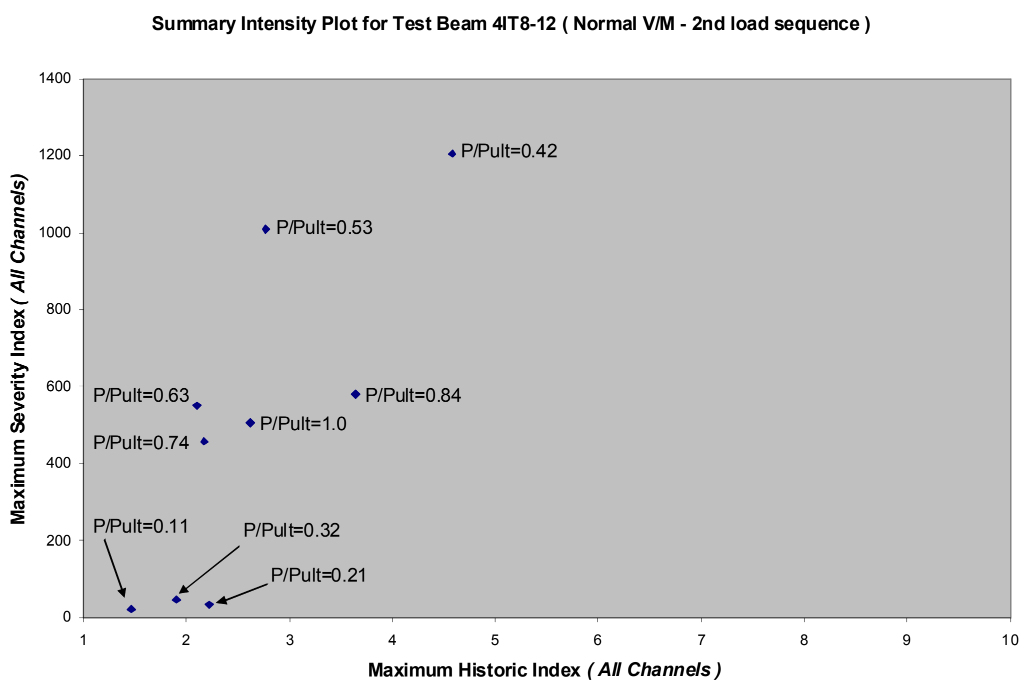

Figure 3.175 Summary of maximum Intensity from all channels over the entire second load protocol for test beam 4IT8-12.

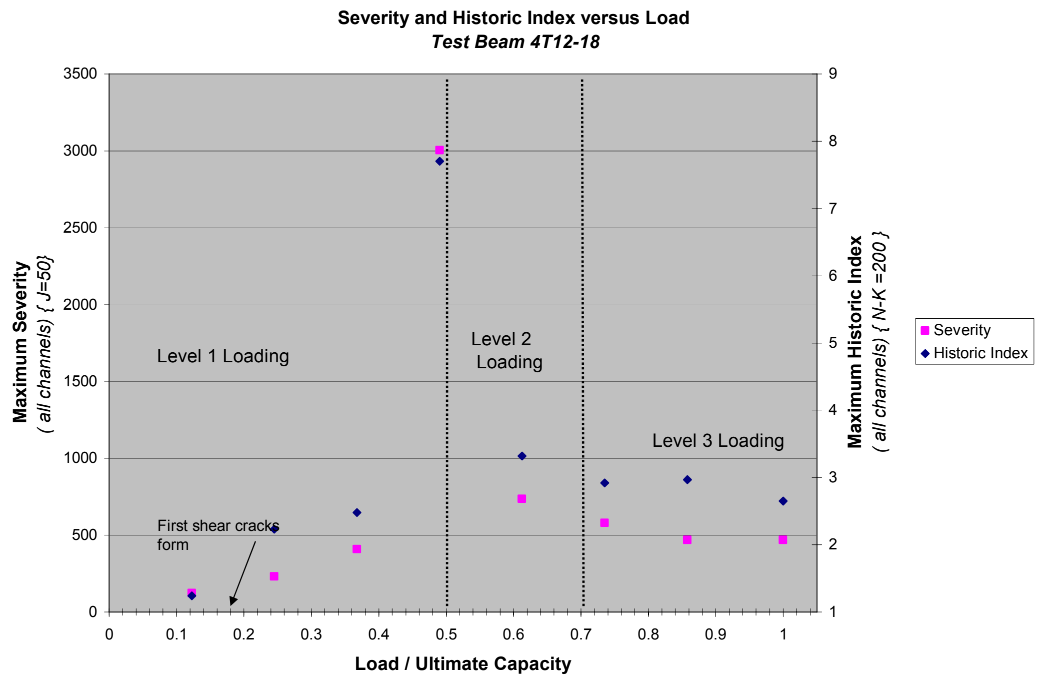

Figure 3.176 Summary of maximum Severity and Historic Index from all channels over the entire load protocol for test beam 4T12-18.

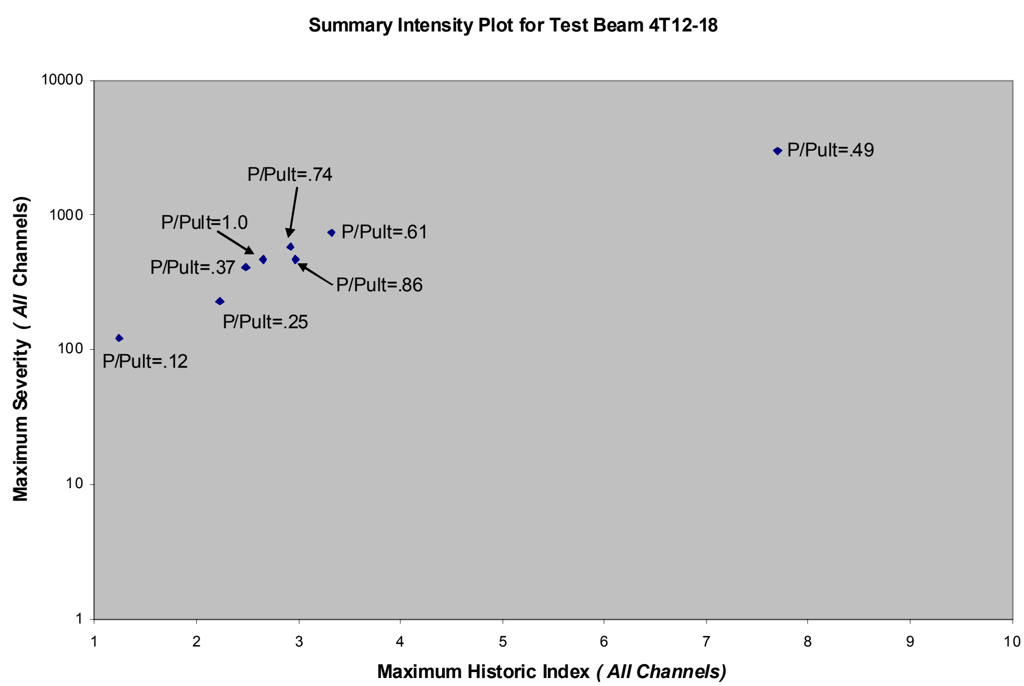

Figure 3.177 Summary of maximum Intensity from all channels over the entire load protocol for test beam 4T12-18.

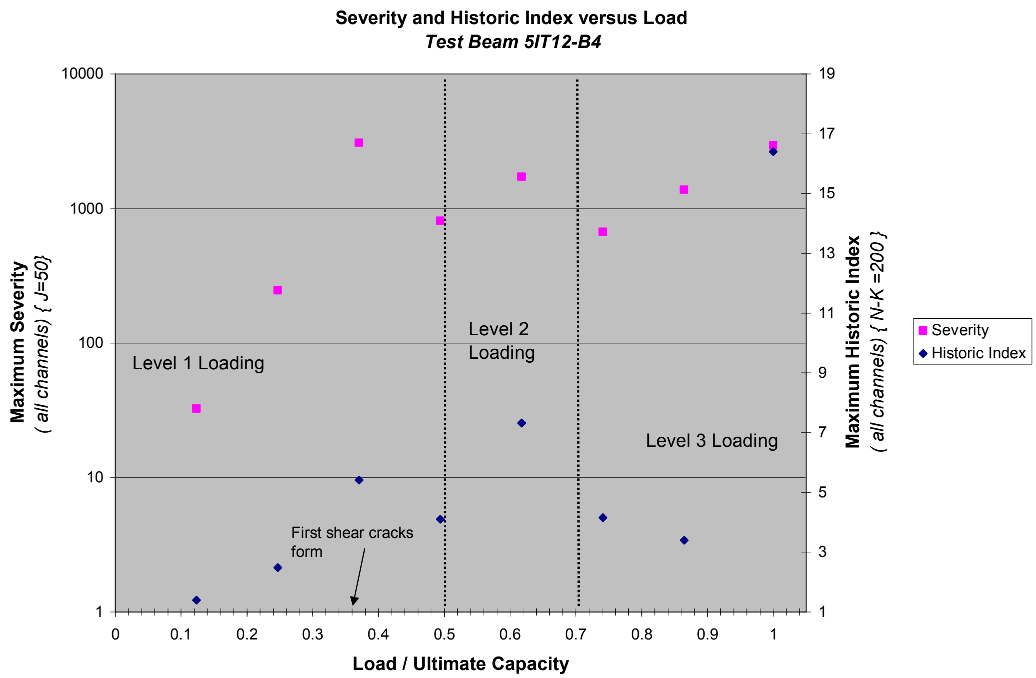

Figure 3.178 Summary of maximum Severity and Historic Index from all channels over the entire load protocol for test beam 5IT12-B4.

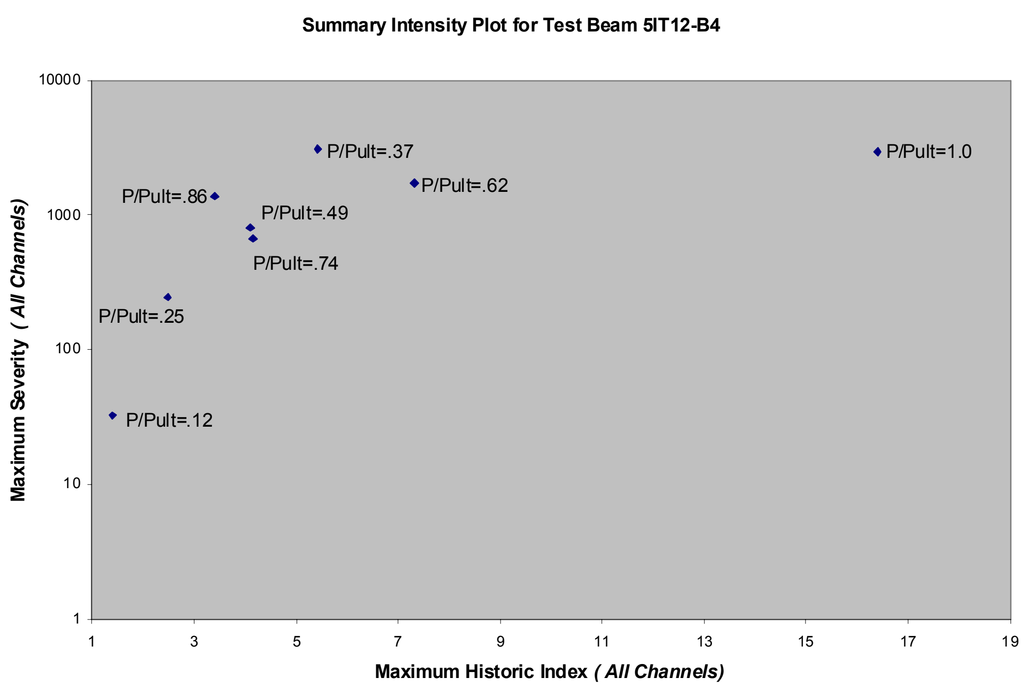

Figure 3.179 Summary of maximum Intensity from all channels over the entire load protocol for test beam 5IT12-B4.

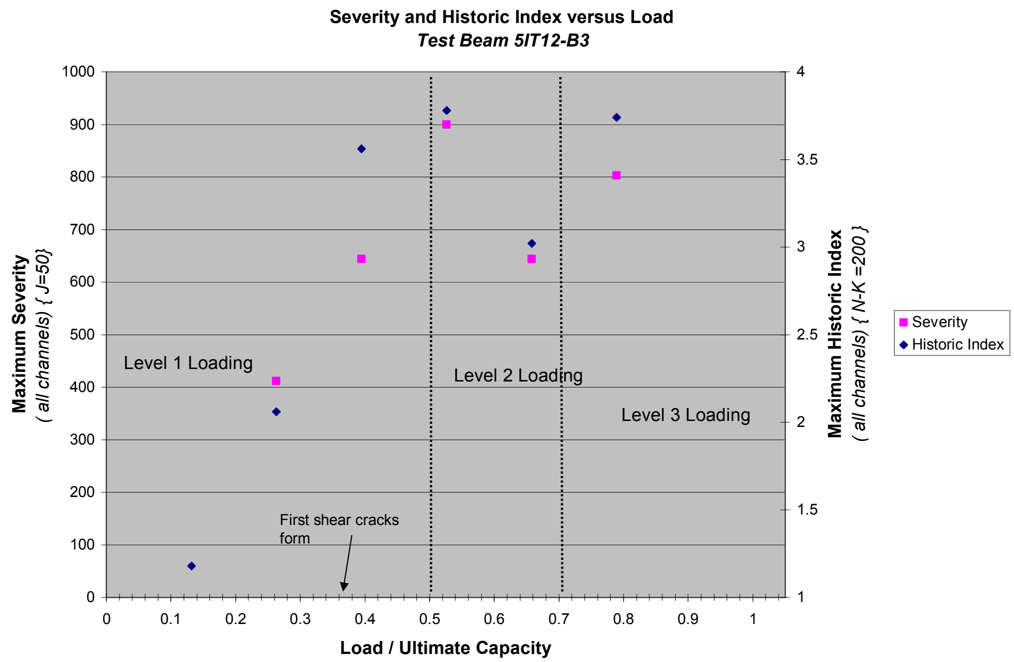

Figure 3.180 Summary of maximum Severity and Historic Index from all channels over the entire load protocol for test beam 5IT12-B3.

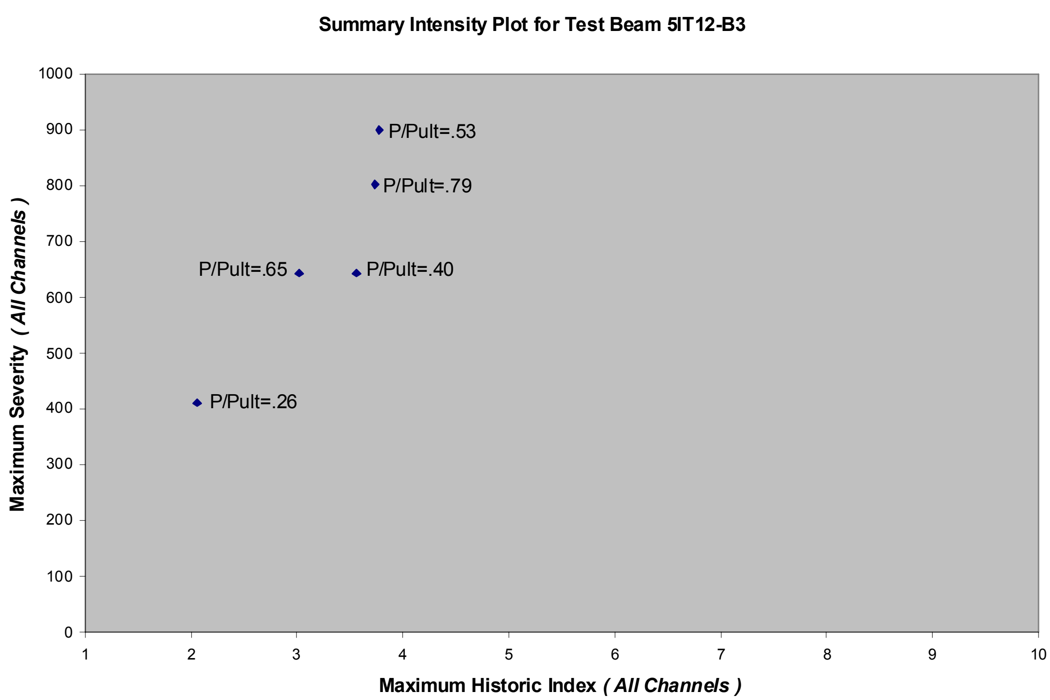

Figure 3.181 Summary of maximum Intensity from all channels over the entire load protocol for test beam 5IT12-B3.

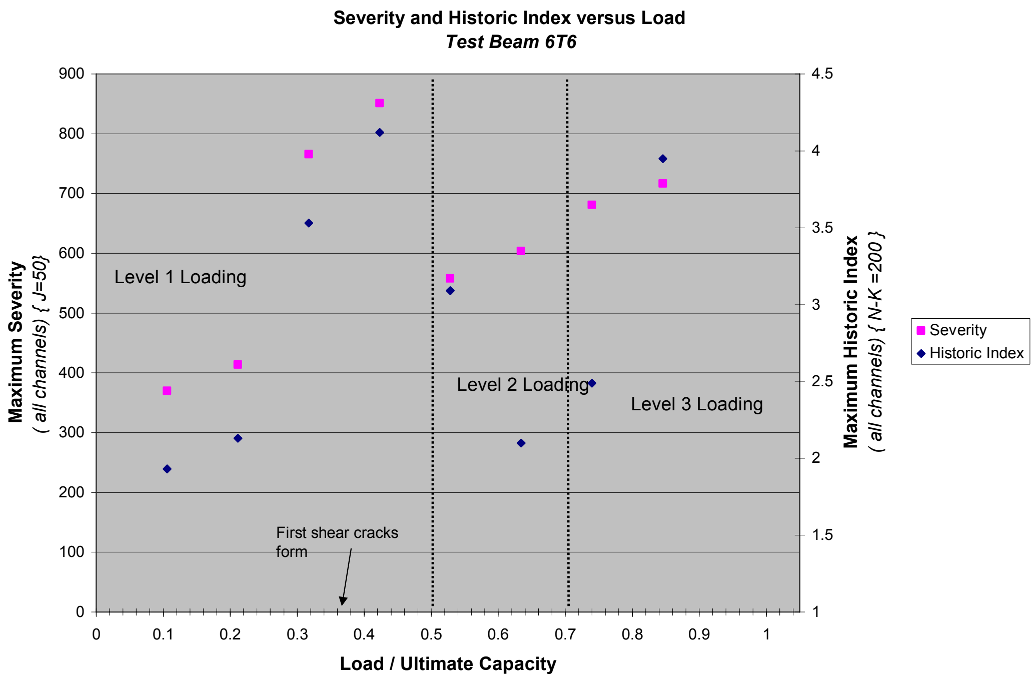

Figure 3.182 Summary of maximum Severity and Historic Index from all channels over the entire load protocol for test beam 6T6.

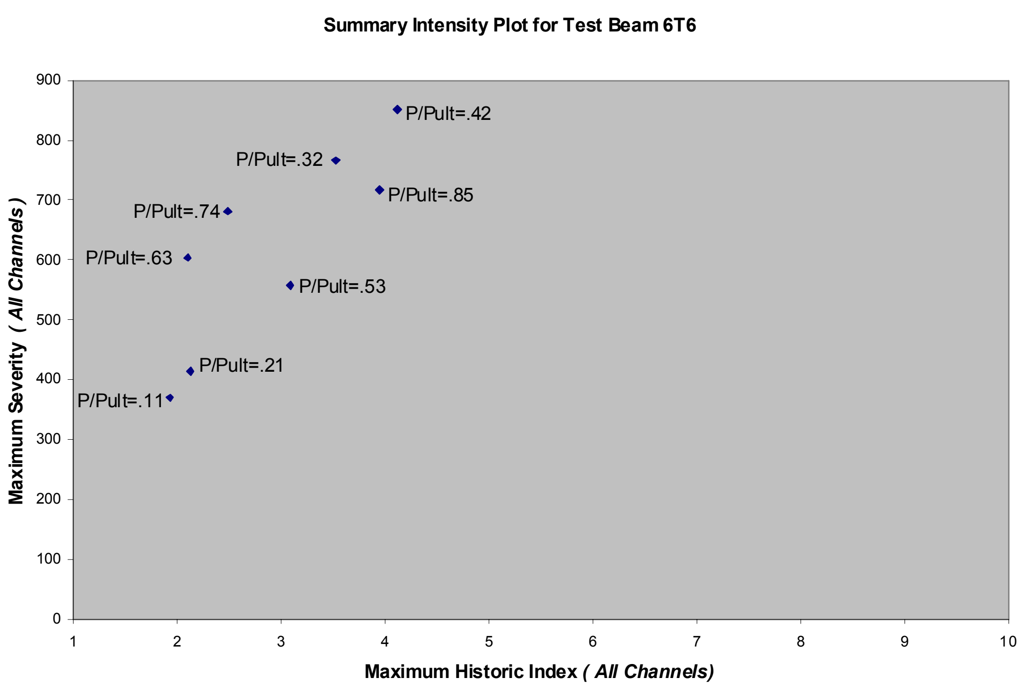

Figure 3.183 Summary of maximum Intensity from all channels over the entire load protocol for test beam 6T6.

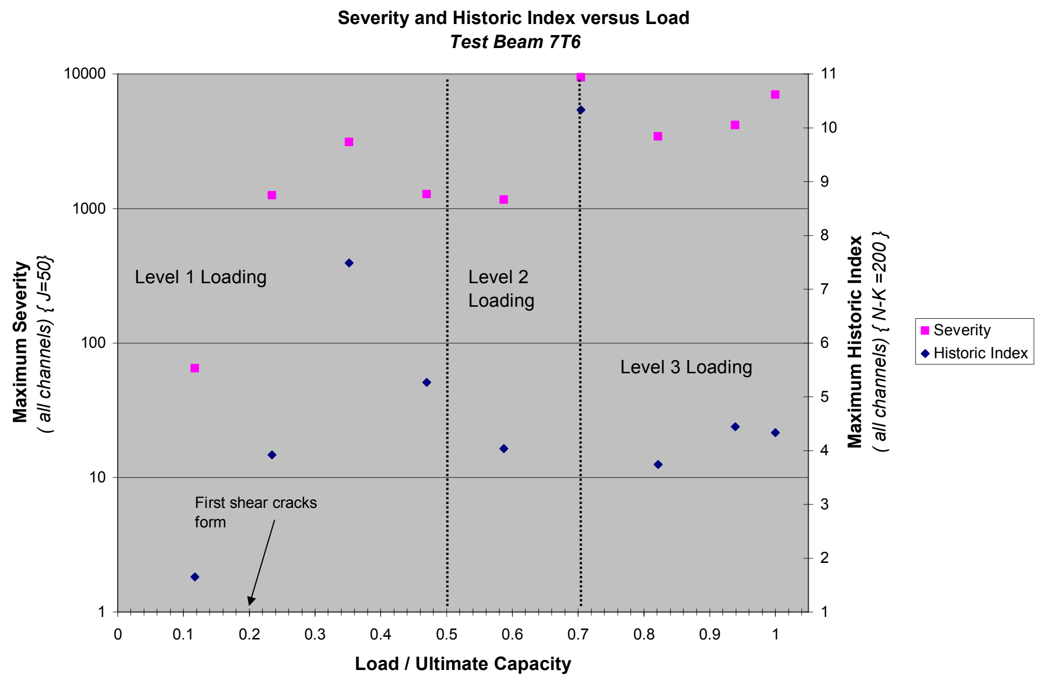

Figure 3.184 Summary of maximum Severity and Historic Index from all channels over the entire load protocol for test beam 7T6.

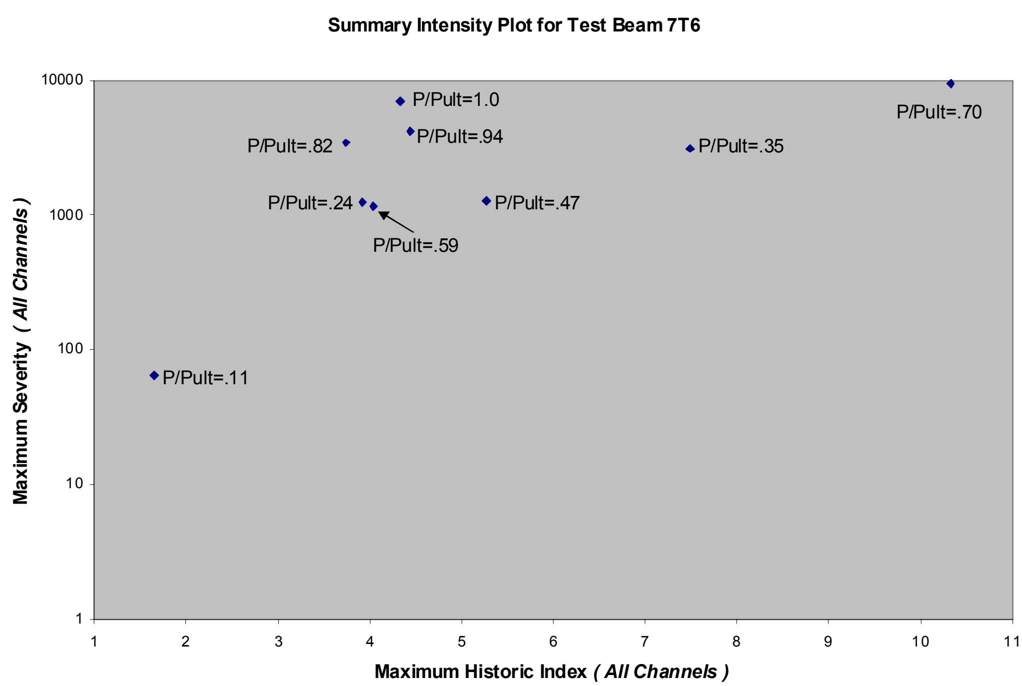

Figure 3.185 Summary of maximum Intensity from all channels over the entire load protocol for test beam 7T6.

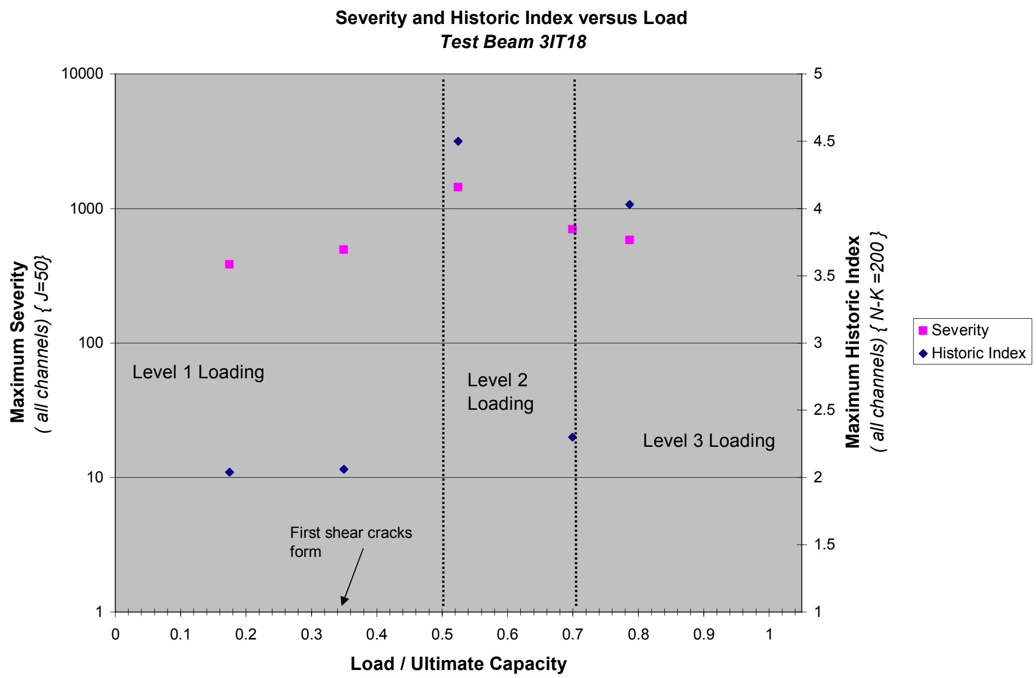

Figure 3.186 Summary of maximum Severity and Historic Index from all channels over the entire load protocol for test beam 3IT18.

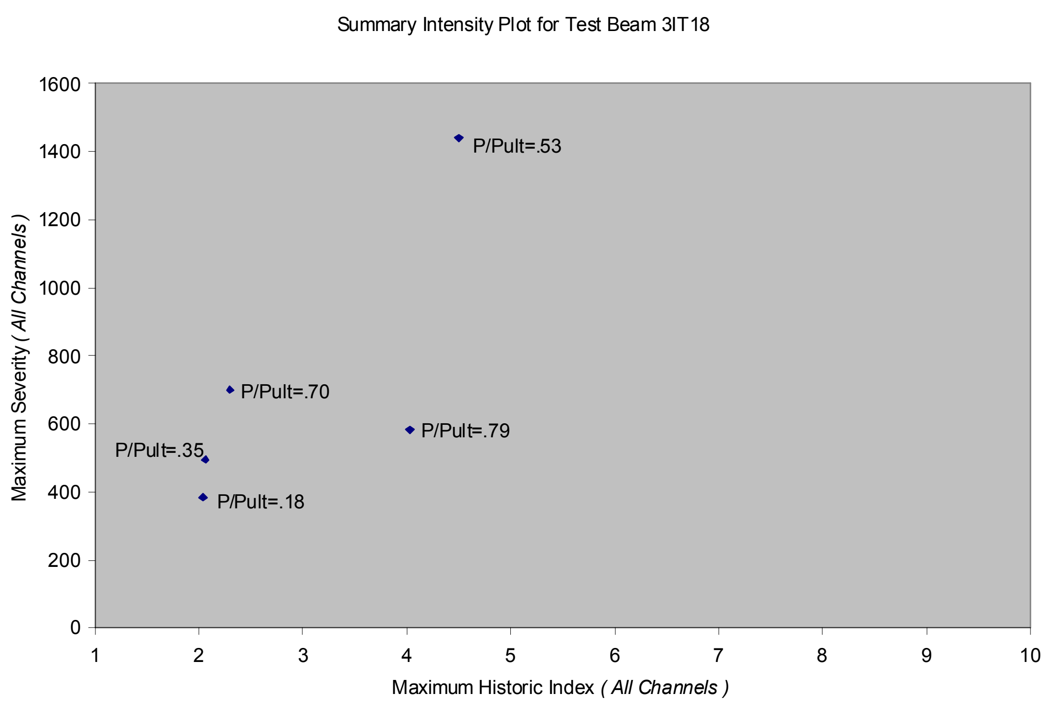

Figure 3.187 Summary of maximum Intensity from all channels over the entire load protocol for test beam 3IT18.

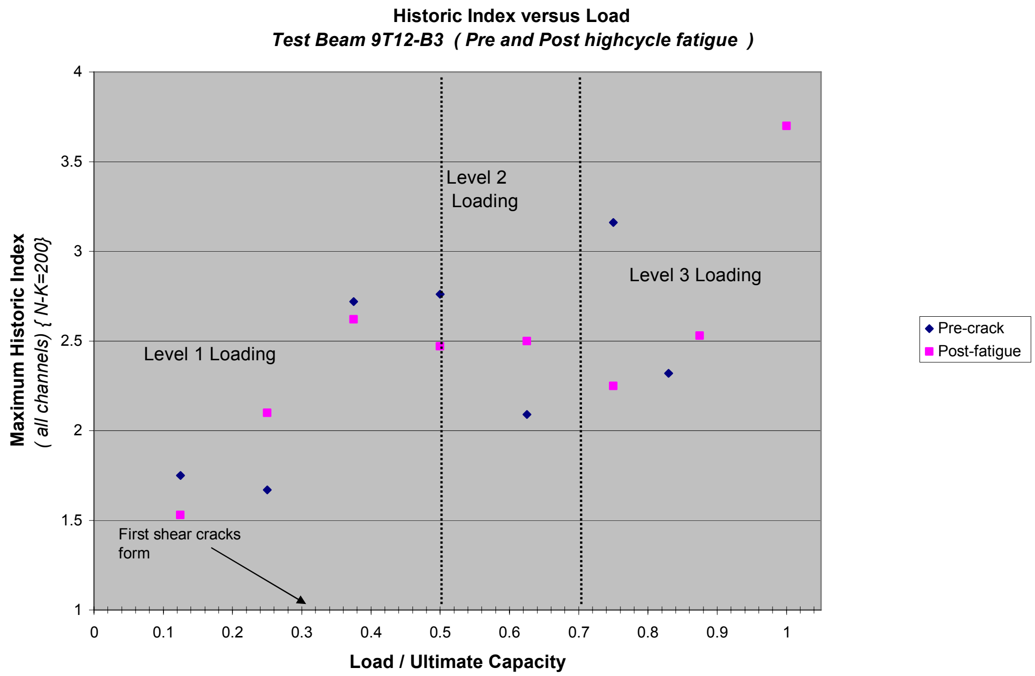

Figure 3.188 Summary of maximum Historic Index from all channels over the entire load protocol for test beam 5IT12-B1.

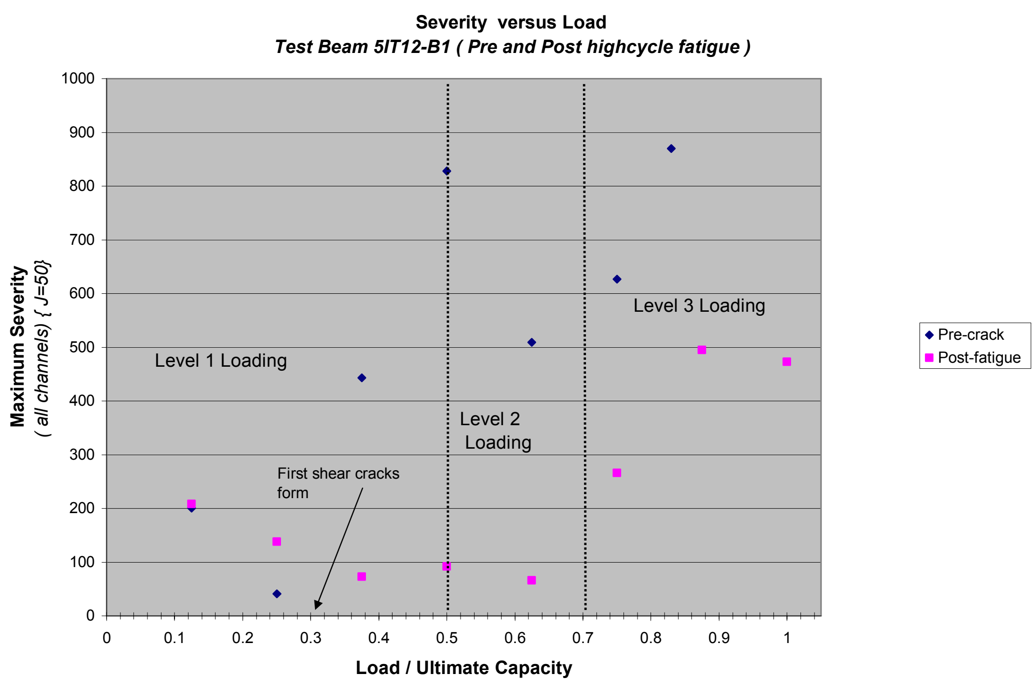

Figure 3.189 Summary of maximum Severity from all channels over the entire load protocol for test beam 5IT12-B1.

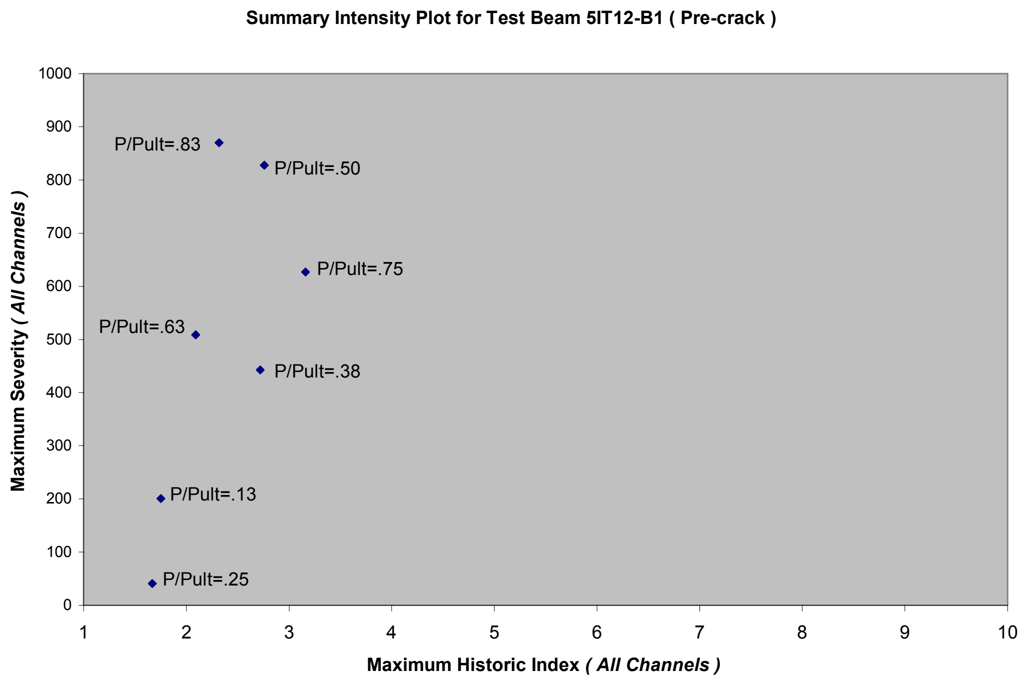

Figure 3.190 Summary of maximum Intensity from all channels over the entire first load protocol for test beam 5IT12-B1.

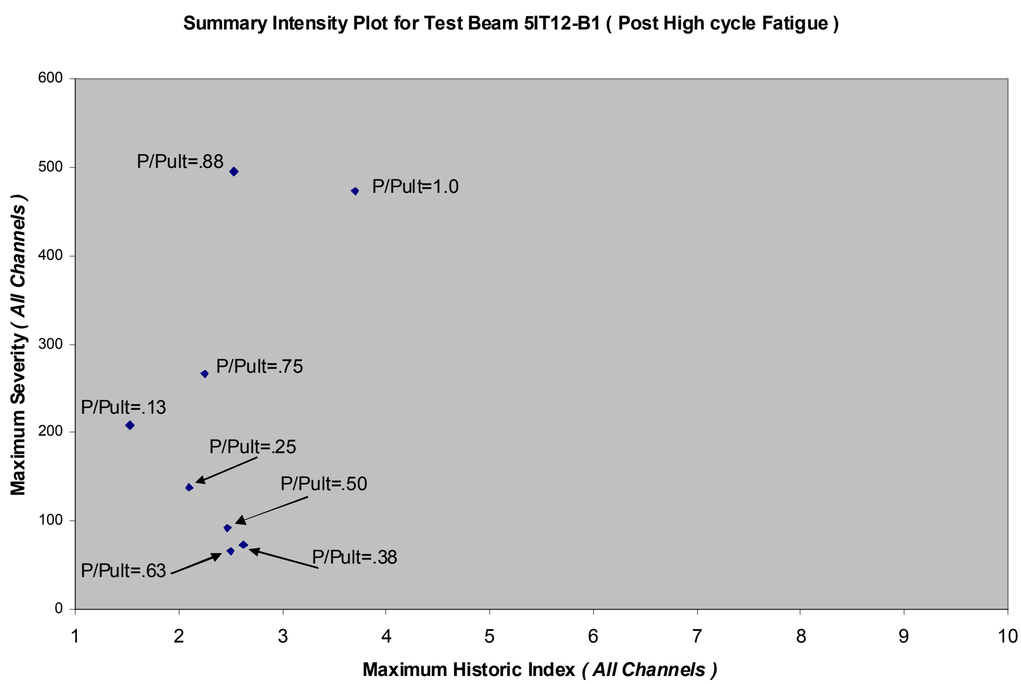

Figure 3.191 Summary of maximum Intensity from all channels over the entire third load protocol for test beam 5IT12-B1.

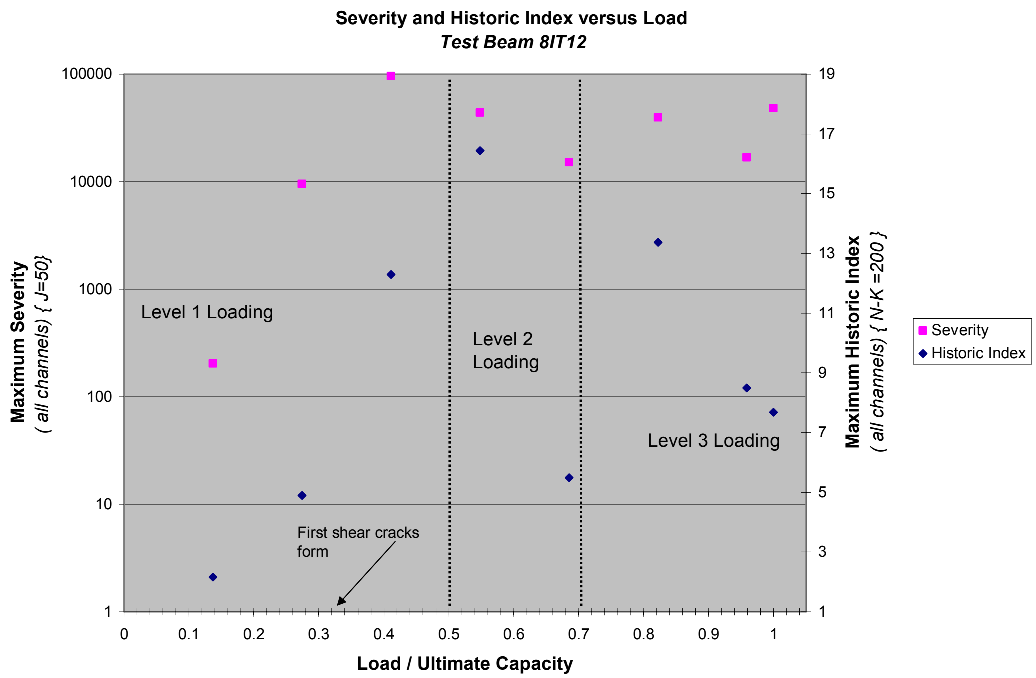

Figure 3.192 Summary of maximum Severity and Historic Index from all channels over the entire load protocol for test beam 8IT12.

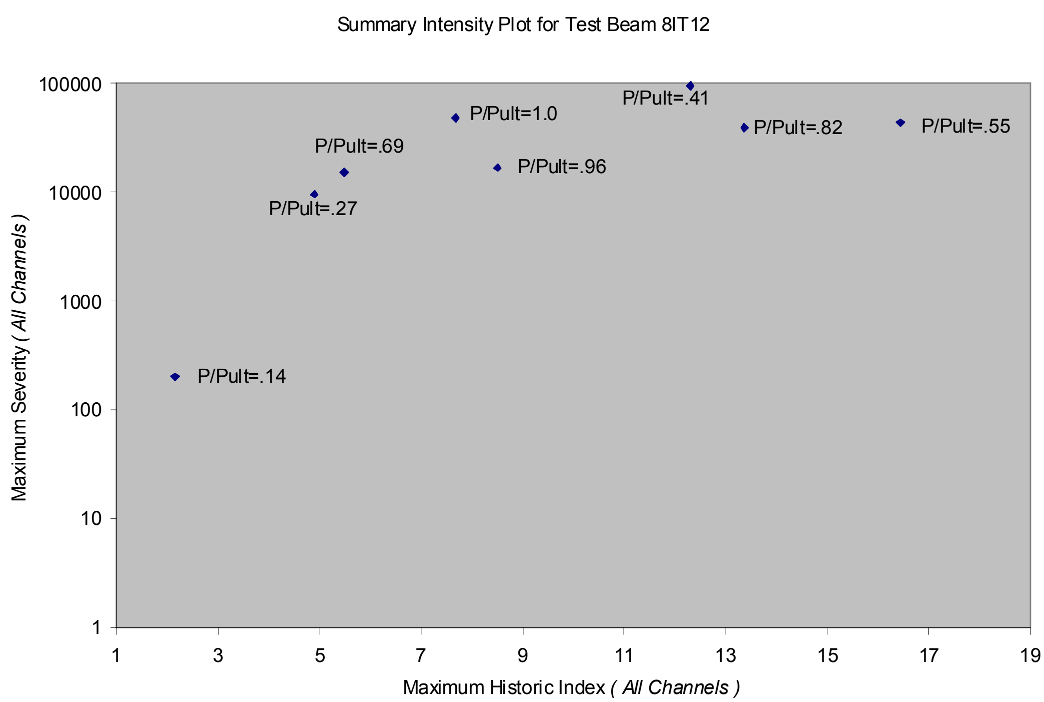

Figure 3.193 Summary of maximum Intensity from all channels over the entire load protocol for test beam 8IT12.

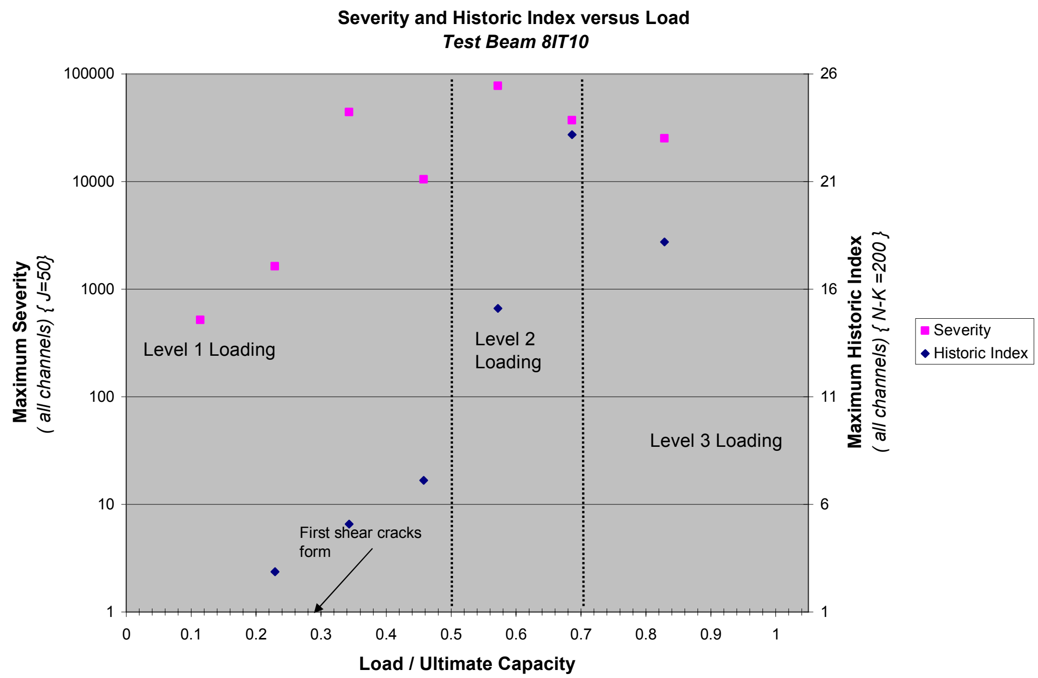

Figure 3.194 Summary of maximum Severity and Historic Index from all channels over the entire load protocol for test beam 8IT10.

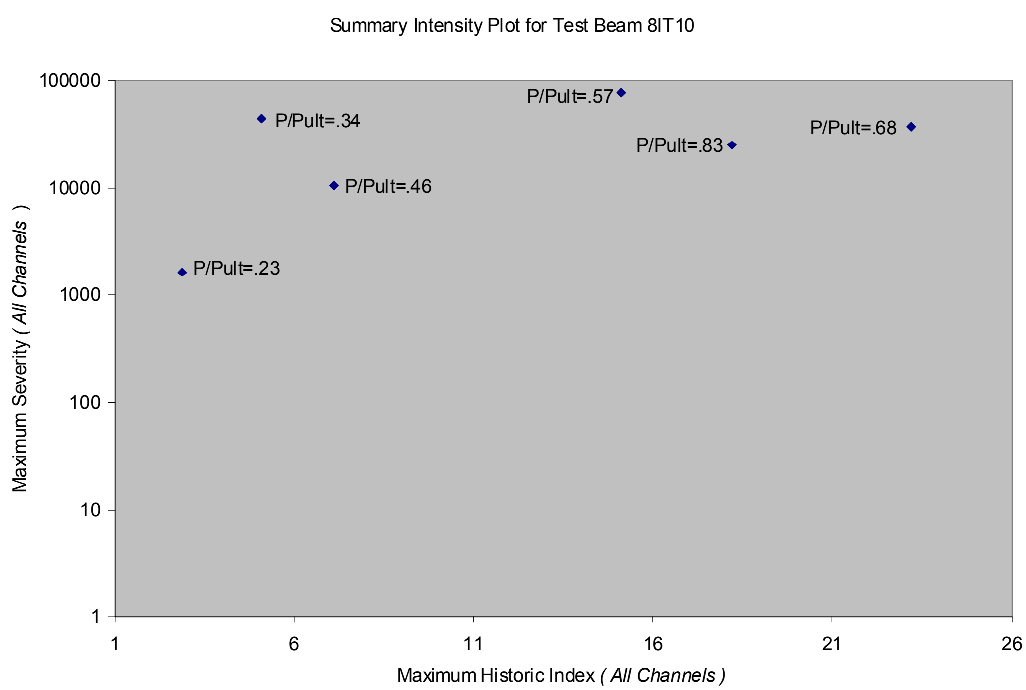

Figure 3.195 Summary of maximum Intensity from all channels over the entire load protocol for test beam 8IT10.

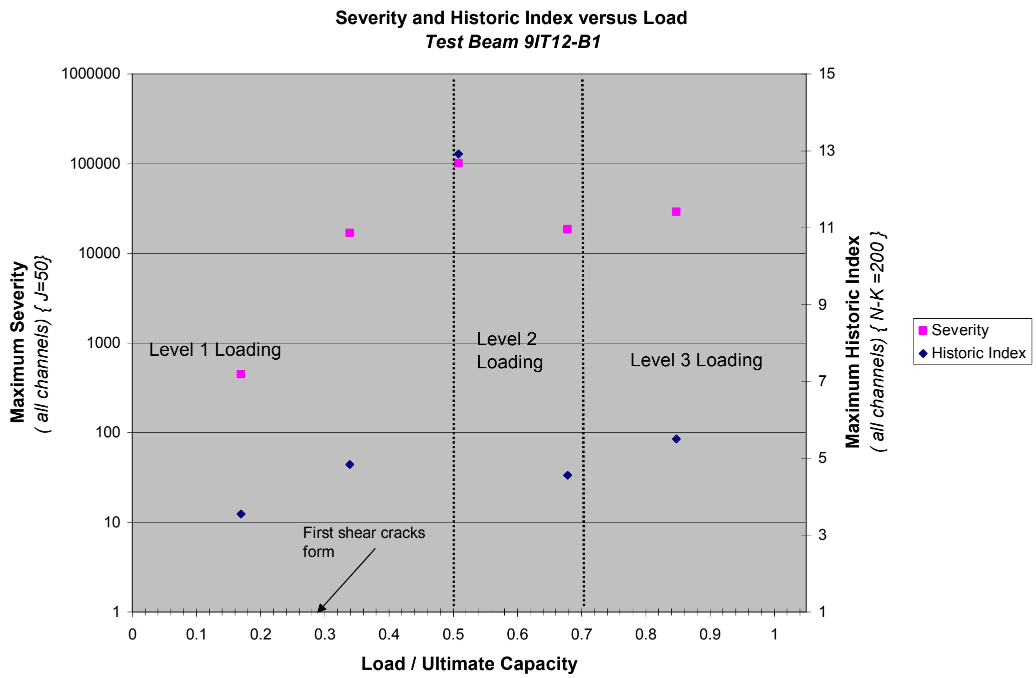

Figure 3.196 Summary of maximum Severity and Historic Index from all channels over the entire load protocol for test beam 9IT12-B1.

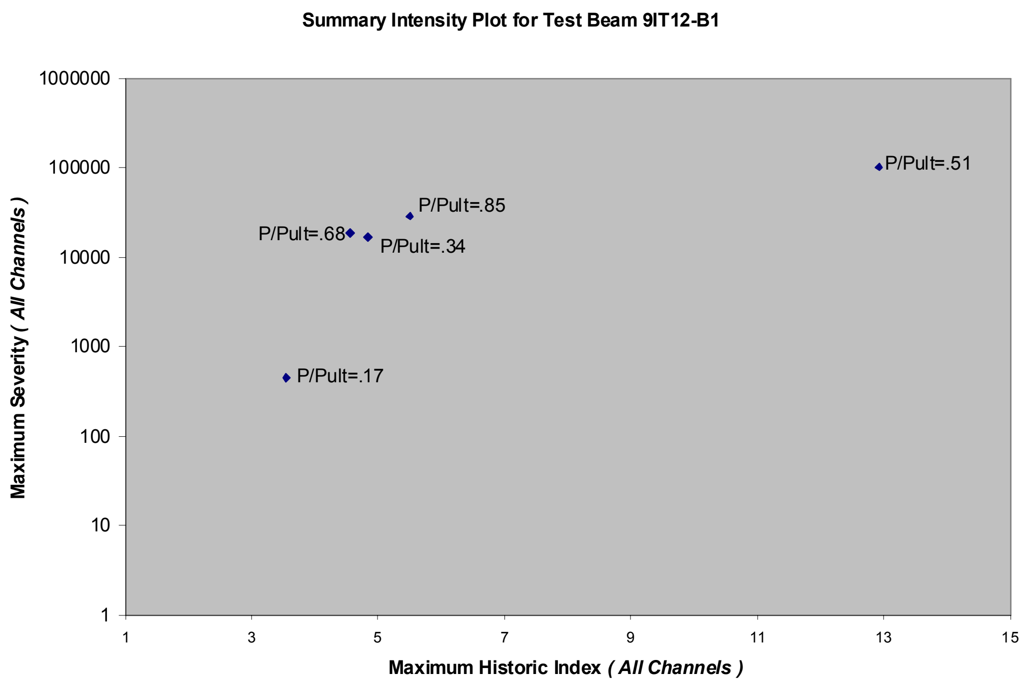

Figure 3.197 Summary of maximum Intensity from all channels over the entire load protocol for test beam 9IT12-B1.

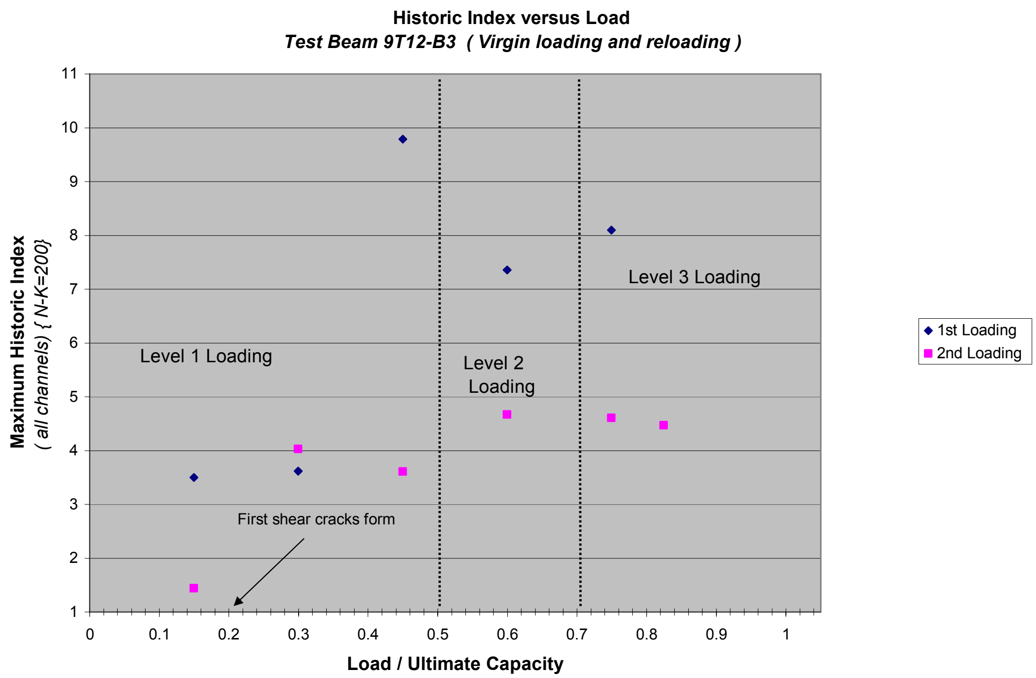

Figure 3.198 Summary of maximum Historic Index from all channels over the entire load protocol for test beam 9T12-B3.

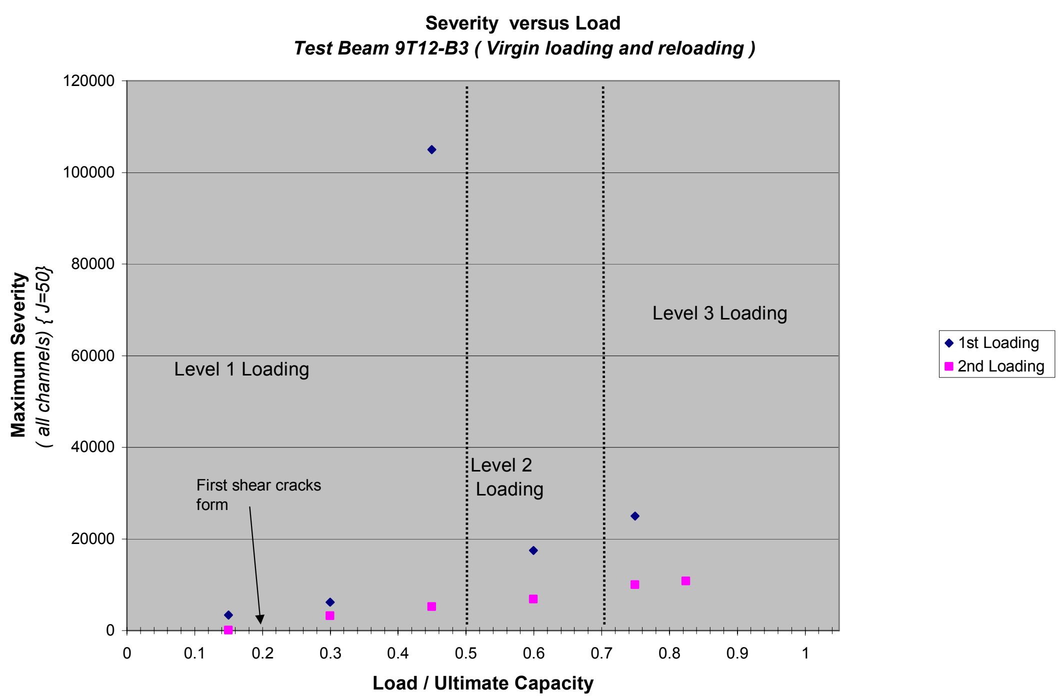

Figure 3.199 Summary of maximum Severity from all channels over the entire load protocol for test beam 9T12-B3.

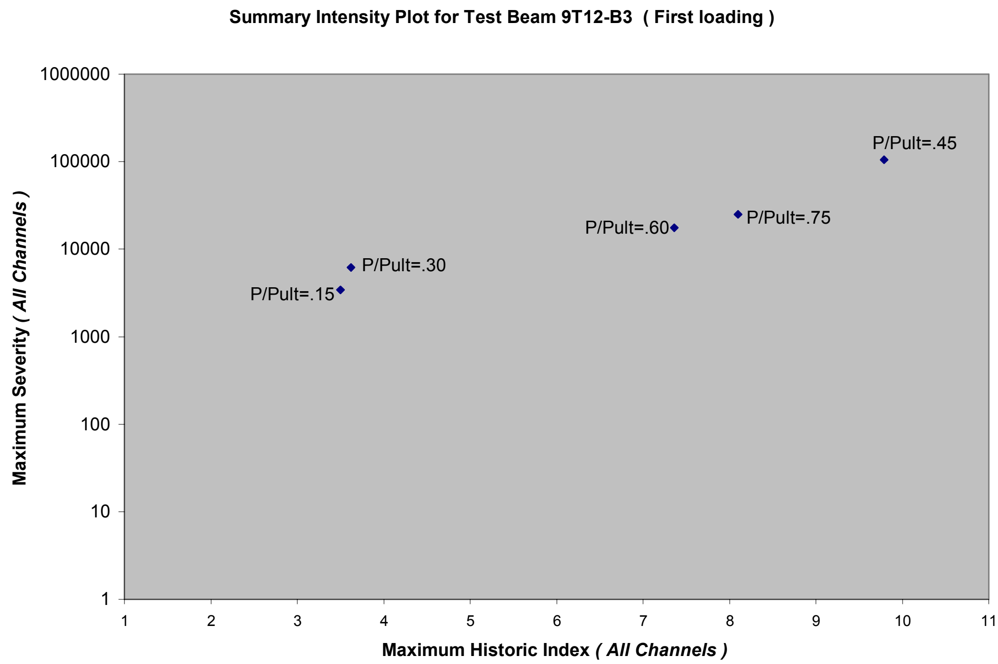

Figure 3.200 Summary of maximum Intensity from all channels over the entire first load protocol for test beam 9T12-B3.

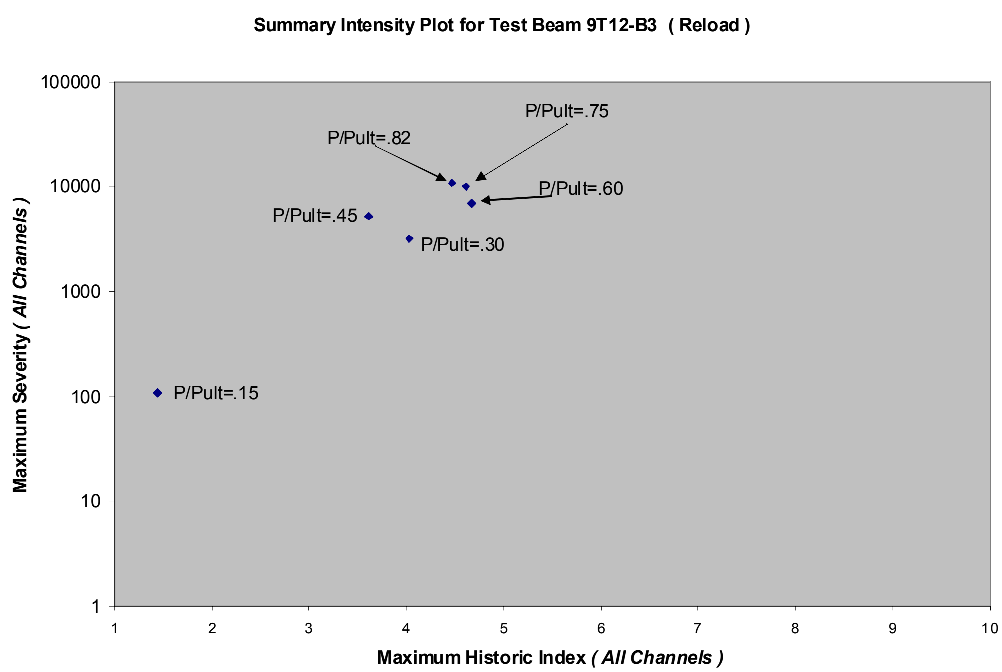

Figure 3.201 Summary of maximum Intensity from all channels over the entire second load protocol for test beam 9T12-B3.

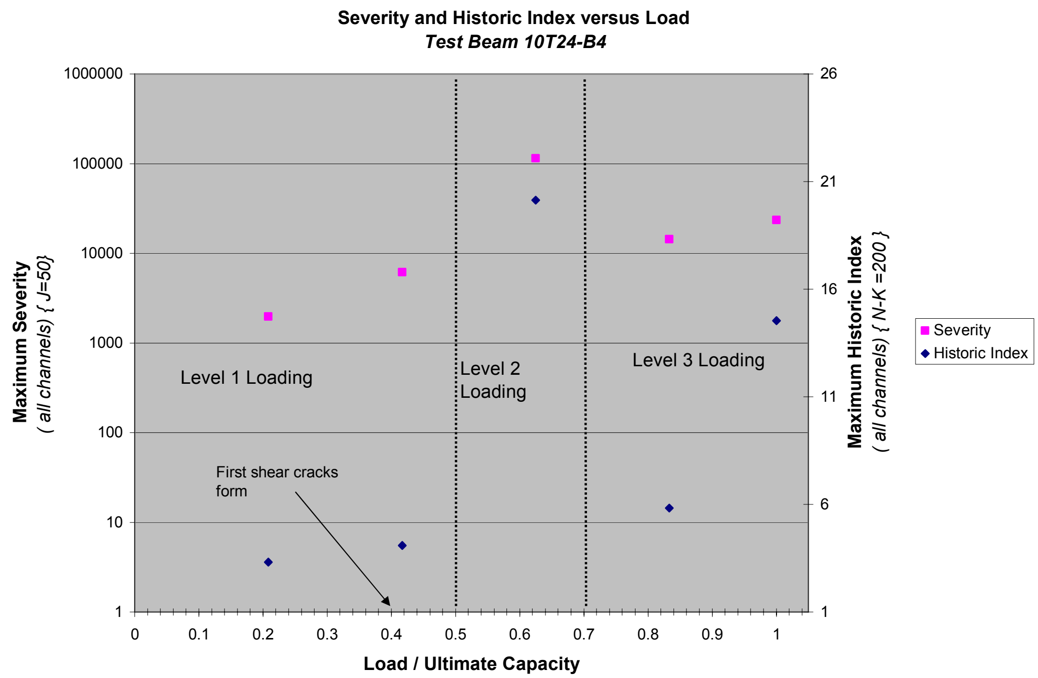

Figure 3.202 Summary of maximum Severity and Historic Index from all channels over the entire load protocol for test beam 10T24-B4.

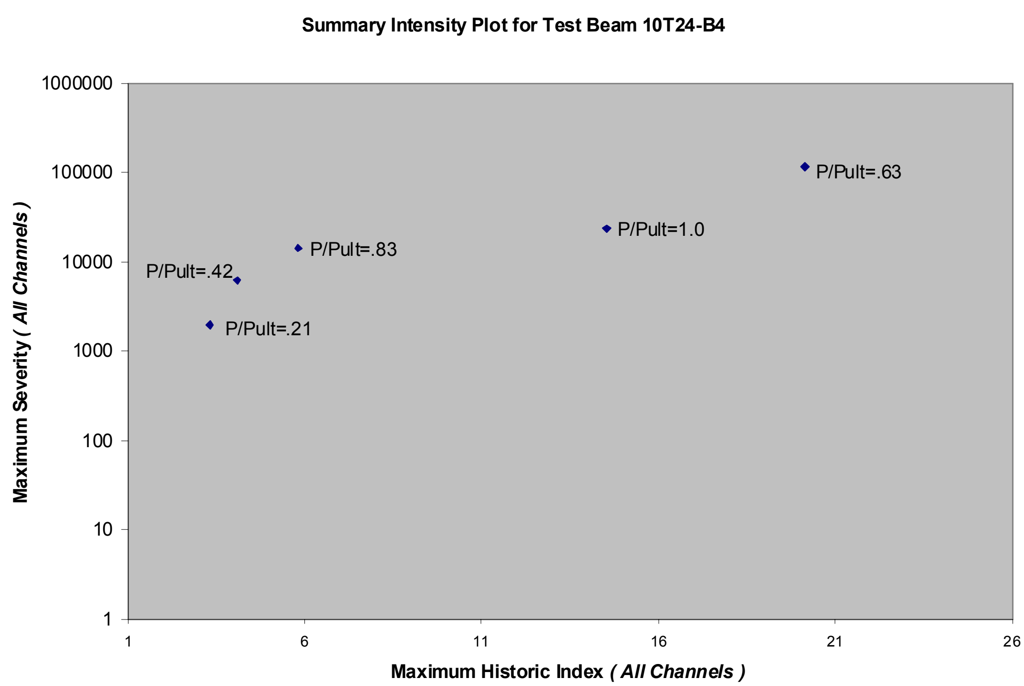

Figure 3.203 Summary of maximum Intensity from all channels over the entire load protocol for test beam 10T24-B4.

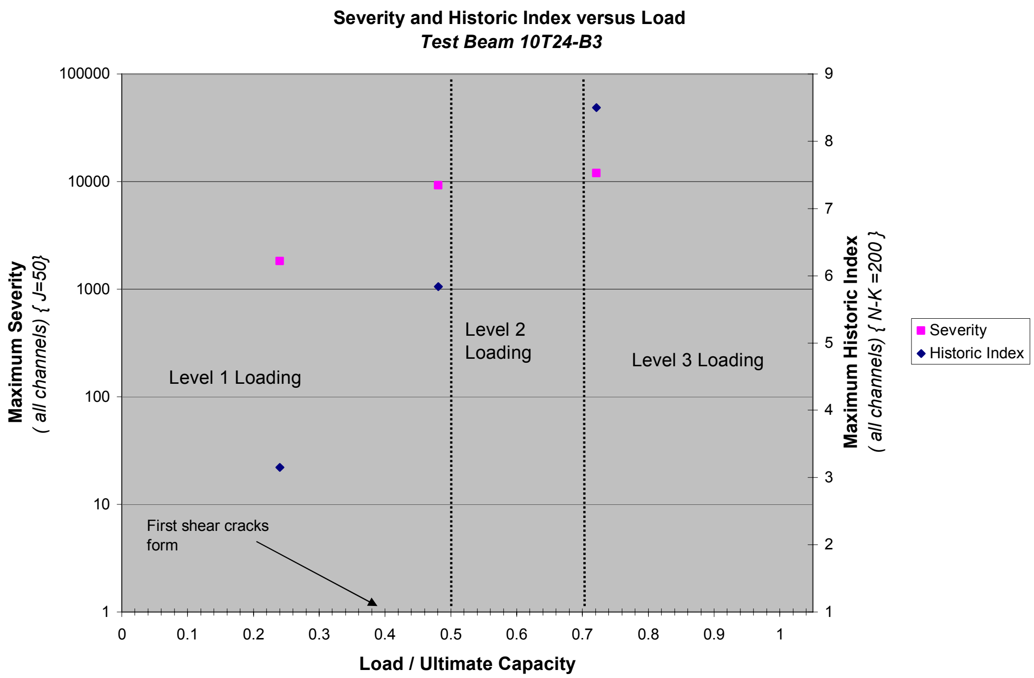

Figure 3.204 Summary of maximum Severity and Historic Index from all channels over the entire load protocol for test beam 10T24-B3.

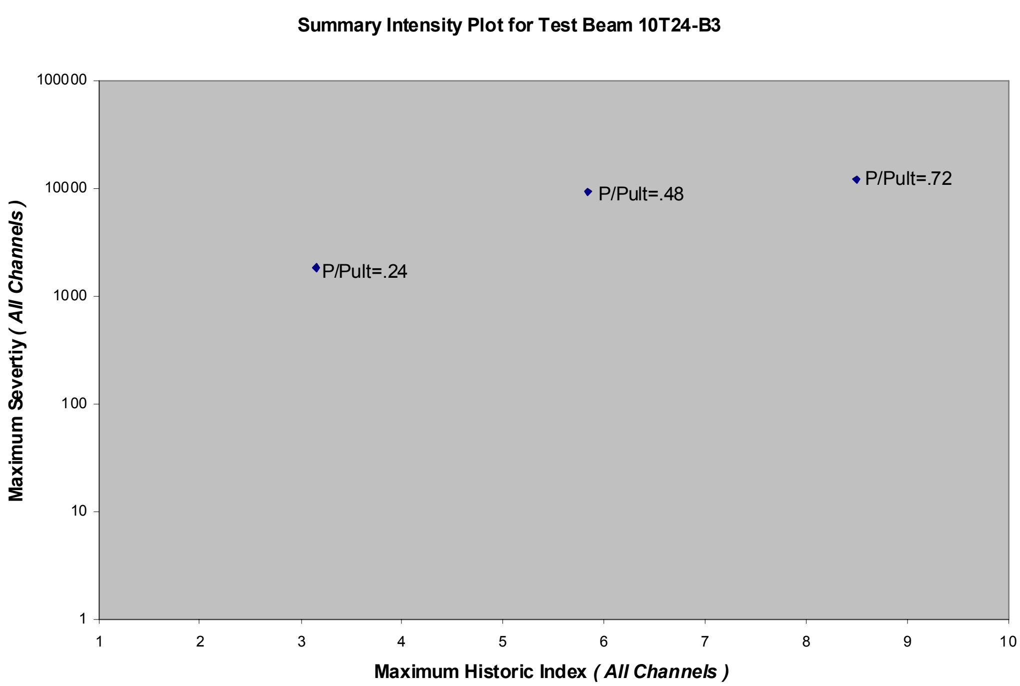

Figure 3.205 Summary of maximum Intensity from all channels over the entire load protocol for test beam 10T24-B3.

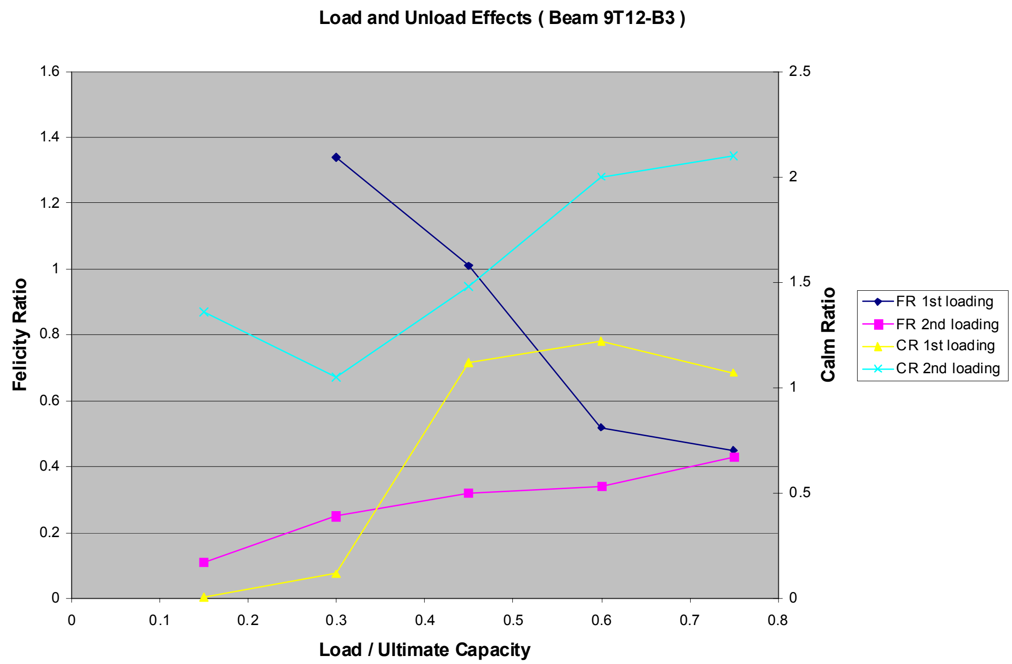

Figure 3.206 Felicity and Calm Ratios for test beam 9T12-B3 , first and second loading sequences.

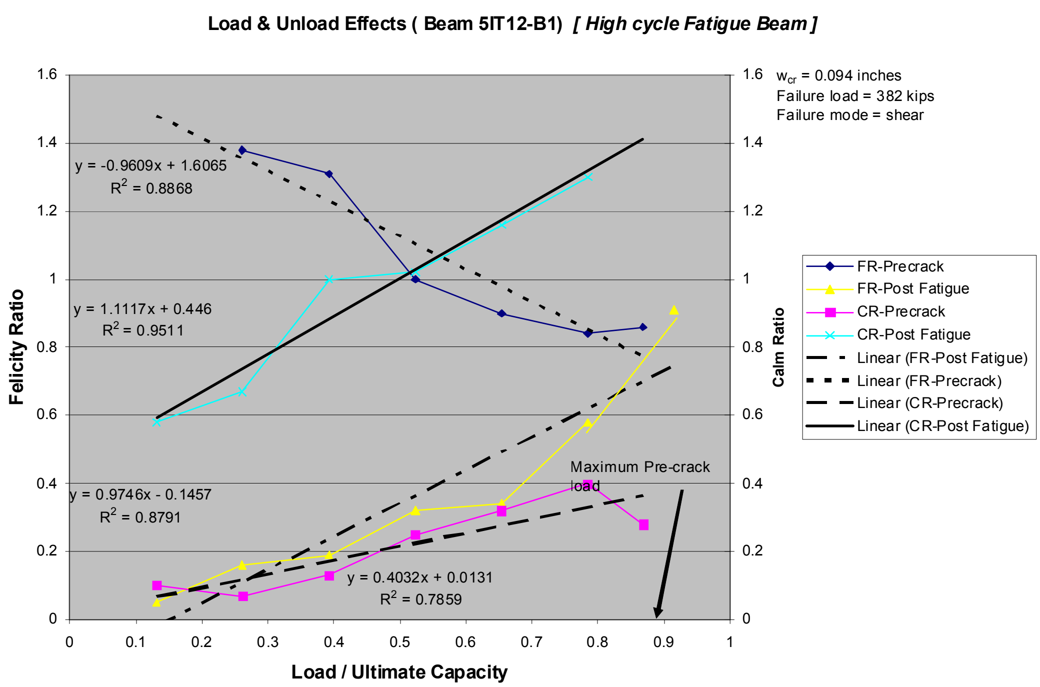

Figure 3.207 Felicity and Calm Ratios for test beam 5IT12-B1, pre-crack and post high cycle fatigue responses.

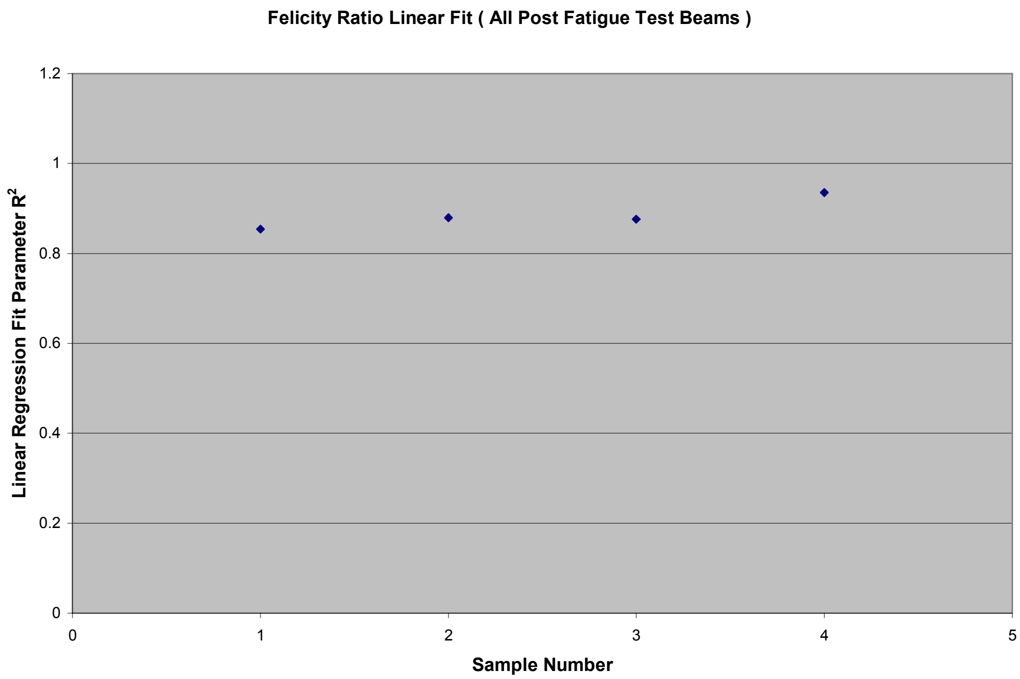

Figure 3.208 Linear regression fit parameter for Felicity ratio on post fatigue test beams (compare to virgin beam response shown in Figure 3.110).

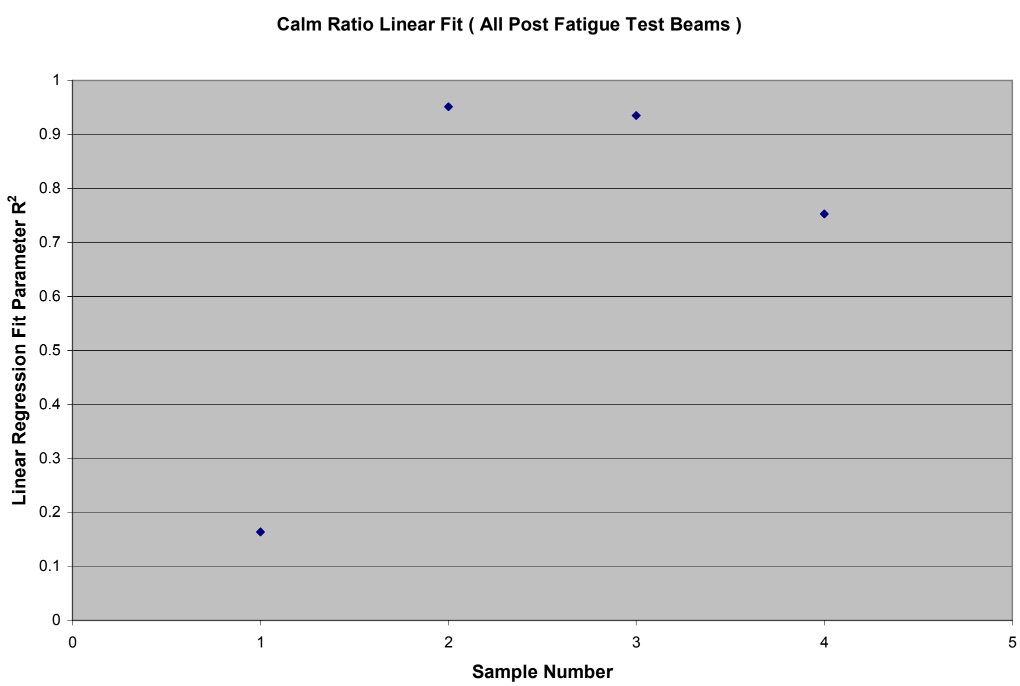

Figure 3.209 Linear regression fit parameter for Calm ratio on post fatigue test beams (compare to virgin beam response shown in Figure 3.111).

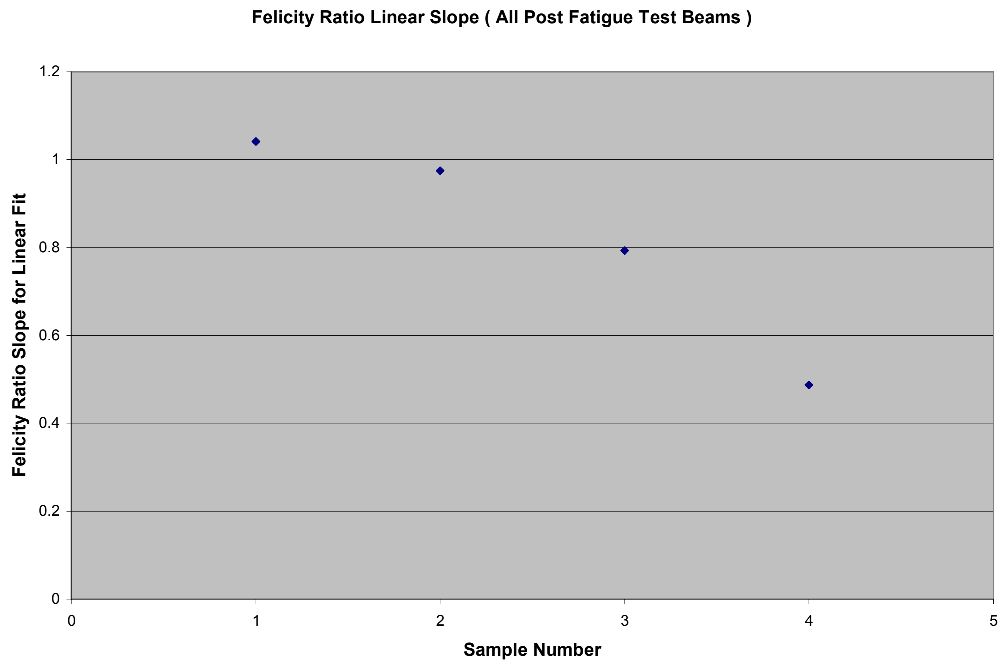

Figure 3.210 Linear regression slope for Felicity ratio on post fatigue test beams (compare to virgin beam response shown in Figure 3.112).

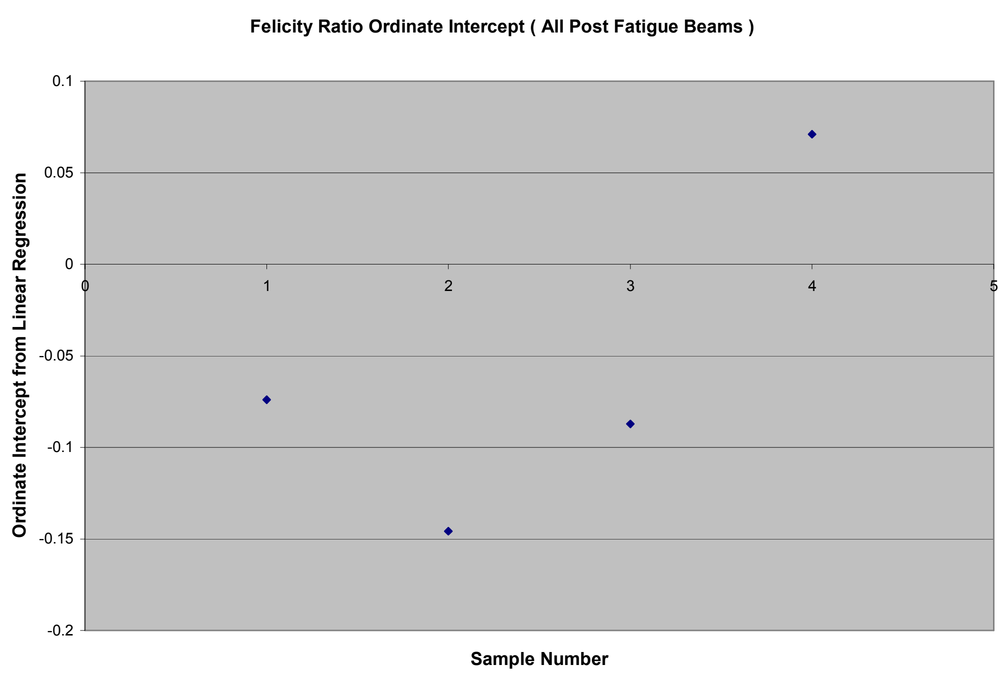

Figure 3.211 Linear regression ordinate intercept for Felicity ratio on post fatigue test beams (compare to virgin beam response shown in Figure 3.113).

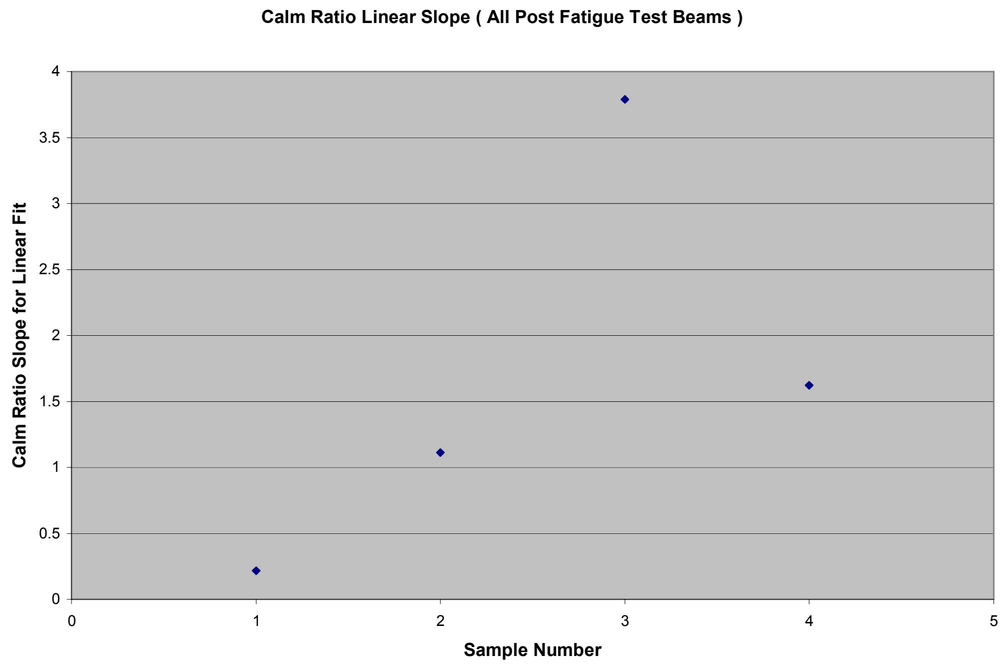

Figure 3.212 Linear regression slope for Calm ratio on post fatigue test beams (compare to virgin beam response shown in Figure 3.114).

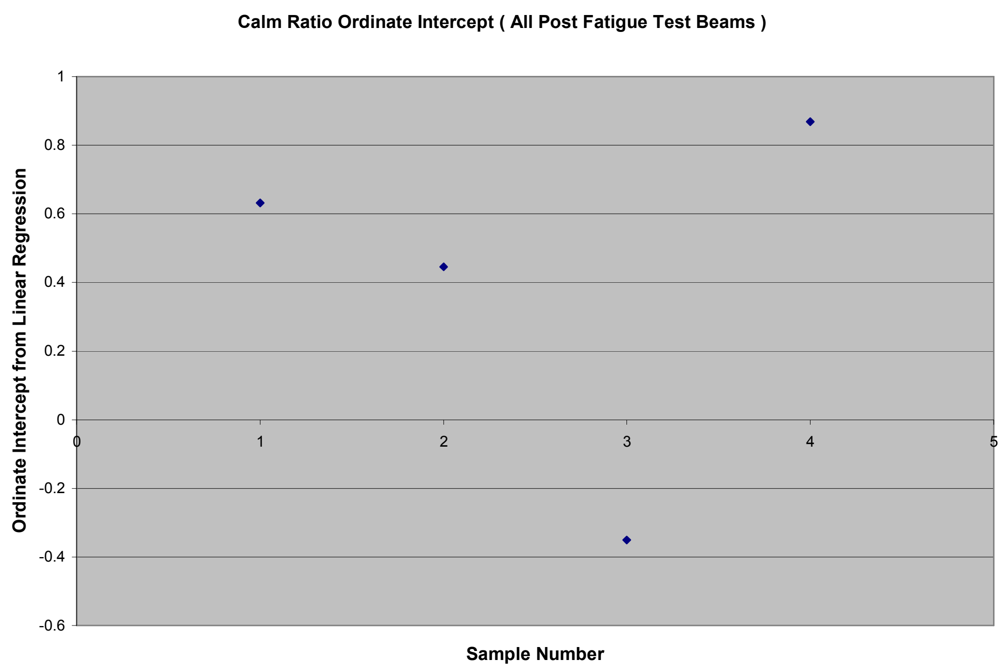

Figure 3.213 Linear regression ordinate intercept for Calm ratio on post fatigue test beams (compare to virgin beam response shown in Figure 3.115).

4 Testing of In-Service Reinforced Concrete Deck Girder Bridges Using Acoustic Emission

4.1 Three Cracked Bridges Selected for Testing

Three RCDG bridges that were exhibiting Level 2 diagonal tension cracking or greater were selected to apply the AE test and evaluation methods developed in Chapter 3 to real in-services bridges. The Luckiamute River bridge was tested first using 14 channels of AE along with CMOD of a prominent shear crack. Static, dynamic and ambient load cases where considered. This bridge has a permanent SHM system that has been in place since 2004. The next bridge tested was the Banzer bridge that was unique from the other two in that it is a two girder system as opposed to four. Again 14 channels of AE were collected along with strain measurements from the shear reinforcing bars that crossed the large diagonal tension crack that was being examined. This proved to be a far superior structural response parameter for correlating with AE compared to CMOD or integrated shear strain. Again static, dynamic and ambient load cases were tested. The final bridge tested used 8 channels of AE along with rebar strain and CMOD focused on a large diagonal tension crack. Test trucks were run in various travel lanes of the bridge in order to vary the loading on the single test girder.

4.2 Acoustic Emissions Testing of the Luckiamute River Bridge, ODOT Bridge # 06653A

4.2.1 Background

Bridge number 06653A carries Highway 99W over the Luckiamute River , located approximately 4 miles south of Monmouth , Oregon. The structure is a typical 1950's era reinforced concrete deck girder (RCDG) configuration with five continuous spans ranging from 46 to 78 feet , supported by four girder lines. This structure shows the signs of the ubiquitous diagonal tension cracking in the high shear zones in the girders near the bents. This particular bridge was fitted with a structural health monitoring (SHM) system in Spring 2004, with emphasis on monitoring the known crack widths and temperatures of the girders and environment.

In addition to the long term SHM system, a series of load tests were performed to quantify the behavior of the most severe shear crack under both controlled and ambient service loads. The response of the structure to these loads will be compared to the response measured during laboratory testing of single, full scale beams of similar construction.

4.2.2 Test Location Description

Figure 4.2.1 shows the plan and elevation drawing for the subject test bridge. Superimposed on the plan drawing are the location markers for the long term shear crack monitoring, cracks C1 thru C5. Crack C3 has the widest crack mouth opening varying from 0.02 to 0.03 inches and spans most of the depth of the beam or girder section. Figure 4.2.2 shows the beam section detail drawing. Crack C3 is located on the West or upstream girder in span 3 (between Bents 3 and 4) approximately 12 feet south of Bent 3 centerline. Figure 4.2.3 shows the detailed crack map with reinforcing steel (rebar) locations relative to the diagonal crack. Figure 4.2.4 shows the approximate location of crack C3 sketched on the beam longitudinal section with the location of the AE sensors. Both faces (upstream and down stream) of the girder were instrumented.

4.2.3 Instrumentation for Structural Load testing

A total of 4 crack mouth open displacement (CMOD) and 14 Acoustic Emission (AE) transducers were installed to measure the response of shear crack C3 to controlled and service or ambient traffic loads.

4.2.3.1 Upstream girder face

The upstream girder face was fitted with three CMOD potentiometers along the length of the crack C3 in addition to 6 AE sensors that formed a planar array approximately 26 inches wide by 40 inches deep encompassing most of the crack C3 as shown in Figure 4.2.5. Resonant 60 kHz sensors were used for this array. The CMOD sensors are potentiometers with a response of 0.1 inch / volt and a range of 0.5 inches. Sensitivity of the CMOD measurement is approximately 0.00025 inches.

4.2.3.2 Downstream girder face

The downstream or inside girder face was fitted with one CMOD located near mid-depth of the girder and 8 AE sensors that formed a planar array approximately 26” by 40” (mirror image of outer array) as shown in Figure 4.2.6. AE sensors at positions 7,8,11,12,13 and 14 use resonant 150kHz AE sensors and positions 9 and 10 use high fidelity AE (displacement type) sensors. Sensor specifications can be found in Appendix A. AE sensors at positions 9 and

10 were used to capture transient wave forms in addition to typical AE measurements. Refer to Figure 4.2.7 for the general arrangement of sensors in both arrays.

The detailed locations of each AE sensor are summarized in Table 4.2.1. A coordinate system is defined as follows for these locations.

Origin – intersection of the bottom – downstream corner of the girder with South face of Bent 3. X-axis runs horizontal in line with the girder line. Y-axis runs vertical, inline with the bent column , Z-axis runs upstream.

Both AE and CMOD data were collected on a Vallen AMSY5 acoustic emission monitoring system with 4 parametric input (16 bit over 10 volts Analog to Digital conversion) and 14 AE channels. AE channels were sampled at 5 MHz. The CMOD were sampled at a minimum of 200 Hz.

4.2.4 Test Procedures

The testing had three distinct activities, 1) Calibration of AE sensors, 2) Controlled loading and 3) Ambient service loading.

4.2.4.1 Calibration of AE sensors

Standard pencil break methods were used to make certain each AE sensor had proper acoustic coupling to the concrete surface. Pencil breaks using 0.5mm lead were performed approximately 2 inches away from each sensor. Three breaks per sensor were performed and recorded. Table 4.2.2 summarizes the peak amplitudes measured at each sensor due to a near by pencil break.

Five controlled load protocols were employed to load the girder being tested, two static and three dynamic.

4.2.4.2 Static load case 1

Three loaded dump trucks (nominally 40,000 lbs GVW) were placed , one at a time , onto span three in such a manner as to cause maximum shear loading on the cracked upstream girder at location C3. Figure 4.2.7 shows the test truck axle weights and configuration. This was accomplished by backing the first truck up from the south end of the bridge until the center of its rearmost axle was 13 feet from the centerline of bent 3. This placed the rear axle at the south end of the shear crack C3. The two remaining trucks were then backed up , one at a time to within a few inches of being bumper to bumper. The upstream tires were centered over the fog line to provide near maximum load distribution to the outermost or upstream girder. The trucks were then driven off the bridge one at a time. Figure 4.2.8 shows the test trucks in position for this load case.

4.2.4.3 Static load case 2

Two loaded dump trucks were placed onto span three much like static load case 1 but with only two trucks. It was determined the third truck had little measurable effect at location C3 during the first static load case. Once the trucks were in place, ambient service loads were allowed to pass in both directions using the downstream lane. This load case was designed to investigate the effects of live loads superimposed on a larger then ambient dead load, i.e. the parked trucks increased the dead load on the girder and the trucks traveling in the opposite lane imparted a live load to the upstream girder via lateral load distribution.

4.2.4.4 Dynamic load case 1

A train of three loaded dump trucks with 10 to 15 foot spacing between trucks were driven Northbound in the Northbound or downstream lane at approximately 5 to 10 mph with the outboard wheels centered over the fog line. This was used to investigate the affects loads in the opposite lane have on the cracked upstream girder.

4.2.4.5 Dynamic load case 2

A train of three loaded dump trucks with 10 to 15 foot spacing between trucks were driven Southbound in the Southbound or upstream lane at approximately 5 to 10 mph with the outboard wheels <u>centered over the fog line</u>. This was to generate a temporally continuous version of Static Load case 1.

4.2.4.6 Dynamic load case 3

A train of three loaded dump trucks with 10 to 15 foot spacing between trucks were driven Southbound in the Southbound or upstream lane at approximately 5 to 10 mph with the trucks <u>centered in the travel lane</u>. This was used to compare with Dynamic load case 2 having a slight decrease in girder loading due to lateral load distribution.

4.2.4.7 Ambient Service loads

Regular traffic was monitored for several hours to capture the affects of typical service loads. Most trucks noted had three axles on the tractor and two to six on the trailers with likely GVW in the 50,000 to 105,500 lbs range. Approximately

60 truck loads were identified over the course of two days of testing. The time of passing, direction of travel and in some cases truck configurations were noted and included in the data for correlation. Figure 4.2.9 shows typical ambient truck configurations. The long term crack width measurements provided by the SHM at crack location C3 are shown in Figure 4.2.10. The upper plot shows crack width and ambient temperature over a 450 day period. The crack width starts at a displacement of 0.022 inches and appears to widen over the period of measurement to 0.030 inches. The lower plot shows the crack width with the mean and three-sigma levels shown. A excursion over the three sigma level can be interpreted as a statistically significant level of widening based on basic process control analyses, thus indicating that even when considering the effects of temperature on the crack width, a permanent amount of crack width increases appears to of developed over the 450 day test period which can be attributed to an accumulation of damage from ambient loading.

4.2.5 Results

4.2.5.1 Load Case Static 1

Analog results

Crack mouth opening displacement ranges from test loading.

Cmod2 (US face top of girder): 6.9×10^{-4} inches
Cmod3 (US face middle of girder): 15.2×10^{-4} inches
Cmod4 (US face bottom of girder): 15.3×10^{-4} inches
Cmod1 (DS face middle of girder): 7.2×10^{-4} inches

AE results

Results	**60 kHz sensors (US face)**	**150 kHz sensors(DS face)**	**High fidelity sensors (DS face)**
Load hits	150	50	60
Unload hits	84	25	33
Peak hit amplitude (dB)	94	59.5	66.5
Calm Ratio	0.56	0.5	0.55
Max.Historic Index	4.4	1.26	1.55
Max. Severity	780	80	520

The correlation of AE hit peak amplitude is shown with CMOD against time with loading and unloading points are shown in Figure 4.2.12. The maximum CMOD measured during loading and unloading was 0.00153 inches. The peak amplitudes ranged from the threshold of 40 dB up to 94 dB. Note the three large bursts of AE centered around 390 seconds on the time scale. These AE came from four different channels, with some from each array. The trucks were still during these bursts and there were no other vehicles on the bridge. After the unloading the CMOD very nearly returns to the starting value. Figure 4.2.13 shows the cumulative hits with time and CMOD. There were 260 hits during loading, 180 hits during load hold and 142 hits during unloading. Note that channels 2 was removed from the data as it was experiencing a large amount of what was found to be spurious threshold crossings resulting from sensor malfunction. Figure 4.2.14, 4.2.15 and 4.2.16 show the Historic Index , Severity and Intensity plot for this load case. Only four sensors detected enough AE activity to calculate these parameters.

4.2.5.2 Load Case Static 2

Analog results

Crack mouth opening displacement ranges from test loading.

Cmod2 (US face top of girder): 9.1×10^{-4} inches
Cmod3 (US face middle of girder): 32.5×10^{-4} inches
Cmod4 (US face bottom of girder): 17.5×10^{-4} inches
Cmod1 (DS face middle of girder): 9.1×10^{-4} inches

AE results

Results	**60 kHz sensors (US face)**	**150 kHz sensors (DS face)**	**High fidelity sensors (DS face)**
Load hits	165	65	74
Unload hits	95	36	37
Peak hit amplitude (dB)	95	64	74
Calm Ratio	0.58	0.55	0.50

Max.Historic Index	3.9	1.98	3.2
Max.Severity	800	169	960

Figure 4.2.17 shows the peak amplitudes correlated with time and CMOD for load case Static 2. Static loading causes the CMOD to open 0.00325 inches. The superimposed ambient or live load in the other lane causes the CMOD fluctuation of 5.5×10^{-4} inches. When the ambient and static trucks are removed, notice that the CMOD does not close back up to the starting value of 0.0261 inches. This is an indication of either irreversible load or temperature effects. Also note the two large AE bursts centered around 325 seconds on the time scale. These occurred under full static load with a small fluctuating load from the opposite travel lane loading with ambient traffic. Peak amplitudes reached 95 dB. Figure 4.2.18 shows the cumulative AE hits with time and CMOD. Static loading accounted for 304 hits, hold with superimposed ambient loading in the opposite lane for 15 minutes registered 320 hits and unloading yield 168 hits. Figures 4.2.19, 4.2.20 and 4.2.21 show the maximum Historic Index, Severity and Intensity plot for this load case. The burst of AE activity during the load hold portion is clearly evident and plots to the far upper right on the intensity plot indicating significant damage may have occurred.

This load case generated AE events that could be located spatially with the planar location algorithm supplied with the post processor, Visual AE. Four planar location sets were considered, the two arrays on the inside and outside face of the stem or web and then two arrays through the thickness of the stem. The outer stem face array which uses the 60 kHz sensors exclusively located five events as shown in Figure 4.2.22. The events appear in the vicinity of the shear crack under investigation. The southern most through thickness array, which uses a combination of 150 and 60 kHz sensors also located four events as shown in Figure 4.2.23.

4.2.5.3 Load Case Dynamic 1

Analog results

Crack mouth opening displacement ranges from test loading.

Cmod2 (US face top of girder): 3.4×10^{-4} inches
Cmod3 (US face middle of girder): 4.4×10^{-4} inches
Cmod4 (US face bottom of girder): 6.0×10^{-4} inches
Cmod1 (DS face middle of girder): 5.0×10^{-4} inches

AE results

Results	**60 kHz sensors (US face)**	**150 kHz sensors (DS face)**	**High fidelity sensors (DS face)**
Load hits	1	0	0
Unload hits	5	6	5
Peak hit amplitude (dB)	42.6	51.1	47.9
Calm Ratio	N/A	N/A	N/A

Max. Historic Index	N/A	N/A	N/A
Max. Severity	N/A	N/A	N/A

Running the test trucks in the opposite lane (Northbound) produced a very small response to the girder section under study. The CMOD had a peak amplitude of 0.0006 inches with very little AE activity as shown in Figure 4.2.24. The cumulative AE hits only amounted to 17 hits on the 13 sensors considered as shown in Figure 4.2.25. Considering the much higher sensitivity to AE in concrete of the 60 kHz sensors, it appears that most of the AE activity occurred within close proximity of the DS girder face since peak amplitudes were larger on the 150 kHz array. Damage parameters could not be properly calculated with such little data. As discussed in Chapter 3 a minimum of 200 hits is needed to provide reliable results for the Calm ratio, Severity and Historic Index.

4.2.5.4 Load Case Dynamic 2

Analog results

Crack mouth opening displacement ranges from test loading.

Cmod2 (US face top of girder): $8.2\text{x}10^{-4}$ inches
Cmod3 (US face middle of girder): $21.5\text{x}10^{-4}$ inches
Cmod4 (US face bottom of girder): $16.0\text{x}10^{-4}$ inches
Cmod1 (DS face middle of girder): $6.9\text{x}10^{-4}$ inches

AE results

Results	**60 kHz sensors (US face)**	**150 kHz sensors (DS face)**	**High fidelity sensors (DS face)**
Load hits	29	6	1
Unload hits	42	70	14
Peak hit amplitude (dB)	88	61.3	66.1
Calm Ratio	N/A	N/A	N/A
Max. Historic Index	2.5	1.22	1.67
Max. Severity	108	72	150

Running the test trucks in the lane (Southbound) which the girder under study bares more support for produced a significant response in both AE and CMOD. The peak to peak change in CMOD was 0.00215 inches, which was the largest excursion recorded during the controlled loading portion of the testing. Figure 4.2.26 shows that the CMOD opens 0.0012 inches as the trucks centers span 2 approaching from the North and then closes 0.0009 inches as the trucks center span 4. As the trucks pass over the cracked section, the CMOD rapidly opens up and then closes again as they leave span 2, returning to the starting CMOD. Nearly all of the AE activity occurs when the CMOD is going from the closed to open positions as the trucks are on the span 2. Figure 4.2.27 shows that a total of 250 AE hits were recorded with peak amplitudes near 88 dB.

Calculation of the calm ratio was not considered to be reliable due to the lack of AE activity. There was barely enough activity to calculate the Historic Index and Severity and the reliability of it us suspect. Nonetheless since these parameters are new to this application the results are shown in Figures 4.2.28 through 4.2.30. This load case produced strong enough AE activity to provide event locations in the 60 kHz array as shown in Figure 4.2.31 with two events calculated.

4.2.5.5 Load Case Dynamic 3

Analog results

Crack mouth opening displacement ranges from test loading.

Cmod2 (US face top of girder): 7.1×10^{-4} inches

Cmod3 (US face middle of girder): 18.1×10^{-4} inches

Cmod4 (US face bottom of girder): 14.2×10^{-4} inches

Cmod1 (DS face middle of girder): 7.3×10^{-4} inches

AE results

Results	**60 kHz sensors (US face)**	**150 kHz sensors (DS face)**	**High fidelity sensors (DS face)**
Load hits	20	9	3
Unload hits	15	17	4
Peak hit amplitude (dB)	62	54.3	54.7

Calm Ratio	N/A	N/A	N/A
Max. Historic Index	N/A	N/A	N/A
Max. Severity	N/A	N/A	N/A

This load case was very similar to the previous one but with slightly less load on the exterior girder because the trucks were centered in the lane as opposed to being over the fog line. Consequently the responses look very similar but lower in magnitude. The CMOD has a peak to peak amplitude of 0.0018 inches and peak AE amplitude of 62 dB as shown in Figure 4.2.32. Figure 4.2.33 shows the total AE hits to be nearly one half that of Dynamic 2 , with 115 hits recorded. Damage parameters were not calculated due to the low AE activity.

4.2.5.6 Ambient Service loads

Analog results

Crack mouth opening displacement ranges from test loading.

Cmod2 (US face top of girder): 9.1×10^{-4} inches
Cmod3 (US face middle of girder): 25.1×10^{-4} inches
Cmod4 (US face bottom of girder): 15.6×10^{-4} inches
Cmod1 (DS face middle of girder): 9.5×10^{-4} inches

AE results

Results	**60 kHz sensors (US face)**	**150 kHz sensors (DS face)**	**High fidelity sensors (DS face)**
Total hits	3115	1657	421
Peak hit amplitude (dB)	94	88.5	84
Max. Historic Index	3.28	2.78	1.93
Max. Severity	1550	225	1340

The response to ambient service loads in both lanes of traffic were measured and recorded for a period of 83 minutes. During this period approximately 50 heavy trucks crossed the bridge with two thirds of them heading Southbound over the instrumented girder section. Specific truck configurations and directions of travel were labeled into the data set to the extent practical. Figure 4.2.34 shows the peak AE hit amplitudes correlated with time and CMOD. The maximum peak to peak CMOD is 0.00251 inches which is very similar to the response from Dynamic 2 load case. These loads were applied at highway speeds as opposed to 10 m.p.h. during the controlled testing. Peak AE hit amplitudes reached 94 dB which correspond with the larger crack motions. The CMOD appears to gradually open up 0.0003 inches on CMOD1 over the course of the test run. This is thought to result from thermal effects as opposed to live load damage due to the gradual nature of the increase. Figure 4.2.35 shows that a total of 5200 AE hits were recorded during this period.

Calm ratios can only be calculated for individual load – unload sequences i.e. individual truck crossings. Identifying individual trucks based only on CMOD would be difficult for this particular data set and was not done. The Historic Index and Severity were calculated over the entire load set and are shown in Figures 4.2.36 and 4.2.37 respectively. Each sensors appears to respond to different trucks which shows the applicability of the zone intensity processing (ZIP) approach discussed in Chapter 3. Figure 4.2.38 shows the intensity plot for the ambient loads.

Many AE events were located from this data set as shown in Figures 4.2.39 and 4.2.40, most of which have moderately high peak amplitudes. Figure 4.2.39 shows the outer stem surface array location results with most of the higher amplitude events locating near the top and bottom of the diagonal shear crack under study. Figure 4.2.40 shows that these located events occurred predominately from the interior portion of the stem in the thickness direction.

The truck load that produced the largest CMOD during the ambient load sequence is shown in Figure 4.2.41 correlated with peak amplitudes and correlated with cumulative hits in Figure 4.2.42. The truck load that produced the largest amount of AE activity is shown correlated with peak amplitudes in Figure 4.2.43 and cumulative hits in Figure 4.2.44.

4.2.6 Discussion of Results

Because this particular bridge is located on a highway of low to moderate use, traffic could be stopped for short periods while static and dynamic load cases were be imposed. The static load cases allowed for clearly defined calculation of the Calm ratio for the loads that produced enough AE activity. The Calm ratio was found to be near 0.5 indicating a moderate level of accumulated damage.

Loading was correlated by measuring CMOD of the main diagonal tension crack that the sensors were covering. This proved to be adequate but lacks the sensitivity and ease of correlation that could be achieved using rebar strain. The CMOD approach is very convenient and easy to apply whereas attaching strain gages to rebar inside the beam requires more effort and skill.

The Historic Index and Severity provided interesting responses to the load cases that produced adequate AE activity and where found to have excellent sensitivity to potentially damaging events. More research will be needed to provide grading categories for the specific levels of response before damage grading can be quantitatively applied to the results. The test data, along with the laboratory test data and other field tests will provide a very good starting point for developing these criteria.

4.2.7 Conclusions

The load cases imposed during this field test including the controlled and ambient loads produced significant AE activity such that meaningful measurements of the load specific and accumulate damage were made. Even though specific damage levels have yet to be developed for the Intensity analysis, the other data including CMOD and number of AE hits and peak amplitudes give a clear indication that this bridge is structurally sound and not experiencing major damage as a result of the loads tested. These loads well represent the legal service loads this structure is required to carry.

Employing rebar strain as the primary physical parameter used to correlate load and AE responses is a very desirable approach and will be included on the remaining bridge tests.

The 60 kHz resonant type AE sensors proved to be much better suited to the lower levels of AE activity found during the testing of in-service bridges when compared to the 150 kHz sensors. The high fidelity sensors also showed much lower sensitivity but are useful for the capturing of transient wave forms which can be of interest for research into the nature of the emissions.

Table 4.2.1 AE sensor type and locations

Girder Face	**Ch#**	**Sensor type**	**Band-pass (kHz)**	**X (inch)**	**Y (inch)**	**Z (inch)**
Upstream	1	Resonant 60kHz	20-850	105.3	62.8	15
Upstream	2	Resonant 60kHz	40-850	131.3	62.0	15
Upstream	3	Resonant 60kHz	40-850	106.7	44.9	15
Upstream	4	Resonant 60kHz	40-850	130.8	42.9	15
Upstream	5	Resonant 60kHz	40-850	103.6	20.38	15
Upstream	6	Resonant 60kHz	40-850	131.6	22.7	15
Downstream	7	Resonant 150kHz	95-850	128.0	62.5	0
Downstream	8	Resonant 150kHz	95-850	108.0	62	0
Downstream	9	DECI S1000H	20-850	130.4	38.6	0
Downstream	10	DECI SE9125	20-850	106.3	38.6	0
Downstream	11	Resonant 150kHz	95-850	130.4	43.9	0
Downstream	12	Resonant 150kHz	95-850	107.3	40.9	0
Downstream	13	Resonant 150kHz	95-850	132	27.3	0
Downstream	14	Resonant 150kHz	95-850	102.6	21.7	0

Table 4.2.2 Summary of AE sensor calibrations using 0.5mm pencil breaks.

Position of pencil break	Peak Amplitudes	Number of other channels triggered	Location of Data in Primary (.PRI) File (Data set No.)
Channel 1	93.8, 93.8, 93.8 *	3	14877, 14897, 15075
Channel 2	93.8, 93.8, 93.8 *	7	15172, 15202, 15237
Channel 3	93.8, 93.8, 93.8 *	6	15355, 15397, 15418
Channel 4	93.8, 93.8, 93.8 *	7	15527, 15552, 15583
Channel 5	93.8, 93.8, 93.8 *	7	15897, 15946, 15972
Channel 6	93.8, 93.8, 93.8 *	7	16093, 16119, 16149
Channel 7	92.3, 94.9, 96.8	8	1387, 1486, 1523
Channel 8	82.9, 85.6, 80.2 **	7	6124, 6148, 6183
Channel 9 (SE-1000)	80.6, 81.7, 79.1	7	1946, 2175, 2397 ***
Channel 10 (SE-9125)	99.8, 99.8, 99.8*	9	3522, 3824,3907 ***
Channel 11	95.1, 97.9, 99.8	9	1947, 2176, 2396
Channel 12	96.4, 91.5, 91.9	11	3528, 3825, 3908
Channel 13	99.8, 99.6, 99.8 *	8	2590, 2660, 2735
Channel 14	87, 91.5, 83.6	9	5996, 6009, 6030 **

*saturation
** after adjustment
*** same breaks as channels 11, 12 respectively

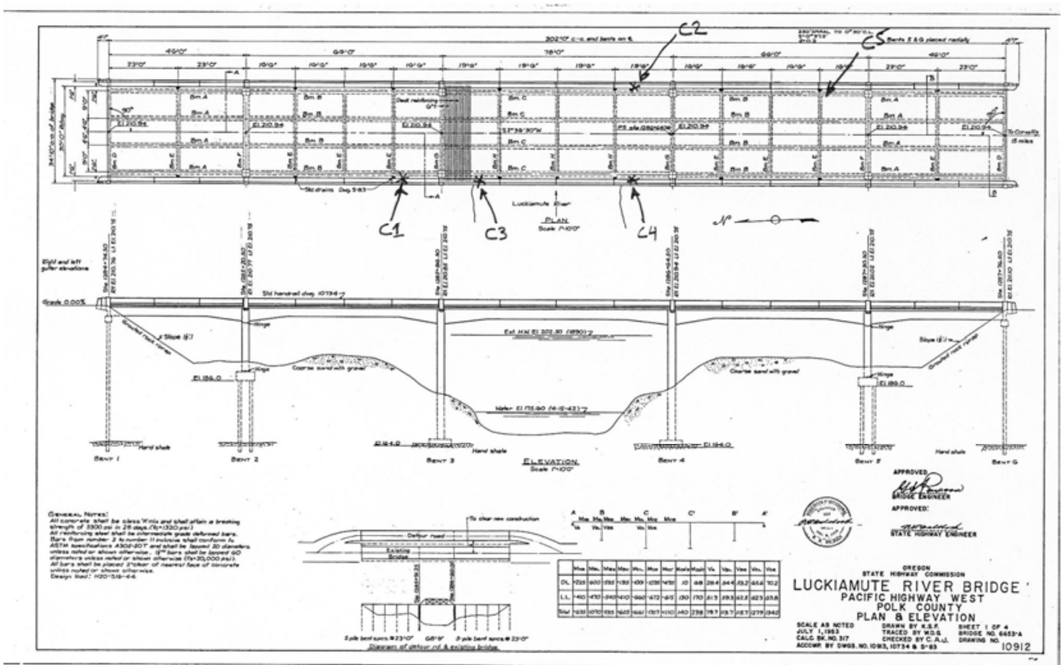

Figure 4.2.1 Plan and elevation drawing for Br. 06653A. Shear cracks C1 thru C5 that have long term crack width monitoring are shown superimposed.

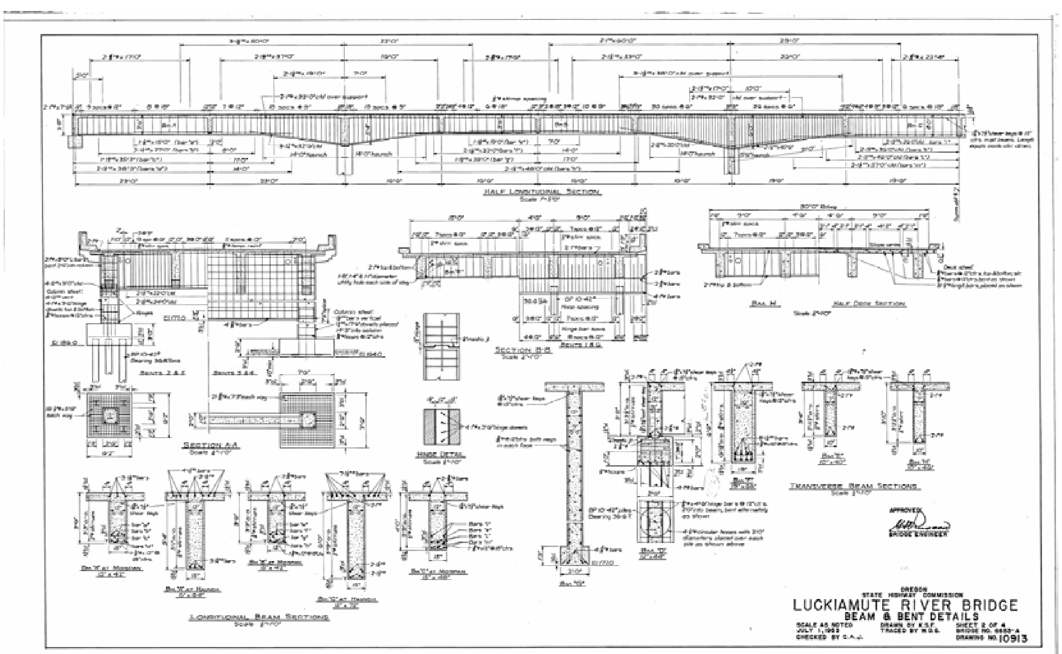

Figure 4.2.2 Beam and bent detail drawing for Br. 06653A.

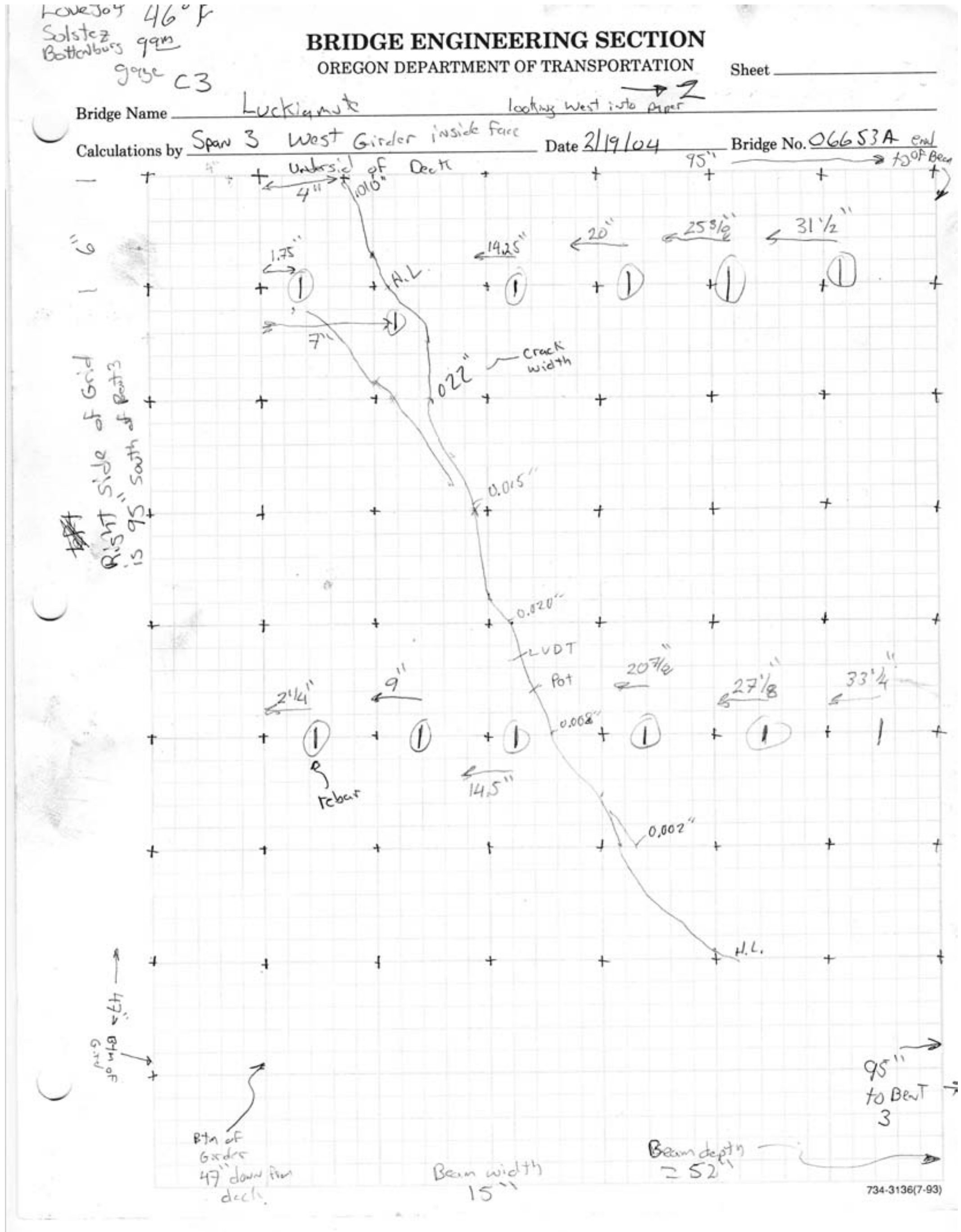

Figure 4.2.3 Crack map for crack C3.

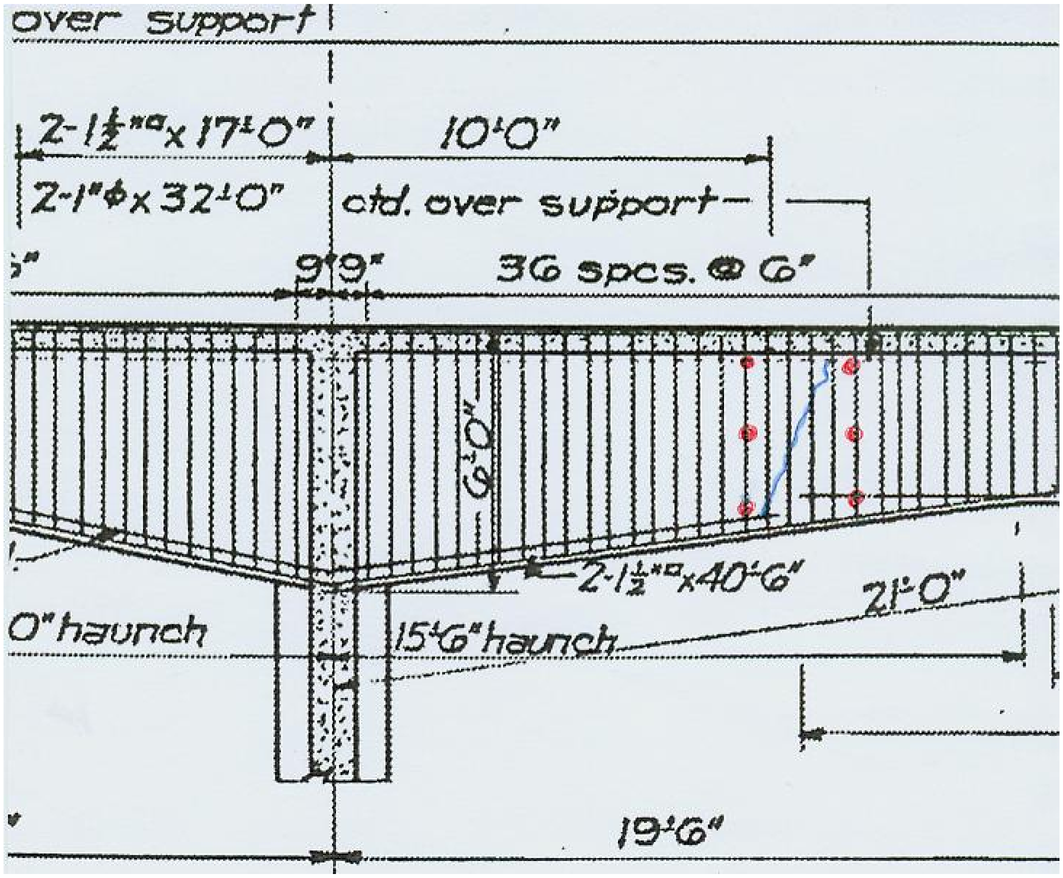

Figure 4.2.4 Enlarged view of longitudinal beam section of span 3 with crack C3 (blue line) and AE sensor locations (red dots) shown.

Figure 4.2.5 Instrumentation of outside or upstream face of girder at crack C3. AE sensors are numbered 1 thru 6 as shown with #1 at the top left , #2 top right , #3 middle left , #4 middle right , #5 bottom left and #6 bottom right. These are KRN 60 kHz resonant AE sensors.

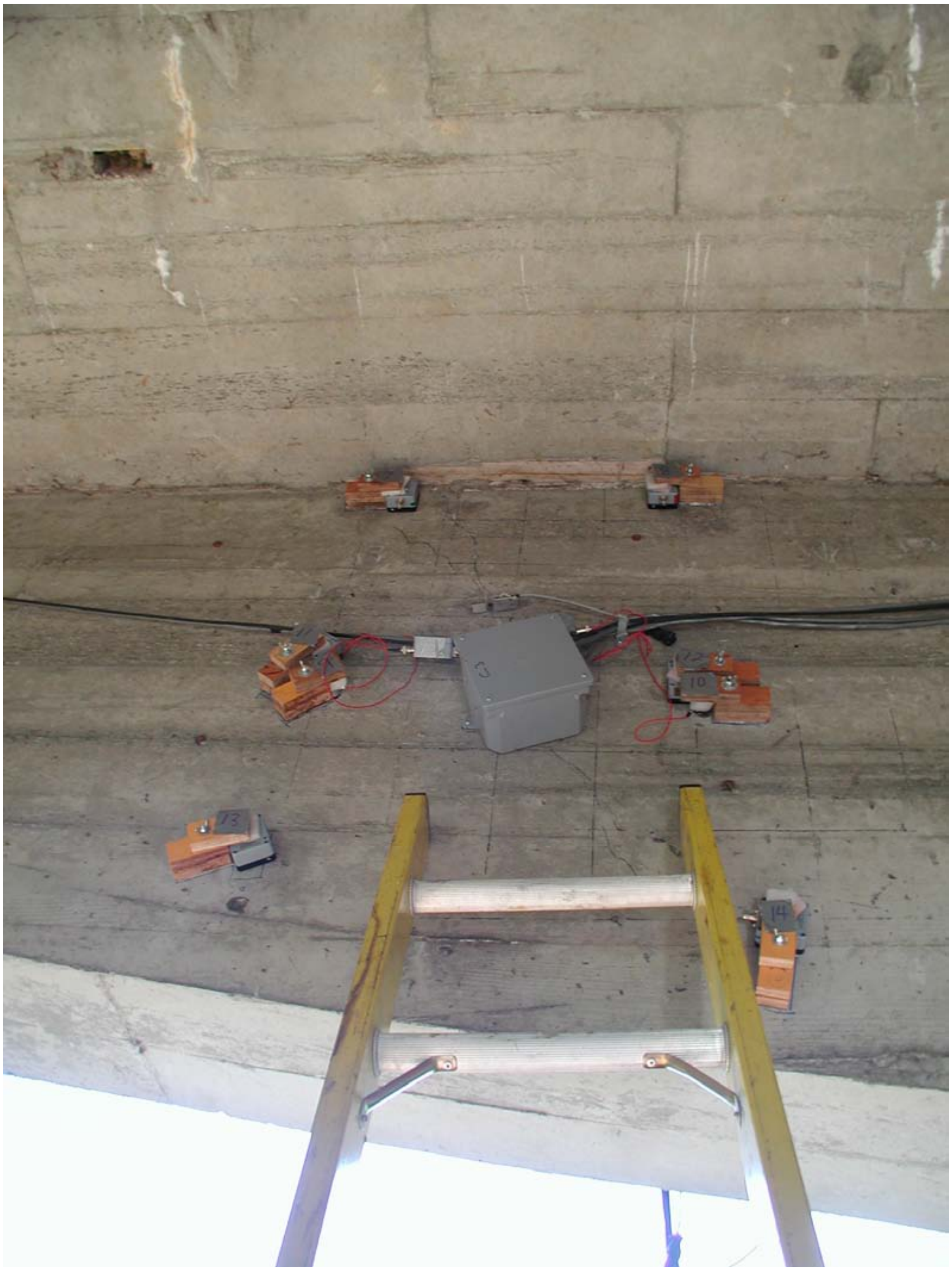

Figure 4.2.6 Instrumentation of inside or downstream face of girder at crack C3. AE sensors are numbered as follows: #7-top left , #8-top right , #11 upper-middle left , #12 upper middle right , #9 lower-middle left , #10 lower-middle right , #13 – lower left and #14 – lower right. The large gray box is part of the long term SHM system. The CMOD is measured just above this box.

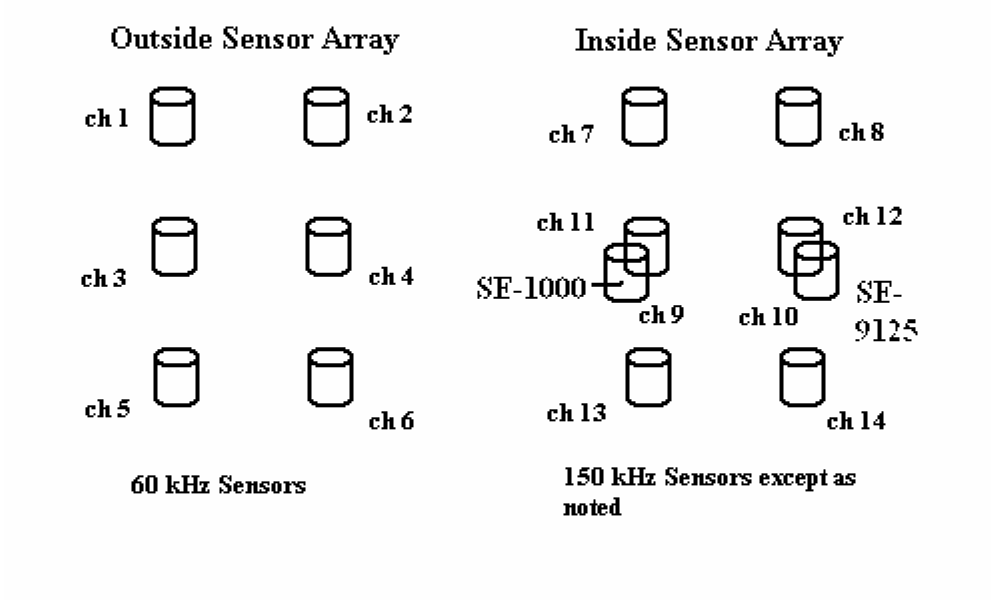

Figure 4.2.7 Schematic representation of sensor layout.

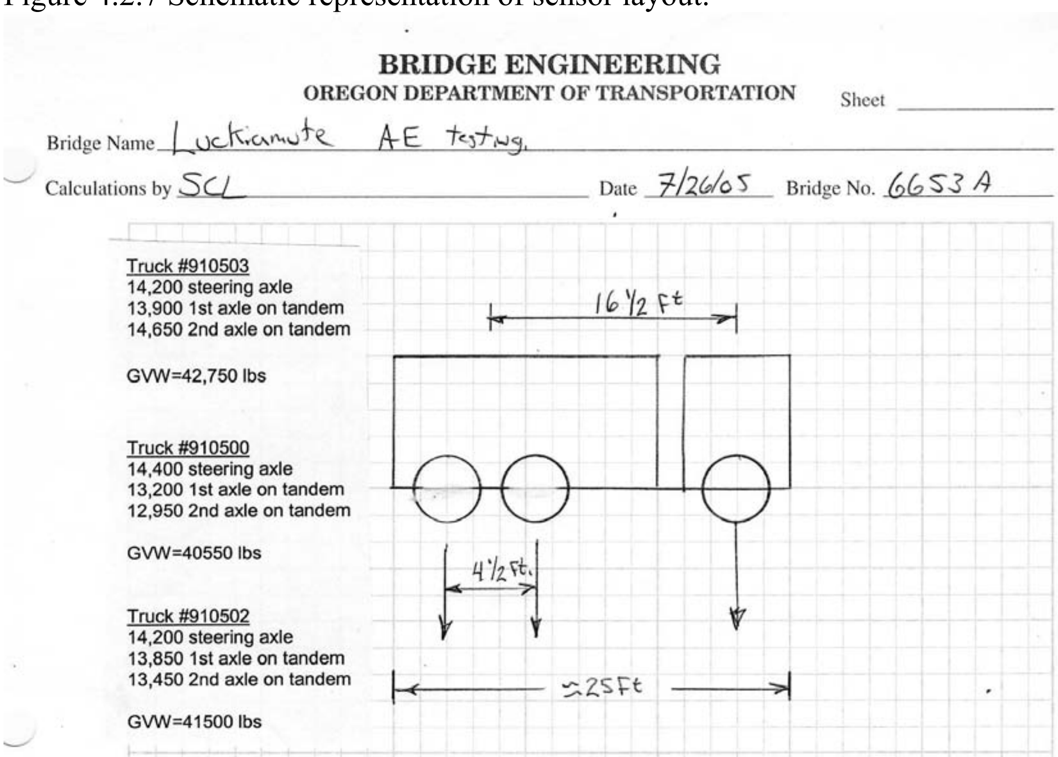

Figure 4.2.7 Configuration and axle weights of test trucks.

Figure 4.2.8 Static load case 1 Truck placement.

Figure 4.2.9 Typical 80,000 lbs GVW ambient service loads

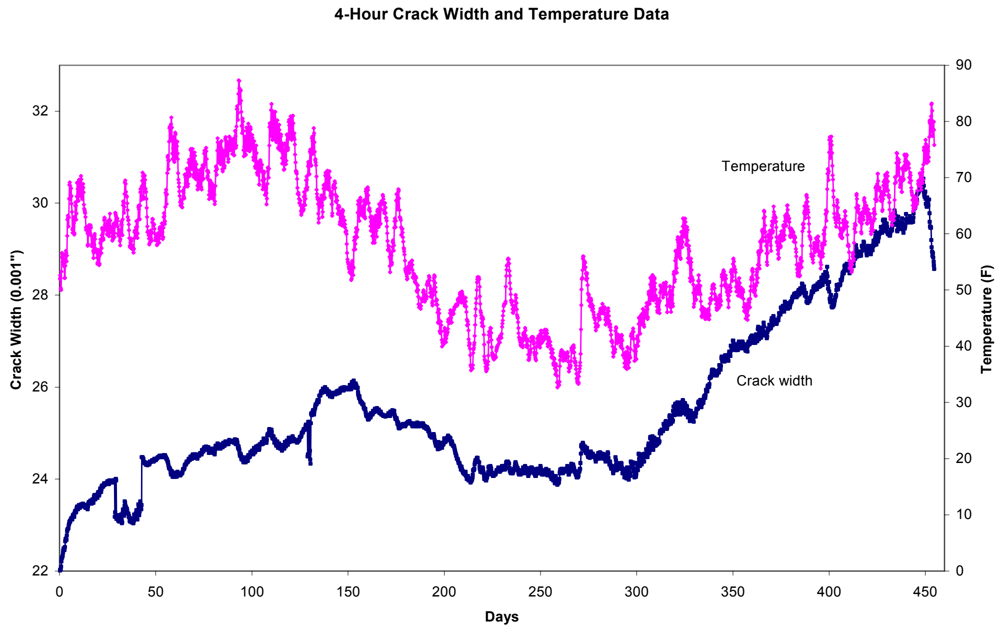

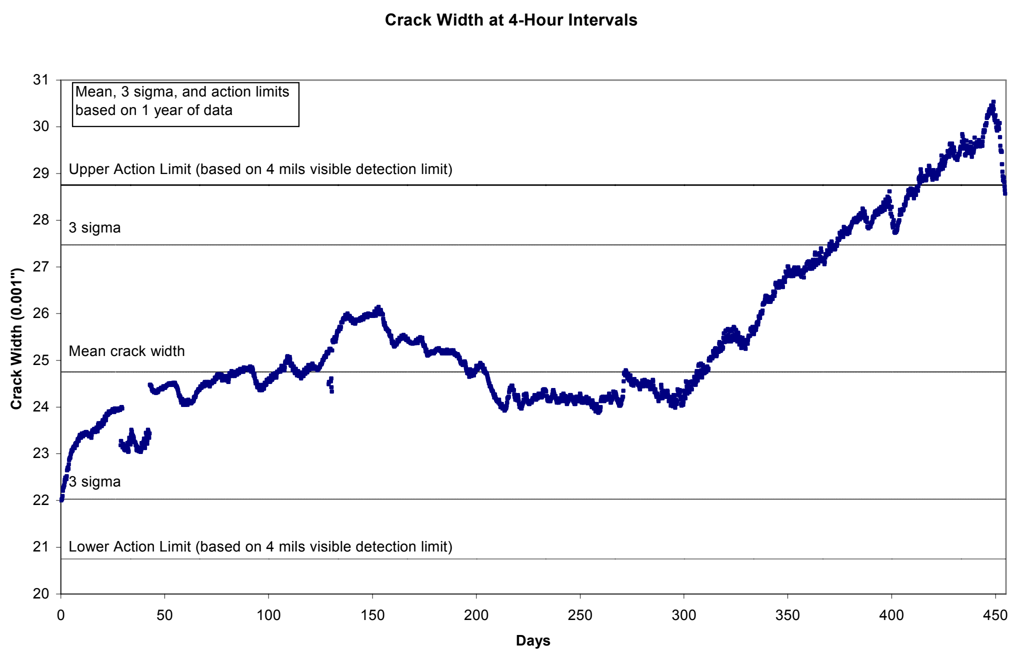

Figure 4.2.10 Long term crack width monitoring results from crack C3.

.

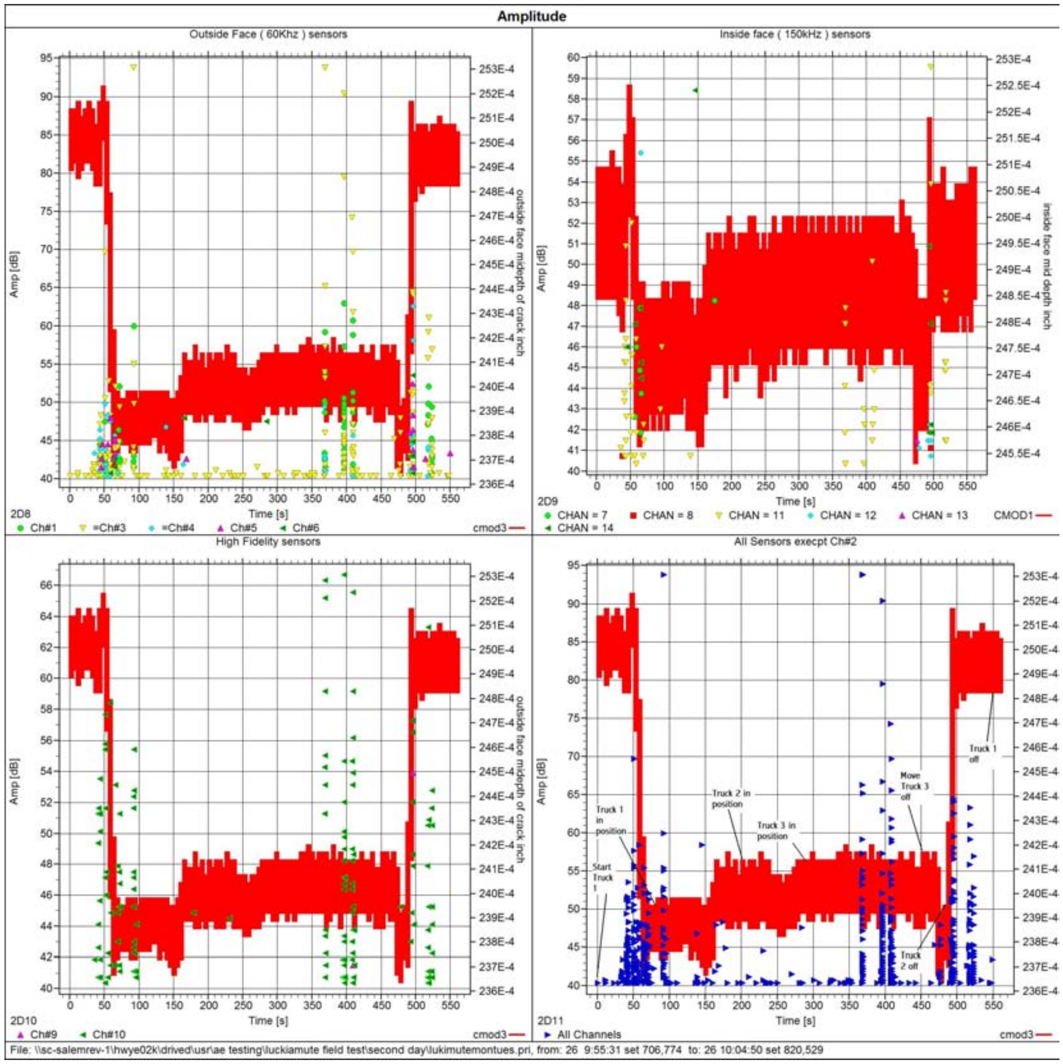

Figure 4.2.12 Load case Static 1 , peak amplitude and crack mouth opening displacement.

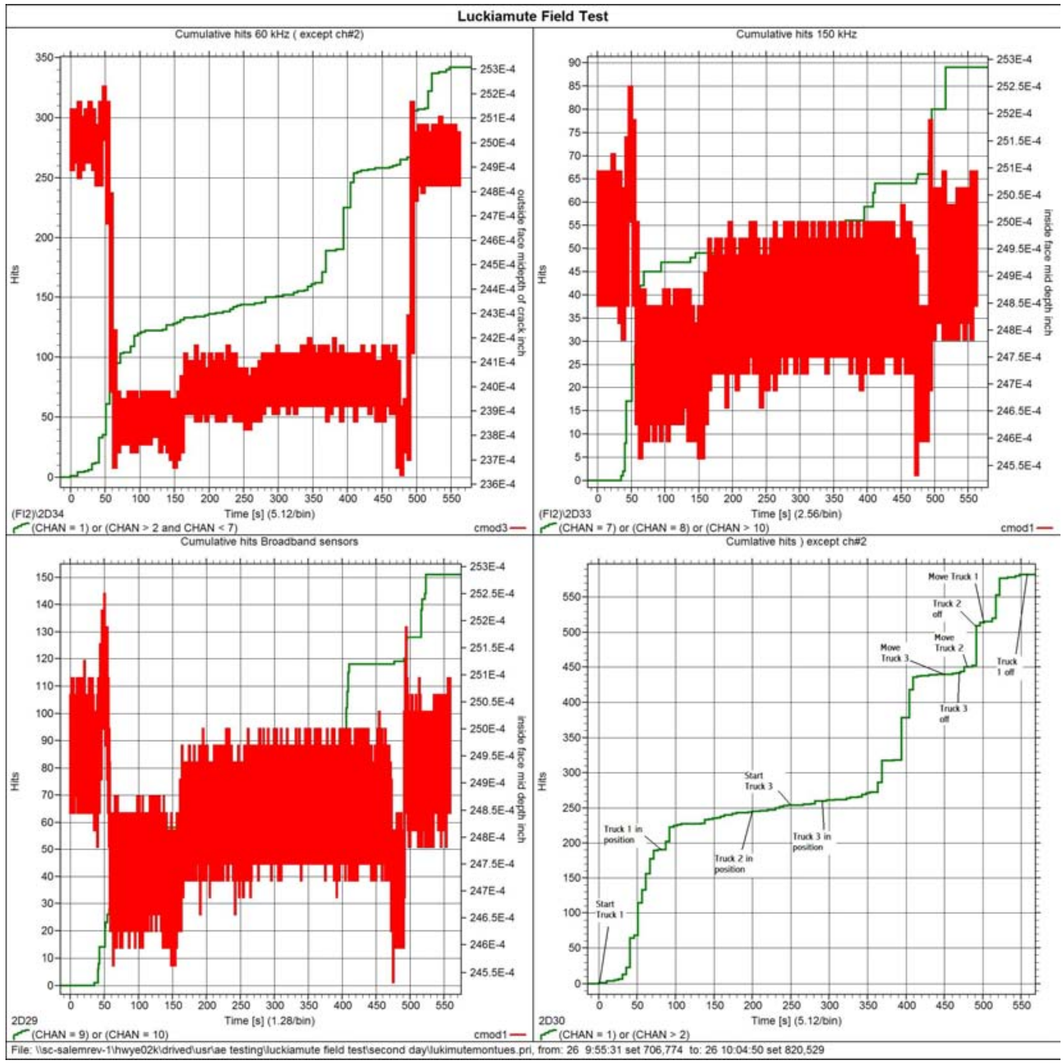

Figure 4.2.13 Load case Static 1 , cumulative AE hits and crack mouth opening displacement.

.

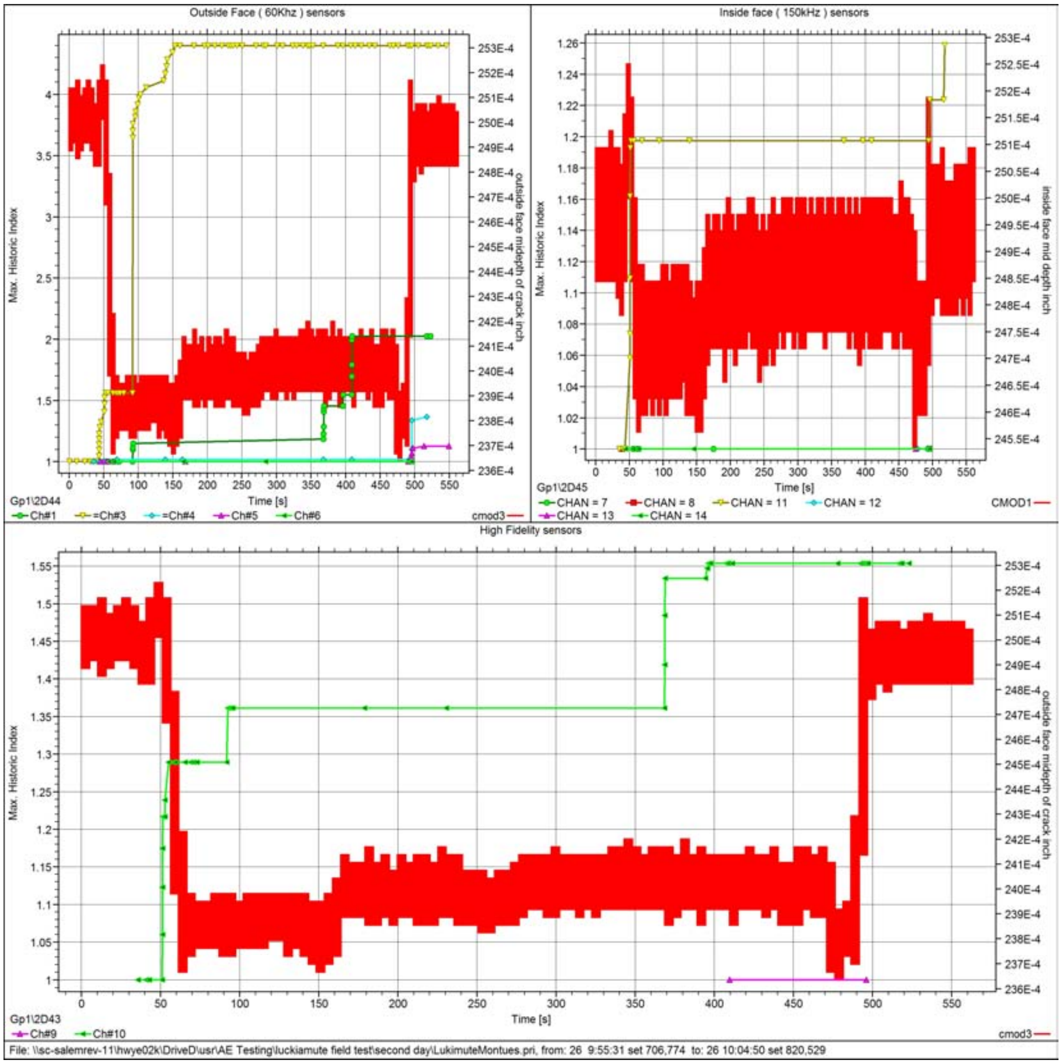

Figure 4.2.14 Load case Static 1 Historical Index.

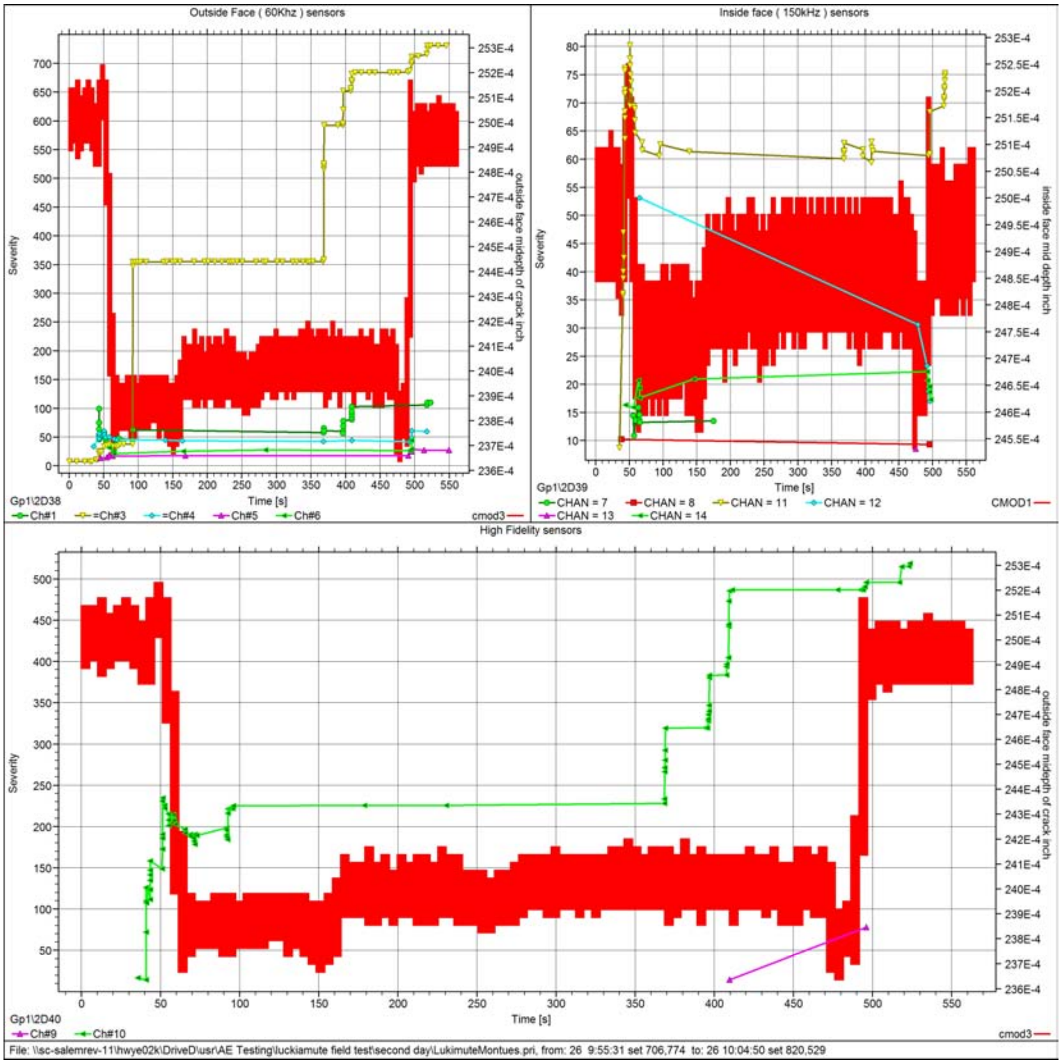

Figure 4.2.15 Load case Static 1 Severity.

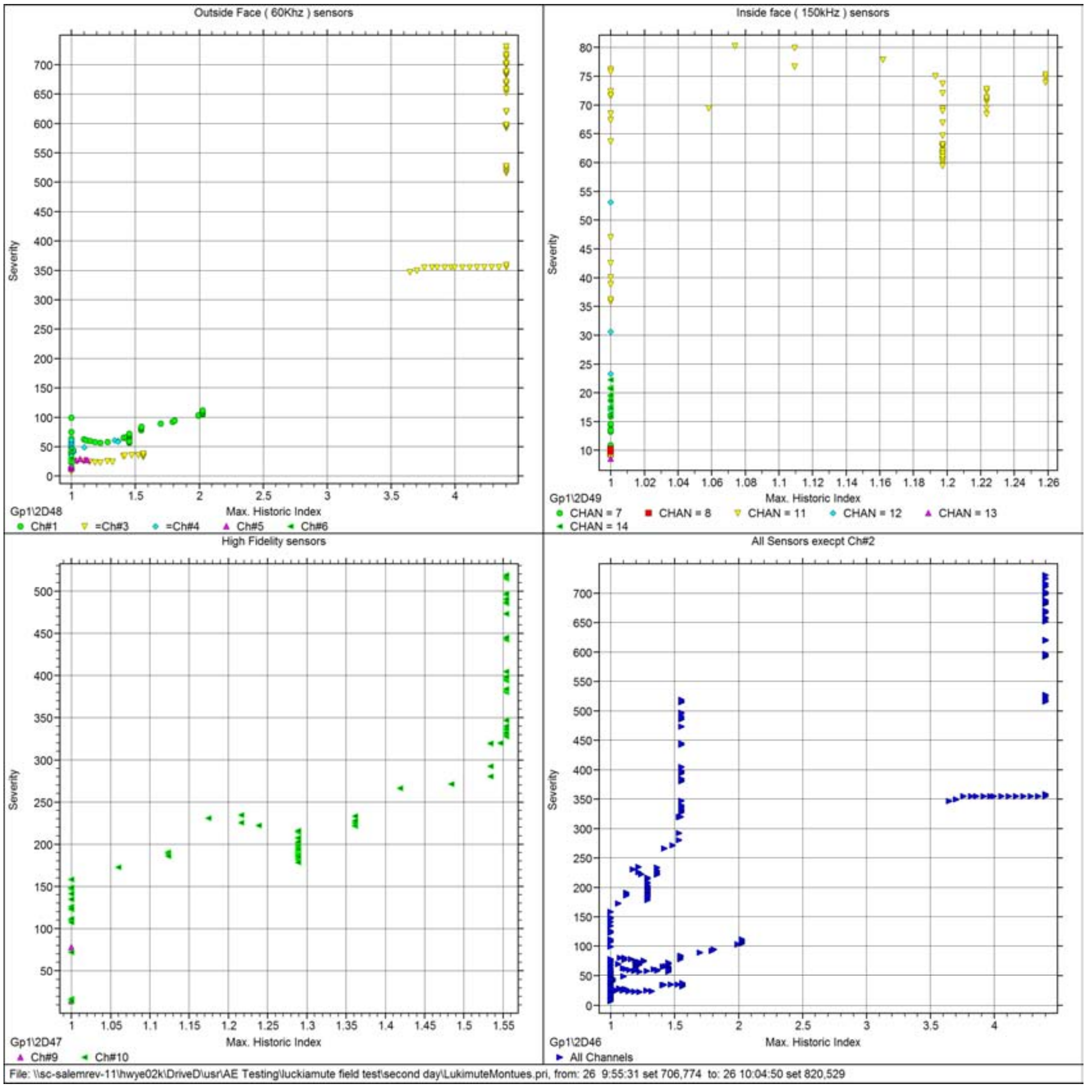

Figure 4.2.16 Load case Static 1 Intensity Plot.

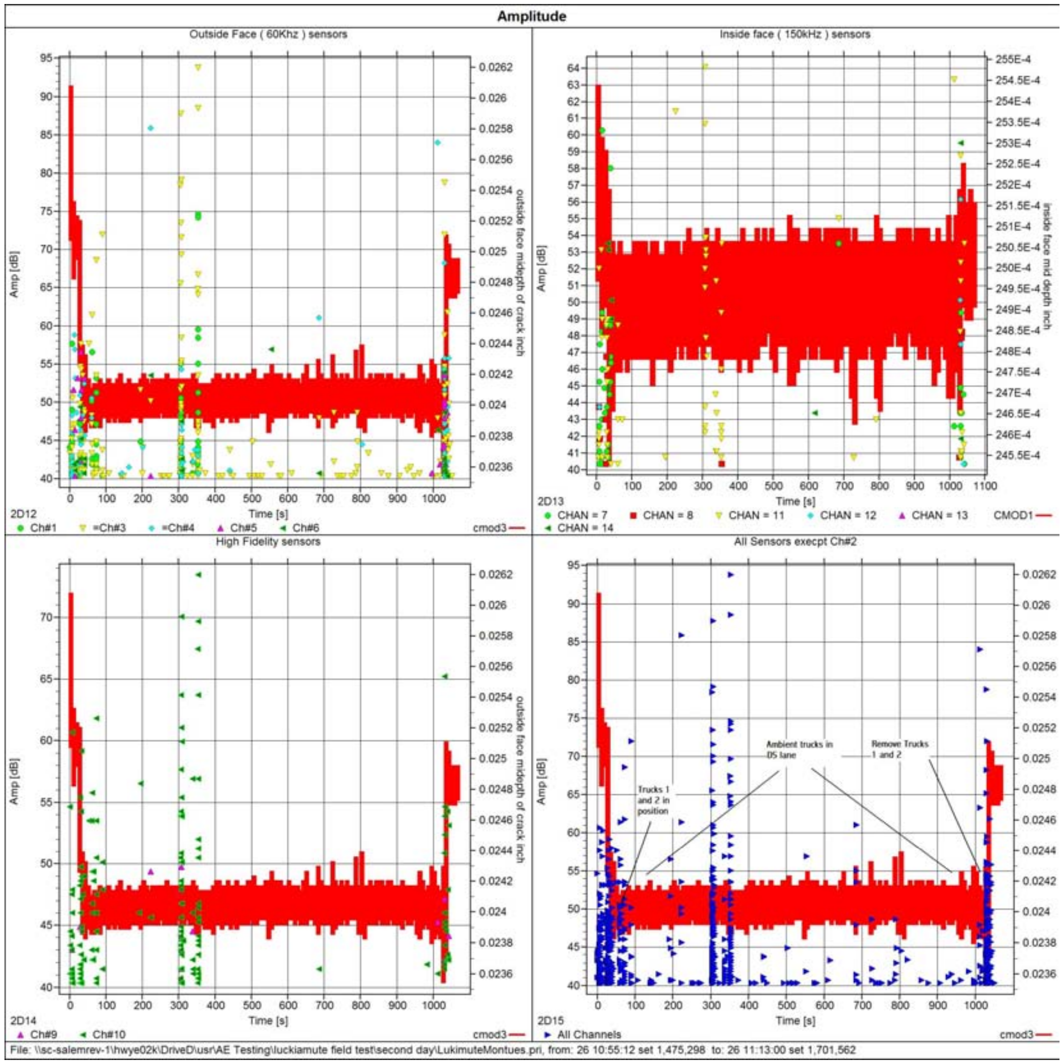

Figure 4.2.17 Load case Static 2 peak amplitudes and cmod3 motion. Note large amount of AE activity between 300 and 400 seconds. Also note that the crack gage does not return to its original value after the static load is removed.

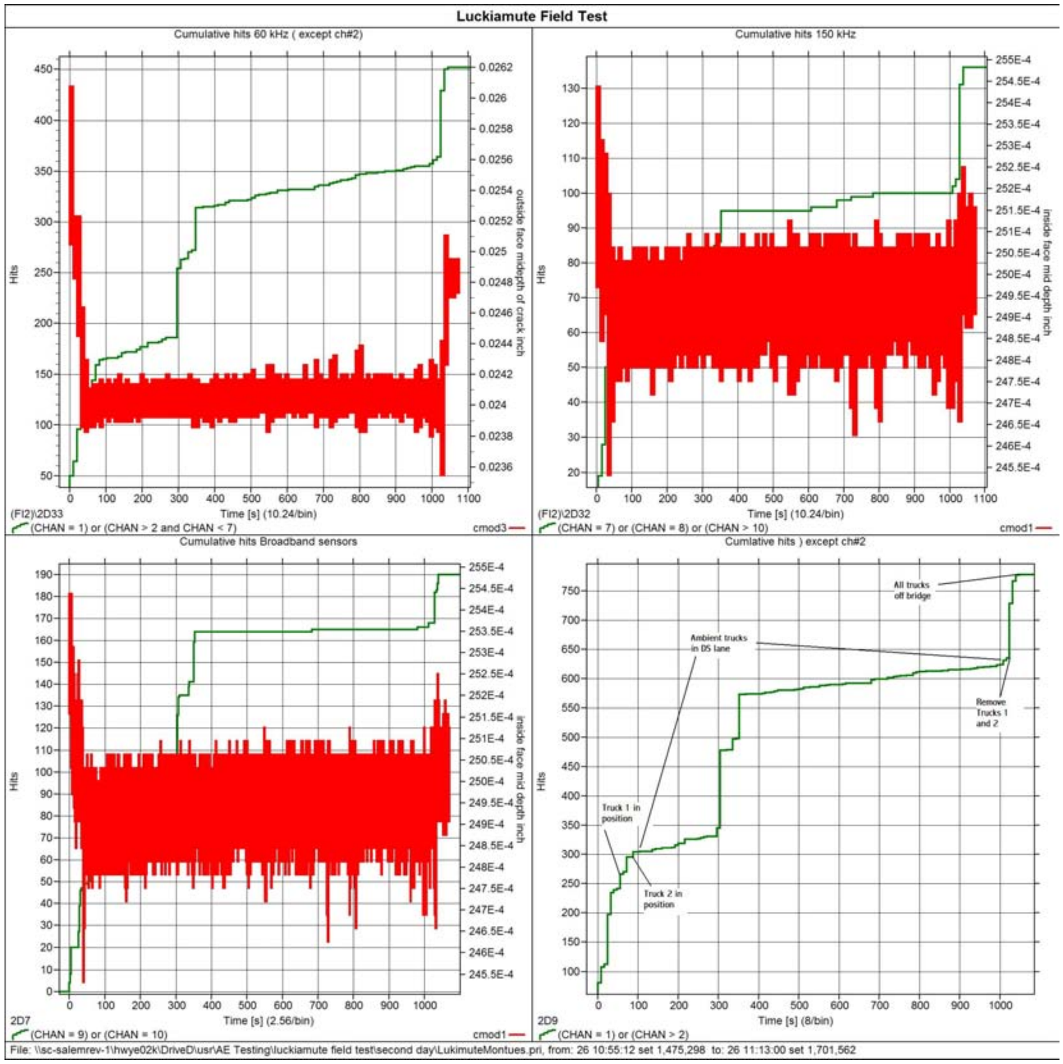

Figure 4.2.18 Load case Static 2 cumulative AE hits.

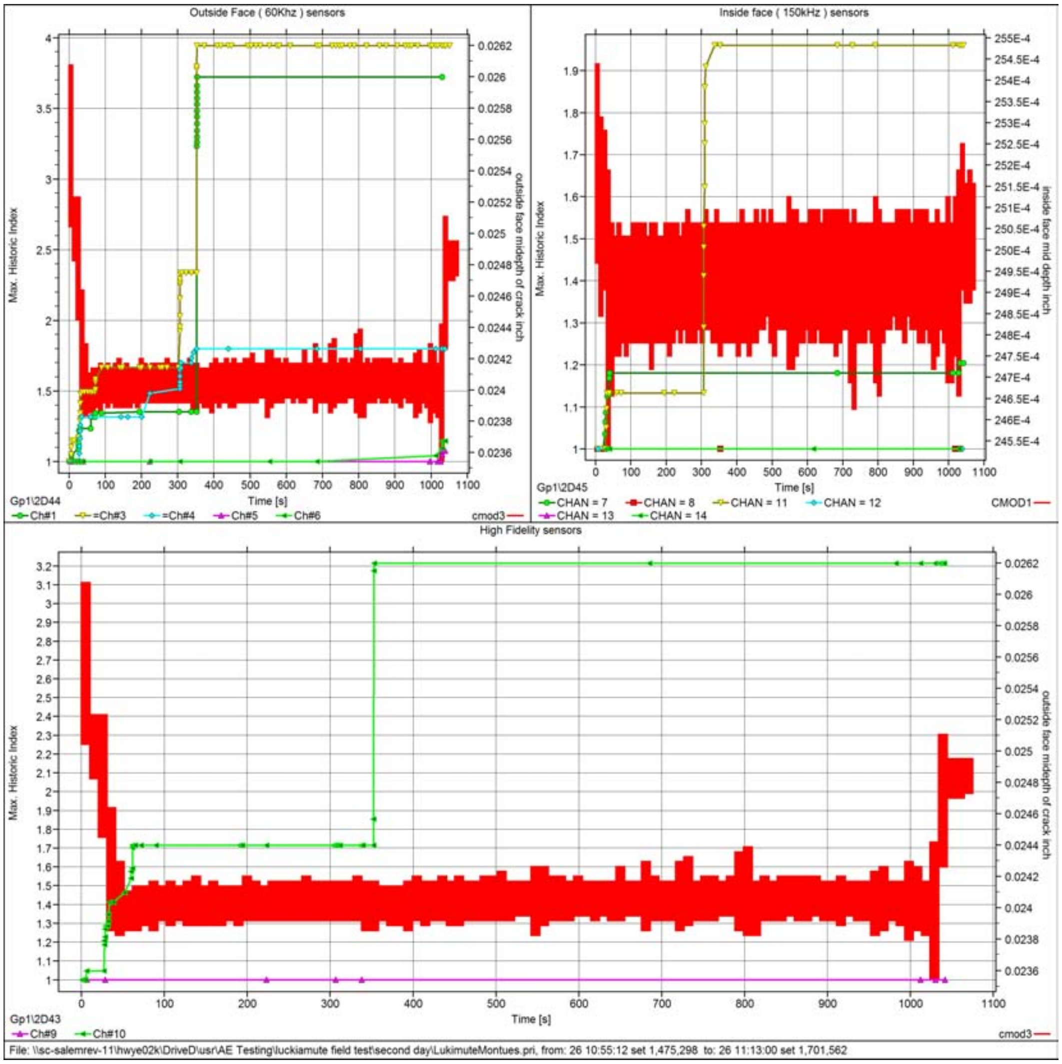

Figure 4.2.19 Load case Static 2 Historical Index.

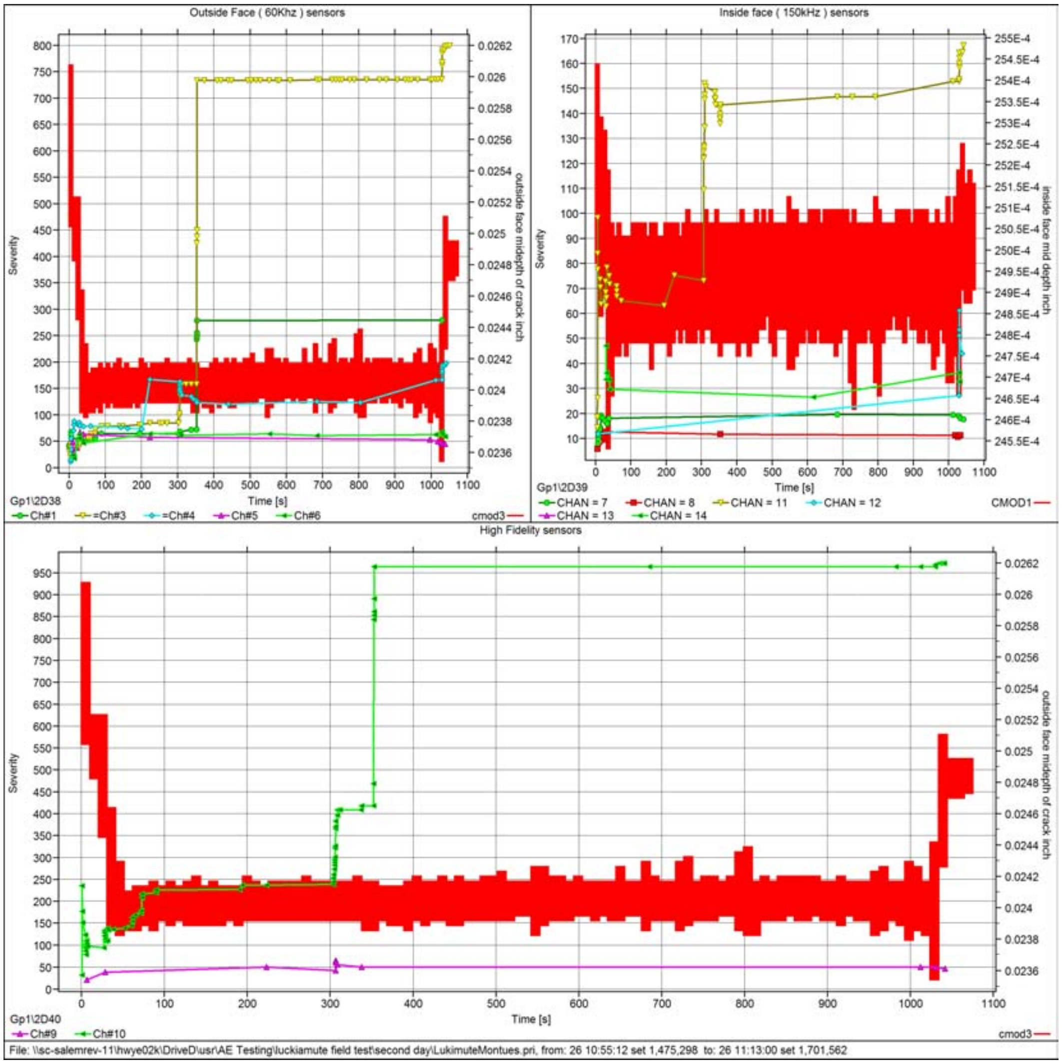

Figure 4.2.20 Load case Static 2 Severity.

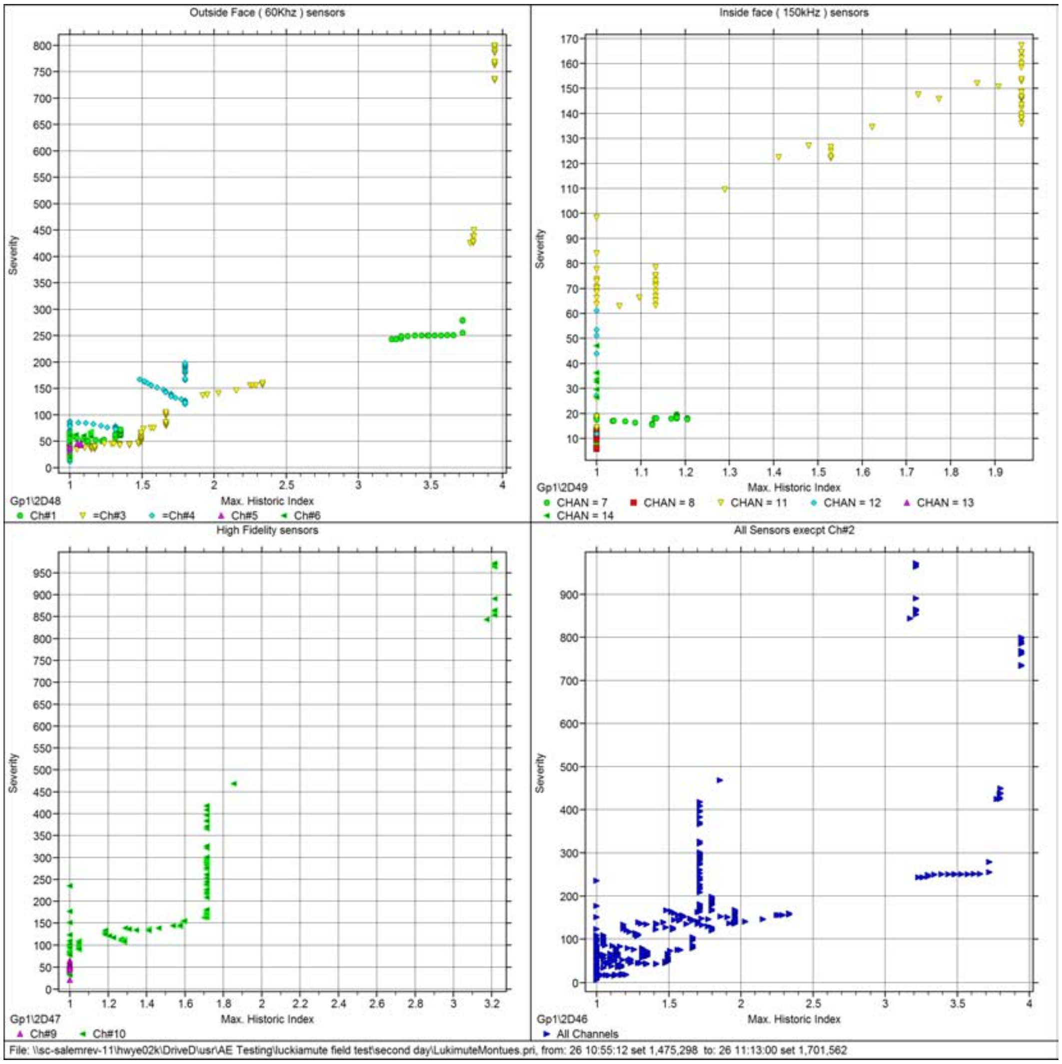

Figure 4.2.21 Load case Static 2 Intensity Plot.

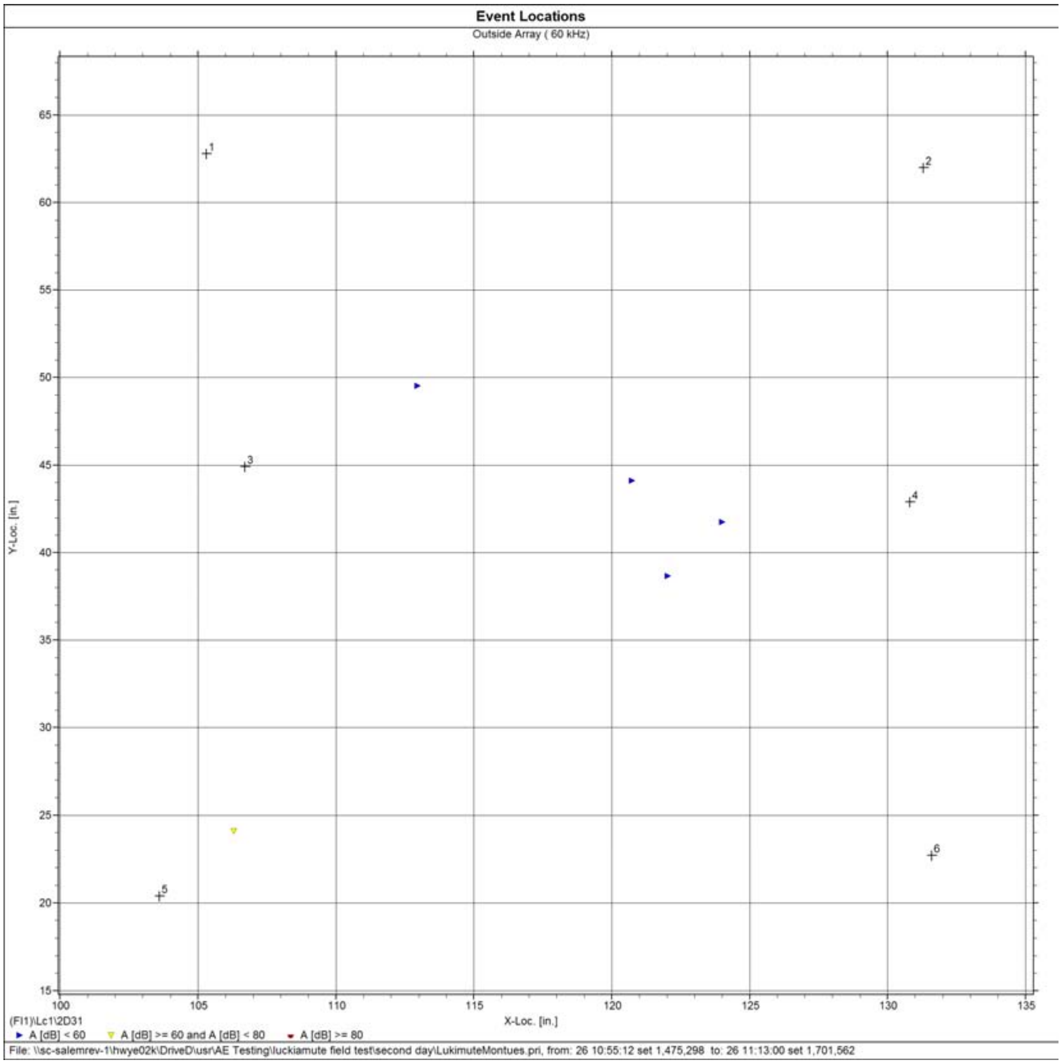

Figure 4.2.22 Load case Static 2 event locations from outside face planar array (60 kHz sensors) .

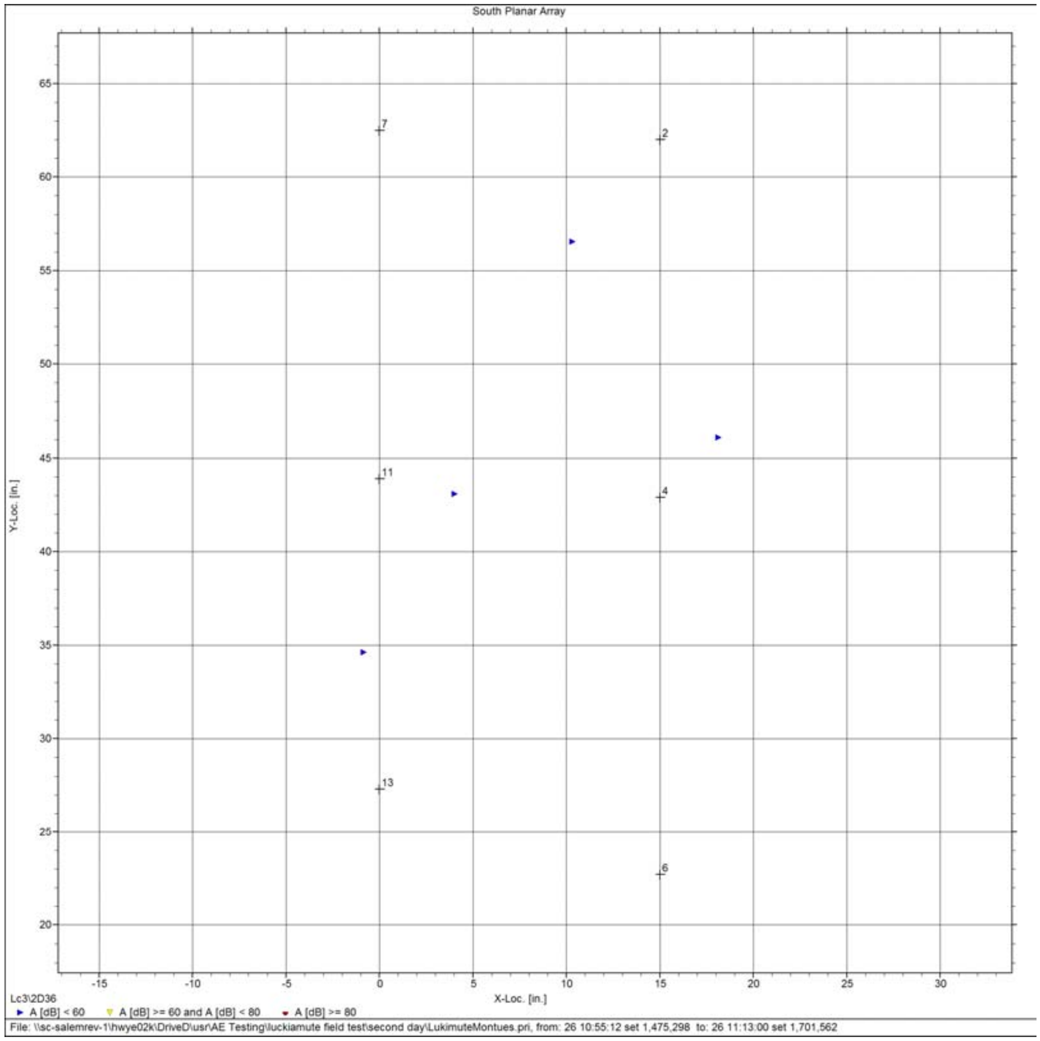

Figure 4.2.23 Load case Static 2 event locations from thru-thickness planar array

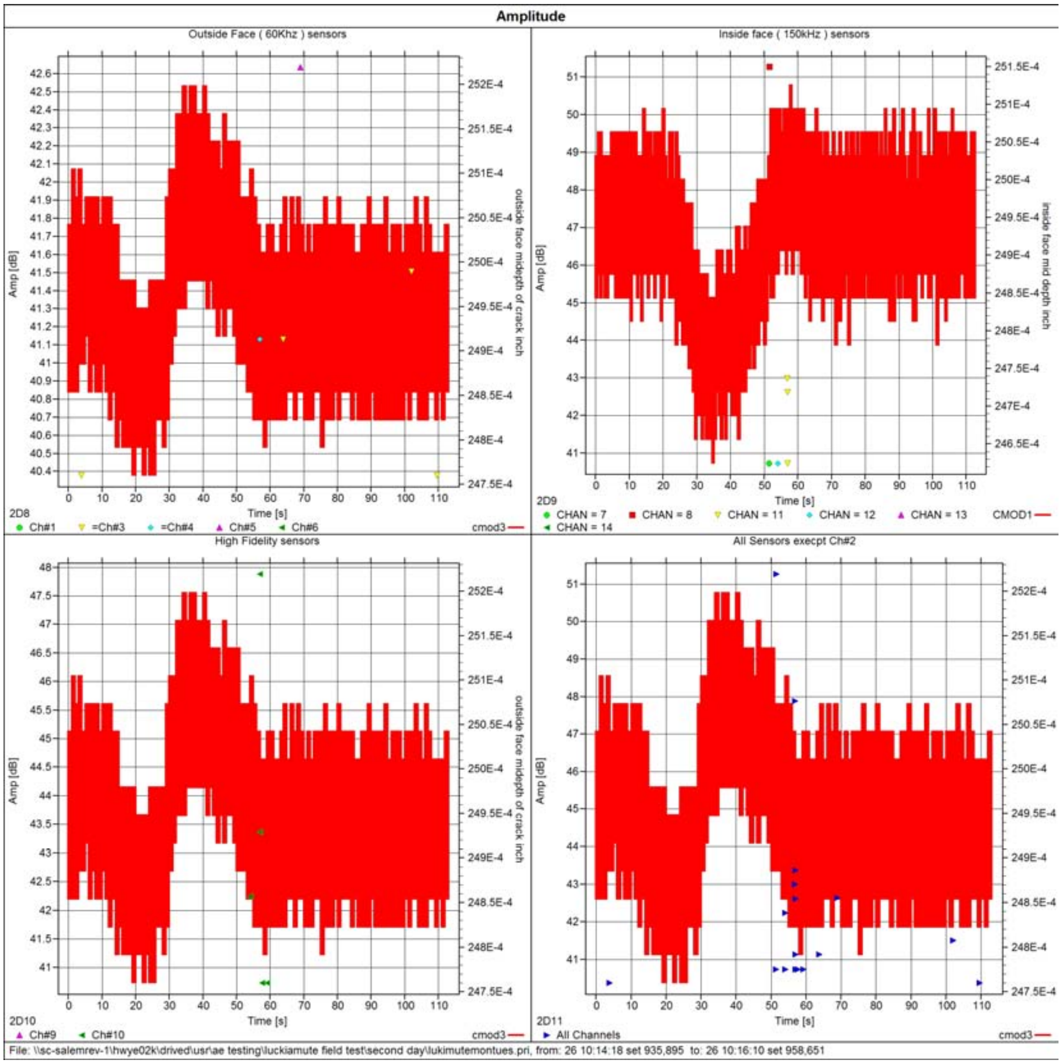

Figure 4.2.24 Load case Dynamic 1 peak amplitude and CMOD.

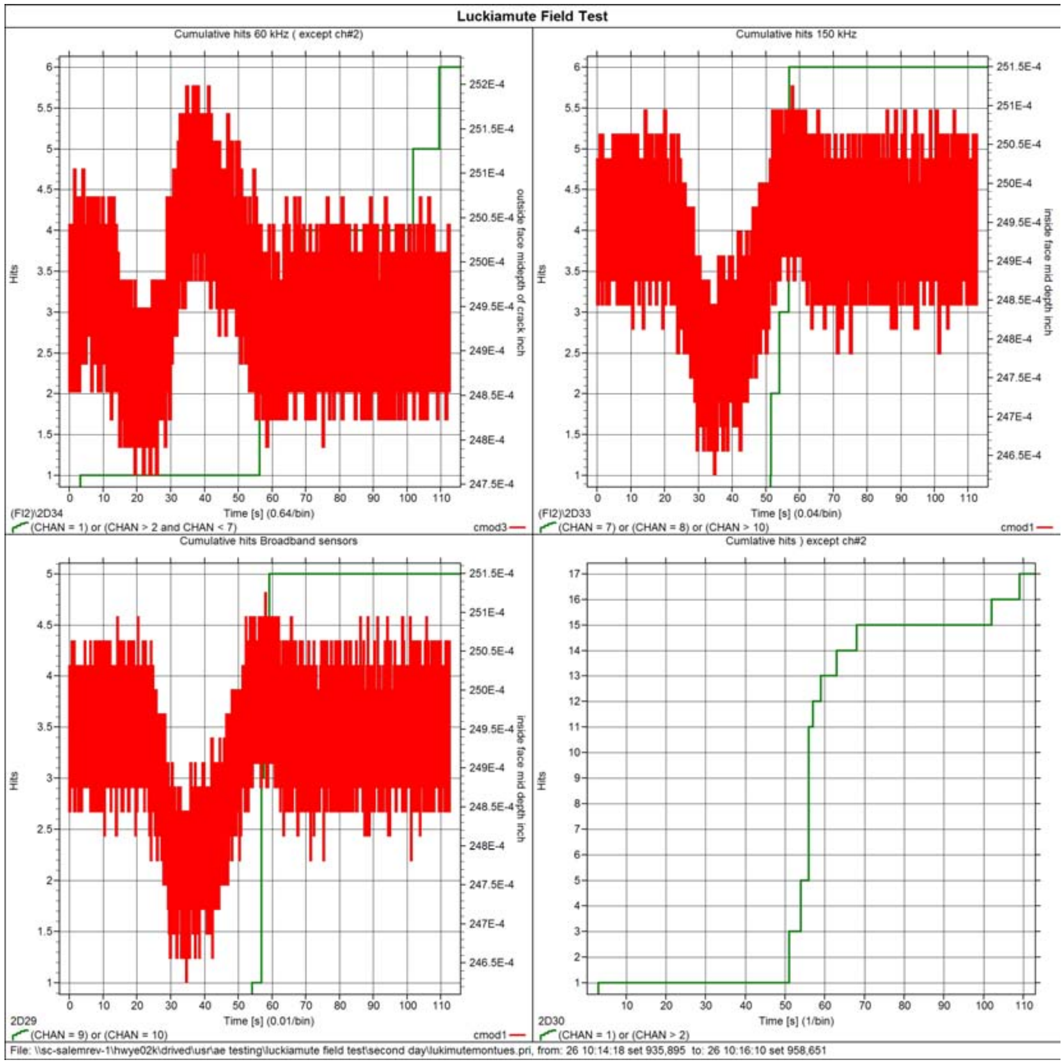

Figure 4.2.25 Load case Dynamic 1 cumulative hits and CMOD.

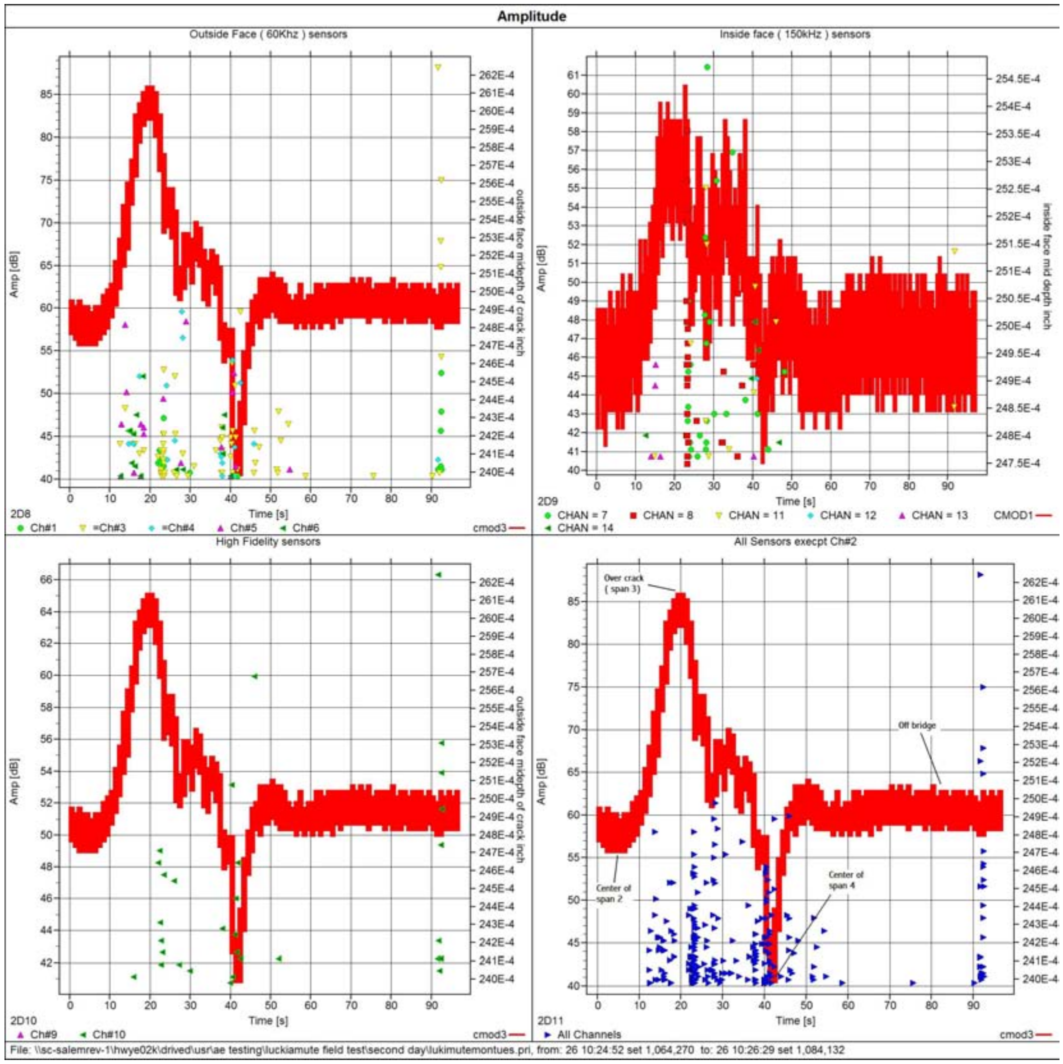

Figure 4.2.26 Load case Dynamic 2 peak amplitude and CMOD

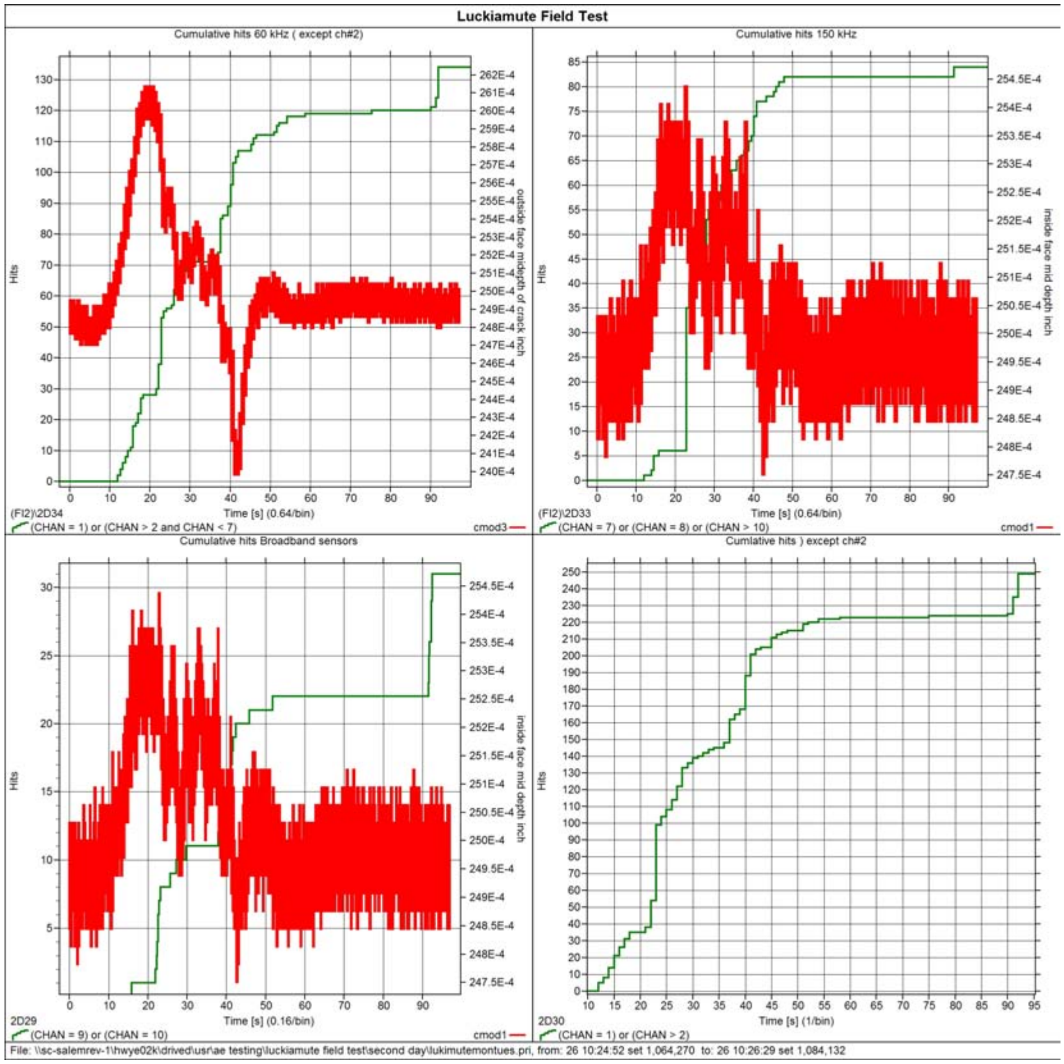

Figure 4.2.27 Load case Dynamic 2 cumulative hits and CMOD.

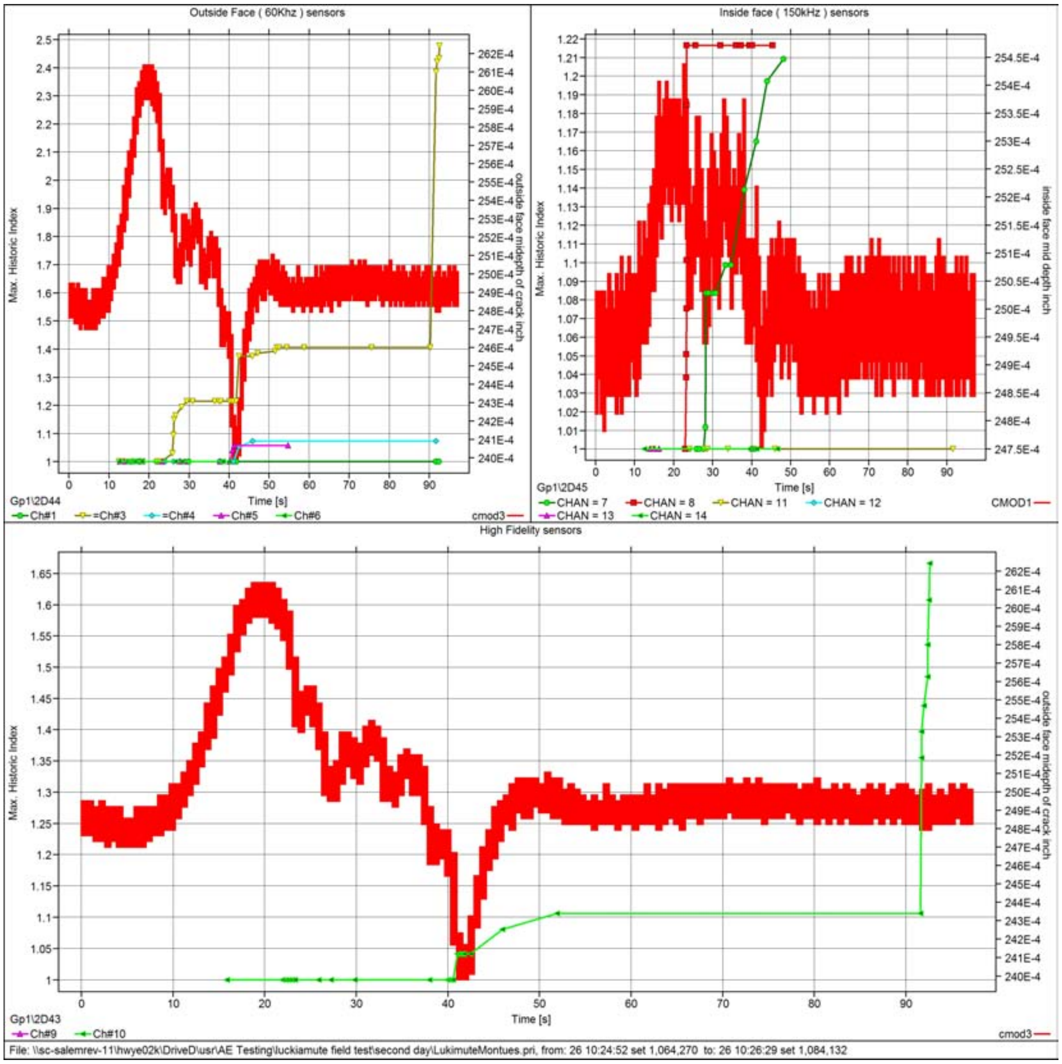

Figure 4.2.28 Load case Dynamic 2 Historical Index.

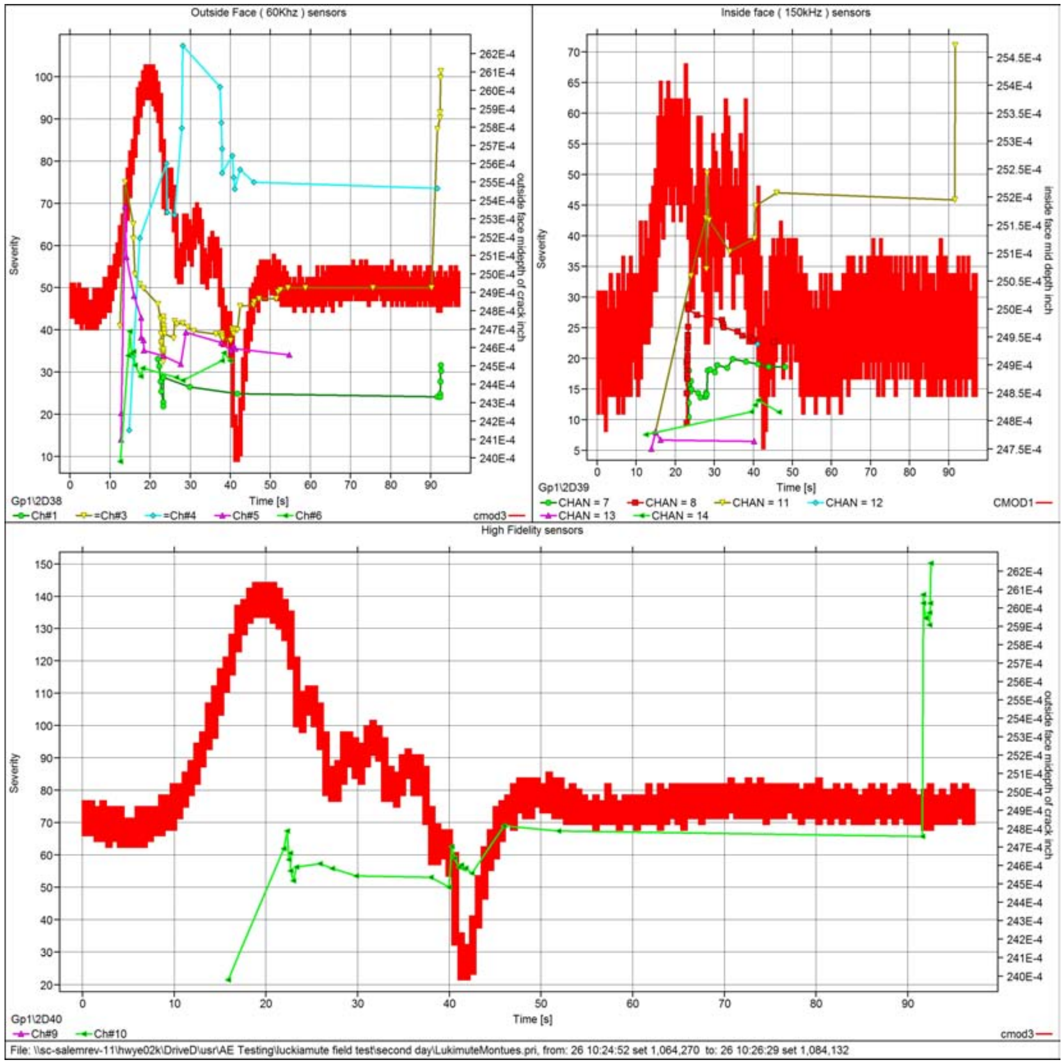

Figure 4.2.29 Load case Dynamic 2 Severity.

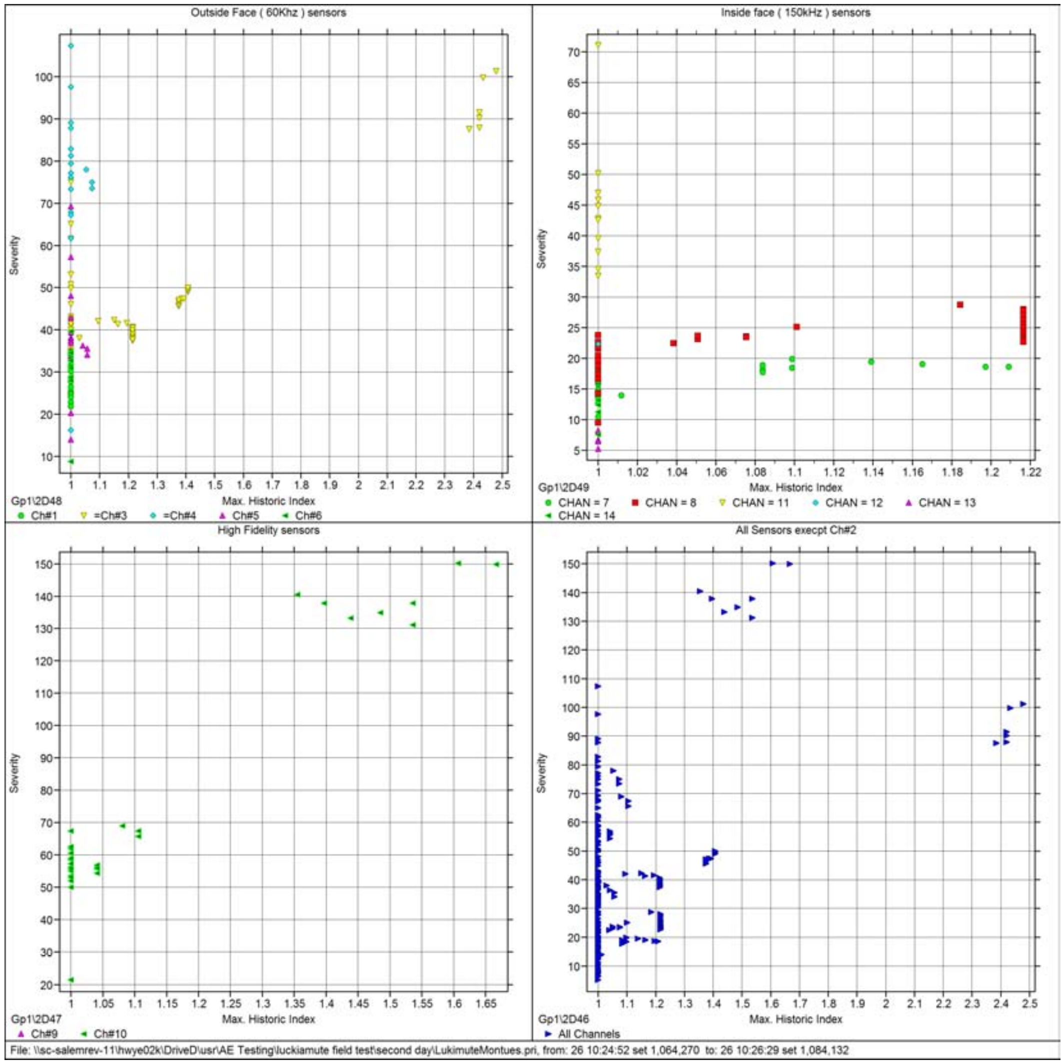

Figure 4.2.30 Load case Dynamic 2 Intensity Plot.

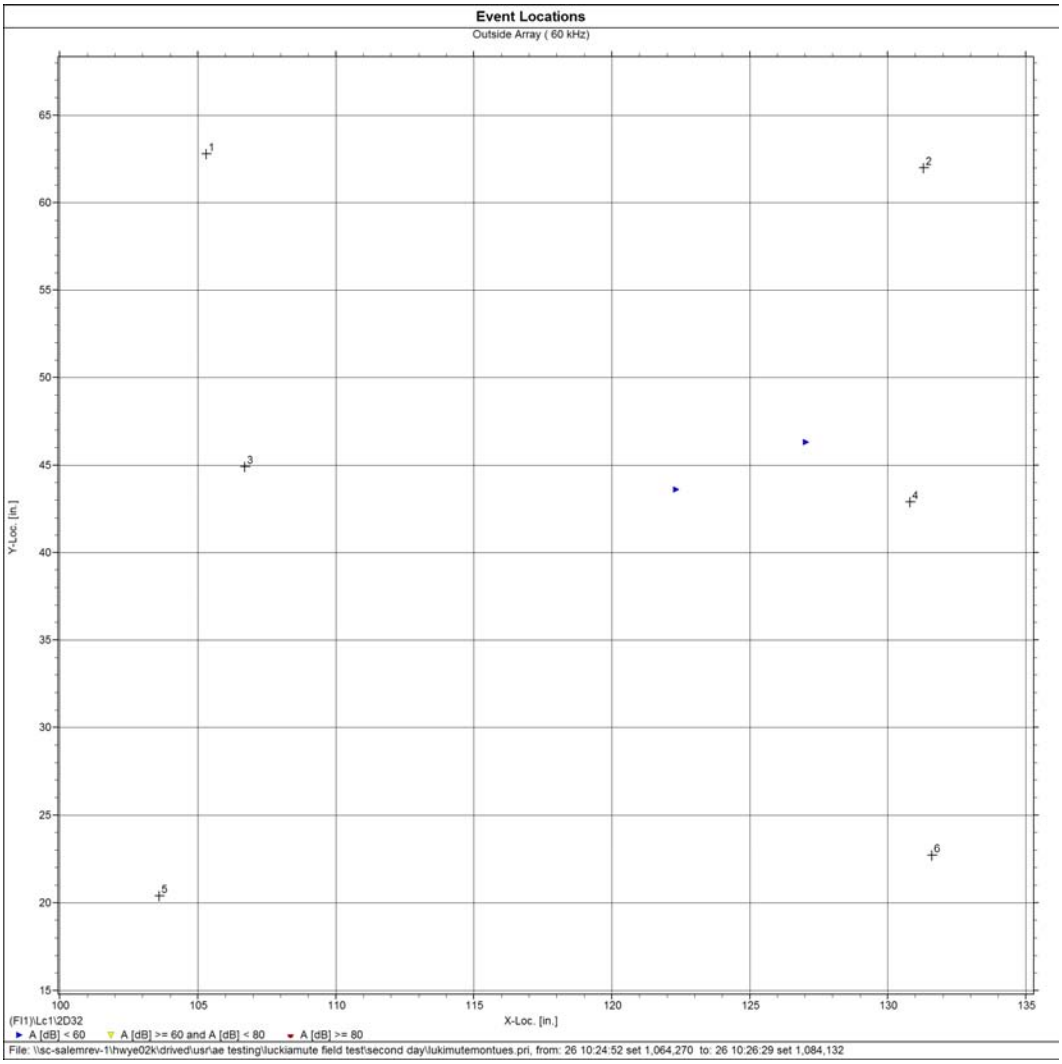

Figure 4.2.31 Load case Dynamic 2 event locations from outside face planar array (60 kHz sensors) .

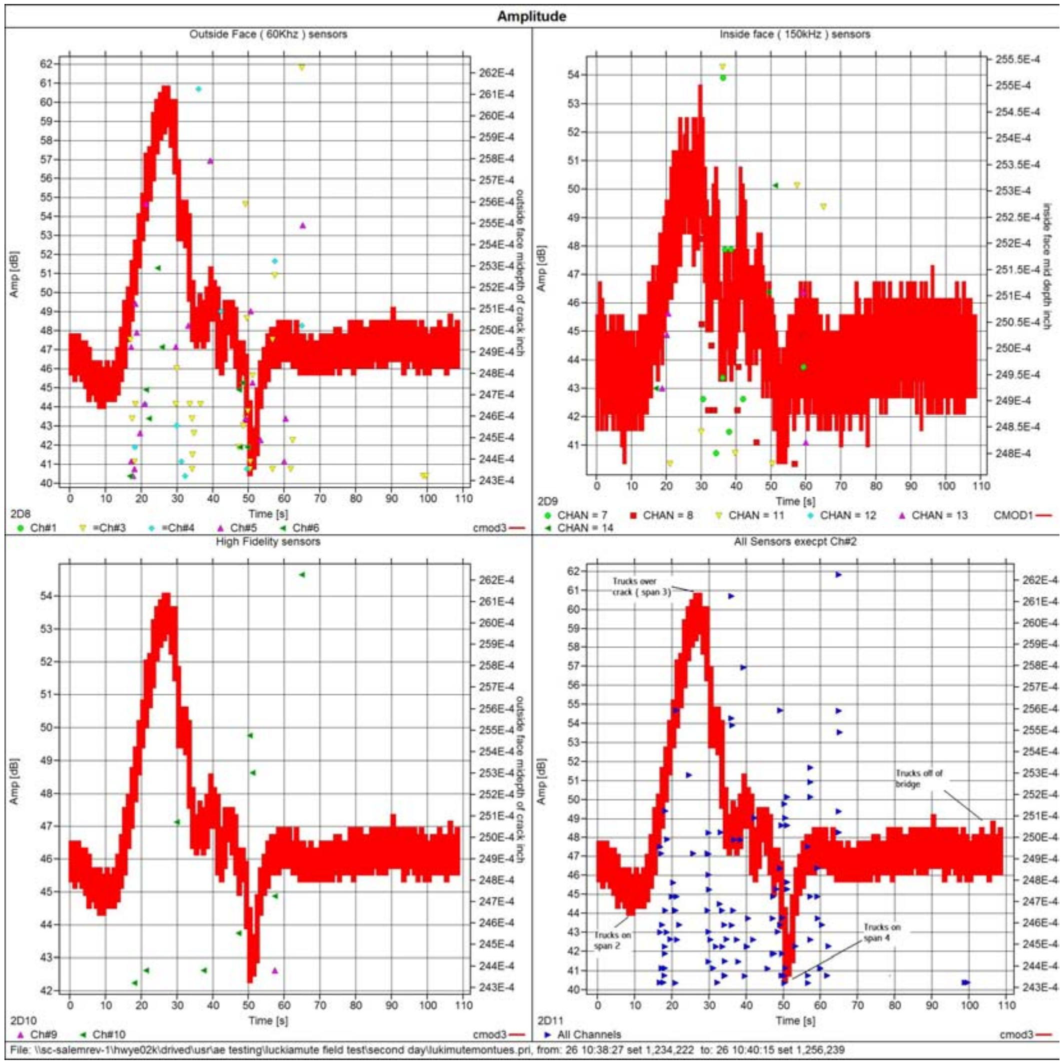

Figure 4.2.32 Load case Dynamic 3 peak amplitude and CMOD.

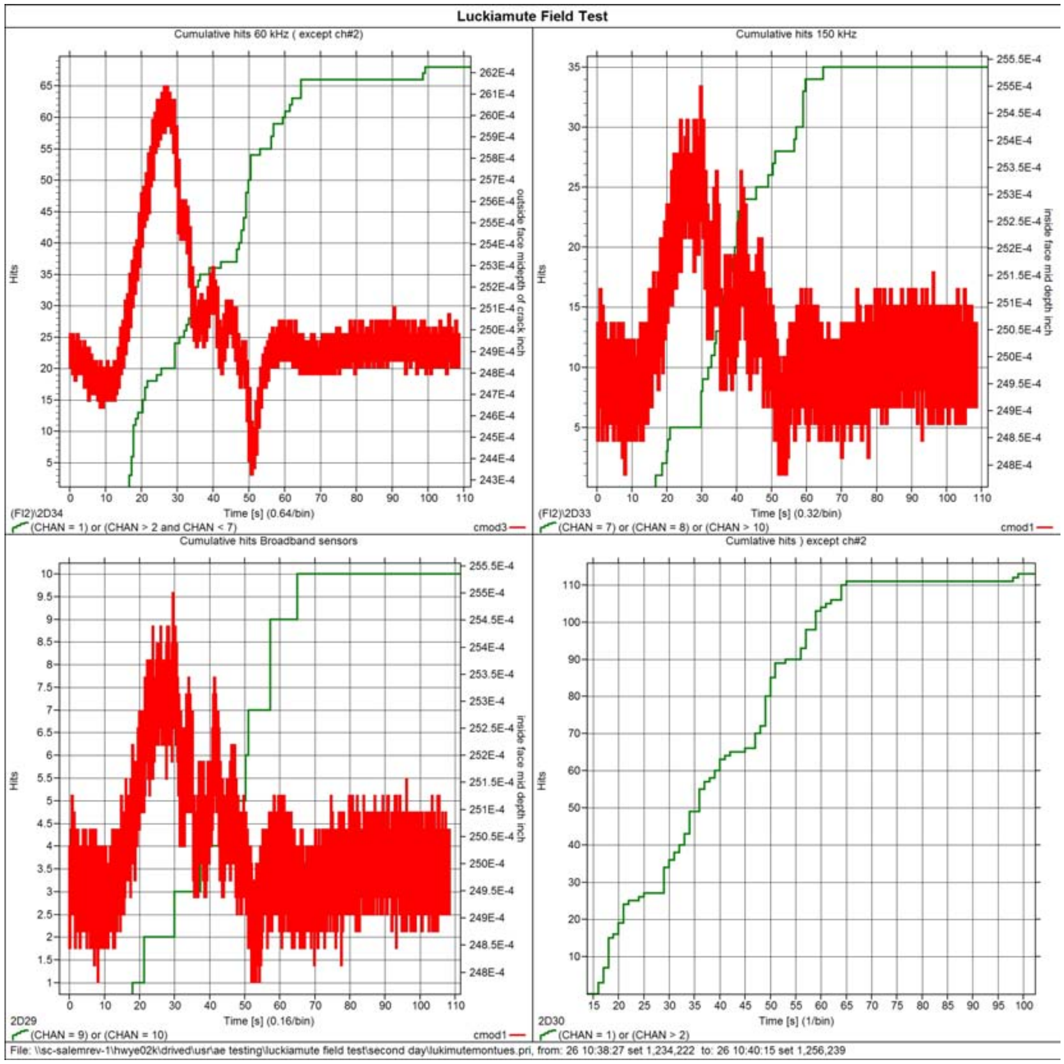

Figure 4.2.33 Load case Dynamic 3 cumulative hits and CMOD.

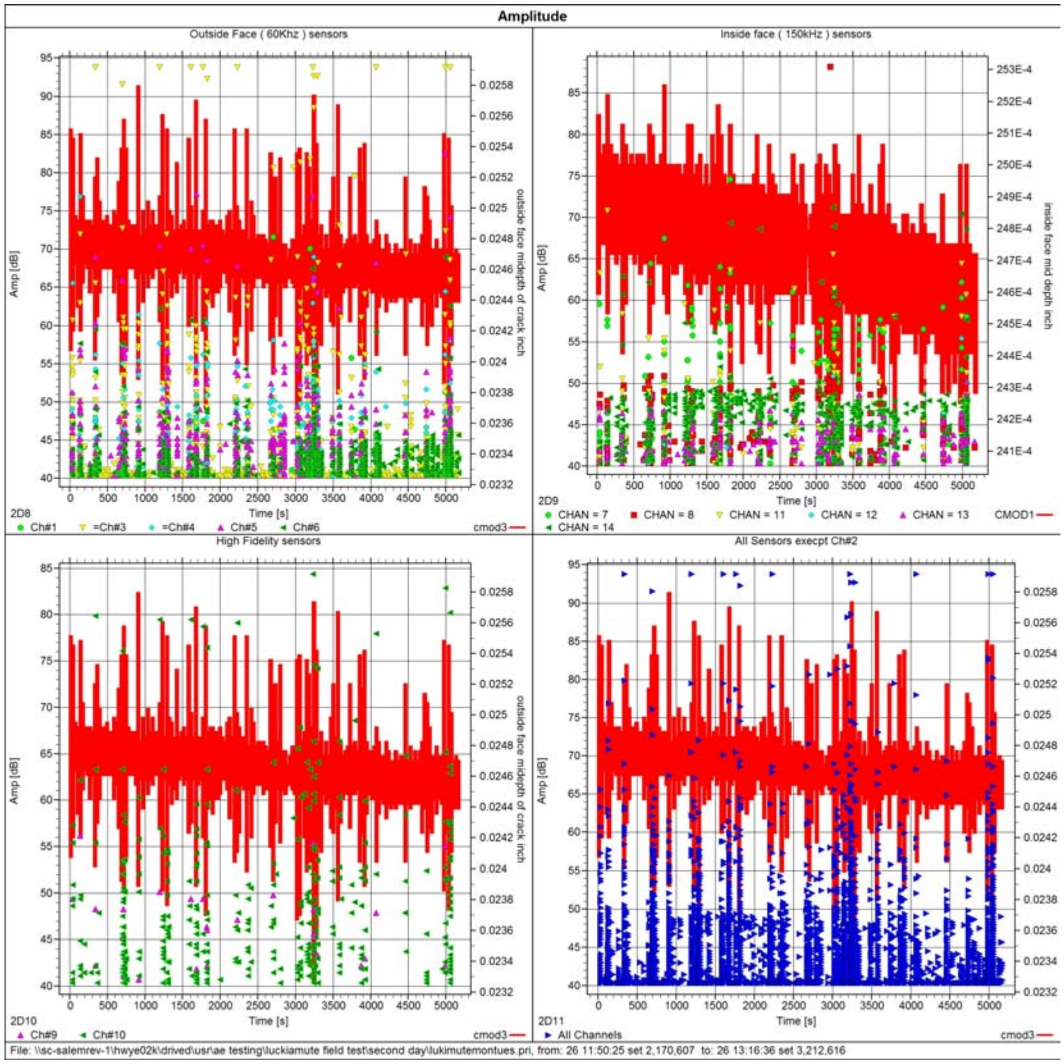

Figure 4.2.34 Ambient loading peak amplitude and CMOD.

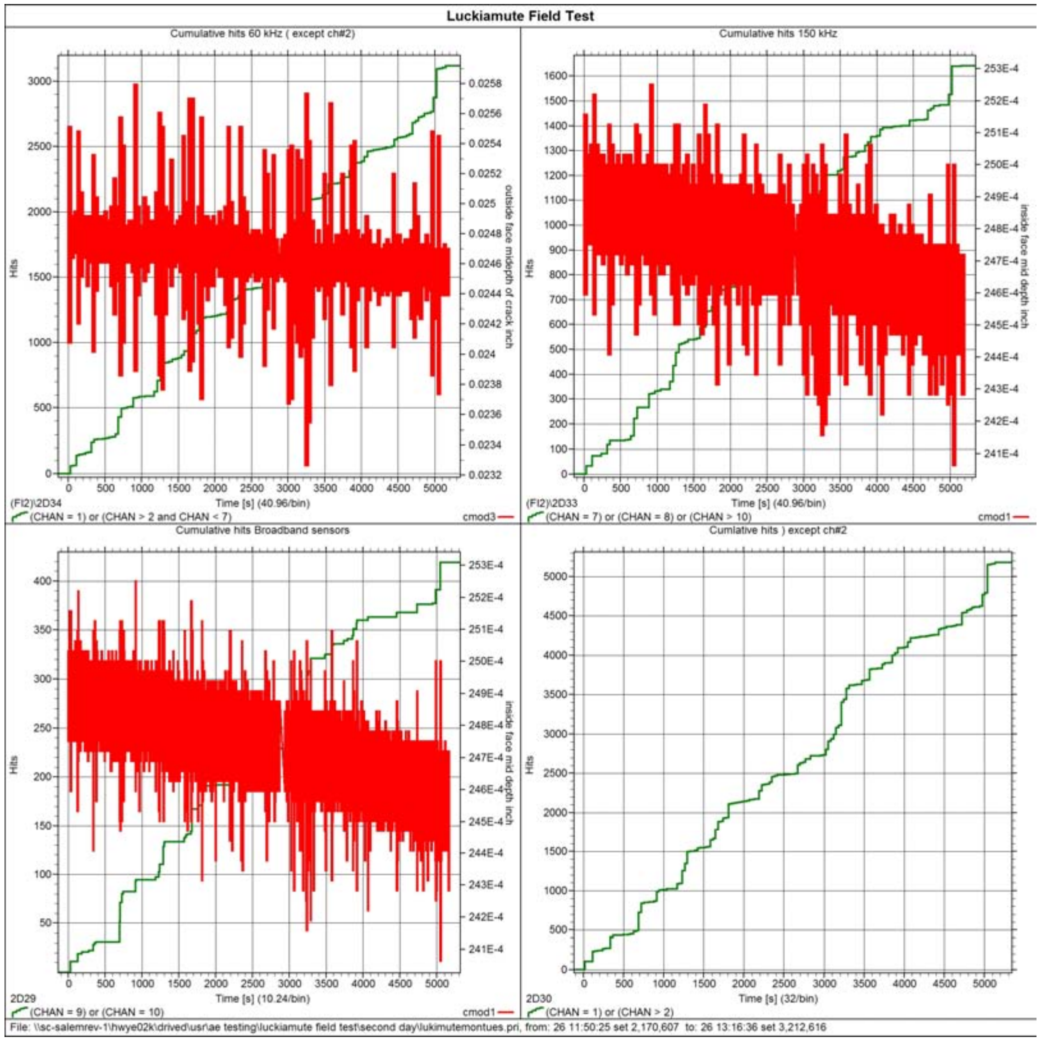

Figure 4.2.35 Ambient loading cumulative hits and CMOD.

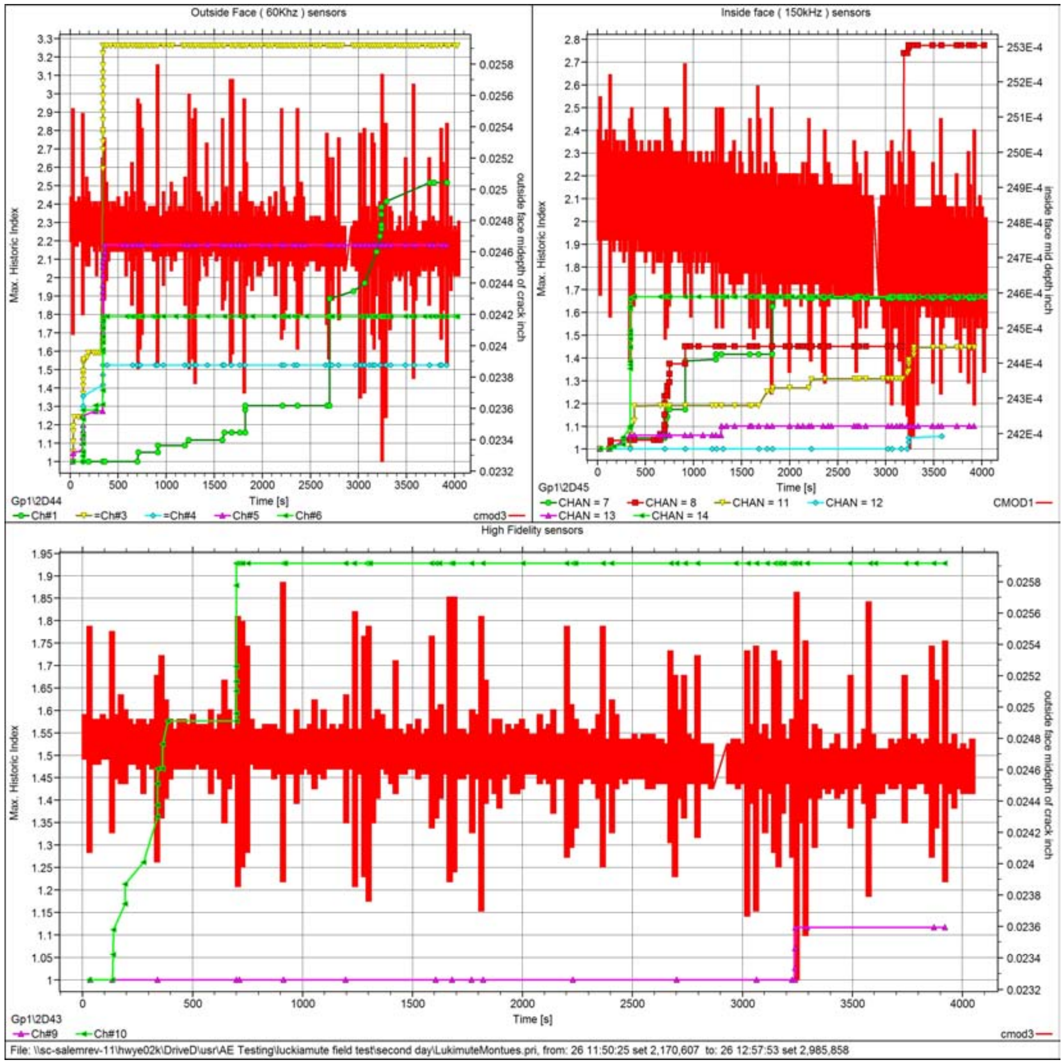

Figure 4.2.36 Ambient loading Historic Index.

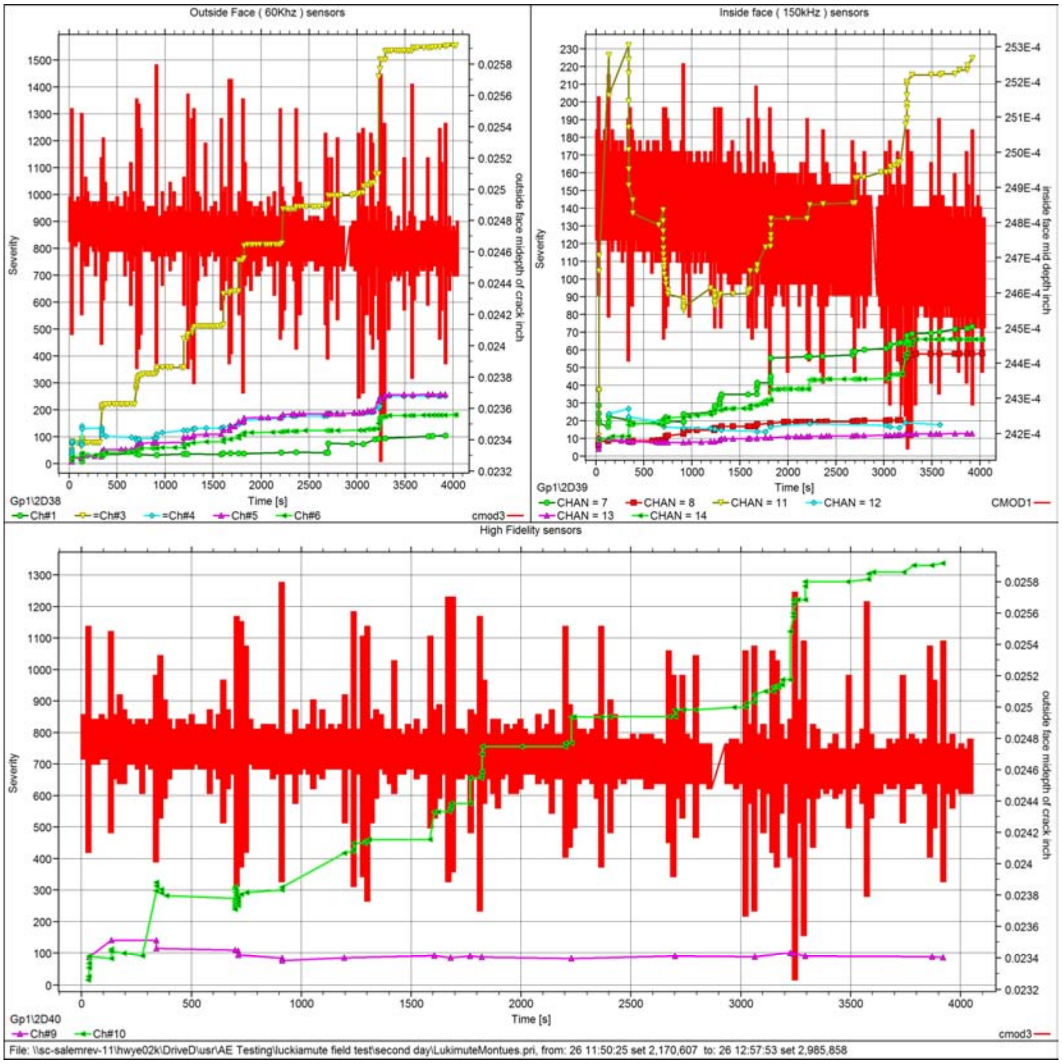

Figure 4.2.37 Ambient loading Severity.

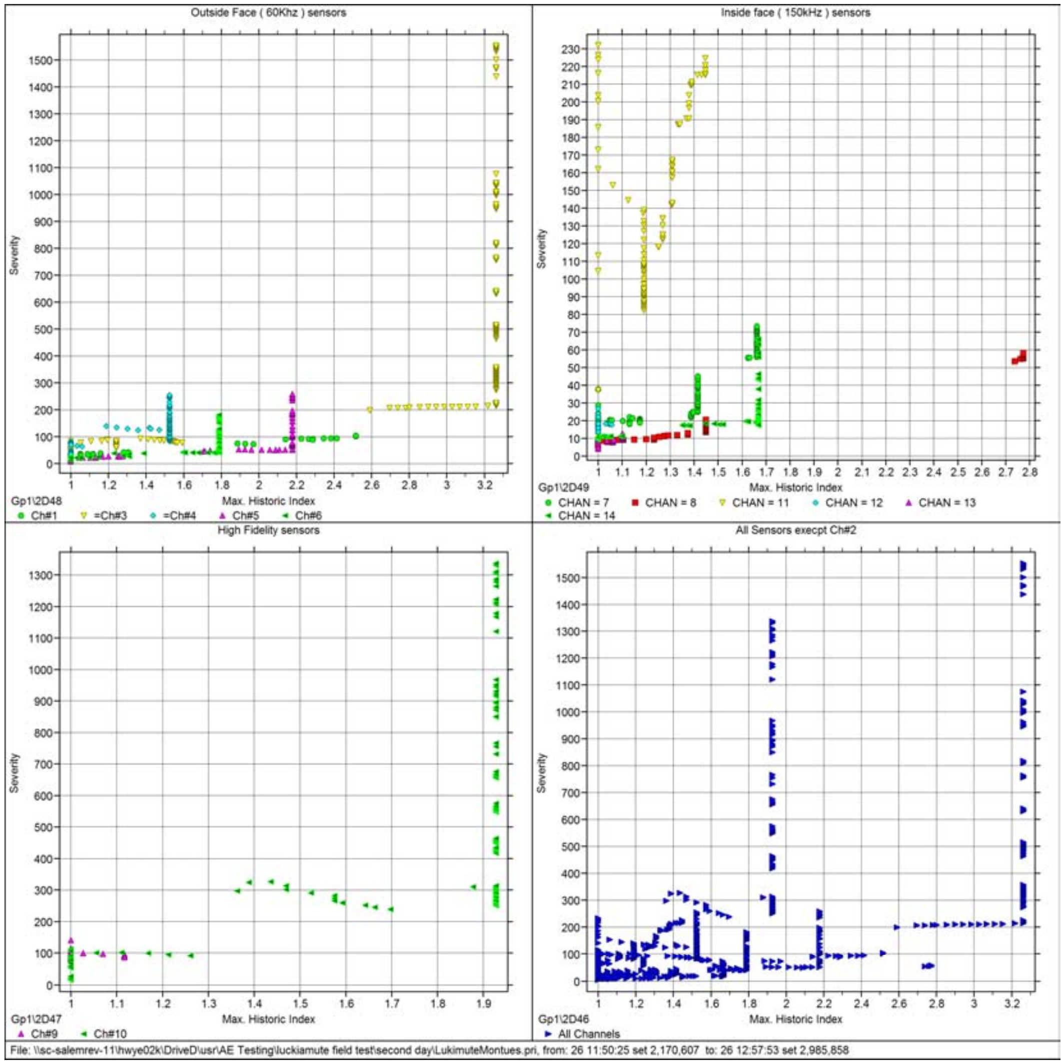

Figure 4.2.38 Ambient loading Intensity Plot.

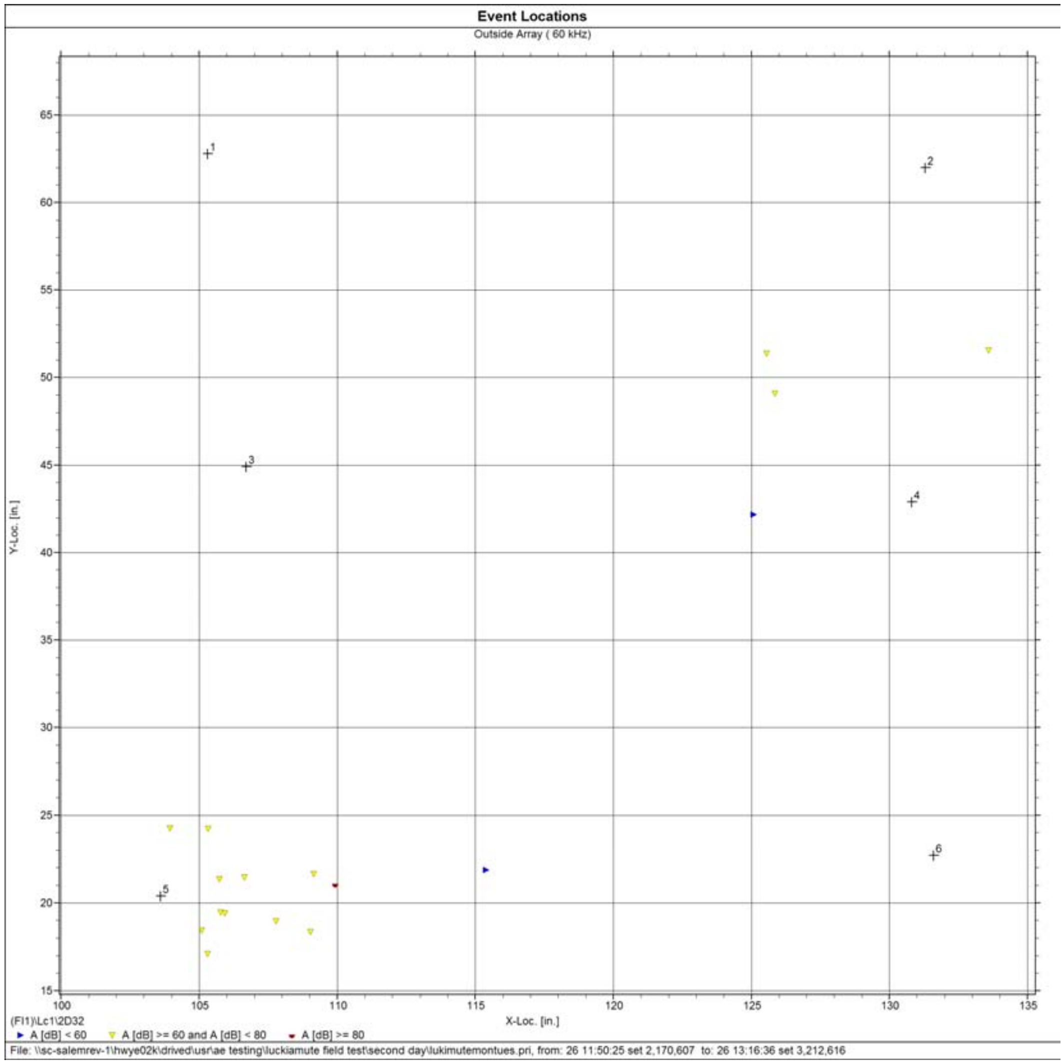

Figure 4.2.39 Ambient loading event locations on outer face.

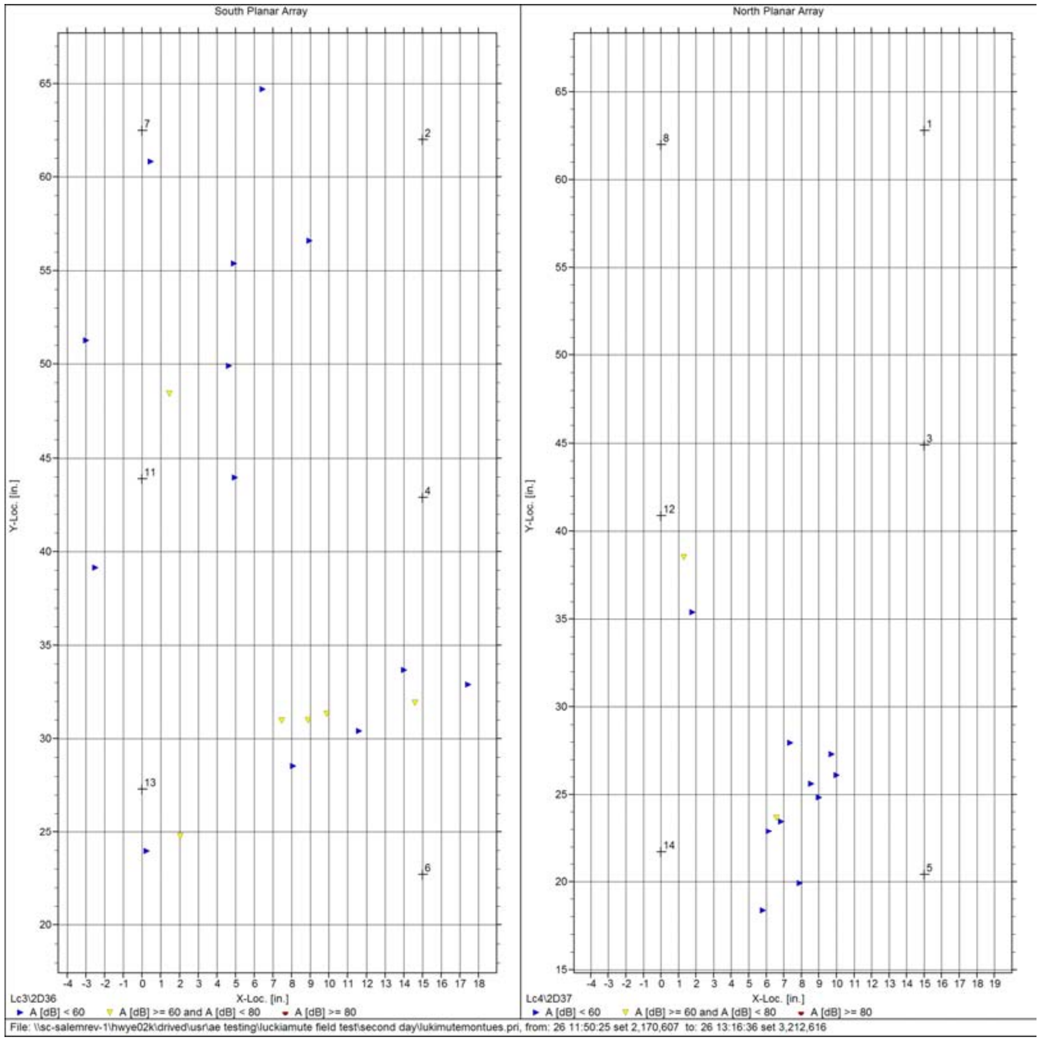

Figure 4.2.40 Ambient loading event locations through stem thickness.

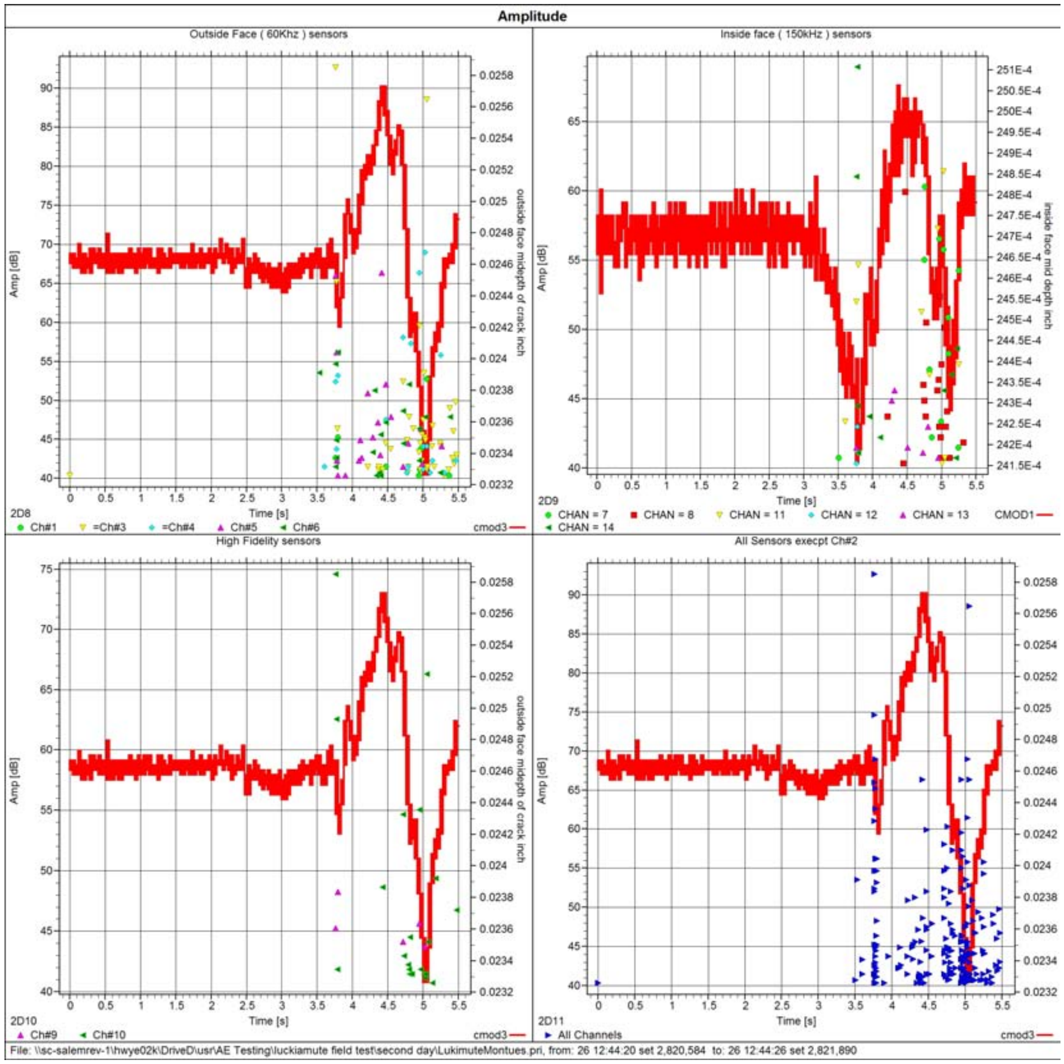

Figure 4.2.41 Peak amplitudes for ambient load that produced the largest CMOD.

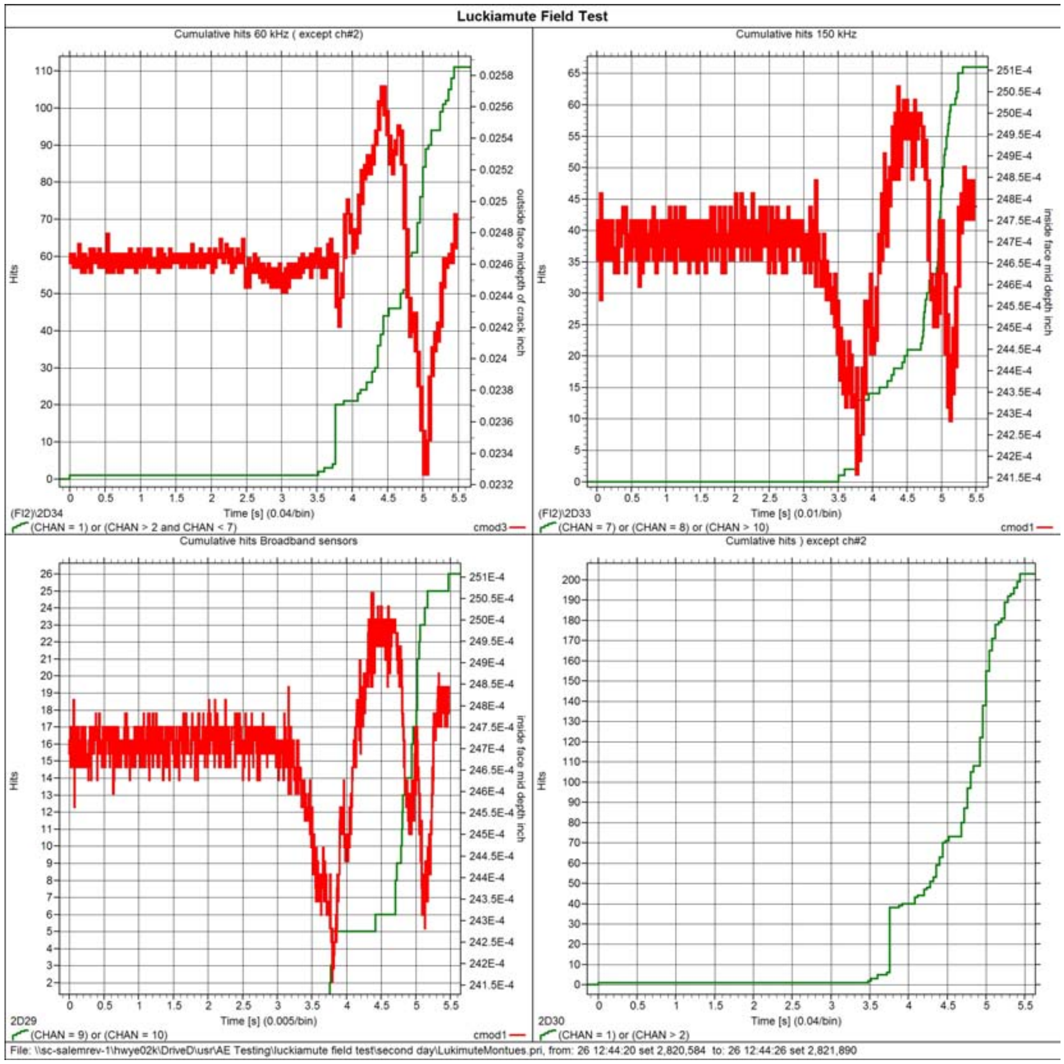

Figure 4.2.42 Cumulative hits for ambient load that produced the largest CMOD.

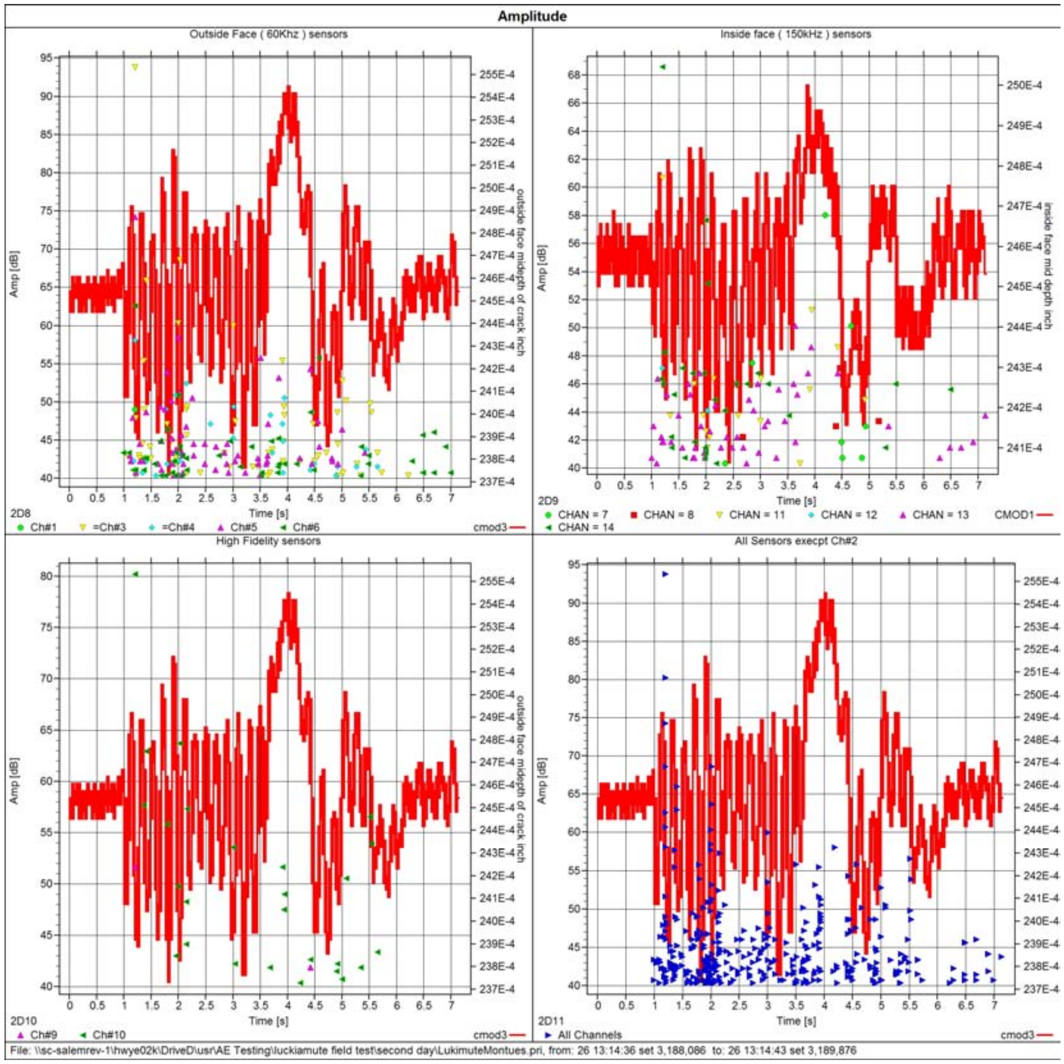

Figure 4.2.43 Peak amplitudes for ambient load that produced the most AE activity.

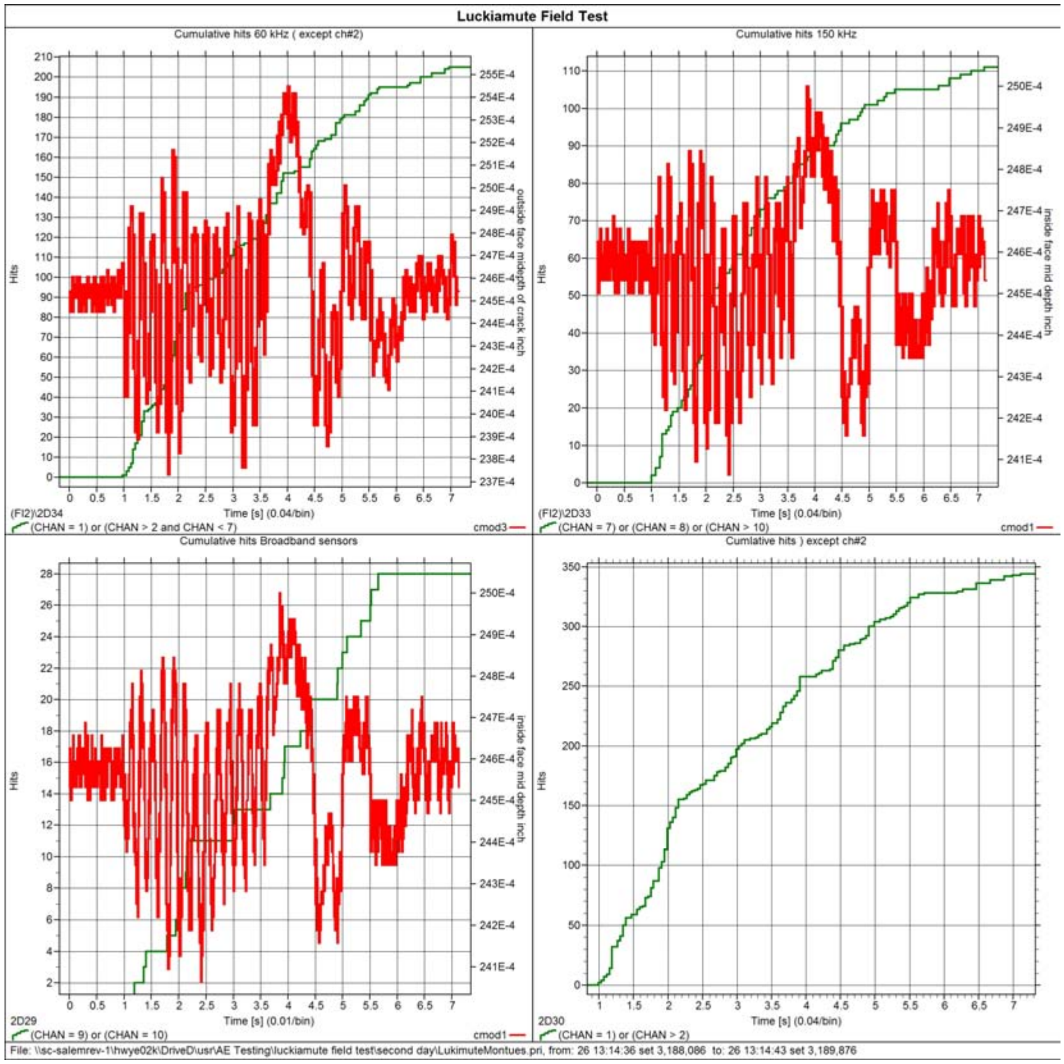

Figure 4.2.44 Cumulative hits for ambient load that produced the most AE activity.

4.3 Acoustic Emissions Testing of the Banzer Bridge ODOT Bridge # 3140A

4.3.1 Background

The Banzer bridge carries Oregon State Highway 102 over the Nehalem River 2 ½ miles West of Mist. The bridge is a three span continuous deck girder design with conventionally steel reinforced concrete girders. The plan and elevation drawing can be seen in Figure 4.3.1 and the girder details seen in Figure 4.3.2. This particular design is somewhat unique for Oregon in that it has only two main girder lines. It was constructed in 1951 and based on a 1999 load rating is unrestricted for legal and permit loads. This bridge is of interest to maintenance engineers in that its main girders have an abundance of fairly large cracks in the concrete. Some of the older cracks have been repaired with epoxy injection methods during the 1980's and have since re-cracked. One particularly large crack is located near the bent 3 end of span 2 on the upstream girder. The diagonal tension crack has a crack mouth opening exceeding 0.070 inches which is considered to be very wide, especially considering the high density of shear steel reinforcement in the section. Refer to Figure 4.3.31 for a crack map of the girder in question.

With the adequate theoretical load capacity rating and the ubiquitous shear and flexural cracks, this bridge was determined to be a good candidate for structural load testing in order to better understand the in-service behavior. In addition to performing a structural load test program, acoustic emissions testing was included as part of an ODOT sponsored research project SPR 633.

4.3.2 Instrumentation description

Both conventional structural instrumentation and acoustic emissions instruments were temporarily installed on a section of span two in order to measure the structures response to both controlled and ambient loads. The location of the test section is shown in Figures 4.3.1, 4.3.3, 4.3.4 and 4.3.6.

4.3.2.1 Conventional structural instrumentation

The upstream steel reinforced concrete girder in span two and adjacent , inboard stringer were fitted with transducers that measured shear strain , crack mouth opening displacement (CMOD) and rebar strain at a section approximately 10 feet West of bent 3. This particular section is in a high shear loading zone and has four nearly full depth shear cracks, the largest of which has a CMOD of 0.08 inches under dead load. The instruments were centered on this particular crack. The locations of internal shear stirrups were located using a rebar locator and the concrete was excavated to gain access to the stirrup for strain gage installation. Refer to Figure 4.3.5 for a photograph of the rebar strain gage installation. The response of these instruments were recorded but only the instruments on the upstream (US) girder were included in the AE data.

4.3.2.2Acoustic emissions instrumentation

A total of 13 AE sensors were attached to the downstream (DS) face of the US girder at the section identified above. Five 60 kHz resonant AE sensors were arranged in a linear array along the beam at mid depth covering a region of approximately 23 feet along the length of the beam from bent 3. Eight 150 kHz resonant sensors were installed in a planar array that surrounded the large shear crack of interest. The linear array was chosen to capture more of a global structural response of the shear zone but also covers a portion of the girder that is subjected to more bending then shear. The planar array focuses specifically on the large shear crack. The area of coverage for the linear array is on the order of 100 ft^2 of girder surface and the planar array covers and area of approximately 10 ft^2.

The sensors were held in place with special clamps that were glued to the concrete surface and acoustically coupled with a silicon grease. AE data in addition to the shear strain, CMOD and rebar strain on the US girder were recorded using a Vallen Systems AMSYS5 AE system. Refer to Figure 4.3.7 for a photograph of the data collection systems. A fourth analog channel was included to identify the presence of known and ambient trucks on the bridge. This was accomplished with a 9 volt supply that was turned on when the trucks came onto the bridge and off when they left the bridge.

A description of each AE sensor location is described in Table 4.3.1. Figures 4.3.3 and 4.3.4 further describe the AE sensor installations.

4.3.3 Calibration of AE sensors

Prior to and after load testing of the bridge most of the AE sensors were checked for proper acoustic coupling using the standard pencil break method. A 0.5mm lead pencil was broken in the close vicinity (approximately 2 inches) from each sensor. (Refer to Figure 4.3.9.) Ideally the peak amplitude measured from each break should be greater then 90 dB and repeatable within 3 dB. Table 4.3.2 summarizes the results of this testing. Due to time limitations with the arriving test trucks not all of the sensors were tested, specifically Channels 1 , 6 and 8 which were at the outer extremes of the linear array. Only 5 of the 13 sensors proved to meet the acceptance criteria with the others not being tested or showing less then desirable amplitudes. It was later determined that low amplitudes were the result of improper couplet selection. The silicon grease used was not the normal Dow vacuum grease which is quit viscous but instead Dow silicon mold release which is not as viscous. The couplet appeared to dry out by absorbing into the concrete.

The compromise in sensor acoustic coupling, though unfortunate , is not a show stopper. It has the effect of reducing coverage of the sensor but not eliminating it. This is especially true with the 150 kHz sensors in the planar array because the sensors were relatively closely spaced together.

4.3.4 Load case description

See Table 3 for test truck configurations and Figure 4.3.8 for photograph of test trucks.

4.3.4.1 Load case 1

Drive truck 1 centered in the upstream lane heading West bound in 20 foot increments across spans 3, 2 and 1.

4.3.4.2 Load case 2

Truck 1 backs up onto span 2 with the nose of the truck at bent 2. Truck is backed up over span 1 to get to this position. Trucks 2 and 3 are moved onto span 2 from the East end of the bridge on at a time in 20 foot increments. All three trucks are then in position on span 2 causing maximum shear loading at the test section. A large ambient truck crosses span 2 heading East in the downstream (DS) lane. Truck 1 is then driven Westbound off of the bridge and returns in the DS lane heading East bound at 5 mph. Truck 1 crosses the bridge and then returns in the DS lane heading West bound at 5 mph. A few more ambient trucks cross the bridge West bound in the DS lane. Trucks 2 and 3 are then driven across span 1 and off of the bridge returning to a no live load condition.

4.3.4.3 Load case 3

Truck 1 drives Eastbound in the upstream (US) lane at 5 mph with left wheel line on the fog line of the lane. The truck is turned around and driven Westbound in the US lane with the right wheel line on the fog line of the lane at 5 mph.

4.3.4.4 Load case 4

Truck 1 is driven Westbound centered in the DS lane across the bridge at 40 mph.

4.3.4.5 Load case 5

Truck 1 is driven Eastbound centered in the US lane across the bridge at 40 mph.

4.3.4.6 Load case 6

Ambient trucks are monitored for a period of 1 hour. The truck causing the largest rebar strain range is identified. Includes the truck causing the largest peak amplitude for AE.

4.3.5 Results

4.3.5.1 Load case 1

Analog results

Peak rebar strain range : 180 $\mu\varepsilon$ (5220 psi)

Peak integrated shear strain: $2.1\text{x}10^{-4}$ inches

AE results

	Planar Array (150 kHz)	Linear Array (60 kHz)
Load hits:	0	33
Unload hits:	4	3
Peak hit amplitude (dB)	53.4	63.2
Calm ratio	NA	.09

Peak hit amplitudes are correlated with rebar strain in Figure 4.3.10. The results from each array and combined results are shown. In general peak amplitudes are fairly low for both AE sensor arrays. The threshold was set at 40 dB for both arrays. In general much more activity is seen in the linear array , which included both shear loading and bending , whereas the planar array is primarily focused on shear response. Also as noted above the area of coverage of the linear array is approximately 10 times that of the planar array. Figures 4.3.11 and 4.3.12 show the differential and cumulative hit activity respectively for load case 1. The linear array recorded almost 9 times the number of hits compared to the planar array. Because no loading hits were recorded in the planar array, a Calm Ratio could not be calculated. The Calm Ratio for the linear array was calculated at 0.09. The validity of the Calm Ratio calculated from a small sample of hits is discussed later in the report.

Event locations were not available for this load case, or any other load cases , due to the low amplitudes of the AE. Only a first hit sensor approach can be used. From the planar array all of the AE activity came from the upper Eastern side of the shear crack. From the linear array most of the AE activity came from the sensor closest to the shear crack , with the remainder coming from the West end of the array which includes bending as well as shear loading.

4.3.5.2 Load case 2

Analog results

Peak rebar strain range : 260 με (7540 psi)

Peak integrated shear strain: 2.6×10^{-4} inches

AE results

	Planar Array (150 kHz)	Linear Array (60 kHz)
Load hits:	9	105
Unload hits:	2	44
Peak hit amplitude (dB)	53.1	66.1
Calm ratio	.22	.42

Peak hit amplitudes are correlated with rebar strain in Figure 4.3.13. This is the most complicated load case so the loading descriptions are annotated on the plot. Amplitudes from both the planar and linear arrays are again fairly low. The peak rebar strain range of 260 με was the largest recorded during the test load protocol and matched the peak strain range measured under ambient loading. The passage of Truck 1 produces the largest amount of AE activity for all of the sub loads that make up this load case. Figures 4.3.14 and 4.3.15 show the differential and cumulative hits results respectively. Though the loading sequence complicates the calculation of the Calm Ratio the planar array has an approximate Calm Ratio of 0.22 and the linear array is 0.42. Base on the first hit sensor approach the AE activity from the planar array shows all of the activity coming from the upper Eastern side of the large shear crack , similar to load case 1. The linear array shows AE activity at all sensor positions but more than half of the total activity comes from channel #10 which , much like load case 1 , which is near the large shear crack.

4.3.5.3 Load case 3

Analog results

Peak rebar strain range : 170 $\mu\varepsilon$ (4930 psi)
Peak integrated shear strain: $2.1\text{x}10^{-4}$ inches

AE results

	Planar Array (150 kHz)	Linear Array (60 kHz)
Load hits:	EB 0 WB 3	EB 35 WB 4
Unload hits:	EB 3 WB 1	EB 3 WB 2
Peak hit amplitude (dB)	EB 45.5 WB 51.1	EB 62 WB 68
Calm ratio	EB NA WB .33	EB 0.09 WB 0.5

Peak hit amplitudes are correlated with rebar strain for load case 3 as shown in Figure 4.3.16. Again peak amplitudes are relatively low. The rebar strain range is identical for each direction of truck travel but the shape of the curve is different due to the axle configuration of the test truck. In theory the East bound passage will produce a higher shear loading on the cracked section then the Westbound passage. Figure 4.3.17 and 4.3.18 show the differential and cumulative hits results respectively. The Eastbound passage produced the most activity for the linear array. Calm Ratios between 0.09 and 0.5 where calculated as shown above.

Based on first hit sensors, the planar array indicates AE activity at both the Eastern and Western sides of the large shear crack near the top, though data is quite limited. The linear array shows AE activity in the shear crack region and Western end of the array which has a lower V/M ratio as discussed above.

4.3.5.4 Load case 4

Analog results

Peak rebar strain range : 110 με (3190 psi)

Peak integrated shear strain: 1.35×10^{-4} inches

AE results

Planar Array (150 kHz) Linear Array (60 kHz)

Load hits: 0

2

Unload hits: 1

4

Peak hit amplitude (dB) 45

49.8

Calm ratio NA

2.0

Peak hit amplitudes for load case 4 are shown in Figure 4.3.19. The differential and cumulative hit results are shown in Figures 4.3.20 and 4.3.21 respectively. Both total AE activity and peak amplitudes are quite low as would be expected because the test truck is running in the lane opposite the girder that is fitted with instruments. The planar array indicates a single hit coming from the upper Eastern end of the large shear crack. The linear array indicates a single hit coming from the large shear crack region and the remaining 5 coming from the Western end of the linear array which has a larger moment contribution. It should be noted that bending moments will tend to distribute laterally more then shear loads, and thus, with a truck in the opposite lane, the mid-span bending loads would be expected to transfer to the US beam more then the shear loads.

4.3.5.5 Load case 5

Analog results

Peak rebar strain range : 200 $\mu\varepsilon$ (5800 psi)

Peak integrated shear strain: $1.52\text{x}10^{-4}$ inches

AE results

<u>Planar Array (150 kHz) Linear Array (60 kHz)</u>

Load hits: 0

12

Unload hits: 0

16

Peak hit amplitude (dB) NA

73

Calm ratio NA

1.3

Peak hit amplitudes for load case 5 are shown in Figure 4.3.22. No AE activity is recorded from the planar array which is interesting considering the shear load on the girder is significant. The linear array recorded significant AE activity at both the large shear crack and further into the moment section of the beam. A moderately high peak amplitude of 73 dB is recorded on channel # 12 which occurs during the unloading portion of the load cycle. The differential and cumulative hit results are shown in Figures 4.3.23 and 4.3.24 respectively. A Calm Ratio of 1.3 was calculated for this load cycle.

4.3.5.6 Load case 6A

Analog results

Peak rebar strain range : 260 με (7540 psi)

Peak integrated shear strain: 0.9×10^{-4} inches

AE results

<u>Planar Array (150 kHz) Linear Array (60 kHz)</u>

Load hits: 14

36

Unload hits: 5

34

Peak hit amplitude (dB) 54

65.1

Calm ratio 0..36

0.94

Peak hit amplitudes for load case 6A are shown in Figure 4.3.25. The strain range was 260 με and was the largest strain range measured under ambient loading which happened to match the strain range from load case 2. The peak amplitudes from both arrays were relatively low. Most of the planar array hits occurred near the upper Eastern side of the large shear crack, but a few hits were also recorded lower in the girder section and on the Western side as well. The majority of AE activity from the linear arrays occurred in the vicinity of the large shear crack, but all sensors recorded activity under this load case. Figures 4.3.26 and 4.3.27 show the differential and cumulative hit results. Calm Ratios of 0.36 and 0.94 were calculated for the planar and linear arrays respectively.

4.3.5.7 Load case 6B

Analog results

Peak rebar strain range : 220 με (6380 psi)

Peak integrated shear strain: 35.0×10^{-4} inches

AE results

Planar Array (150 kHz) Linear Array (60 kHz)

Load hits: 4

25

Unload hits:	1	
	18	
Peak hit amplitude (dB)	53	
	83.3	
Calm ratio	.25	
	0.72	

Peak hit amplitudes for load case 6B are shown in Figure 4.3.28. Even though the rebar strain range was 23% lower than that recorded in load case 6A both the peak amplitudes and cumulative hits were higher. The planar array recorded AE activity in the upper Eastern side of the large shear crack. The linear array recorded AE activity at all sensor locations but most of the activity, including the large amplitude 83.3 dB hit came from the Western end of the array which has a large bending component of load. Figures 4.3.29 and 4.3.30 show the differential and cumulative hits results respectively. Calm Ratios of 0.25 and 0.72 were calculated for the planar and linear arrays.

4.3.6 Discussion of results

Using rebar strain as the primary analog input for correlating AE data with loading proved to be much more effective then using only CMOD as was the case with the field test at Luckiamute described in Section 4.2. The strain in the rebar is much more sensitive to the truck loading especially at the moment the wheel load crosses the portion of the girder that has the large shear crack. It is much more difficult to install rebar strain gages then a crack motion gage but worth the effort.

Even though the three test trucks used for the loading sequences produced reasonably high strain ranges in the rebar there was very little AE activity recorded compared to the Luckiamute River bridge test described in Section 4.2.

Part of this lack of measured activity can be attributed to poor sensor acoustic coupling discussed in Section 4.3.3. The load rating for this structure indicates that the girders have plenty of capacity for legal loads, and thus the legal loads used for the testing would not be expected to cause much damage. Clearly this bridge has experienced very heavy, illegal loads in the past considering the extent and severity of the cracking. Most of the load cases did not produce enough AE activity to make an accurate measurement of the Calm Ratio, but the three load cases that did , cases 5, 6A and 6B indicate a Calm Ratio close to or greater then 1.0. Based on the laboratory test results found in Chapter 3, this level of Calm Ratio is indicative of heavy accumulated damage, which was observed in the field. Neither the Severity or Historic Index were calculated for these tests due to the lack of AE data which , neglecting the poor sensor coupling, supports the load rating which concludes legal loads are not damaging to this structure.

4.3.7 Conclusions

A high level of accumulated damage exists in this bridge as seen by the cracking and indicated by the high Calm ratio. Legal loads do not impart significant damage to the girders as indicated by the load rating and the low level of AE measured. It is very likely that over weight loads are have crossed and continue to cross this bridge due to its unique location which is very isolated and surrounded by logging activity. A permanent Structural Health Monitoring System is currently being installed on the structure to capture and characterize these suspected over loads. The data collected from this test will provide a baseline for legal loads and can be used to identify illegal loads.

Table 4.3.1 AE channel descriptions.

AE Ch. #	**Sensor position #**	**Sensor type**	**X position (in) From West face of Bent 2**	**Y position (in) From bottom of US beam**
1	1	60 kHz	33	46
9*	2	60 kHz	83	44
10	3	60 kHz	128	47
12	5	60 kHz	175.5	46
6	6	60 kHz	228	48.4
2	7	150 kHz	85	36.5
3	8	150 kHz	102	36
4	9	150 kHz	93.8	48
5	10	150 kHz	107.6	46.8
7	11	150 kHz	99.1	59.5
8	12	150 kHz	113	58.7
13	13	150 kHz	109	68
14	14	150 kHz	122	64.5

* AE Channel 9 was not used in the analysis due to excessive sensor noise

Table 4.3.2 Sensor calibration check with 0.5mm pencil breaks within 2 inches of sensor.

Sensor Position #	**Sensor type**	**AE Channel**	**Peak Amplitudes dB**	**Location of Data in Primary (.PRI) File (Data set No.)**
1	60 kHz	Channel 1	Did not check	
7	150 kHz	Channel 2	81.4, 76.9, 78.8	29222, 29258, 29372
8	150 kHz	Channel 3	85.2, 89.3, 85.9	74493, 74521, 74940 **
9	60 kHz	Channel 4	80.0, 84.0, 81.0	28000, 28152, 28254
10	150 kHz	Channel 5	87.8, 88.9, 86.3	29746, 30017, 30160
6	60 kHz	Channel 6	Did not check	
11	150 kHz	Channel 7	81.7, 84.8, 86.3	30869, 31403, 31698
12	150 kHz	Channel 8	Did not check	
2	60 kHz	Channel 9	99.8*, 99.8, 99.8	70255, 70261, 70339
3	150 kHz	Channel 10	96.8, 96.0	72287, 72291
		Channel 11	Not used	
5	60 kHz	Channel 12	99.8*, 99.8, 99.8	62291,62393, 62460
13	150 kHz	Channel 13	90.0, 86.3, 92.3	74561, 74587, 74596 **
14	150 kHz	Channel 14	97.9, 99.8*., 99.1	74607, 74634, 74645 **

* saturation   ** after remounting

Table 4.3.3 Test truck axle weights.

Test Truck #	**Serial #**	**Front axle weight (lbs)**	**Rear axle weights (lbs)**	**GVW (lbs)**
1	01-509	17420	15940+16800	50160
2	98-501	16400	16220+16680	49300
3	97-1516	15120	Combined 31300	46420

Axle spacing front to rear = 16.5 ft. , front rear to rear = 4.5 ft.

Overall length approximately 25 ft.

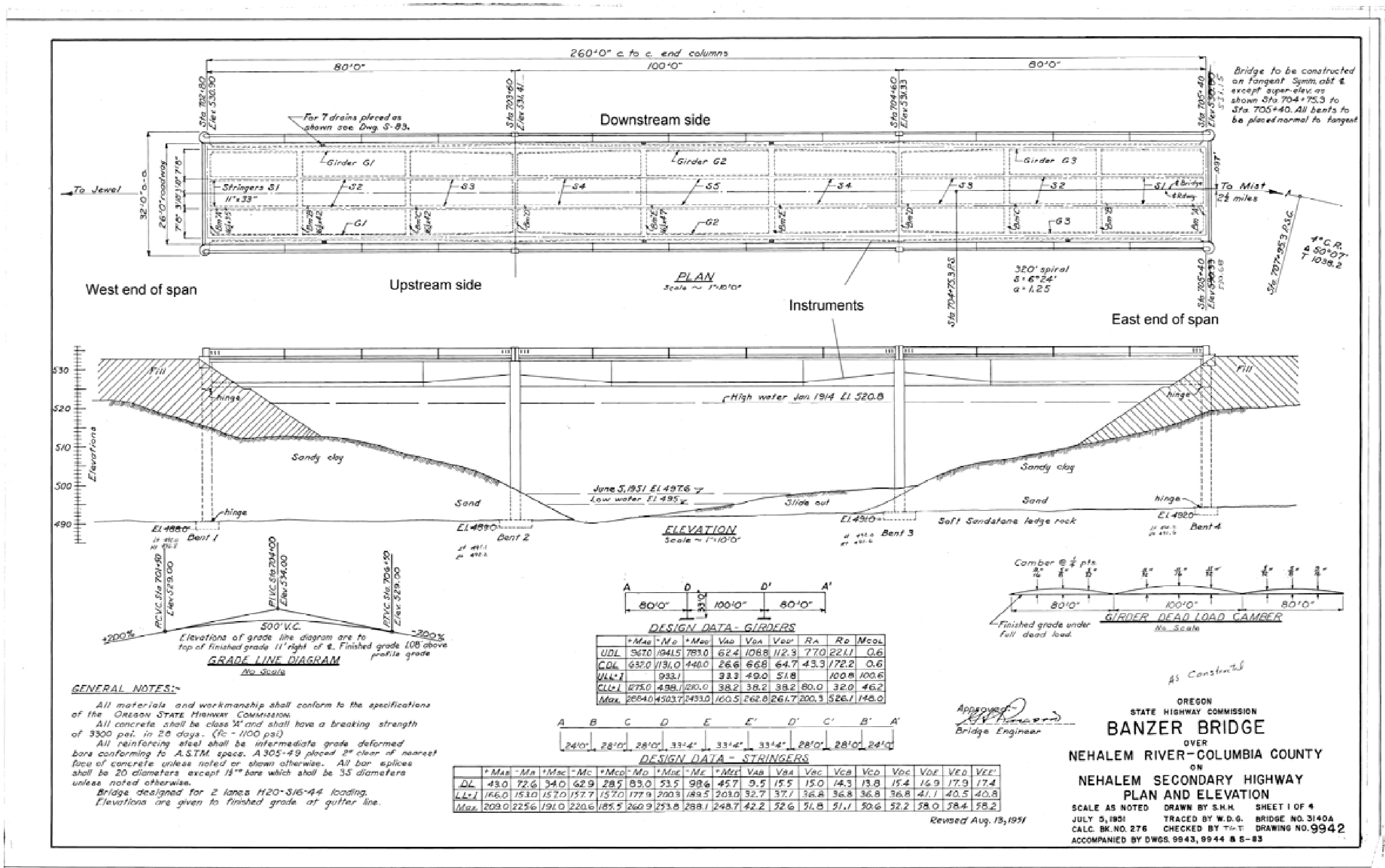

Figure 4.3.1 Plan and elevation drawing of Br. 3140A.

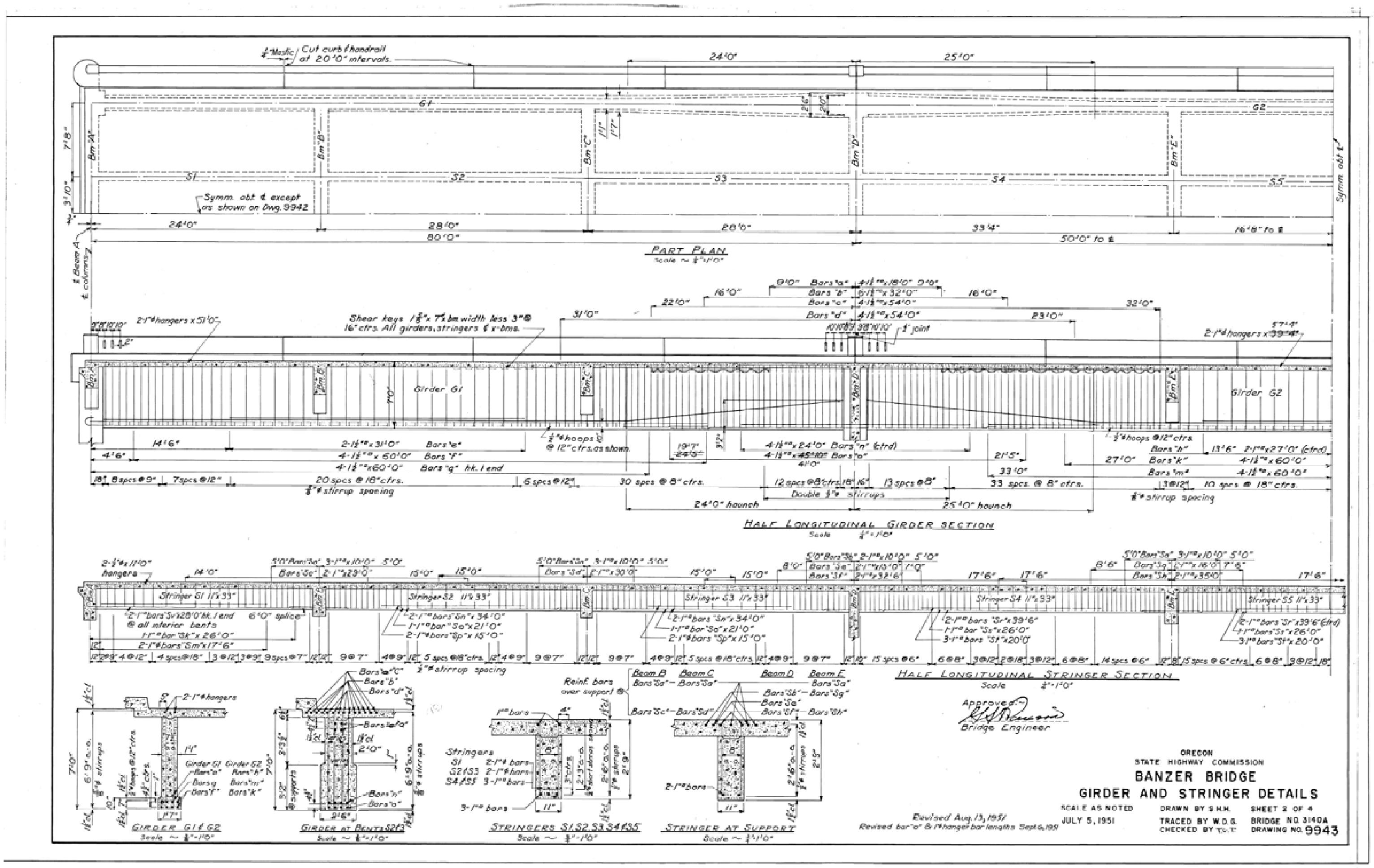

Figure 4.3.2 Beam sections.

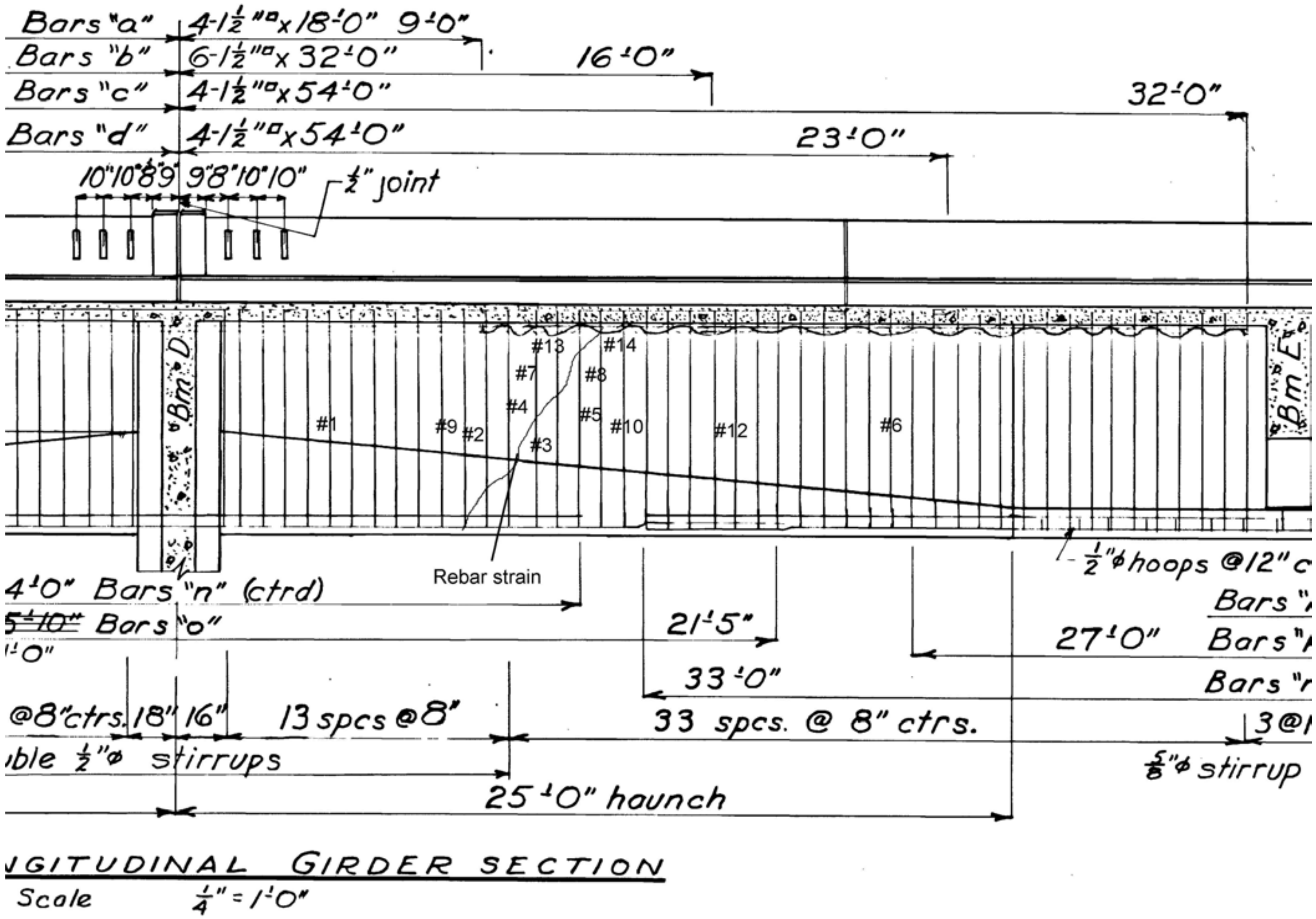

Figure 4.3.3 Approximate AE and strain sensor locations shown on span 2 beam section near bent 2.

Figure 4.3.4 Sensor installation.

Figure 4.3.5 Close up view of the rebar which was exposed and had a strain gage installed between deformations. Output from this gage was the primary analog input used to correlate shear load and AE data.

Figure 4.3.6 Upstream side view of bridge looking West (Note the shear crack that was instrumented is shown).

Figure 4.3.7 Data collection center was setup under span 3 (East end of bridge). Left to right are Richard Nordstrom (PSU) , Steven Solstez (ODOT) and Chris Higgins (OSU).

Figure 4.3.8 Test trucks are being positioned on span to induce a known load.

Figure 4.3.9 Richard Nordstrom performs a sensor check after test loads are finished. Access was provided with an ODOT bridge walker.

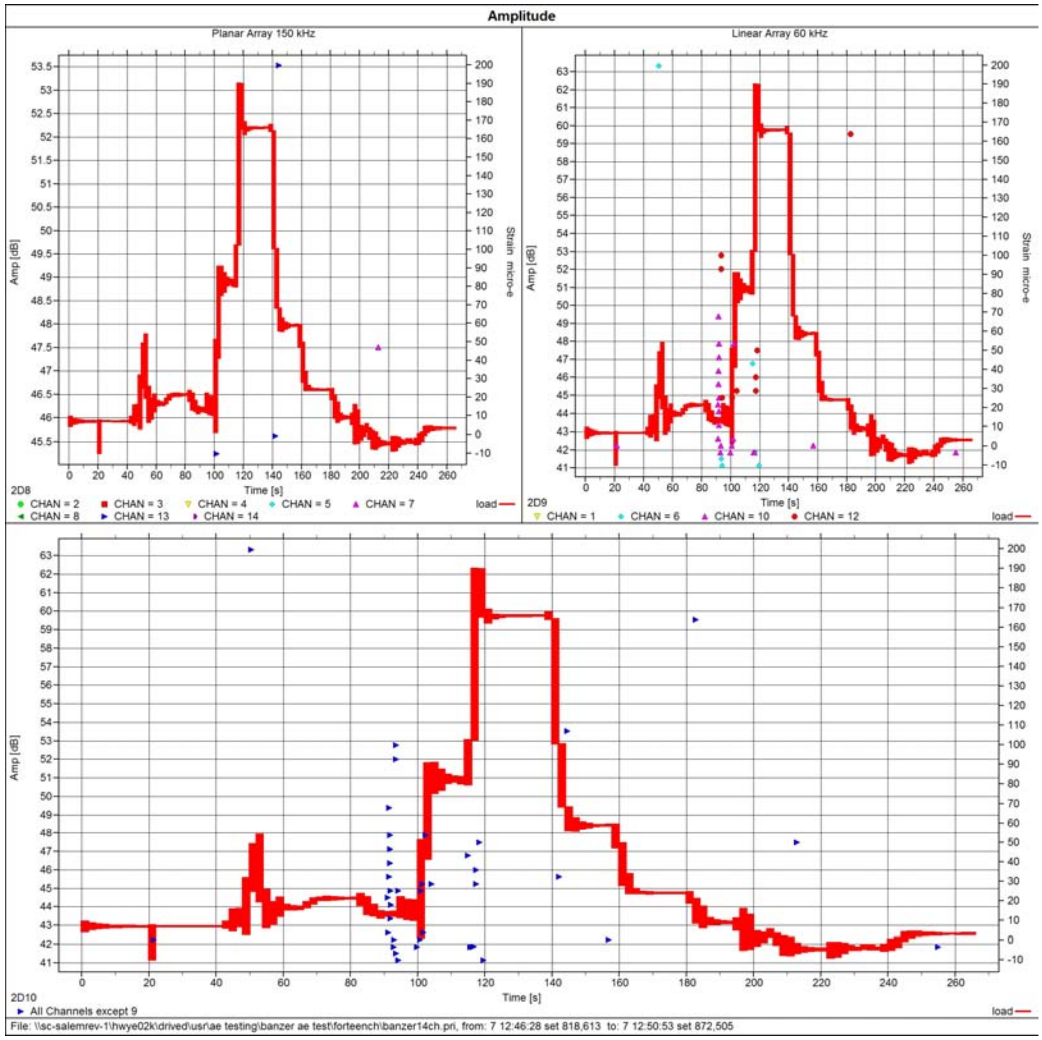

Figure 4.3.10 Load case 1 Peak amplitudes correlated with rebar strain , upper left plot shows planar array results and upper right plot shows linear array results and lower plot shows combined results. Load case 1 is a single test truck crossing bridge in US lane heading Westbound.

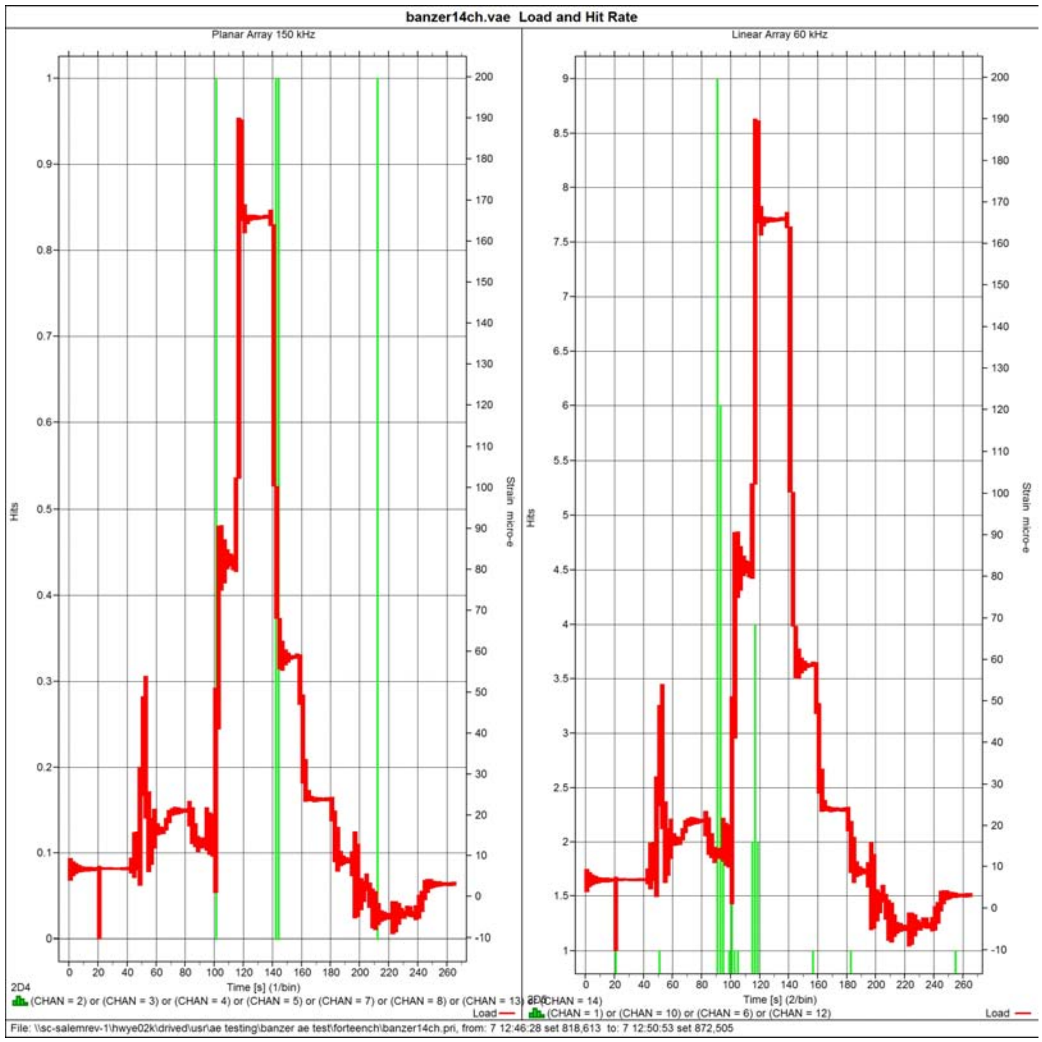

Figure 4.3.11 Load case 1 Differential hits distributed with rebar strain. Left plot are the planar array results and right plot are the linear array results.

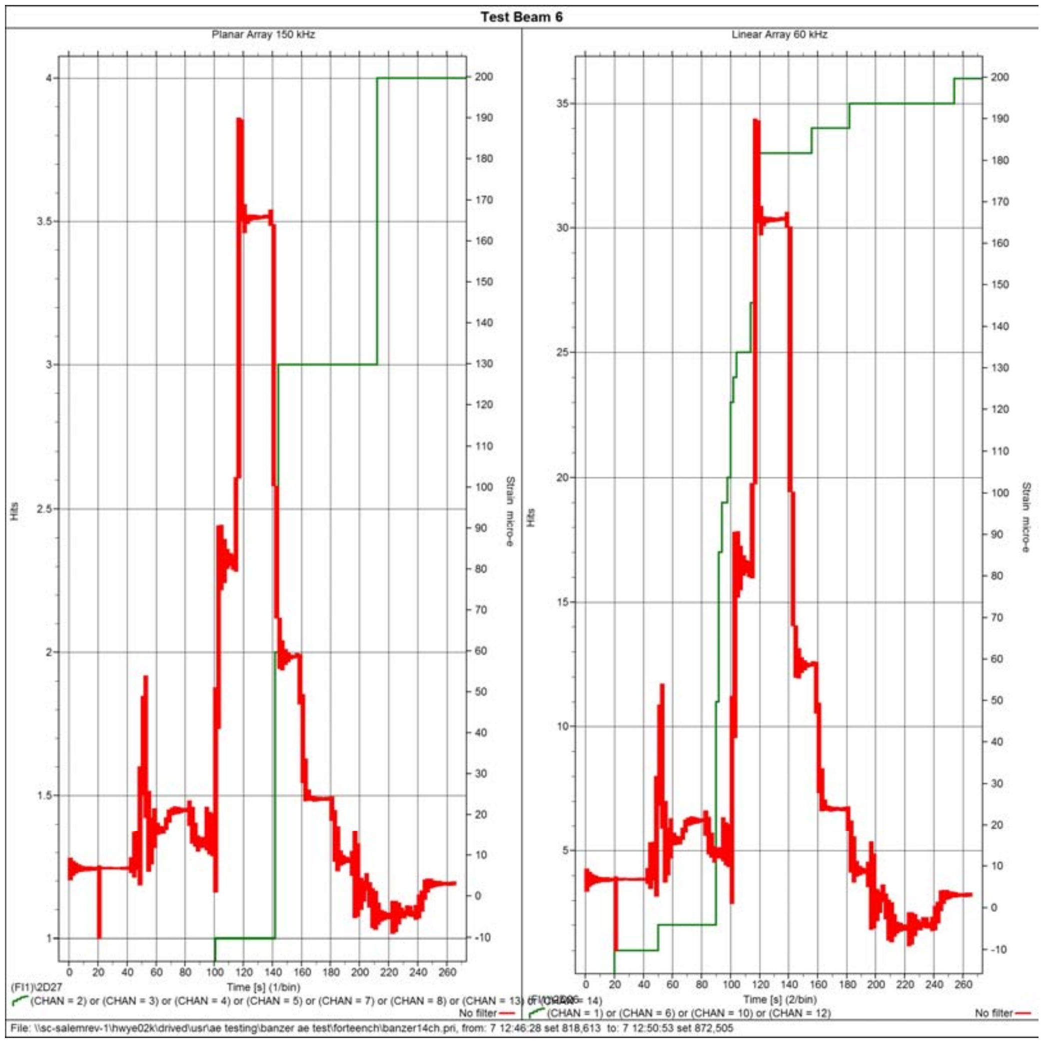

Figure 4.3.12 Load case 1 cumulative hit results distributed with rebar strain. Left plot shows planar array results and right plot show linear array results.

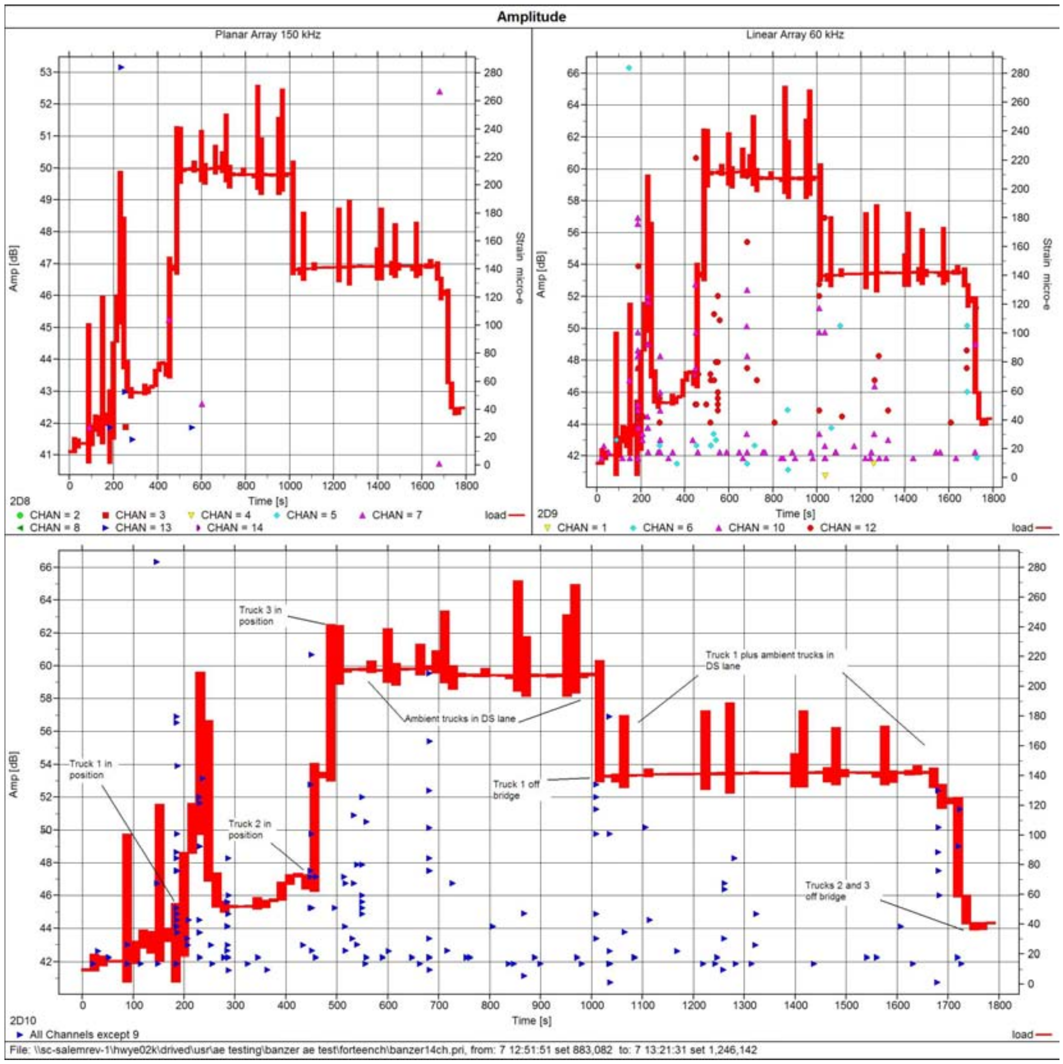

Figure 4.3.13 Load case 2 Peak amplitudes correlated with rebar strain , upper left plot shows planar array results and upper right plot shows linear array results and lower plot shows combined results. Load case 2 has all three test trucks placed on span 2 centered in the US lane followed by removal of truck 1 , passing truck 1 in the DS lane , with ambient trucks as well in the DS lane. All trucks are removed at the end of the load case. These events are labeled in the lower plot only but apply to all three plots.

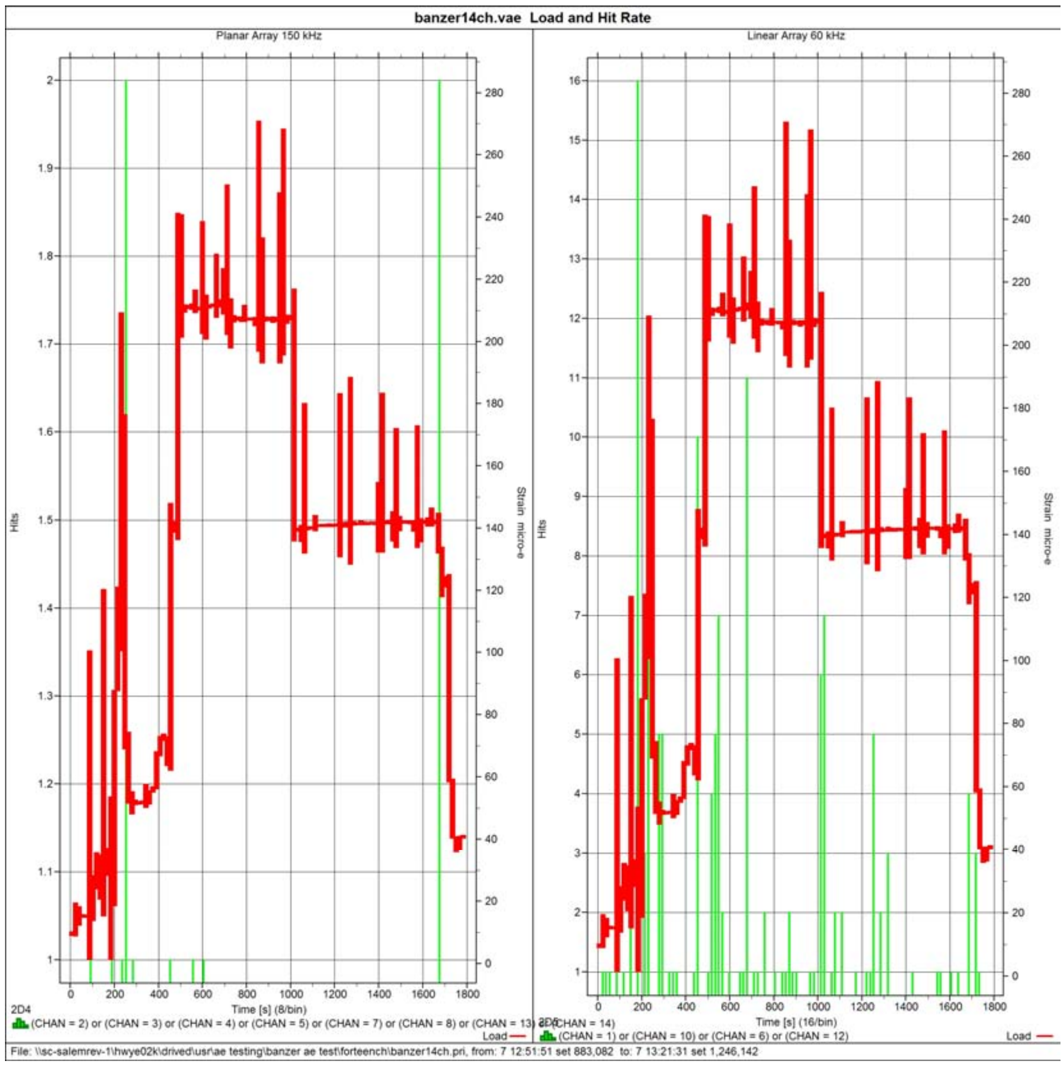

Figure 4.3.14 Load case 2 Differential hits distributed with rebar strain. Left plot are the planar array results and right plot are the linear array results.

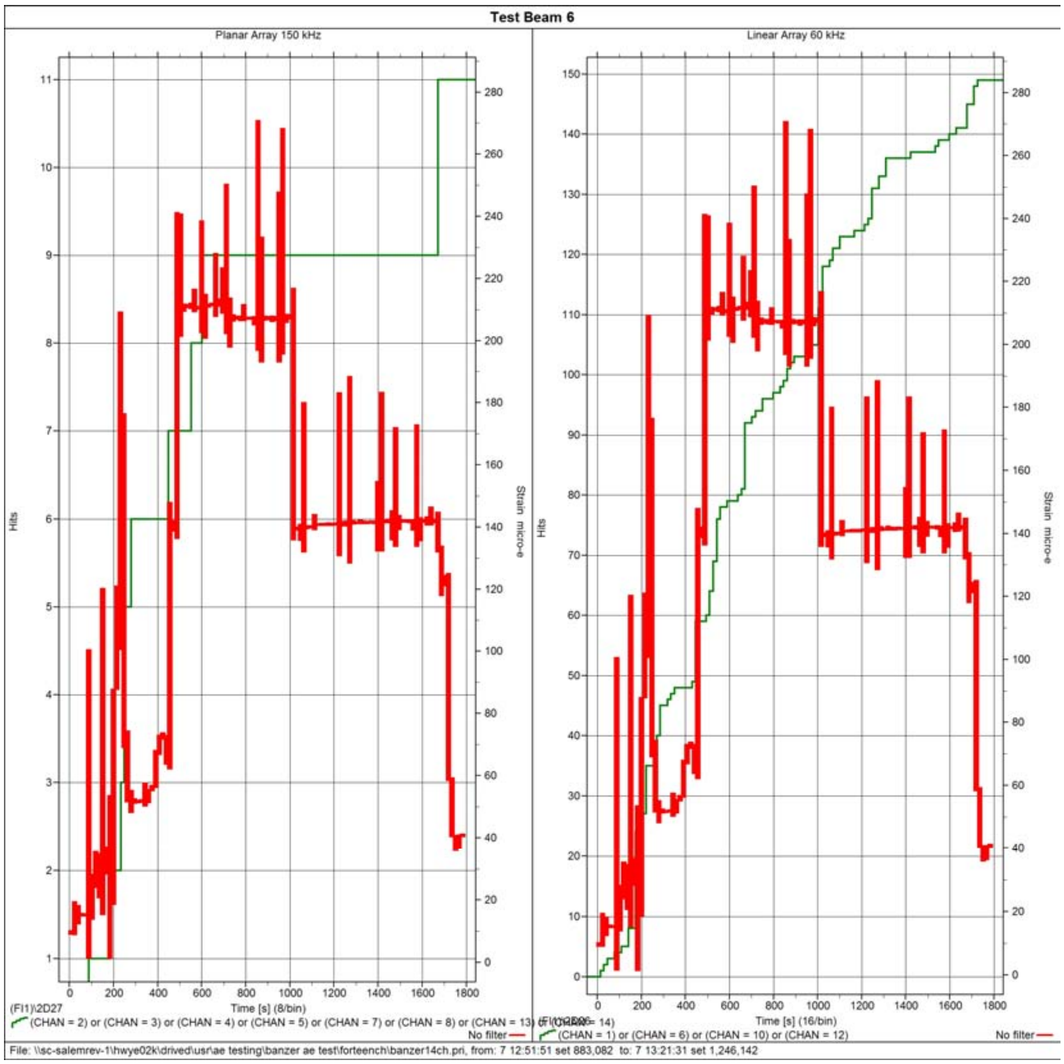

Figure 4.3.15 Load case 2 cumulative hit results distributed with rebar strain. Left plot shows planar array results and right plot show linear array results.

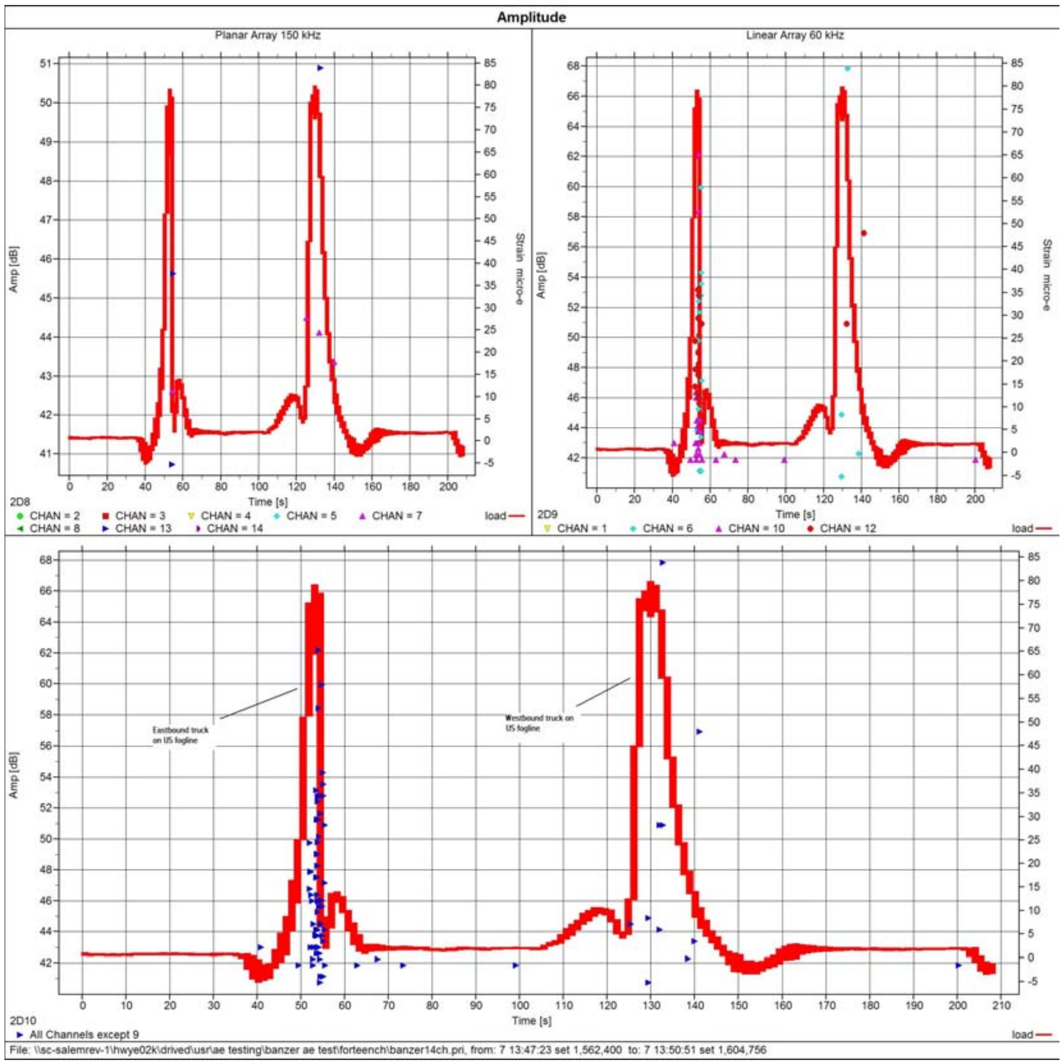

Figure 4.3.16 Load case 3 Peak amplitudes correlated with rebar strain , upper left plot shows planar array results and upper right plot shows linear array results and lower plot shows combined results. Load case 3 has truck 1 driving across the bridge in the US lane with outer wheel line on the lane fog line. Left strain excursion is for the Eastbound case and right strain excursion is for the Westbound case.

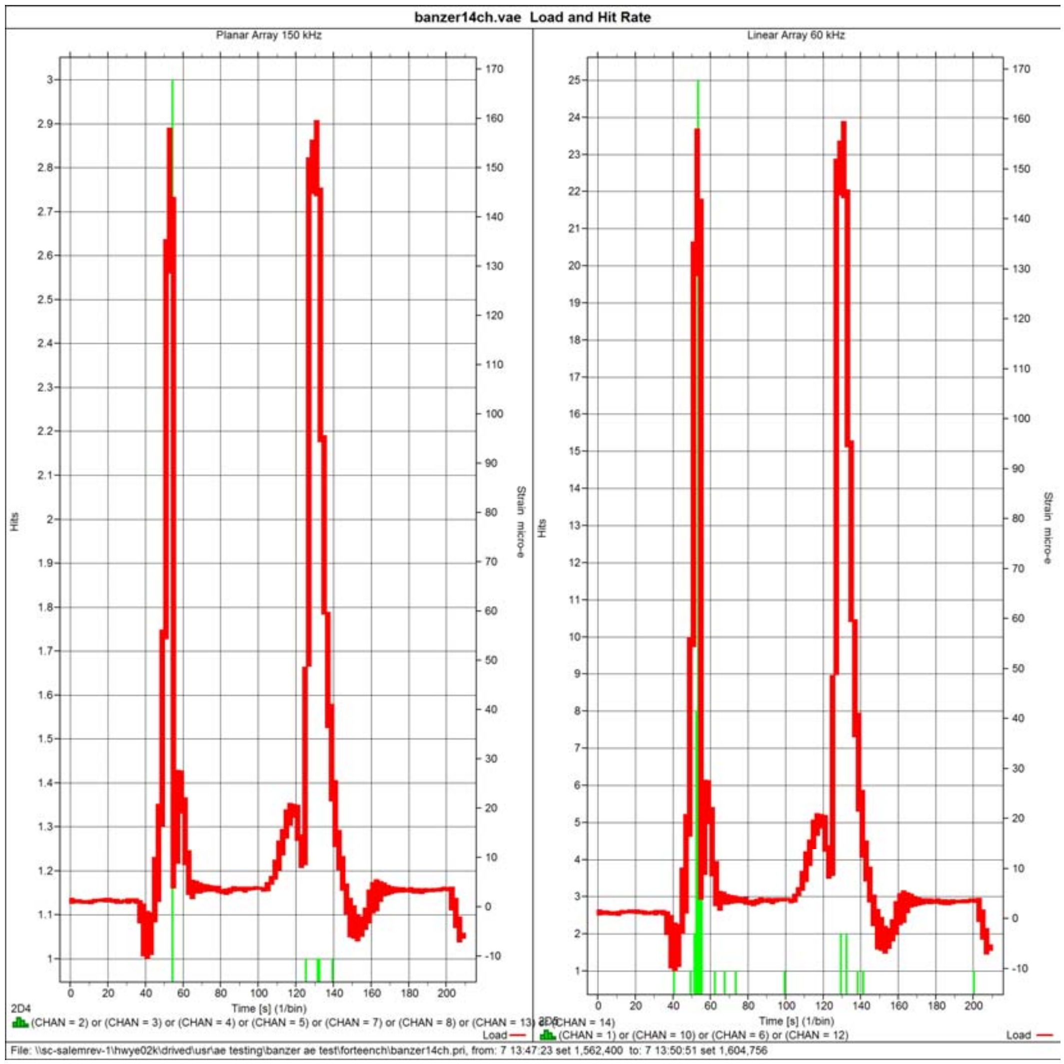

Figure 4.3.17 Load case 3 Differential hits distributed with rebar strain. Left plot are the planar array results and right plot are the linear array results.

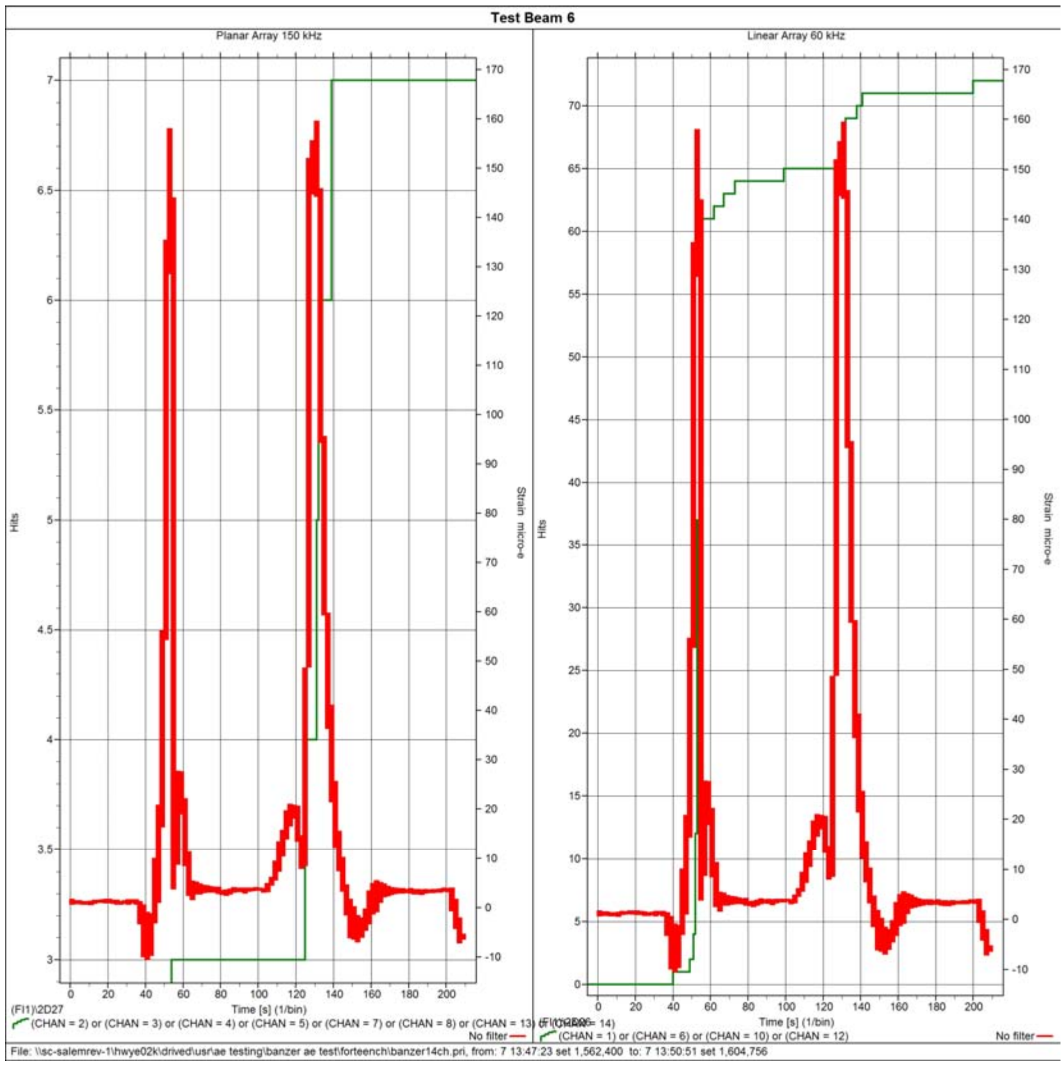

Figure 4.3.18 Load case 3 cumulative hit results distributed with rebar strain. Left plot shows planar array results and right plot show linear array results.

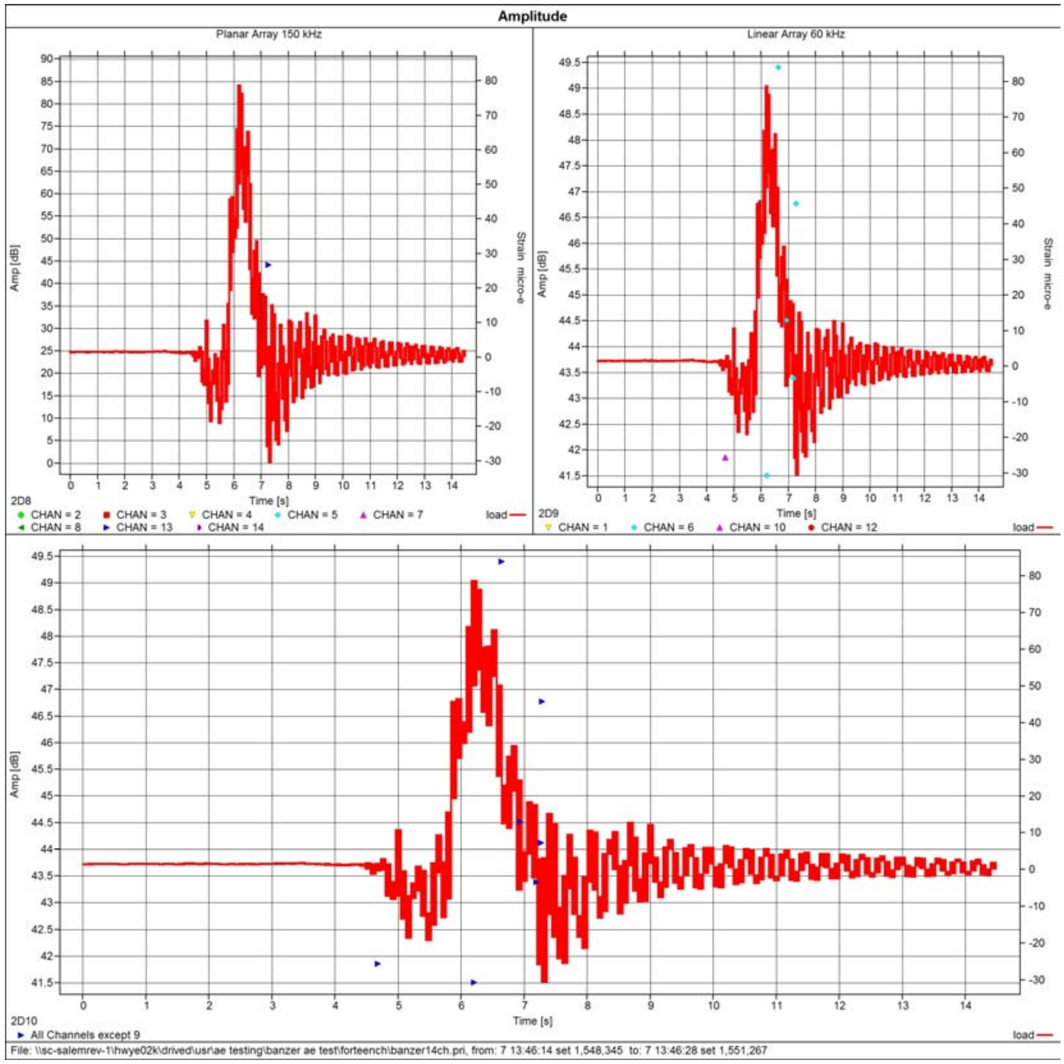

Figure 4.3.19 Load case 4 Peak amplitudes correlated with rebar strain , upper left plot shows planar array results and upper right plot shows linear array results and lower plot shows combined results. Load case 4 has truck 1 driving across the bridge in the DS lane heading Westbound at 40 mph.

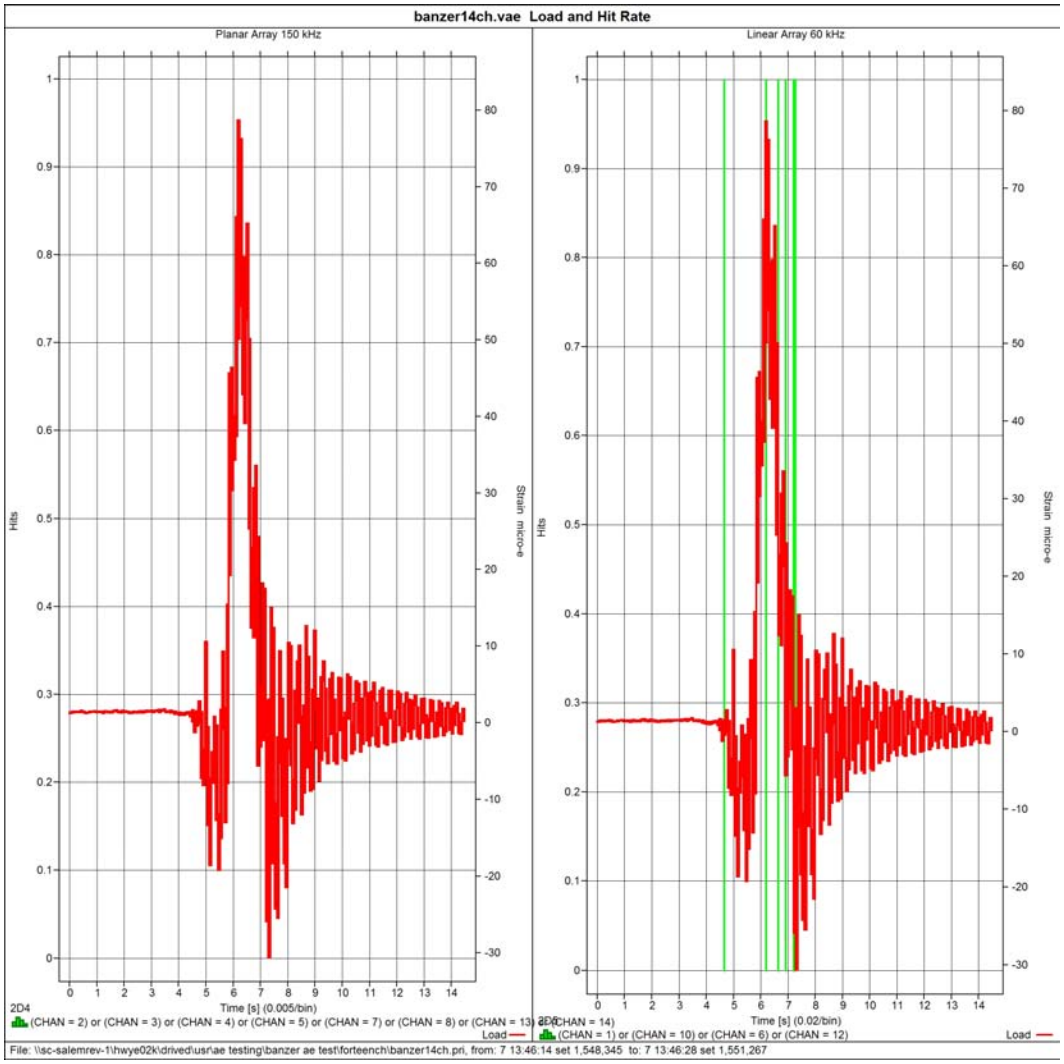

Figure 4.3.20 Load case 4 Differential hits distributed with rebar strain. Left plot are the planar array results and right plot are the linear array results.

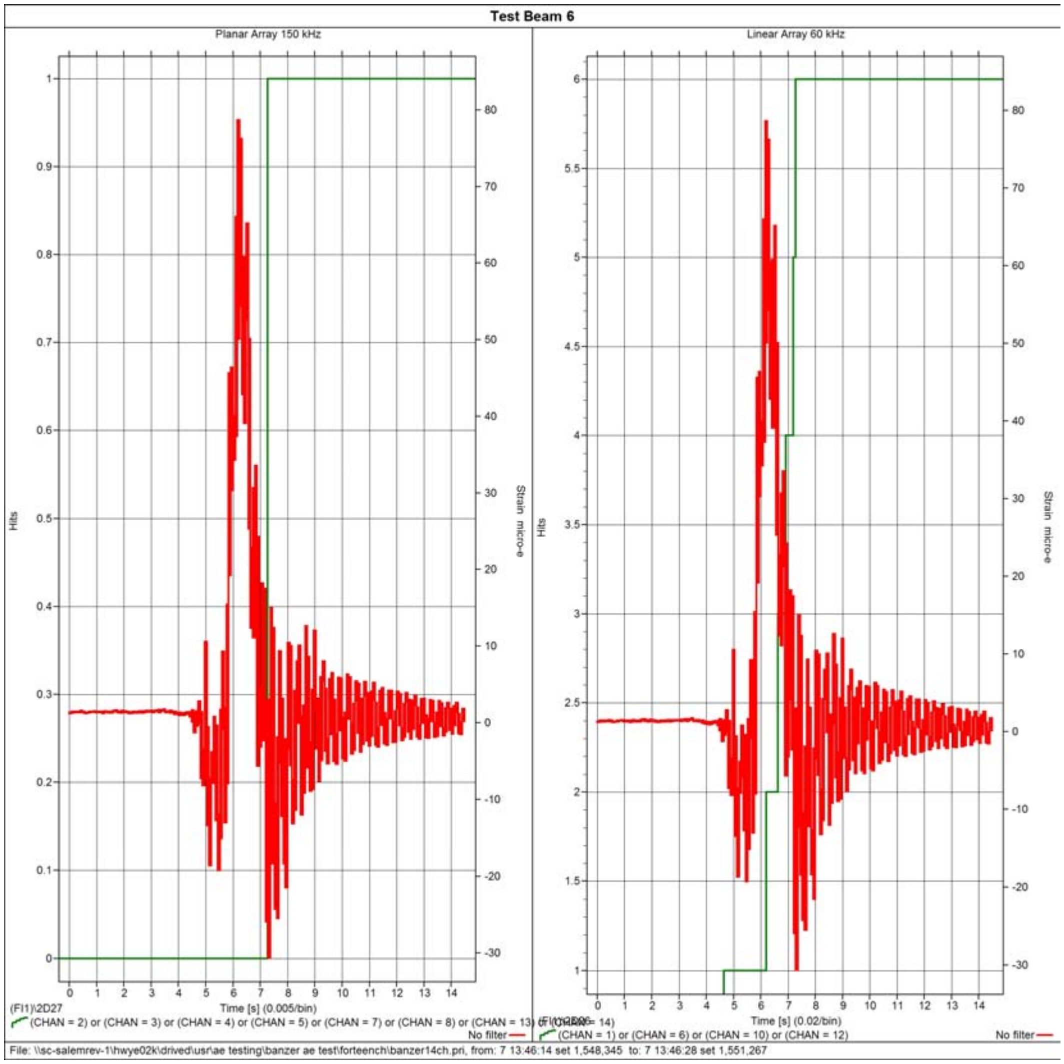

Figure 4.3.21 Load case 4 cumulative hit results distributed with rebar strain. Left plot shows planar array results and right plot show linear array results.

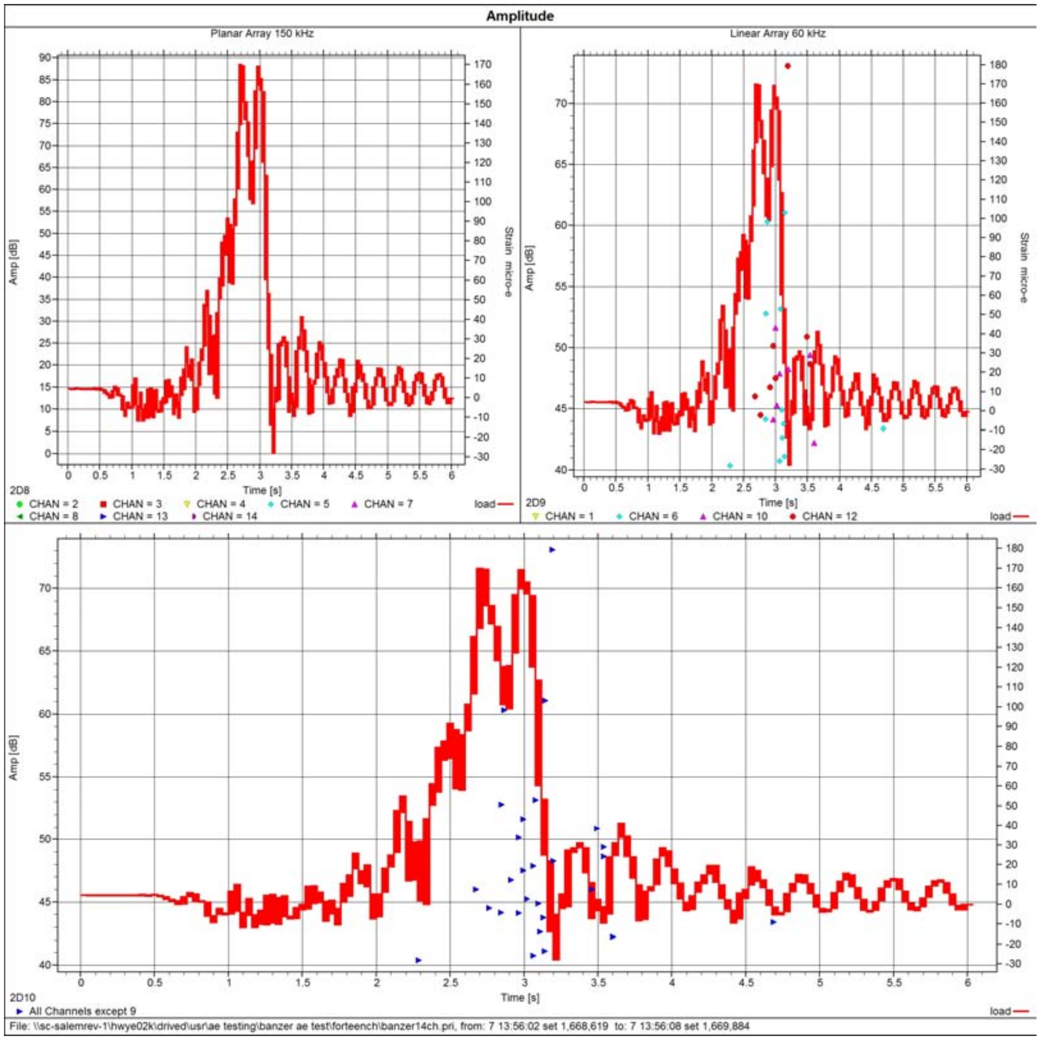

Figure 4.3.22 Load case 5 Peak amplitudes correlated with rebar strain , upper left plot shows planar array results and upper right plot shows linear array results and lower plot shows combined results. Load case 5 has truck 1 driving across the bridge in the US lane heading Eastbound at 40 mph.

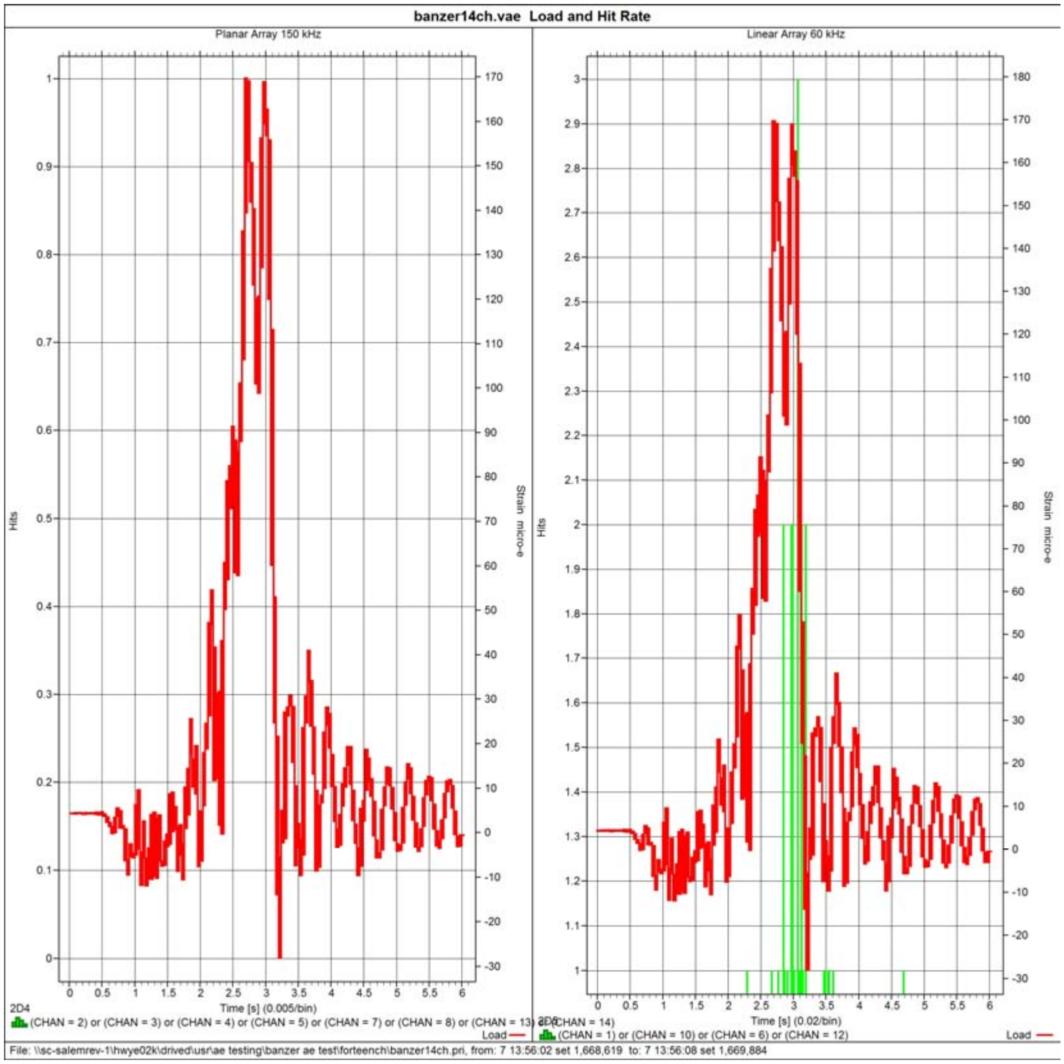

Figure 4.3.23 Load case 5 Differential hits distributed with rebar strain. Left plot are the planar array results and right plot are the linear array results.

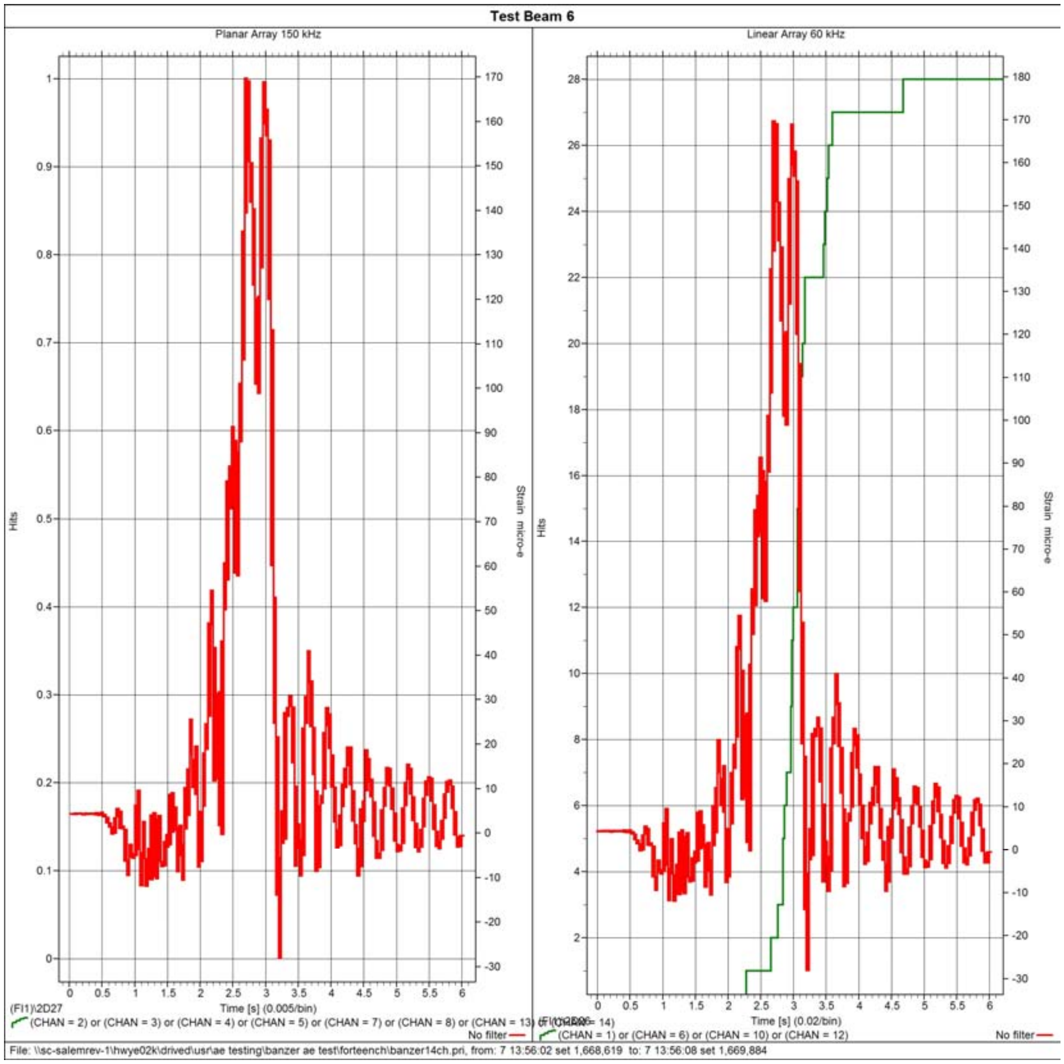

Figure 4.3.24 Load case 5 cumulative hit results distributed with rebar strain. Left plot shows planar array results and right plot show linear array results.

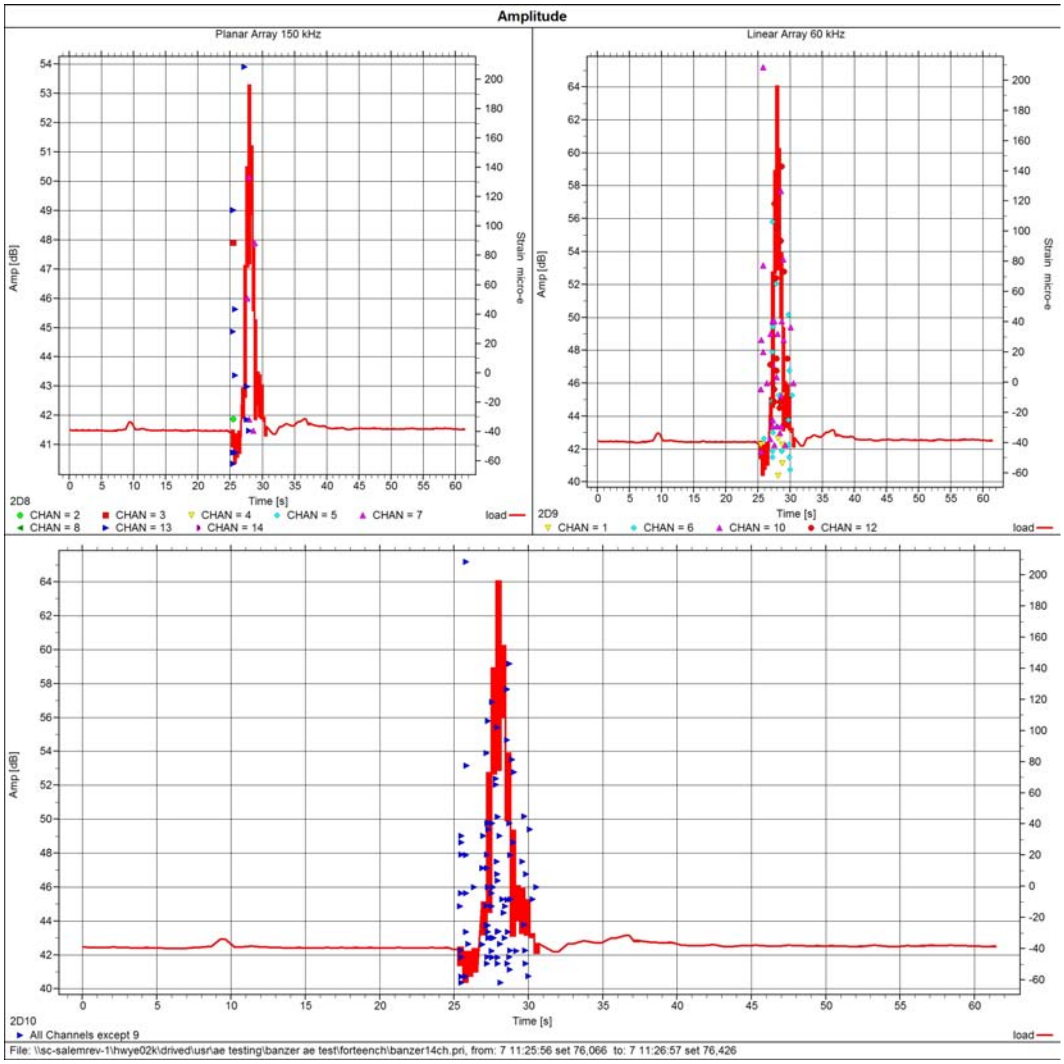

Figure 4..3.25 Load case 6A Peak amplitudes correlated with rebar strain , upper left plot shows planar array results and upper right plot shows linear array results and lower plot shows combined results. Load case 6A is an ambient truck crossing the bridge in the US lane heading Eastbound. This particular load produced the largest rebar strain range recorded.

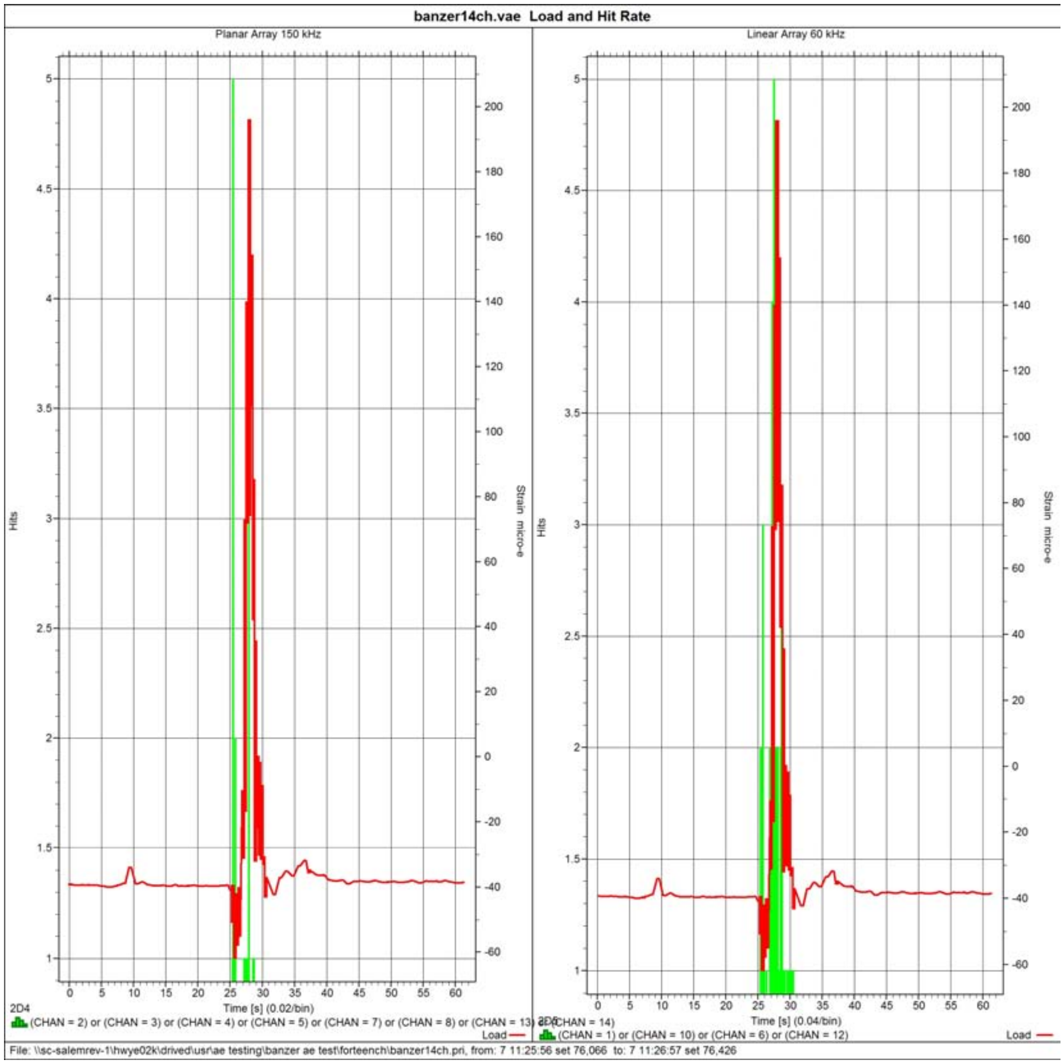

Figure 4.3.26 Load case 6A Differential hits distributed with rebar strain. Left plot are the planar array results and right plot are the linear array results.

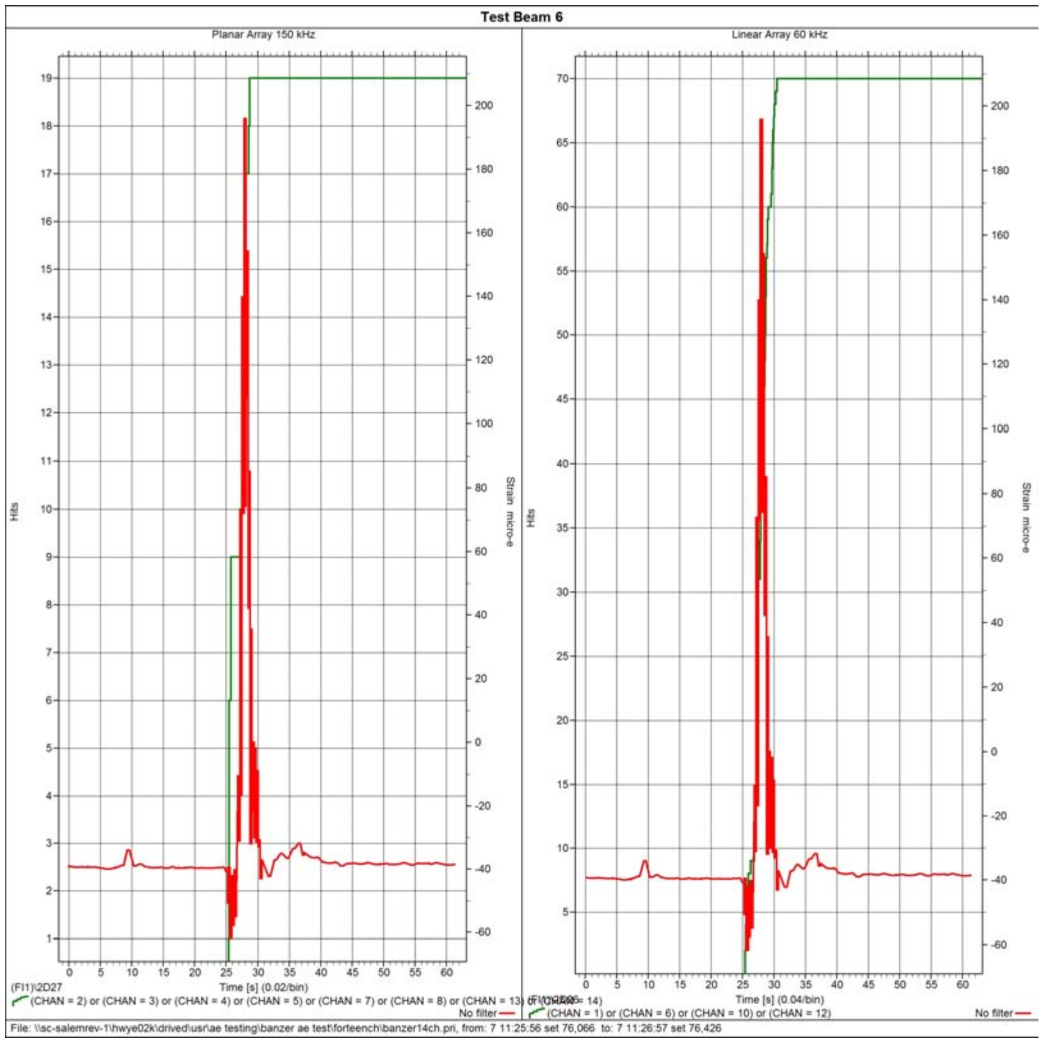

Figure 4.3.27 Load case 6A cumulative hit results distributed with rebar strain. Left plot shows planar array results and right plot show linear array results.

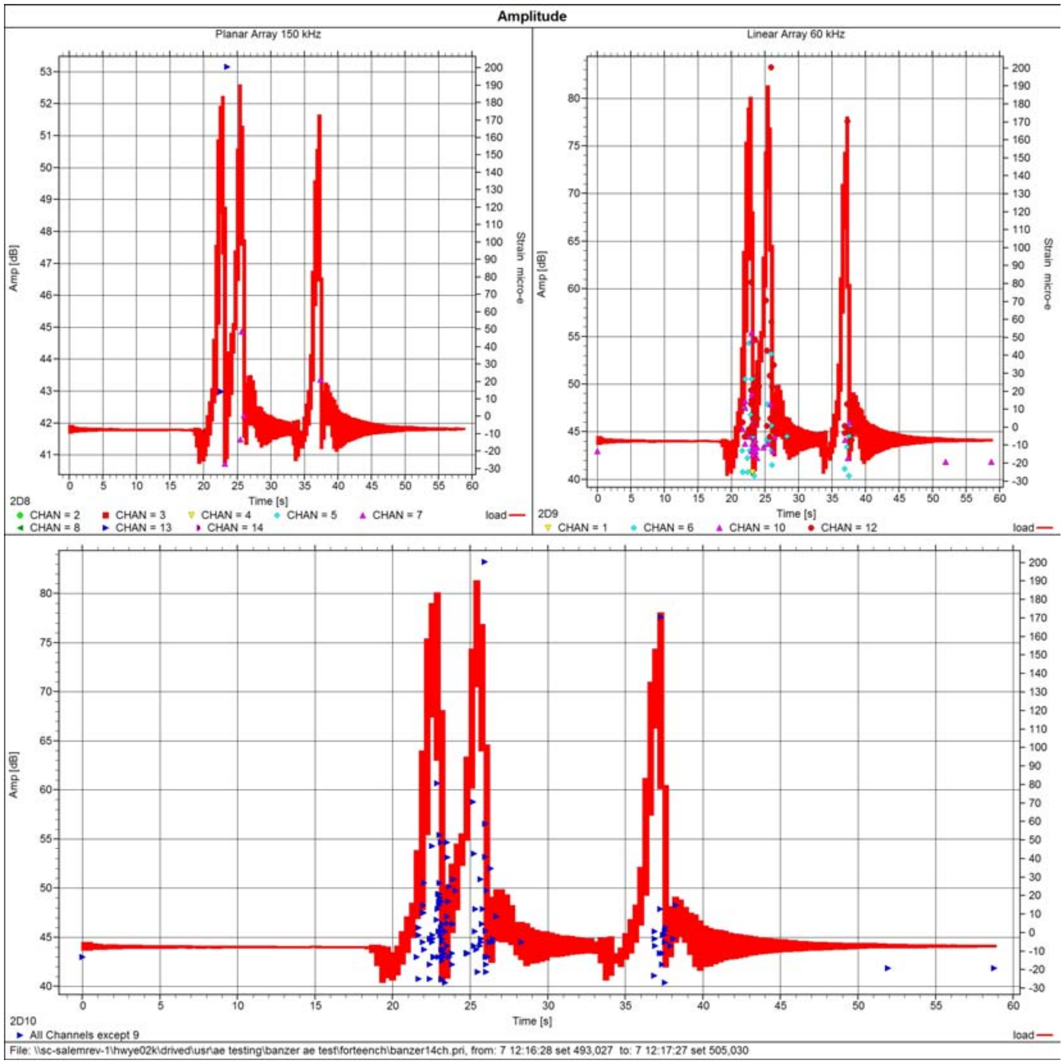

Figure 4.3.28 Load case 6B Peak amplitudes correlated with rebar strain , upper left plot shows planar array results and upper right plot shows linear array results and lower plot shows combined results. Load case 6B is an ambient truck crossing the bridge in the US lane heading Eastbound. This particular load produced the largest peak amplitudes recorded.

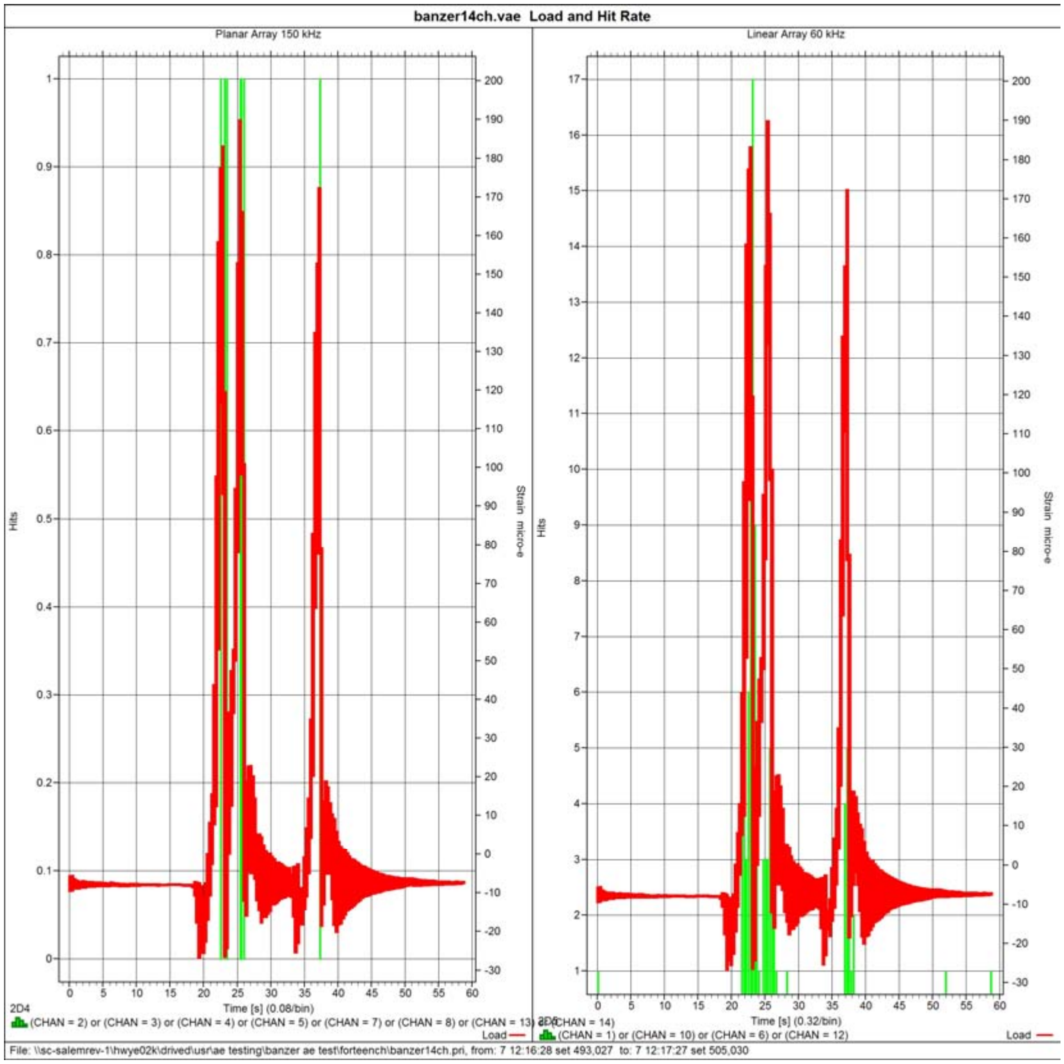

Figure 4.3.29 Load case 6B Differential hits distributed with rebar strain. Left plot are the planar array results and right plot are the linear array results.

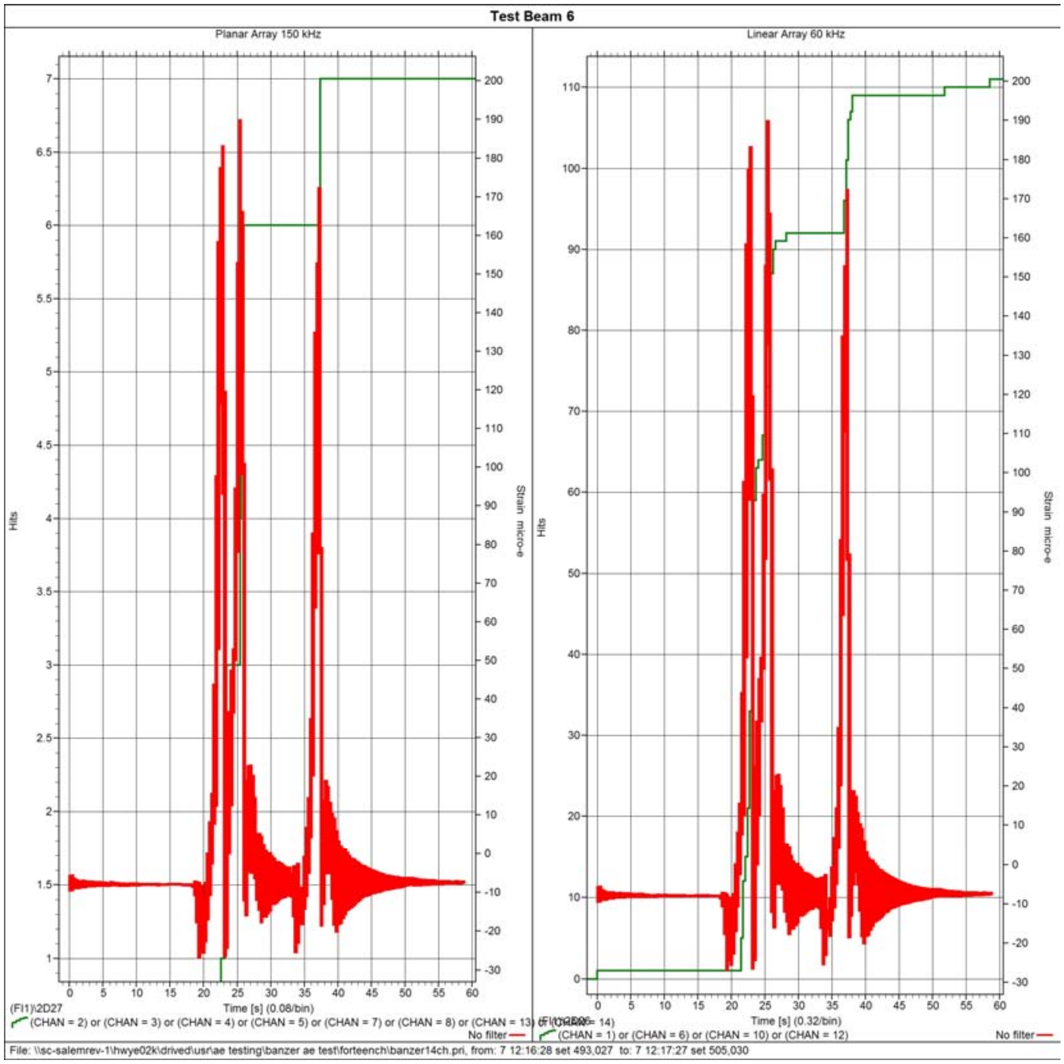

Figure 4.3.30 Load case 6B cumulative hit results distributed with rebar strain. Left plot shows planar array results and right plot show linear array results.

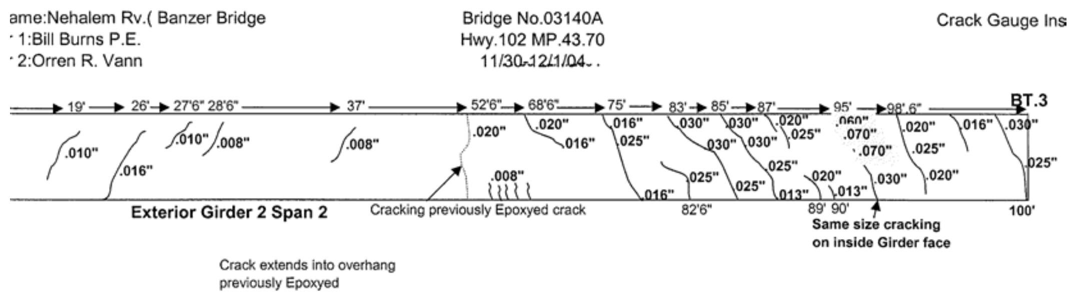

Figure 4.3.31 Crack diagram for upstream girder of span 2.

4.4 Acoustic Emissions Testing of the Pacific Highway Over Crossing of Main Street Bridge, ODOT Bridge # 07863

4.4.1 Background

Bridge number 07863 carries Interstate 5 Southbound over Main street in Cottage Grove, Oregon with an average daily traffic count exceeding 35,000 vehicles per day with 10% of this being heavy trucks. The superstructure is three spans continuous RCDG with span lengths of 65 feet for the exterior spans and 83 feet for the center span. The structure was constructed in 1954 and contains the vintage detailing and sections found in the bridges studied in SPR 350. A retrofit was applied in 1995 that added an exterior girder to each side and strengthened the bent caps. This retrofit was applied due to load ratings that indicated a lack of capacity for permit loads and minor to moderate diagonal tension cracking of the girders and bent caps. The structure now has six girder lines. Though scheduled for replacement this structure in the retrofitted condition has the structural capacity to safely carry all legal loads including permits as was found with a more recent load rating using the methods described in SPR 350. A special in-service structural load test was performed to validate the new load rating that justifies leaving the structure open to all legal loads prior to replacement. Acoustic Emissions testing was including in the structural testing.

4.4.2 Test Location Description

Figure 4.4.1 shows the plan and elevation drawing for the original construction of the bridge. Figure 4.4.2 shows the beam section details. Diagonal tension cracks can be found in all of the original girders in the high shear zones near each of the bents. The cracked sections nearest bent 2 in the center span were chosen for study because the size and shape of each cracked section crossed at least 2 stirrups for good strain measurements and the access was good.

4.4.3 Instrumentation for Structural Load Testing

CMOD transducers and rebar strain gages were attached to each of the four original girders at the section containing diagonal tension cracks which was approximately 13 feet into the center span from bent 2. This is the region of maximum shear stress, and each girder contained one main crack that was on average 0.025 to 0.03 inches wide which is considered to be an ODOT level 3 crack. The diagonal tension crack on Girder 5 was fitted with AE sensors in addition to the CMOD and strain. This girder carries the largest portion of the load from trucks which use the "B" or slow lane as required by law. Figure 3 shows a typical heavy truck passing over the bridge in the B lane. The trucks tractor rear wheels are approximately over the instrumented section of the center span.

An 8 channel Vallen AMSYS5 AE system was used to collect both AE and the parametric data from Girder 5 and a separate system collected data for the other girders as shown in Figure 4.4.4 located directly below the instrumented section. A total of 8 , 60 kHz resonant type AE sensors were deployed around the large crack on Girder 5. Figure 4.4.5 shows the sensors located on the West face and bottom flange. Figure 4.4.6 shows a close up view with channel numbers labeled. Notice the CMOD and strain gage which are also labeled. Figure 4.4.7 shows a close up view of the sensors on the East face with the bottom flange sensors. The diagonal tension crack, which goes through the thickness of the beam, is highlighted. The sensor array geometry was purposely applied in an unsymmetric manner around the crack in order to achieve the best possible event locations which is being investigated and developed under SPR 633. The 60 kHz AE sensors were chosen for maximum sensitivity based on experience from the previous field tests and the work covered in Appendix B and C.

Sensor locations are defined in Table 4.4.1. The origin is located at the intersection of Girder 5 and bent 2 on the South face of bent 2 and at the base of the girder mid-thickness. The X-axis runs with the girder line , the Y-axis runs vertical and the Z-axis in the thickness direction.

4.4.4 Test Procedures

The testing had two distinct activities, 1) Sensor coupling check and 2) Controlled structural loading which had a total of 11 test truck crossings. Because this structure carries traffic on the main North – South route in Oregon, stopping ambient traffic during controlled loadings was not possible. However by testing early on a Sunday morning a rolling blockade could be used to slow and hold back traffic while the test truck crossed the spans, thus preventing unknown loads during the controlled loading. The test truck could not come to a stop during the testing and thus allowing for static tests as was done in the previous two field tests. All test runs were done at either 10 mph or 50 mph. The test truck was an ODOT three axle 50,000 lb GVW sand truck that is very similar in weight and axle spacing to the dump trucks used in the previous field tests.

4.4.4.1 Calibration of AE sensors

Once the AE sensor were installed and the data system connected the acoustic coupling of each sensor was checked using the standard pencil break method as was performed on the previous field tests. All sensors met the acceptance criteria.

4.4.4.2 Test Run #1

The first test run placed the truck driving at 10 mph straddling the fog line in the B lane as shown in Figure 4.4.8. This position puts most of the load on girders 5 and 6 with most of it going to the exterior Girder 6.

4.4.4.3 Test Run #2

The second test run placed the truck driving at 10 mph with the passenger side wheels on the fog line of the B lane as shown in Figure 4.4.9. This was similar to the first test run but with more load being transferred to the test Girder 5.

4.4.4.4 Test Run #3

This test run placed the truck centered in the B lane, shown in Figure 4.4.10, which is where most trucks cross. This position puts the maximum load on to the test girder(5). The truck crossed at 10 mph.

4.4.4.5 Test Run #4

The truck is centered over the skip line which separates the B (truck) and A (passenger car) lanes traveling at 10 mph as shown in Figure 4.4.11. Girder 5 still carries a large portion of this load.

4.4.4.6 Test Run #5

This test run placed the truck centered in the A lane traveling at 10 mph as shown in Figure 4.4.12. Most of the load is on Girders 2 and 3.

4.4.4.7 Test Run #6

This test run placed the truck with the driver side wheels on the A lane fog line traveling at 10 mph as shown in Figure 4.4.13. This places the least amount of load on Girder 5.

4.4.4.8 Test Run #7

This test run placed the truck centered in the B lane traveling at 50 mph as shown in Figure 4.4.14. It was intended to be a more dynamic version of Test Run # 3.

4.4.4.9 Test Run #8

This test run place the truck centered in the A lane traveling at 50 mph as shown in Figure 4.4.15 producing a more dynamic version of Test Run # 5.

4.4.4.10 Test Run #9

This was a repeat of Test Run # 7.

4.4.4.11 Test Run #10

This was a repeat of Test Run #8

4.4.4.12 Test Run #11

This was a second repeat of Test Run #7.

4.4.5 Results

4.4.5.1 Test Run #1

Peak amplitudes for each AE channel are correlated with rebar strain as shown in Figure 4.4.16. The cumulative hits are shown in Figure 4.4.17. The Maximum Historic Index and Severity are shown in Figure 4.4.18 and 4.4.19. The resulting Intensity plot is shown in Figure 4.4.20. The rebar strain goes into compression relative to the dead load condition as the truck crosses the approach span indicating negative bending. As the truck enters the instrumented center span and crosses the cracked section, the rebar strain rapidly goes into tension, and both the passing of the front and rear axles can be seen. Keep in mind the dead load super imposes a tensile strain of approximately 300 $\mu\varepsilon$ which is not shown in the plots. As the truck crosses the center span the live load tensile stress in the rebar drops back down to the zero or dead load level. Some small amplitude oscillations from vibration of the structure are then seen. A summary of the peak responses of the parametric and AE results are listed below.

Parametric results

Peak rebar strain range:	80 $\mu\varepsilon$ (2,320 psi)
Peak CMOD range:	7.0×10^{-5} inches

AE results

	All Channels
Load hits:	150
Unload hits:	293
Peak hit amplitude (dB):	81

Calm ratio:	1.95
Maximum Historic Index:	2.08
Maximum Severity:	215

4.4.5.2 Test Run #2

Peak amplitudes for each AE channel are correlated with rebar strain as shown in Figure 4.4.21. The cumulative hits are shown in Figure 4.4.22. The Maximum Historic Index and Severity are shown in Figure 4.4.23 and 4.4.24. The resulting Intensity plot is shown in Figure 4.425. This test run imparted 10% more load onto the test girder then the previous test run. A summary of the peak responses of the parametric and AE results are listed below.

Parametric results

Peak rebar strain range:	88 με (2,552 psi)
Peak CMOD range:	6.0×10^{-5} inches

AE results

	All Channels
Load hits:	240
Unload hits:	300
Peak hit amplitude (dB):	83
Calm ratio:	1.25
Maximum Historic Index:	2.40
Maximum Severity:	268

4.4.5.3 Test Run #3

Peak amplitudes for each AE channel are correlated with rebar strain as shown in Figure 4.4.26. The cumulative hits are shown in Figure 4.4.27. The Maximum Historic Index and Severity are shown in Figure 4.4.28 and 4.4.29. The resulting Intensity plot is shown in Figure 4.4.30. This test run put the maximum load onto the test girder. A summary of the peak responses of the parametric and AE results are listed below. Note that even though the peak rebar strain was nearly 50% larger then the previous test run, the CMOD range is the same showing that rebar strain is a much more sensitive parametric input to correlate load then CMOD.

Parametric results

Peak rebar strain range:	130 $\mu\varepsilon$ (3,770 psi)
Peak CMOD range:	6.0×10^{-5} inches

AE results

	All Channels
Load hits:	300
Unload hits:	475
Peak hit amplitude (dB):	84
Calm ratio:	1.58
Maximum Historic Index:	2.76
Maximum Severity:	152

4.4.5.4 Test Run #4

Peak amplitudes for each AE channel are correlated with rebar strain as shown in Figure 4.4.31. The cumulative hits are shown in Figure 4.4.32. The Maximum Historic Index and Severity are shown in Figure 4.4.33 and 4.4.34. The resulting Intensity plot is shown in Figure 4.4.35. This test run imparted a slightly lower load onto the test girder then the previous test run. A summary of the peak responses of the parametric and AE results are listed below.

Parametric results

Peak rebar strain range: 115 με (3,335 psi)

Peak CMOD range: 6.0×10^{-5} inches

AE results

	All Channels
Load hits:	300
Unload hits:	340
Peak hit amplitude (dB):	80
Calm ratio:	1.13
Maximum Historic Index:	2.29
Maximum Severity:	104

4.4.5.5 Test Run #5

Peak amplitudes for each AE channel are correlated with rebar strain as shown in Figure 4.4.36. The cumulative hits are shown in Figure 4.4.37. The minimum number of hits (200) to calculate the AE based damage parameters (Calm ratio, Historic Index and Severity) were not produced from this test run due to the low magnitude of the load on the test girder. A summary of the peak responses of the parametric and AE results are listed below.

Parametric results

Peak rebar strain range: 25 με (725 psi)

Peak CMOD range: 3.0×10^{-5} inches

AE results

	All Channels
Load hits:	46
Unload hits:	96
Peak hit amplitude (dB):	66
Calm ratio:	N/A
Maximum Historic Index:	N/A
Maximum Severity:	N/A

4.4.5.6 Test Run #6

Peak amplitudes for each AE channel are correlated with rebar strain as shown in Figure 4.4.38. The cumulative hits are shown in Figure 4.4.39. The minimum number of hits (200) to calculate the AE based damage parameters (Calm ratio, Historic Index and Severity) were not produced from this test run due to the low magnitude of the load on the test girder. A summary of the peak responses of the parametric and AE results are listed below.

Parametric results

Peak rebar strain range:	20 $\mu\varepsilon$ (580 psi)
Peak CMOD range:	4.0 x 10^{-5} inches

AE results

	All Channels
Load hits:	45
Unload hits:	72
Peak hit amplitude (dB):	57
Calm ratio:	N/A
Maximum Historic Index:	N/A
Maximum Severity:	N/A

4.4.5.7 Test Run #7

Peak amplitudes for each AE channel are correlated with rebar strain as shown in Figure 4.4.40. The cumulative hits are shown in Figure 4.4.41. The Maximum Historic Index and Severity are shown in Figure 4.4.42 and 4.4.43. The resulting Intensity plot is shown in Figure 4.4.44. This test run was similar to Test Run #3 with the exception of truck speed which was 5 times faster. Peak strain, CMOD and AE hits and amplitudes were found to be slightly lower when compared to the slower test run. A summary of the peak responses of the parametric and AE results are listed below.

Parametric results

Peak rebar strain range:	100 $\mu\varepsilon$ (2,900 psi)
Peak CMOD range:	8.0 x 10^{-5} inches

AE results

	All Channels
Load hits:	150
Unload hits:	340
Peak hit amplitude (dB):	74
Calm ratio:	2.2
Maximum Historic Index:	2.29
Maximum Severity:	196

4.4.5.8 Test Run #8

Peak amplitudes for each AE channel are correlated with rebar strain as shown in Figure 4.4.45. The cumulative hits are shown in Figure 4.4.46. The minimum number of hits (200) to calculate the AE based damage parameters (Calm ratio, Historic Index and Severity) were not produced from this test run due to the low magnitude of the load on the test girder. A summary of the peak responses of the parametric and AE results are listed below.

Parametric results

Peak rebar strain range:	28 $\mu\varepsilon$ (812 psi)
Peak CMOD range:	4.0 x 10^{-5} inches

AE results

	All Channels
Load hits:	57
Unload hits:	125
Peak hit amplitude (dB):	64
Calm ratio:	N/A
Maximum Historic Index:	N/A
Maximum Severity:	N/A

4.4.5.9 Test Run #9

This test run was a repeat of Test Run #7. The parametric responses were nearly identical as were the peak amplitudes and number of AE hits. The Calm ratio was also nearly identical but the Historic Index showed a 10% increase and the Severity showed a 50% decrease compared to Test Run #7. A summary of the peak responses of the parametric and AE results are listed below.

Parametric results

Peak rebar strain range: 100 $\mu\varepsilon$ (2900 psi)
Peak CMOD range: 9.0×10^{-5} inches

AE results

	All Channels
Load hits:	150
Unload hits:	350
Peak hit amplitude (dB):	77
Calm ratio:	2.33
Maximum Historic Index:	2.5
Maximum Severity:	95

4.4.5.10 Test Run #10

This test run was a repeat of Test Run #8. The parametric responses were very similar as were the peak amplitudes. The number of AE hits was higher then Test Run #8 and provided close to the minimum 200 hits needed to calculate the Calm Ratio which showed an increase. The results from the Historic Index and Severity were deemed unreliable due to the lack of AE hits. A summary of the peak responses of the parametric and AE results are listed below.

Parametric results

Peak rebar strain range: 24 με (696 psi)
Peak CMOD range: 4.0×10^{-5} inches

AE results

	All Channels
Load hits:	64
Unload hits:	196
Peak hit amplitude (dB):	62
Calm ratio:	3.06
Maximum Historic Index:	N/A
Maximum Severity:	N/A

4.4.5.11 Test Run #11

This test run was a second repeat of Test Run #7. The parametric responses were nearly identical as were the peak amplitudes and number of AE hits. The Calm ratio was also similar as was the Historic Index and Severity. A summary of the peak responses of the parametric and AE results are listed below.

Parametric results

Peak rebar strain range: 100 με (2900 psi)

Peak CMOD range: 8.0×10^{-5} inches

AE results

	All Channels
Load hits:	150
Unload hits:	370
Peak hit amplitude (dB):	75
Calm ratio:	2.47
Maximum Historic Index:	2.33
Maximum Severity:	223

4.4.6 Discussion of Results

The test procedures, AE and parametric transducer selection and installation used for this test were greatly improved on this test compared to the two previous tests based on those experiences. Even though static testing was not available due to traffic restrictions, the loading protocol systematically applied a wide range of common in-service loading conditions by driving the test truck in the various lanes which imparted different loads on the test girder due to lateral load distribution. The test truck weight and axle configuration, though not as severe as some of the heavier ambient loads, produced adequate loads to measure both the structural and AE responses. Ambient loads and the AE responses were not covered in this report, but 6 days of ambient traffic monitoring with the structural test equipment showed a peak rebar stress of 5200 psi which is not much greater then the maximum stress of 3770 psi measured from Test Run #3. It should be pointed out that 6 days of continuous strain data on a structure of such high use is very representative of service conditions.

Using rebar strain as the primary parametric input for identifying the loading sequence and correlating AE data was very successful as it was during the testing of the Banzer bridge in Section 4.3. Selecting the 60 kHz resonant type AE sensor also proved to be a good choice due to their high sensitivity. Even though the structure does not experience loads in-service that are as severe as those tested in the laboratory, adequate AE data was collected for all but the lightest load cases.

The Calm Ratios measured were found to be significantly higher than the two previous bridge tests with an average value of 1.9 and a standard deviation of 0.5. Previous testing yielded Calm Ratios between 0.5 and 1.0 for data sets with 200 or more hits. Figure 4.4.47 shows the summary of Calm Ratio measurements for this test. Defining the load and unload portions of a test truck passing is not as straight forward as the loading used in the laboratory or even static loading of in-service bridges. For this test and the two previous field tests, loading was defined up to the peak rebar strain or CMOD, and the unloading was defined to occur after the peak. At least consistency was applied so the results between field tests should be very comparable to each other and reasonably comparable to the laboratory data.

Adequate AE data were collected for most of the test runs to calculate reasonable Historic Index and Severity responses. A summary Intensity plot is shown in Figure 4.4.48. As discussed in Chapter 3 developing grading regions that apply to conventionally reinforced concrete bridge girders is still under development but this data will be very useful for achieving that goal, especially for defining the lower end of the damage chart. In general both the Historic Index and Severity increased with increasing load on the test girder.

In addition to the structural and AE parameters measured during this test, AE event locations within the test girder have been calculated as part of SPR 633. This test utilized the latest AE sensor array deployment and P-wave detection methods to calculate 3 dimensional locations of significant AE events during the testing.

4.4.7 Conclusions

Based on the visual inspection of the girders the diagonal tension cracks can be categorized as ODOT level 3 cracks, barely meeting the minimum crack width criteria of greater then 0.025 inches. The Calm Ratio results indicate a fairly high level of accumulated damage with an average value of 1.9 which is at the high end of Level 3 response found in laboratory test results of Chapter 3. Prior to retrofitting these girders likely carried relatively high loads compared to their capacity, especially Girder 5. After the retrofit the capacity was significantly increased and both the ambient and controlled loads are easily supported by the bridge. Qualitatively the Historic Index and Severity support the conclusion of the structural test that service loads are generally not damaging to the girders. The sensitivity of the AE system was great enough to easily detect the crossing of a small passenger car. If an especially heavy truck were to cross this bridge and impart significant damage to the girders, a SHM system that incorporated the equipment and deployment used for this test would very likely detect the event with great reliability.

Table 4.4.1 AE sensor locations

Girder face	Ch#	Sensor type	X (inch)	Y (inch)	Z (inch)
West	1	60 kHz	128.9	51	8.3
West	2	60 kHz	132.7	34.5	8.2
West	3	60 kHz	113.5	30.5	8.7
Bottom	4	60 kHz	142	14.5	3.0
Bottom	5	60 kHz	108.4	11.2	-4.1
East	6	60 kHz	138.8	49.3	-8.1
East	7	60 kHz	127.7	24	-8.4
East	8	60 kHz	119.5	42.5	-8.6

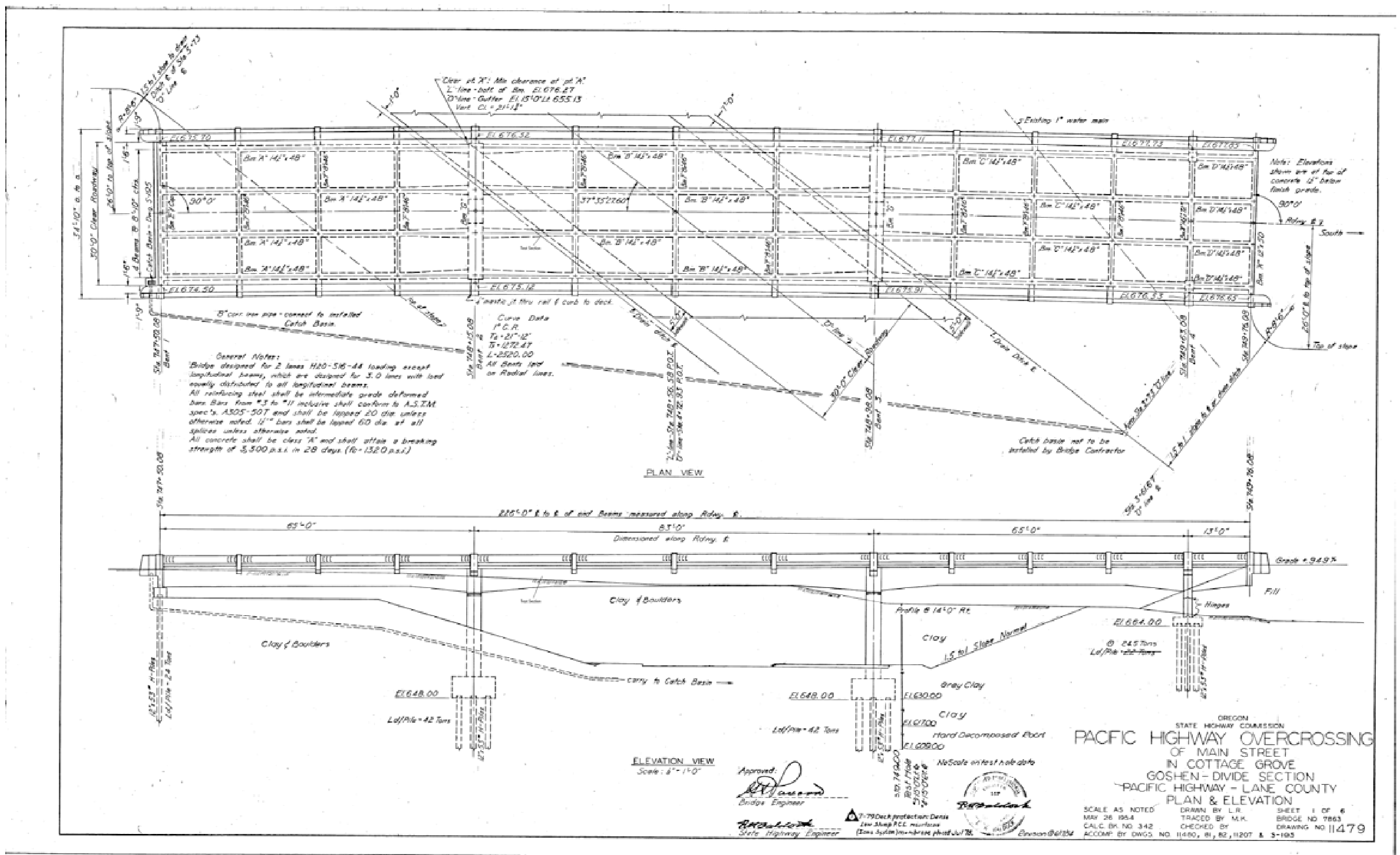

Figure 4.4.1 Plan and elevation view of Br. 07863.

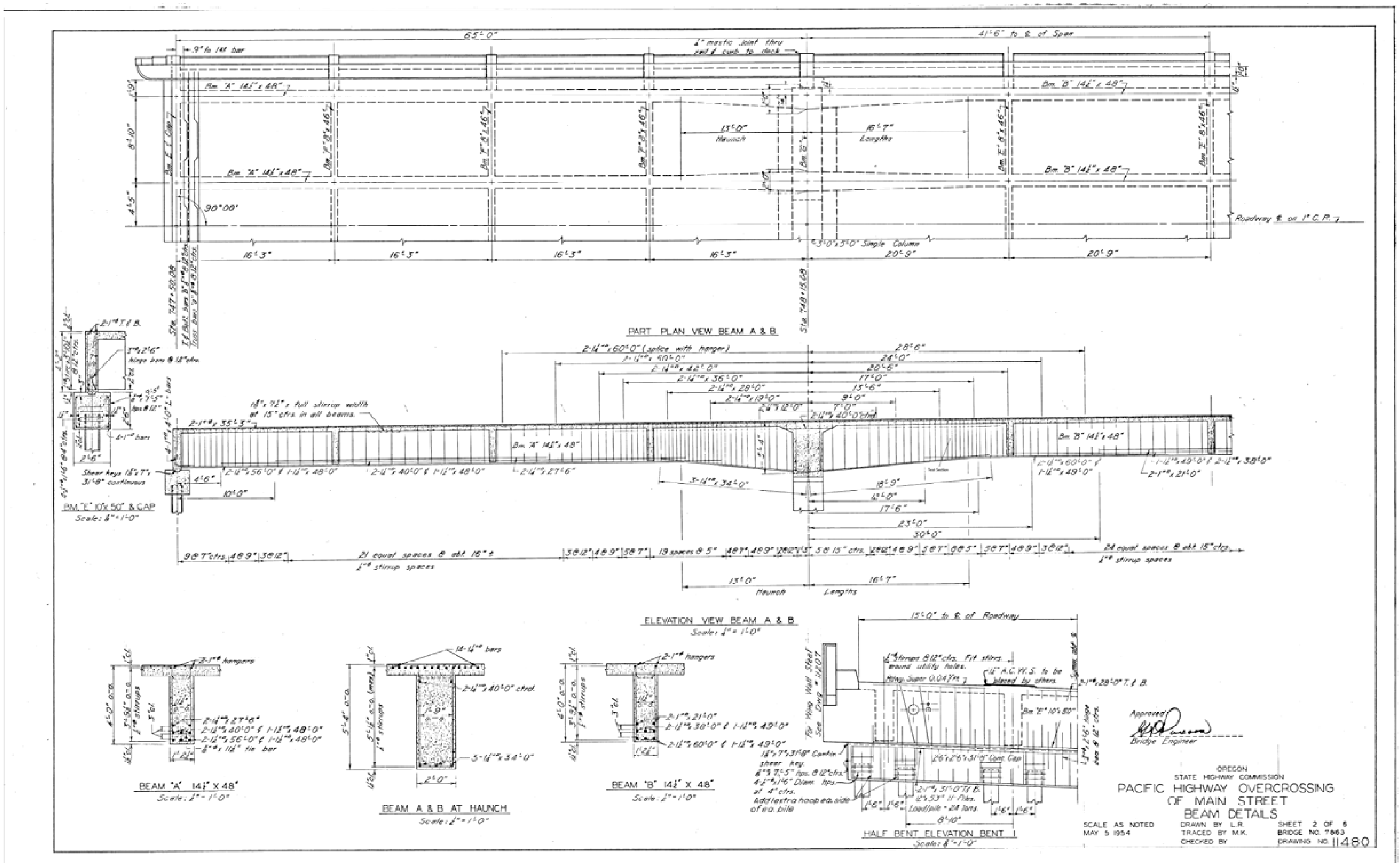

Figure 4.4.2 Beam and bent detail drawing for Br. 07863.

Figure 4.4.3 Photograph of Br. 07863 with ambient loading.

Figure 4.4.4 Data acquisition systems and setup.

Figure 4.4.5 AE sensor deployment on West face of Girder 4 centered around a shear crack.

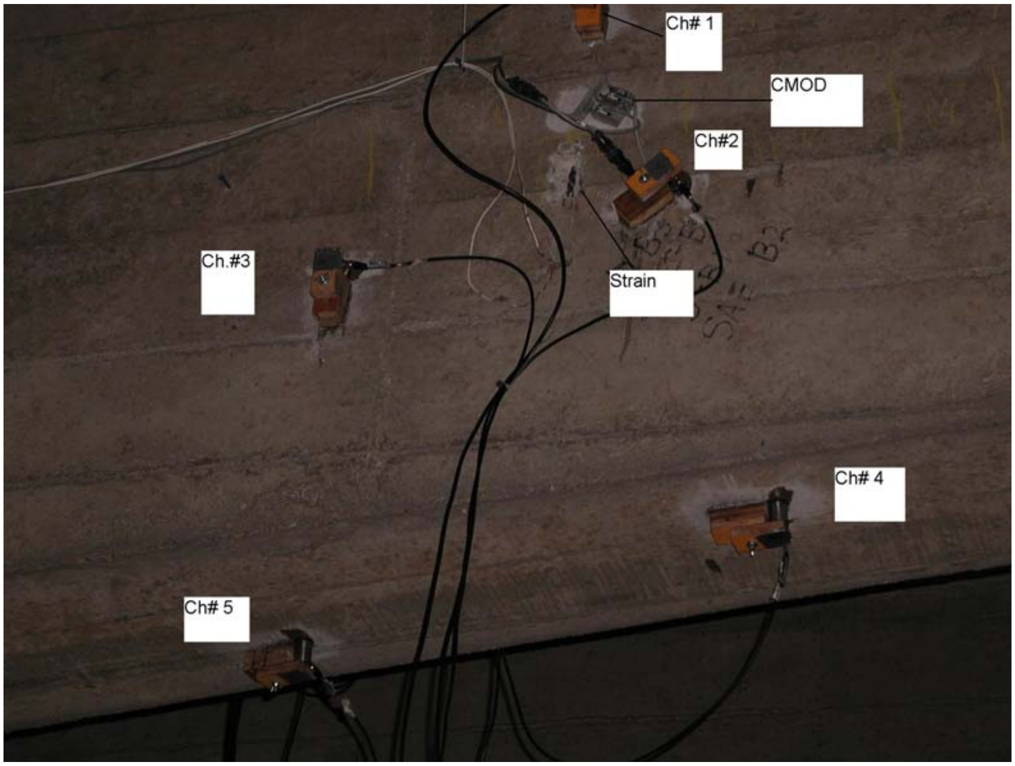

Figure 4.4. 6 Close up view of AE and parametric sensors around shear crack on West face of girder 4.

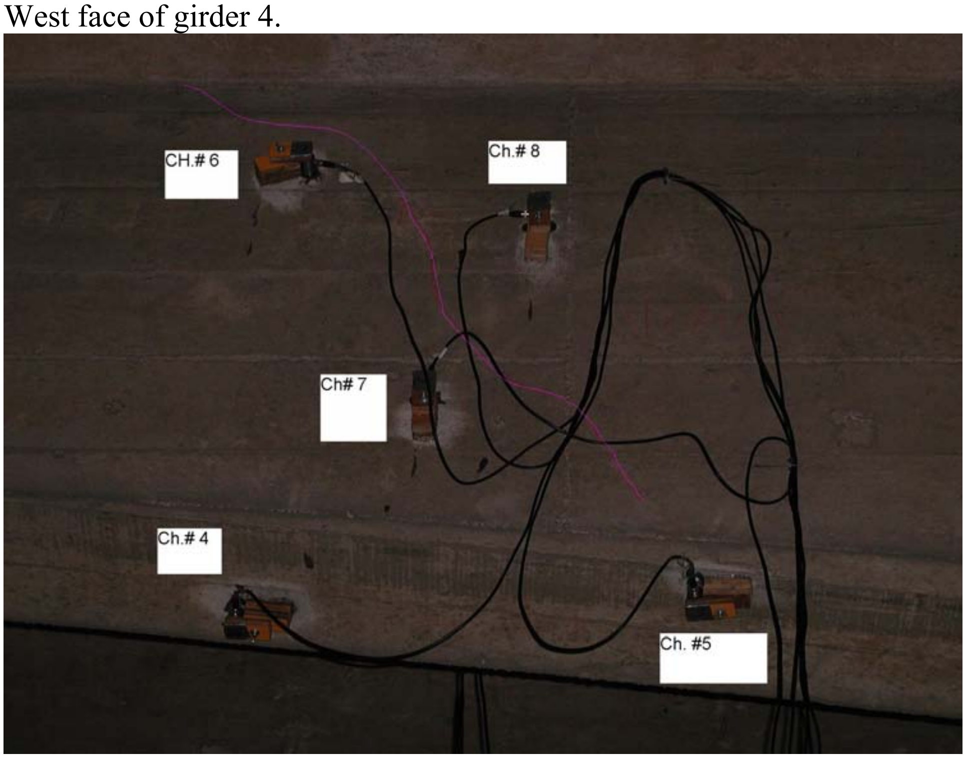

Figure 4.4.7 AE sensor deployment on East face of Girder 4 centered around a shear crack.

Figure 4.4.8 Test Run #1 Passenger wheel over B-lane fog line at 10 mph.

Figure 4.4.9 Test Run #2 Passenger wheel on B-lane fog line at 10 mph.

Figure 4.4.10 Test Run #3 Truck centered in B-lane at 10 mph.

Figure 4.4.11 Test Run #4 Truck centered over skip line at 10 mph.

Figure 4.4.12 Test Run #5 Truck centered in A-lane at 10 mph.

Figure 4.4.13 Test Run #6 Driver wheels on A-lane fog ling at 10 mph.

Figure 4.4.14 Test Run #7 Truck centered in B-lane at 50 mph.

Figure 4.4.15 Test Run #8 Truck centered in A-lane at 50 mph.

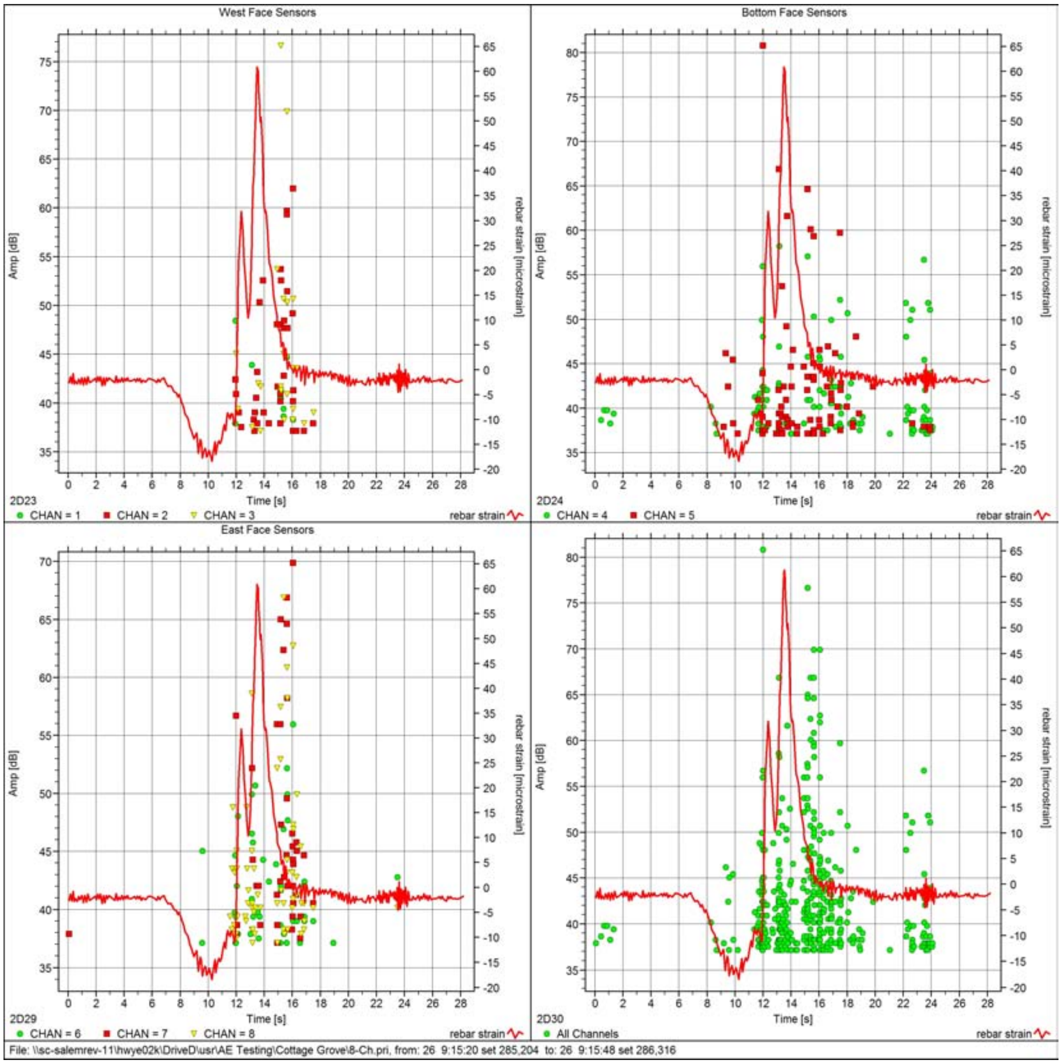

Figure 4.4.16 Peak amplitude correlated with rebar strain for Test Run #1.

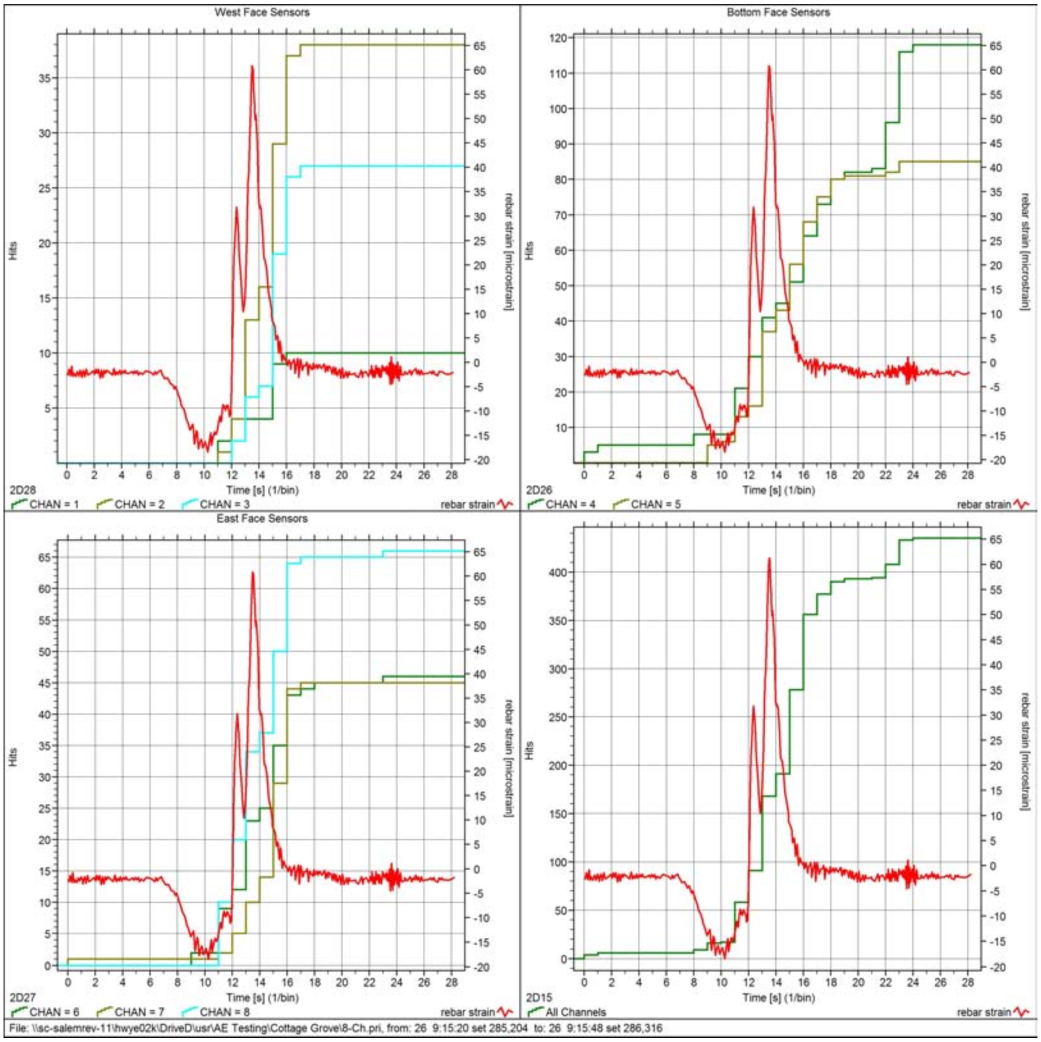

Figure 4.4.17 Cumulative hits correlated with rebar strain for Test Run #1.

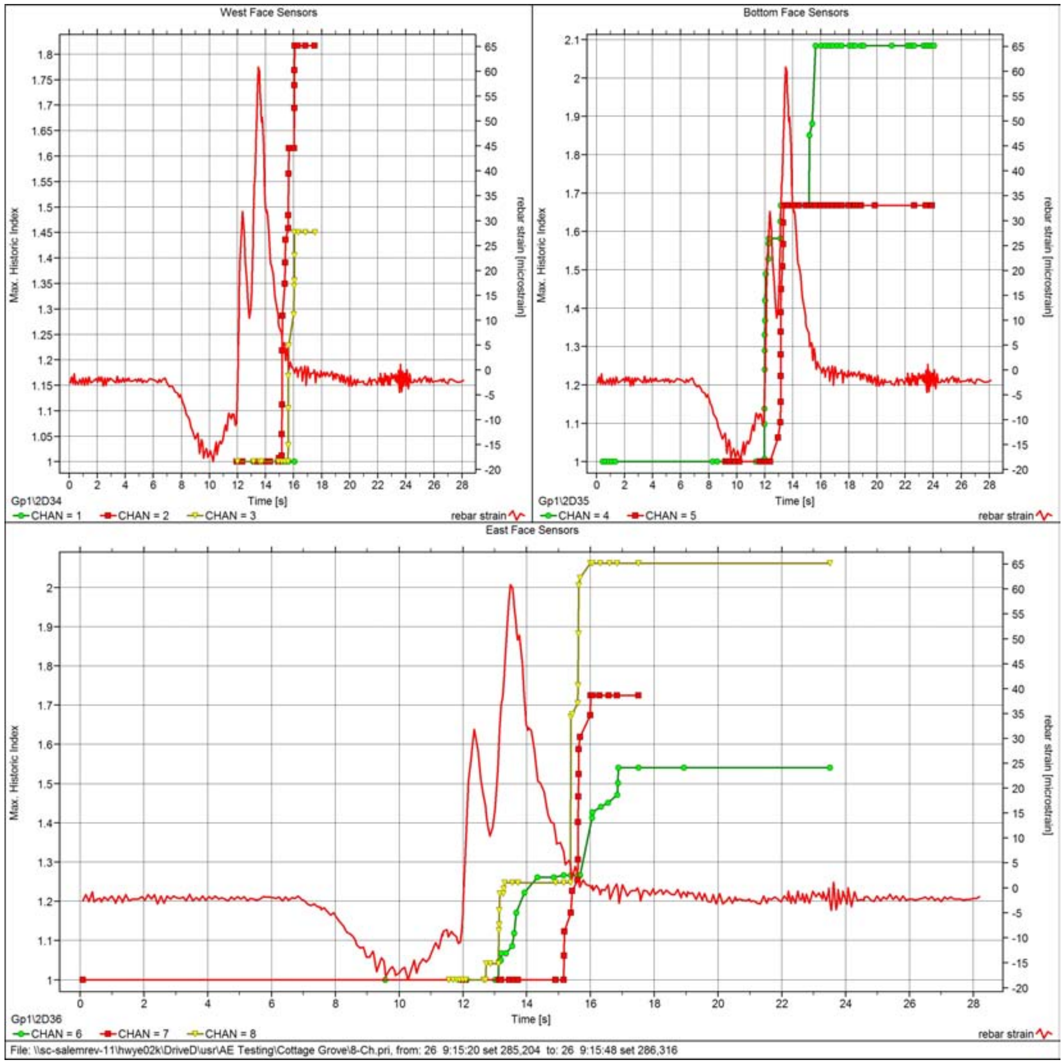

Figure 4.4.18 Maximum Historic Index correlated with rebar strain for Test Run #1.

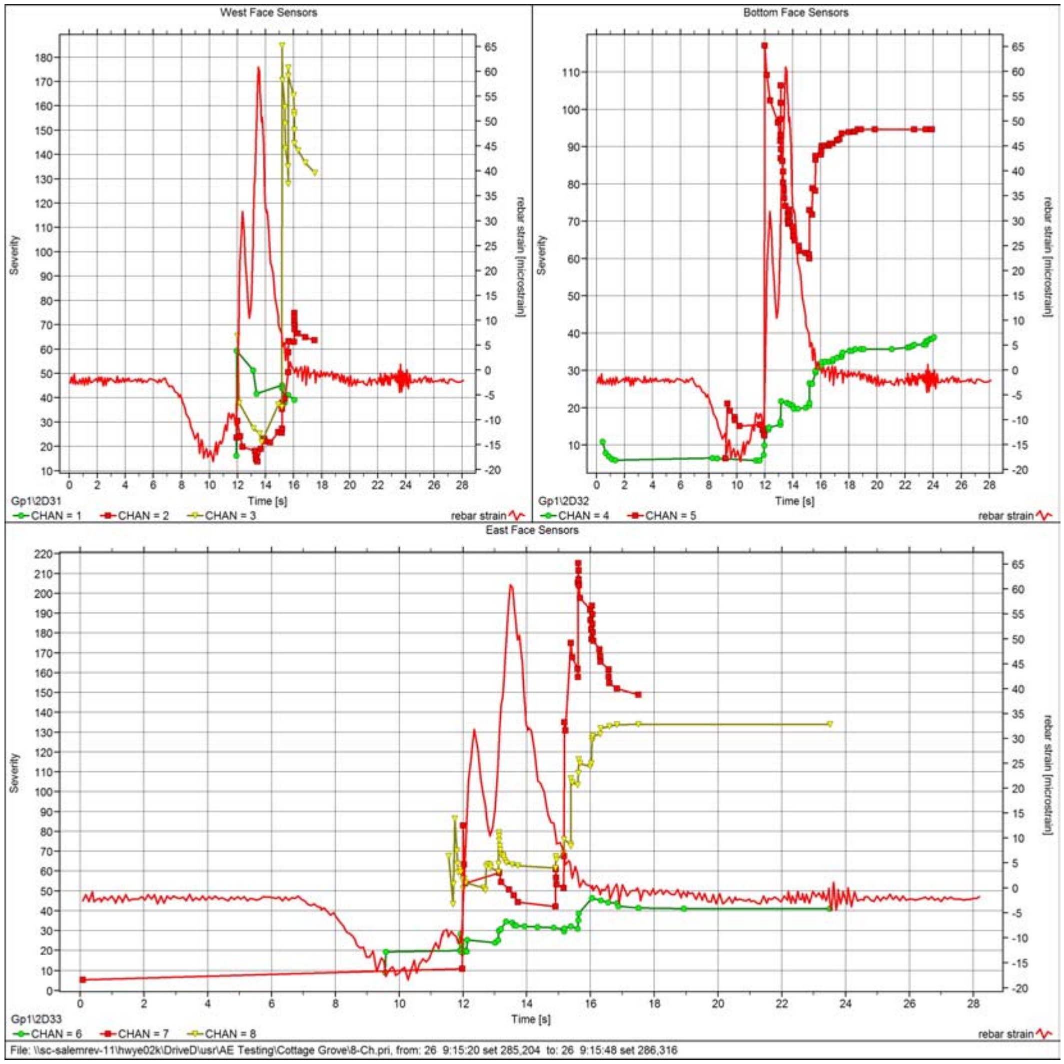

Figure 4.4.19 Severity correlated with rebar strain for Test Run #1.

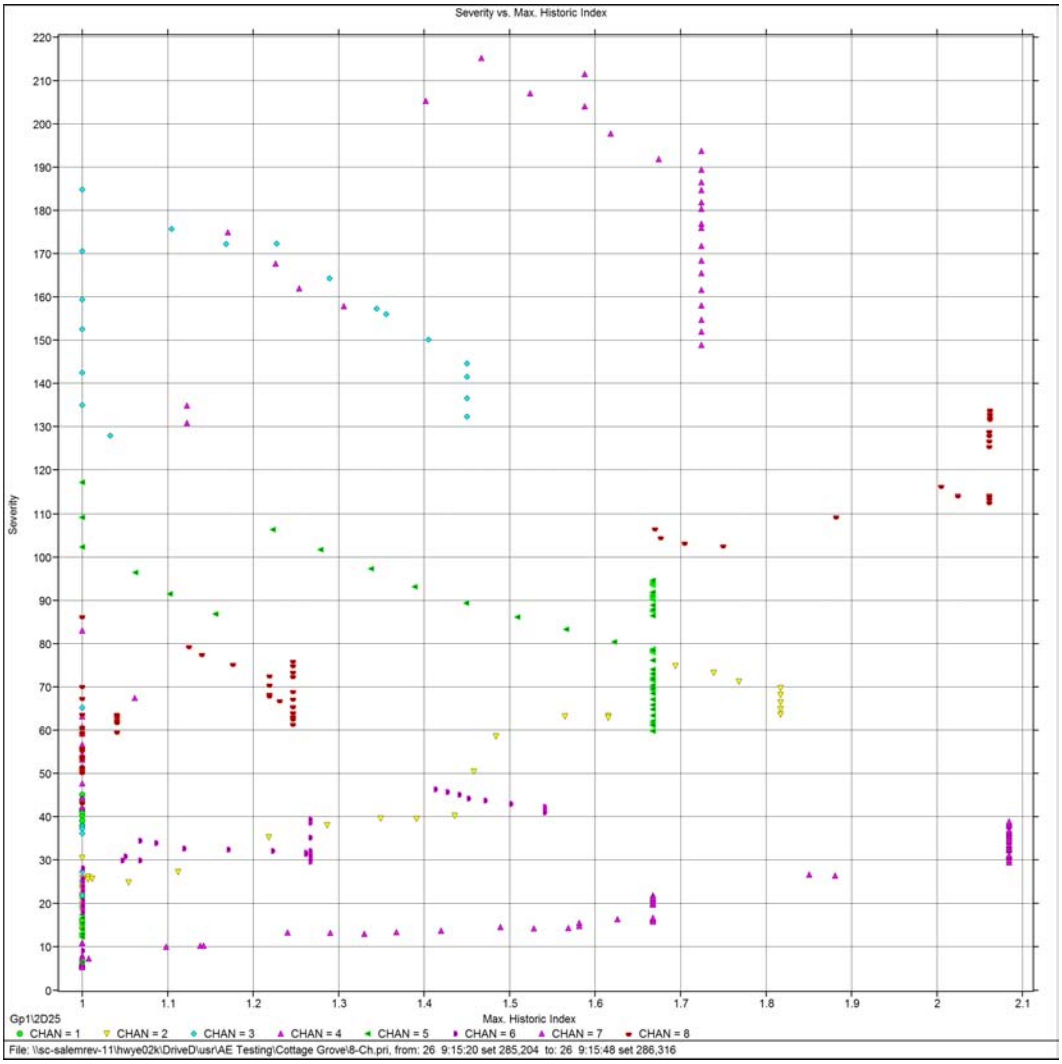

Figure 4.4.20 Intensity plot for Test Run #1.

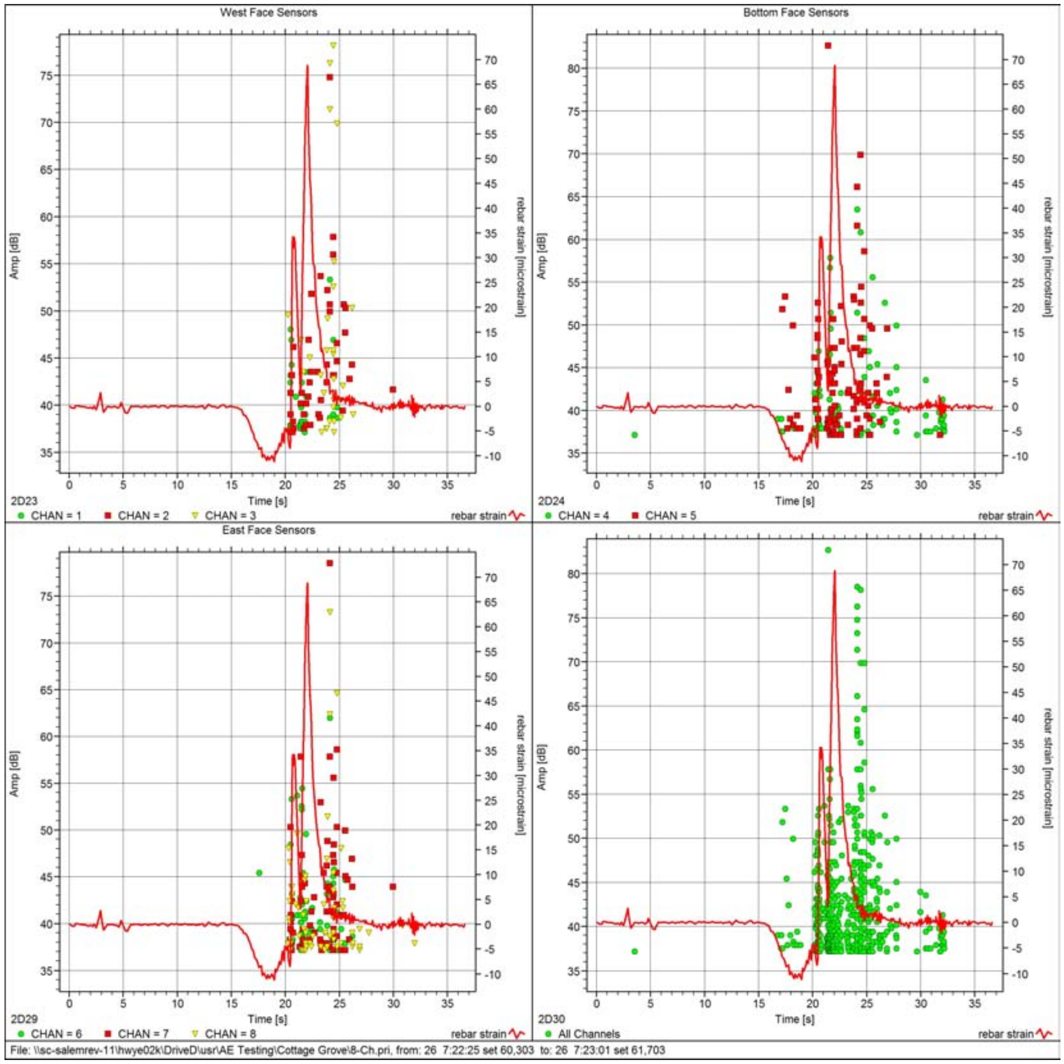

Figure 4.4.21 Peak amplitude correlated with rebar strain for Test Run #2.

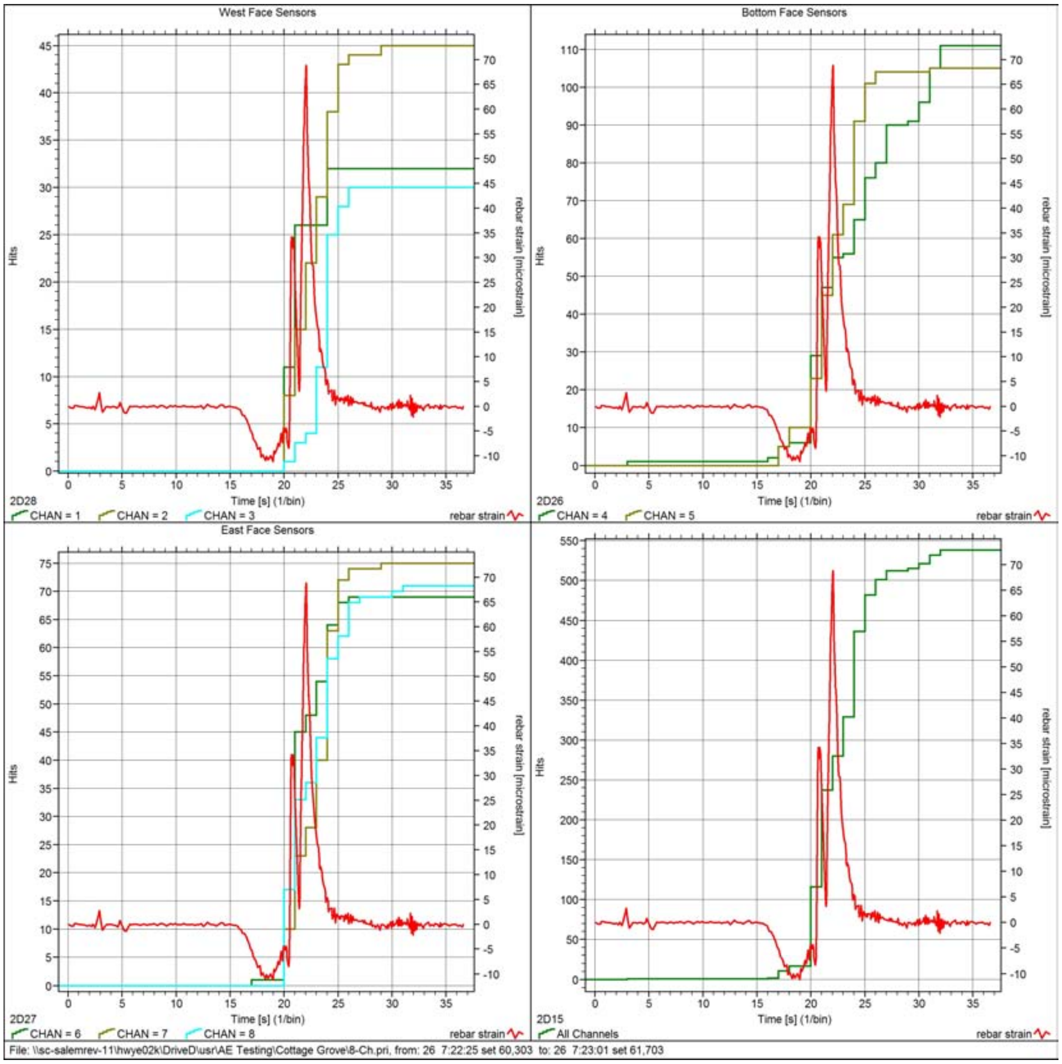

Figure 4.4.22 Cumulative hits correlated with rebar strain for Test Run #2.

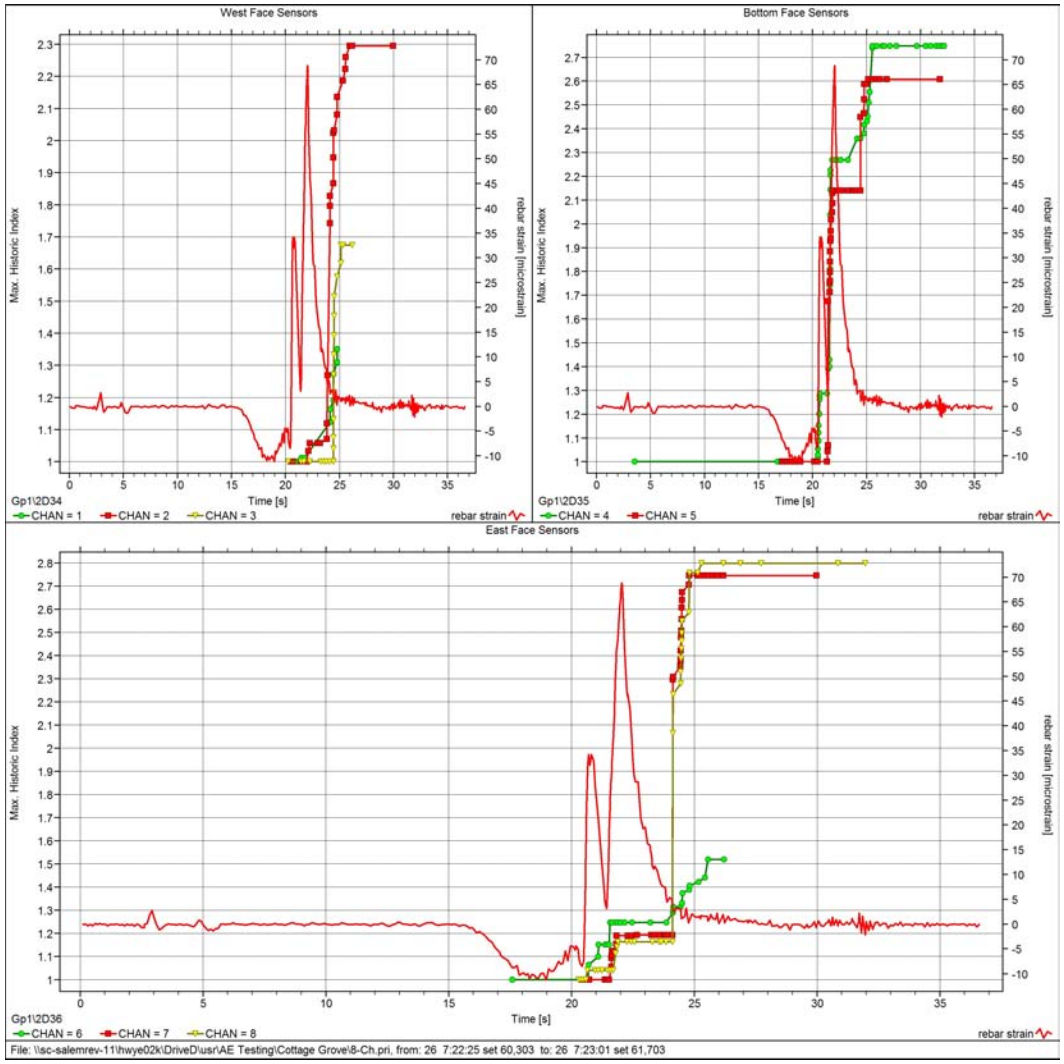

Figure 4.4.23 Maximum Historic Index correlated with rebar strain for Test Run #2.

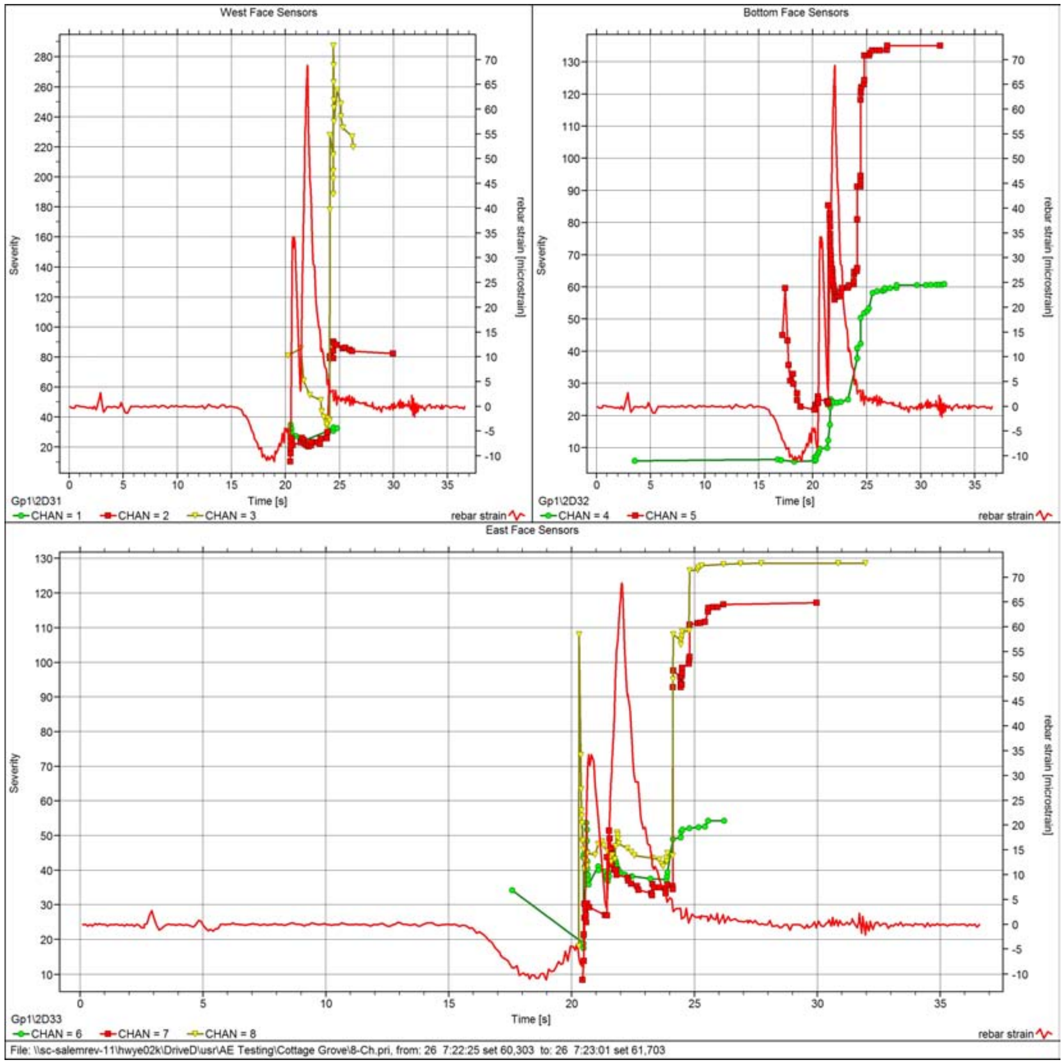

Figure 4.4.24 Severity correlated with rebar strain for Test Run #2

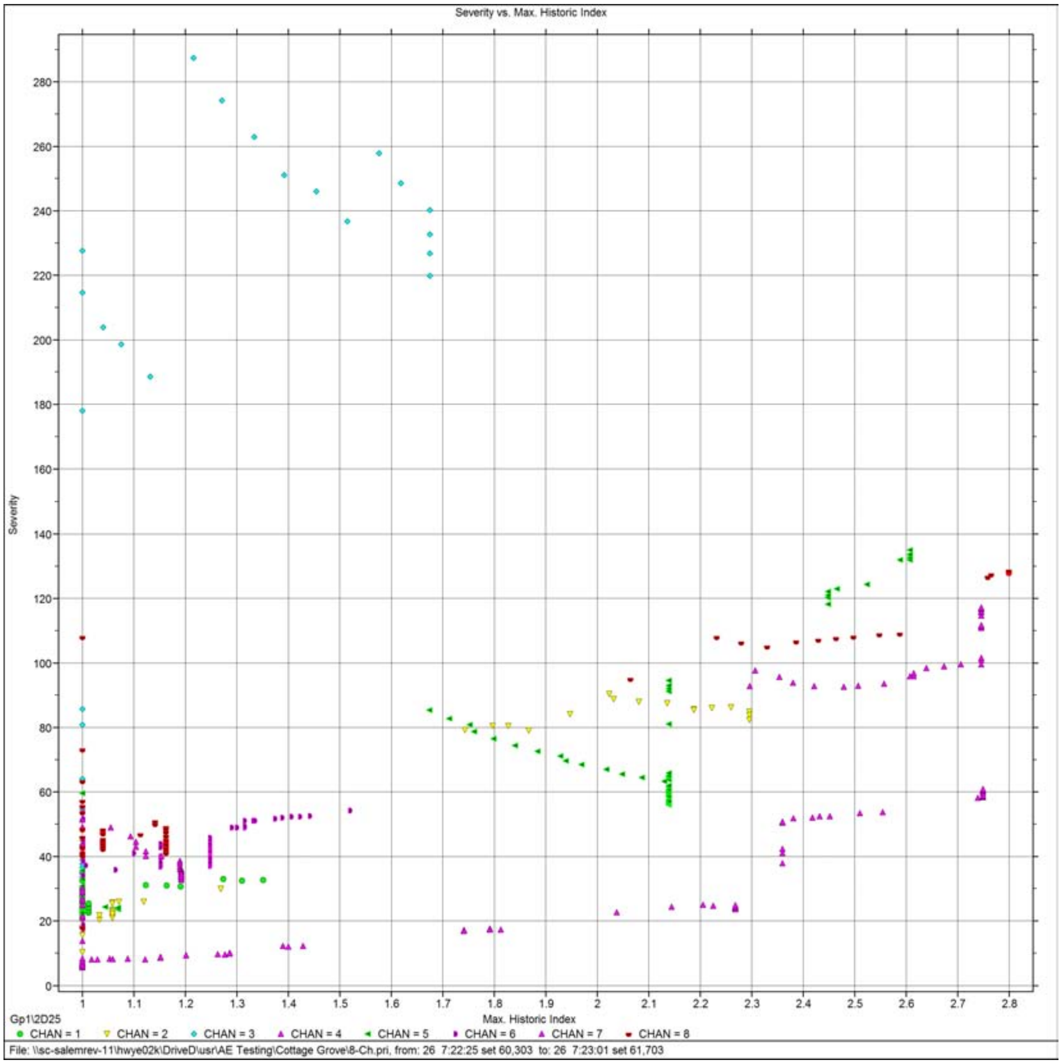

Figure 4.4.25 Intensity plot for Test Run #2.

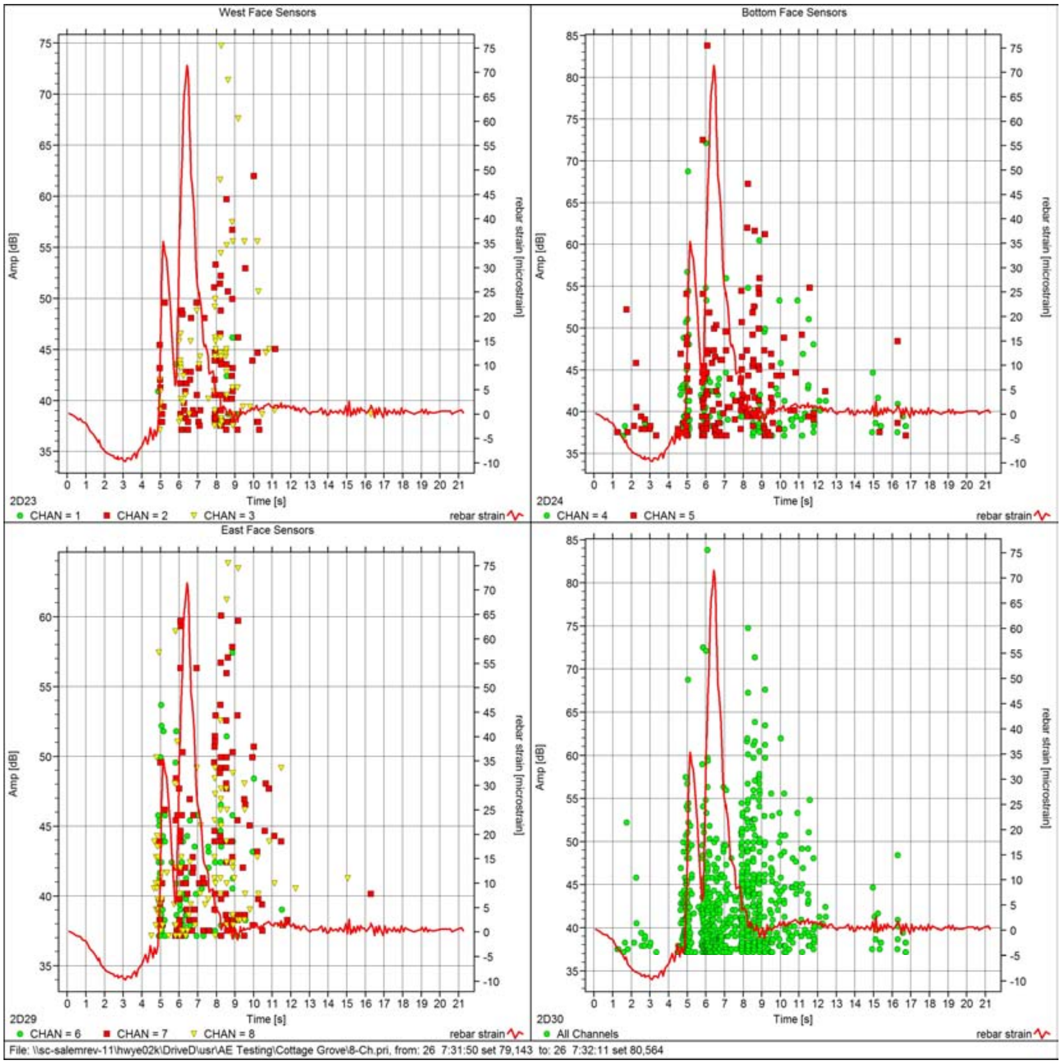

Figure 4.4.26 Peak amplitude correlated with rebar strain for Test Run #3.

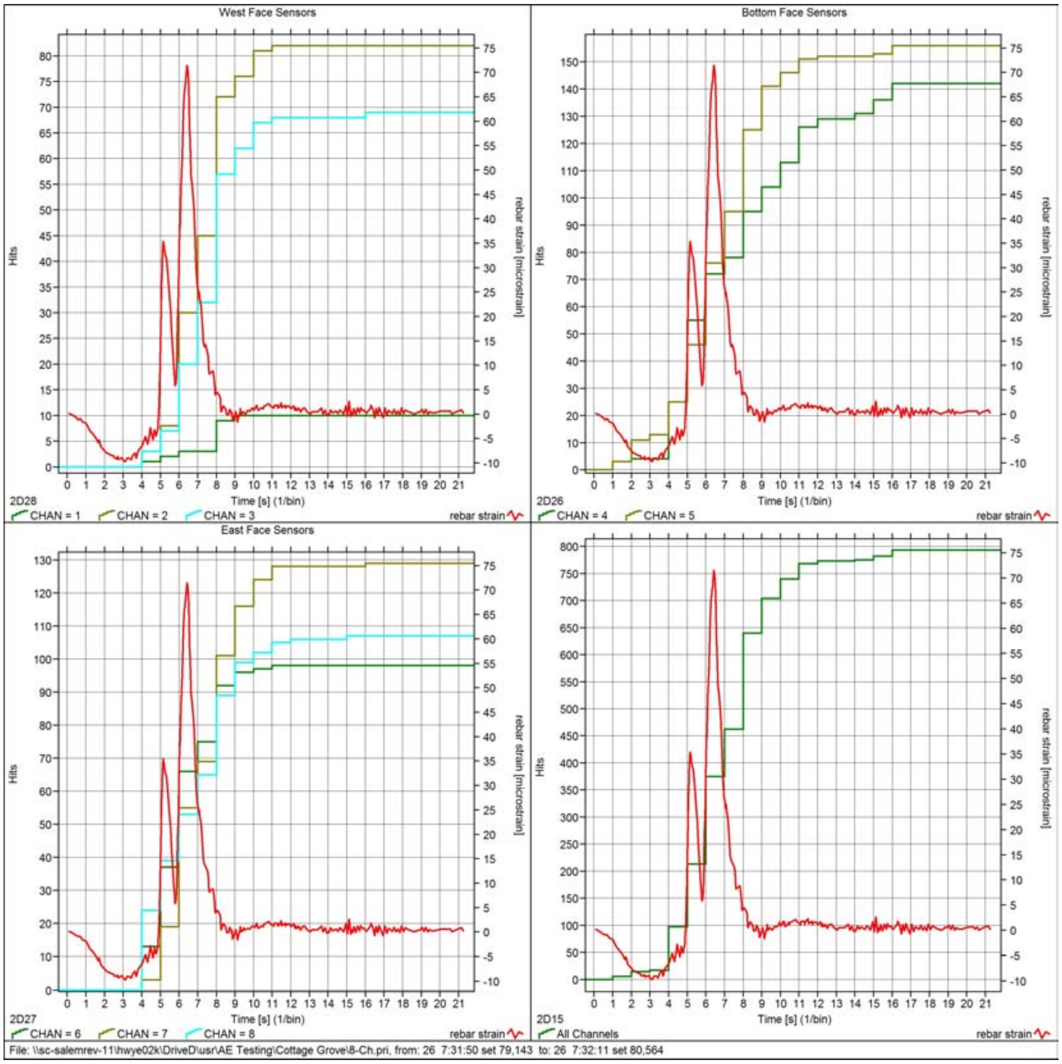

Figure 4.4.27 Cumulative hits correlated with rebar strain for Test Run #3.

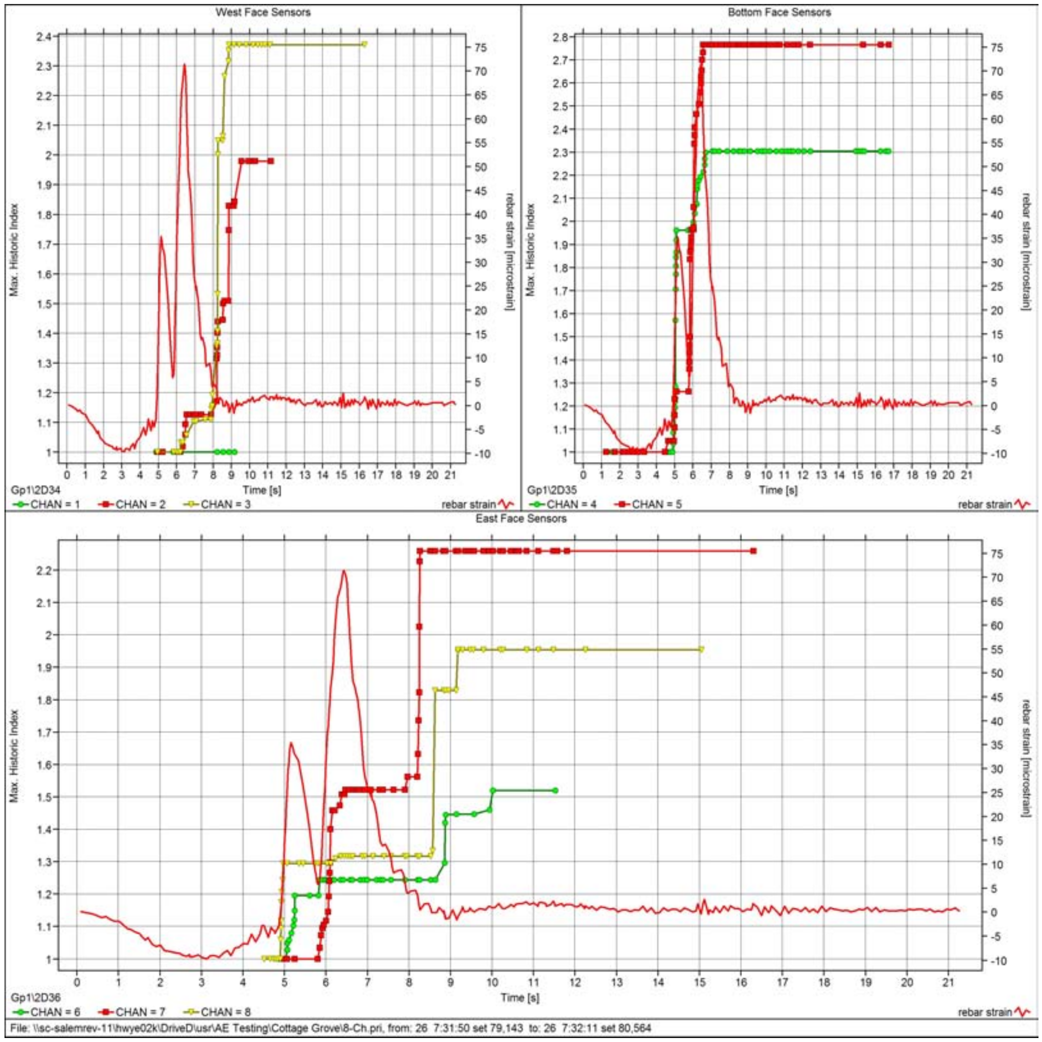

Figure 4.4.28 Maximum Historic Index correlated with rebar strain for Test Run #3.

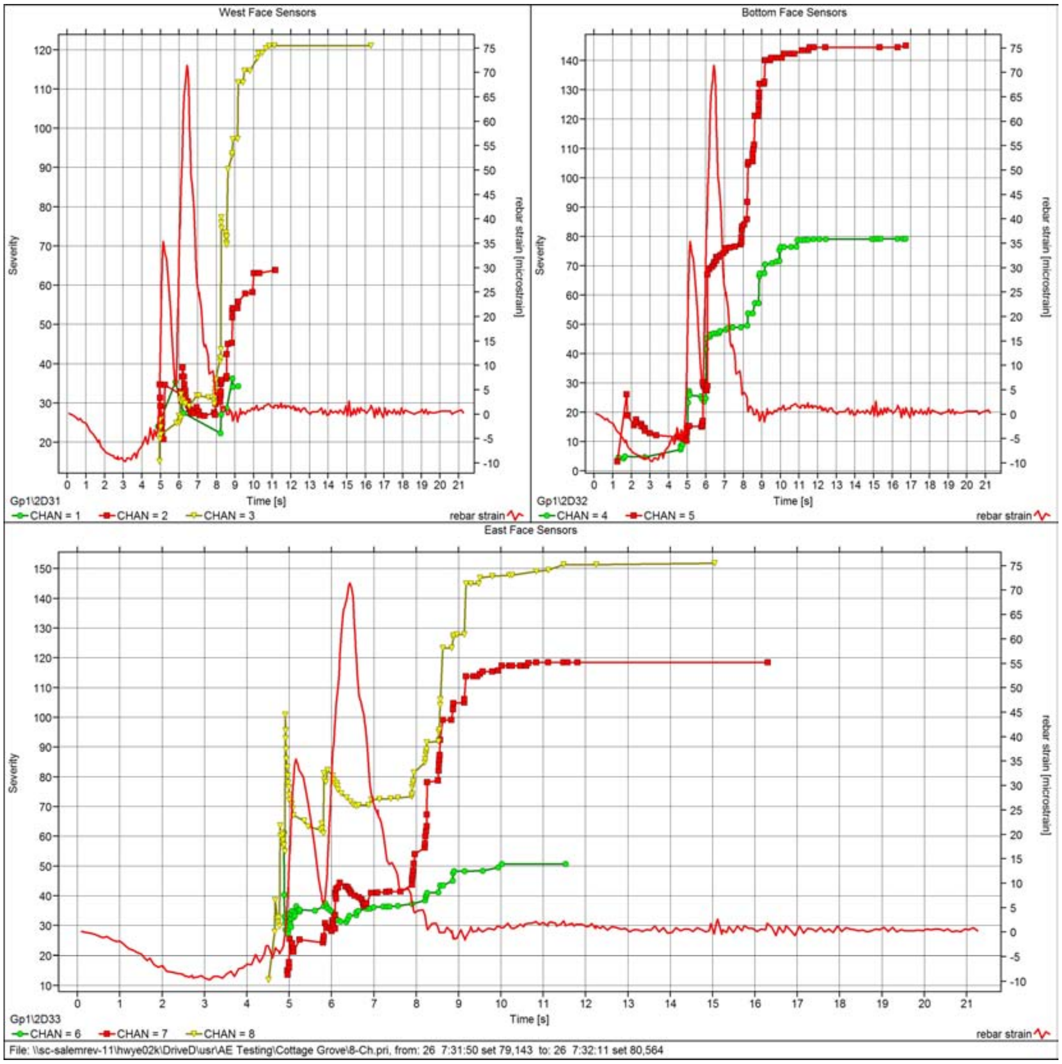

Figure 4.4.29 Severity correlated with rebar strain for Test Run #3.

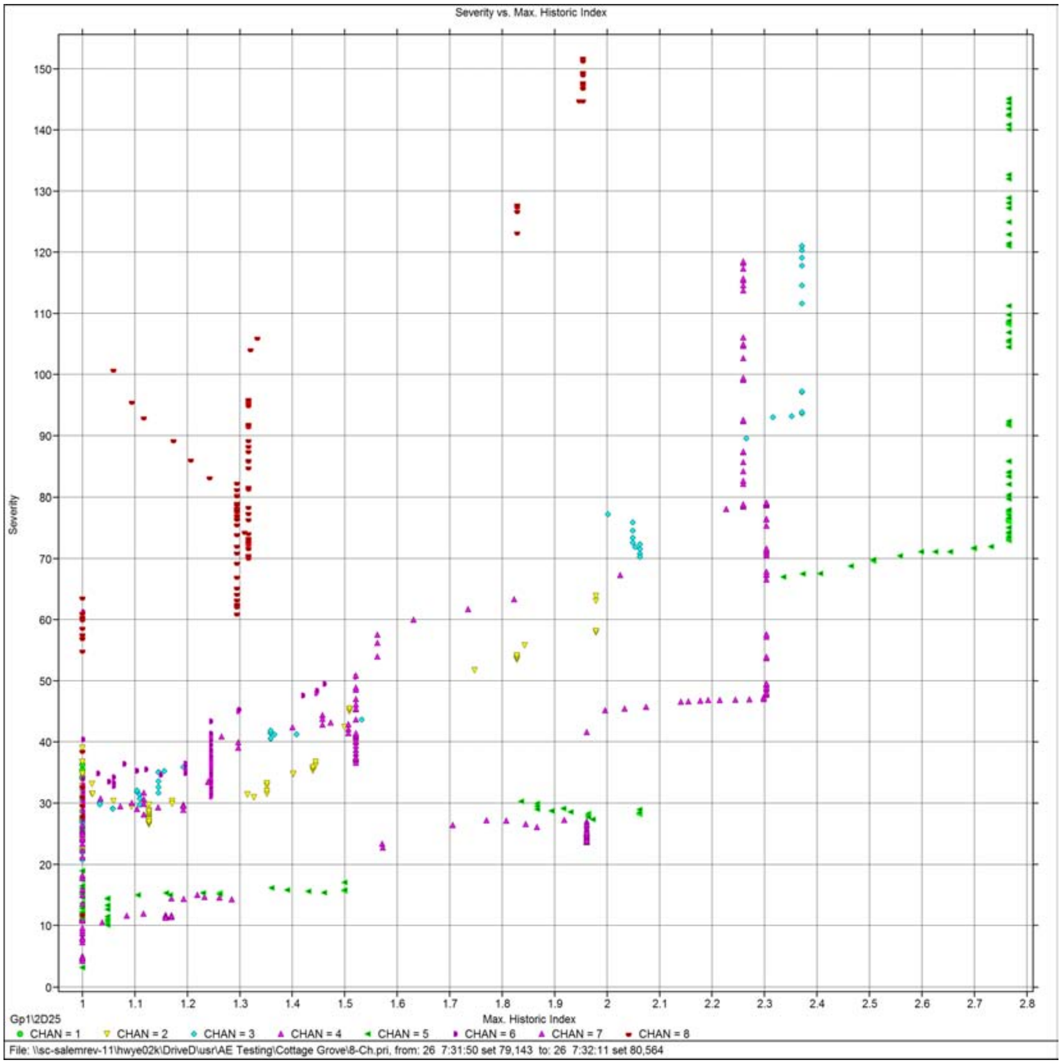

Figure 4.4.30 Intensity plot for Test Run #3.

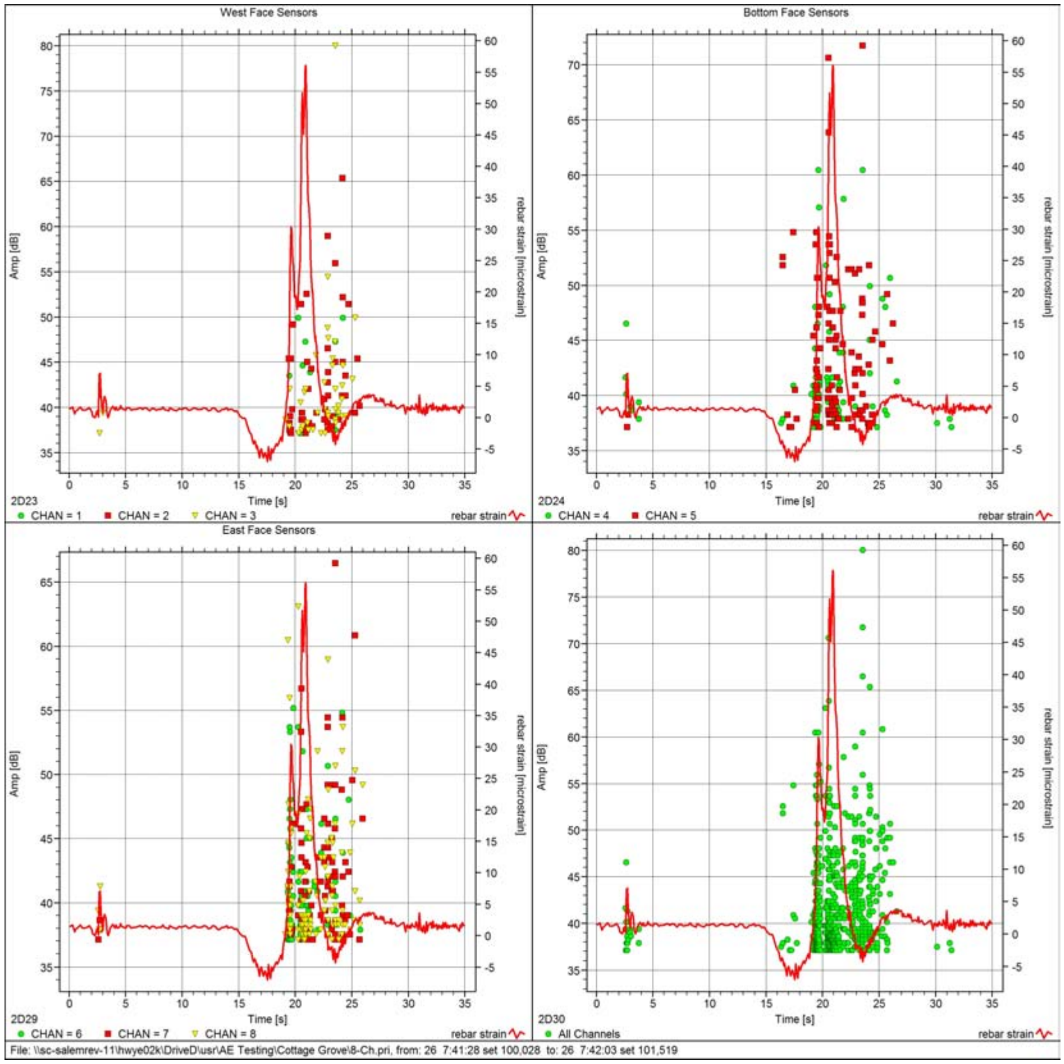

Figure 4.4.31 Peak amplitude correlated with rebar strain for Test Run #4.

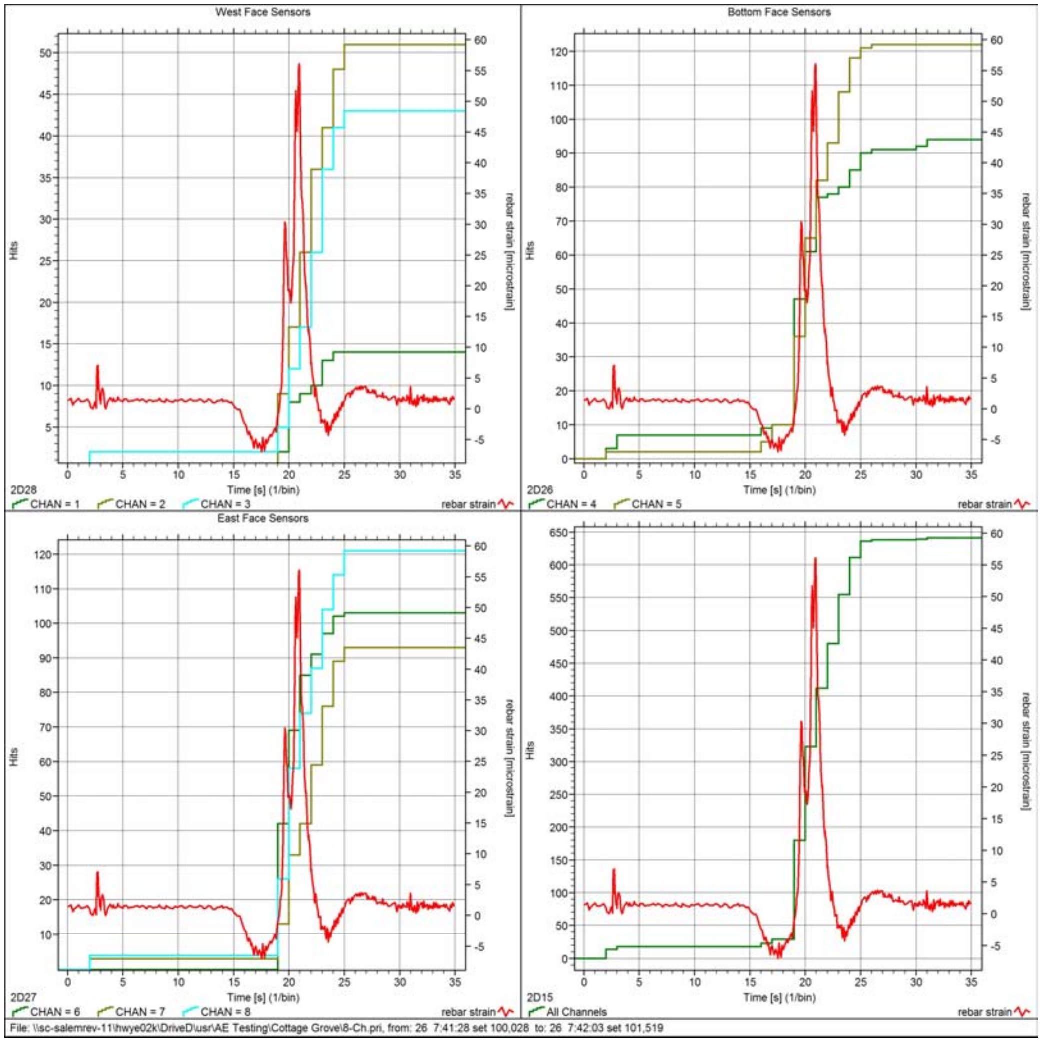

Figure 4.4.32 Cumulative hits correlated with rebar strain for Test Run #4.

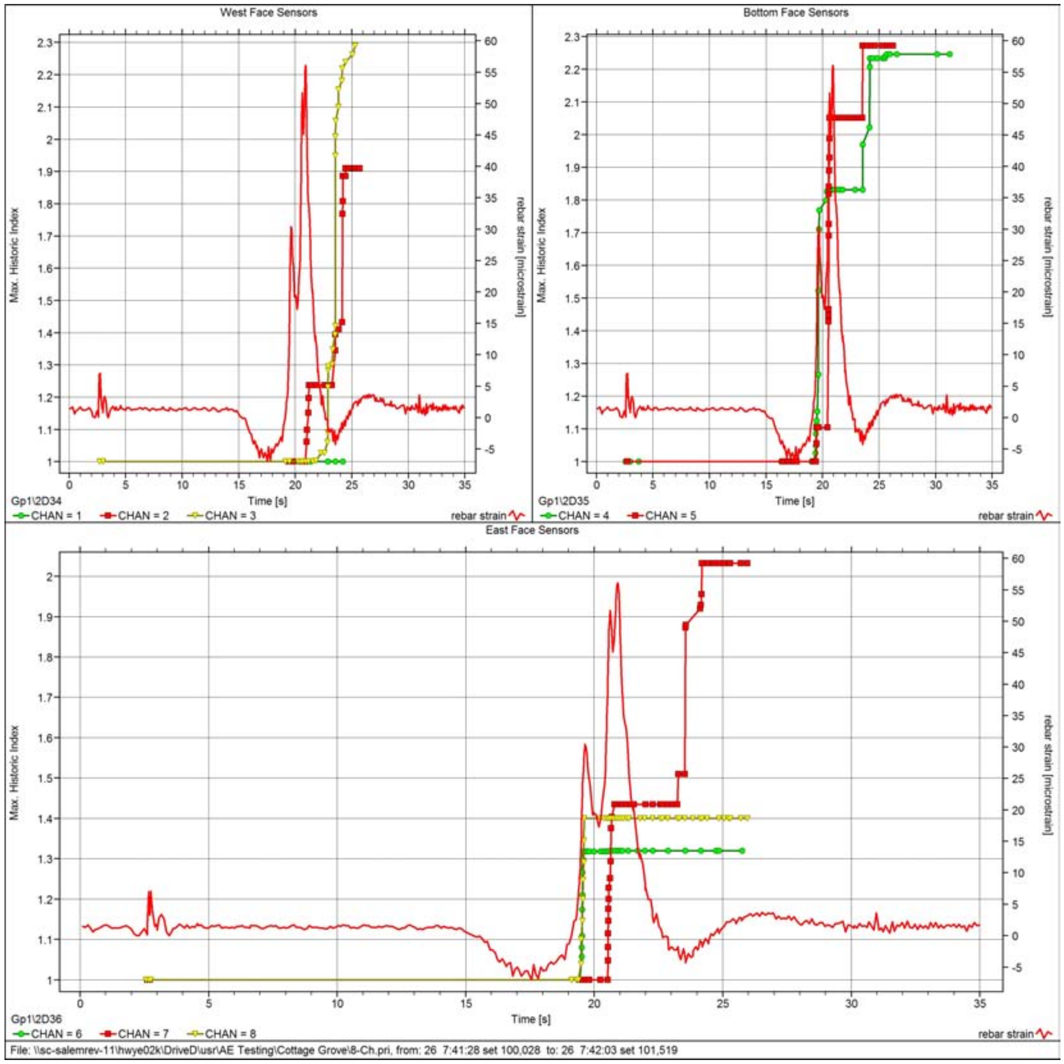

Figure 4.4.33 Maximum Historic Index correlated with rebar strain for Test Run #4.

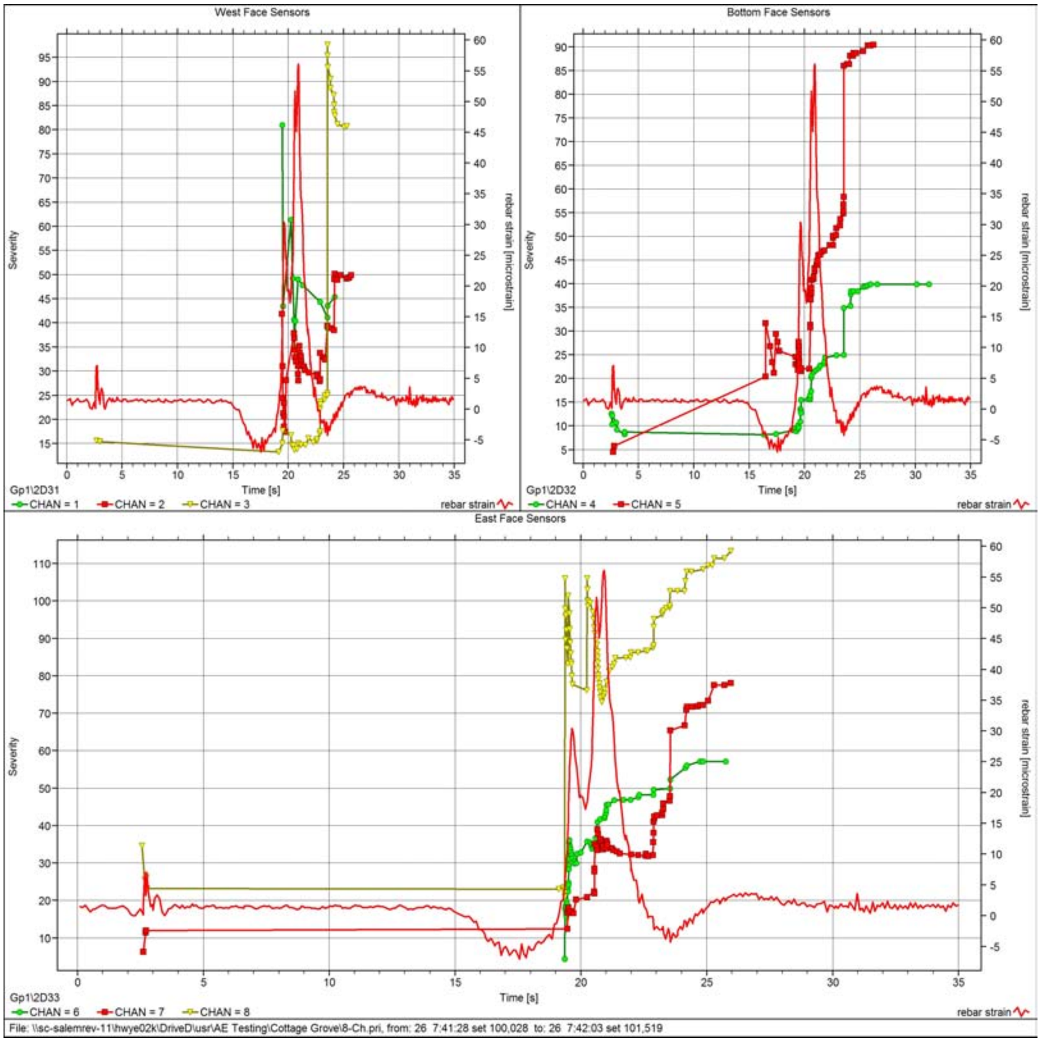

Figure 4.4.34 Severity correlated with rebar strain for Test Run #4

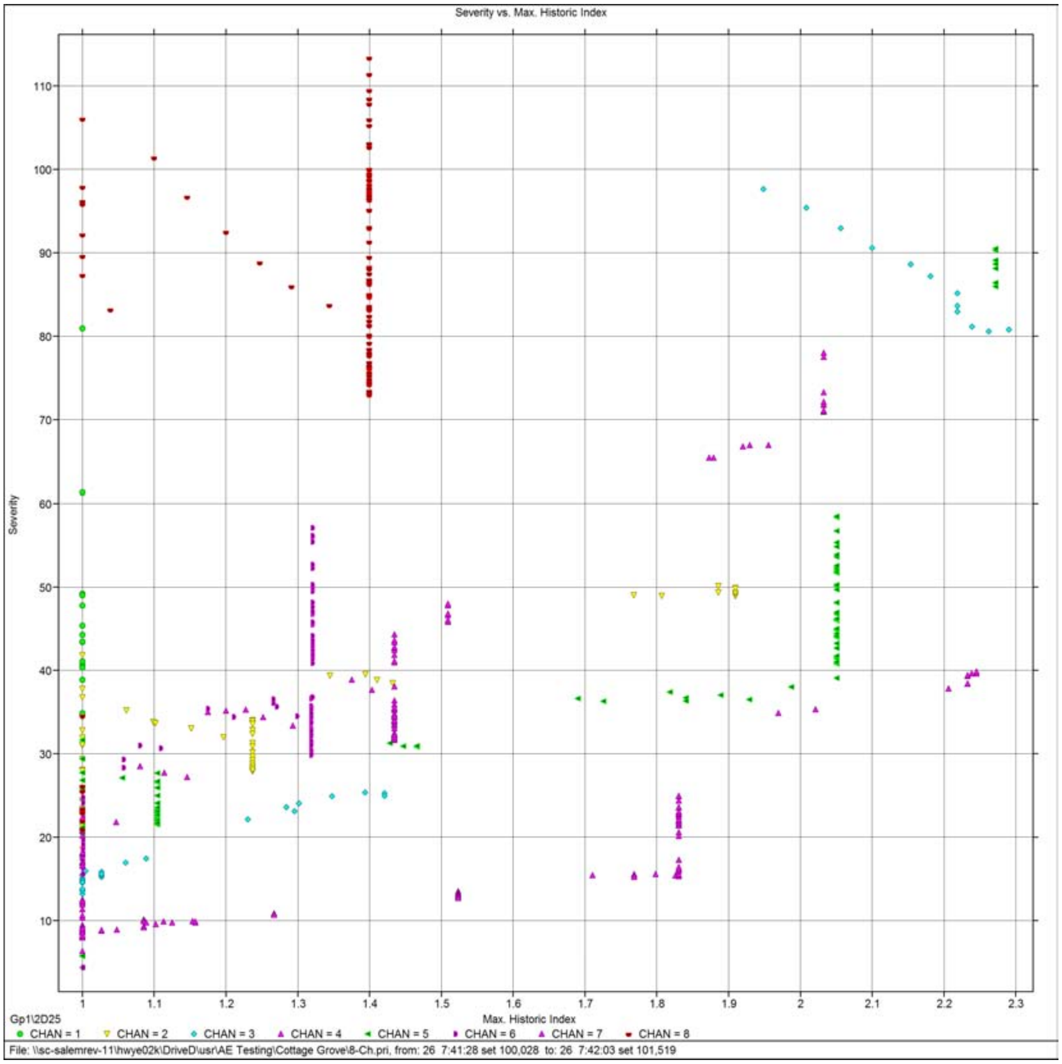

Figure 4.4.35 Intensity plot for Test Run #4.

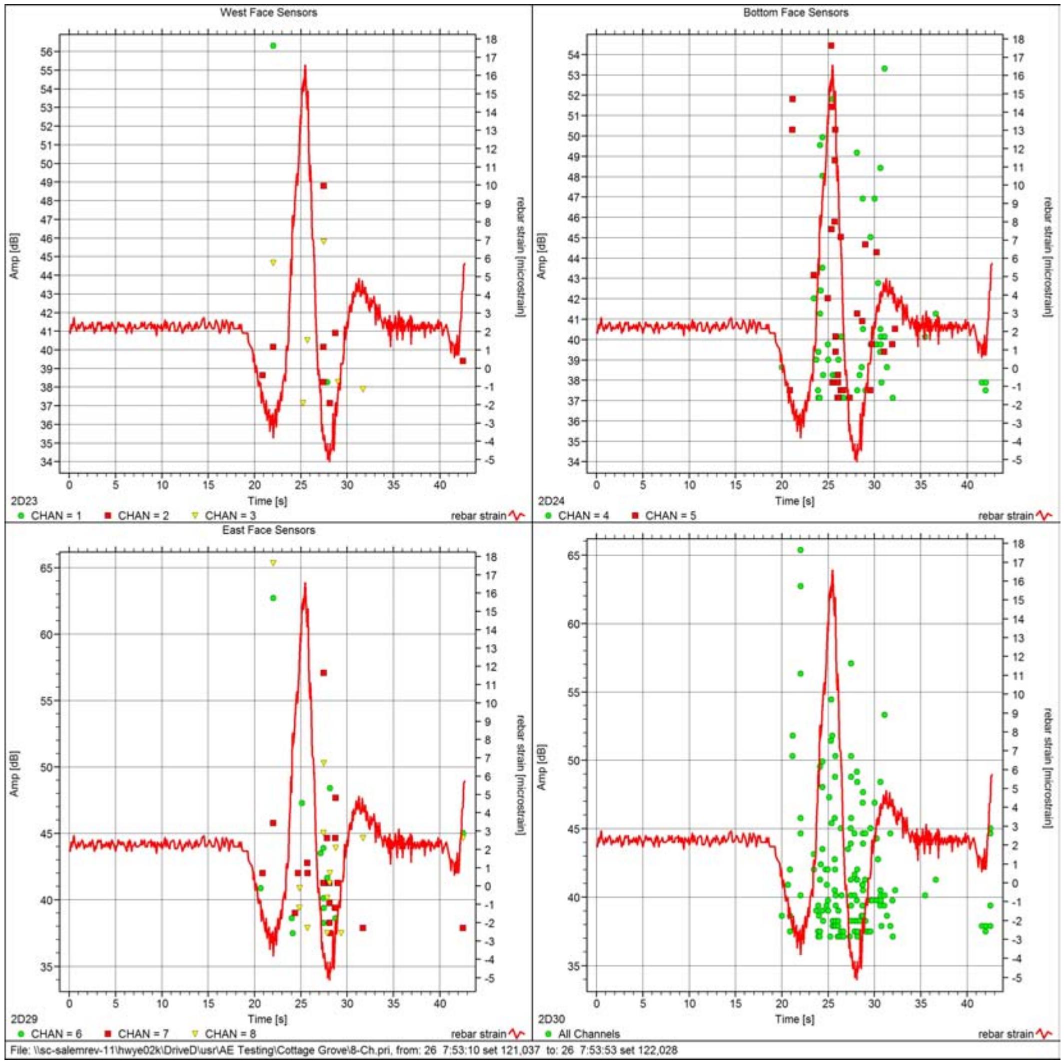

Figure 4.4.36 Peak amplitude correlated with rebar strain for Test Run #5.

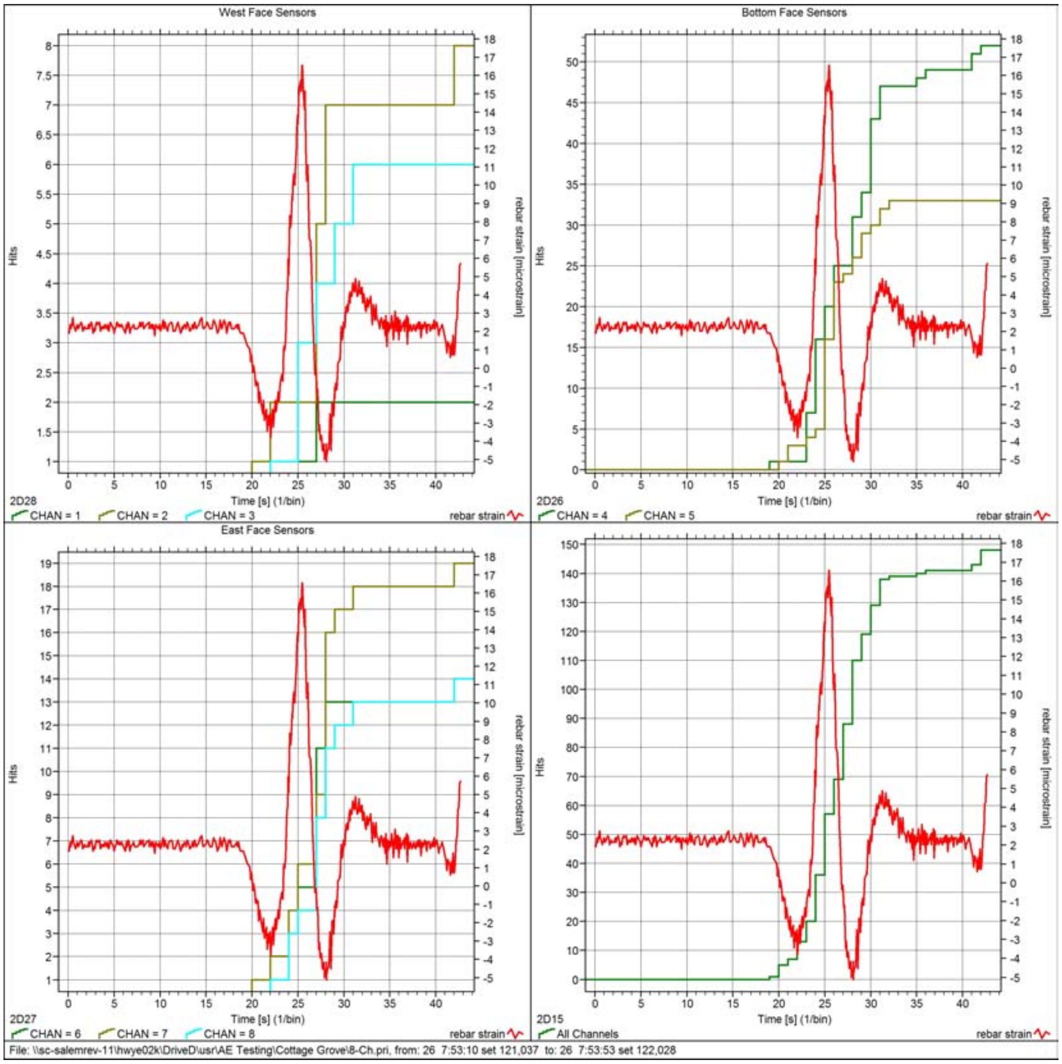

Figure 4.4.37 Cumulative hits correlated with rebar strain for Test Run #5.

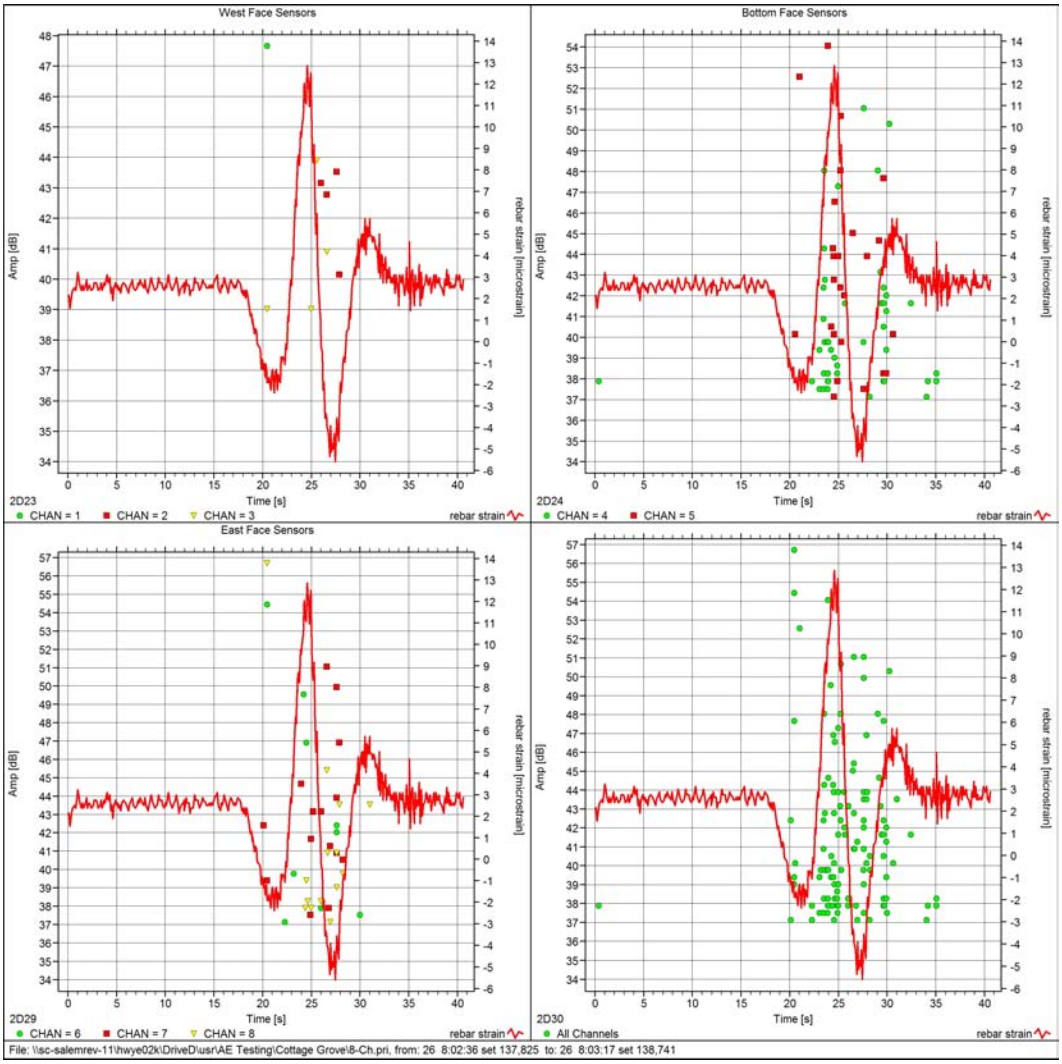

Figure 4.4.38 Peak amplitude correlated with rebar strain for Test Run #6.

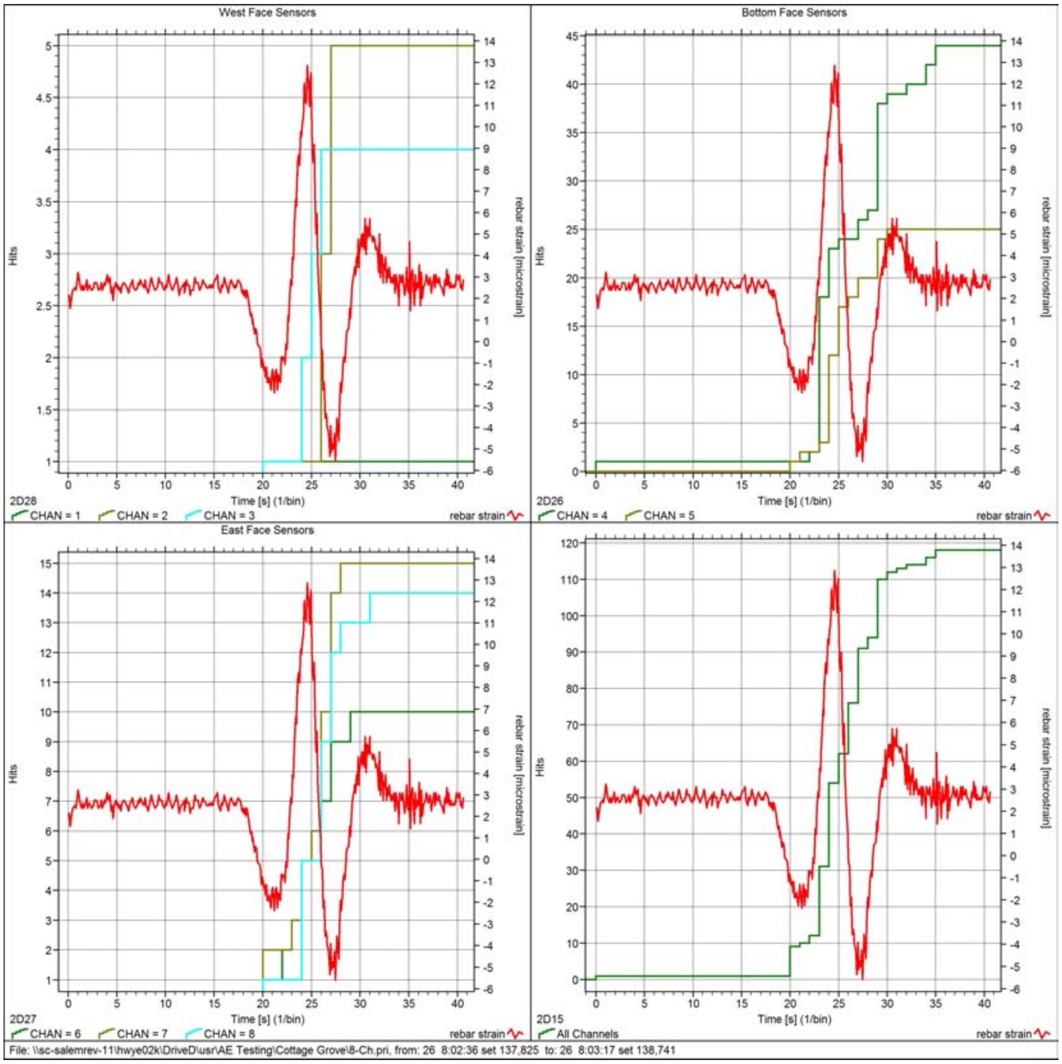

Figure 4.4.39 Cumulative hits correlated with rebar strain for Test Run #6.

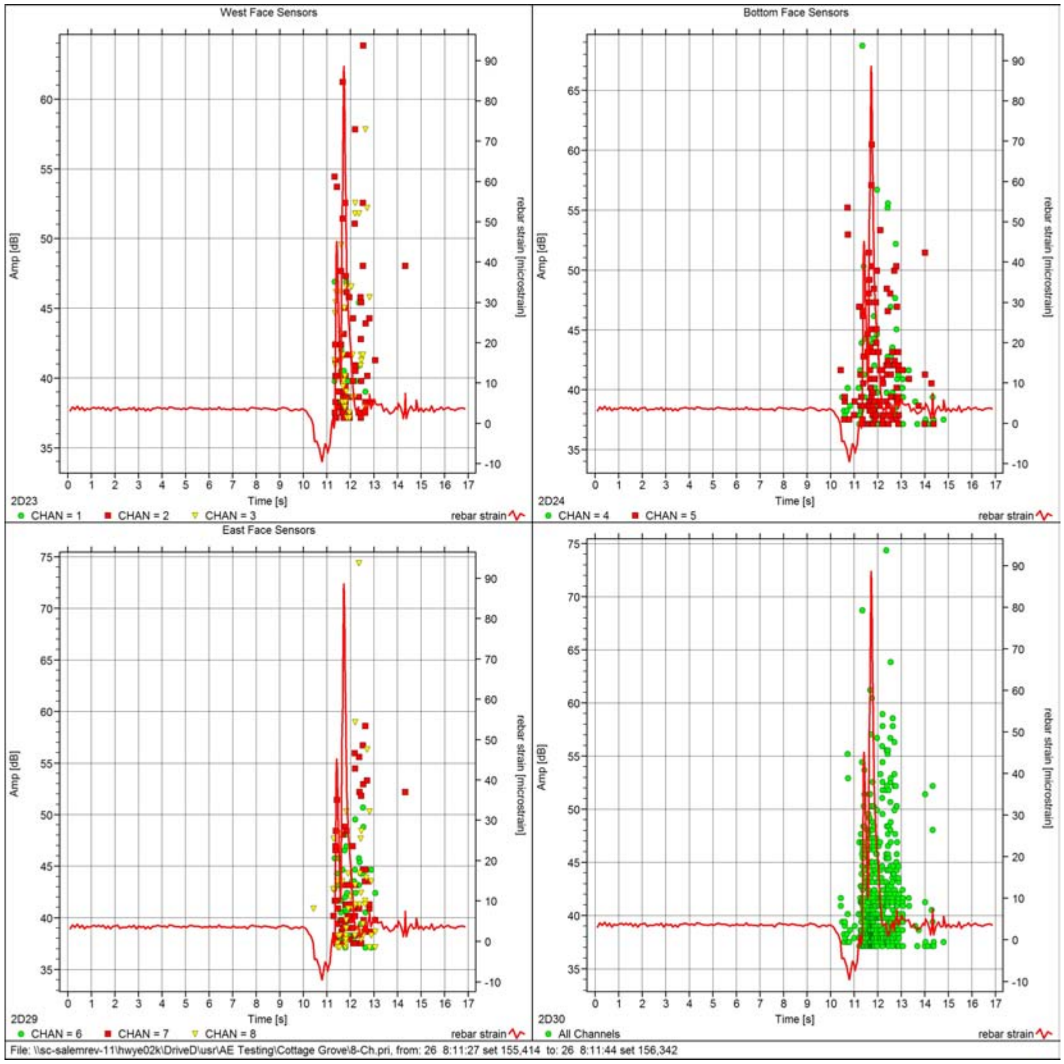

Figure 4.4.40 Peak amplitude correlated with rebar strain for Test Run #7.

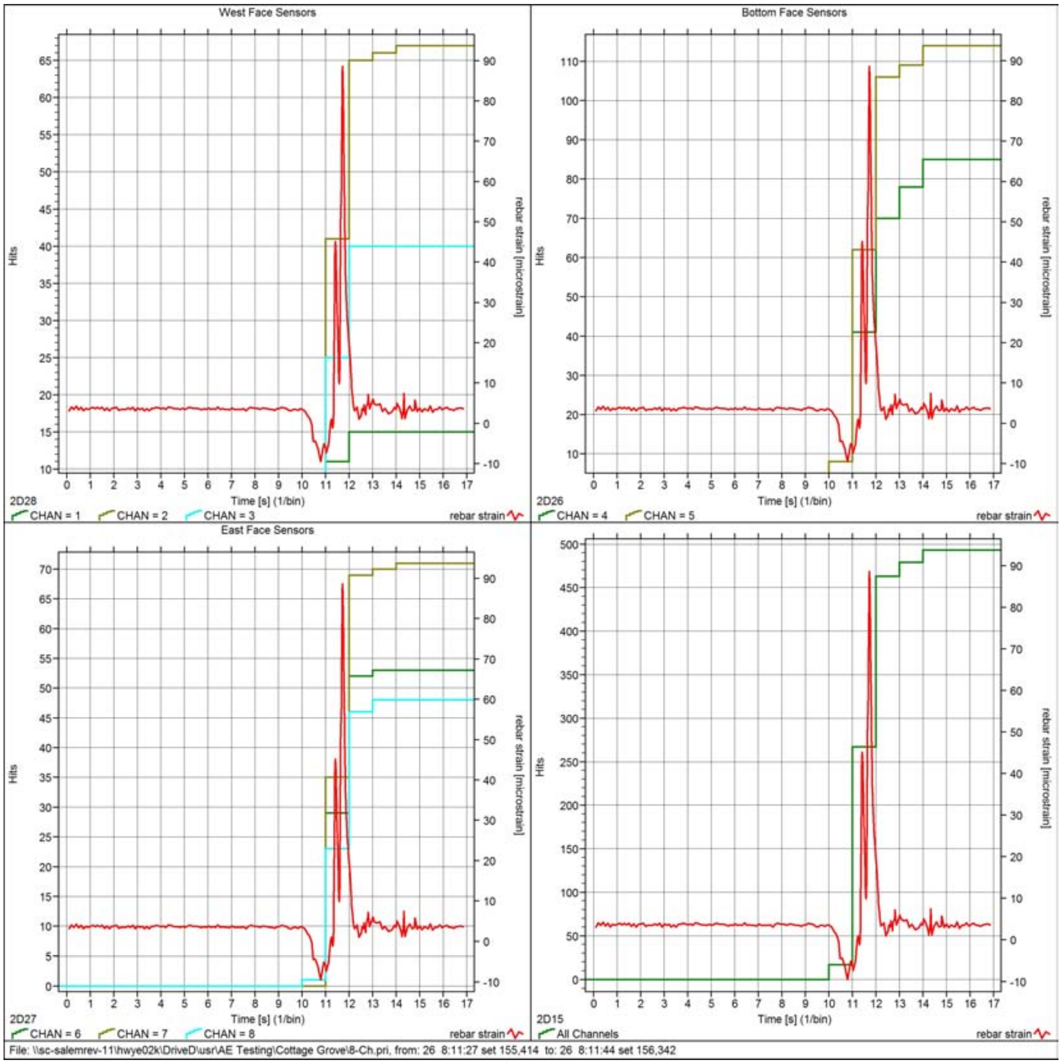

Figure 4.4.41 Cumulative hits correlated with rebar strain for Test Run #7.

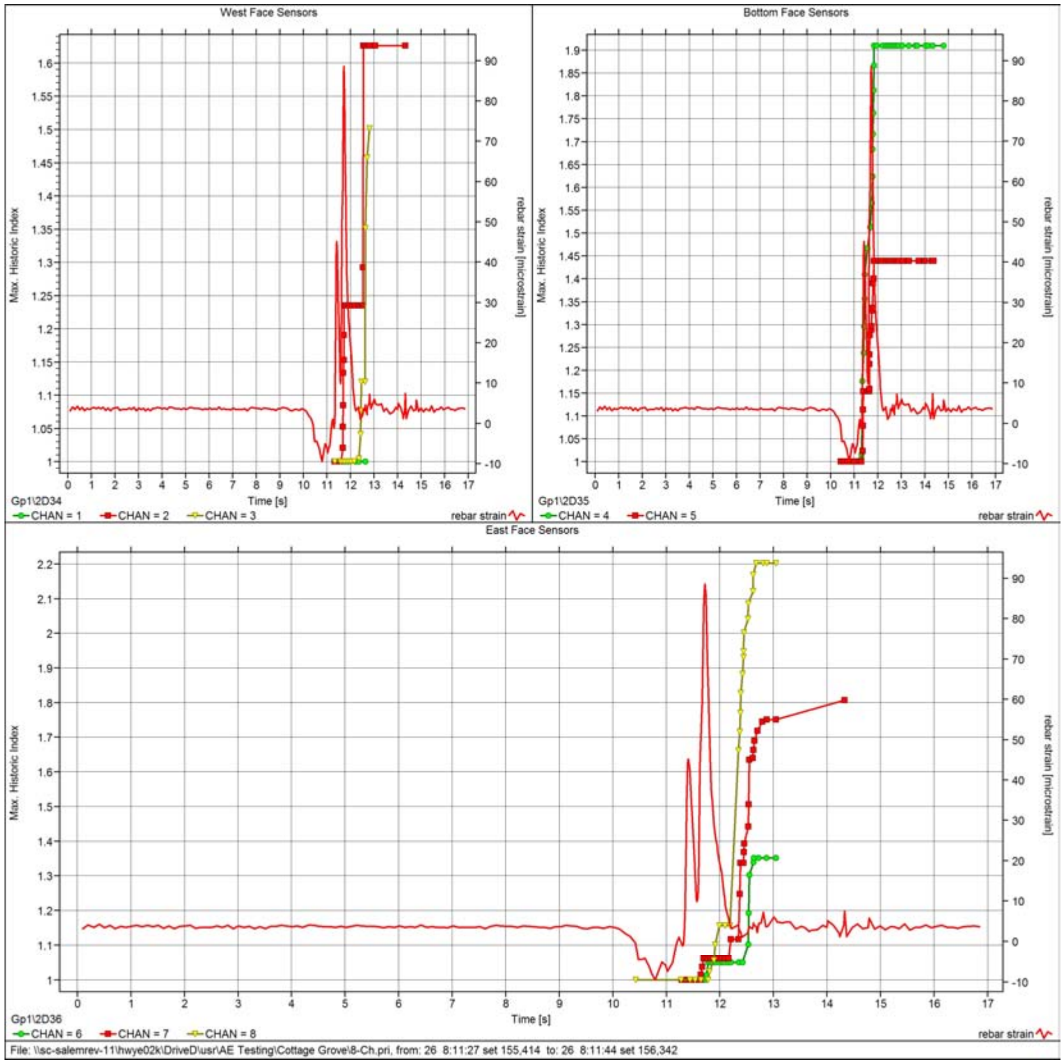

Figure 4.4.42 Maximum Historic Index correlated with rebar strain for Test Run #7.

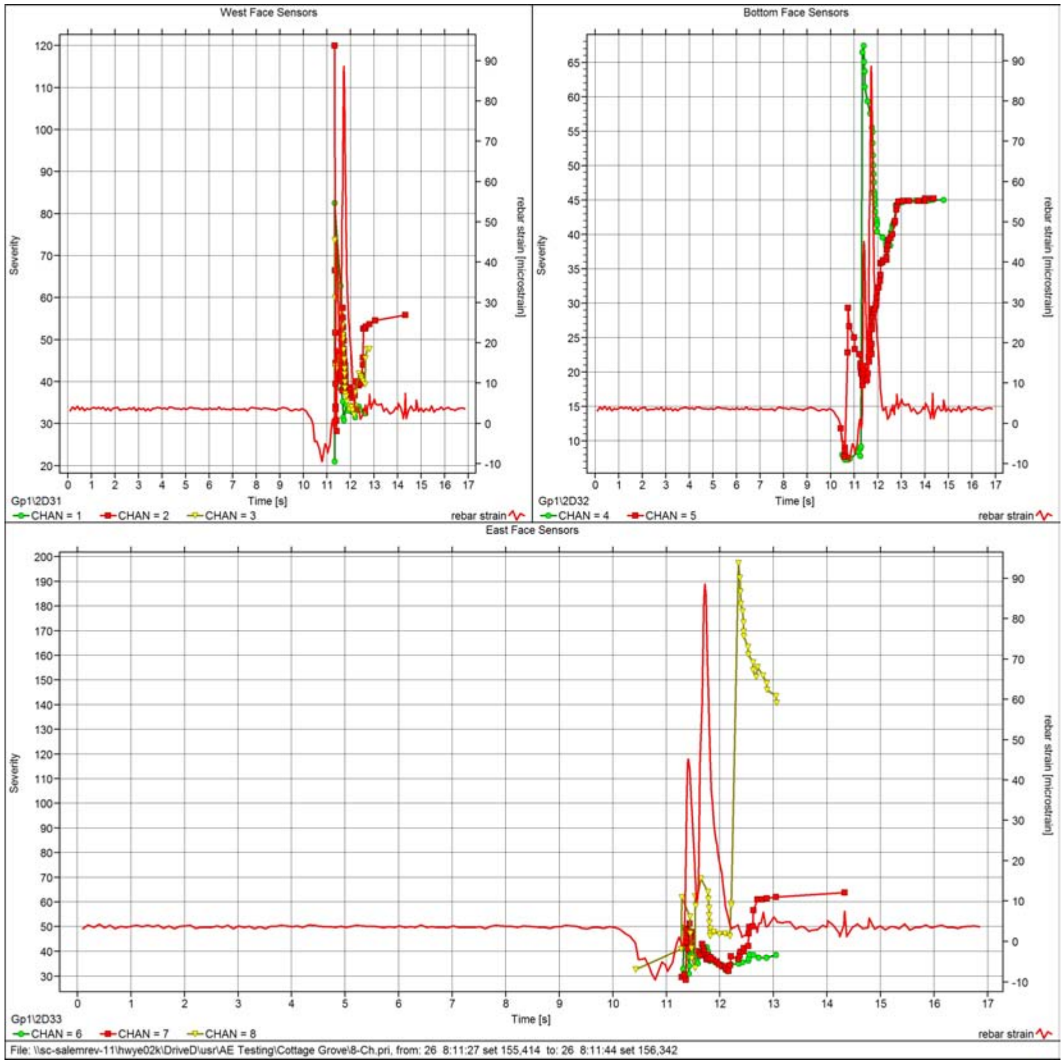

Figure 4.4.43 Severity correlated with rebar strain for Test Run #7.

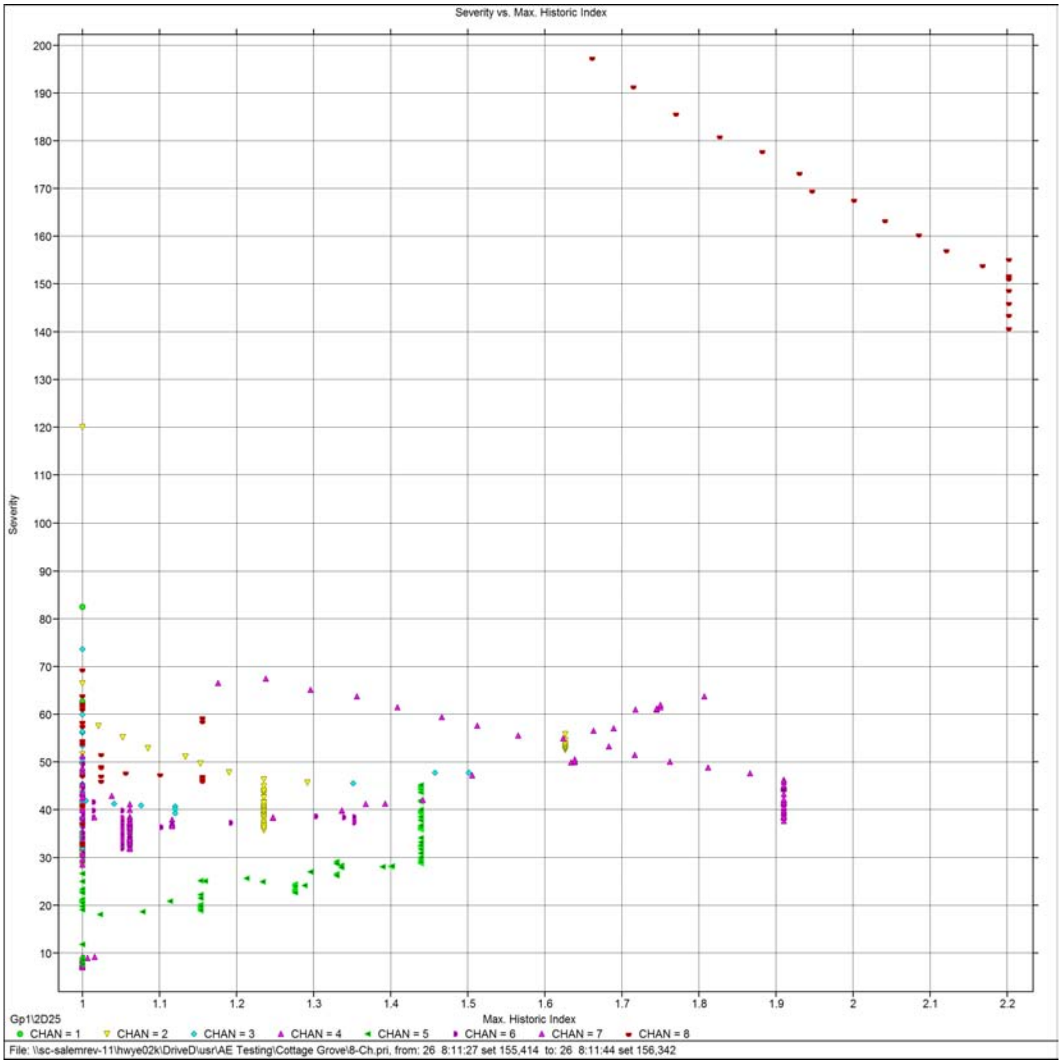

Figure 4.4.44 Intensity plot for Test Run #7.

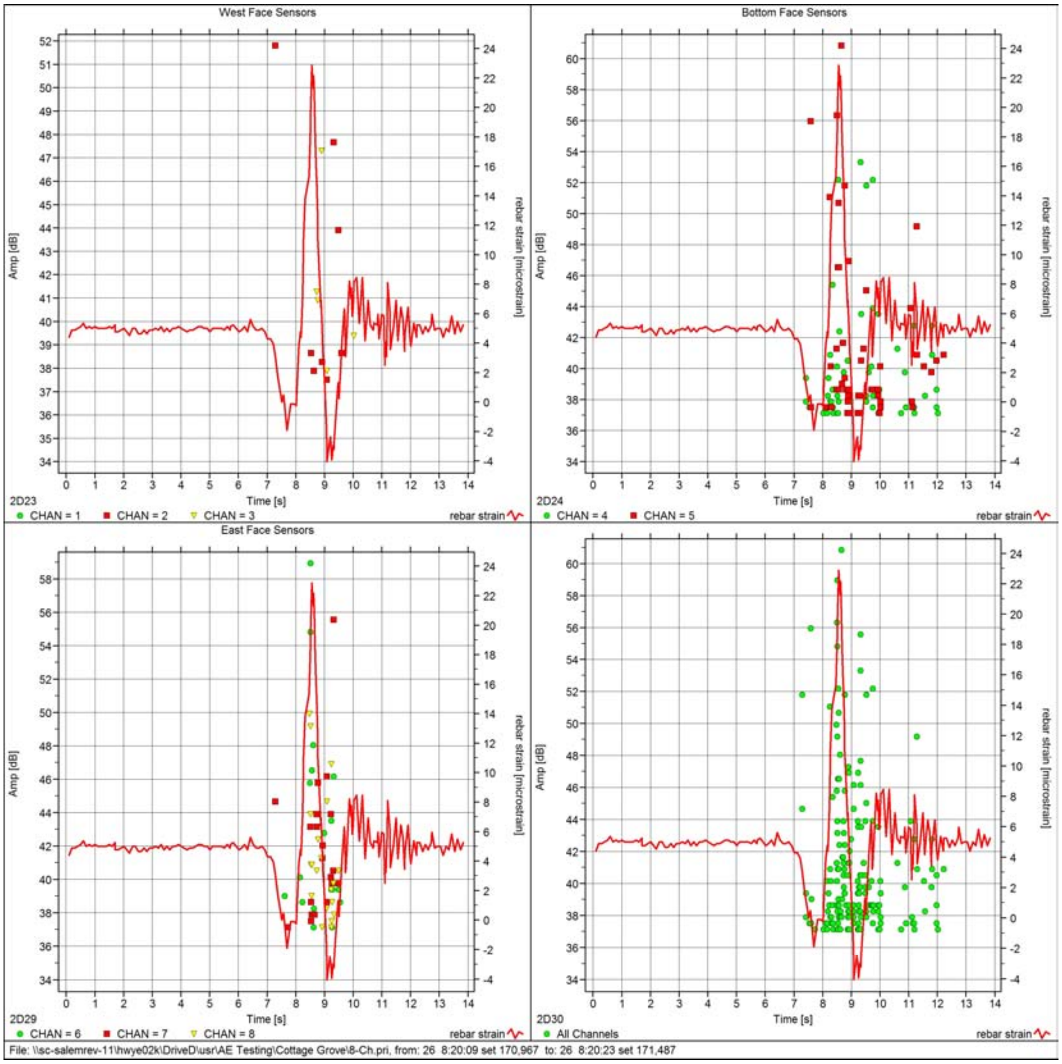

Figure 4.4.45 Peak amplitude correlated with rebar strain for Test Run #8.

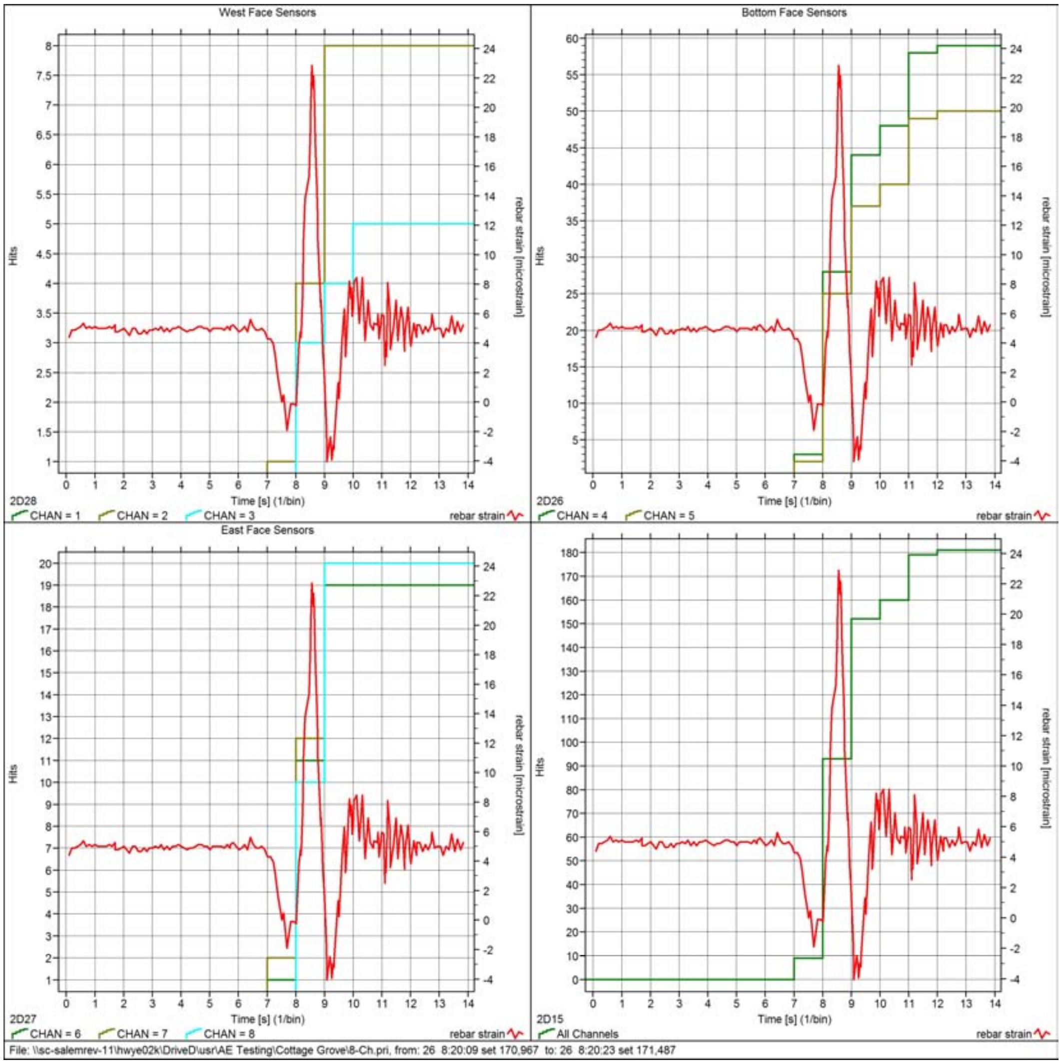

Figure 4.4.46 Cumulative hits correlated with rebar strain for Test Run #8.

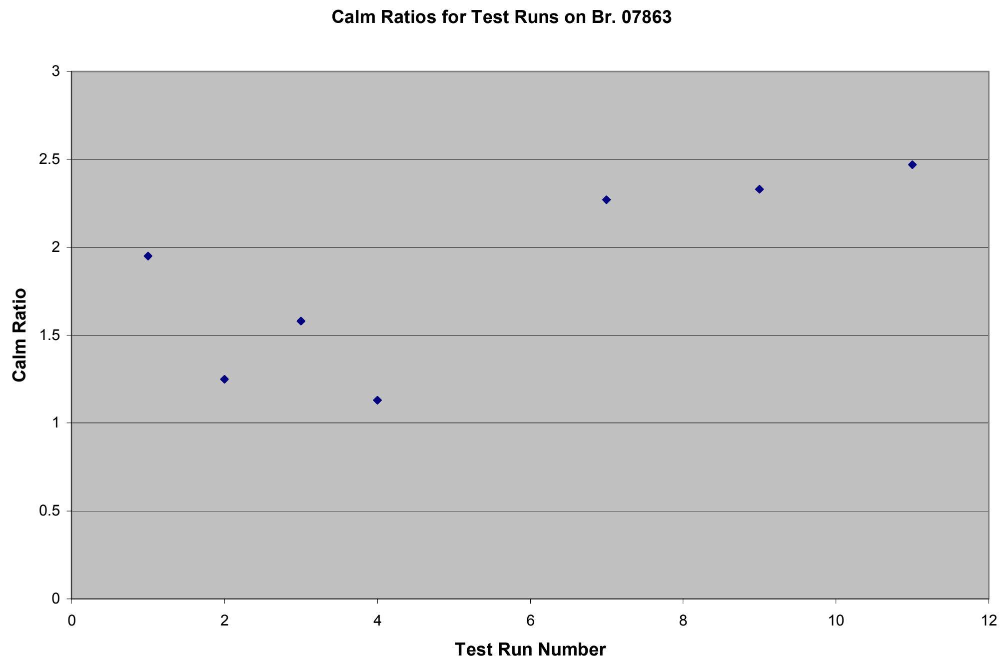

Figure 4.4.47 Summary of Calm Ratios measured during controlled loading.

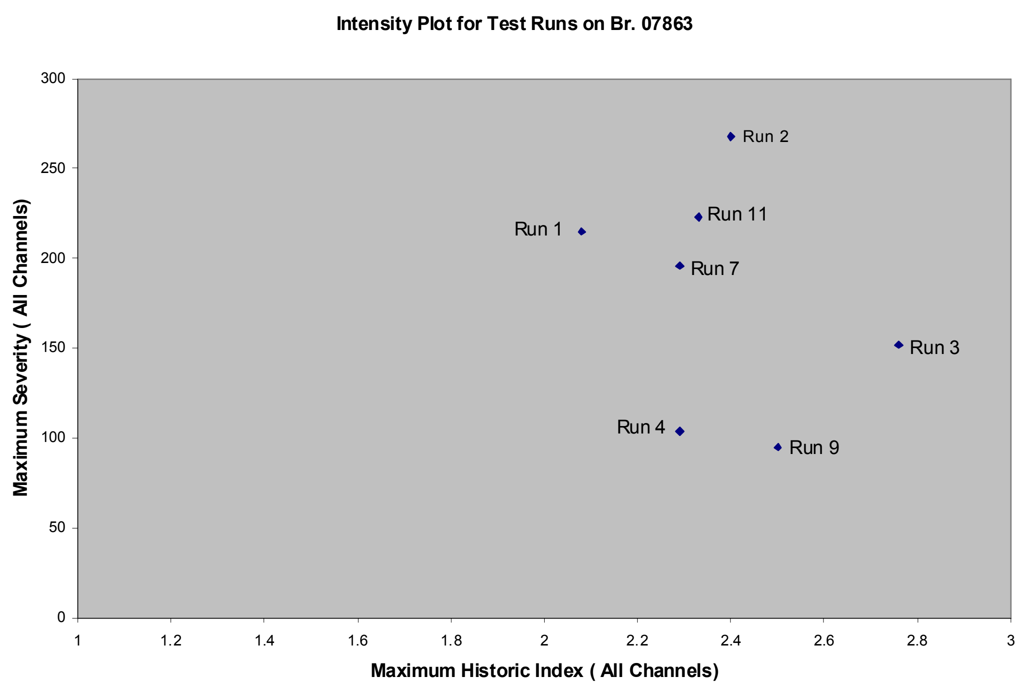

Figure 4.4.48 Summary Intensity plot for controlled loading.

5 Summary and Discussion of Laboratory and Field Testing Results

5.1 Stress wave propagation in concrete

Before attempting to implement AE monitoring schemes on RCGD bridges or test specimens, a basic understanding of how the three main types of stress waves that can exists in a semi-infinite solid medium propagate through and reveal themselves on the surface of structural concrete must first be obtained. The dilation or P-wave, the distortion or S-wave and the Rayleigh or R-wave travel at different speeds, attenuate in different manners and produce different vertical components of surface displacement when appearing on a measurable free surface. Five separate but related laboratory test projects were developed in order to quantify the responses of these parameters in a concrete solid medium.

5.1.1 Acoustic Emission Sensors and Their Calibration of Concrete Structures

Three different types of AE sensors were used for this project, a 150 kHz and 60 kHz resonant type and a high-fidelity type. The resonant sensors have much greater sensitivity especially to surface velocity and acceleration. They are most useful for applications of parameter based AE analysis which was the primary approach used. The high-fidelity sensors primarily respond to surface displacement at the cost of sensitivity and are most useful for laboratory work focused on stress wave propagation and attenuation. Foremost, AE sensors act as receivers, picking up the structures surface response to AE sources applied remote from the sensor. Breaking mechanical pencil leads on a free surface generates a strong and sharp disturbance much like a step or impulse function. Using this accepted method of providing an AE source in the structure, both the AE sensors acoustic coupling to the structure and attenuation of stress waves in the structure can be quantified. One advantage the pencil break source has is that it can develop responses that can be compared to analytic solutions to Lamb's problem. A disadvantage is that it is typically applied by hand with some variation in the source function. Another means of providing an AE source in a structure is to use one of the AE sensors as a driver and input a brief sinusoidal impulse into the structure. This approach has an advantage of great consistency between input sources. Also from a practical standpoint sensors can be pulsed remotely during a test and not require direct access to the test surface. This is an important feature when the alternative is a 30 foot ladder on semi level ground under a bridge. Because these sensors are basically electro-mechanical oscillators, the AE source that is input to the structure must be a sinusoid of some form. The calibration pulses developed for this purpose are well suited to create strong and sharp inputs, but they are not a step function like the pencil break, and thus identifying the multiple oscillations as they travel in the various forms available to them (P,S and R wave) can be more difficult to decipher and interpret.

This sub project which is covered in Appendix A quantified the basic responses of these AE sensors when mounted on concrete structures using both pencil lead breaks and calibration pulses.

5.1.2 Investigation of Surface Waves in Concrete from Pencil Lead Breaks

A second sub project was conducted to focus on surface wave propagation in concrete and make comparisons to analytic solutions of Lamb's problem. This work provides the experimental portion of the project which was used to support the analytical work done by Kennedy , et. al. [49]. The high fidelity type sensor was used as a receiver to characterize the vertical surface motion resulting from a pencil lead break on the same surface at a remote location. Both P and R-waves were clearly identified from the input source. P-waves were found to travel on the surface at 150 in/ms and typically could only be detected with in a few inches of the source due to rapid attenuation in the concrete and the small vertical component of motion produced by the P-wave. P-waves were found to have a very broad frequency spectrum as determined by FFT analysis with a frequency band ranging from 50 to 500 kHz. R-waves were found to propagate at a speed of 83 in/ms and suffered much less attenuation with detection capabilities exceeding 18 inches for pencil lead break sources. R-waves are more narrow banded in frequency content then P-waves with the higher frequencies attenuating rapidly and then traveling and oscillating in a monochromatic nature. Within a few inches of propagation, the R-wave was found to have a frequency band of 50 to 340 kHz which rapidly attenuated down to a frequency of 50 kHz after only 7 inches of propagation and continued in this manner. Based on the measurement of the P and R-waves in addition to physically measuring the mass density of the concrete used, the propagation speed of the S-wave was calculated to be 88 in/ms. The S-wave is often difficult to identify in transient wave forms due to its subtle motion characteristics. Knowing when to expect its arrival proved to be useful for the analytical modeling of stress waves propagating through the thickness of the full size test specimens covered in Appendix E. Knowledge of how these stress waves propagate and attenuate in concrete is very useful for selecting the appropriate AE sensors and array deployment on real bridges.

5.1.3 Surface Wave Propagation in Concrete Using Resonant Sensors and Calibration Pulses

The next logical step to developing an understanding of AE sensors applied to concrete structures is to repeat the means used in the previous section but incorporate the more sensitive resonant type sensors which can be found in Appendix C. Calibration pulses were used, replacing the pencil break as an AE source in order to increase repeatability and better quantify attenuation over larger areas. A high-fidelity sensor was used as a driver because its input source contained the fewest number of oscillations and was most easily characterized for the analytical project running in parallel with this project. The source was placed on the center of a large concrete block and both resonant and high-fidelity receivers were placed around the source at various distances. Responses such as P and R-wave arrivals, peak amplitudes and propagation speeds were measured for all sensor types and over different regions of the assumed homogeneous test block. Automated wave speed measuring methods commonly employed in AE testing were examined and compared to the results found by examining transient wave forms. The automated method almost always misses the arrival of the first P-wave oscillation generated from the calibration pulse for practical propagation distances and typically triggers on a later higher amplitude wave, thus under predicting the actual wave speed. The different sensors each responded in a different manner. The more sensitive resonant type would trigger on the second or third P wave oscillation giving an indicated speed of around 120 in/ms out to a propagation distance of 12 to 16 inches after which they would tend towards the R-wave speed in the range of 80 in/ms. The high-fidelity sensors would trigger on the second and third P-wave oscillation out to approximately 5 inches and then trigger on the first R-wave oscillation out past 18 inches. The far field attenuation for the 150 kHz, 60 kHz and high-fidelity sensors on the concrete test block surface was found to be 2.4 , 1.5 and 2.3 dB per inch of propagation distance, respectively. Rayleigh wave geometric attenuation is 0.52 dB/in, thus a significant amount of material attenuation (scatter and friction loss) is evident in the data. Variations in wave speed and attenuation in the as cast concrete test block were also investigated and found to be very uniform over the 16 square feet of surface area.

This sub project quantified the attenuation rates for each sensor type when mounted on concrete at practical sensor spacing. It also demonstrated the limitation of the automated wave speed measurement methods when used with calibration pulses for AE sources. Both of these factors must be understood to design and employ an AE test on a real bridge.

5.1.4 Effects of Aggregate Gradation of the Propagation of Bulk Wave in Concrete.

Concrete, being a mixture of various gradations of aggregate, sand, water and cement can be expected to be very non-homogenous on a macro distance scale. Based on the results discussed in Chapter 2, the propagation of stress waves through such a medium are not terribly affected by variations in aggregate gradation provided the frequency range of propagation is held within certain bounds, especially at the high end. A significant number of tests have been performed and results published confirming this observation as presented in Chapter 2. It is the larger aggregate that could have the greatest effect on the propagation of stress waves if higher frequencies are collected, above approximately 500 kHz. However, at the time this project was started, very little information was available for the effects of aggregate gradations with maximum sizes exceeding ¼ inch. The AASHTO Class-A structural concrete specified for the construction of the vintage RCDG bridges studied contains a significant amount of aggregate that is larger then ¼ inch, with up to 50% by weight exceeding ¼ inch and maximum aggregate sizes of ¾ inch.

This sub project was designed and implemented to characterize the effects of common aggregate gradations on the propagation of dilatational waves through specimens of usefully large proportions as found in Appendix D. Twelve inch diameter concrete test specimens were cast up using 5 different concrete mix designs and in three different lengths. The lengths were cast at 3, 6 and 12 inches. The mix designs only varied in maximum aggregate size ranging from the commonly specified ¾" minus gradation down to a mix with the maximum aggregate size being that of sand or less then ¼ inch. A high-fidelity AE transducer was used as a driver at one end of each test specimen to introduce an AE source with a calibration pulse. A second high-fidelity sensor was placed as a receiver at the other end of the specimen to capture and record the surface displacements resulting from the stress wave after it propagated through the height of the test cylinder. Individual wave forms were analyzed for each test and the P-wave speed, frequency content and amplitude were measured. The test method proved to be very repeatable with low variation between results for a particular cylinder. The overall effects of the aggregate gradation were much more uniform in the 12 inch cylinders when compared to the 3 and 6 inch cylinders. The twelve inch cylinders are likely more representative of the concrete used in construction because the longer propagation distance allows for sampling of more defects and thus tends to average out better then the shorter cylinders. A typical minimum thickness for the vintage RCGD structures is 12 to 14 inches.

Measured P-wave speeds ranged from 140 to 163 in/ms over the entire range of aggregate gradation for the 12 inch specimens. This is surprisingly small variation considering large differences in maximum aggregate size. P-wave amplitude attenuation among the different gradations was also quit small, differing by less then a factor of 2 for all 12 inch specimens. This amounts to 6 dB at twelve inches. The plot shown in Figure D22 of Appendix D portrays the small variations well. Again the measured attenuation is much greater then pure geometric attenuation revealing that other loss mechanisms dominate. As seen though, these loss mechanisms do not vary strongly with the aggregate gradations studied. Finally, the primary frequency peak in the FFT of each P-wave shows a range of 100 to 175 kHz for all aggregate sizes after 12 inches of propagation.

This sub project showed that the observations of previous research, that the maximum aggregate size on the propagation of dilatation waves in concrete does not strongly effect the results if a upper bound of frequency range is used, can be extended to common structural concrete that contains aggregates with maximum sizes up to ¾ inches. In other words, for the frequency ranges used in AE testing of concrete bridges, the concrete can be reasonably treated as a homogenous material when it is in the un-cracked condition.

5.1.5 Effects of Reinforcing Steel on the Propagation of Bulk Waves in Concrete

A final sub project was designed and implemented to quantify the effects that reinforcing steel may have on the propagation of P and S waves through a concrete medium. All bridge structures studied incorporate ½ inch diameter (No. 4) steel rebars to carry a portion of the shear loads in the girder once the girder stem is cracked. These bars are typically set 2 inches in from the outer faces of the stem on both sides with spacing ranging from 24 to 6 inches. Stem thickness is typically 12 to 16 inches. AE sensors must be placed on exposed surfaces for practical application of in-service bridges. The vast majority of real AE events caused by structural damage will originate from the interior of the girder stem as opposed to the outer surfaces and thus will have the opportunity to intercept a stirrup or rebar prior to manifesting itself onto the surface to be sensed. Granted that even at the low end of rebar spacing, these vintage beams have much more concrete volume then steel volume and from a stress wave propagation perspective could be considered to be lightly reinforced when compared to concrete structures such as columns which contain large amounts of steel reinforcing.

To quantify the effects of the steel, two test specimens were cast each of which were very representative of the high shear region found in both the full scale laboratory specimens and in the field. One test specimen was un-reinforced and the other had steel reinforcing at the low end of spacing, which is 6 inches and thus represents the highest steel-to-concrete ratio found in service and on the full scale specimens. A high-fidelity AE transducer was used as a driver and input an AE source on one side of the stem. The resulting stress waves were allowed to propagate through the thickness of the stem and were received by a second high-fidelity AE sensor. The sending sensors position was fixed and the receivers position was varied. The extent of position variation was such that the effects from the test steel reinforced specimen would capture at least one stirrup. Variations in the P-wave amplitude on the receiving surface were compared both with position and with and without reinforcing steel. The results showed that the test procedure was very repeatable with little variation at particular receiver locations but the amplitudes did significantly vary between positions and with the addition of the steel reinforcing bars. Peak amplitude variations of 300% were measured between reinforced and un-reinforced specimens. This equates to nearly 10 dB. This is a significant difference and could have a measurable effect on localization methods. For parameter based AE which is not concerned with identifying the arrival of the P-wave, the effect is likely much less significant. Analytic models are being develop to better understand these effects and also help sort out the vertical components of surface displacement from P and S-wave striking the surface at various angles of incidence. The effects of rebar spacing on parameter based AE are also being investigated with more laboratory testing being performed by Higgins et. al. [50].

5.2 Full Scale Laboratory Beam Testing

With a basic understanding of AE sensor performance and stress wave propagation in a concrete medium achieved the next step was to apply this knowledge to the full scale laboratory beams that were tested under SPR 350. The goals of this portion of the research were to validate the damage assessment methods presented in NDIS-2421 when applied to beams that are designed specifically to fail from shear overload as opposed to flexure, establish new damage criteria for this mode of failure and gain experience with different AE sensors and sensor deployments. Once these features are better understood from the laboratory work, then they can be applied to in-service structures.

5.2.1 Variations in the Laboratory Testing of Full Scale Beams

Several variables were incorporated into this test program including beam design, beam loading, AE sensor type and array deployment.

5.2.1.1 Beam Specimen Design Variations

All test beams had the same physical dimensions that included a length of 26 feet, a depth of 4 feet, a flange that was 3 feet wide and 6 inches deep and a stem that was 14 inches thick. Two basic configurations were used, the T-beam which simulated positive flexure when loaded in four point bending and the IT or inverted T-beam that simulated negative flexure. In all cases the flange represented the deck portion of the RCDG. The primary variable for these test beams was shear stirrup spacing which ranged from 6 inch to 24 inch spacing. Other variables such as debonded stirrups, under developed flexural steel and continuity variations in the stem to flange connections were also tested.

5.2.1.2 *Loading Variations*

The primary loading protocol consisted of slow monotonic loading to a predetermined maximum load followed by a hold period and then unloading. With each load cycle the maximum load was incrementally increased until failure or a predetermined amount of damage based on diagonal tension crack width was met. Under this loading protocol variations in loading rate, shear-to-moment ratios and reloading were tested. High cycle fatigue testing was included by first pre-cracking the test specimen to a specified level of damage, followed by 2 million cycles of simulated heavy truck loads and followed with monotonic loading to failure.

5.2.1.3 *Variations in AE Sensor Type and Array Deployment*

Three different AE sensor types were used for these tests; 1) high fidelity sensors, 2) 150 kHz resonant type sensors and 3) 60 kHz resonant type sensors. These sensors were deployed in six different manners. The primary manner used a planar arrangement that covered the expected shear failure region at one end of the test beam. Two variations of this arrangement were used including rectangular and skewed rectangular coverage. A third type of planar array focused all sensors around the crack tip of a major diagonal tension crack after it had formed. Three different linear arrays were also used. The primary linear array placed all sensors horizontally at mid-depth of the stem and were spaced such that the entire beam was covered. A second type placed all sensors in a vertical array mounted directly over a stirrup that was located in the high shear zone. A third linear array placed all sensors horizontally over the high shear zone of the stem at one end of the beam.

5.2.2 Example Static Beam Test

In order to understand the calculation of damage assessment parameters based on AE measurements, a basic understand of AE measurements and their responses to load is required. The test setup and data presentation for all 31 beams tested with AE were conducted in a similar manner. A typical example of a complete monotonic loading protocol up to failure was presented in detail. Parameters that are important to damage assessment such as number of AE hits, peak amplitudes and other parametric representations of transient wave forms were explained and their corresponding responses to various levels of loading demonstrated. The various plots shown can be used as a starting template of analysis of the AE data when applied to these types of structures.

5.2.3 Damage Assessment Using AE

Prior work by others [2,5,8,9,12,17,46,47,48] have demonstrated that damaging processes and damage accumulation in concrete structures can be identified and to some extent quantified through the interpretation of AE data taken during loading processes. The most mature method that has been applied to such structures is that specified in the Japanese non-destructive testing standard NDIS-2421 which uses two parameters that are calculated from AE test data to categorize the accumulated level of damage in a conventionally reinforced concrete structure. The research that led to this standard used test data from beams that were designed to fail in flexure. A major portion of this research was focused on developing damage criteria that was specific to the particular class of bridge and service conditions that are of concern to ODOT, with diagonal tension cracking being of particular interest.

A second damage assessment approach was also considered which came out of the FRP pressure vessel industry called Intensity Analysis [46]. The promising features of this approach are that it had been very well developed and became a test standard for this industry. It too was focused on testing composite materials and had recently been applied to concrete bridges with promising results [47,48].

5.2.3.1 Damage Assessment Using the Felicity and Calm Ratios

As detailed in Chapter 3 the Felicity Ratio is a good indicator of the breakdown of the Kaiser effect which in turn indicates damage accumulation in many materials. It is determined from the loading portion of the load cycle. One of the practical difficulties with measuring the Felicity Ratio is defining the exact onset of AE activity during the loading cycle. This is particularly true with conventionally reinforced concrete structures. A practical and consistent method for defining the onset of AE activity was developed and applied to all of the data sets. The Calm Ratio is a damage indicator that considers both the loading and unloading portions of the load cycle as developed by Ohtsu et. al. [2]. Its definition is much less subjective then the Felicity Ratio and is more practical to measure on in-service bridges.

Ohtsu found that the number of AE hits measured during a loading cycle was proportional to the CMOD in concrete test beams. The number of diagonal tension cracks and their corresponding crack mouth widths are fundamental physical damage assessment measurements taken by bridge engineers on RCDG bridges that exhibit distress. Thus, AE data can be related to physical damage on these bridges. Both the Felicity and Calm Ratios can be used for damage assessment individually or combined into the damage assessment chart developed in NDIS-2421.

The relationship between either of these AE parameters and normalized peak load was found to be quite linear over the in-service load ranges for most of the test beams, including those that were subjected to high cycle fatigue loading. A relationship for damage level and each of these AE parameters was developed. Three different damage levels were defined for loading level, Felicity and Calm Ratio based on the ODOT crack comparator tool used for bridge inspection. Thus, a set of damage criteria using the Felicity and Calm Ratios was developed specifically for the common vintage RCDG bridge found in ODOT inventory. These two AE parameters can be used to characterize the current state of structural damage accumulation in concrete structures and can be used to identify particular loading events that impart damage by examining the change in each of the parameters before and after the loading. For each of the three damage levels, a recommended response was developed ranging from do nothing up to invoking more refined structural analyses which may result in load restrictions or retrofitting. An important aspect of the recommended responses is that invoking load restrictions or retrofitting needs to be determined by a detailed structural analysis and not the AE results alone. One of the more recent AE tests on concrete bridges suggested that bridge replacement resulted from the AE test results. This response would be appropriate for more developed applications of AE such as the Intensity analysis applied to FRP pressure vessels discussed in the next section but not for concrete bridges. At the current state of development, AE should be used to invoke more refined analysis or other NDE methods and not bridge replacement.

5.2.3.2 Intensity Analysis

A more recent application of AE testing on concrete bridge girders uses the Intensity Analysis which appears to be very sensitive to the occurrence of structural damage. Again two parameters are calculated from the AE data but this time include peak amplitudes i.e. signal strength, as well as the number of AE hits. These two parameters are called the Historic Index and Severity. As with the Felicity and Calm Ratios each of these parameters is useful in itself and can also be combined to determine the Intensity of a particular AE source. The Intensity is a measure of the structural significance of an AE source. The Historic Index and Severity are calculated directly from the parameter based AE data (real time if necessary). An application specific factor is used for the calculation of each of these two parameters. Once they are calculated, they are correlated on an Intensity grading chart. Application specific grading criteria are then applied to determine the Intensity of each AE source or hit recorded.

Since the application of Intensity analysis to conventionally reinforced concrete is in its early stages of development very little guidance is available for choosing the appropriate factors for calculating the Historic Index and Severity, and to the author's knowledge, no guidance is available for the grading criteria needed to determine Intensity for the application at hand. The Historic Index and Severity were calculated for numerous test beam specimens and loading conditions. The responses and general magnitudes were examined and presented for a particular test beam in some detail. Overall results for all test beams were summarized.

The results showed that using the factors for calculating the Historic Index and Severity that were used by Fowler when applied to FRP pressure vessels provided reasonable results and behaved in the same manner through the loading ranges. The peak magnitudes for these parameters were found to be AE sensor type specific. Both of these parameters proved to be very sensitive and reasonably stable indicators of structural damage as it occurred. More research will be required to develop Intensity grading levels for this particular application, but monitoring both the Historic Index and Severity have immediate use in the application of Structural Health Monitoring systems to these bridges based on the laboratory and field testing results. Further analysis of these test data will likely lead to a preliminary set of Intensity grading criteria specific to this application.

5.3 In-service Bridge Testing

Having tested 31 laboratory beams to failure using AE to monitor the damage progress, the final phase of this project assembled all of the sensor installation and data reduction methods develop and applied them to three in-service vintage

RCDG bridges that were showing Level 2 or worse damage in the form of diagonal tension cracking. Gaining physical access to these structures to install sensors and apply controlled test loads requires a serious effort. Working for ODOT made this task reasonable by using State owned access equipment, maintenance personal to provide traffic control and loaded dump trucks for controlled loads. Each of the three tests provided a wealth of structural and AE test data and the experience needed to get quality data.

5.3.1 Testing of the Luckiamute River Bridge

The first bridge tested had already been fitted with ODOT's first Structural Health Monitoring system that was designed and installed by the author. This system had been monitoring and recording CMOD at five diagonal tension crack locations for 1 year prior to the AE test. The data indicated that some of these cracks had experienced measurable increases in CMOD over the year. CMOD was chosen as the primary structural parameter to monitor and correlate with the AE data during the testing. This approach proved to be practical and useful but lacked the sensitivity that could be had by using rebar strain. Because this bridge is located on a State Highway that has low to moderate traffic flow, greater latitude in loading protocols could be used which included static and dynamic loads. The highway was temporarily closed for each load case so the effects of each load could be monitored without influence from ambient loads. A rather severe load case was used that placed three heavily loaded dump trucks bumper to bumper on the main span. A large amount of ambient loading was also recorded.

By combining two AE systems a total of 14 AE channels were used for this test. The test section contained a Level 2 diagonal tension crack and was fitted with two planar arrays , one on each face of the stem surrounding the entire crack. One array used 60 kHz sensors and the other used a combination of 150 kHz and high-fidelity sensors. Though a significant quantity of AE data was measured, the amount and signal strengths were found to be much lower then those experienced in the laboratory testing when new cracks were forming and extending. This is in agreement with the load rating calculations that do not predicted diagonal tension cracking to result for the test loads applied. The damage state, as calculated by the Calm Ratio, was in reasonable agreement with the physical condition of the girder being tested. Enough AE data was produced to also calculate the Historic Index and Severity for many of the load cases. The 60 kHz sensors proved to be far more sensitive then the other sensors used as was suggested from the laboratory work.

5.3.2 Testing of the Banzer Bridge

The second bridge tested with AE was of a unique design which has only two main girders as opposed to the typical four. The load rating on this structure indicated that no capacity issues were present but physical inspection of the girders showed extensive and severe diagonal tension cracking with a maximum CMOD of over 0.07 inches. In fact, many of these cracks had been repaired by epoxy injection and then recracked. The design drawings indicate a very high density of shear stirrups in the cracked sections. This bridge is located in a very remote area that is surrounded by logging activity. Given the high load rating and the abundance of large cracks, illegal overloads were the suspected cause of the cracking. So even though this bridge has many features that differ significantly from the typical vintage RCDG bridge, it was thought to be an excellent candidate to apply AE.

Based on the experience from the previous field test, rebar strain was selected for correlating the AE data with loading. Again, a 14 channel AE system was used with one planar array focused on a major diagonal tension crack using 150 kHz sensors and a linear array that covered over 20 feet of the test girder using 60 kHz sensors. Access to the test section was more difficult on this bridge requiring the use of a special designed mobile access platform. Again due to the low traffic count the highway was temporarily shut down during controlled loading which included both static and dynamic loads.

Very little AE activity was measured during this test as a result of the controlled and ambient loads. Part of the reason for the reduced amount of AE data was due to the acoustic coupling between the AE sensors and the concrete had dried up over night and was thus compromised to some degree. Post loading calibration tests on the sensors coupling indicated a 10 dB loss in acoustic coupling on the 150 kHz sensors which is significant but not a complete failure. Again the 60 kHz sensors provided the vast majority of the AE data and the post-test sensor calibrations indicated good acoustic coupling. None of the controlled or ambient load cases provided enough AE data to make a high quality determination of the Calm Ratio which was found to require a minimum of 200 hits and neither the Historic Index or Severity could be calculated. Using rebar strain to determine loading condition proved to work very well.

Even though there was not enough AE data collected to make quality assessments of the AE damage indicators, the lack of data is consistent with the applied loads which load rating calculations indicate can easily be carried by the bridge. It is very likely that illegal heavy loads continue to use this structure on a regular basis. Of course these loads will not pass when there is a strong ODOT presence on the structure. Based on the results of these tests, the structural load rating and the presence of large cracks a Structural Health Monitoring system was designed and is currently being installed on this structure in anticipation of characterizing the overloads and possibly taking action to prevent future over loads.

5.3.3 Testing of the Pacific Highway Over Crossing of Main St. in Cottage Grove, OR

The third and final bridge tested with AE carries I-5 Southbound which has very high traffic volume. The structural details of this bridge are consistent with vintage RCDG designs. Moderate diagonal tension cracking has occurred with crack width at the border between Level 2 and Level 3. One cracked section of one of the 6 girders on the main span were fitted with 8-60 kHz AE sensors deployed in a 3 dimensional array surrounding a significant diagonal tension crack. Both rebar strain and CMOD were employed to correlate load with AE results. Controlled loads were limited to slow and fast dynamic loading using a rolling blockage on the highway to restrict ambient loads during the controlled loading. The test truck was run crossing the bridge in different lane positions which in turn loaded the test girder to different levels. The load rating on this structure indicates plenty of capacity for all but the heaviest permit loads and even these very heavy loads can be safely carried. The test truck produced moderate loading with the peak rebar stress range being less then 4 ksi. For reference the endurance limit of this rebar is 20 ksi.

All load cases produced a measurable amount of AE data due to the high sensitivity of the 60 kHz sensors. Even small passenger cars could be easily detected. For most of the test runs, enough AE data was generated to provide quality calculations of the AE damage parameters. Calm Ratio results indicate a fairly high level of accumulated damage with values in the 0.5 to 2.5 range. The maximum Severity measured was relatively low for 60 kHz sensors, and the Historic Index was in the range of 2 to 3 which was similar to Luckiamute river bridge. These are reasonable results considering the current physical condition of the test girder and the relatively light loading induced by the test truck. This test incorporated all of the experience gained from both the laboratory and previous field testing and is thus a very high quality set of AE data. Intensity plots were developed and presented in Chapter 4 and should prove useful for future development of grading criteria.

6 Conclusions and Recommendations for Testing RCDG Bridges Using Acoustic Emissions

6.1 Conclusions from Stress Wave Propagation in Concrete Testing

Even though structural concrete is very non-homogeneous on a macroscopic level, previous research has found that stress wave propagation in the frequency range applicable to Acoustic Emissions testing is not severely altered by the variation in aggregate gradation for aggregate sizes up to ¼ inch. Results from this research project has shown that this observation can be extended up to aggregate sizes of ¾ inch which is commonly found in the concrete used to construct vintage RCDG bridges. For all concrete mixes tested, attenuation of the stress wave amplitudes is significantly greater than pure geometric attenuation resulting from loss mechanisms primarily attributed to friction losses. Dilatation waves travel and attenuate faster than Rayleigh waves and are composed of a much broader frequency spectrum than Rayleigh waves. Dilatation waves are more practically detected with AE sensors when they strike the measuring surface with a significant normal component and can be measured over propagation distances exceeding 1 foot for strong sources such as pencil lead breaks or calibration pulses from other AE sensors. Dilatation waves that propagate parallel to the measuring surface can only be detected a few inches away from the source. Rayleigh waves can be detected over propagation distances exceeding 2 feet with resonant type sensors.

The 60 kHz resonant AE sensor proved to have much greater sensitivity for detecting stress wave propagation in concrete compared to the 150 kHz and high-fidelity AE sensors. It should be mentioned that the high attenuation of stress waves in concrete is not always detrimental to AE testing. It does limit the effective range of each sensor but also virtually eliminates spurious noise rejection problems which dominate AE testing on less attenuative materials such as steel and aluminum.

The effects of steel reinforcing bars inside a concrete matrix can have a measurable and significant effect on the transmission of dilatation waves as they reveal themselves on the measured surface. More research is needed to quantify this effect which is currently under way. Overall, the effect is not too significant for parameter based AE analysis but likely is significant when accurate localization of AE sources is required.

6.2 Conclusions from Laboratory Testing of Full Scale Concrete Beams

Laboratory testing of full scale beams confirmed that the Kaiser effects does exist in conventionally reinforced concrete structures subjected to increasing loads and that AE activity is proportional to damage that is quantified by crack mouth opening displacement. The state of accumulated damage can be tracked using either or both the Felicity and Calm Ratios. To a reasonable degree each of these parameters can infer the previous maximum load a particular RCDG beam has experienced. Also, for the load ranges that are of interest to in-service bridges, these two parameters behave in a surprisingly linear manner with load. On virgin test beams the Felicity Ratio always decreases with increasing maximum load, and the Calm Ratio always increases with increasing load. On test beams that have been pre-cracked and subjected to high cycle fatigue loading and then retested with a monotonic increasing load protocol, the Felicity Ratio was found to start out at a value well below 1.0, indicating high damage, and then increase with increasing load as damage was imparted to new sections of the beam. The Calm Ratio was found to start at a level near where it finished with the pre-cracking and then continue to increase up to near failure.

The formation and extension of diagonal tension cracks in every test beam produced very large quantities of high amplitude AE hits at high hit rates even when large sensor spacing was used. The Severity and Historic Index appear to do a very nice job of characterizing this phenomenon, with the Severity comparing the strength of the current sample of hits to the entire load data set and the Historic Index comparing the same with the previous sample. Thus, both relative signal strength and how fast it comes on are characterized.

These two parameters are most useful for assessing whether a particular load cycle produces structural damage that is significant. This can also be achieved by looking at changes in the Calm or Felicity Ratios if a second loading can be performed and with much less sensitivity. At this stage of development in the application of Intensity analysis of vintage RCDG beams, the Severity and Historic Index are purely qualitative just as they were when first being applied to the pressure vessel industry. But in a similar fashion, their usefulness for RCDG testing is very apparent and, based on the results for testing the laboratory beams, ready for implementation into testing and monitoring of in-services bridges. In time the author believes that quality grading criteria, which can be used to define Intensity levels that correlate well with damage associated with diagonal tension cracking, can be developed and practically implemented into structural health monitoring.

6.3 Conclusions from Field Testing of Concrete Bridges

Three in-service RCDG bridges that exhibited ODOT Level 2 to 3 diagonal tension cracking were tested with AE. Several variations in AE sensor type, array deployments, parametric inputs for tracking load and loading protocols were used based on those used in the laboratory testing. In general the AE measured in these tests is of much smaller quantity and lower signal strength than that measured in the laboratory. The loads imposed during the field tests would not be expected to form additional diagonal tension cracks, and thus strong bursts of AE should not be expected. However, a significant amount of data was collected and correlated with loading. The quantity and signal strength was consistent with that of the test beams being cycled at a low load level after having been pre-cracked. The Felicity Ratio is not easily calculated for in-service bridge testing because the maximum prior load is not known, though it could be estimated by current CMOD. The Calm Ratio was calculated for many load cycles, and when sufficient AE activity is measured,(more then 200 hits), it was found to reasonably correlate with the damage level in the beam being tested based on crack widths.

The Severity and Historic Index were calculated for two of the three bridge tests and proved to be very sensitive yet stable qualitative indicators of AE source intensity. Both parameters responded to increasing loads on the tested girders. When the test truck passed over the bridge in the lane that produced the maximum load on the test girder, the Severity had peak magnitudes up to 223 and the Historic Index maximum was 2.5. One of the static load cases on the Luckiamute river bridge produced a strong burst of AE during the load hold portion when three test trucks were on the test span. When the trucks were removed the CMOD gage indicated that the crack opening did not return all of the way back to its gap prior to the loading which is good evidence some structural damage may have occurred as a result of this load case. The AE data clearly identify this event’s occurrence in real time which produced a maximum Severity of 750 and maximum Historic Index of 4.4 over a three hour sample of ambient traffic which included a large number of apparently heavily loaded, though legal, trucks. The maximum Severity recorded was 1600 and the maximum Historic Index was 3.3. The CMOD ranges measured during the ambient loads were approximately 75% larger then the controlled loads indicating more severe loading, which is also indicated by the Severity and Historic Index.

Using the strain measured from a steel stirrup that crosses a diagonal tension crack is decidedly the best means of correlating load with the AE data. Installation of the gage and measurement of this parametric input is non-trivial and requires good access to the test section and a skilled person to make it work reliably. Measuring the crack mouth displacement is also a viable alternative which is much easier to apply but considerably less sensitive and not as direct a measurement of load.

Using 60 kHz resonant sensors produces much more useable AE data then either the 150 kHz or high-fidelity sensors. The latter two can be used for tightly spaced arrays centered close to a damage site of interest with reasonable results, but for general application and greater coverage, the 60 kHz sensors proved to be far superior. The reasons for this were clearly determined in the study of stress wave propagation in concrete found in Appendices A through E.

Loading protocol is very important for establishing a base line response for a particular bridge. Even though many of the bridges of concern are very similar in construction, both to each other and the laboratory test specimens, controlled loads should first be applied to calibrate the monitoring system. This is no different then requiring a separate structural load rating to be performed on each bridge even though many of them are identical in many features. Having a quality load rating that characterizes the test loads imposed in conjunction with the AE data can be very useful for determining acceptable service limits for bridges whose capacities are in question or of concern.

6.4 Recommendations for Testing and Monitoring of RCDG Bridges Using AE

Based on the laboratory and in-service bridge test results determined from this research a set of recommend guidelines for testing vintage RCGD highway bridges the are subject to diagonal tension cracking was developed and is described below.

6.4.1 Visual Inspection of Bridge

A visual inspection of the bridge, in accordance with National Bridge Inspection Standards, should first be performed to identify the general physical condition, identify, locate, map and measure all visually detectable cracks or other forms of damage. Even if a recent bridge inspection report is available, it should be verified with an inspection prior to planning the testing procedures. Review of maintenance activities over the life span of the bridge is also desirable.

6.4.2 Structural Load Rating

The most current load rating for the bridge should be obtained and the sections with the lowest rating factors should be compared to the physical damage observed in the inspection and determine if there is reasonable correlation. Preferably the rating was performed using one of the more modern codes such as LRFR (Load Resistance Factor Rating) or better yet using the procedures specified in SPR 350. The loads considered in the rating should be compared to both the real ambient loads and the loads that can be practically applied with test trucks. A load rating performed using the exact test trucks weights, axle configurations and load placement is highly desirable for making the best use of the test data.

6.4.3 Select Test Section on Girders

Based on the visual inspection and load rating data the appropriate test section on the bridge girder lines should be selected. The ideal section will contain significant diagonal tension cracks that are all spaced approximately the same distance for the nearest vertical support structure, i.e. bent or pier on each girder line. The cracks should cross nearly the full depth of the stem at an angle, preferably close to 45 degrees, with one or more shear stirrups crossing the crack. If several of these sections are present then choose one considering maximum crack width and / or ease of access. Ideally strain gages and / or CMOD transducers can be installed on each girder line at the chosen section with the strain gage attached to a shear stirrup that crosses a diagonal tension crack and measuring CMOD near the strain gage location.

6.4.4 Select AE Sensor Type and Array Deployment

If 60 kHz resonate type sensors are available, their use is preferred due to greater sensitivity and potential coverage then higher frequency units. High-fidelity sensors are generally not sensitive enough to be of practical use for field testing. The array deployment should be decided considering the sensor type, number of sensors and desired area of coverage. For general application when more then one crack is present, a widely spaced linear array deployment centered at mid depth of the stem will provide the greatest coverage. Sensor spacing up to approximately 6 feet can be used with the 60 kHz sensors and 1 ½ to 2 feet for 150 kHz sensors. Depending on the number of sensors available and the locality of cracks, using more then one linear array, e.g. one array on each girder line, maybe desirable. Using the ZIP analysis discussed in Chapter 3 would best be applied using these types of array deployments.

If there is one particular crack or other damage feature that is of concern then using planar arrays that cover the defect area are preferable. Ideally enough sensors can be employed to deploy two or more planar arrays of 3 channels or more around the defect area. When determining the exact location of each sensor, it should be kept in mind that non-symmetric sensor placement around the defect will provide the greatest accuracy for localization algorithms if they are to be used. Mounting sensors on both sides of the stem and the bottom face is desirable for optimal coverage of the damaged region. It is also desirable to locate and mark on the girder stem the location of all stirrups in the test area using a rebar locator.

Another factor to consider is access to the test surfaces. Bridges will typically require access equipment ranging from ladders to man lifts. In many instances use of these tools will involve traffic control which may be the deciding factor sensor placement. Safe access is a must because installation of the parametric and AE sensors and related lead wires is time consuming work that requires comfortable and steady access.

6.4.5 Data Acquisition Equipment Location

A location to setup the data acquisition equipment should be selected that is safe to work from for both the operators and equipment. Lead wire runs must also be considered when choosing the location. The AE system can tolerate lead wire runs exceeding 200 feet if necessary, but typically CMOD and particularly strain transducers will not unless signal conditioning can be applied at the transducer. If a medium to long term health monitoring system is to be employed, then vandalism and theft of the expensive test equipment must also be considered.

6.4.6 Mount and Check the parametric and AE sensors

The parametric sensors should be installed prior to mounting the AE sensors ,especially if strain gages are to be used. This will reduce the chances of damaging the AE sensors. The AE sensor fixtures should be mounted in the sensor locations determined in Section 6.4.4. The concrete surface must be cleaned with a wire brush or grinding stone to remove the paste from the surface and expose any surface voids. Mounting sensors directly over voids should be avoided. Using a quality cyanoacrylate adhesive of medium to thick viscosity with a quick setting activator works very well for adhering the AE sensor clamp to the prepared concrete surface. Laboratory grade vacuum grease is the preferred acoustic couplant to be used between the AE sensor aperture face and the concrete surface. A minimum clamping force of 4 lbs is required for good acoustic coupling. Once the sensors are mounted and lead wires run, the acoustic coupling of each sensor should be checked using the pencil lead break method discussed in Chapter 4 and ASTM E-650. The responses of the parametric input transducers should be zeroed and checked.

6.4.7 Set AE Thresholds

With the data acquisition system up and running the triggering thresholds for each AE channel should be set. Ideally five minutes of data with no alternating loads on the structure should be measured. The RMS levels from each sensor can be used to determine the lowest threshold levels which for a quality AE system and sensor should be around 3 times the RMS value. Floating threshold levels can be implemented with good success on AE systems so equipped. Once the thresholds are set ambient traffic should be allowed to cross the structure. The recording threshold, which is typically higher then the detection threshold, can be set by observing the response of the system to insignificant loads such as small passenger cars.

6.4.8 Run Controlled Load Cases

Once the data acquisition system is fully operational and threshold set, the controlled loading can be conducted. It is almost mandatory that no other alternating and preferable no additional static load are on the test span or the attached approach spans during the application of the controlled loads. With highway bridges this can be challenging and will require proper planning of traffic control. On high volume highways the rolling blockage performed in low volume hours of operation is recommended. Typically under these conditions static load cases cannot be applied. If permitted, static load cases are desirable for unambiguous calculations of the Calm Ratio. Quality field notes should be taken during the test runs so there is no ambiguity regarding which loading case corresponds too which data set. Photographs of each load case are very useful for post processing of the data.

6.4.9 Ambient Load Cases

Typically the controlled loads will not be as severe as the upper end of the ambient loads. For this reason it is desirable to collect at least 100 ambient load cases. Often times the most severe loads will occur when a combination of trucks are on the span at the same time. This event is probabilistic and thus requires a significant amount of loading to capture. A full time structural health monitoring system will provide the best chances of capturing such events.

6.4.10 Calculate Damage Parameters

For each controlled load case the Calm Ratio, Severity and Historic Index should be calculated. The Calm Ratio is a single parameter that characterizes the current state of accumulated damage in the test section. This parameter represents the entire load case and generally will not change unless more damage is imparted to the test section. If insufficient AE activity is recorded, i.e. less then

200 hits, then the value can vary greatly, though typically on the orders of 0.1 to 10. A stable calculation of the Calm Ratio should be repeatable in the range of 0.1 to 1.0.

The Severity and Historic Index for each AE channel should be calculated over each load case data set. Using J=50 and N-K=200 is a good starting point for the factors needed to calculate the Severity and Historic Index respectively. Expect the lighter load cases, i.e. test truck crossing being mostly supported by non-instrumented girders, to not yield reliable or for that manner any results with these two parameters. Again more then 200 hits are required to begin calculating these parameters, especially the Historic Index. The data are calculated per channel and typically presented that way especially if ZIP analysis is to be employed. Peak values from all channels over the entire load case are also a useful way to present the overall results.

6.4.11 Compare Parametric Data to Load Rating

Preferable rebar strain was recorded so that the actual loads imposed on the test girder(s) can be compared with calculated results from the load rating. The more sophisticated the load rating the better they will agree. It is also acceptable to apply the strain data to the load rating for fine tuning if it is done in the manner prescribed in LRFR. Load rating factors can now be confidently assigned to each test load case.

6.4.12 Developing Intensity Grading Criteria

If the measured loads can be brought within reasonable agreement with load rating results then acceptable operational limits or threshold can be assigned to the Severity and Historic Index responses. Base lines can be established from the test data by assigning Intensity grading criteria for each of the controlled load cases based on the load rating factors. These grading criteria will only be directly applicable to the maximum level of loading applied during the controlled loads. As previously discussed ambient loads will likely exceed these levels. Based on the ambient data collected, a representative range of maximum Severity and Historic Index can be determined and applied as a threshold level for a structural health monitoring system. Because many of these bridges are very similar in design and construction, test results from one bridge to another can at least be compared to help refine or extend the loading ranges that the Intensity grading criteria cover and thus mature over time much like it has in the pressure vessel industry.

6.4.13 Implementation of AE Testing into a Structural Health Monitoring System

There are at least two reasons to proceed with the design and installation of a structural health monitoring system after the above described testing has been completed. The first and primary reason is that the calculated load rating predicts an under capacity structure for carrying the expected loads. This would be especially true if the load rating in question was refined with strain gage data and still predicted a under capacity situation. When this occurs, it is often not feasible to limit loads on the bridge due to political reasons, and repairs or replacement will take time to implement. Assuming the owners do not fear the bridge will pose safety issues, (i.e. potential collapse or excessive deflections, which will likely be the case for the subject bridges), a structural health monitoring system can provide reliable assurance that the structure is performing adequately under the service loads until the repairs or replacement can be implemented. Past practice under these conditions have been addressed by sending out a bridge inspector to the structure on an increased frequency. NBIS standards require a maximum of 2 year periods between inspections. In some cases this has been reduced by owners to a period of 7 days. Though sending a real person to a troubled structure who knows what to look for on a very repetitive cycle does provide a level of comfort for the owners, it is very impractical, expensive and technically speaking, of questionable value.

For bridge structures that have moderate to high use and value, a more effective and efficient approach is to install a structural health monitoring system that can continuously measure important structural responses such as stirrup strain, CMOD and AE. Such systems, as are currently being implemented on several ODOT bridges, can provide real time continuous monitoring that can be easily accessed by maintenance engineers from the office. Not only is this far more convenient then constant physical inspection, it is more effective because the monitoring is continuous. Historic trends are also more easily identified form the data which can warn of increasing damage accumulation, rebar stress ranges and CMOD. Thresholds on both the structural and AE data can be set, and the system can notify the owner when they have been exceeded, thus causing a real person to investigate the structure physically.

By establishing Intensity grading criteria, AE could be readily implemented for this purpose. No other means of non-destructive testing currently available is better suited to detect the occurrence of structural damage over a large area in real time then AE when properly applied. Results from this research has shown that the formation and significant extension of diagonal tension cracks in RCDG's can be readily detected and approximately located when using ZIP analysis. The Severity can be expected to increase 1 to 3 orders of magnitude during such an occurrence when compared to load cycles that do not impart such damage. The Historic Index has been found to increase by a factor of 3 to 7 from such damage. Using these two AE parameters along with rebar strain and / or CMOD to confirm a service load produced the AE as opposed to other sources such as electrical interference or environmental conditions, can provide the grounds for a very sensitive and reliable structural health monitoring system on the subject structures.

Another practical application for implementing a structural health monitoring system can be for detecting and quantifying overloads on structures. The Banzer bridge discussed in Chapter 4 is a good example of this application. Both the load rating and testing of this bridge indicate adequate structural capacity for legal loads. Physical inspection of the bridge shows extensive accumulated damage. It is very likely illegal heavy loads are using this remotely located bridge and causing this damage. Providing weight enforcement at this remote location is neither practical nor likely effective. A structural health monitoring system is currently being installed on this structure for full time monitoring. At this time the system will only monitor and record structural transducers and not AE transducers. This is due to the fact that such systems are relatively new to ODOT and keeping the first few installations simple and moderately priced were self imposed requirements. The system will however have the ability to provide threshold exceedance notification as well as real time remote monitoring of the data. Both AE and triggered video cameras can be included at a future time if the first year or two of monitoring justifies such action.

6.5 Recommendation for Further Research

Many of the results and conclusions from this research can be directly applied to structural health monitoring of vintage RCDG bridges as described above. The most immediate need for research will be focus on developing Intensity grading criteria for these structures. The test data from both the laboratory work and field testing will provide a solid basis to begin developing these criteria. Once a more firm understanding of these parameters is achieved when applied to concrete structures, more field testing and applications should allow the Intensity analysis approach to be developed into an accepted test standard for such applications.

Bibliography

1. Luangvilai , Kritsakorn , Punurai , Wonsiri and Jacobs , Laurence J. , " Guided Lamb Wave Propagation in Composite Plate / Concrete Component," Technical Notes , Journal of Engineering Mechanics , pp. 1337-1341. Dec. 2002.

2. Ohtsu , Masayasu , Uchida , Masakatsu , Okamoto , Takahisa and Yuyama , Shigenori , " Damage Assessment of Reinforced Concrete Beams Qualified by Acoustic Emission, " ACI Structural Journal Vol. 99 , No.4 pp 411-417 , August 2002.

3. Landis , Eric N. and Baillon , Lucie , " Experiments to Relate Acoustic Emission Energy to Fracture Energy of Concrete," Technical Notes , J. of Engineering Mechanics pp 698-702 , June 2002.

4. Jacobs , Laurence J. and Owino , Joseph O. , " Effect of Aggregate Size on Attenuation of Rayleigh Surface Waves in Cement-Based Materials, " J. of Engineering Mech. pp 1124-1130 , Nov. 2000

5. Yuyama , Shigenori , Okamoto , Takahisa , Shingeishi , Mitsuhiro , Ohtsu , Masayasu , and Kishi , Teruo , " A Proposed Standard for Evaluating Structural Integrity of Reinforced Concrete Beams By Acoustic Emission , " Acoustic Emission: Standards and Technology Update , ASTM STP 1353 pp. 25-40 1999.

6. Landis , Eric N. , " Micro-macro Fracture Relationships and Acoustic Emissions in Concrete," Construction and Building Materials Vol. 13 , pp. 65-72 , 1999.

7. Ohstu , Masayasu , Okamoto , Takahisa , and Yuyama , Shigenori , " Moment Tensor Analysis of Acoustic Emission for Cracking Mechanisms in Concrete," ACI Structural Journal , Vol. 95 , No. 2 , March-April 1998.

8. Ohtsu , M. , " The History and Development of Acoustic Emission in Concrete Engineering", Magazine of Concrete Research , Vol. 48 , No. 177 , pp. 321-330 , Dec. 1996.

9. Balazs , G.L. , Grosse , U.C. , Koch , R. , and Reinhardt , H.W. ," Damage Accumulation on Deformed Steel Bar to Concrete Interaction Detected by Acoustic Emission Technique," Magazine of Concrete Research , Vol. 48 , No. 177 , pp. 311-320 , 1996.

10. Suaris , W. , Van Mier , J.G.M. , " Acoustic Emission Source Characterization in Concrete Under Biaxial Laoding," Materials and Structures , Vol. 28 , pp. 444-449 , 1995.

11. Landis , Eric N. and Shah , Surendra P. , " Frequency-Dependent Stress Wave Attenuation in Cement-Based Materials, " J. of Engineering Mech. pp 737-743 , June 1995.

12. Balazs , G.L. , Grosse , U.C. , Koch , R. , " Deterioration in Fatigue Detected by Acoustic Emission Technique, " Proceedings , IABSE Symposium San Francisco , 1995 , pp. 1289-1294.

13. Maji , A.K. , Sahu , R. " Acoustic Emissions from Reinforced Concrete" , Experimental Mechanics, Vol. 34 , No. 4 , pp. 379-388 , Dec. 1994

14. Landis , Eric N. , Shah , Surendra P. , " Recovery of Microcrack Parameters in Mortar Using Quantitative Acoustic Emission," Journal of Nondestructive Evaluation , Vol. 12 , No. 4 pp.219-232 , 1993.

15. Maji , A.K. , "Determination of In-Situ Stresses From Acoustic Emissions, " Proceeding of Engineering Mechanics, pp 405-408 , 1992.

16. Glaser , S.D. and Nelson , P.P. , " High-Fidelity Waveform Detection of Acoustic Emissions from Rock Fracture, " Materials Evaluation , pp. 353-360 , March 1992.

17. Ouyang, Chengsheng , Landis , Eric , and Shah , Surendra P. , " Damage Assessment in Concrete Using Quantitative Acoustic Emission, " Journal of Engineering Mechanics , Vol. 117 No. 11 , pp. 2681-2698 , 1991.

18. Ohtsu , Masayasu , "AE Application to Fracture Mechanics," Trans. Of the Japan Concrete Institute , Vol. 11 , pp. 141-146 , 1989.

19. Yoshikawa , Sumio , and Mogi , Kiyoo , " Experimental Studies on the Effect of Stress History on Acoustic Emission Activity – A Possibility for Estimation of Rock Stress," Journal of Acoustic Emission Vol. 8 , No. 4 pp 113-123 , 1989.

20. Maji , A. K. , Ouyang , C. , Shah , S. P. , " Fracture Mechanisms of Quasi-Brittle Materials Based on Acoustic Emission, " J. Mater. Res. , Vol. 5 , No. 1 , pp 206-217 , Jan. 1990.

21. Benz , Rudiger , Niethammer , Marc , Hurlebaus , Stefan and Jacobs , Laurence J. " Localization of Nothces with Lamb Waves," J. Acoust. Soc. Am. 114 (2) pp 677-685 , Aug. 2003.

22. Scarpetta , E. , Sumbatyan , M.A. , " In-Plane Wave Propagation Through Elastic Solids with a Periodic Array of Rectangular Defects," Journal of Applied Mechanics Vol. 69 , pp. 179-188 , March 2002.

23. Neithammer , Marc and Jacobs , J. Laurence , "Time-frequency representation of Lamb waves, " J. Acoust. Soc. Am. , Vol. 109 , No. 5 Pt. 1 , pp 1841-1847 , May 2001.

24. Neithammer , Marc and Jacobs , J. Laurence , "Time-frequency representation of Lamb Waves Using the Reassigned Spectrogram, " J. Acoust. Soc. Am. , Vol. 107 , No. 5 Pt. 1 , pp L19-L24 , March 2000.

25. Enoki , M. and Kishi , T. , " Theory and Analysis of Deformation Moment Tensor Due to Microcracking, " International Journal of Fracture , Vol. 38 , pp. 295-310 , 1998.

26. Maji , A.K. , Satpathi , D. , and Kratochvil , T. , " Acoustic Emission Source Location Using Lamb Wave Modes, " J. of Engineering Mech. pp. 154-161 , Feb. 1997.

27. Littles , Jerrol W. , Jr. , Jacobs , Laurence J. and Qu , Jianmin , " Experimental and Theoretical Investigation of Scattering From a Distribution of Cracks, " Ultrasonics Vol. 33 No. 1 pp. 37-43 , 1995.

28. Landis , E. , Ouyang , C. and Shah , S. P. ," Automated Determination of First P-wave Arrival and Acoustic Emission Source Location," Journal of Acoustic Emission , Vol. 10 , No. 1-2 , pp. 97-103 , 1992.

29. Jacobs, Laurence J. " Characterization of Acoustic Emission Signals From Mode I Crack" , Journal of Engineering Mech. , Vol. 117 , No. 8 , pp. 1878-1889 , 1991.

30. Jacobs, Laurence J. , Scott , William R. , Dianne , Granata M. and Martin , Ryan J. , "Experimental and Analytical Characterization of Acoustic Emission Signals," Journal of Nondestructive Evaluation , Vol. 10 , No. 2 , pp 63-70, 1991.

31. Jacobs , Laurence J. " Characterization of Acoustic Emission Signals," Mechanics Computing in the 1990's and Beyond , pp. 949-953 , 1991.

32. Ohtsu , M. and Ono , K. , " AE Source Location and Orientation Determination of Tensile Cracks from Surface Observation," NDT International Vol. 21 Number 3 , pp. 143-150, June 1988.

33. Ohtsu , Masayasu , " Mathematical Theory of Acoustic Emission and Its Application," Mem Fac Eng. Kumamoto Uni 1987; 32:1-28.

34. Hsu , N. N. , Simmons , J. A. , and Hardy , S.C. , " An Approach to Acoustic Emission Signal Analysis-Theory and Experiment," Materials Evaluation pp. 100-106 , Oct. 1977.

35. Moser , Fredrich , Jacobs , Laurence , Qu , Jianmin , " Modeling Elastic Wave Propagation in Waveguides with the Finite Element Method, " NDT&E International Vol. 32 , pp. 225-234 1999.

36. Prosser , W.H. , Hamstad , M.A. , Gary , J. and O'Gallagher , A. , " Finite Element and Plate Theory Modeling of Acoustic Emission Waveforms," Journal of Nondestructive Evaluation , Vol. 18 , No.3 pp. 83-90 , 1999

37. .Hamstad , M.A. , O'Gallagher , A. and Gary , J. , " Modeling of Buried Monopole and Dipole Sources of Acoustic Emission with a Finite Element Technique," Journal of Acoustic Emission , Vol. 17 No. 3/4 , pp. 97-110 , Dec. 1999.

38. Prosser , W.H. , Hamstad , M.A. , Gary , J. and O'Gallagher , A. , "Reflections of AE Waves in Finite Plates: Finite Element Modeling and Experimental Measurements," Journal of Acoustic Emission , Volume 17 , No. 1-2 , pp. 37-47 , June 1999.

39. Hamstad , M.A. , Gary , J. , and O'Gallagher , A., " Far-field Acoustic Emission Waves by Three-Dimensional Finite Element Modeling of Pencil-Lead Breaks on a Thick Plate," Journal of Acoustic Emissions , Vol. 14 No. 2 , pp. 103-114 , June 1996.

40. Gary , John and Hamstad , Marvin , " On the Far-field Structure of Waves Generated by a Pencil Lead Break on a Thin Plate," Journal of Acoustic Emission Vol. 12 , No. 3/4 pp. 157-170 Dec. 1994.

41. Fracture and Size Effect in Concrete and Other Quasibrittle Materials , Zdenek P. Bazant , Jaime Planas , CRC Press New York , 1998.

42. Bond and Development of Reinforcement , A Tribute to Dr. Peter Gergely , ACI International , SP-180.

43. Nondestructive Testing Handbook Volume Five Acoustic Emission Testing , 2nd Edition , ASNT, 1987.

44. Wave Motion in Elastic Solids , Karl F. Graff, Ohio State University Press, 1975.

45. Stress Wave Propagation in Solids an introduction , Richard J. Wasley , Marcel Dekker , Inc. , NY 1973.

46. Fowler, T. J. , Blessing, J.A. , Conlisk, P.J. , “ New Directions in Testing”, Proc. 3rd International Symposium on Acoustic Emissions from Composite Materials , Paris , France , 1989.

47. Texas Department of Transportation “ Procedure for Acoustic Emissions Monitoring of Pre-stressed Concrete Girders” , 2001. Journal of Acoustic Emissions Volume 19 (CD-ROM).

48. Golaski, L. , Gebski, P. , Ono, K. , “ Diagnostics of Reinforced Concrete Bridges by Acoustic Emission”, Journal of Acoustic Emissions , Volume 20 , pp. 83-98 , 2002.

49. Strategic Planning and Research report “Acoustic Emissions Testing of Concrete Bridges”,SPR-633, Oregon Department of Transportation, due for publication August 2007.

50. Strategic Planning and Research report “ Assessment Methods for Diagonally Cracked Reinforced Concrete Deck Girders”, SPR-350, Oregon Department of Transportation, 2005.

51. Kuennen, Tom, “ Taming Oregon’s Cracked Bridges”, Better Roads Magazine , pp. 54-63, April 2006

52. Strategic Planning and Research report “ Remaining Service Life of Reinforced Concrete Beams with Diagonal Tension Cracks”, SPR-341, Oregon Department of Transportation, 2005.

53. Breckenridge, Franklin R., Tschiegg, Carl E., and Greenspan, Martin, “ Acoustic emission: some applications of Lamb’s problem.”, J. Acous. Soc, Am, Vol 57, No.3 pp 626-631, 1975.

54. Ohtsu, Masayasu and Ono, Kanji, “ A Generalized Theory of Acoustic Emission and Green’s Functions in a Half Space”, J. of Acoustic Emission , Vol. 3 No. 1, pp. 27-40, 1984.

55. Mooney, Harold M. ,”Some Numerical Solutions for Lamb’s Problem”, Bulletin of the Seismology Society of America, Vol. 64, No. 2 pp. 473-491, April 1974.

56. Pekeris, C.L. , “ The Seismic Surface Pulse” Geophysics Vol. 41, pp 469-480, 1955.

57. Pekeris, Chaim L. and Lifson, Hanna, “ Motion of the Surface of a Uniform Elastic Half-Space Produced by a Buried Pulse”, Journal of the Acoustical Society of America, Vol. 29, No. 11, pp. 1233-1238, Nov. 1957.

58. Pekeris, C.L. “ A Pathological Case in the Numerical Solution of Integral Equations”, Mathematics, Vol. 26, pp. 433-437, 1940.

59. Farhey, Daniel N., “ Bridge Instrumentation and Monitoring for Structural Diagnostics”, SAGE Publications Vol. 4(4): 0301 18, 2005.

60. Chang, Peter C., Flatau , Alison and Liu, S.C., “ Review Paper: Health Monitoring of Civil Infrastructure”, SAGE Publications Vol. 2(3): 0257-267, 2003.

61. Philippidis, T.P. and Aggelis , D.G.,” Experimental study of wave dispersion and attenuation in concrete”, Elsevier Ultrasonics Vol. 43 pp 584-595, December 2004.

62. Chang, Ta-Peng, Lin, Huang-Chin, Chang, Wen-Tse and Hsiao, Ju-Fang,”Engineering properties of lightweight aggregate concrete assessed by stress wave propagation methods”, Elsevier Cement & Concrete Composites Vol.28 pp. 57-68, August 2005.

63. Wu, T.T., Fang, J.-S., Liu, G.-Y. and Kuo, M.-K, “ Determination of elastic constants of concrete specimen using transient elastic waves”, J. Acous. Soc. Am. Vol. 98 No. 4, pp. 2142-2148, October 1995.

64. Owino, Joseph O. and Jacobs, Laurence J., “ Attenuation Measurements in Cement-Based Materials Using Laser Ultrasonics”, Journal of Engineering Mechanics Vol. 125 , No. 6, pp. 637-647, June 1999.

65. Ohtsu, Masayasu, “ Acoustic Emission for Structural Integrity of Concrete from Fresh to Damaged”, Key Engineering Materials Vols. 279-273, pp. 543-548, 2004.

66. Kurz, Jochen, H., Finck, Florian, Grosse, Christian U. and Reinhardt, Hans-Wolf, “ Stress Drop and Stress Redistribution in Concrete Quantified Over Time by the b-value Analysis”, SAGE Publications Vol. 5(1): 0069 13 , pp. 69-81, 2006.

67. Colombo, Sabrina, Forde, Michael C., Main, Ian, G. and Hill, Brian, “ AE Monitoring of Boghall Concrete Bridge, Scottish Borders”, University of Edinburgh, 2002.

68. Colombo, Sabrina, Main, I..G. and Ford, M.C. , “ NDT integrity and load carrying assessment of concrete bridges”, Highways Agency, Contract No. 3/320, University of Edinburgh, Scotland, UK, 2002.

69. Rayleigh, J.W.S, “ On waves propagated along the plane surface of an elastic solid.” , Proc. Lond. Math. Soc. Vol. 17, pp. 4-11, 1887.

70. Lamb, H. " On the propagation of tremors over the surface of an elastic solid" , Phil. Trans. R. Soc. A203, pp. 1-42, 1904.

Appendices

Appendix A Acoustic Emission Sensors and Their Calibration on Concrete Structures

An Acoustic Emission (AE) sensor is a transducer that is mounted to an exposed surface on the structure of interest and develops an electrical signal output that is a function of the surface kinematics directly under the sensors receiving surface or aperture. There are two general types of sensors in practical use, the resonant sensor and the hi-fidelity sensor.

Resonant AE sensors

In general the resonant type consists of a mass loaded piezoelectric crystal that develops relatively high output signals in the resonant frequency band of the sensor. These sensor types most often respond to velocity and acceleration more then displacement. The sensitivity of these sensor types is commonly expressed in output voltage per unit pressure input on the aperture and expressed in decibels due to the large range of sensitivity experienced over the useable frequency band. Resonant type sensors typically have highly variable sensitivity over the frequency band of use with peaks occurring at the resonant frequencies of the sensor. As a consequence they will often " ring ' when excited at or near the resonant frequencies much like an under damped spring – mass –damper system.

Two different resonant type AE sensors were used in this study : 1) the Vallen VS-150 and 2) The KRN i060. The former is a relatively broad band resonant sensor with a useable frequency range of 100 to 375 kHz and a peak sensitivity near 150 kHz. A typical calibration sheet for a VS-150 sensor is shown in Figure A1. The later resonant sensor type is more narrow banded with a useable frequency range of 40 to 150 kHz and a peak sensitivity near 60 kHz as shown in a typical calibration sheet for this sensor in Figure A2.

In summary resonant AE sensors have the advantage of very high sensitivity to surface motions but in general their output signals cannot be meaningfully compared to a quantifiable surface motion. They are primarily used in the practical application of AE to structural health monitoring because of the wide sensor spacing that can be used.

Hi-fidelity AE sensors

Hi-fidelity AE sensors develop a much more linear and un changing response to surface motions over the frequency band of use then resonant types. There are several different types of hi-fidelity AE sensors in common use with most of them using a piezoelectric crystal that is mounted and loaded in such a manner as to have a very broad and constant output sensitivity. Some types, including those used in this study have outputs that are directly proportional to surface displacement as opposed to velocity and or acceleration. Such sensors have a sensitivity expressed in voltage output per unit aperture displacement and again are expressed in decibels to cover the broad frequency range in which they are applied. The particular hi-fidelity sensors used in this study are DECI S1000H and a typical calibration sheet is shown in Figure 3.

Though the absolute value of surface displacement is not as accurately resolved compared to some of the conical type or not contact laser inferometer sensors the relative motion is well resolved and traceable to the National Institute for Standards and Testing (NIST). For the 30 to 250 kHz range these sensors yield an output of 126 to 224 μV/Pico meter or the inverse which is 8.0 to 4.4 Pico meters / millivolt.

In summary hi-fidelity AE sensors can be purchased that primarily respond to displacement and are much more linear over the frequency range of use compared to resonant type sensors. Their primary use is in characterizing surface motions for comparison to analytic models and for getting an unbiased representation of the frequency content of particular AE sources. Their reduced sensitivity compared to the resonant type generally limit there use to laboratory work when the medium being studied is concrete.

Sensor mounting to structures

Because all of these sensors respond to surface motions it is imperative that the sensor be properly mounted to the structure of interest with good acoustic coupling between the surface and the sensor. In general the surface must be relatively flat, smooth and free of defects larger then 1/16 inch. A coupling material is used to accommodate surface irregularities between the sensor and surface. The coupling material used for these studies was laboratory grade vacuum grease. The sensor must also be held firmly in place with a clamping force of at least 4 lbs in order to minimize the couplant gap. Once installed the sensors acoustic coupling is checked by inputting AE sources into the structure and measuring the response of the sensor. The response must be of sufficient magnitude and repeatability before the sensor mounting is accepted. Details of AE sensor mounting are discussed in ASTM E-650. Various means of providing AE sources are discussed below.

Acoustic Emission Source Generation for Calibrating Mounted Sensors

Two primary methods of developing AE sources in concrete structures were used in this study , the pencil lead break and the sensor calibration pulse. Each has its advantages and disadvantages. There are three main responses that are sought after in the use of calibration tests :1) signal recognition 2) wave speed measurement and 3) amplitude attenuation.

With signal recognition the measured sensor response can be compared to analytic models in order to help identify the arrival of the various stress waves such at dilatation, distortion and surface waves. This can greatly aid in accurately measuring the wave speeds and attenuation. Wave speeds are important as they are a direct result of the material properties of the medium being tested. This information is used to optimize the recording parameters and determining the locations of AE sources when more then one sensor is being used. Characterizing the attenuation with respect to both frequency content and spatial location is important to test sensor mounting and selecting sensor spacing.

<u>Pencil lead breaks for AE source</u>

One of the well known analytical solutions for stress wave propagation in a semi-infinite medium is known as Lamb's Problem which develops the surface displacement time histories for various points on the surface resulting from a step force applied to the surface. Figure A4 shows the analytic solution for a force suddenly applied and released (impulse type) onto the surface. Only the vertical displacements at a position significantly away from the source (far –field response) are shown. The arrivals of the dilatation or P-wave, distortion or S-wave and the Rayleigh or surface wave are shown. Most AE sensors including the units used in this study are only sensitive to the vertical component of the surface displacement. The pencil break test is very similar to Lamb's problem for impulse loading.

Figures A5 through A7 show the response of a hi-fidelity sensor resulting from a 0.5mm 2H lead break 1 3/8 inches from the sensor center with the sensor on the same plane as the source. Figure A5 shows the total response from arrival to full decay. The frequency band of a pencil break is relatively broad band and has significant components from 40 kHz to 400 kHz. Figure 6 shows a time expanded view featuring the arrival of the first P , S and Rayleigh waves. Visual identification of the S-wave is considerably less obvious than the other waves in most time histories studied and this is a particularly good example. Figure A7 shows a further time expanded scale at the arrival of the first P-wave. The horizontal lines at + and – 0.05 mV indicate the fixed threshold used for triggering the recorder for this event. The arrival of the first P-wave can be seen clearly at this short of a propagation distance. At distances farther then 3 inches with 0.5mm pencil breaks it becomes difficult to detect visually.

This response is typical for surface wave in a concrete medium. The vertical component of the P-wave is typically very small and only detectable with in a few inches of a strong source such as a pencil lead break. As is presented in Appendix B and C, the 150 kHz resonant sensor can detect this same wave out to approximately 8 inches. Also discussed is the fact that the Rayleigh wave can be easily detected at propagation distances exceeding 18 inches with both hi-fidelity and resonant type sensors. More often then not the S-wave is located by calculating the expected arrival time based on the more identifiable P and Rayleigh wave.

Figure A8 shows the peak amplitudes measured from pencil lead breaks 6 inches from the AE senor with varying lead diameter and sensor type. As is expected the peak amplitudes increase with increasing pencil lead diameter. The two resonant sensors show greater sensitivity with the 60 kHz sensor showing saturation with the 0.5 and 0.7mm leads. All three lead diameters work well on concrete.

The advantages to the pencil lead break are : 1) it can readily be compared to familiar analytic solutions , 2) it has a broad and fairly flat frequency band that is similar to fracture type AE , 3) it is reasonably energetic and hence can be detected out to practical distances , and 4) it is very easy to apply in both the laboratory and field.

The disadvantages of the pencil lead break are : 1) there is a significant portion of the loading time history after the break occurs that is difficult and impractical to quantify , 2) each break is not identical, varying mostly in peak amplitude when conducted properly, and 3) an additional AE sensor is needed if absolute wave speeds are to be measured as the source is not timed with the receiver and 4) a step or impulse source can created numerical difficulties when applied to finite element analysis.

Despite the disadvantages listed the pencil lead break is a very useful and practically repeatable source for studies using AE on a concrete media.

Calibration Pulse from AE Transducer

Another practical method of inputting AE sources into a structure is the use of a calibration pulse. Some AE sensors have pulse through capability meaning that not only can they act as a receiver but if they are provided with calibration pulse signal (typically 40 to 400 volts peak to peak) they will behave as a source or speaker. This has some distinct advantages over the pencil lead break in that the source can now be easily timed with the receiving sensors and is very repeatable with little to no variation pulse to pulse.

The Vallen AMSYS5 AE system has two options for providing calibration pulses to a AE transducer , normal and low , referring to the frequency content of the signal sent. In each case a sinusoidal voltage is sent to the AE sensor selected.

The shape and frequency content of the source signal has been optimized to generate maximum energy over a specified frequency band. The actual wave form of the source as it is input into the structure to which the AE sensor is mounted depends very strongly on the type of AE sensor used. A particular sensors response to the calibration signal can be quantified by acoustically coupling the sensor to be tested to a hi-fidelity AE sensor and then pulsing the sensor which one wants to test.

This test was applied to using both a hi-fidelity and resonant type sensor excited with a calibration pulse signal. Figure 9 shows the test setup for quantifying the response of hi-fidelity sensor. Both sensors shown are DECI S1000H hi-fidelity sensors, one being pulsed into the other. Since the receiving hi-fidelity sensor primarily responds to displacement it does a suitable job of quantifying the actual motion of the aperture on the pulsed unit. Figure A10 shows the calibration source signal (upper plot) and the response to the pulse as generated from the pulsed sensor (lower plot) , both in the temporal and frequency domains. The calibration pulse sent was using the normal frequency band. The signal sent to the pulser can generally be described as a time decaying sinusoid with a frequency band of 80 to 300 kHz and a strong peak near 150 kHz. The motion of the pulser can be inferred from the lower plot which appears very similar in shape but has significant components in both the 150 kHz and 340 kHz regions. The second peak in frequency appears to be related to reflected waves between sensors as the magnitude of this peak was strongly related to sensor alignment. The magnitude of the aperture displacement is on the order of 240 Pico meters based on the calibration sheet for the receiving sensor. Overall the hi-fidelity AE sensors appears to accurately generate the calibration pulse , especially in the frequency band of less then 300 kHz which is applicable to concrete media.

Figure A11 shows the results using the low frequency calibration pulse. This signal is very similar to the previous but extends the energy content down to 100 kHz. The apparent aperture motion from this pulse does not follow the signal quit as well as the normal pulse but is still reasonably similar. Again reflections appear to occur in the higher frequency ranges.

As discussed above resonant type AE transducers develop very good sensitivity at the cost of ringing after the source has diminished. This effect can be demonstrated by using a hi-fidelity sensor to pulse into a resonant sensor. The test setup is shown in Figure A12 where the receiver is a 150 kHz resonant sensor seen on the left and the pulser is a hi-fidelity sensor seen on the right. The hi-fidelity sensor is given a normal calibration pulse which we have seen produces an aperture motion very similar to the signal sent. Figure 13 shows the sent signal in the upper plot and the resonant transducers response in the lower plot. The resonant sensor rings down for more then 12 cycles after the input source has diminished. A similar effect can be expected if the resonant sensor was used to provide the calibration signal into the structure.

The advantages of using calibration pulses as AE sources are 1) the source and receivers are timed together, 2) the magnitude and wave form of the source are very repeatable and 3) a sinusoidal AE source is easier to model with finite element analysis when compared to a step or impulse source and 4) the source can be input remotely from the structure being tested once the sensor are installed.

The disadvantages of using calibration pulses as AE sources are 1) the actual shape and frequency content of the input source is strongly tied to the sensor type being pulsed, 2) the arrival of the various waves (P , S and Rayleigh) is more difficult to interpret at the receiver do to multiple presence i.e. not a single cycle like an impulse function and 3) the input source is essentially monochromatic so the proper frequency must be chosen.

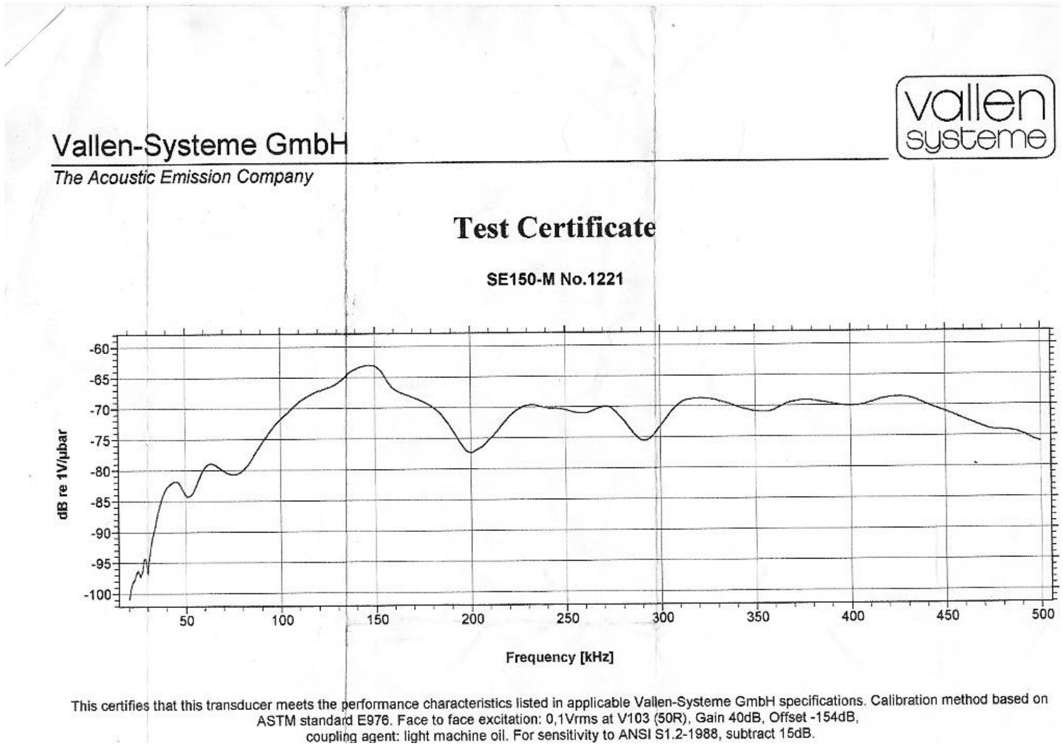

Figure A1 Frequency response for a 150 kHz resonant AE sensor.

KRN SERVICES

Sensor Functional Test Data

Preamp 40 to 44 dB gain

Model number: KRNi060
Serial Number 03026 - Repair

Test Equipment:

	Model Number	Serial No.	Cal. Date
Function Generator: Rep Rate = 14 mSec V_{RMS} = 71mV Width = 11-495 kHz	LG Precision FG-8002	8061038	N/A
Multimeter	BK Precision 5360	70907040	01/07
Source Crystal:	Panametrics V101-RB	230166	N/A
Signal Capture:	Keithley KPCI-3110	0896305	7/05
Spectrum Analyzer:	HEM Snap Master	Ver. 3.5.13	N/A

Spectral Response:

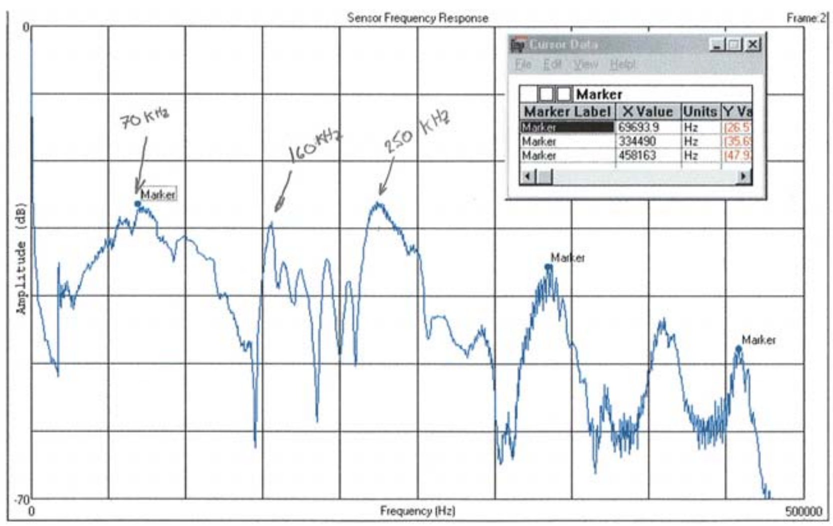

Form SensTest 150 / 060 Rev1 1-06 **Tested By:** C.M. Nickolaus CMN **Date:** January 16, 2006

2000 LOGSTON BLVD ◆ RICHLAND, WA 99354 ◆ PHONE 509-545-3268 ◆ FAX 509-375-4838

Figure A2 Frequency response for a 60 kHz resonant AE sensor.

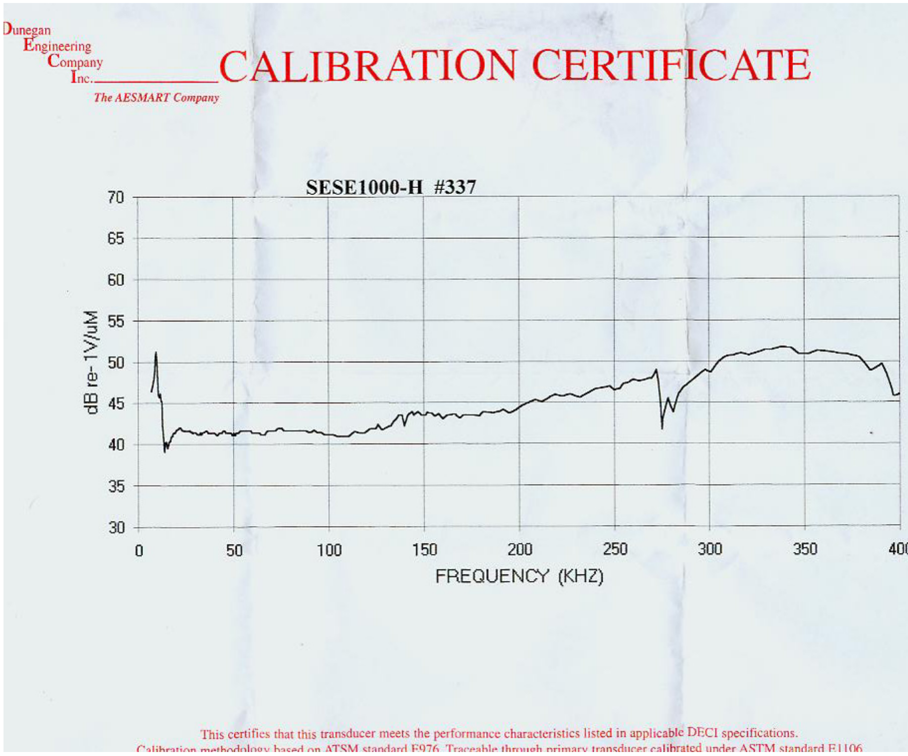

Figure A3 Frequency response for a Hi-fidelity AE sensors.

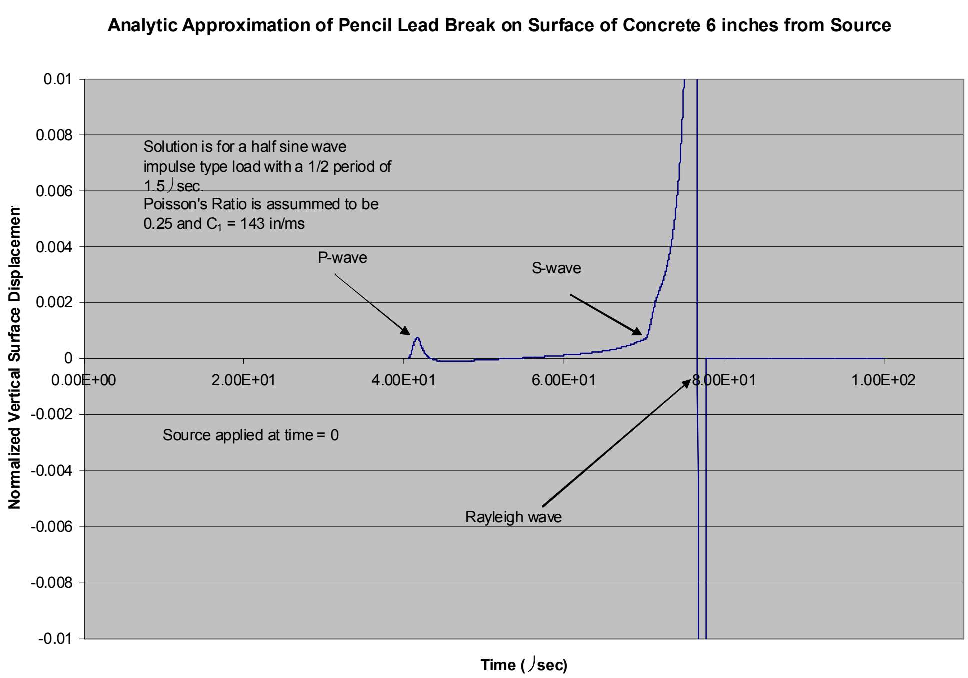

Figure A4 Analytical solution to Lamb's Problem of impulse force applied on the surface of a semi-infinite elastic medium.

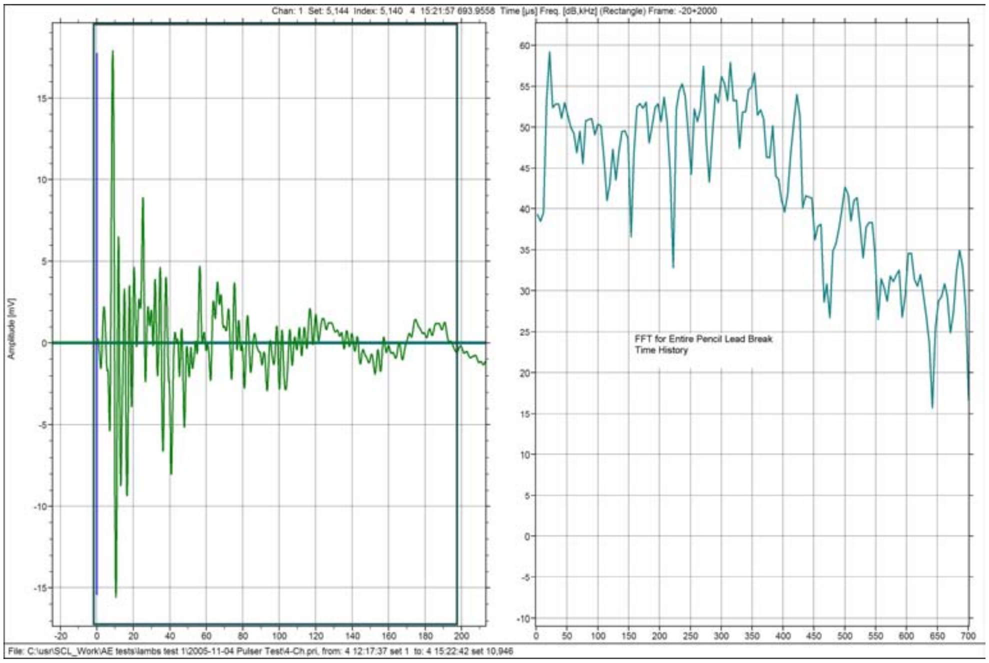

Figure A5 Measured response of a hi-fidelity AE sensor from a 0.5 mm pencil lead break on concrete measure 1 3/8 inches away.

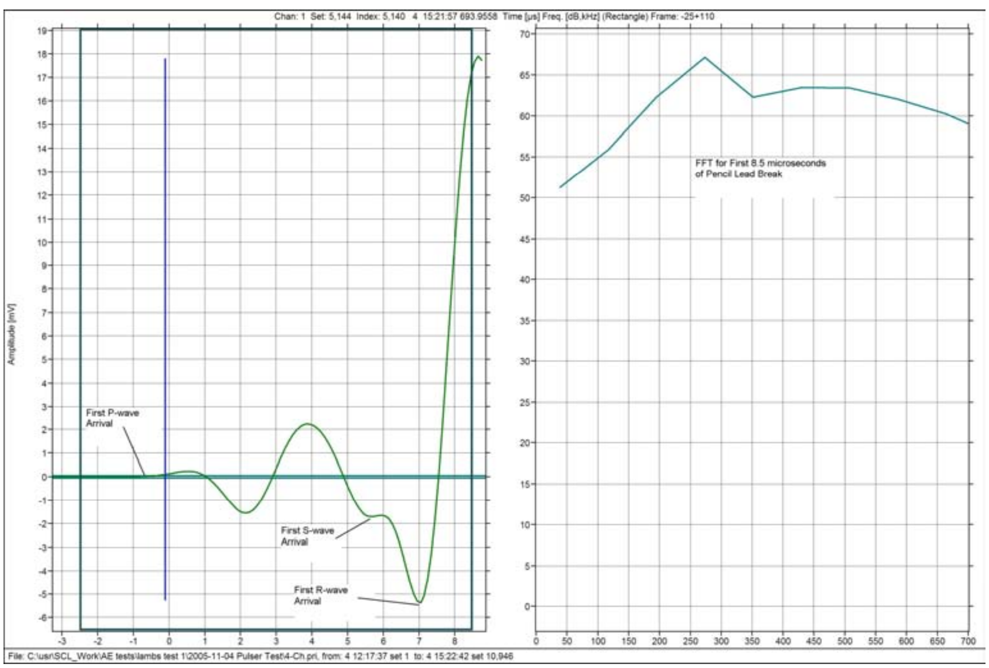

Figure A6 Time expanded view of pencil lead break near the arrival of the first P , S and Rayleigh waves.

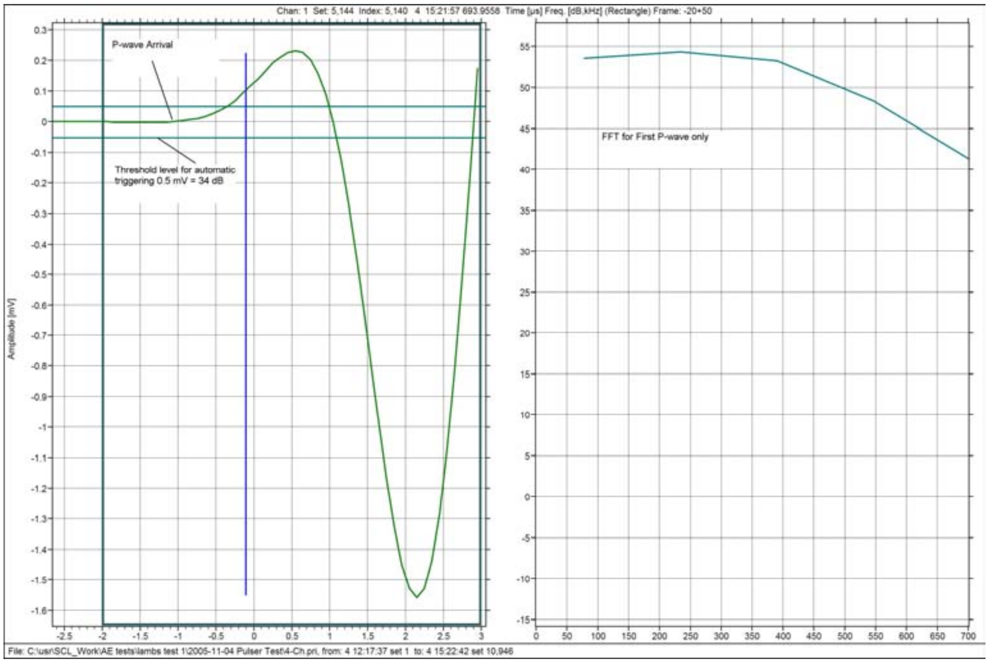

Figure A7 Time expanded view of the pencil lead break with detail of the first P-wave arrival.

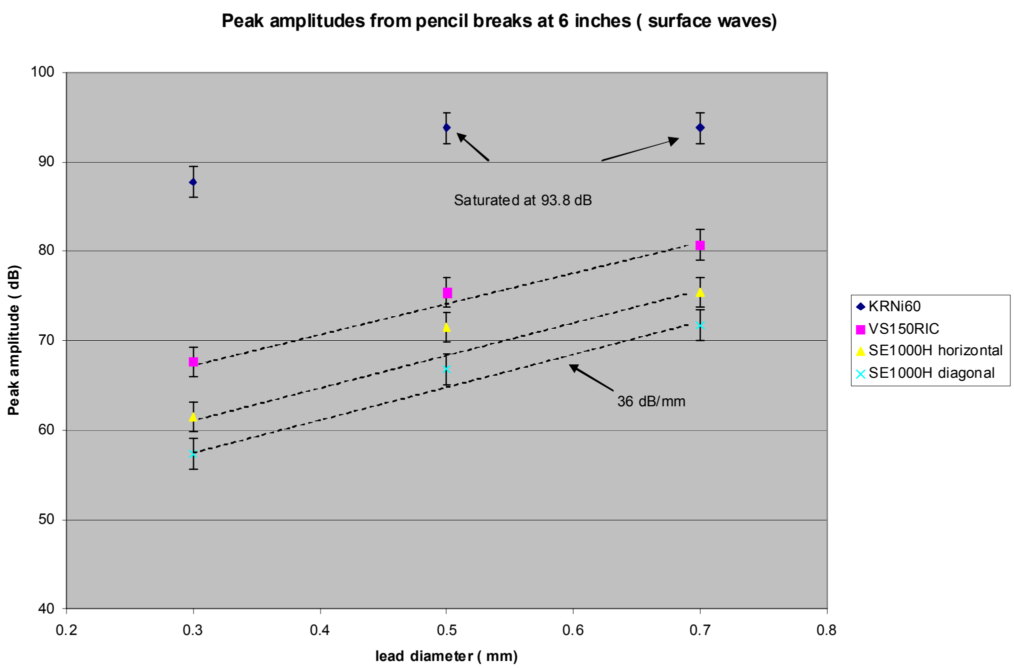

Figure A8 Peak amplitudes from various pencil lead diameters as measured by both hi-fidelity and resonant AE sensors. Error bands show extreme range five samples.

Figure A9 Photograph of AE sensor calibration pulse response test setup for hi-fidelity sensor.

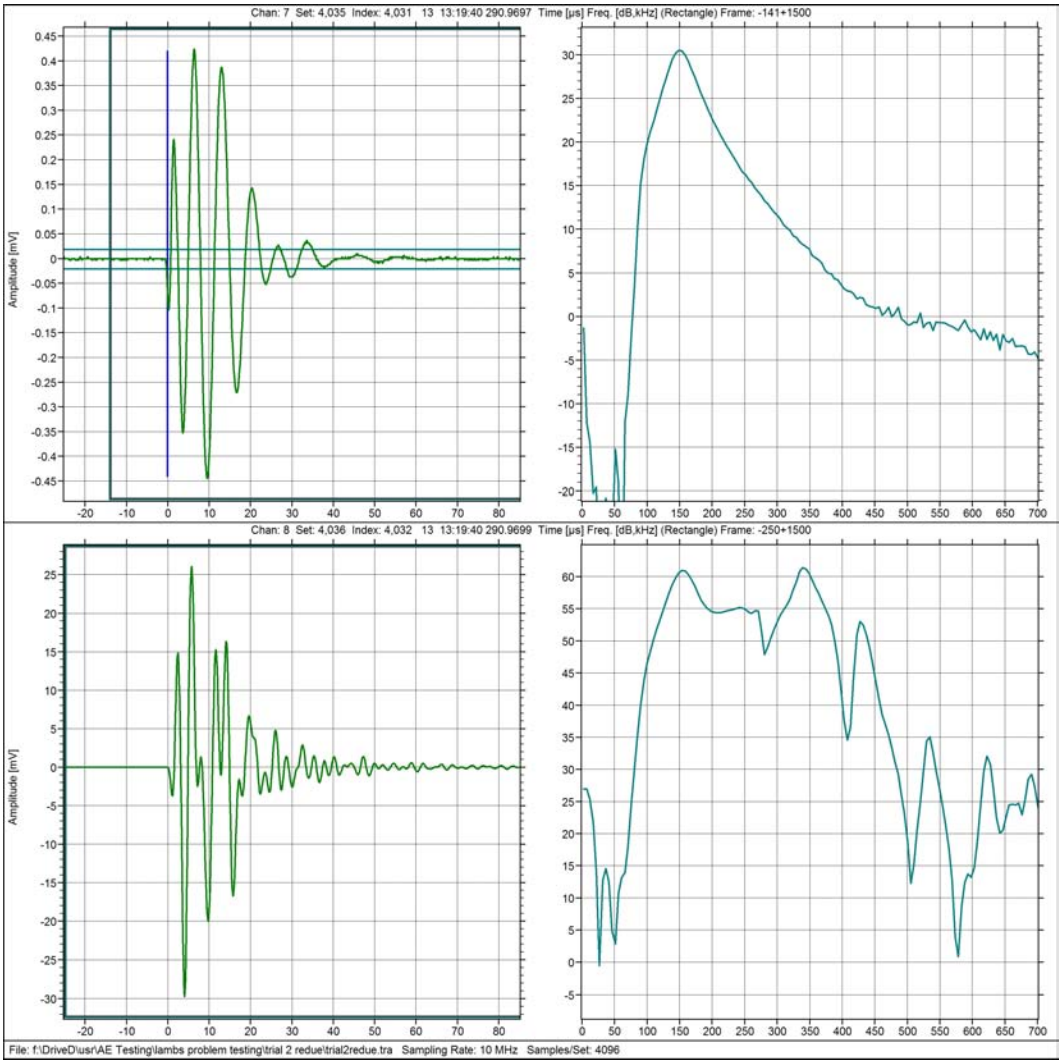

Figure A10 Normal calibration pulse signal (top plot) and response signal from a hi-fidelity AE transducer (bottom plot).

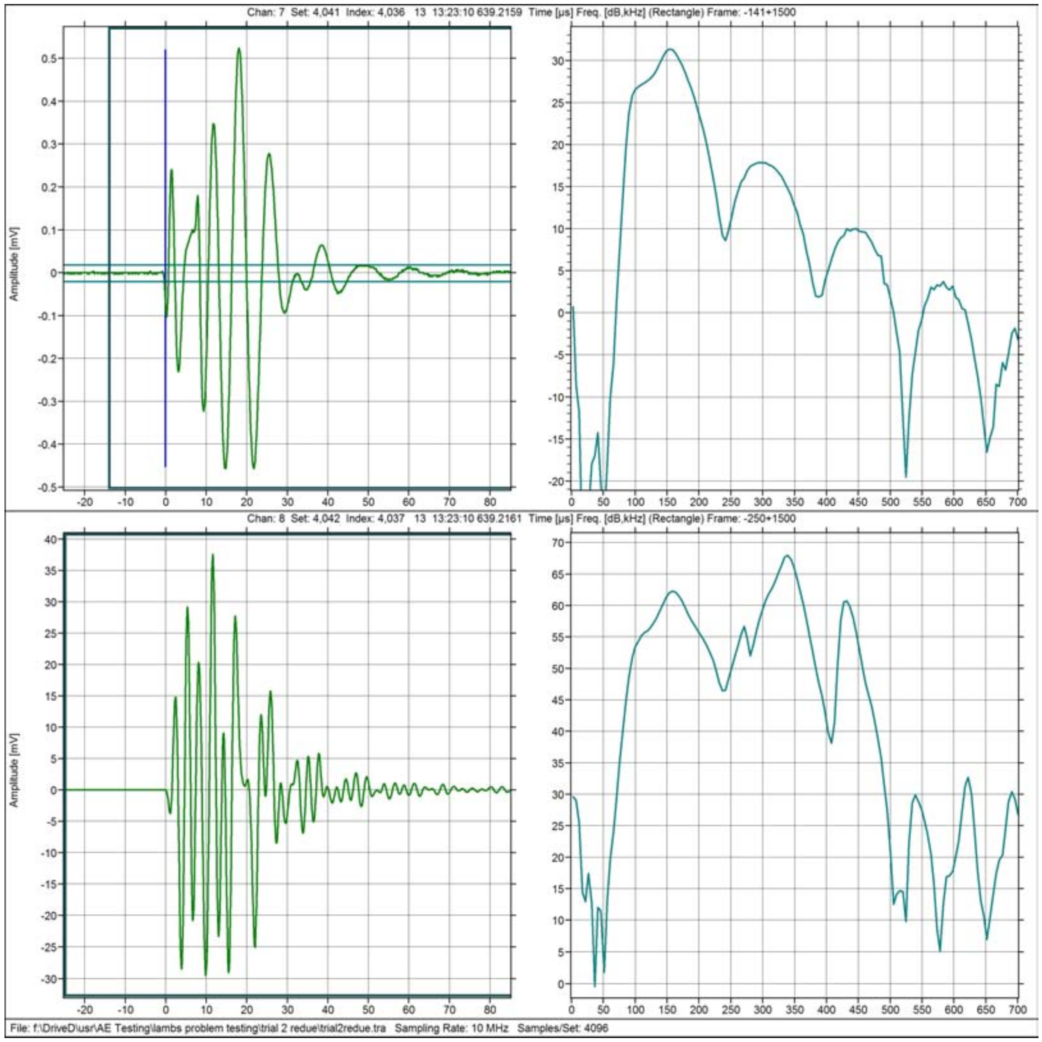

Figure A11 Low calibration pulse signal (top plot) and response signal from a hi-fidelity AE transducer (bottom plot).

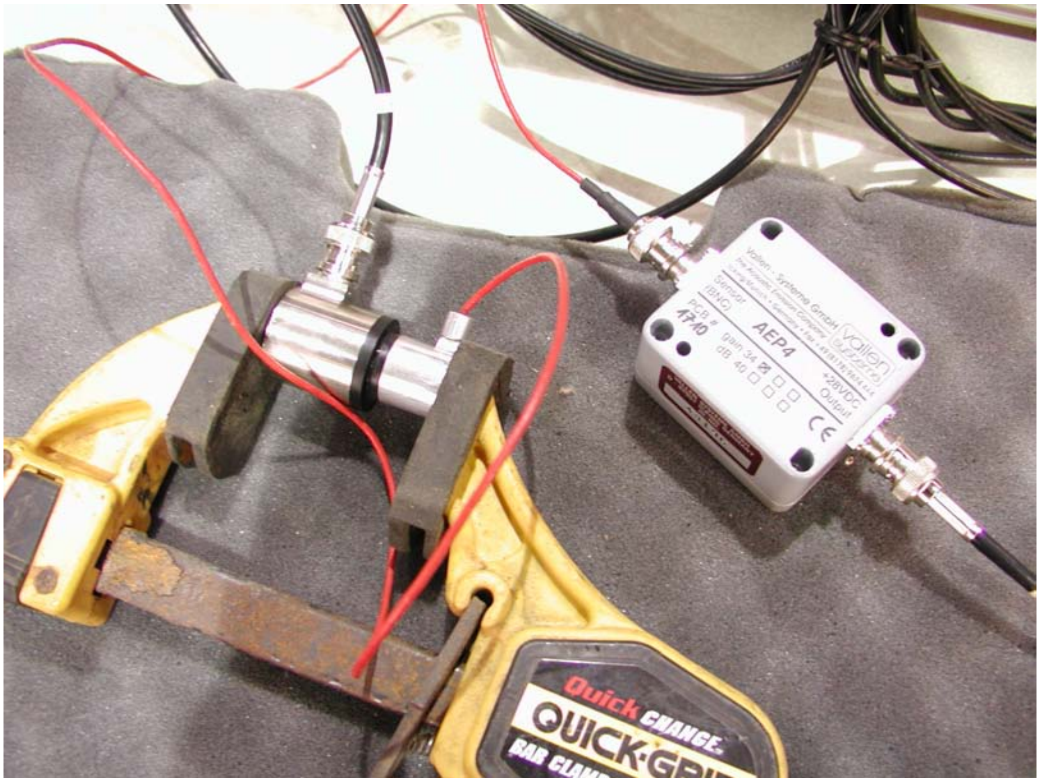

Figure A12 Photograph of AE sensor calibration pulse response test setup for resonant sensor.

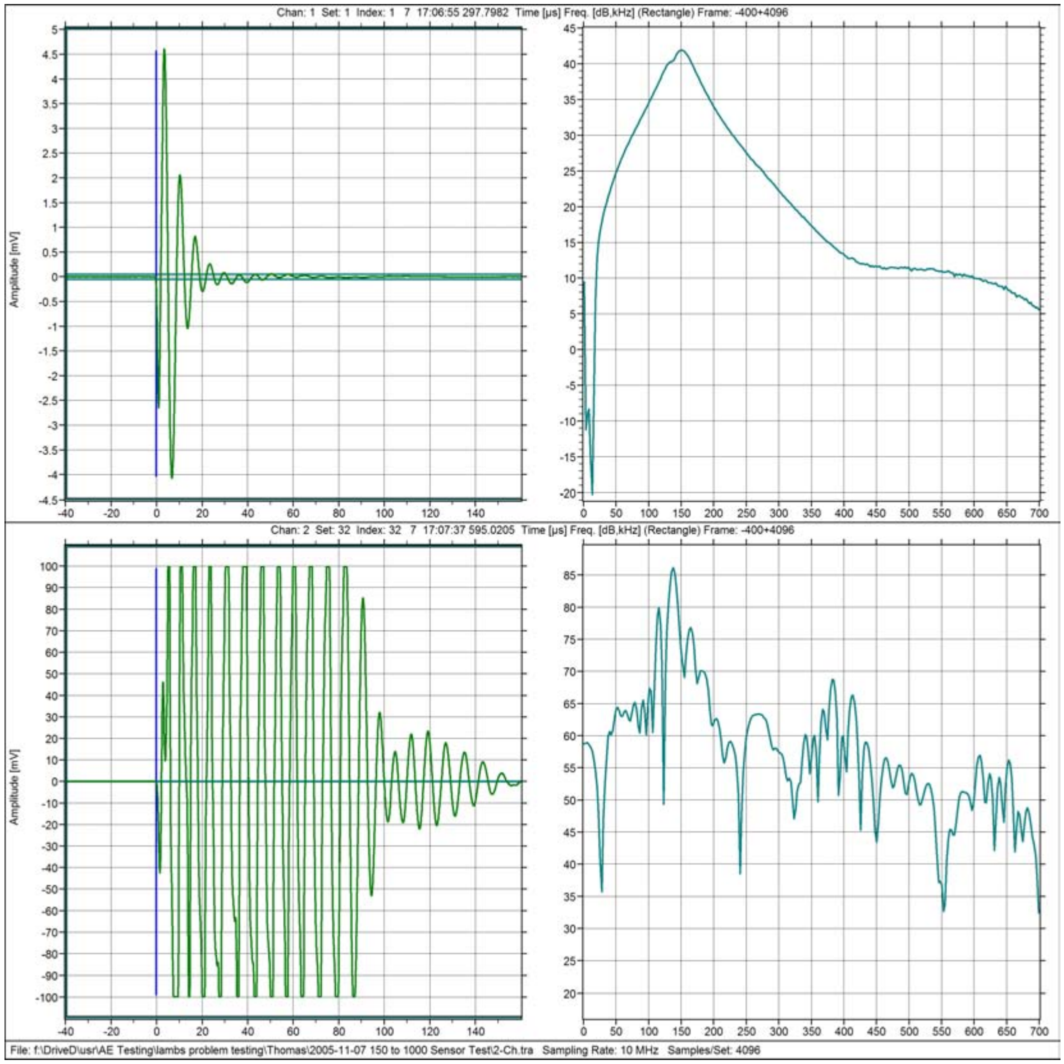

Figure A13 10 Normal calibration pulse signal (top plot) and response signal from a 150 kHz resonant AE transducer (bottom plot).

Appendix B Investigation of Surface Wave Propagation in Un-reinforced Concrete Block Using Pencil Lead Breaks as an AE Source

Purpose of Test

The purpose of this series of tests was to quantify the P and Rayleigh wave propagation speed and frequency content in concrete. Using measured values of the P and Rayleigh wave speed the S-wave speed and elastic constants for the concrete can be calculated.

Test Apparatus

Test Block

An un-reinforced concrete block 48” x 48” by 14 “ was used as the test block. The concrete mix used was same mix used for all testing of the full scale beams and can be characterized as having an aggregated gradation of ¾” minus , a weigh density of 141 lbf / ft^3 , and a minimum compressive strength at 28 days of 3300 psi. The test surfaces of the block were prepared by removing rough sections with a hand operated grinding stone. The upper surface was sectioned and scales marked using permanent markers.

AE System

A Vallen AMSYS5 AE test system with 8 AE channels was used to collect the data. Each channel is equipped with a transient recorder sampling at a rate of 10 MHz and 16-bit digitization. The hi-fidelity sensors respond to displacement and have a very constant sensitivity over the listed frequency range. They are used to calibrate the frequency responses of other transducers as well as studying surface displacements from various disturbances in the test medium. The resonant sensors typically respond to velocity and or acceleration and have much more sensitivity and sensitivity variation with frequency. They are more commonly used is actual applications of AE due to the increased sensitivity over the hi-fidelity type transducers. The hi-fidelity transducers are used in the laboratory to quantify the displacements from various AE sources and the resonant sensors are used for comparison with the intent of applying their use on real structures. Only hi-fidelity AE sensors were used for this test.

Test Procedures

The sensors were acoustically coupled to the surface of the concrete test block using a laboratory grade vacuum grease and an applied minimum normal force of 4 lbs. Figure B1 shows the test block with attached AE sensors. Figure B2 shows a schematic of the sensor layout and locations of applied pencil lead breaks on the x-axis. Pencil lead breaks were applied from x = -1 to -15 inches on the axis in one inch increments. A minimum of 5 pencil lead breaks were applied at each location and the transient surface disturbance propagations measured at the fixed AE sensor locations. Two sensors were used to provide a timing gate of known distance for wave speed calculations. The range of propagation distance between the source and middle of the timing region varied from 2.5 to 16.5 inches.

Results

The transient surface disturbance wave forms from each of the two sensors are shown in Figures B4 through B18 for pencil lead breaks applied from x= -1 to -15 inches. Only the first source location at x = -1 inch provided a strong enough P-wave to be visibly detectable in the wave forms of both receiving sensors as seen in Figure B4. The measure P-wave speed was 150 in/ms which is consistent with the value measured in the bulk wave test found in Appendix E. All source locations yielded a measured Rayleigh wave speed. Rayleigh wave arrivals were determined by visually comparing the wave form to the analytic solution shown in Figure B3 which is expected to be very similar up to and including the arrival of the first Rayleigh wave. After the arrival of this wave the measured wave forms continue to oscillate due to the impulse nature of the pencil break compared to the step nature of the analytical solution.

For each source location the wave speeds are calculated and summarized in Figure B38. The far field Rayleigh wave speed can be seen to be very constant at a value of 83 in/ms. At source locations with less then 4 inches of propagation to the center of the timing region the measured wave speed reduces down to 62.5 in/ms. This is likely due to difficulty in identifying the exact arrival time of the Rayleigh wave at the sensor located closest to the source. The difficulty is thought to occur due to both near field effects and the complicated transients of the source occurring after the break. These higher frequency components tend to damp out quickly making measurements beyond 4 inches of propagation unambiguous.

The frequency content of each wave form was investigated using the Fast Fourier Transform (FFT) on specific portions of each time history. The purpose of this analysis was to determine what frequency band the P and Rayleigh waves propagate in when concrete is the medium. Have this knowledge allows proper selection of AE transducers and test setups.

Figure B19 shows a close up view of the P-wave arrival at a propagation distance of 1 inch. The FFT analysis is windowed on the first complete oscillation and the frequency spectrum is shown to the right of the time history. The results show that the P-wave portion of the disturbance is broad band, meaning a compilation of many frequencies, with a slight peak near 350 kHz. Figure B20 shows the same wave form with emphasis on the arrival of the Rayleigh wave which the FFT is again windowed on. The frequency content as shown in the FFT is still fairly broad band but starts to rapidly attenuate above 550 kHz. Slight peaks can be seen at 120 and 350 kHz. From 2 to 3 inches of propagation the P-wave is visibly identifiable but has a very low signal to noise ratio and is not identifiable beyond 3 inches of propagation. Thus the frequency content of the surface propagating P-wave was only measurable at 1 inch of propagation for these tests.

The frequency content of the first Rayleigh waves were calculated out to a propagation distance of 18 inches which can be seen in detail in Figures B20 through 37. The farther the wave propagates the lower and more narrow banded the frequency content becomes. Figure B39 shows a summary of the P and Rayleigh wave frequency content variation with propagation distance. Beyond 6 inches of propagation the frequency spectrum is very monochromatic at a constant frequency of 50 kHz.

The shear wave speed and elastic properties of the concrete can be calculated once the P and Rayleigh wave speeds are know. Figure B40 shows a summary of these calculations. The calculated S-wave speed is 88 in/ms

Conclusions

Using pencil lead breaks as an AE source for measurement of surface disturbances found the near field P-wave speed of the concrete test block to be 150 in/ms and the far field S and Rayleigh wave speeds to be 88 and 83 in/ms respectively. The frequency content of the P-wave was found to be very broad band with a frequency range of 20 to 700 kHz. The frequency content of the Rayleigh wave disturbance was found to be broad banded near the source but rapidly became monochromatic as a frequency of 50 kHz beyond 6 inches of propagation. Thus for practical applications of measuring surface waves on concrete structures an AE sensor with good sensitivity in the 40 to 100 kHz frequency band is recommended.

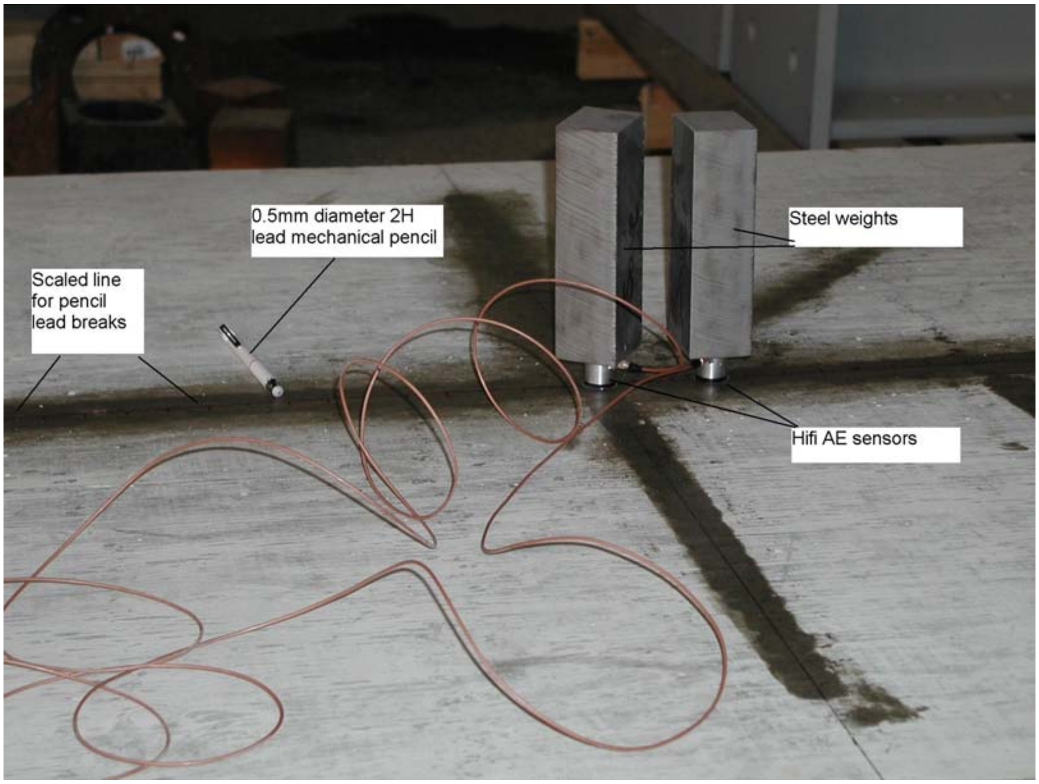

Figure B1 Photograph of test setup.

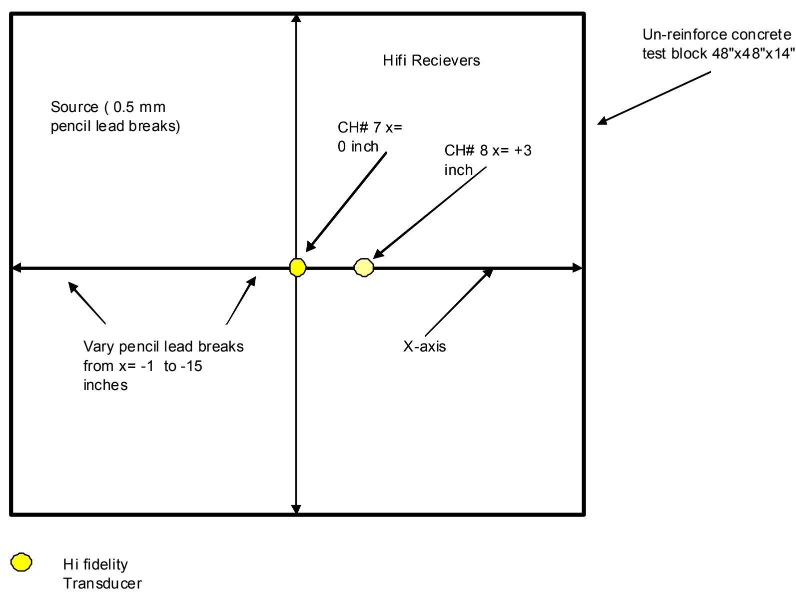

Figure B2 Schematic of test setup.

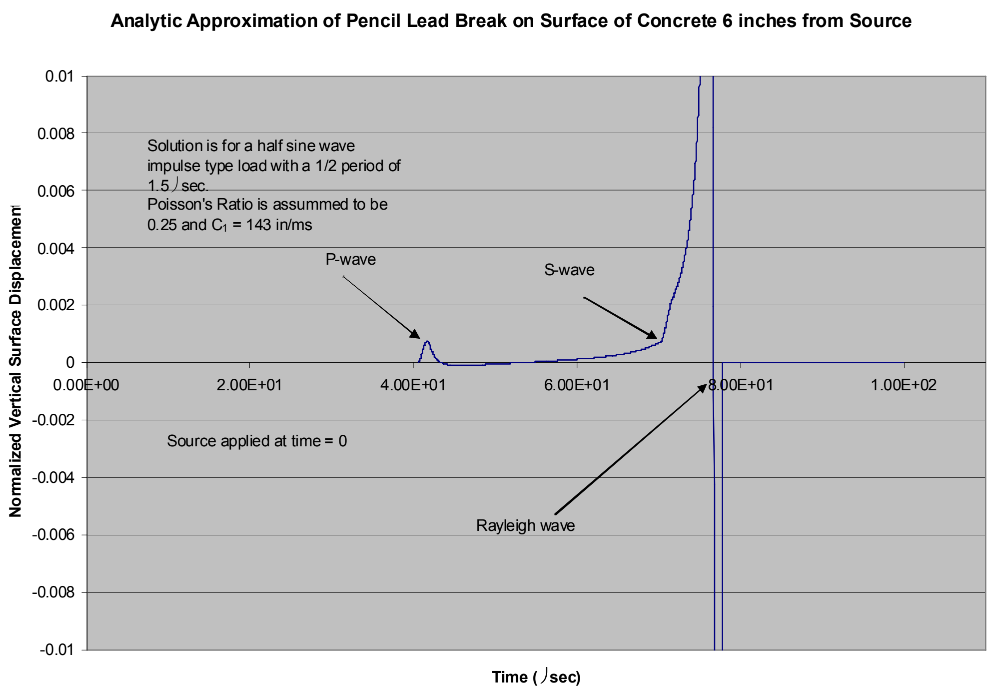

Figure B3 Analytic solution for impulse type surface disturbance.

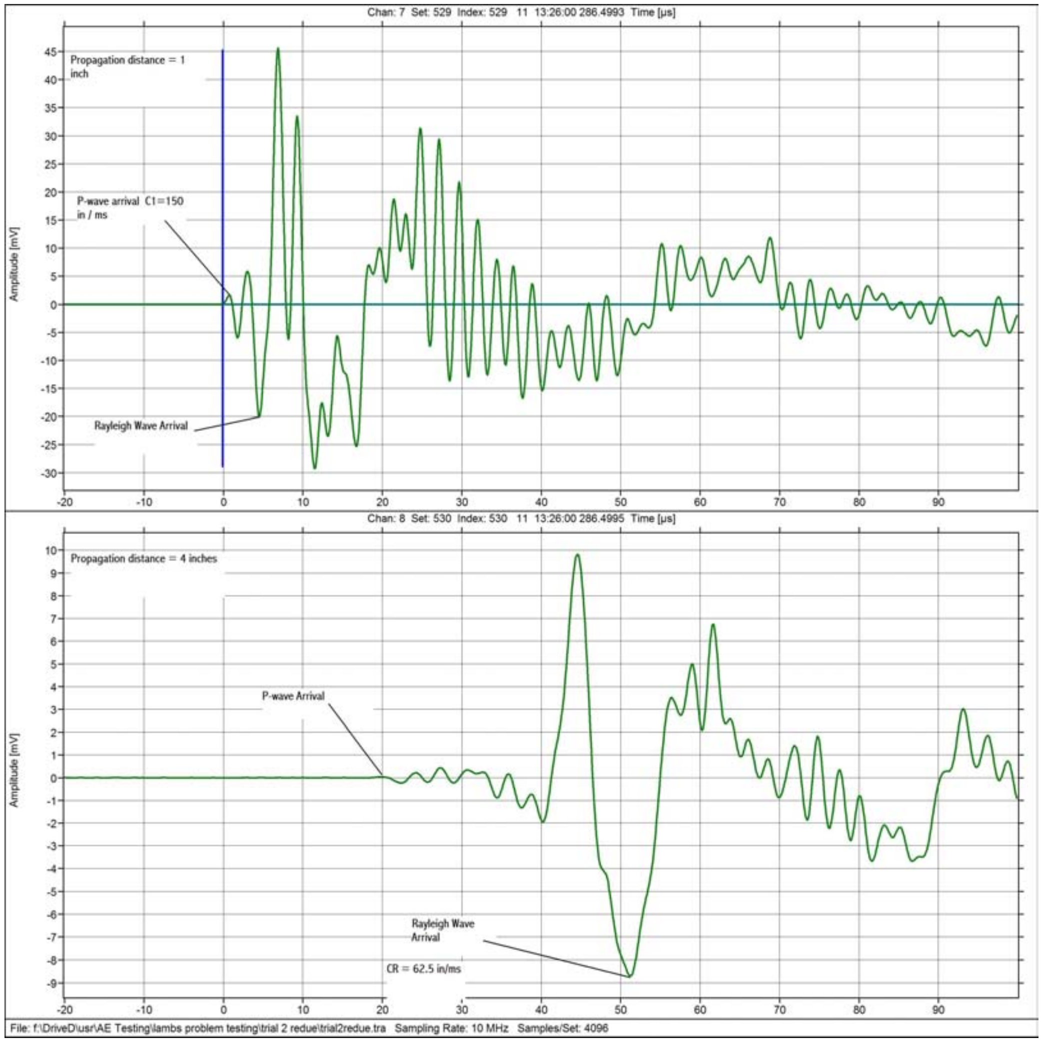

Figure B4 Wave form for 0.5 mm pencil lead break at x = - 1 inch.

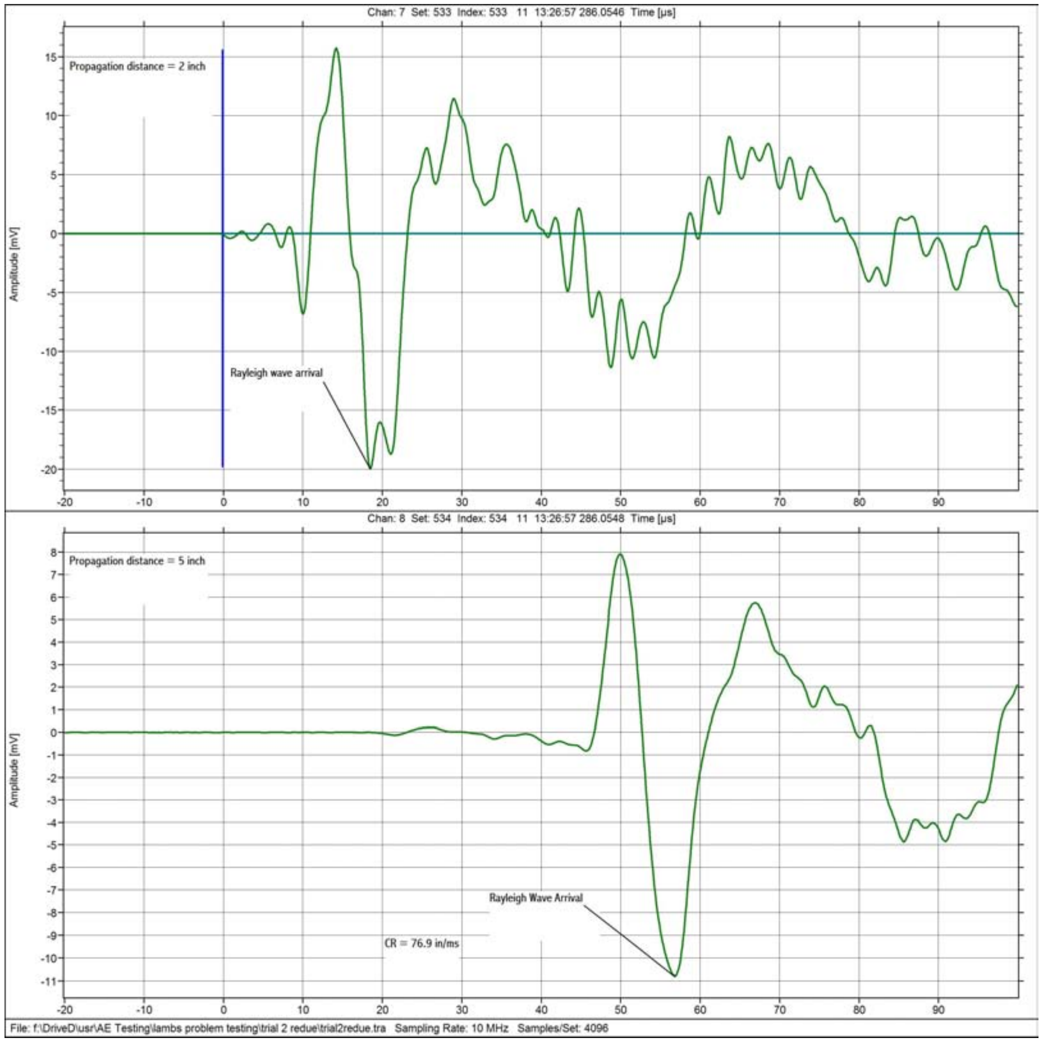

Figure B5 Wave form for 0.5 mm pencil lead break at x = - 2 inch.

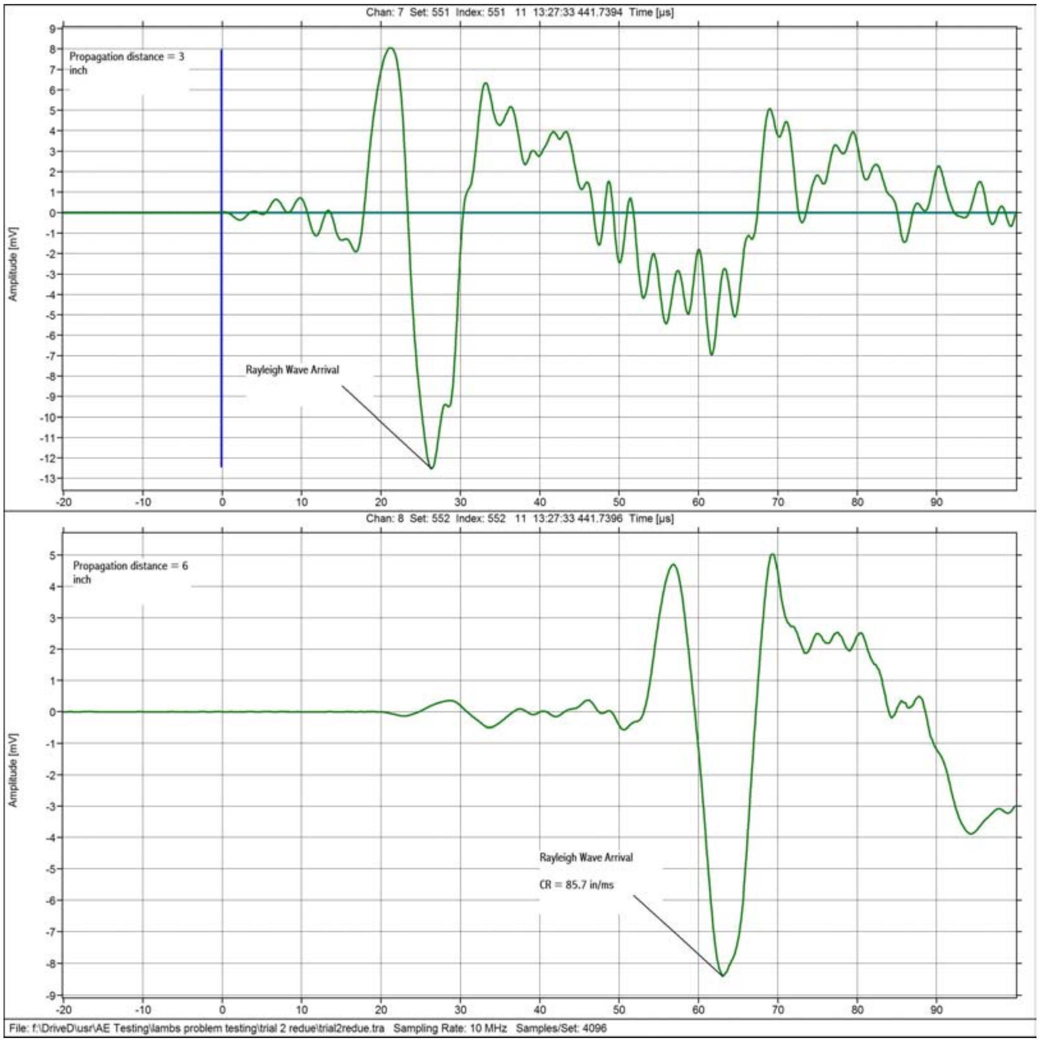

Figure B6 Wave form for 0.5 mm pencil lead break at x = - 3 inch.

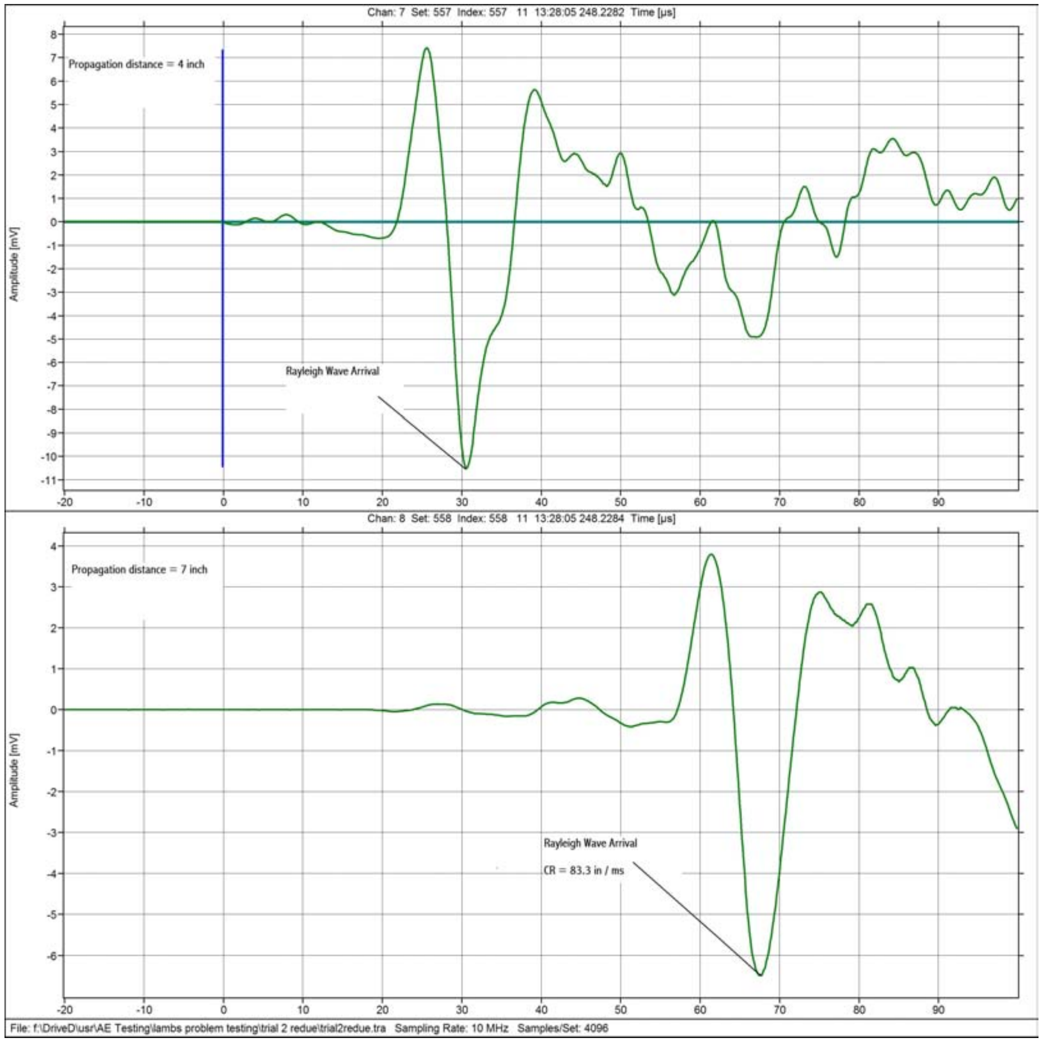

Figure B7 Wave form for 0.5 mm pencil lead break at x = - 4 inch.

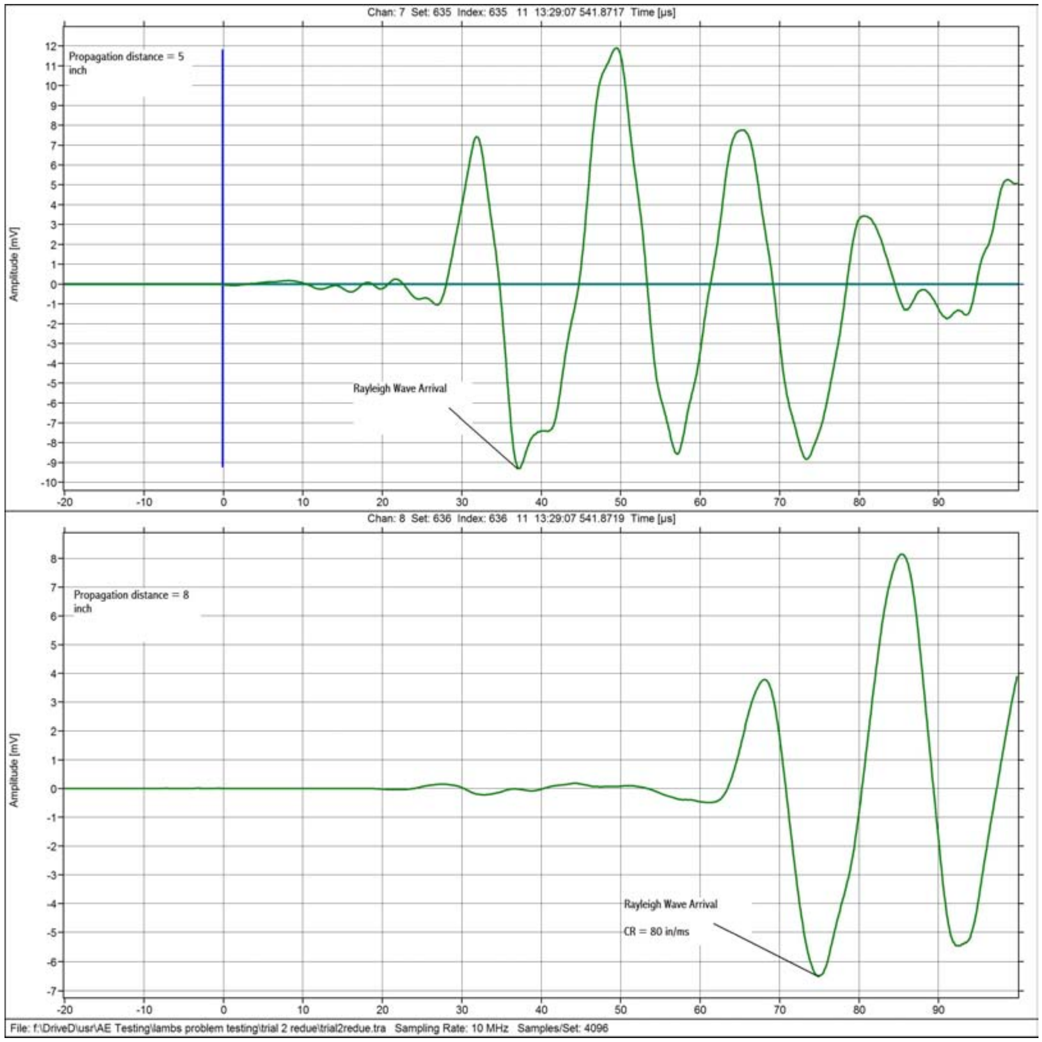

Figure B8 Wave form for 0.5 mm pencil lead break at x = - 5 inch.

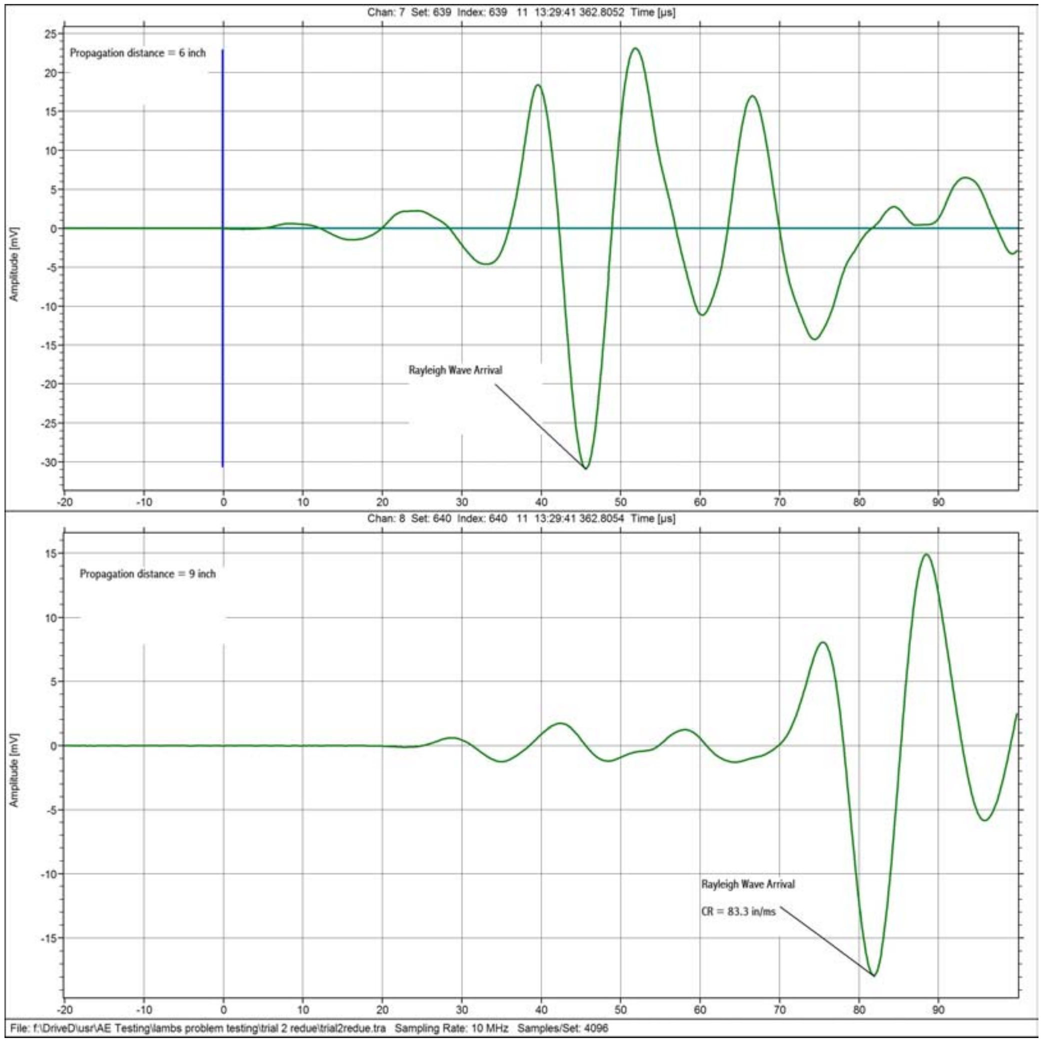

Figure B9 Wave form for 0.5 mm pencil lead break at x = - 6 inch.

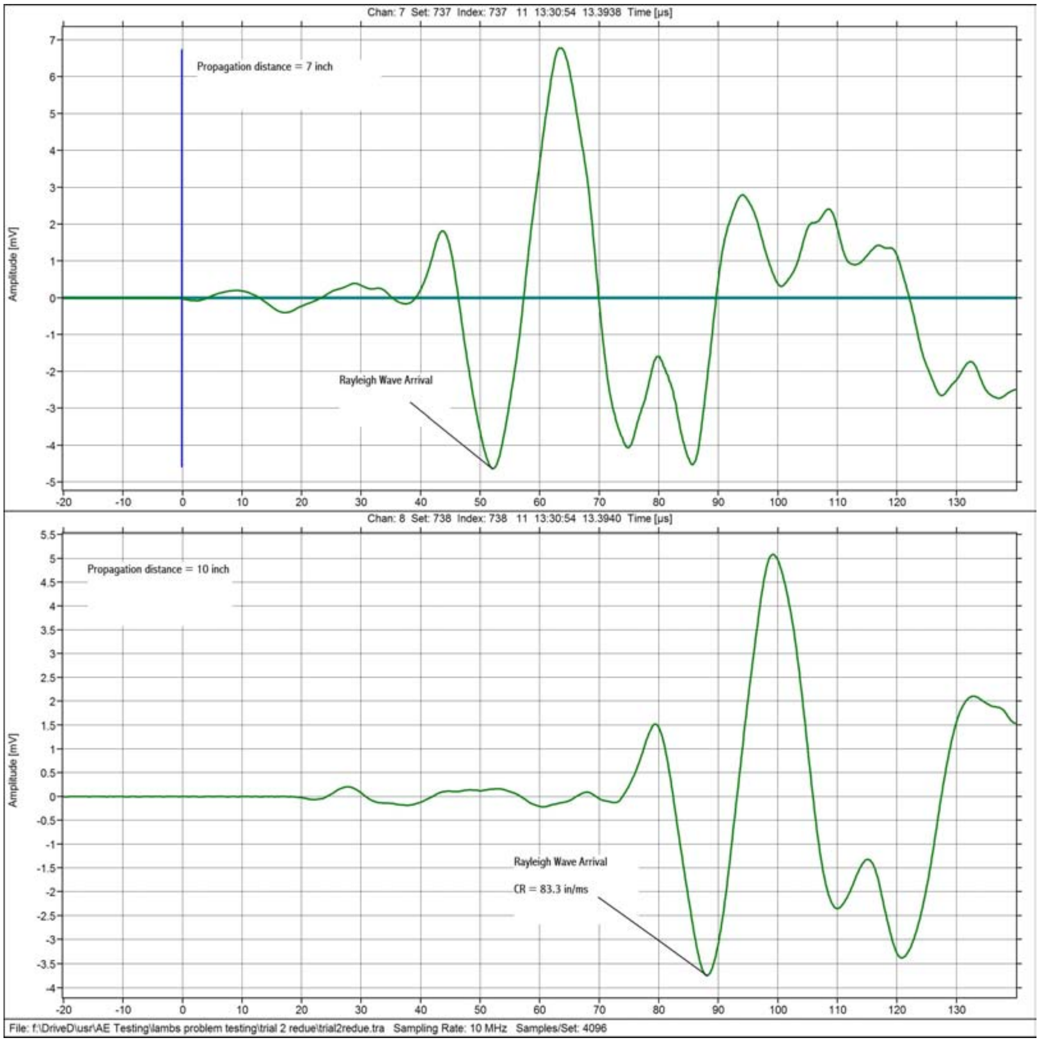

Figure B10 Wave form for 0.5 mm pencil lead break at x = - 7 inch.

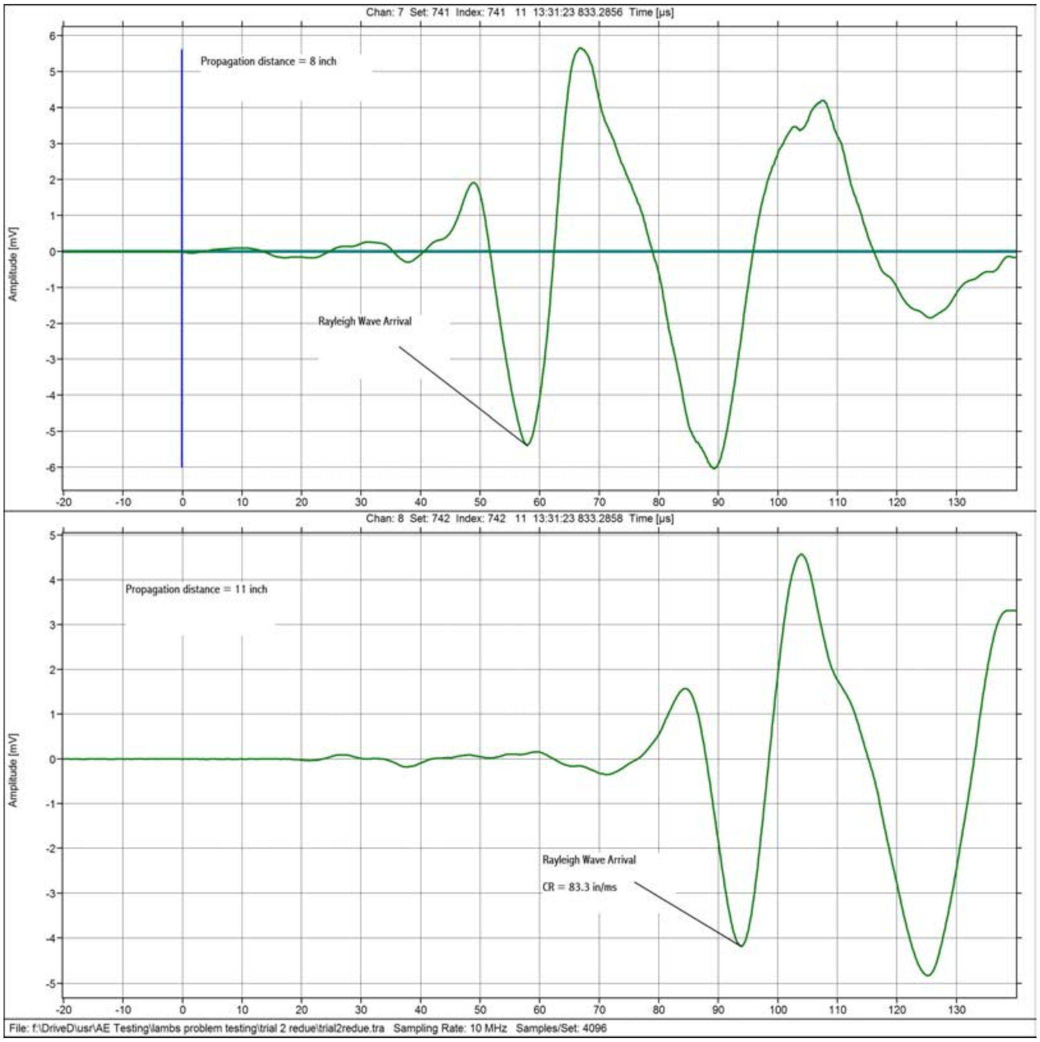

Figure B11 Wave form for 0.5 mm pencil lead break at x = - 8 inch.

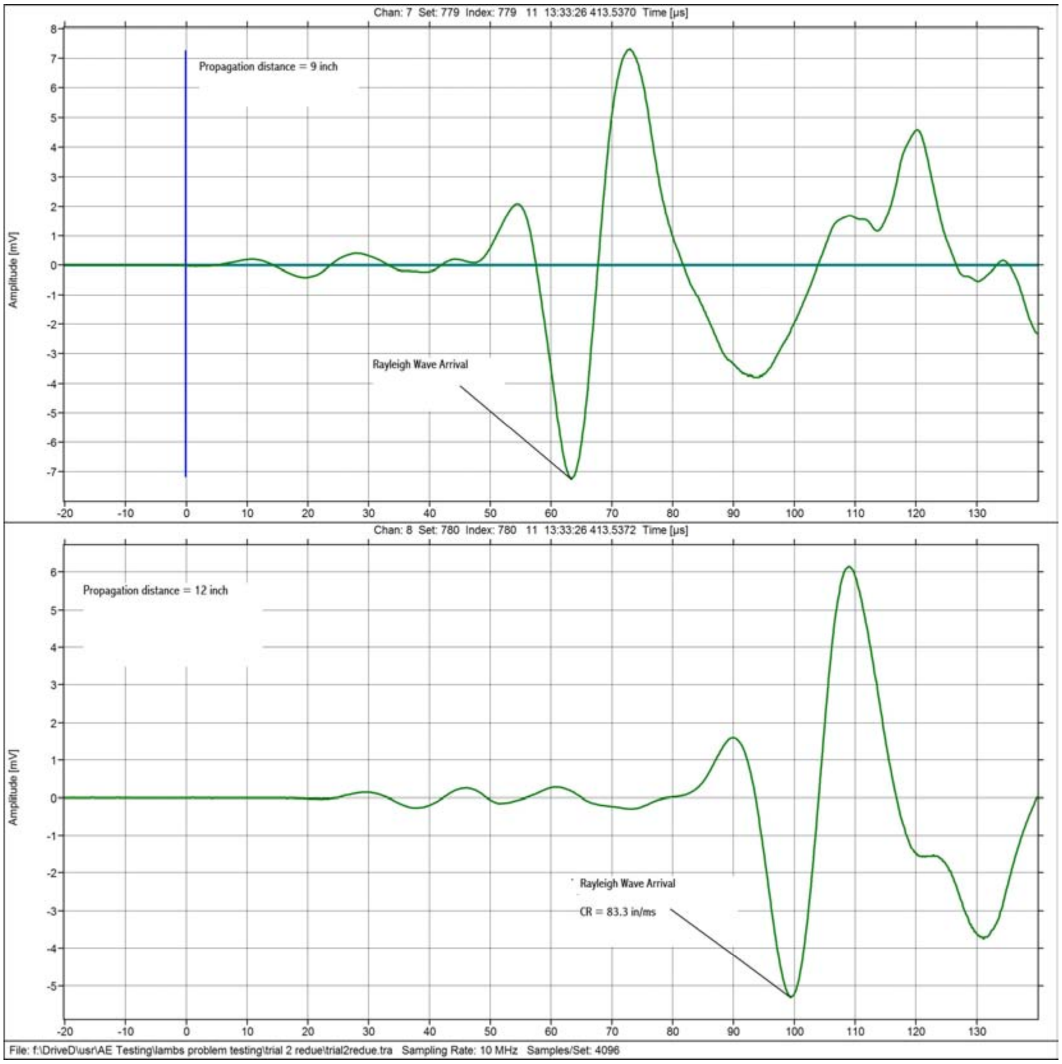

Figure B12 Wave form for 0.5 mm pencil lead break at x = - 9 inch.

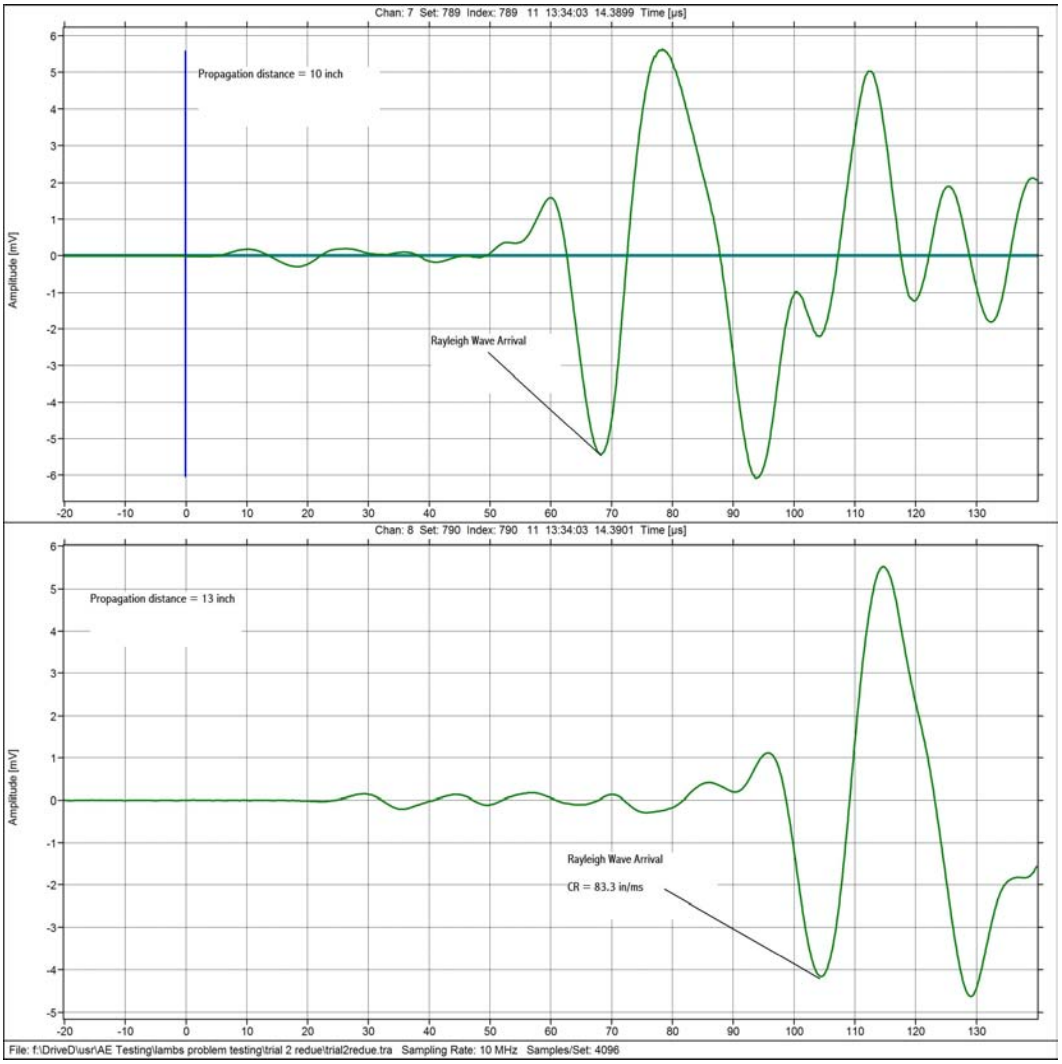

Figure B13 Wave form for 0.5 mm pencil lead break at x = - 10 inch.

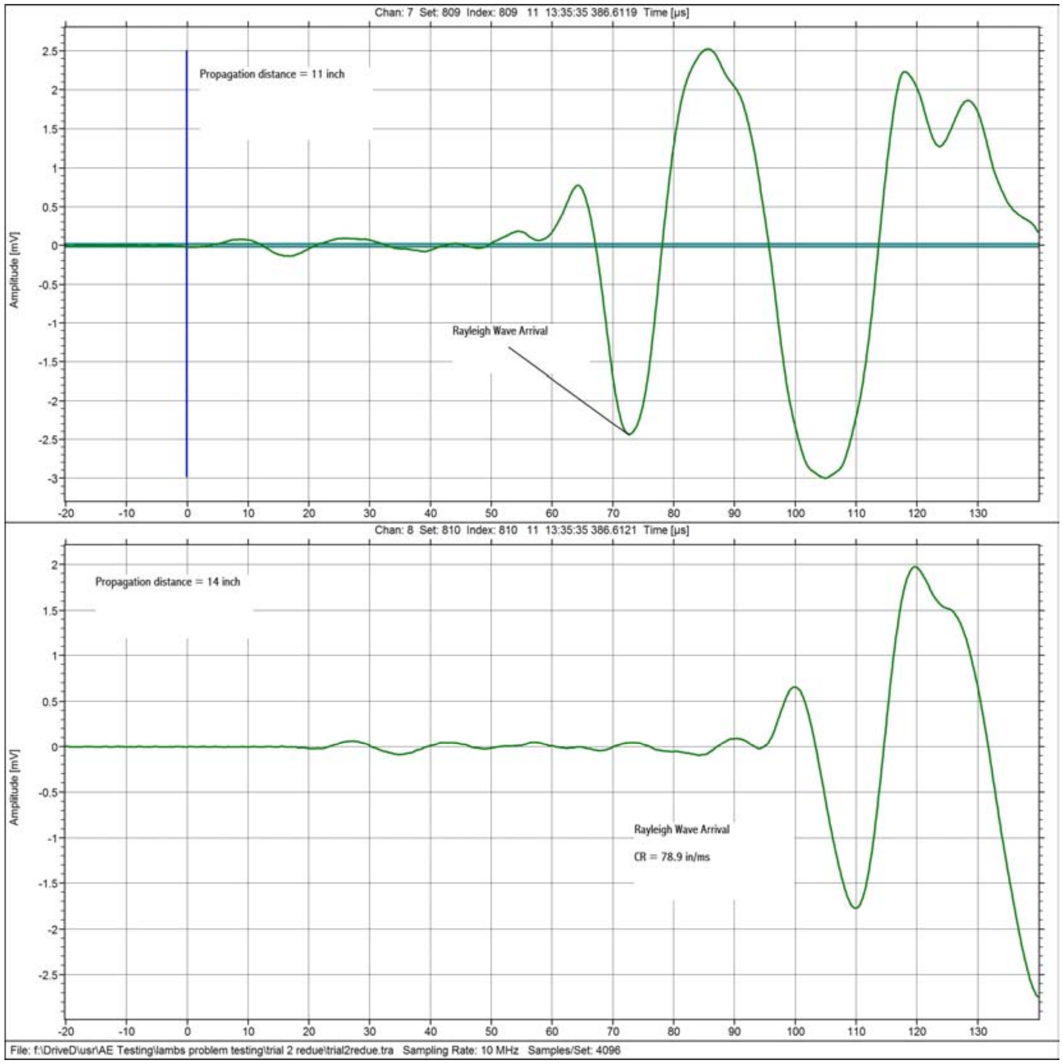

Figure B14 Wave form for 0.5 mm pencil lead break at x = - 11 inch.

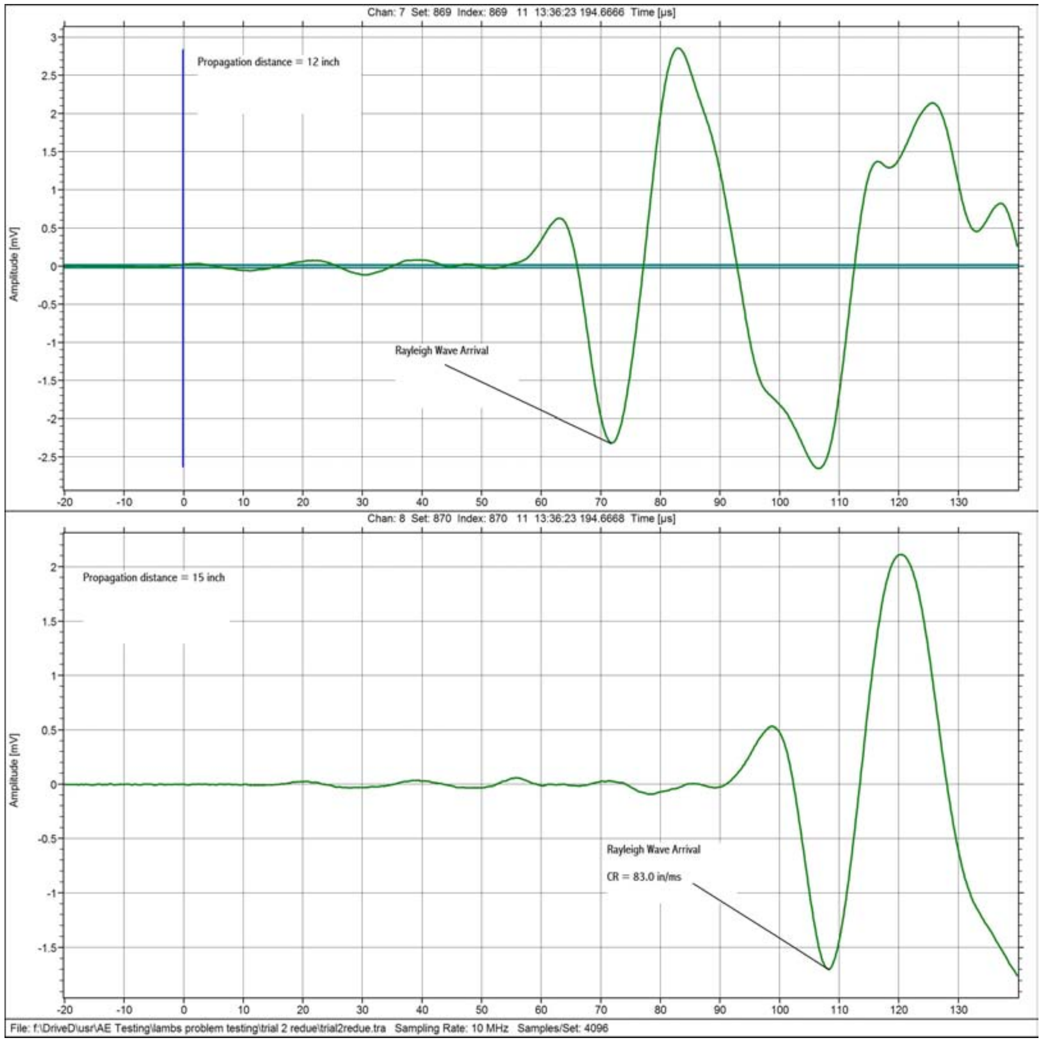

Figure B15 Wave form for 0.5 mm pencil lead break at x = - 12 inch.

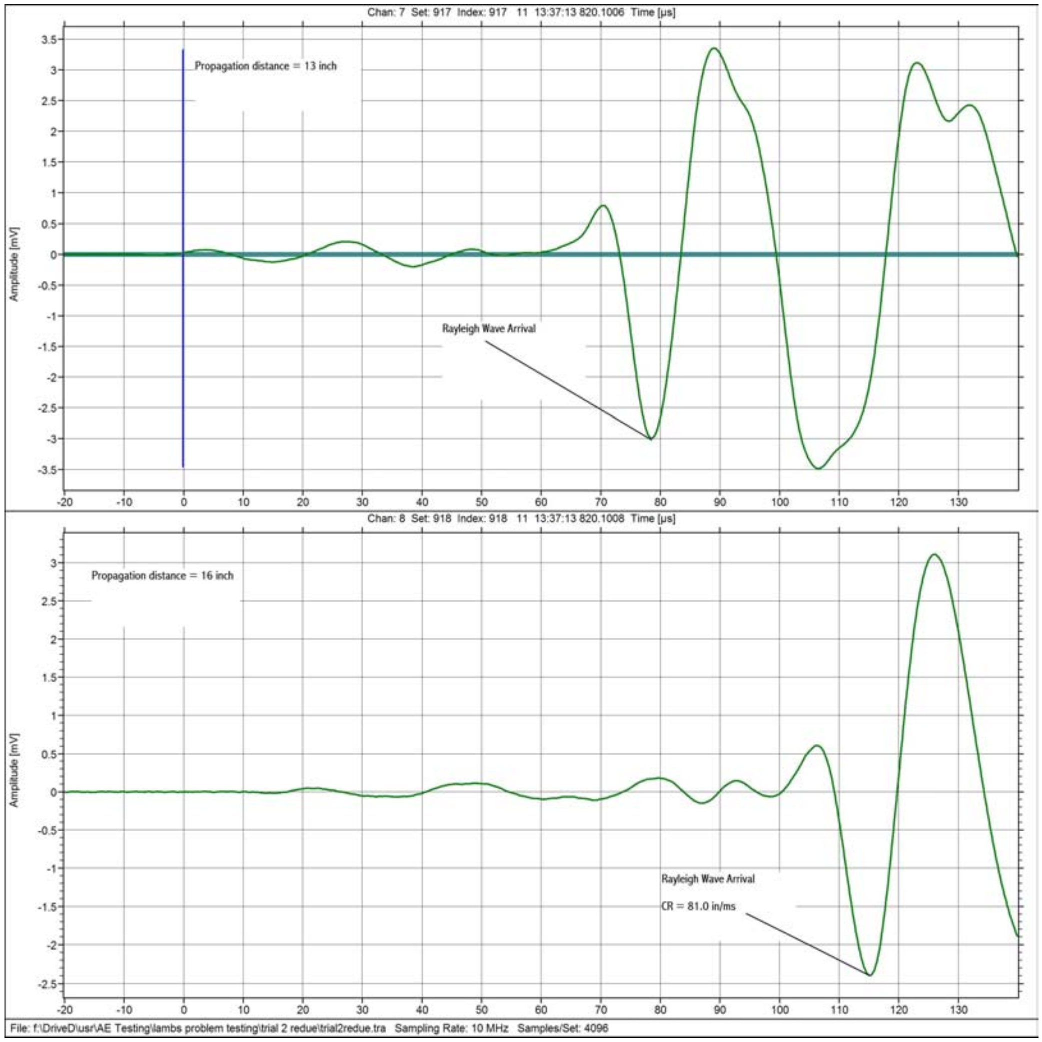

Figure B16 Wave form for 0.5 mm pencil lead break at x = - 13 inch.

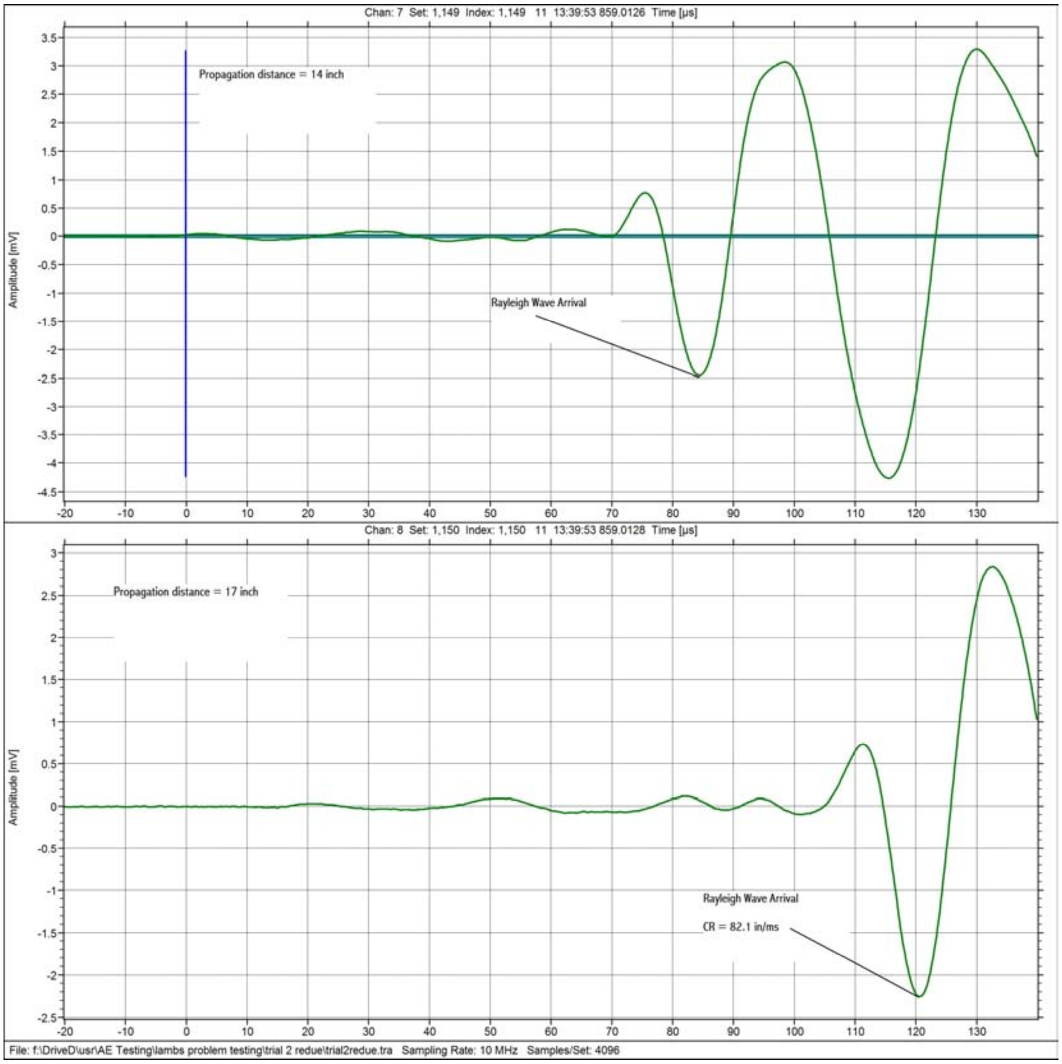

Figure B17 Wave form for 0.5 mm pencil lead break at x = - 14 inch.

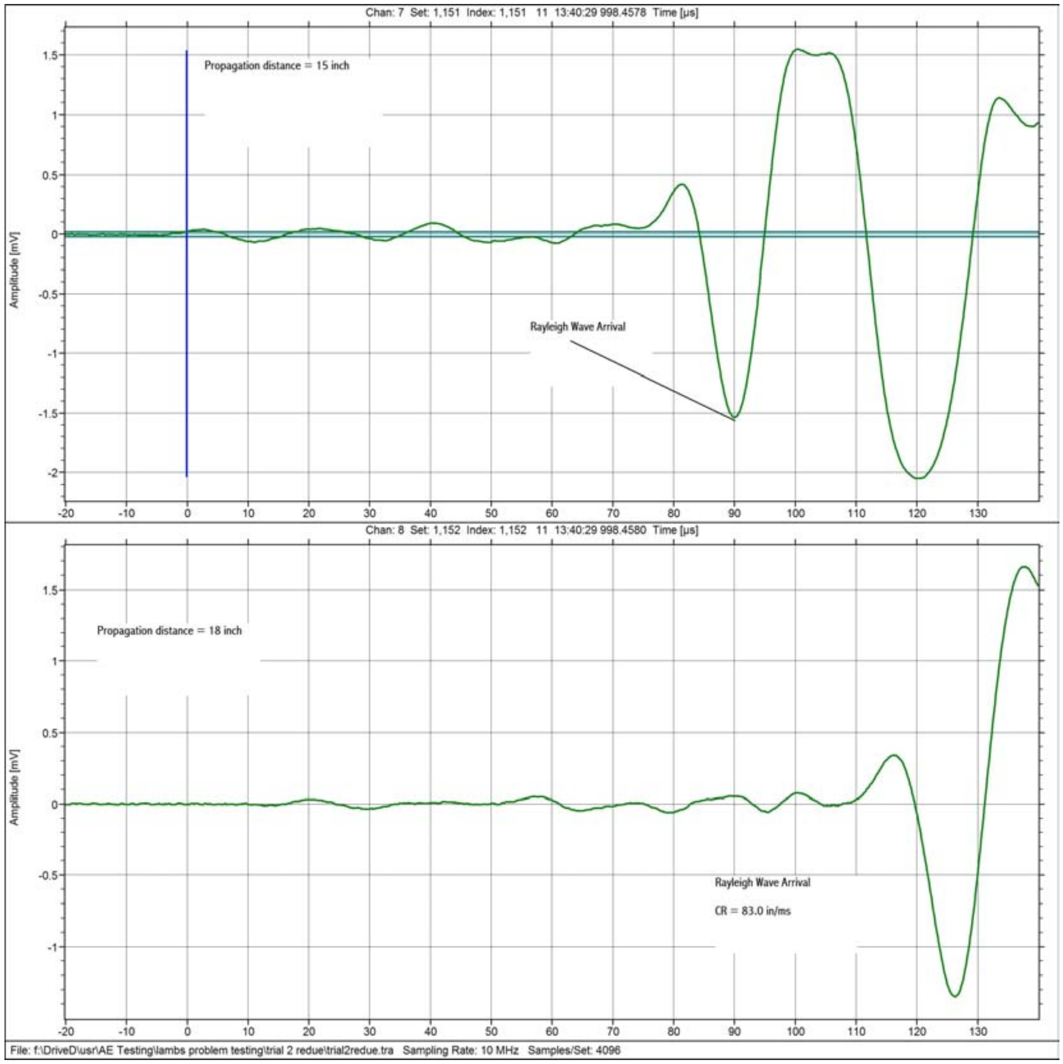

Figure B18 Wave form for 0.5 mm pencil lead break at x = - 15 inch.

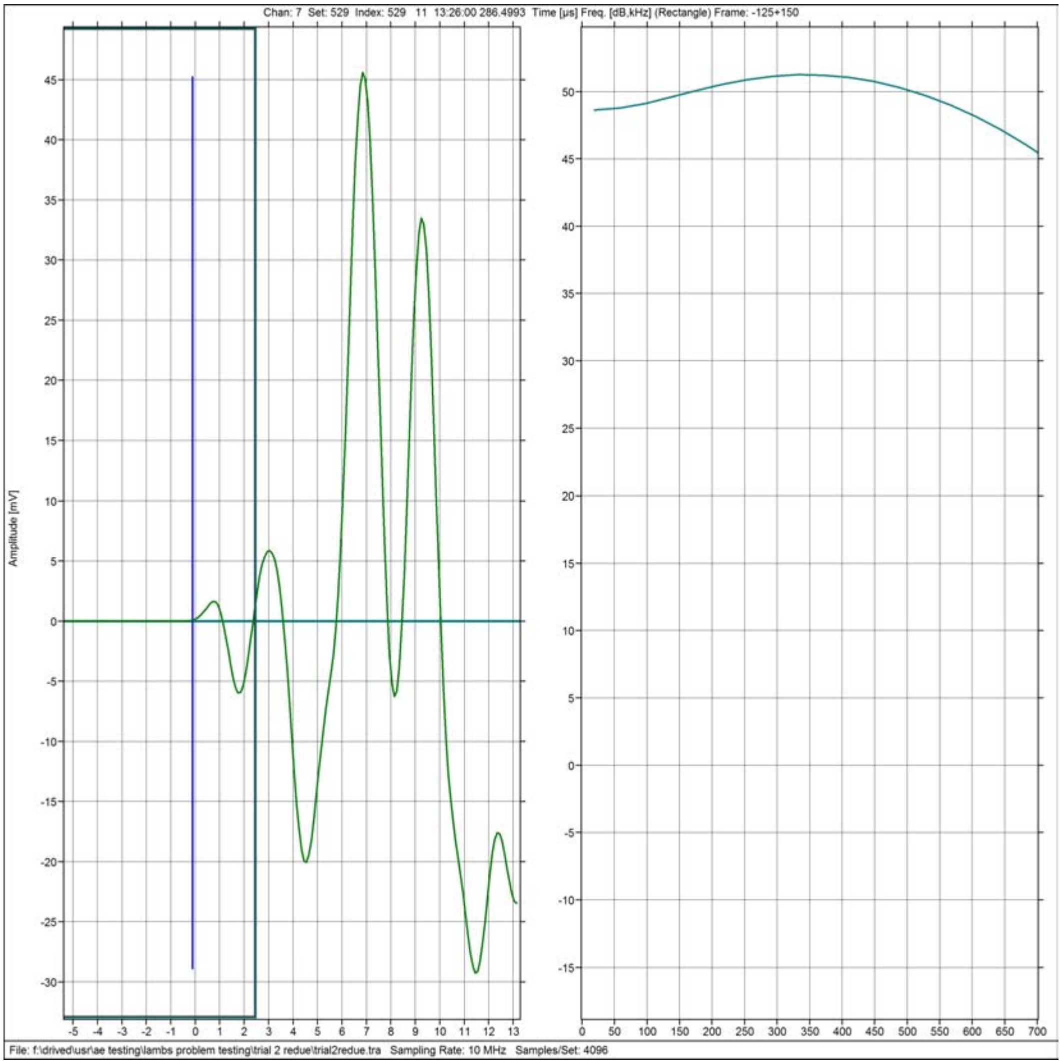

Figure B19 Wave form and FFT of P-wave arrival at a propagation distance of 1 inch.

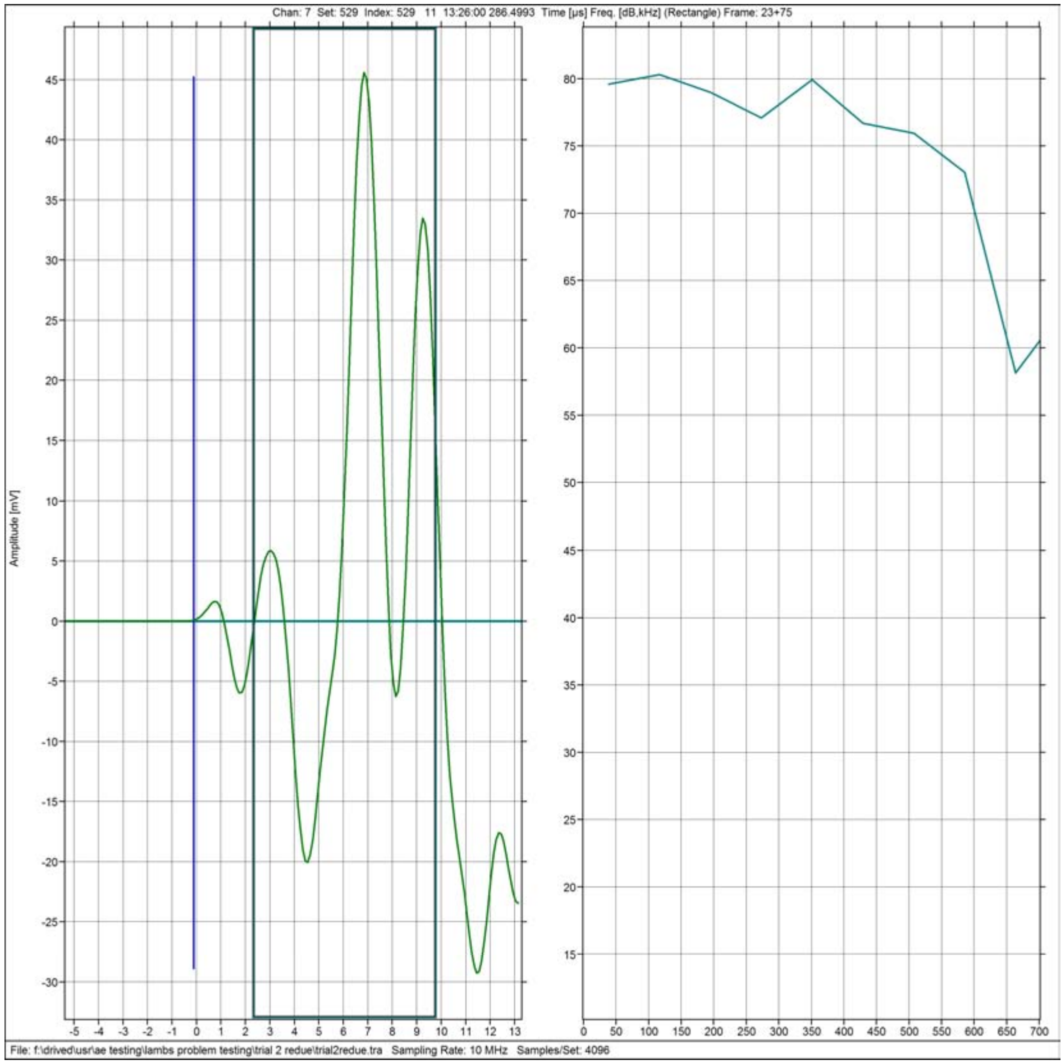

Figure B20 Wave form and FFT of R-wave arrival at a propagation distance of 1 inch.

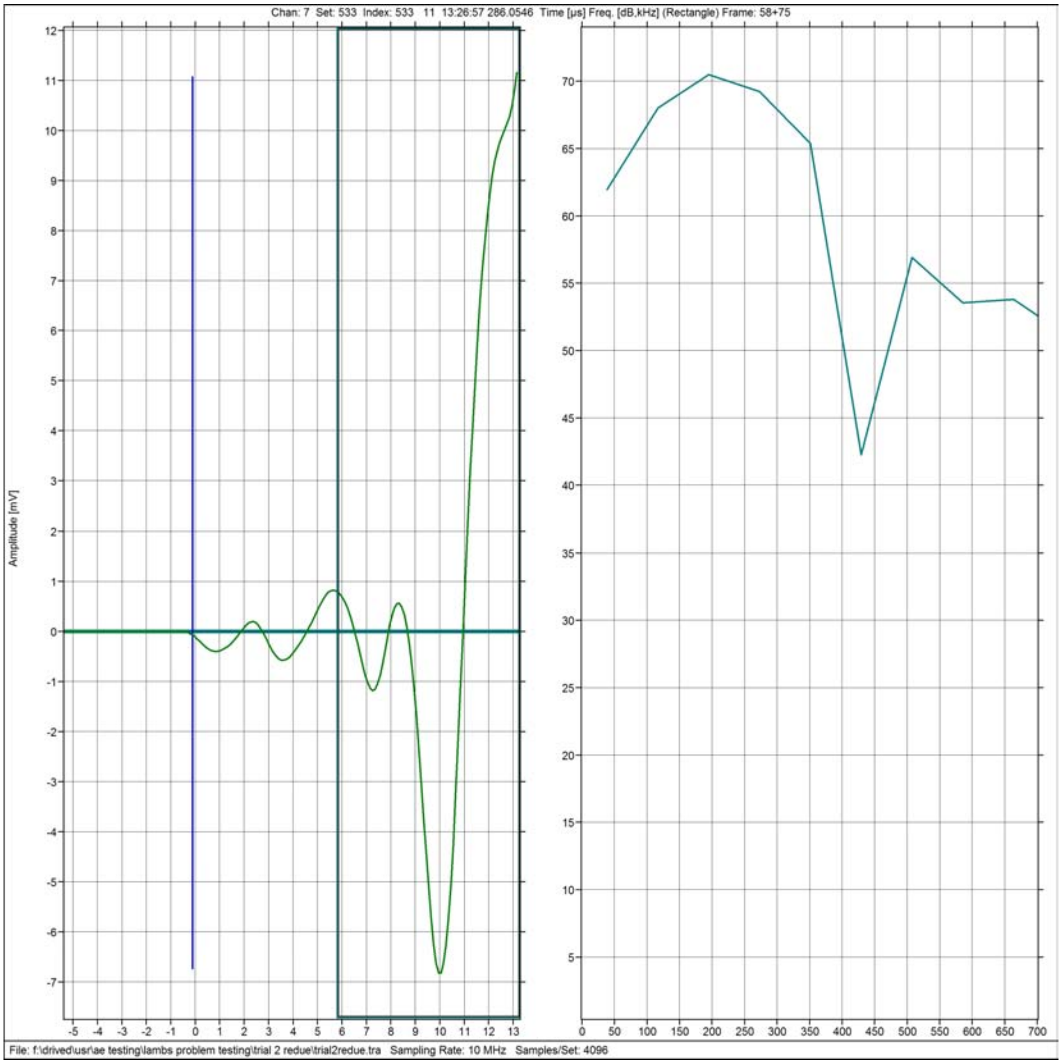

Figure B21 Wave form and FFT of R-wave arrival at a propagation distance of 2 inch.

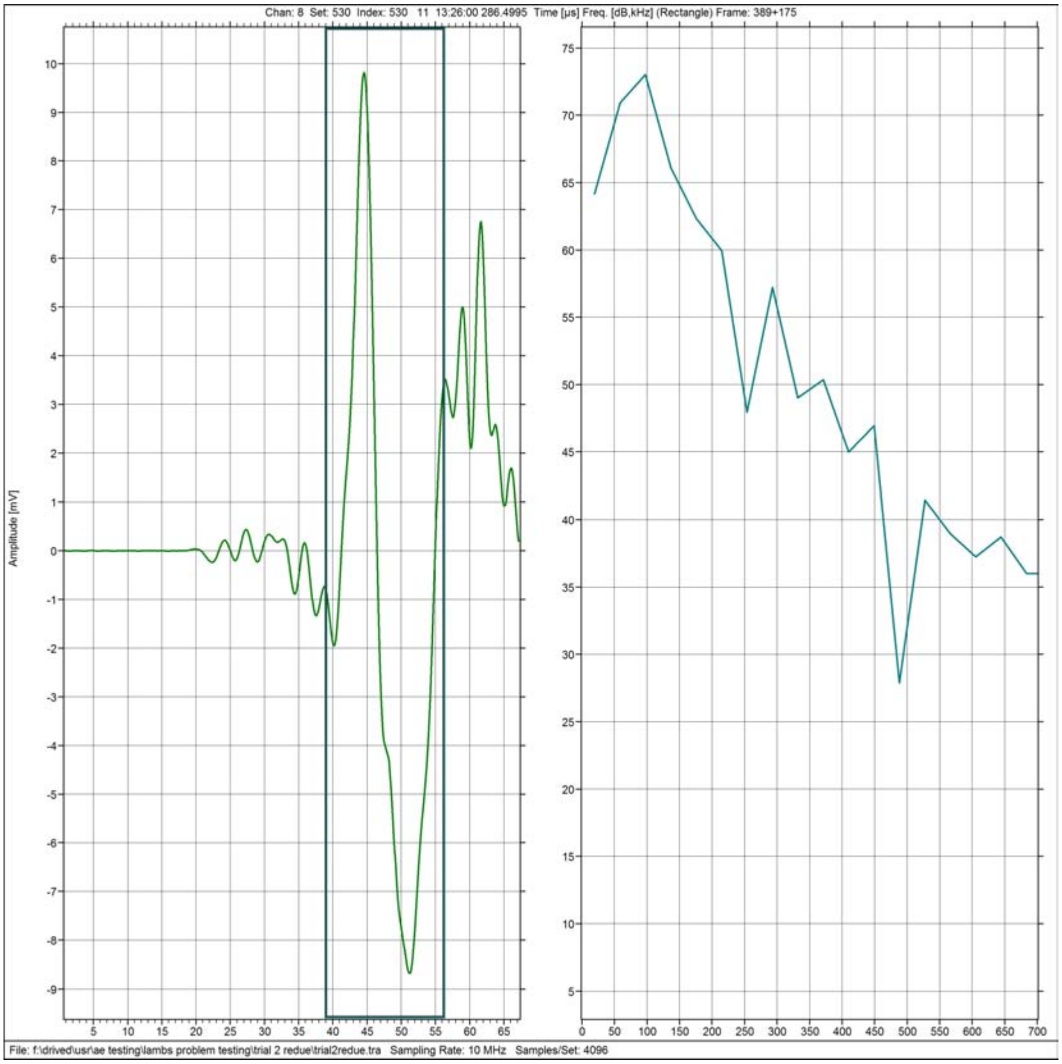

Figure B22 Wave form and FFT of R-wave arrival at a propagation distance of 3 inch.

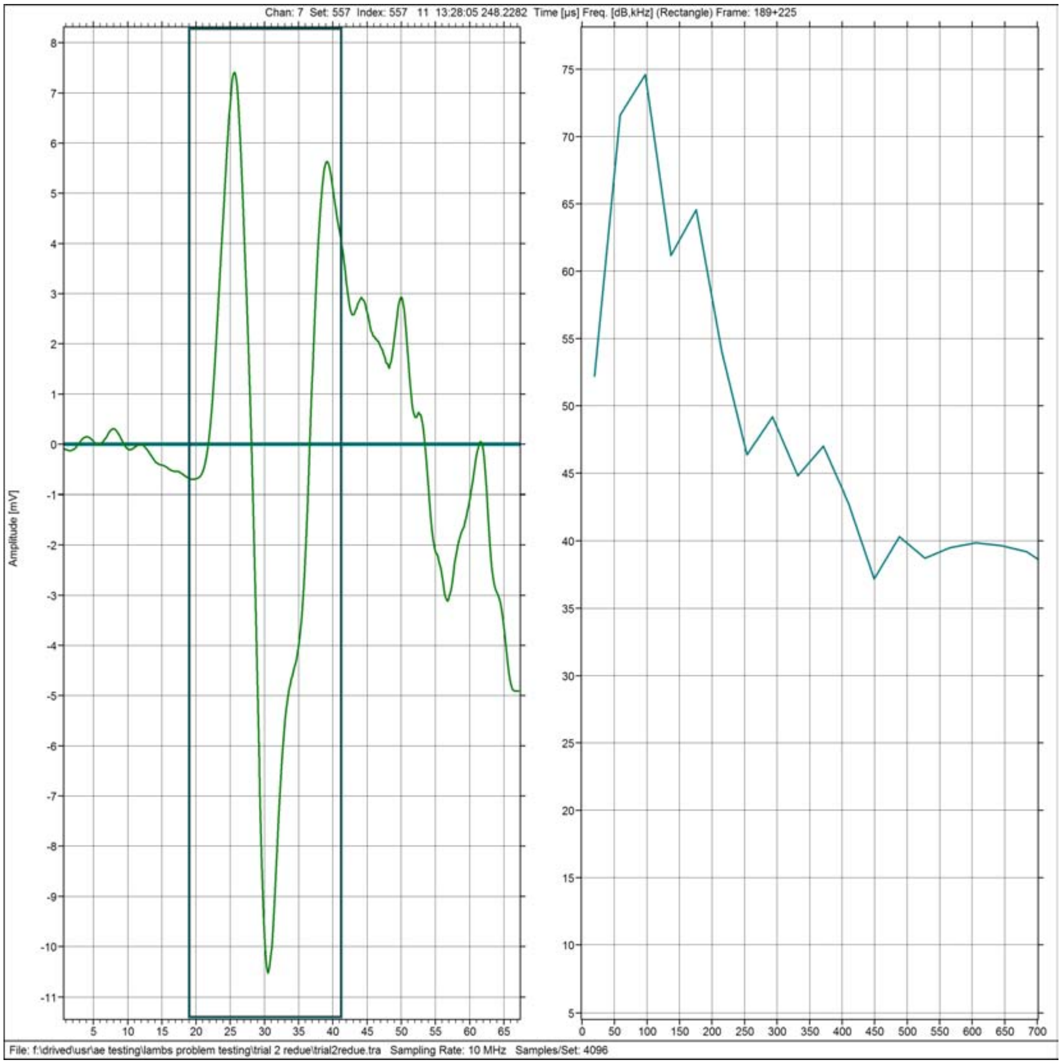

Figure B23 Wave form and FFT of R-wave arrival at a propagation distance of 4 inch.

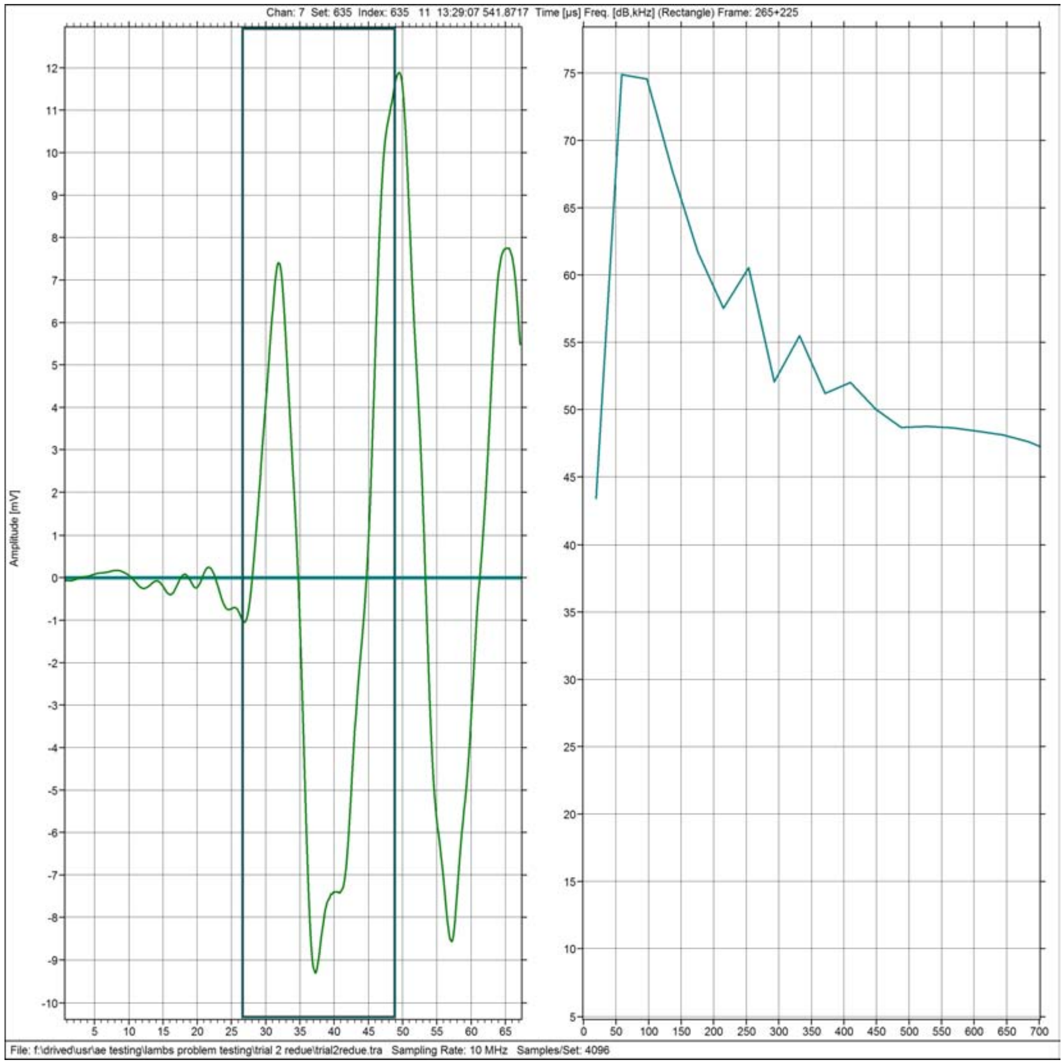

Figure B24 Wave form and FFT of R-wave arrival at a propagation distance of 5 inch.

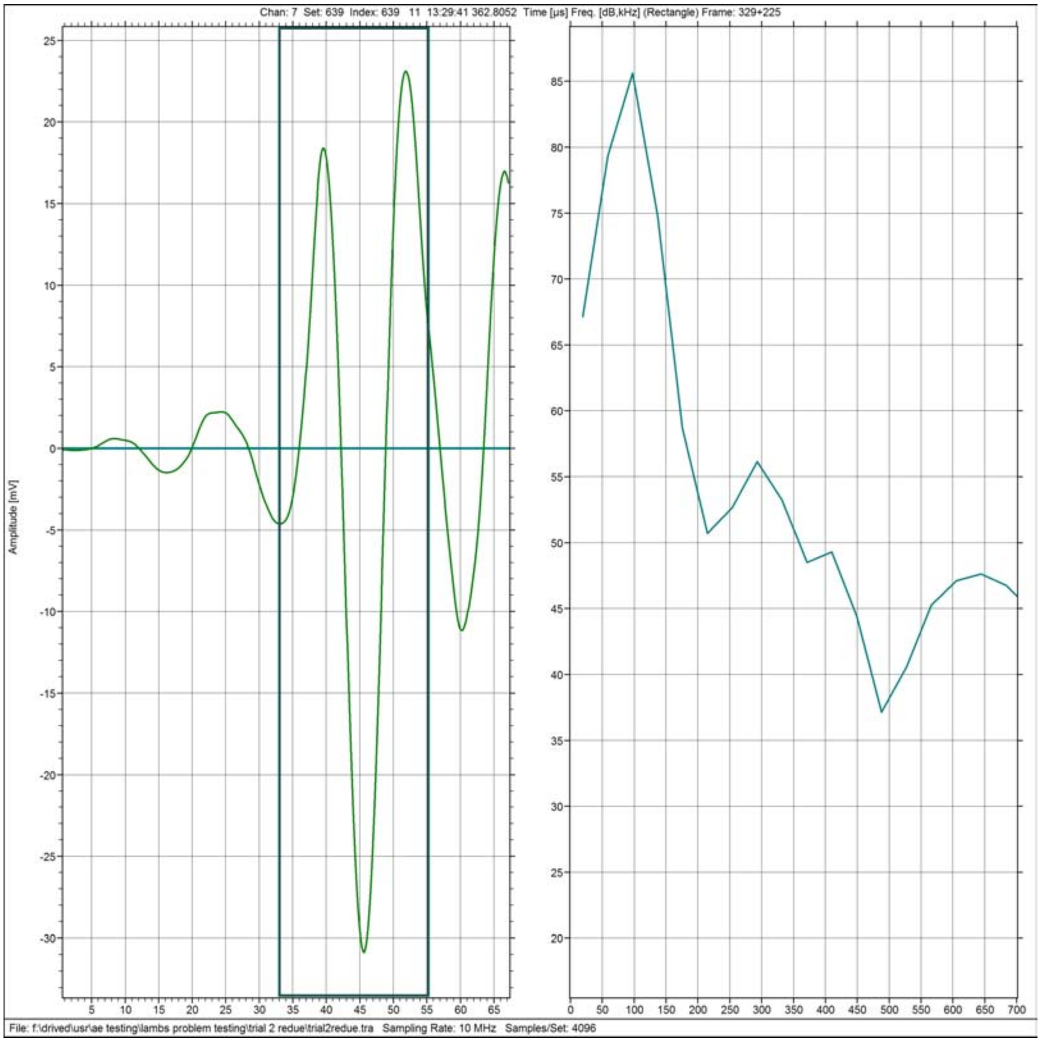

Figure B25 Wave form and FFT of R-wave arrival at a propagation distance of 6 inch.

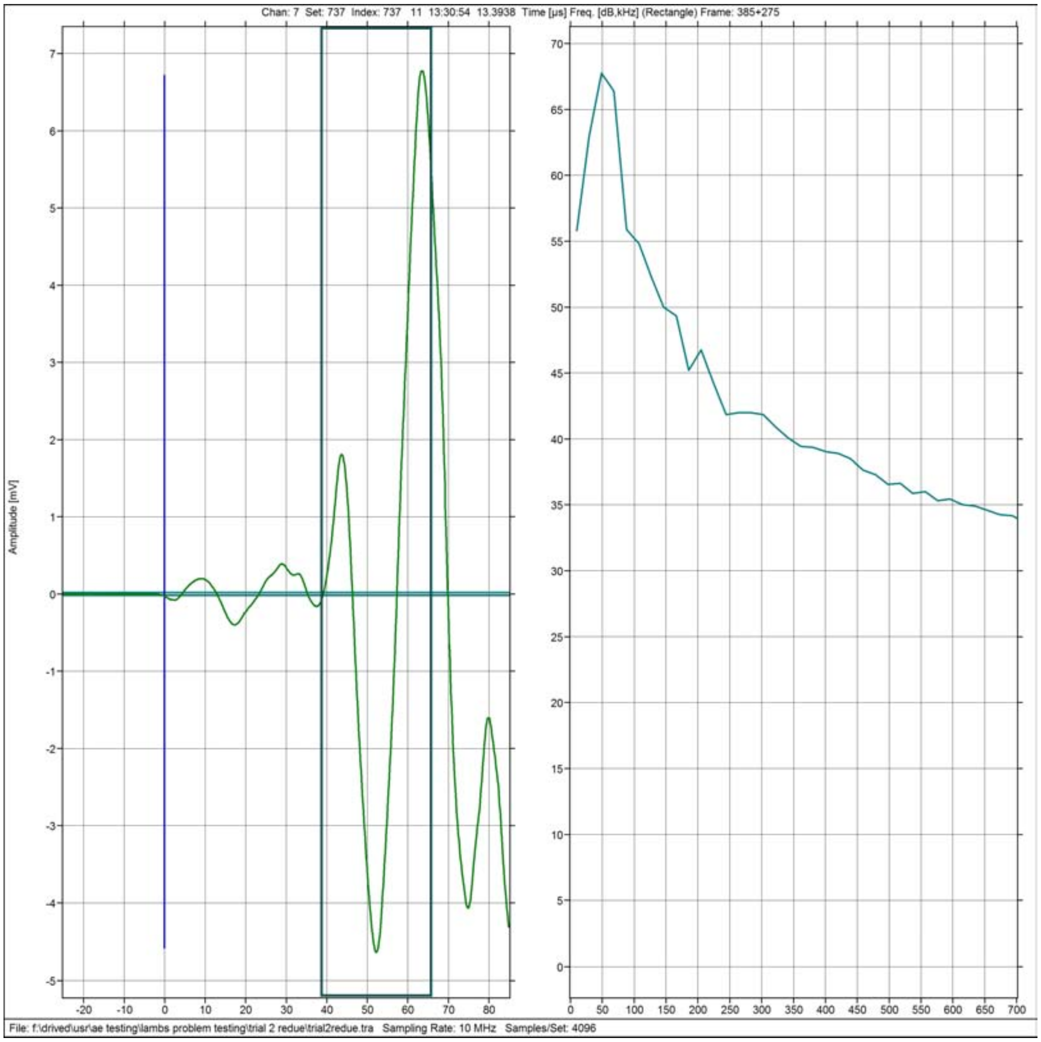

Figure B26 Wave form and FFT of R-wave arrival at a propagation distance of 7 inch.

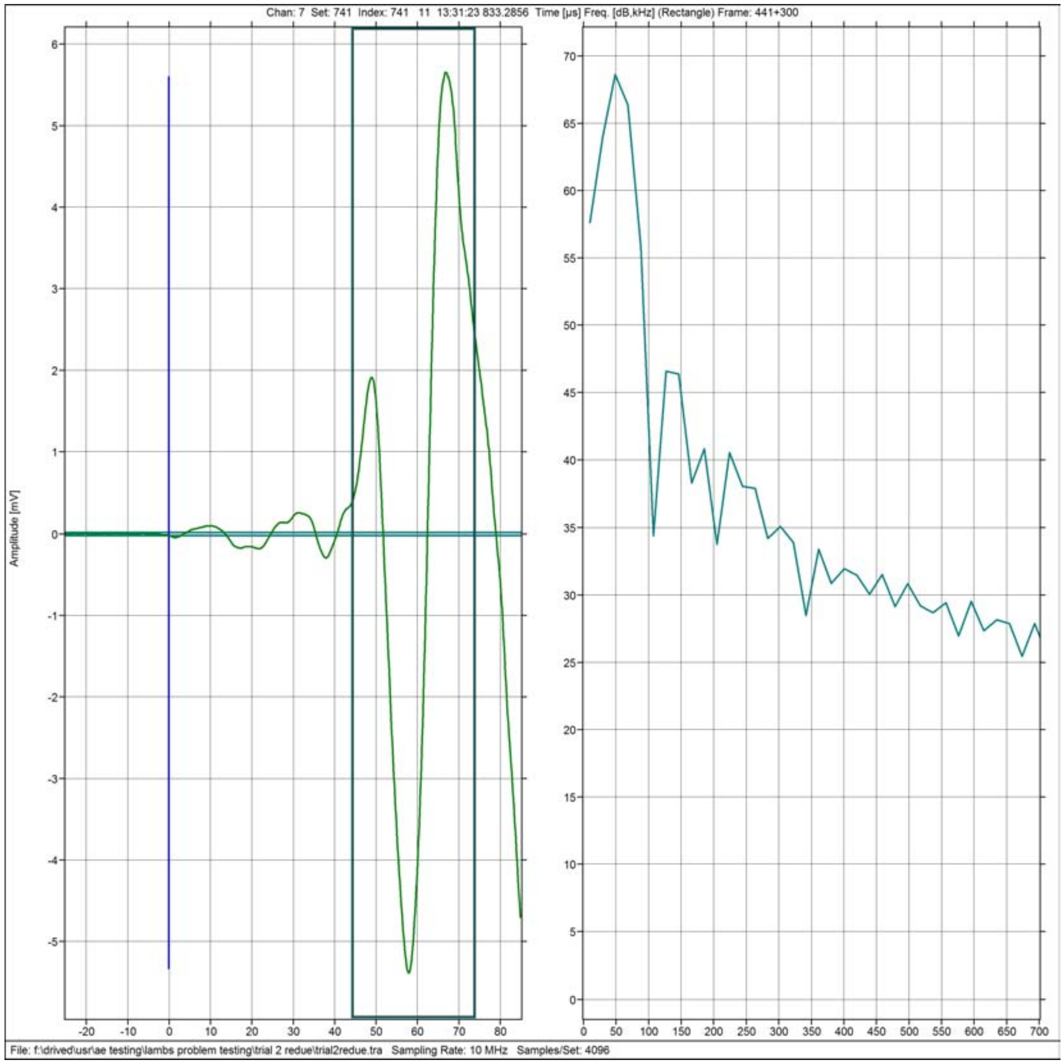

Figure B27 Wave form and FFT of R-wave arrival at a propagation distance of 8 inch.

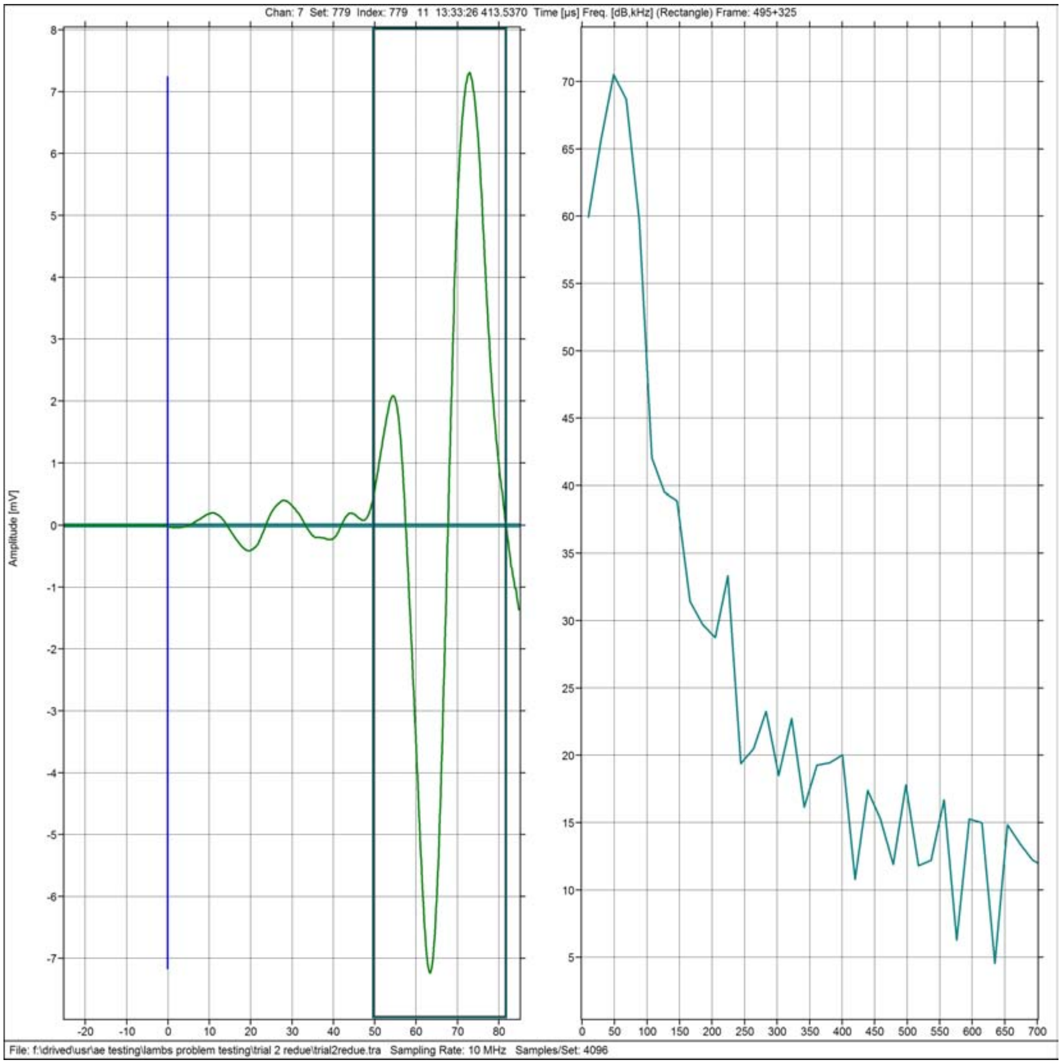

Figure B28 Wave form and FFT of R-wave arrival at a propagation distance of 9 inch.

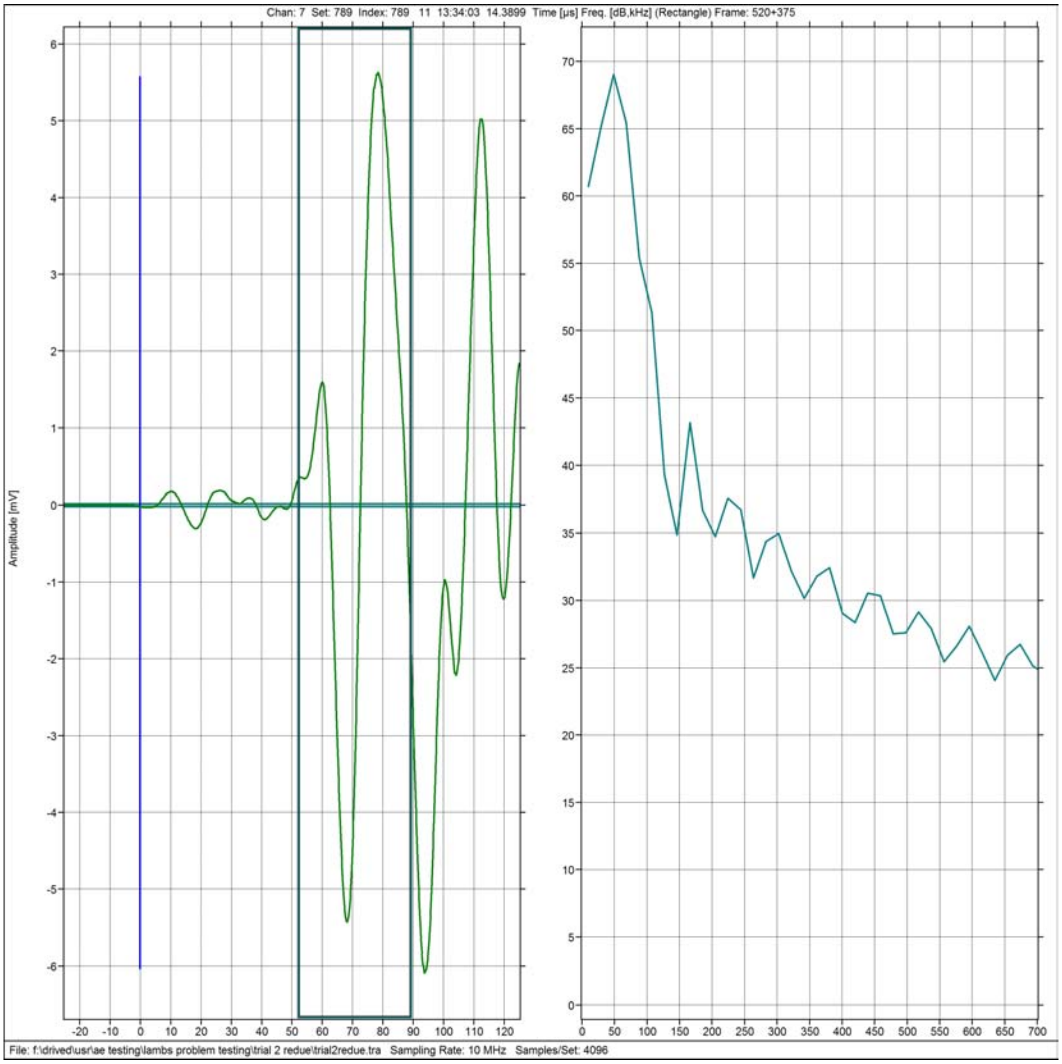

Figure B29 Wave form and FFT of R-wave arrival at a propagation distance of 10 inch.

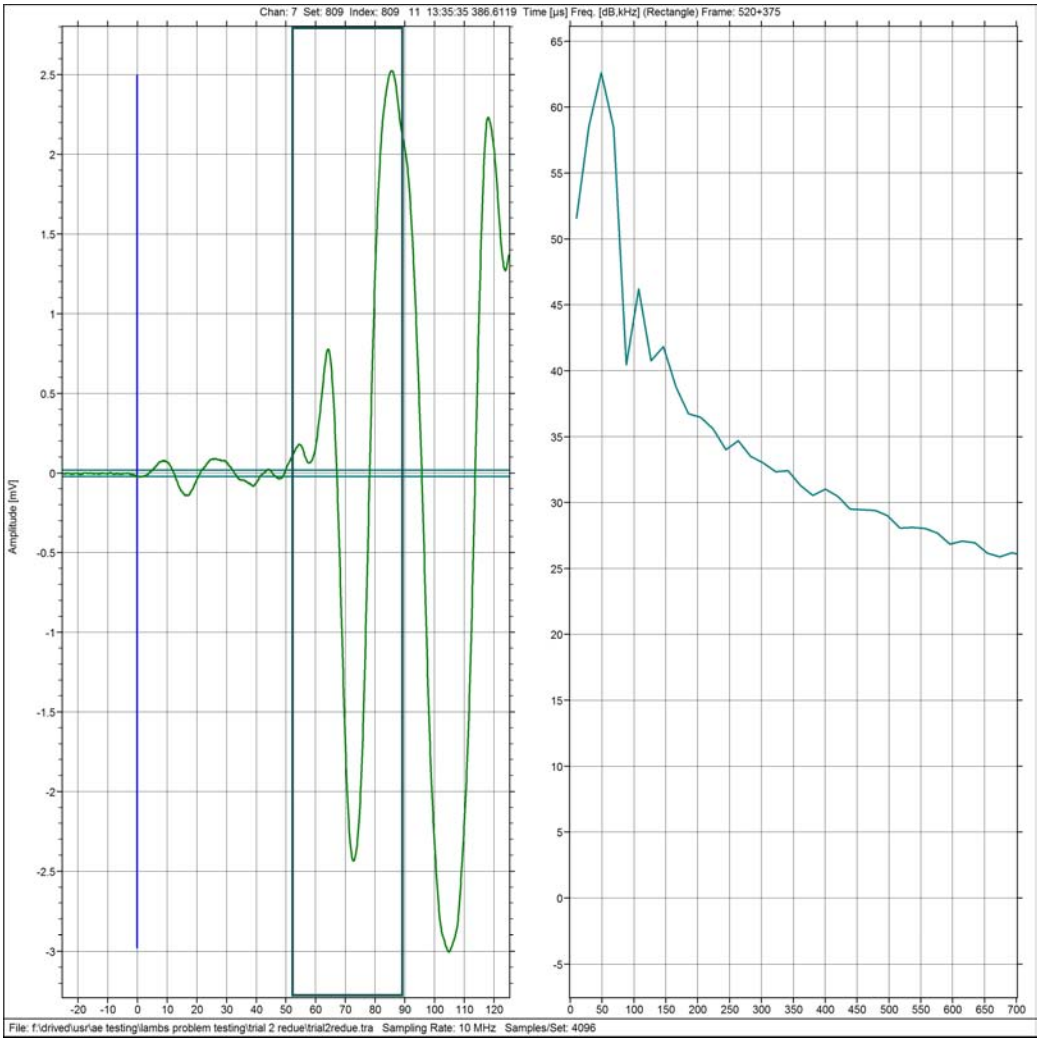

Figure B30 Wave form and FFT of R-wave arrival at a propagation distance of 11 inch.

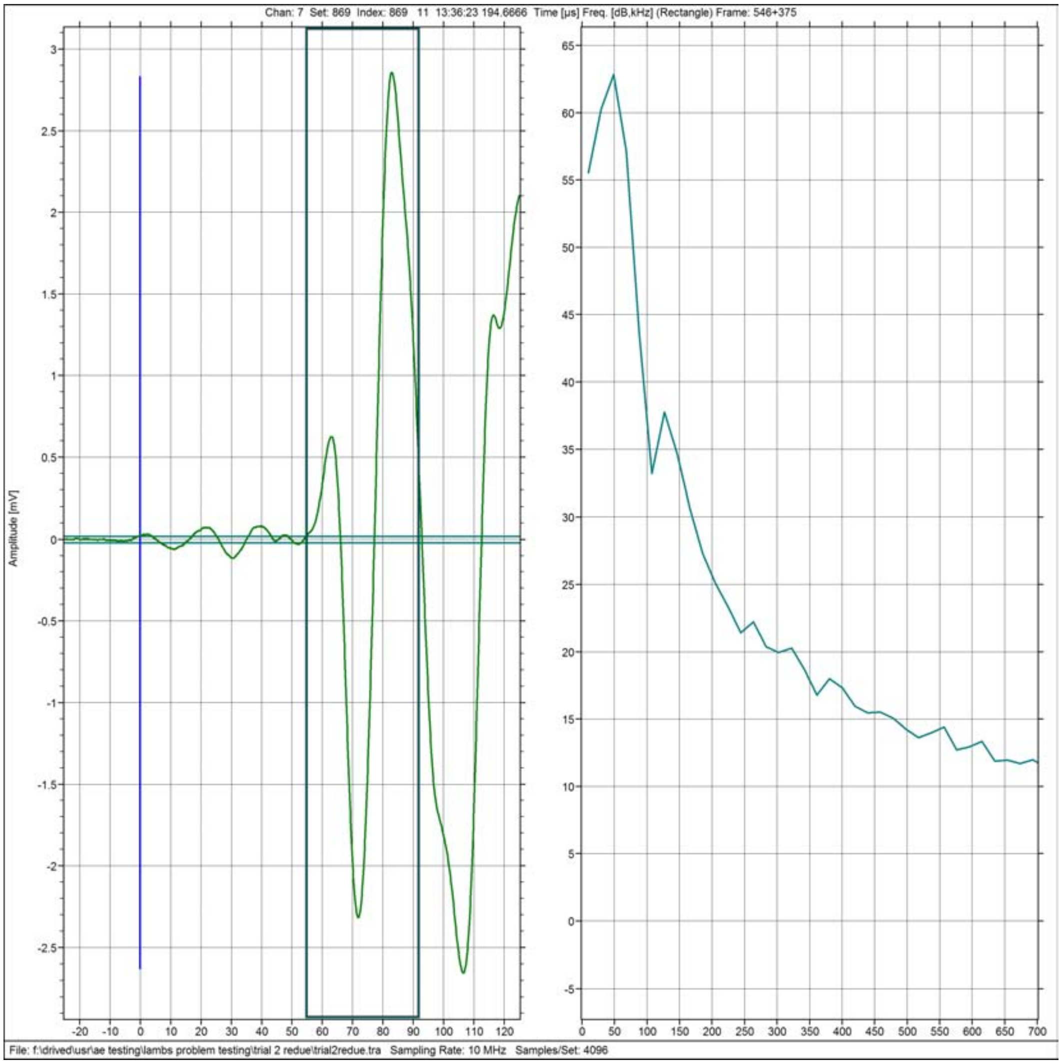

Figure B31 Wave form and FFT of R-wave arrival at a propagation distance of 12 inch.

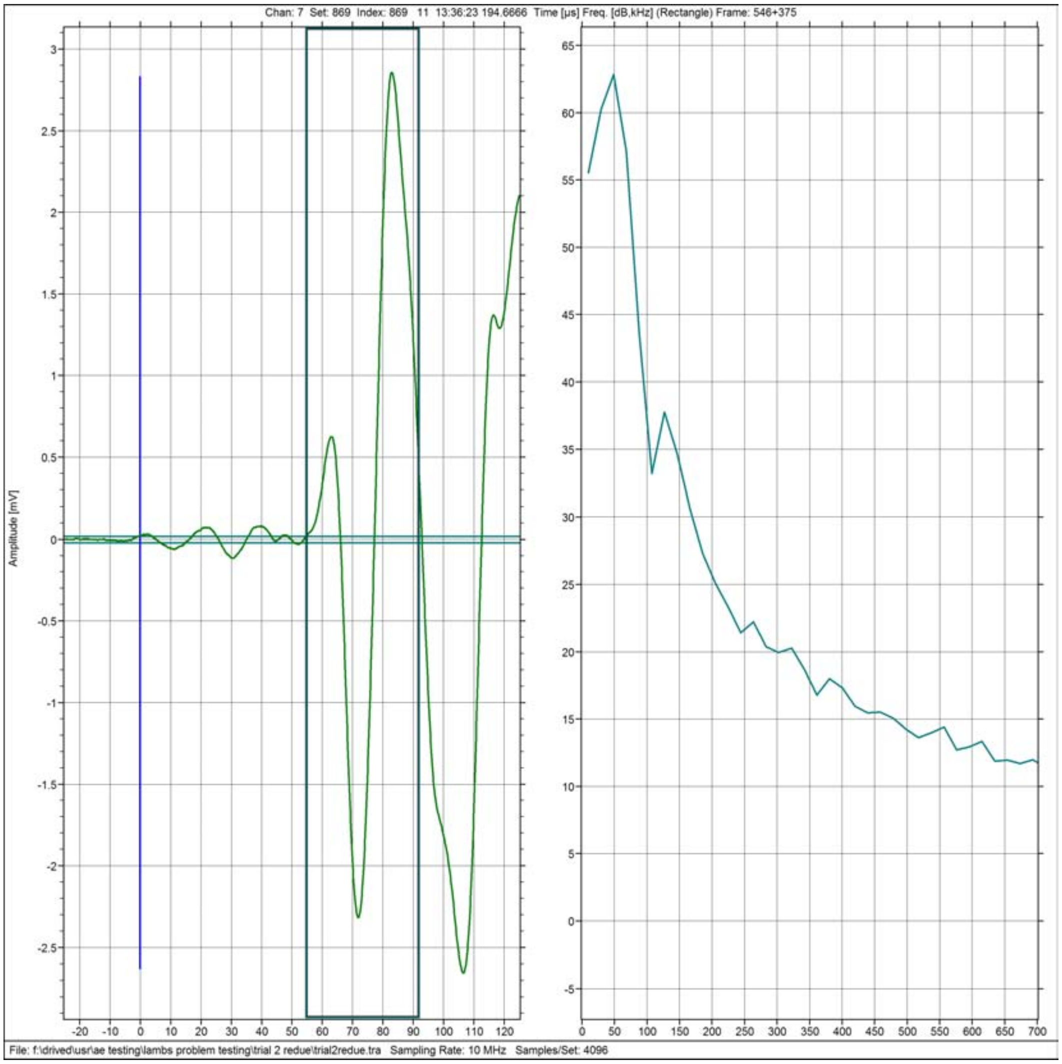

Figure B32 Wave form and FFT of R-wave arrival at a propagation distance of 13 inch.

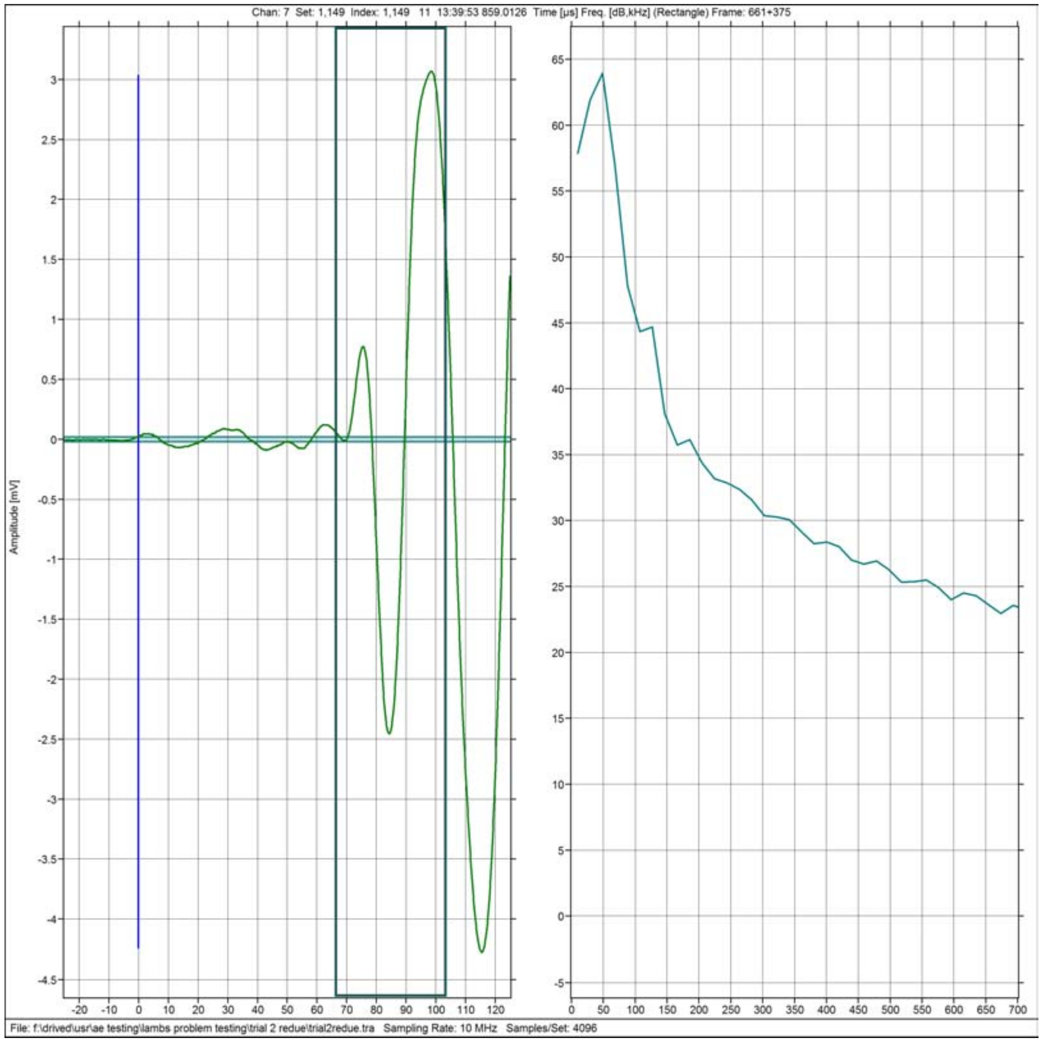

Figure B33 Wave form and FFT of R-wave arrival at a propagation distance of 14 inch.

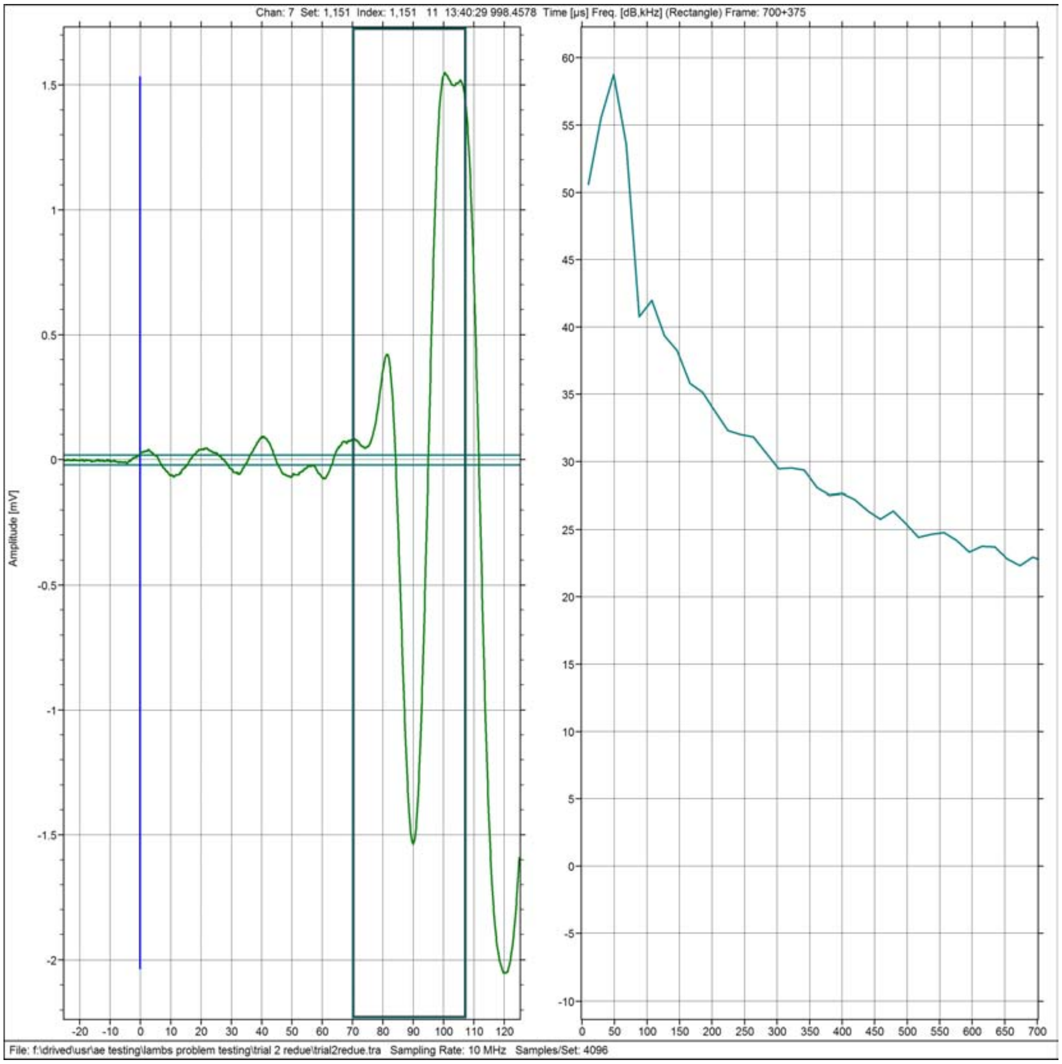

Figure B34 Wave form and FFT of R-wave arrival at a propagation distance of 15 inch.

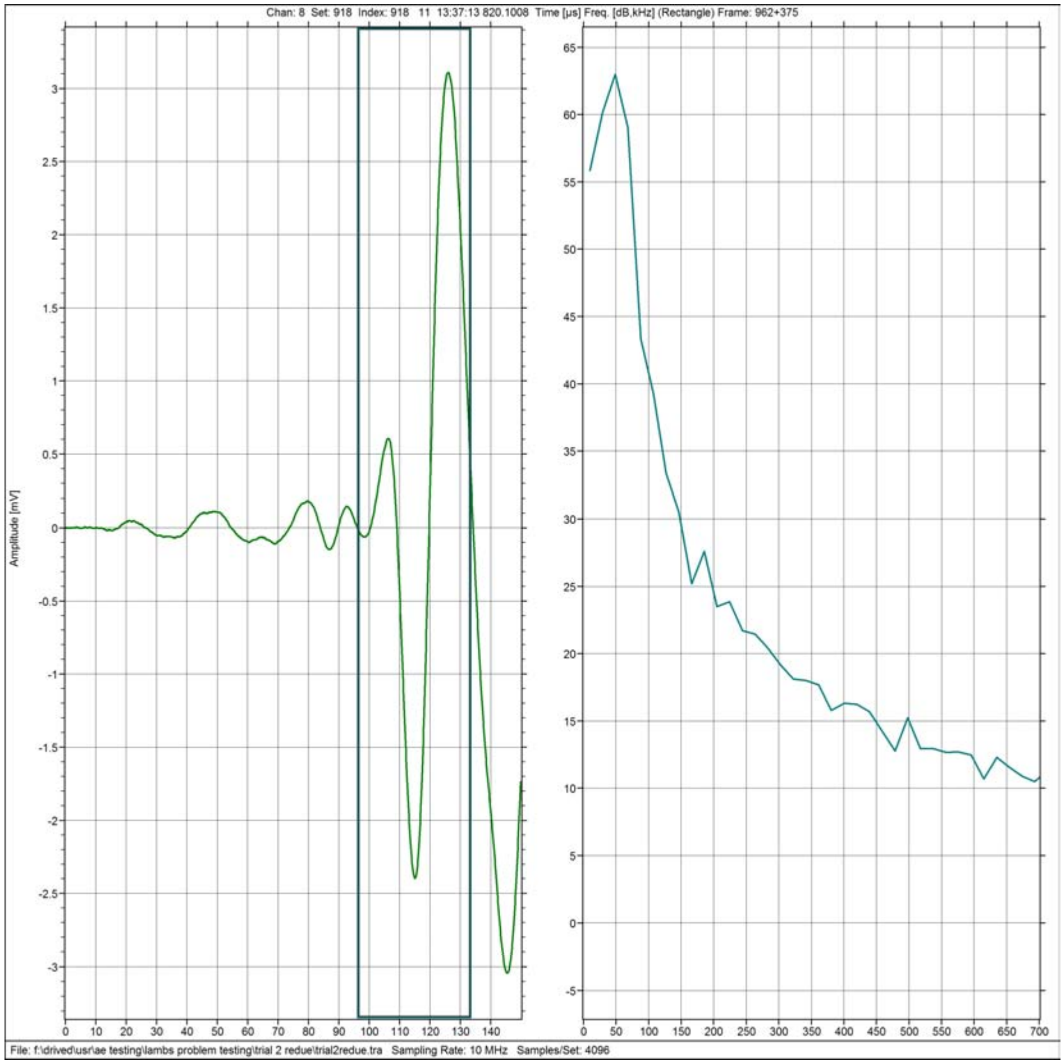

Figure B35 Wave form and FFT of R-wave arrival at a propagation distance of 16 inch.

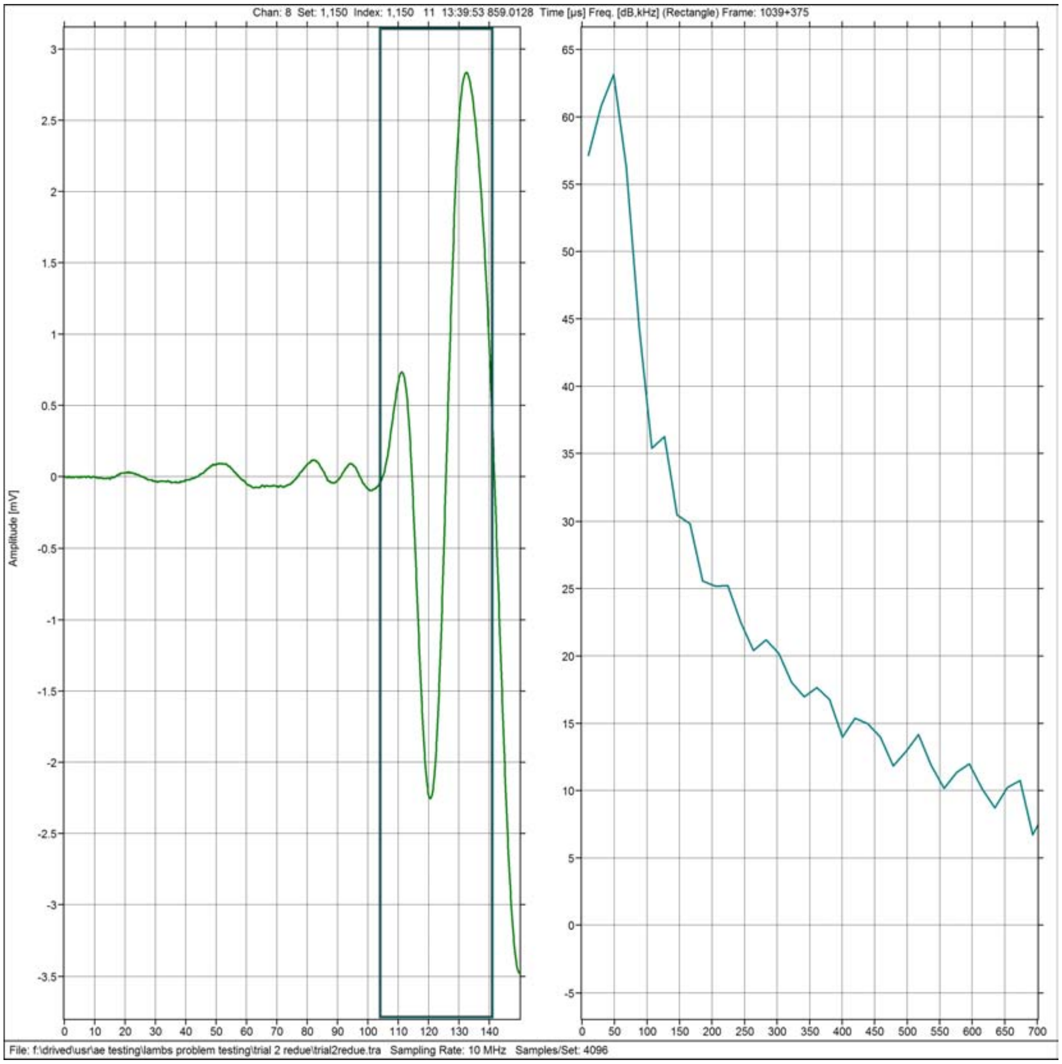

Figure B36 Wave form and FFT of R-wave arrival at a propagation distance of 17 inch.

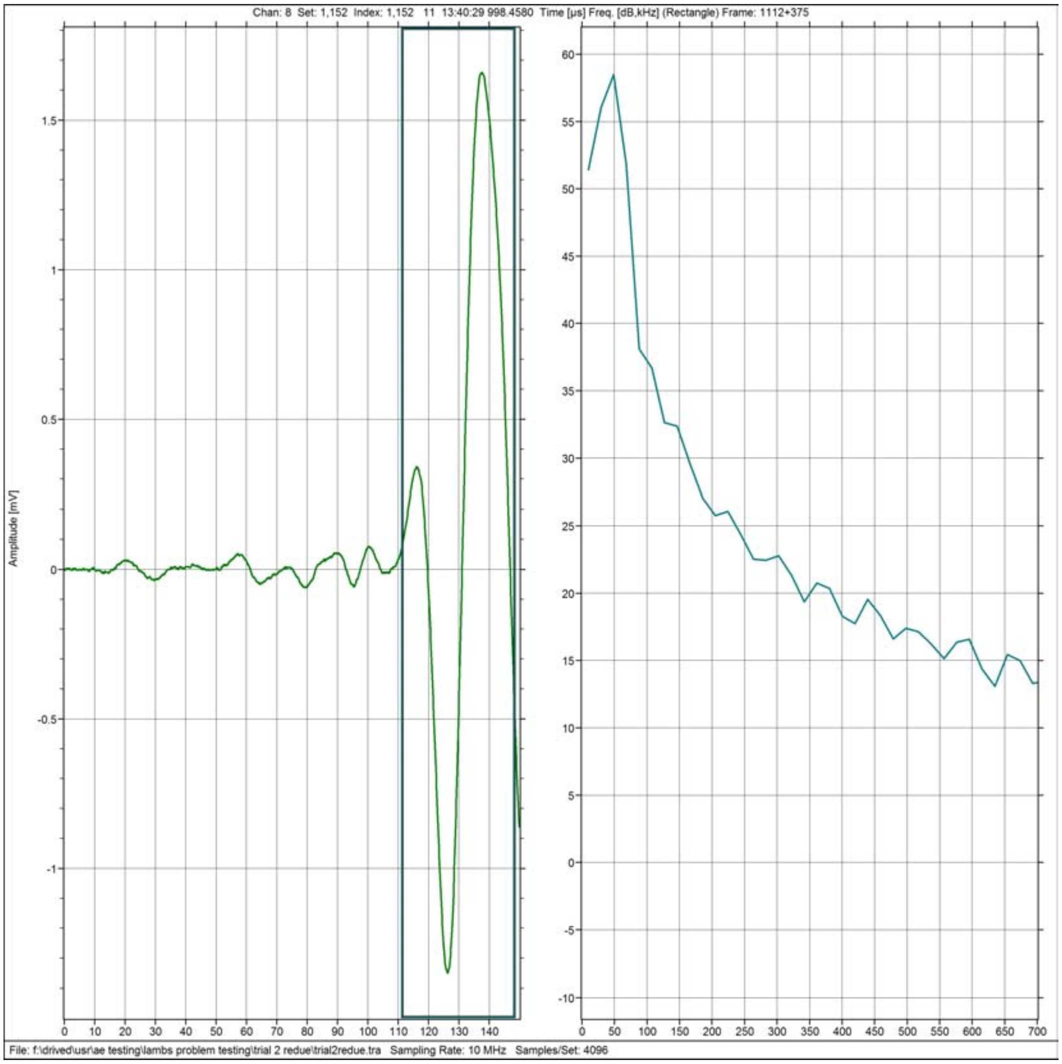

Figure B37 Wave form and FFT of R-wave arrival at a propagation distance of 18 inch.

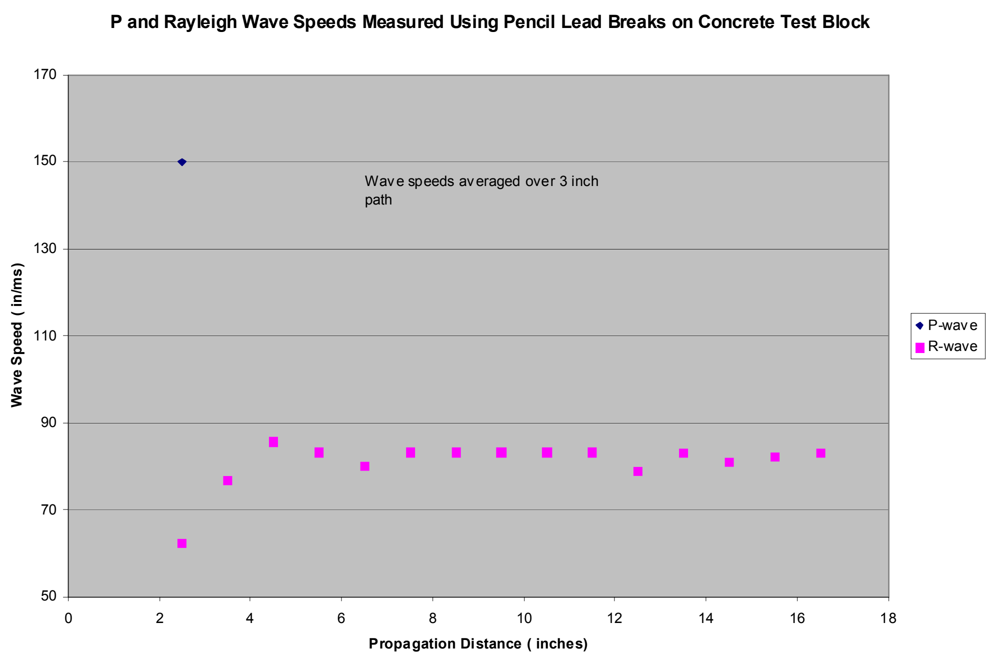

Figure B38 Rayleigh wave speed variation with propagation distance.

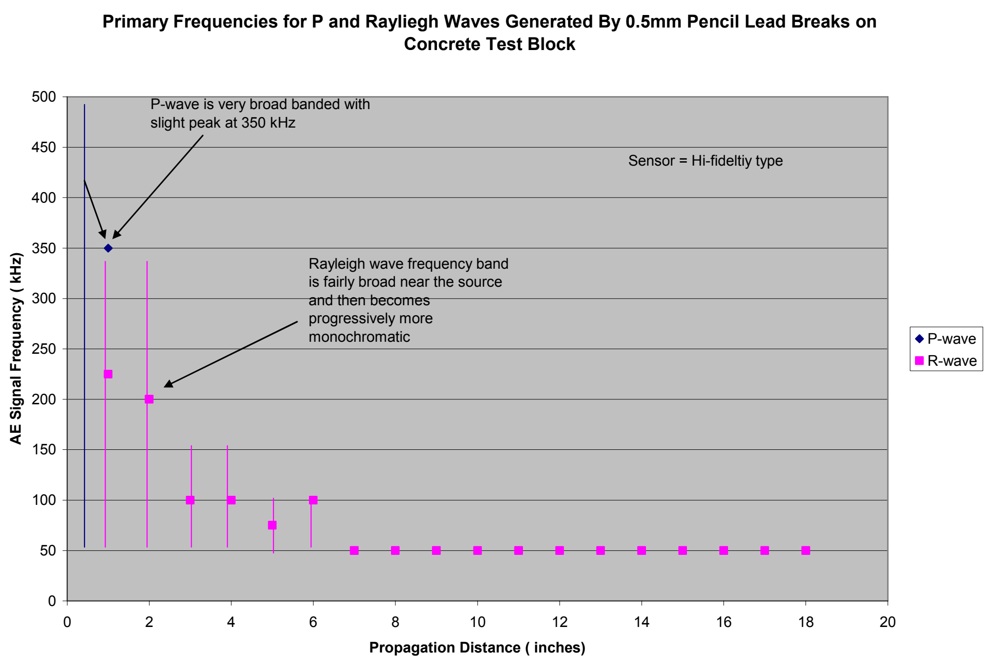

Figure B39 P and Raleigh wave primary frequency components.

Determination of Material Properties Using AE

1 Input

Unit Weight:	$\rho := 141.0 \frac{lb}{ft^3}$	$\rho = 2.259 \times 10^3 \frac{kg}{m^3}$	
Speed of P-Wave (Primary Wave):	$c_P := 150.0 \frac{in}{ms}$	$c_P = 3.81 \frac{m}{ms}$	Lit.: 3.5 m/ms < c_P < 5 m/ms
Speed of R-Wave (Rayleigh Wave):	$c_R := 83.0 \frac{in}{ms}$	$c_R = 2.108 \frac{m}{ms}$	

2 Equations

$$c_S := 0.5 \cdot \sqrt{-\frac{2 \cdot c_R^2 \cdot \left(-12 \cdot c_P^2 + 16 \cdot c_R^2\right)}{12 \cdot c_P^2 - 16 \cdot c_R^2} + 2 \cdot \sqrt{\frac{4 \cdot c_P^2 \cdot c_R^4}{12 \cdot c_P^2 - 16 \cdot c_R^2} + \frac{c_R^4 \cdot \left(-12 \cdot c_P^2 + 16 \cdot c_R^2\right)^2}{\left(12 \cdot c_P^2 - 16 \cdot c_R^2\right)^2}}}$$

$$\nu := \frac{c_P^2 - 2 \cdot c_S^2}{2 \cdot \left(c_P^2 - c_S^2\right)}$$

$$E_c := 2 \cdot \left(c_S^2 \cdot \rho + c_S^2 \cdot \nu \cdot \rho\right)$$

3 Results

Speed of S-Wave (Shear Wave):	$c_S = 88.041 \frac{in}{ms}$	$c_S = 2.236 \frac{m}{ms}$	
Poisson's Ratio:	$\nu = 0.237$		Lit.: 0.15 < ν < 0.25
Modulus of Elasticity:	$E_c = 4.054 \times 10^6 \frac{lbf}{in^2}$	$E_c = 2.795 \times 10^4 \frac{N}{mm^2}$	

Figure B40 Calculations for determining shear wave speed and elastic constants.

Appendix C Investigation of Surface Wave Propagation in Un-reinforced Concrete Block Using a Calibration Pulse as an AE Source

Purpose of Test

The purpose of this series of tests was to quantify the stress wave speed and displacement amplitude attenuation of a sinusoidal forcing source as it propagates on the surface of a large un-reinforced concrete block as measured by both hi fidelity and resonant AE receivers. Variations in different sections of the test block were also quantified.

Test Apparatus

Test Block

An un-reinforced concrete block 48” x 48” by 14 “ was used as the test block. The concrete mix used was same mix used for all testing of the full scale beams and can be characterized as having an aggregated gradation of ¾” minus , a weigh density of 141 lbf / ft^3 , and a minimum compressive strength at 28 days of 3300 psi. The test surfaces of the block were prepared by removing rough sections with a hand operated grinding stone. The upper surface was sectioned into quarters and scales marked using permanent markers.

AE System

A Vallen AMSYS5 AE test system with 8 AE channels was used to collect the data. Each channel is equipped with a transient recorder sampling at a rate of 10

MHz and 16-bit digitization. Both hi fidelity and resonant type AE transducers were used for these tests as summarized in Table C1.

The hi-fidelity sensors respond to displacement and have a very constant sensitivity over the listed frequency range. They are used to calibrate the frequency responses of other transducers as well as studying surface displacements from various disturbances in the test medium. The resonant sensors typically respond to velocity and or acceleration and have much more sensitivity and sensitivity variation with frequency. They are more commonly used is actual applications of AE due to the increased sensitivity over the hi-fidelity type transducers. The hi-fidelity transducers are used in the laboratory to quantify the displacements from various AE sources and the resonant sensors are used for comparison with the intent of applying their use on real structures.

The sensors were acoustically coupled to the surface of the concrete using a laboratory grade vacuum grease and an applied minimum normal force of 4 lbs. Figure C1 shows the test block with attached AE sensors.

Test Procedures

<u>Test 1 - Variation with AE Sensor Type</u>

A time decaying sinusoidal forcing sources was input into the top surface of the concrete test block at the geometric center. This source was generated by coupling a hi-fidelity transducer to the center of the blocks upper surface and exciting it with a hi voltage calibration pulse generated by the AE system. The pulse causes the aperture of the transducer to oscillate in a predictable manner as was discussed in Appendix A. A very accurate timer is started as soon as the pulse is triggered and the receiving AE sensors start recording awaiting the arrival of the surface waves as the propagate out radially from the source. Figure 2 shows a schematic of the test setup. Hi-fidelity and resonant transducers were placed at various distances from the source ranging from 3 to 18 inches away as shown. The response at each position was recorded. A minimum of 5 pulses per test position were used to assure consistent responses. If peak amplitudes measured from each of these 5 pulses varied more then 0.5 dB the sensor was remounted and retested until consistent results were obtained.

<u>Test 2 – Variation with As-Cast Properties in Test Block</u>

A second test setup was used to quantify the response variation over different section of the block using the same hi-fidelity receivers. Concrete can be considered either homogenous or in-homogeneous depending on the condition of the concrete and the frequency range of interest. This test quantifies the variations for a typical as-cast block and the frequency range of interest for physical testing of concrete structures as discussed in Appendix B,D and E. Figure 3 shows a schematic of this test setup. Again a single hi-fidelity AE transducer is used to provide a source input at the geometric center of the top surface. The surface displacement response is measured in four different directions outward radially from the source between 3 and 18 inches.

Results of Testing

<u>Test 1 – Variation with AE Sensor Type</u>

In order to discuss the measured responses over the entire range of testing variations it is first helpful to exam the transient response wave forms at a particular distance from source to receiver in order to describe how the various results are measured and calculated.

Figure C4 shows the transient response of the source pulse *signal* and the receiver displacement response of the hi-fidelity sensor at a distance of 6 inches. To the right of each transient signal is the corresponding representation in the frequency domain as calculated by the Fast Fourier Transform (FFT) method. This distance is chosen to represent a point in the early portion of the far field response. It is important to understand that the upper plot depicts the electrical signal sent to the source AE transducer and not the actual motion of the forcing function. As discussed in Appendix A the actual motion of sensors diaphragm is very similar to this signal in shape for the hi-fidelity transducers and thus can be meaningfully compared to the response at the various receivers. The lower plots shows the temporal and frequency responses as measured by a hi-fidelity AE transducer and thus can be directly related to surface displacement.

The calibration signal has two frequency peaks , one at 100 kHz and the other at 175 kHz and was chosen to stimulate both the low frequency (60 kHz) and middle frequency (150 kHz) resonant AE transducers. The response of the hi-fidelity sensor shows peaks at 72 , 92 and 150 kHz respectively.

Figure C5 shows a close up view of the hi-fidelity sensor response near the arrival of the first P-wave oscillation. Based on the bulk wave studies in Appendix D the measured P-wave oscillation propagation speed for this particular test specimen was found to be 150 in/ms and thus the arrival of the first P-wave oscillation on the surface is expected to arrive 40 μs after the calibration source pulse is initiated. Due to the high attenuation in concrete and the reduced sensitivity of the hi-fidelity AE sensor the arrival of this first wave is not detectable at a distance of 6 inches as seen in the time history. Visual inspection of the wave form shows the first detectable wave arrival at 48.5 μs which corresponds to the second oscillation of the source. At 66.8 μs the surface motion amplitude is large enough to cross the triggering threshold of the AE data acquisition system. This corresponds to the anticipated arrival of the first Rayleigh wave oscillation. Table C2 summarizes the expected arrival times of the first three P and Rayleigh wave oscillation peaks at a propagation distance of 6 inches.

Figure 6 shows the transient response of the 60 kHz resonant sensor at a distance of 6 inches. To the right of each transient signal is the corresponding representation in the frequency domain. Peaks in the frequency domain are seen to be at 50 and 75 kHz. Figure C7 shows a close up view of the resonant AE sensors response near the arrival of the first P-wave oscillation. The first visibly detectable P-wave oscillation arrival occurs at 47 μs after the initiation of the source pulse which is very similar to hi-fidelity AE sensor, which again is very near the expected arrival of the second oscillation of the source. The first threshold crossing occurs at 55.7 μs. The threshold for the 60 kHz resonant sensors is set at nearly twice the level of the other sensors due to a lower signal to noise ratio of this particular brand of sensor. This time corresponds half way between the expected arrival of the second and third P-wave oscillation but significantly before the expected arrival of the first Rayleigh wave oscillation.

Figure C8 shows the transient response of the 150 kHz resonant sensor at a distance of 6 inches. To the right of each transient signal is the corresponding representation in the frequency domain. The primary peak in the frequency domain occurs at 170 kHz.

Figure C9 shows a close up view of the resonant AE sensors response near the arrival of the first P-wave oscillation. In this case the first visibly detectable P-wave oscillation arrival corresponds with the anticipated arrival to within 1 μs.

The first threshold crossing occurs at 44.3 ms which is only 3.3 ms delayed from the expected first P-wave oscillation arrival and 4.7 ms preceding the expected arrival of the second P-wave oscillation. The measured arrival times of the first visibly detectable wave and threshold crossing are summarized in Table C3 for each sensor type at a propagation distance of 6 inches.

Examining these AE sensor response time histories shows that detection of the first P-wave oscillation from the calibration pulse on the surface of the concrete is difficult compared to the arrival of the Rayleigh wave oscillation which has much larger amplitude. The hi-fidelity sensors can barely resolve the arrival of the first P-wave oscillation out to a few inches of propagation and detection is achieved by visually inspection of the signal time history. The resonant type sensors are much more sensitive and thus the first P-wave oscillation can be detected out to approximately 12 inches with visual inspection of the wave form and 6 inches using the threshold crossing method. This statement is true for the 150 kHz resonant sensor only. Though the 60 kHz resonant sensor comes close to detecting the first P-wave oscillation arrival it is only able to trigger on the threshold crossing on the 2nd and 3rd P-wave oscillations.

Figure C10 shows a summary of the wave speeds as measured by each transducer type over the range of wave propagations. With the exception of the 150 kHz resonant sensor within 6 inches of the source the threshold crossing occurs from the second or third P-wave oscillation or the S or Rayleigh wave oscillation as the propagation distance increases. The hi-fidelity sensors are predominately picking up the Rayleigh wave oscillation after 6 inches.

Figure C11 shows the attenuation of the peak amplitude as a function of propagation distance and sensor type. Based on visual examination of the wave forms the peak amplitude typically corresponds to the 2nd Rayleigh wave oscillation. Bulk waves such as P and S-waves will decay geometrically with the inverse of the distance of propagation and Rayleigh wave oscillations decay geometrically with the inverse of the square root of propagation distance. The geometric decay rate for Rayleigh wave oscillations is shown in the figure for comparison. It is clear that there are attenuation mechanisms other then geometric in the concrete. The 60 kHz resonant sensor shows the lowest attenuation at 1.5 dB/inch average. The 150 kHz resonant and hi-fidelity sensors show an average attenuation of 2.4 and 2.3 dB/ inch.

Test 2 – Variation with As-Cast Properties in Test Block

Figure C12 shows the measured wave speeds using a hi-fidelity sensors to pulse and receive along different paths on the test block surface. Again the first P-wave oscillation is missed using the threshold detection method for all distances of propagation. Between 3 and 8 inches the 2nd and 3rd P-wave oscillation are triggering the detection. Passed 8 inches triggering primarily occurs on the first or second Rayleigh wave oscillation. From 12 to 18 inches the results are very similar for each path.

Figure 13 shows the peak amplitude attenuation as a function of propagation distance. All four paths show very similar attenuation which is again compared to geometric only attenuation.

Conclusions

Using an AE transducer to input an AE source into a concrete structure provides an excitation that is repeatable in both amplitude and timing. This is very useful for measuring wave speeds and attenuation with various receivers and receiver positions. The hi-fidelity sensor can only detect the P-wave oscillation for propagation distances of less then 6 inches. The resonant sensors can extend this range out to approximately 18 inches. The Rayleigh wave oscillations could easily be detected by all sensor types out beyond 18 inches.

The practical range of using the threshold crossing method of detecting the P-wave oscillation from this source is very limited (2 inches for the hi-fidelity and 6 inches for the 150 kHz resonant sensors). By visually examining the receivers response time history one or all of the first 3 P-wave oscillations can be identified out to a greater range (6 inches for the hi-fidelity and up to 18 inches for the resonant sensors).

Surface wave amplitudes were found to attenuate significantly faster then what is expected from solely geometric attenuation. When considering the peak amplitudes of the Rayleigh wave showed the least attenuation with the 60 kHz resonant transducers at a value of approximately 3 times that of geometric attenuation , 1.5 dB/in versus 0.52 dB/in. The 150 kHz resonant and hi-fidelity sensors showed much greater attenuation of the peak Rayleigh wave at 2.4 and 2.3 dB/in respectively.

Measuring wave speeds and attenuation in various sections of the test block showed relatively little variation considering the non-homogenous structure of concrete. Wave speed measured using the threshold crossing method produced a fair amount of variation with in 6 inches of the source and then rapidly converged to the Rayleigh wave speed from 6 to 18 inches for all sections. The peak amplitude attenuation for all four sections was found to be very consistent.

Table C1 Summary of AE Transducers used for these tests.
* Calibration sheets for each sensor can be found in Appendix A

Sensor type	Brand	Model	Frequency range (kHz) *	Apperature diameter (inch)
Hi-fidelity	DECI	SE1000 H	20 to 325	0.06
Resonant	KRN	i060	40 to 140	0.75
Resonant	Vallen	VS150	90 to 500	0.63

Table C2 Summary of expected surface wave arrival times at a distance of 6 inches.
* Estimated from measured C_1 speed and material properties

Wave description	**Expected arrival time (μs)**
1st oscillation P-wave	41
2nd oscillation P-wave	49
3rd oscillation P-wave	62
1st oscillation Rayleigh wave	70*
2nd oscillation Rayleigh wave	79*
3rd oscillation Rayleigh wave	82*

Table C3 Summary of measured wave arrival times.

AE Sensor type	**1st visibly detectable wave (μs)**	**1st threshold crossing (μs)**
Hi-fidelity	48.5	66.8
60 kHz resonant	47.0	55.7
150 kHz resonant	40	44.3

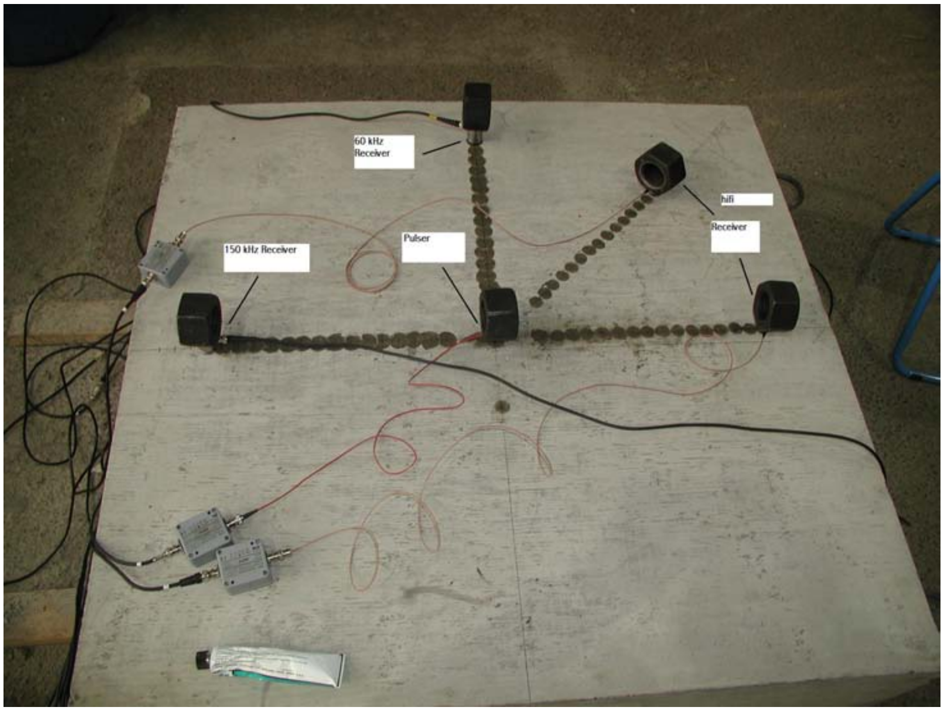

Figure C1 Photograph of test block and AE sensors .

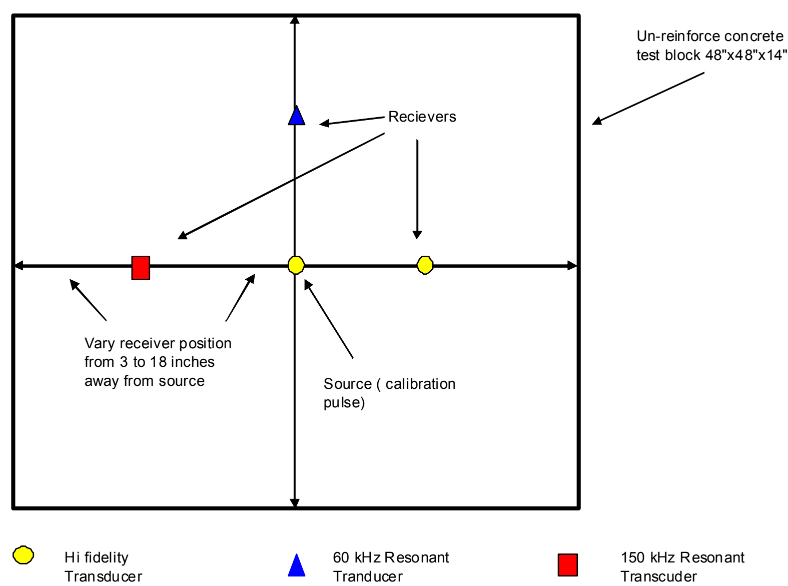

Figure C2 Schematic of Test 1 setup to investigate the variation of different sensor types to an input calibration pulse.

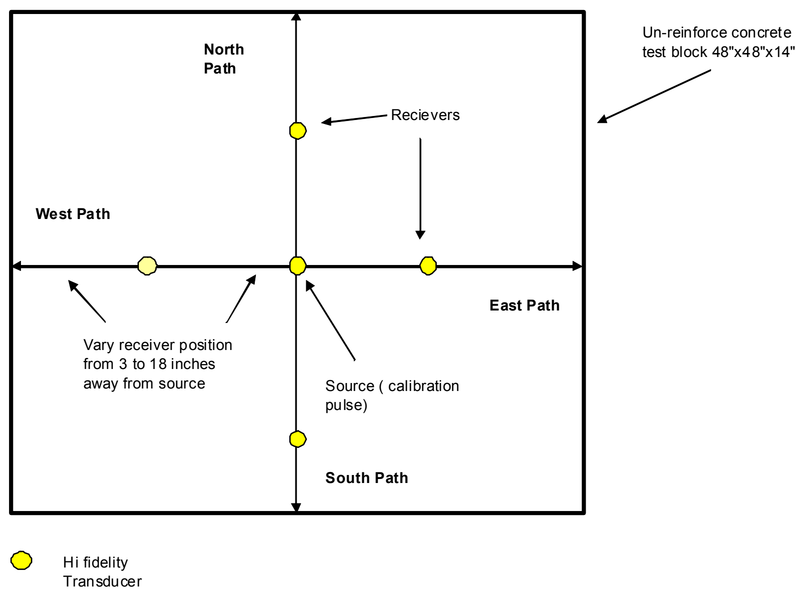

Figure C3 Schematic of Test 2 setup to investigate the variation of as-cast concrete stress wave propagation properties.

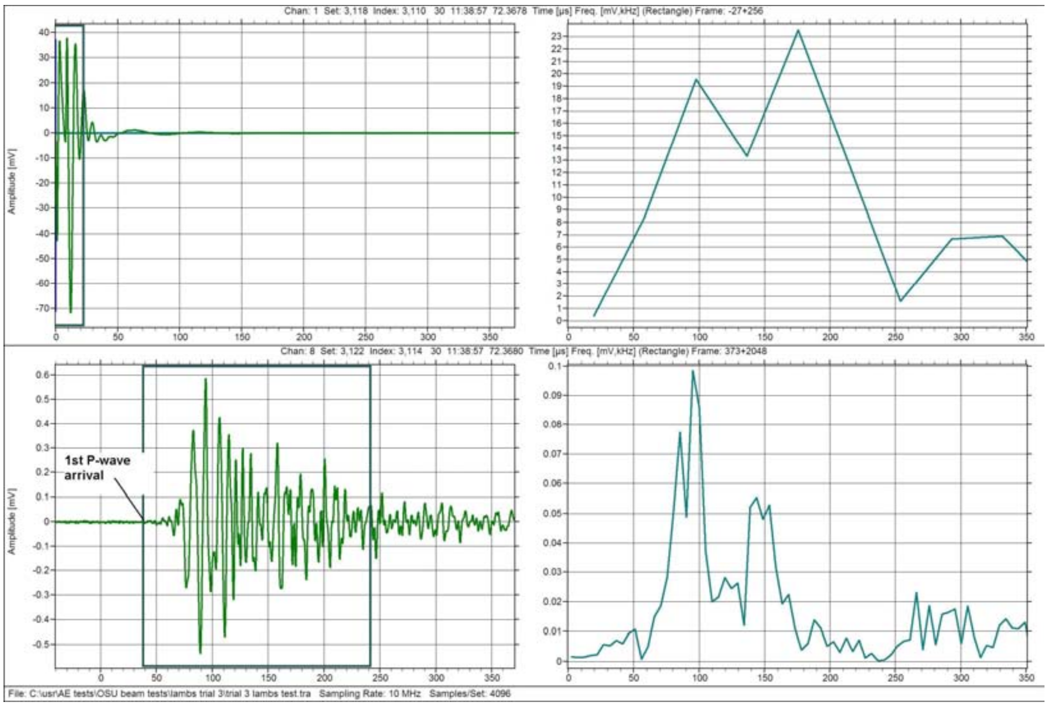

Figure C4 Response of hi-fidelity transducer to calibration pulse at a distance of 6 inches from source to receiver shown in temporal and frequency domains. The upper plots correspond to the source signal and the lower plots to the receiver.

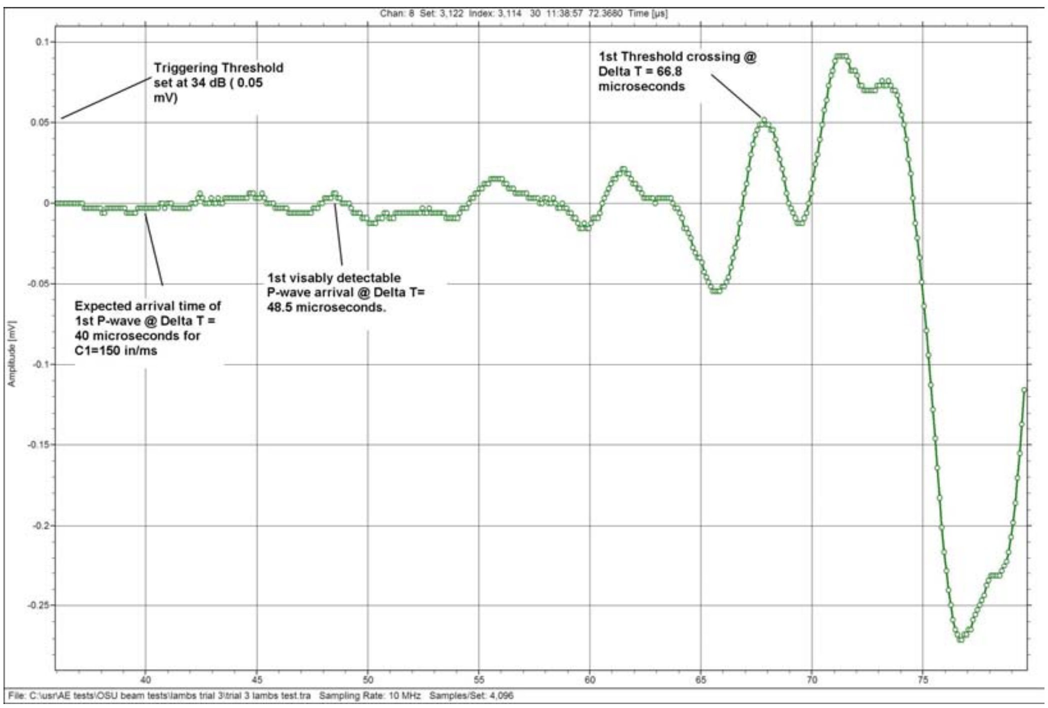

Figure C5 Close view of hi-fidelity AE receiver at 6 inches from source. The first visibly detectable arrival of a P-wave occurs 48.5 μs after the source pulse is initiated. The first threshold crossing occurs 66.8 μs after the source pulse is initiated. Note that individual data points are identified with circles to show the sampling rate relative to the response.

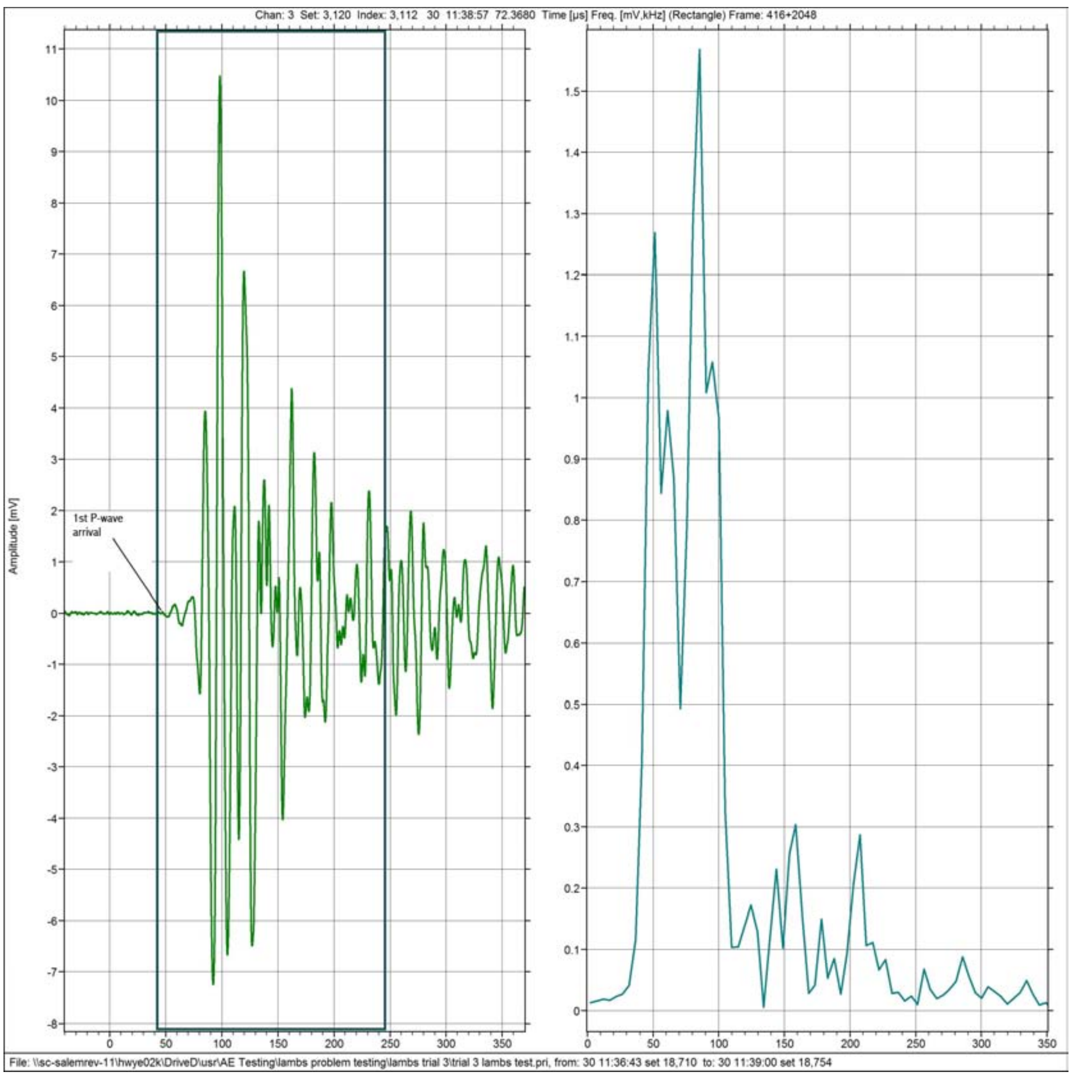

Figure C6 Temporal and frequency response of the 60 kHz resonant sensor to the source pulse at a distance of 6 inches.

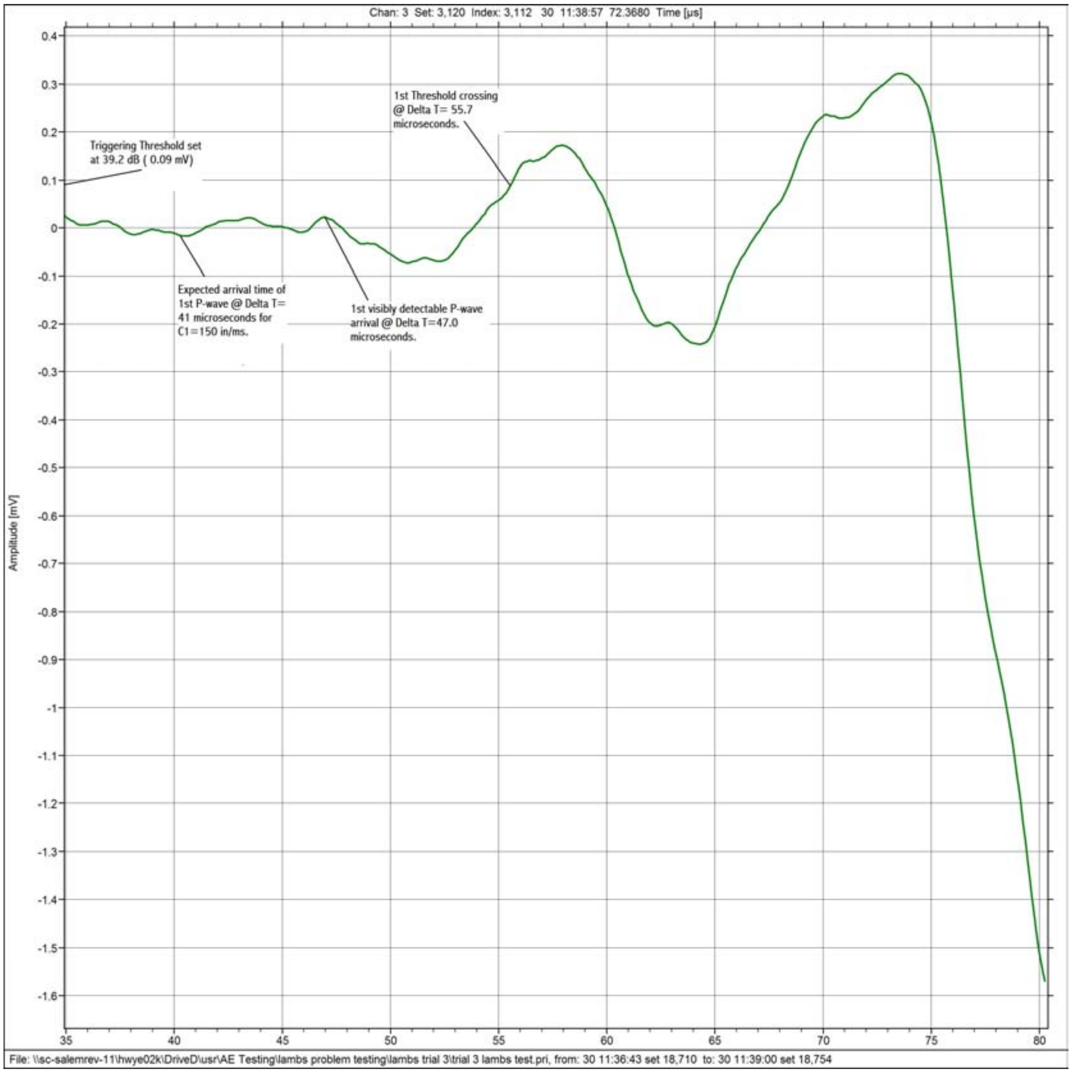

Figure C7 Close up view of the 60 kHz resonant sensor transient response.

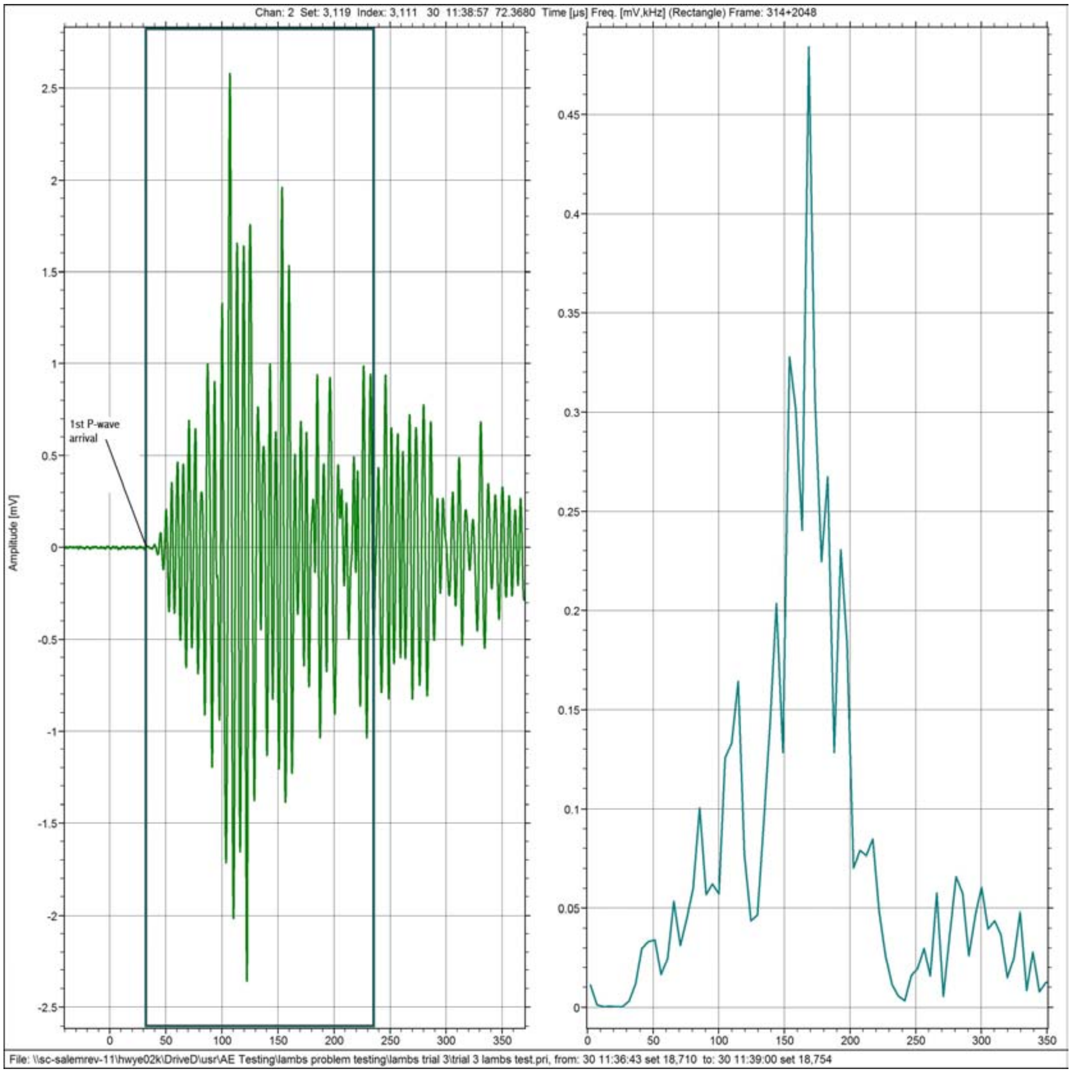

Figure C8 Temporal and frequency response of the 150 kHz resonant sensor to the source pulse at a distance of 6 inches.

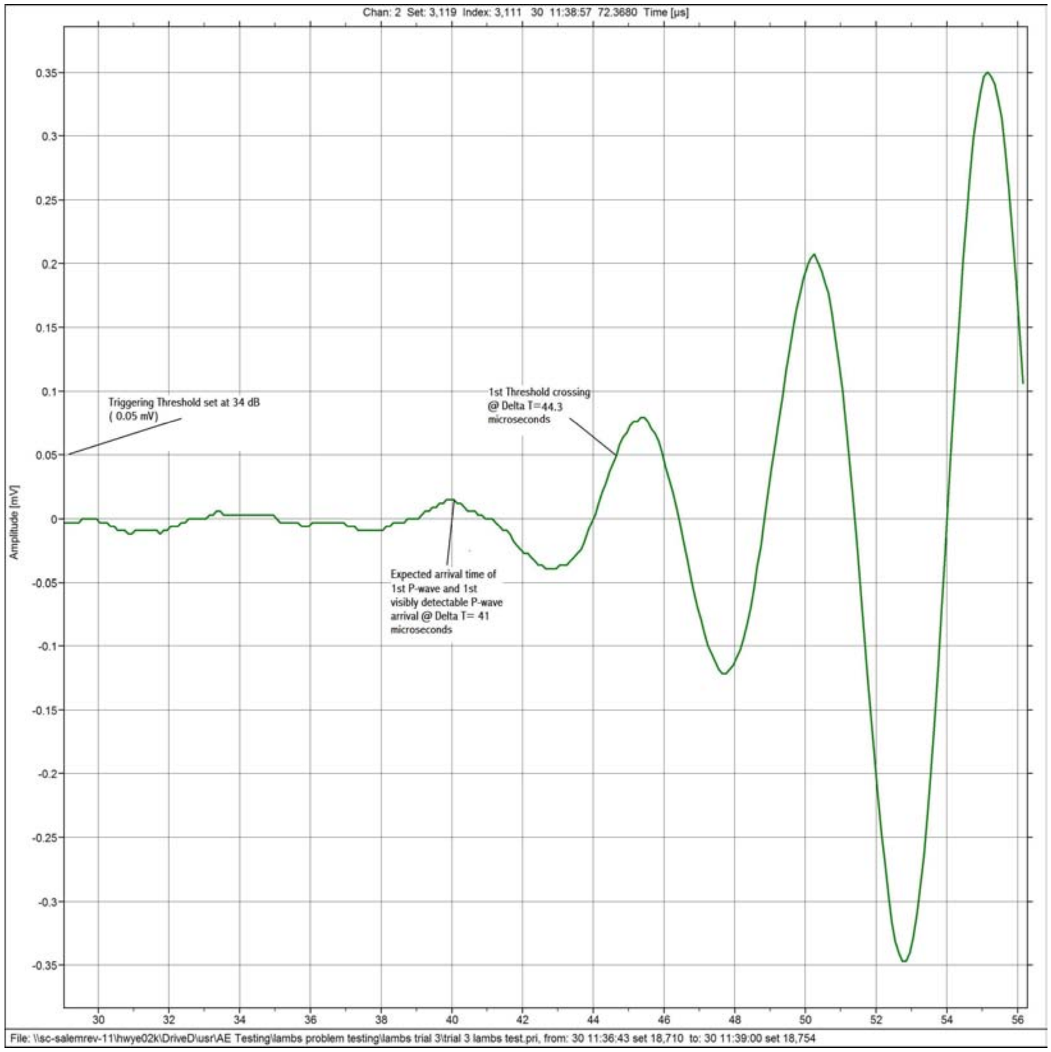

Figure C9 Close up view of the 150 kHz resonant sensor transient response.

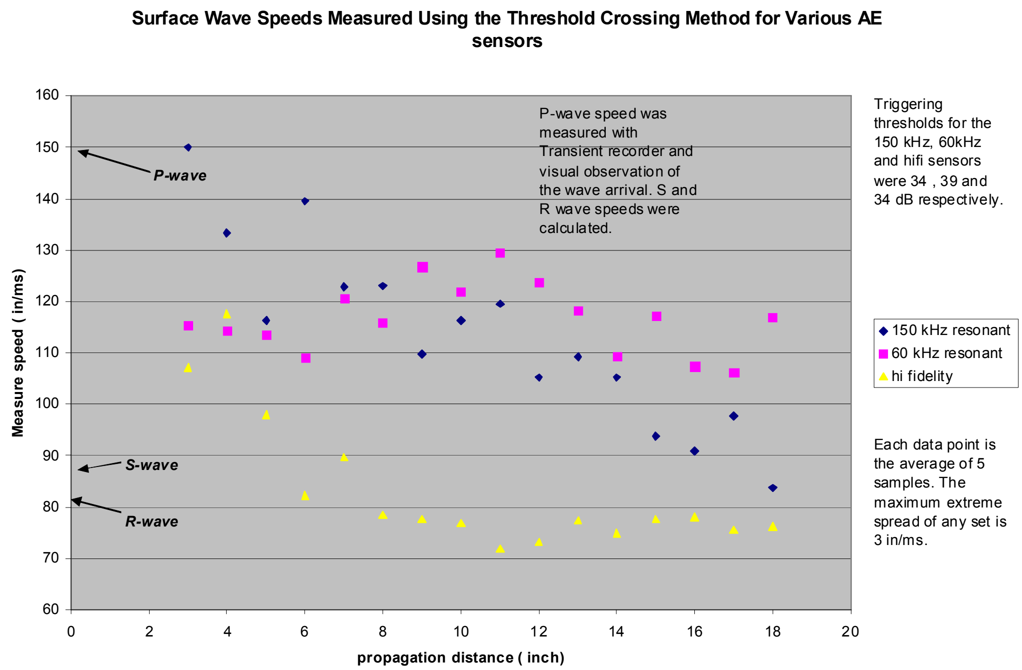

Figure C10 Surface wave speeds measured on concrete test block with various AE sensors.

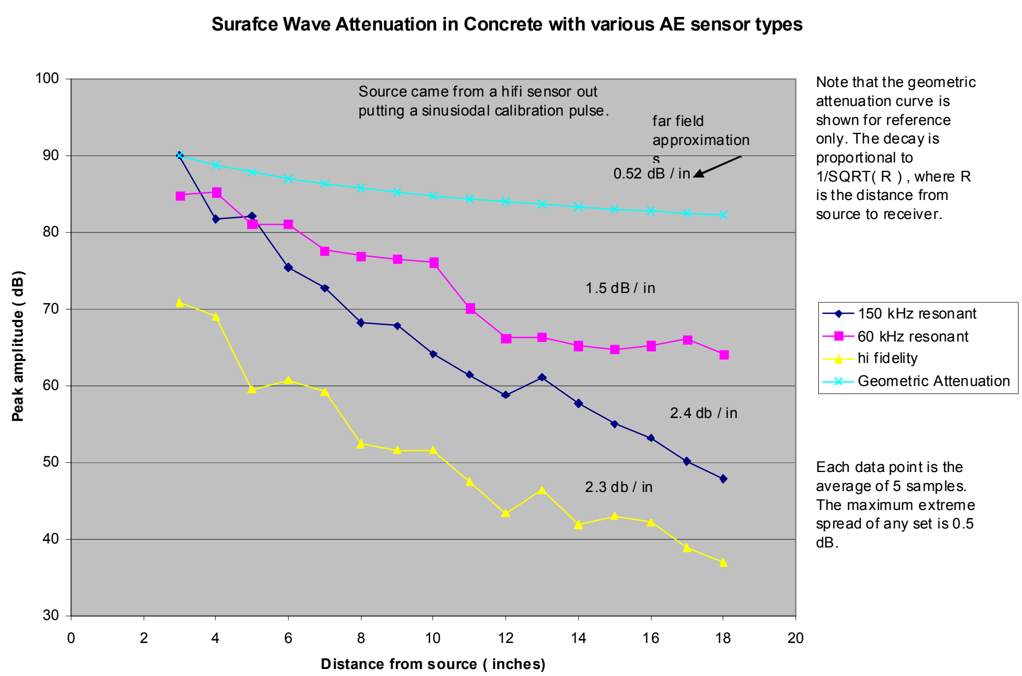

Figure C11 Surface wave amplitude attenuation on concrete test block with various AE sensors.

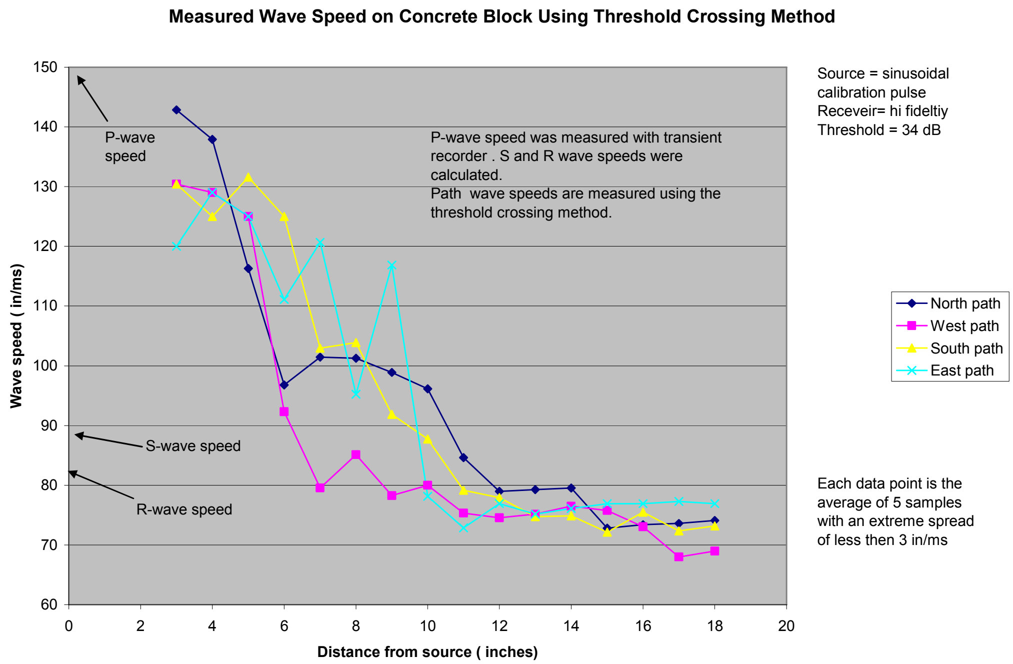

Figure C12 Surface wave speeds measured on concrete test block in various directions and locations.

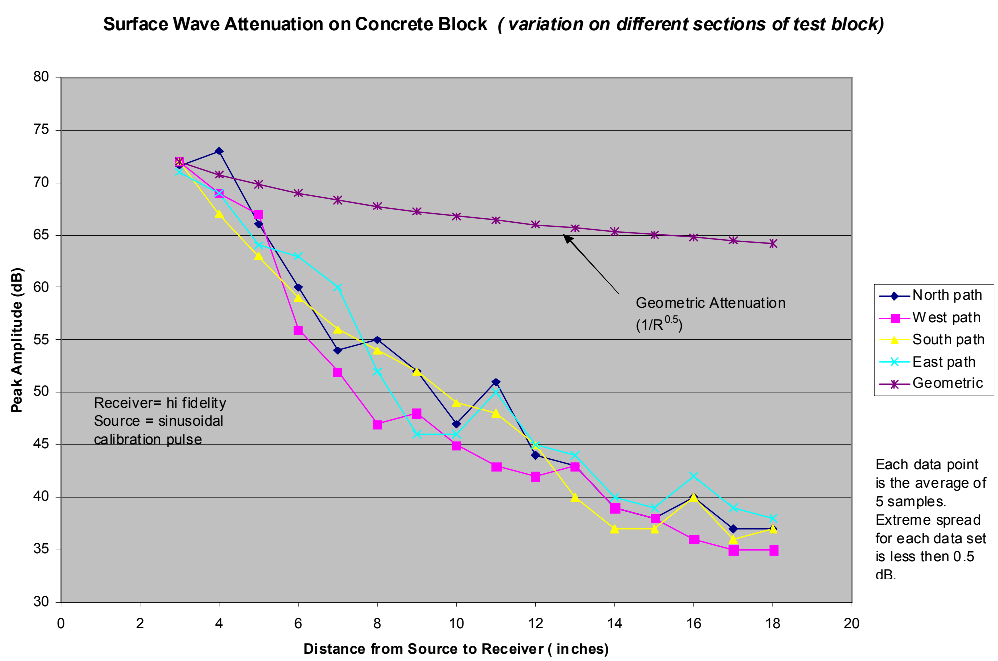

Figure C13 Surface wave amplitude attenuation on concrete test block with various directions and locations.

Appendix D Investigation of the Effects of Aggregate Gradation on the Propagation of Dilatation Waves in Structural Concrete

Purpose of Test

The purpose of this series of tests was to quantify the effects of varying the maximum aggregate size in the standard laboratory concrete mix design on the propagation of dilatation waves. Wave speed, amplitude and frequency content are investigated.

Test Apparatus

Two AE hi-fidelity AE transducers were mounted on the opposite ends of a concrete test cylinder, facing each other. One transducer was used an AE source using the low calibration pulse and the other as a receiver as shown in Figure D1. Stress waves were input into one side (AE channel #7), allowed to propagate through the height of the cylinder and surface motion measured on the opposite surface. Both cylinder height and concrete aggregated gradation were varied.

Test Specimens

A total of 15 concrete cylinder test specimens were fabricated. The diameter of each specimen was 12 inches with 5 specimens each at specific heights of 3, 6 and 12 inches. Figures D2 through D4 show the AE transducers mounted on the different test cylinder heights. The dimensions of the test cylinders were chosen such that the arrival of the dilatation wave on the opposite face would not be contaminated with waves reflected off of the sides or back face.

For each height the 5 specimens had different maximum aggregate size in the mix. Figure D5 shows the concrete suppliers standard concrete mix design used for testing of full size beams and test blocks used during the various research projects at OSU for ODOT. It can be characterized as an AASHTO Class-A concrete consisting of cement, sand , aggregate and water. The maximum aggregate size is ¾ inch. This mix was chosen to best represent the concrete used in the construction of the vintage RCDG bridges owned by ODOT.

The raw materials needed to produce this concrete mix were acquired from the supplier. The aggregate and sand were graded by size and the weight percentages of each gradation range were calculated. Table D1 shows the weight percentages for the aggregate and sand for the Standard mix. Five separate batches were then mixed with the first batch containing the entire gradation as supplied, the second containing only the aggregate and sand passing the ½" screen , the third containing only the aggregate and sand passing the 3/8 " screen, the fourth with aggregate and sand passing the ¼ " screen and the fifth passing only the 1/8th inch or number 8 screen. The weigh percentages for each batch are shown in Table D1. The ends of each test cylinder were ground smooth in the center for consistent AE sensor mounting.

<u>AE System Setup</u>

A Vallen AMSYS5 AE test system was used to record the wave forms from the receiver and to apply the calibration pulse to the pulser. Data were sampled at 10 MHz and 16-bit digitization. Both the pulsing and receiving AE transducers were DECI S1000H hi-fidelity type sensors.

Test Procedures

A laboratory grade vacuum grease was used as a complaint between the sensor aperture face and the concrete. A minimum normal force of 4 lbs between the sensors and the test block was applied by hand. A total of 10 calibration pulses were sent and received for each specimen to assure consistency and repeatability. All 15 specimens were tested 90 days after they were cast to assure adequate concrete curing time.

Results

Figure D5 shows the low calibration signal sent to the AE transducer acting as a pulser , Channel #7 , with the corresponding representation in the frequency domain. As discussed in Appendix A the actual forcing function put into the structure is very similar in shape and frequency content to the signal when pulsed through a hi-fidelity AE transducers , though the exact magnitude is not known. The energy put into the structure from this pulse is concentrated in the frequency range of 100 to 450 kHz.

The surface displacement responses on the opposite end of the cylinder are grouped by aggregate gradation and shown in Figures D6 through D20. The transient wave form is only shown near the arrival of the first P-wave for clarity. With each transient response the FFT is calculated for the first P-wave oscillation and presented to the right of the wave form. The time scale origin starts with the beginning of the calibration pulse for all plots. Figures D6 through D8 show the results for the **sand** Mix for 3 , 6 and 12 inch cylinder heights respectively. Figures D9 through D11 show the results for the **¼" minus** Mix for 3 , 6 and 12 inch cylinder heights respectively. Figures D12 through D14 show the results for the **3/8" minus** Mix for 3 , 6 and 12 inch cylinder heights respectively. Figures

D15 through D17 show the results for the **½ " minus** Mix for 3 , 6 and 12 inch cylinder heights respectively. Figures D18 through D20 show the results for the **¾ " minus** Mix for 3 , 6 and 12 inch cylinder heights respectively. In all responses the arrival of the first P-wave oscillation is clearly identifiable.

Because the amplitude of the first P-wave oscillation is large enough to easily detect with the equipment and methods used the fixed threshold method of automatically calculating the time delay between the calibration pulse and response on the opposite can be used with excellent results. Each test specimen was given 10 calibration pulses and the extreme spread in measured time delays was less then 1 μsec for all test specimens. Thus the P-wave speeds measured have extreme spreads of less then 5%, 2.5% and 1.25% for the 3 , 6 and 12 inch specimens respectively. The results from the fixed threshold method were checked my visual examination of the wave form and found to be in excellent agreement.

Figure D21 shows a summary of the measured P-wave speeds for each test specimen. Variation between the various aggregate gradations is largest for the 3 inch specimens with P-wave speeds between 118 and 219 in/ms. The larger the test cylinder height becomes the less the variation in wave speed is seen. At the 12 inch cylinder height the wave speed range from 140 to 164 in/ms. The ¾ inch minus or standard mix gradation is found to have the slowest P-wave speed and all other gradations are shown to have very similar results at a slightly higher speed. The larger cylinders are statistically more likely to represent the effects of gradation variation because more of the in-homogenous material is being sampled. Thus the larger variation at the smaller cylinder heights is not unexpected especially considering the maximum aggregate size is 1/4th of the total propagation distance. Dilatation wave speed measurements in the standard concrete as mixed by the supplier shows a speed of 150 in/ms which is very comparable to the 140 in/ms measured in these test specimens mixed at ODOT.

The amplitudes of the first P-wave oscillations were measured by visual inspection of the wave forms and converted to an approximate surface displacement using the AE sensors calibration factor. These amplitudes are summarized in Figure D22 showing the variation of both cylinder height and aggregate gradation. These amplitudes are in the range of 0.1 to 10 Pico meters. At the more representative cylinder height of 12 inches the ¾" minus or standard gradation has measurably greater attenuation then the other gradations but is still similar. For reference the amplitude decay rate of geometric only attenuation is show plotted. Clearly all of the aggregate gradation mixes have much greater attenuation then strictly geometric.

Figure D23 shows the frequency peaks for the P-wave as calculated by the FFT. As expected the higher frequency components tend to attenuate with increasing propagation distance ranging from 250 kHz on the 3 inch specimens down to near 135 kHz at 12 inches. The ¾ inch minus or standard mix showed the greatest attenuation of high frequencies.

Conclusions

The test method proved able to produce very repeatable results. The 12 inch specimens showed much less range in wave speeds and amplitudes between the various aggregate gradations and are likely most representative of the bulk behavior of these mixes. From a practical applications perspective the variation in test results between the various aggregate gradations is not particularly significant for the mixes used and frequency ranges investigated. This fact adds credibility to the assumption that a large concrete specimen can be treated as a homogenous material with respect to stress wave propagation and the practical application of using AE to monitor and locate AE sources in the material.

Table D1 Weight percentages for the various gradations of aggregate used for the test cylinders. All batches have 12.2% cement and 6.7% water.

Batch	¾"(% weight)	½ " (%weight)	**3/8 "(% weight)**	¼ "(% weight)	**sand** (% weight)
Standard (¾- minus)	4	6	10	25	35
½ - minus	0	10	10	25	35
3/8 – minus	0	0	20	25	35
¼ - minus	0	0	0	45	35
sand	0	0	0	0	80

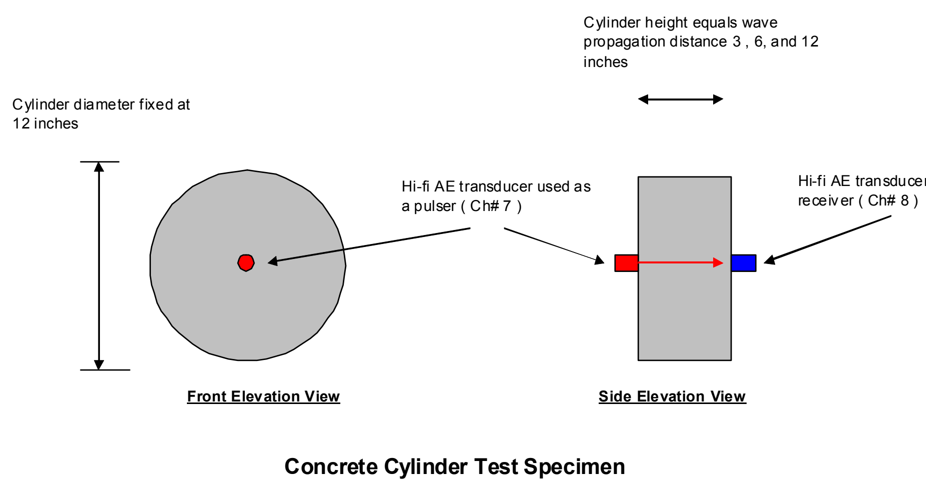

Figure D1 Schematic of test setup for studying dilatation wave propagation through various concrete mix designs and propagation distances.

Figure D2 Photograph of 3 inch cylinder being tested.

Figure D3 Photograph of 6 inch cylinder being tested.

Figure D4 Photograph of 12 inch cylinder being tested.

Added 8/18/04

MORSE BROS.

Mix ID Number: 031-30N16000

Concrete Mix Design

MIX DESIGN QUANTITIES

Material	Product/Source	Spec Grav	English Units Weight	English Units Volume	Metric Units Mass	Metric Units Volume
Cement	Glacier Dalian, Type I-II	3.15	470 lb	2.39 ft^3	279 kg	0.089 m^3
Fly Ash	None	2.25	0 lb	0.00 ft^3	0 kg	0.000 m^3
Water(Total)	Corvallis R-Mix Plant 1	1.00	259 lb	4.15 ft^3	154 kg	0.154 m^3
3/4 - #4 Round	Corvallis (Bui 22-001-2	2.60 *	1740 lb*	10.72 ft^3	1032 kg*	0.397 m^3
Fine Aggregate	Corvallis (Bui 22-001-2	2.58 *	1389 lb*	8.63 ft^3	826 kg*	0.320 m^3
Admixtures	Grace	1.00	1 lb	0.02 ft^3	1 kg	0.000 m^3
	Air(Entrap/Entrain)	4.0 %	3860 lb	1.08 ft^3	2291 kg	0.040 m^3
	Total Mix Volume:			27.00 ft^3		1.000 m^3

ADMIXTURES

Product	ProductName/Type	Dosage Rate	Dosage (English)	Dosage (Metric)
Air Entrainment	Grace Daravair 1000	0.30 oz/cwt**	1.4 oz/cy**	54.5 mL/m^3**
Water Reducer	Grace WRDA-64	4.00 oz/cwt**	18.8 oz/cy**	727.3 mL/m^3**

MIX DESIGN PROPERTIES

Aggregate Properties

		Spec Grav	Abs	FM	Dry Rodded Unit Wt	
3/4 - #4 Round	2003-0.750-000#4-001	2.60	2.6		99.3 pcf	1591 kg/m^3
Fine Aggregate	2003-00000-0SAND-001	2.58	3.8	3.05		

STATE

Plastic Properties:

	English	Metric
Slump:	5.0 ± 1.0 inch	125 ± 25 mm
Air Content:	4.0 ± 1.5 %	
Unit Weight:	143 pcf	2291 kg/m^3

Design Properties:

	English	Metric
Required Strength (f'c):	3000 psi @ 28 days	21 MPa @ 28 days
Total Cementitious:	470 lb 5 Sack	279 kg
Fly Ash %:	0.0 %	
W/C Ratio:	0.55 (incl Admix)	

Project:

Contractor:

Comments:

Footnotes: *SSD Weights and Spec Gravities. ** Admixture dosage rate will be adjusted according to manufacturer's recommendations to accommodate varying field conditions.

Submitted By:

Designed By:

Date Submitted: 8/17/2004

Figure D4 Standard concrete mix design for all full size beam test. This mix produces a concrete very similar to that used in constructing the vintage RCDG bridges in Oregon.

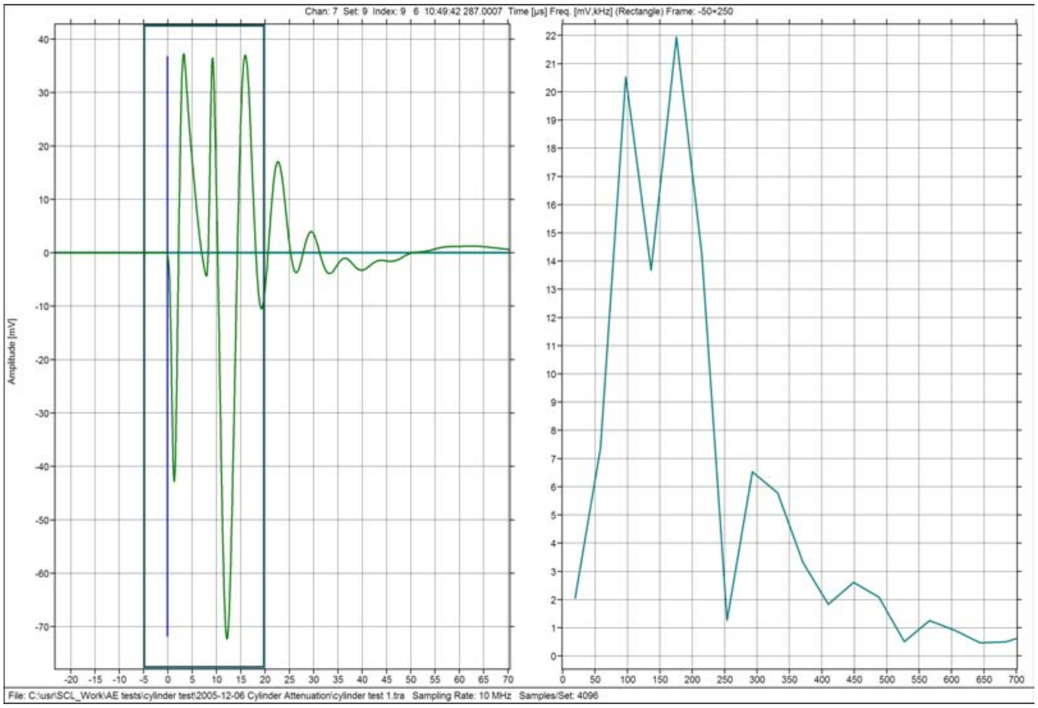

Figure D5 Wave form and FFT of calibration pulse signal sent to hi-fidelity AE transducer.

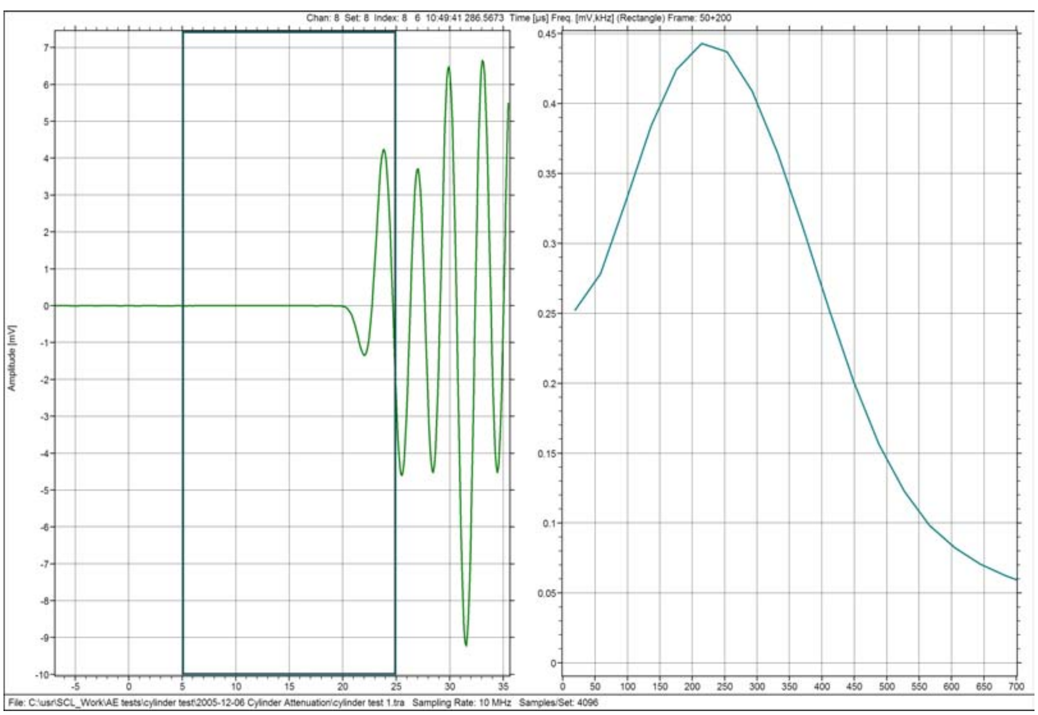

Figure D6 Wave form and FFT from receiver for **3 inch** cylinder height with a **Sand Mix**.

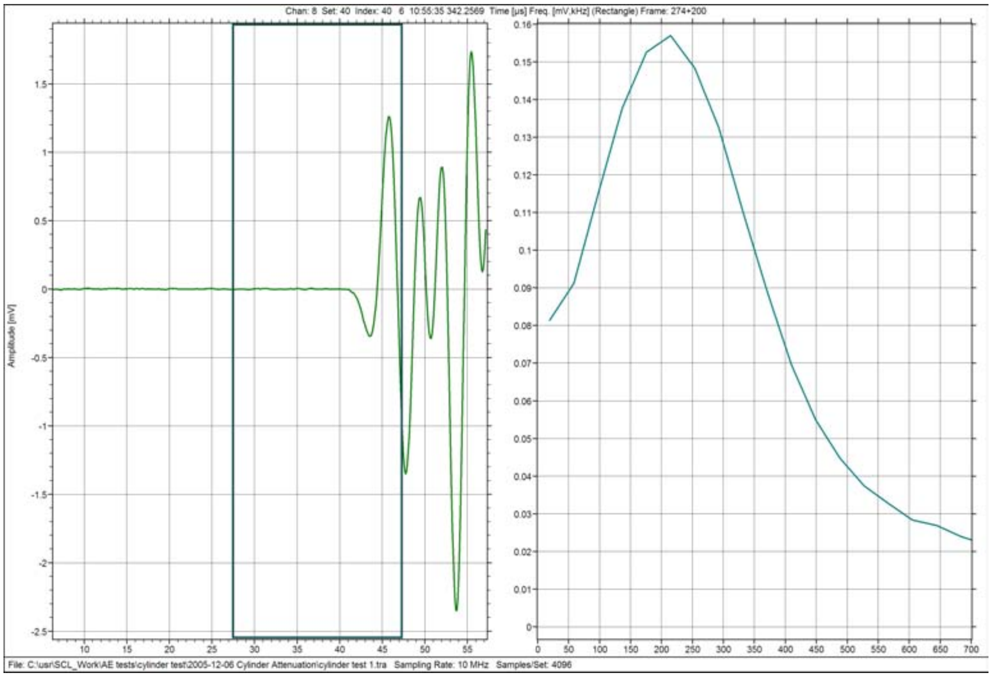

Figure D7 Wave form and FFT from receiver for **6 inch** cylinder height with a **Sand Mix**.

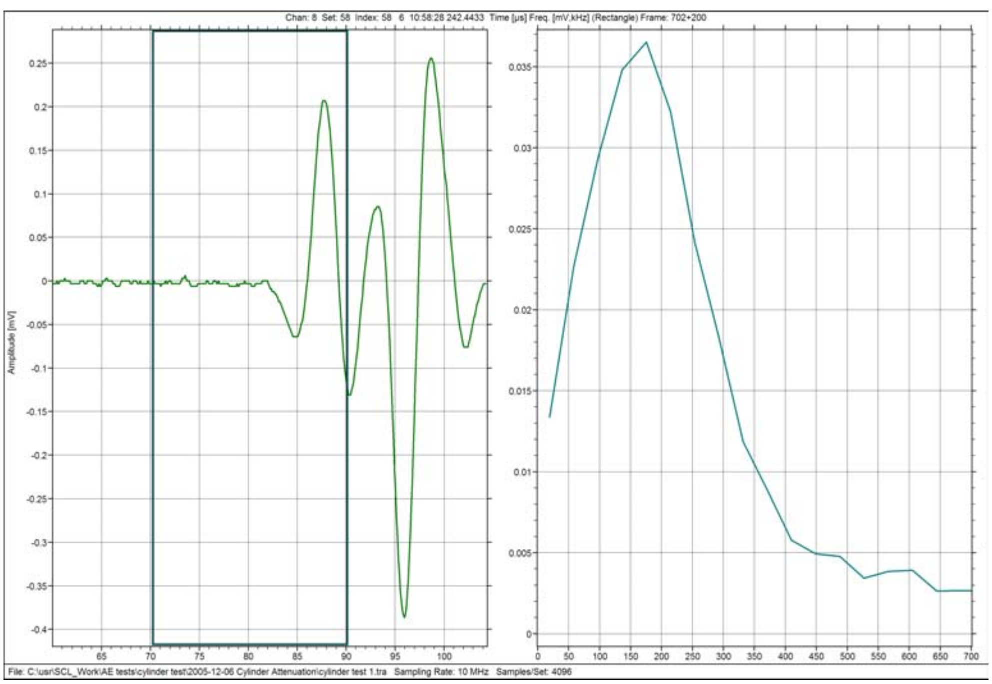

Figure D8 Wave form and FFT from receiver for **12 inch** cylinder height with a **Sand Mix**.

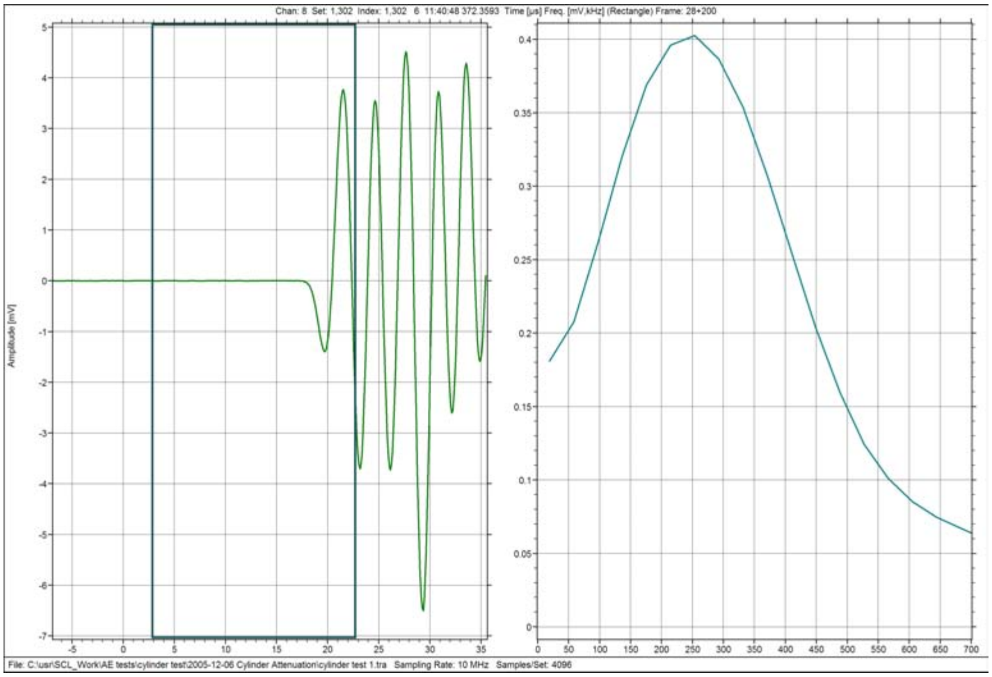

Figure D9 Wave form and FFT from receiver for **3 inch** cylinder height with a **¼" minus Mix**.

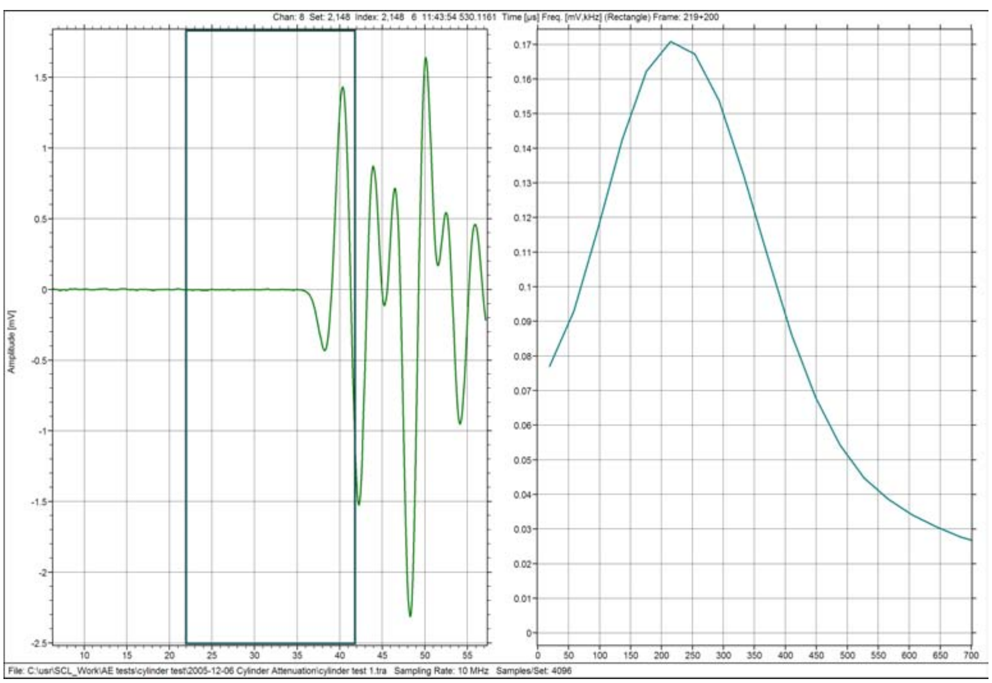

Figure D10 Wave form and FFT from receiver for **6 inch** cylinder height with a **¼" minus Mix**

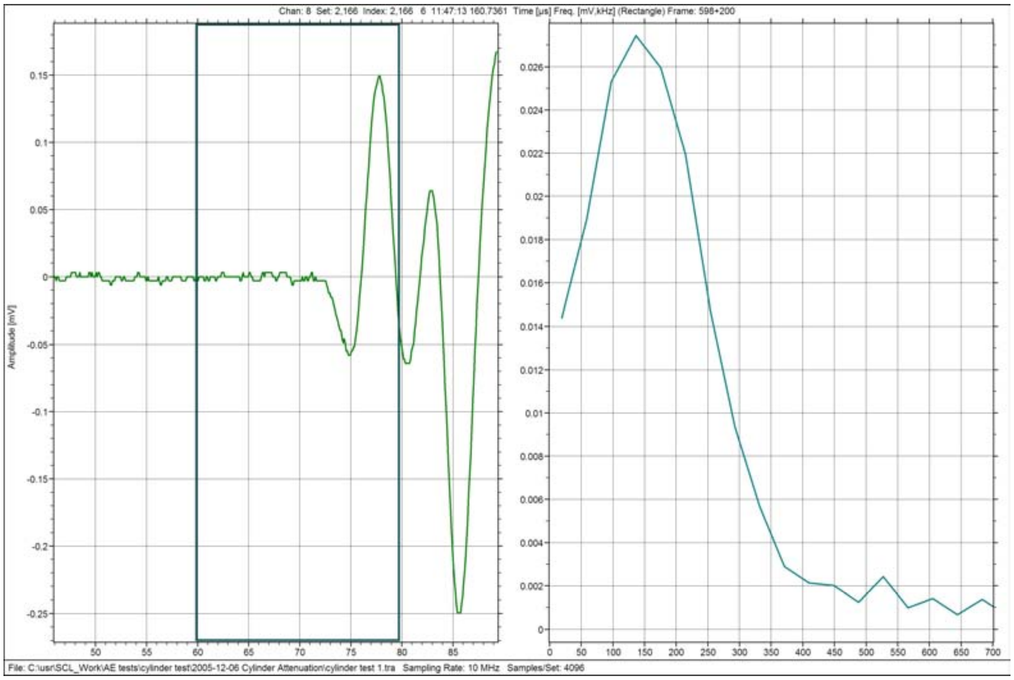

Figure D11 Wave form and FFT from receiver for **12 inch** cylinder height with a **¼" minus Mix**.

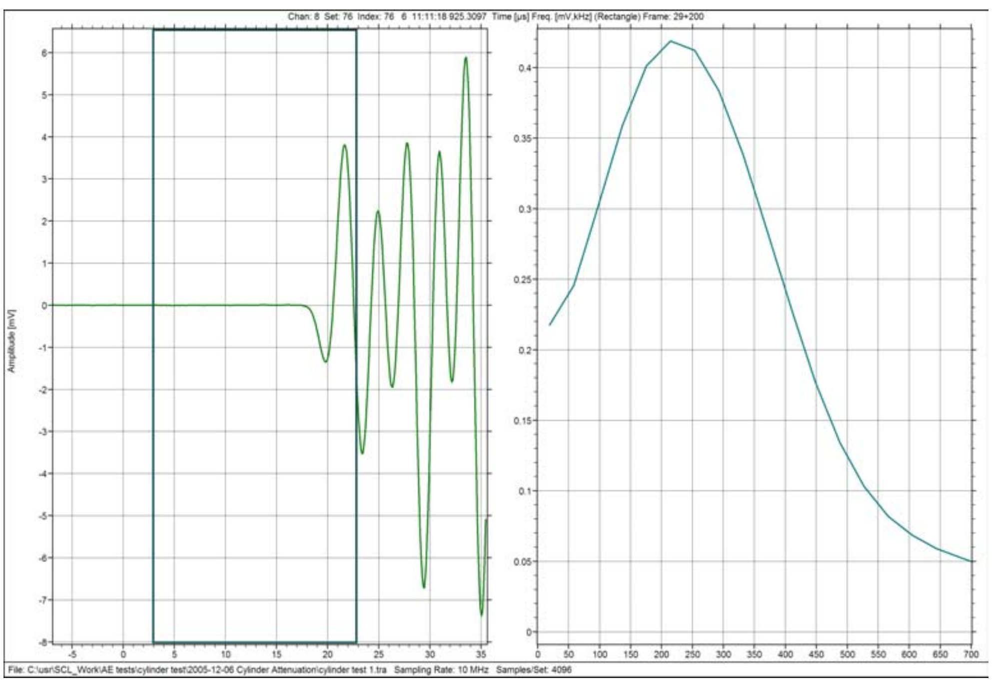

Figure D12 Wave form and FFT from receiver for **3 inch** cylinder height with a **3/8" minus Mix**.

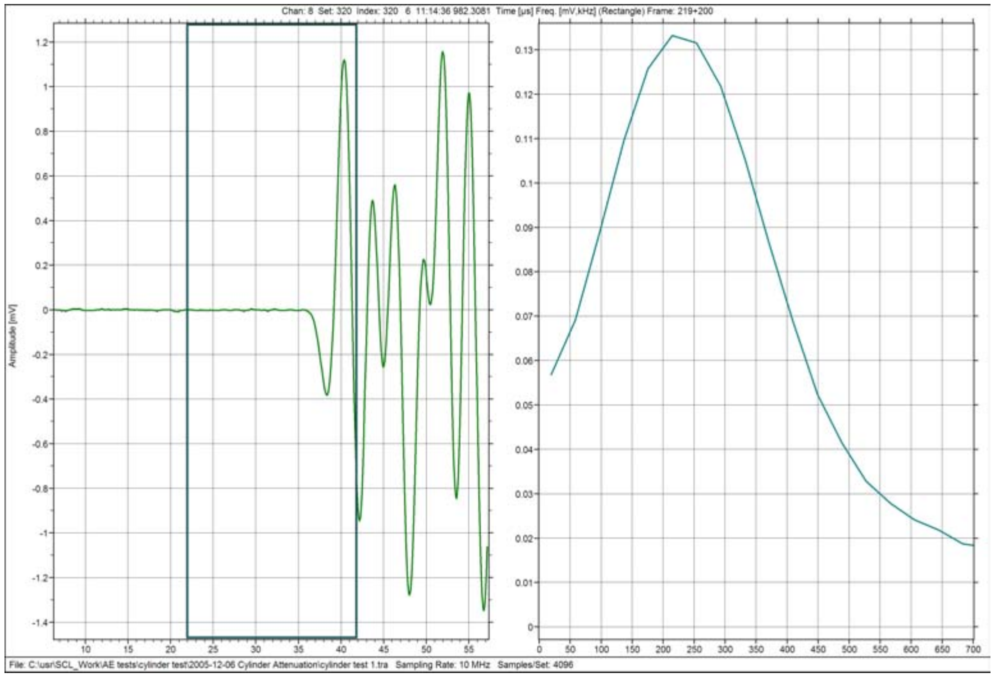

Figure D13 Wave form and FFT from receiver for **6 inch** cylinder height with a **3/8” minus Mix**

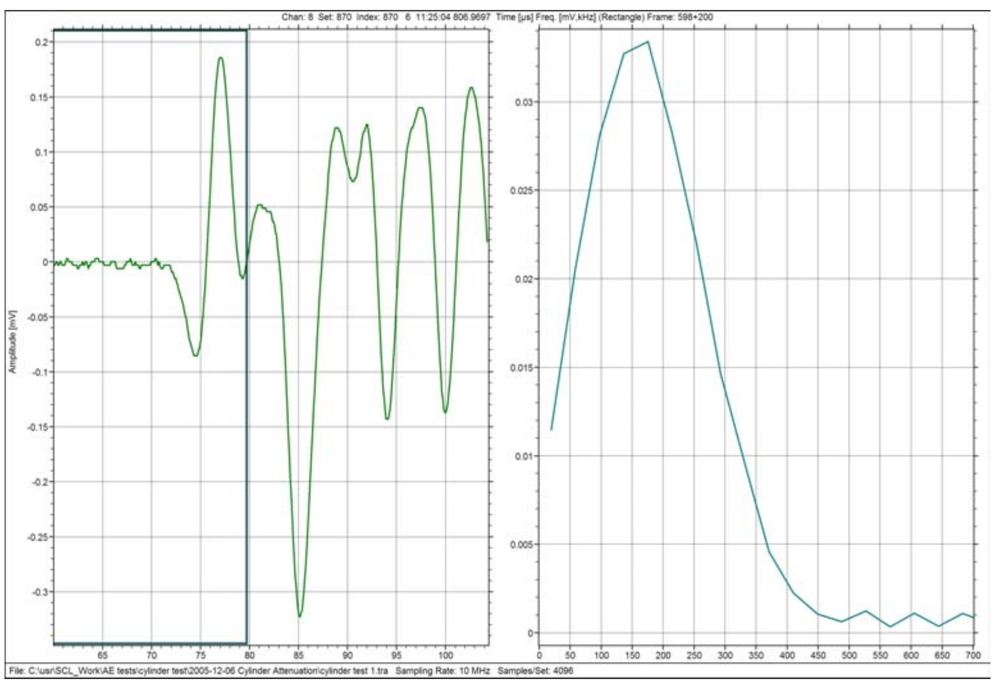

Figure D14 Wave form and FFT from receiver for **12 inch** cylinder height with a **3/8” minus Mix**.

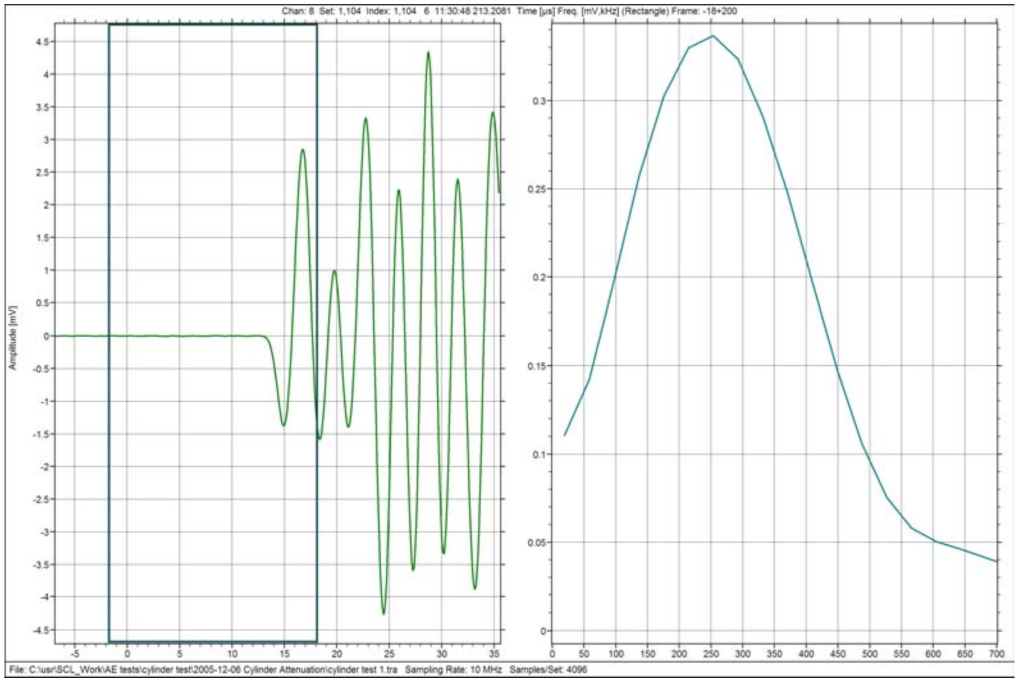

Figure D15 Wave form and FFT from receiver for **3 inch** cylinder height with a **1/2" minus Mix**.

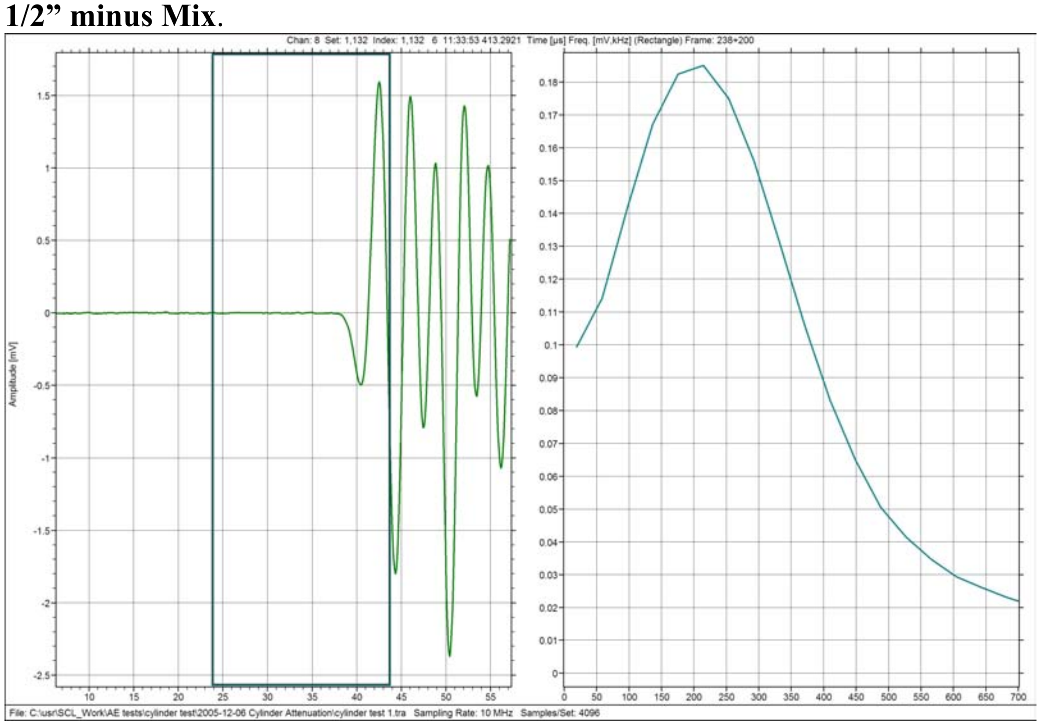

Figure D16 Wave form and FFT from receiver for **6 inch** cylinder height with a **1/2" minus Mix**

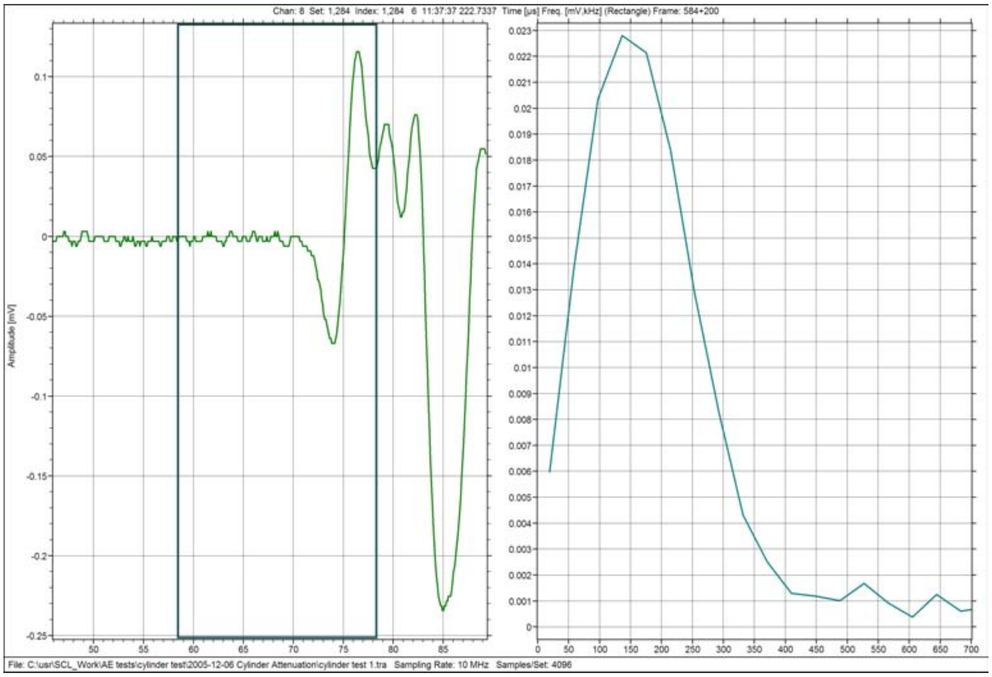

Figure D17 Wave form and FFT from receiver for **12 inch** cylinder height with a **1/2 " minus Mix**.

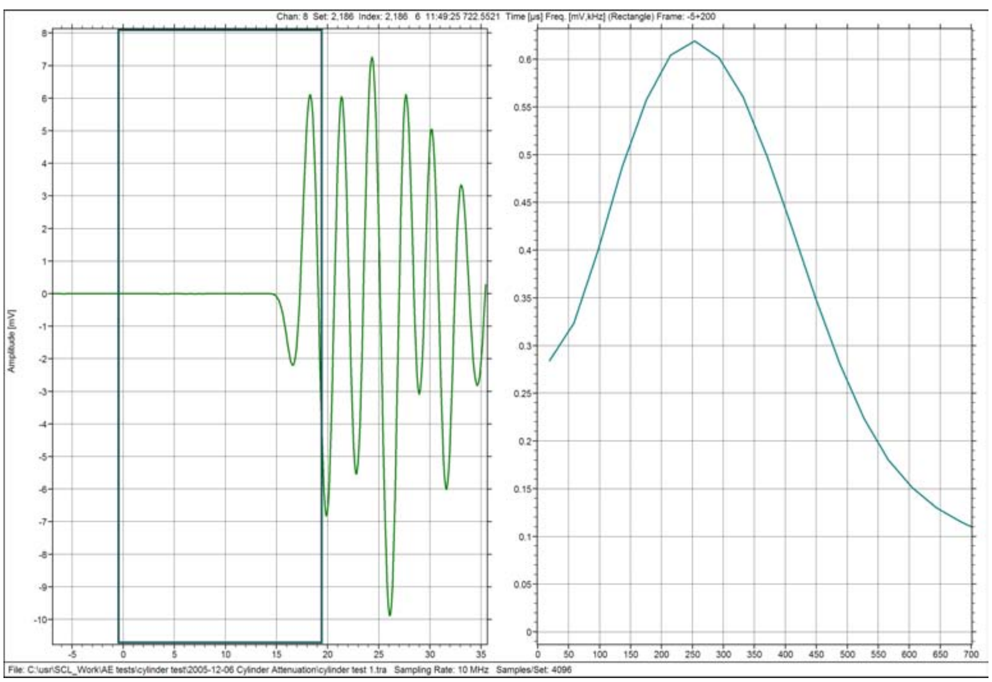

Figure D18 Wave form and FFT from receiver for **3 inch** cylinder height with a **¾ " minus *(Standard*) Mix**.

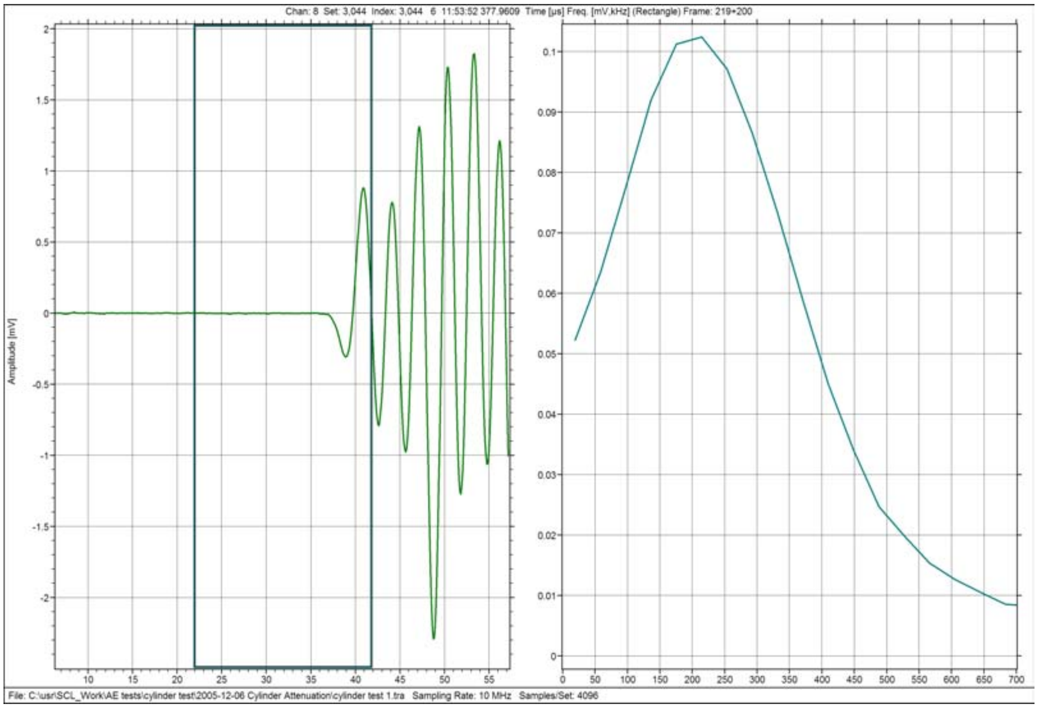

Figure D19 Wave form and FFT from receiver for **6 inch** cylinder height with a **¾ " minus *(Standard*) Mix**

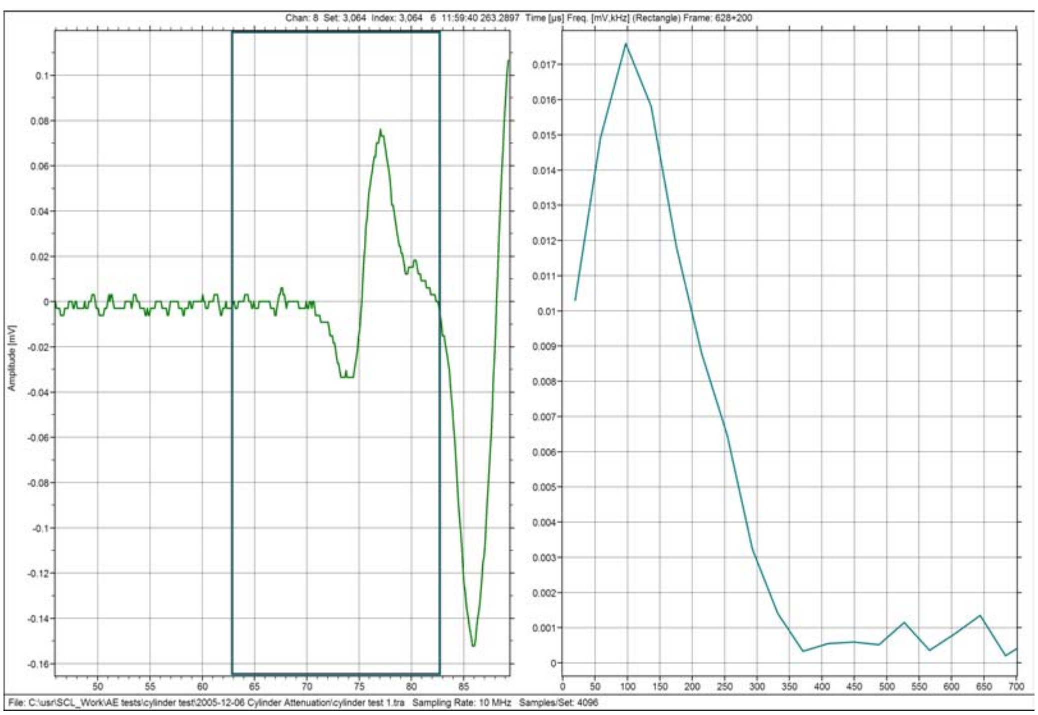

Figure D20 Wave form and FFT from receiver for **12 inch** cylinder height with a **¾ " minus *(Standard*) Mix**.

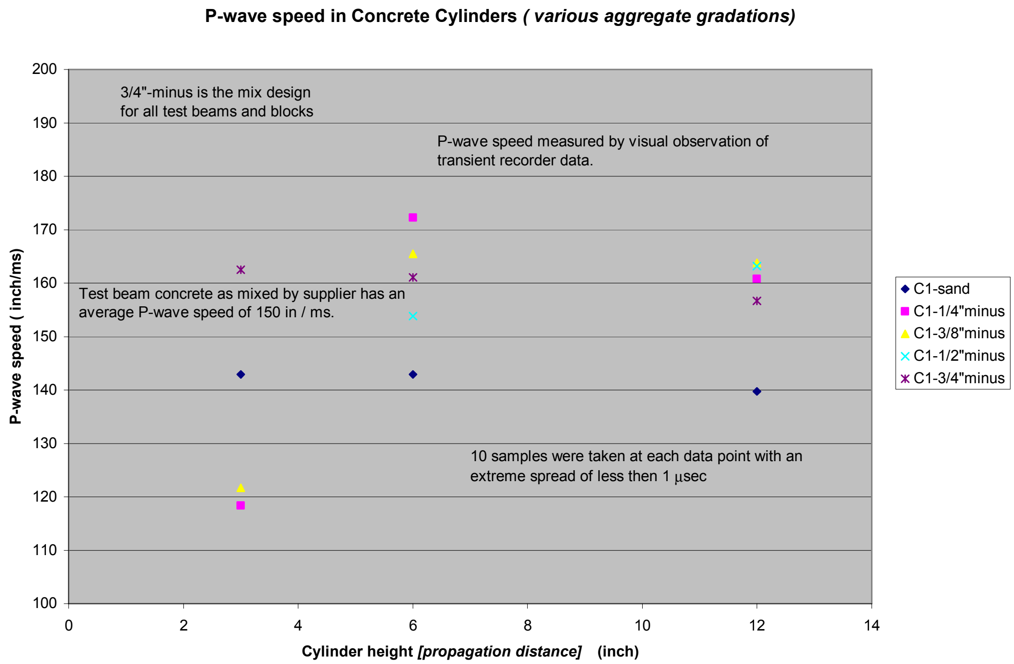

Figure D21 Measured dilatation wave speeds in concrete test cylinders.

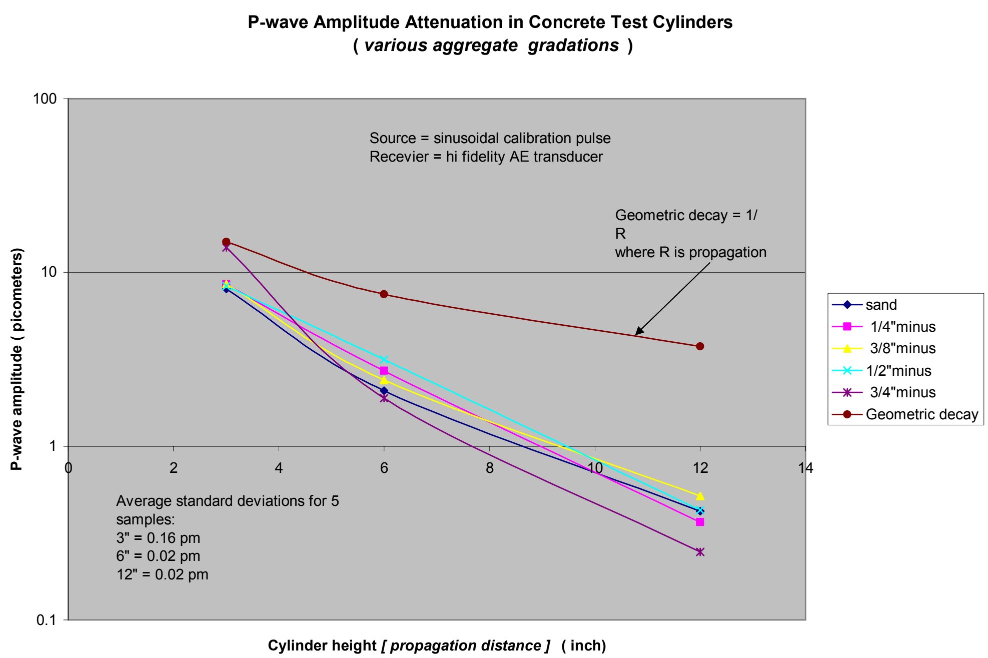

Figure D22 Measured dilatation wave amplitude attenuation in concrete test cylinders.

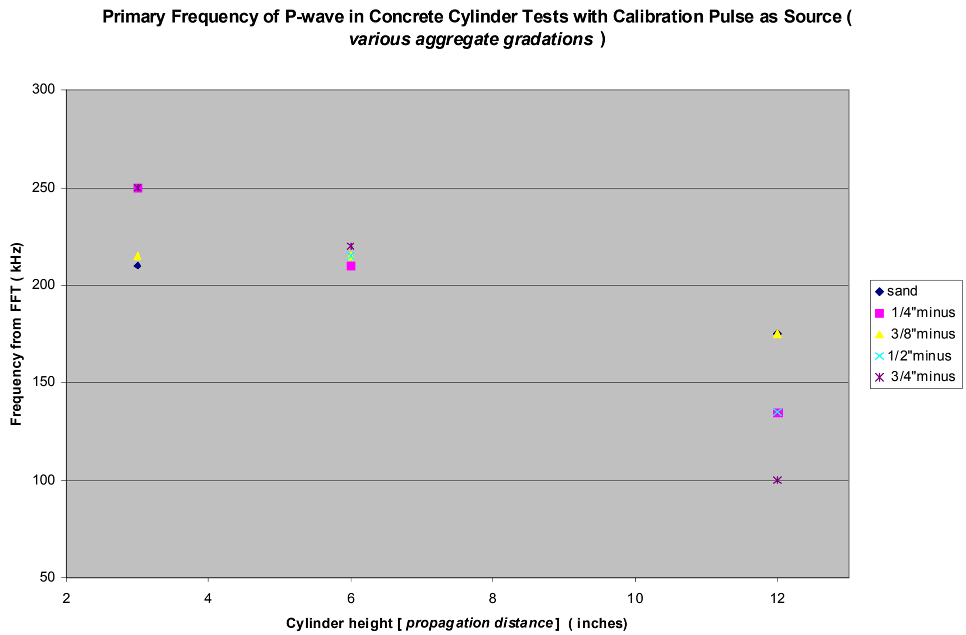

Figure D23 Measured dilatation wave frequency peaks from FFT in concrete test cylinders.

Appendix E Investigation into the Effects of Steel Reinforcement on the Stress Wave Propagation in Concrete Structural Members

Purpose of Test

The purpose of this test series was to determine the measurable effect, if any , of having steel reinforcement bars embedded in a concrete slab on stress wave propagation as measured from the surface of the test block. Typical concrete bridge girders as are being studied under this research project have shear steel reinforcement in the critical shear zones. The density of the shear stirrups range from 6 to 24 inches on centers using a ½ inch diameter (#4) reinforcing bars positioned 2 ¼ inch from the surface of the concrete beams stem or web to the center of the bar. AE generated on the interior of the beam as it is loaded must pass through the "rib like" shear reinforcing cage prior to interacting with the outer surface of the stem where it is detected and measured by the AE sensors. Knowledge of the effects of the steel cages effects on the surface motions is useful for determining proper sensor placement during laboratory and field application of AE to structural health monitoring.

Test Apparatus

Two separate concrete test blocks were used for these tests. Both had exterior dimensions very similar to the critical shear zones of the full scale test beams discusses in Chapter 3 with a width and height of 48 inches and thickness of 14 inches. The concrete used was from the same mix design as used in the full scale test beams. One test specimen was un-reinforced and the other has shear steel reinforcement with the closest bar spacing found in service of 6 inches on center with #4 bars. AE testing was performed on the test specimens far enough from the perimeter edges such that stress wave reflections inside of the test specimen form the edges was no of concern and thus behaved like an infinitely large slab of constant thickness. AE sensors were mounted onto the test specimens to measure surface disturbances input into the test specimens from both pencil lead breaks and AE transducers calibration pulses as discussed in Appendix A,B and C.

<u>AE System Setup</u>

The Vallen AMSYS5 AE system was setup using two channels with transient recorders sampling at 10 MHz. The AE transducers were the hi-fidelity type DECI S1000H.

Test Procedures

The first test used two AE channels both acting as receivers, each one places nearly opposite of the other on each side of the stem as shown in Figure E1. Channel 7 was slightly offset by a distance of 1 inch to allow the use of a pencil lead break as the location shown in the figure. Channel 7 thus acted as a trigger to start the timing clock for the other receiver, Channel 8 on the opposite side of the stem. With this setup the P-wave speed through the thickness of the test specimen could be calculated. Also of interest is the frequency content of the P-wave at both the near by sensor , Channel 7 , located on the same surface as the broad band AE source and the P-wave as it arrived having traveled through the thickness of the stem as measured at Channel 8. This late information can be used for optimal AE sensor selection.

The second test used two AE channels with the same receiver, Channel 7 , but with Channel 8 located on the opposite side of the stem acting as a pulser. The position of the receiver was varied in the direction shown in Figure E2 thus measuring the impact of the calibration pulse on the opposite side of the stem form the AE source at varying angles of approach. The farther from normal the measurement is made the more measurable effect the S-wave could possibly impart onto the measuring surface.

The third test used the same measurement setup as the second but instead was applied to the concrete test block that contained the steel reinforcement. The sensor position were chosen such that the maximum effect of the steel reinforcement has on the stress wave propagation through the thickness of the stem could be resolved as shown in Figure E3. Figure E4 shows a photograph of the top (thickness section) of the test block that contained the steel reinforcement. Figure E5 show the varying positions of the receivers with pulses being input on the opposite side of the stem at a fixed location.

Results

Pencil lead break AE source

Figure E6 show the surface responses to pencil lead break at x = 0 inch with the upper plot showing the response on the same surface as the pencil lead break at a distance of 1 inch and the lower plot showing the response on the opposite side of the stem directly opposite the pencil lead break , having propagated through the 14 inch thickness of the test block. Steel reinforcing was not included in this test. The measured P-wave speed was found to be 150 in/ms. Two the right of each wave form is the corresponding frequency domain representation. The P-wave disturbance measured near the source on the same plane shows a broad frequency content from 60 to 700 kHz with slight emphasis on frequencies below 350 kHz.

The lower right hand plot shows that after propagating through the stem thickness the frequency content of the P-wave has shifted significantly to the lower frequency range of 20 to 200 kHz. The amplitude of the P-wave has also decayed significantly and is approaching the limit of detection using automated fixed threshold methods but is clearly detectable in the transient wave form.

Based on the testing and analysis presented in Appendix B the shear or S-wave speed was calculated from the P and Rayleigh wave speeds measured to be 88 in/ms in this particular batch of concrete. Using these results the wave form and FFT on the far surface is shown with the expected S-wave selected for frequency content. The frequency domain shown to the right of the wave form shows the frequency content of the S-wave to be narrow banded with a peak near 145 kHz. Note that the wave form shows the entire surface response up to and including the S-wave arrival and the S-wave portion of the wave form is boxed in to show the FFT sample region.

Calibration pulse source

Using one of the two AE sensors as a pulsed AE source and the other as a receiver allowed the studying of varying the angle of impact of the P and S-waves onto the receiver surface. Figures E8 through E18 show the wave forms of the calibration pulse signal applied to one surface of the stem in the upper plots and the received signal from the opposite surface in the lower plot from a normal impact (90 degrees) at position 0 to an a 32 degree impact at position 9 , all in the test block that had no steel reinforcement. The observed P-wave arrivals are shown at each receiver position along with the expected arrival of the first S-wave pulse. The peak amplitudes of the P and S-waves are comparable in magnitude but the S-wave generally shows larger peak amplitudes as the angle of impact decreases from 90 to 32 degrees. For all angles tested the P-wave speed was a nearly constant 150 +/- 3 in/ms .

The same test procedures were applied to the concrete test block that contained steel reinforcement. Figures E19 through E27 show the wave forms of the calibration pulse signal applied to one surface of the stem in the upper plots and the received signal from the opposite surface in the lower plot from a normal impact (90 degrees) at position 0 to an a 27 degree impact at position 7 , all in the test block that had no steel reinforcement. The observed P-wave arrivals are shown at each receiver position along with the expected arrival of the first S-wave pulse.

A comparison of the non-reinforced and steel reinforced test results is shown in Figures E28 through E30. Figure E28 shows the variation of the first P-wave oscillation amplitudes, Figure E29 the second P-wave oscillation and Figure E30 the third P-wave oscillation amplitude respectively. One each plot the anticipated region of steel reinforcement interference is shown and labeled “ rebar region”. The statistical variation of each measurement is also shown on the plots for a sample of 5 data at each point. The maximum variation between un-reinforced and steel reinforced test block results appears to occur between the 0 and 2 inch positions where the P-waves in the steel reinforced specimen have amplitudes two to fives times larger then the same positions in the un-reinforced specimen. In the region were the rebar is expected to possibly influence the through thickness stress wave propagation the differences in peak P-wave amplitudes are much less with a maximum variation of 0.29 Pico meters or a factor of 1.75.

Conclusions

The pencil lead break AE source measurements showed that the P-wave from a pencil lead break can be detected after propagating 14 inches through the test block thickness, which is identical to the full scale test beams in thickness, thought it is on the bottom limit of detection using automated fixed level threshold methods. The frequency content of the P-wave shows attenuation of the higher frequency components as it propagates. The frequency content of the P-wave dropped from over 700 kHz down to the 20 to 200 kHz band upon detection on the opposite surface. The S-wave showed a narrow banded frequency content between 100 and 170 kHz after propagating through the stem thickness.

The calibration pulse AE source measurements showed that both the arrivals of the P and S-waves from the source could be detected and identified on the opposite surface of the stem having propagated through the thickness. Significant differences in the P-wave amplitudes were measured between the un-reinforced and steel reinforced concrete test blocks but primarily in the region where the least influence of the steel would be expected. These results will be considered further by comparing the measured results to the results of finite element analysis in order to better understand the potential influence of reinforcing steel on the stress wave propagation inside the concrete structure.

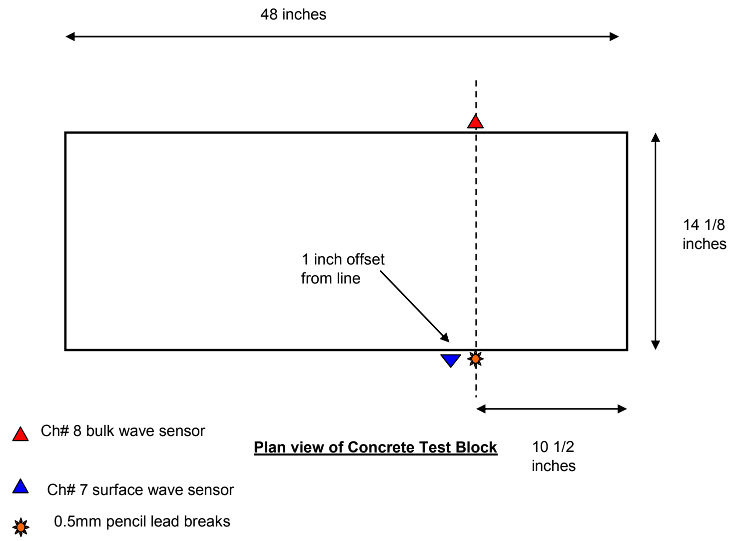

Figure E1 Schematic of test setup for pencil lead breaks through the concrete test block thickness.

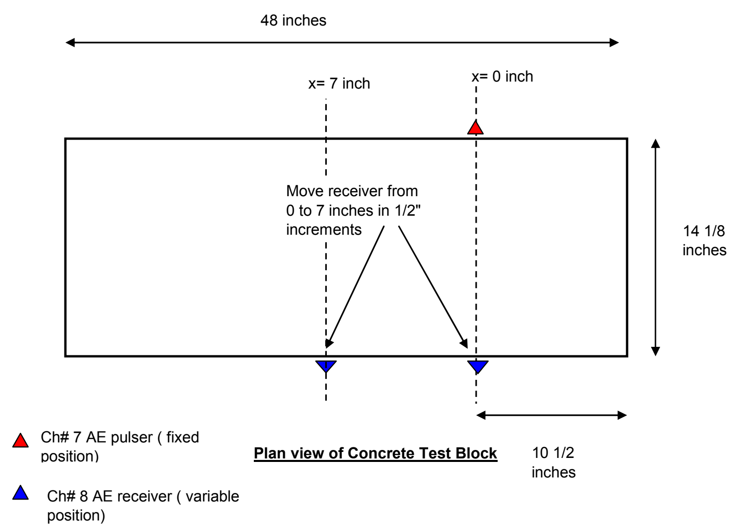

Figure E2 Schematic of test setup for calibration pulses through un-reinforced concrete test block.

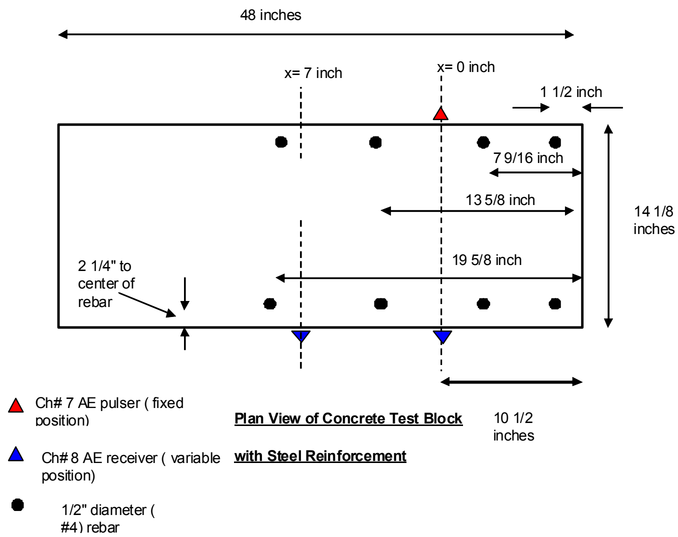

Figure E3 Schematic of test setup for calibration pulses through steel-reinforced concrete test block.

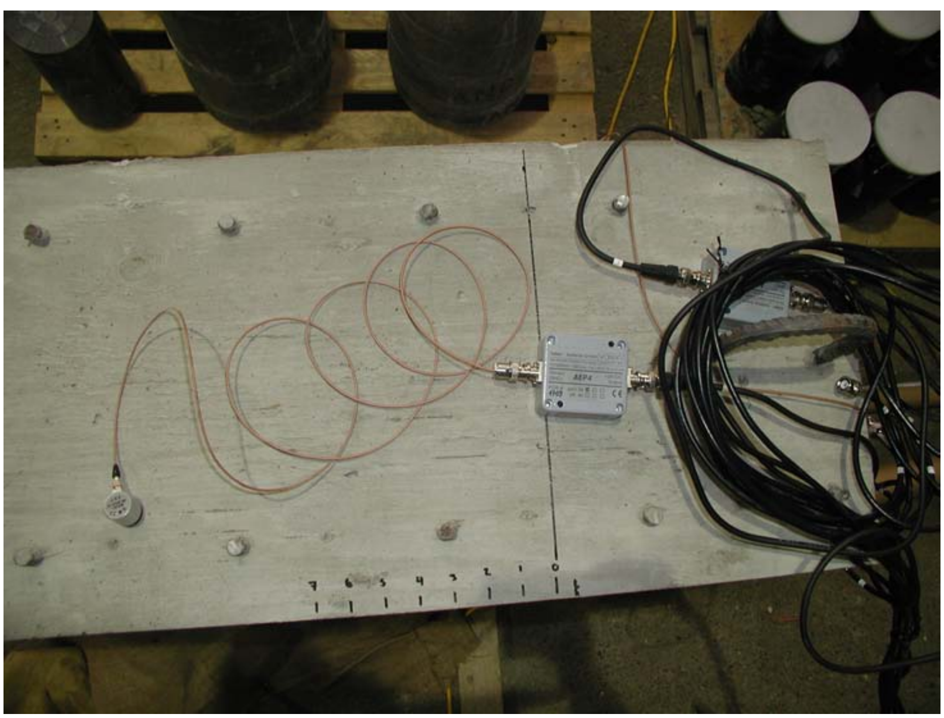

Figure E4 Photograph of steel-reinforced concrete test block.

Figure E5 Photograph of steel-reinforced concrete test block with receiver AE transducer being mounted.

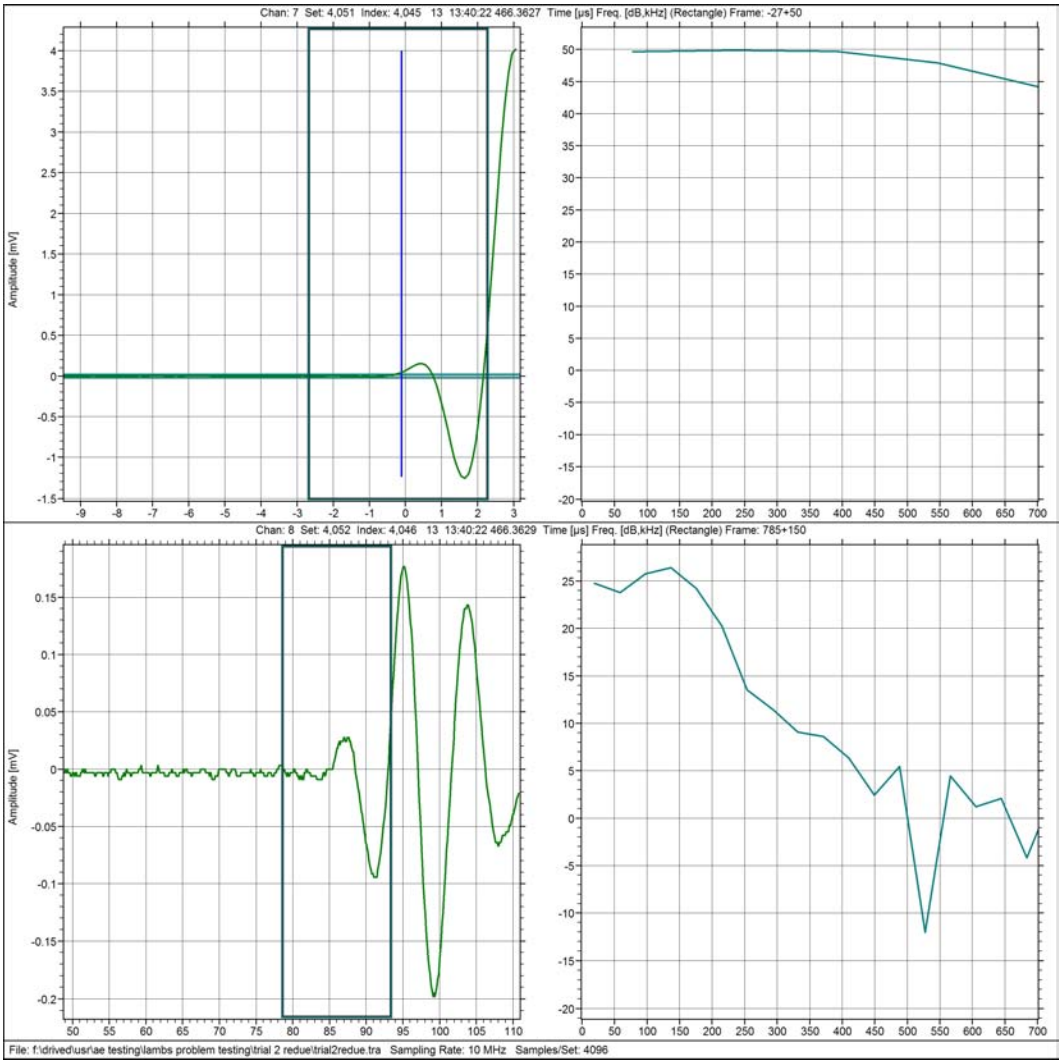

Figure E6 Wave forms and FFT for surface response near pencil lead break (upper plot) and P-wave portion of surface response on opposite side of test block from pencil lead break (lower plot).

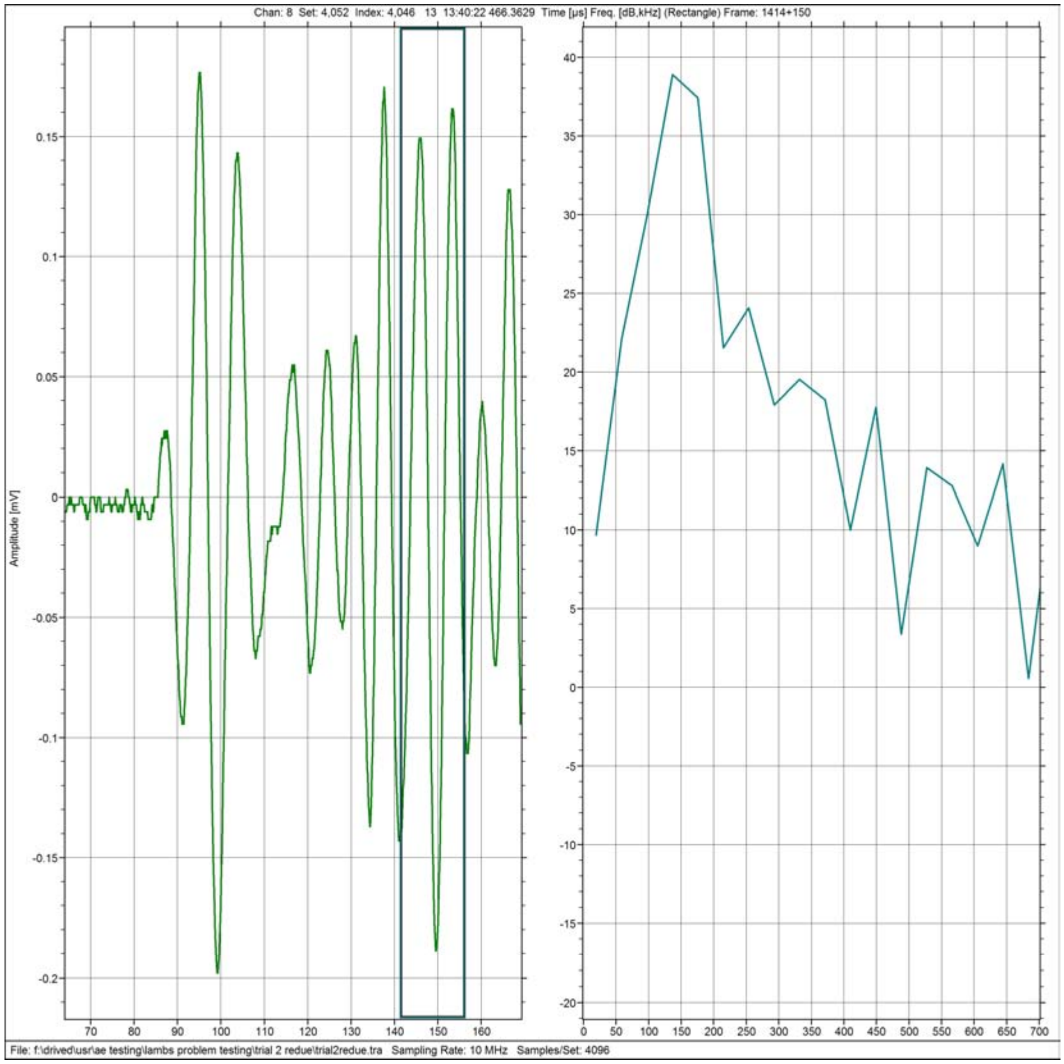

Figure E7 Wave form and FFT for shear wave portion of surface response on opposite side of test block from pencil lead break.

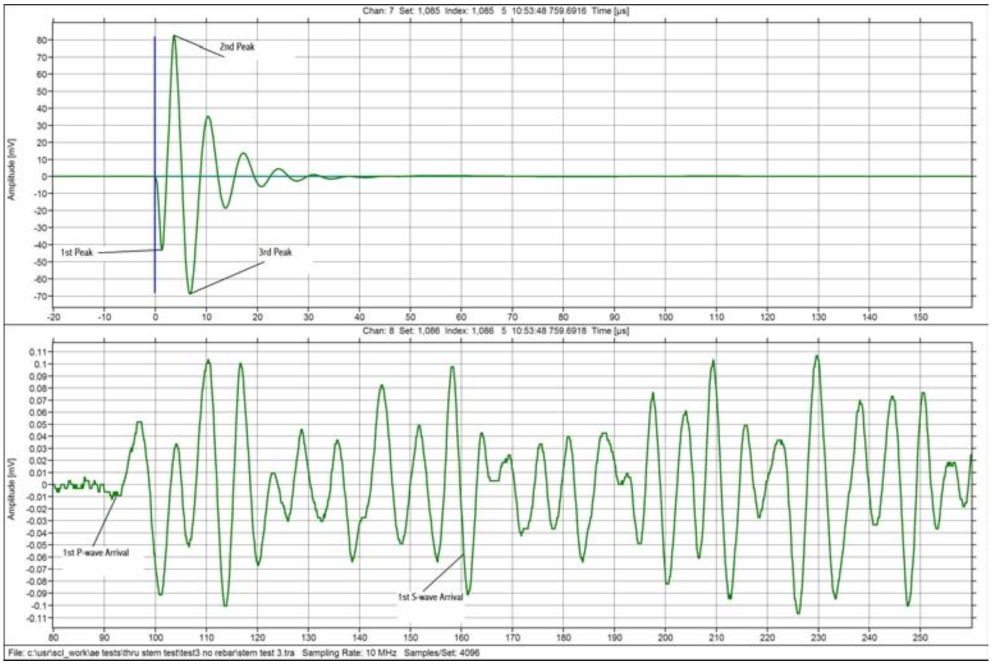

Figure E8 Wave forms of calibration pulse sent to AE pulser (upper plot) and response on opposite side of un-reinforced concrete test block at receiver position 0 (lower plot).

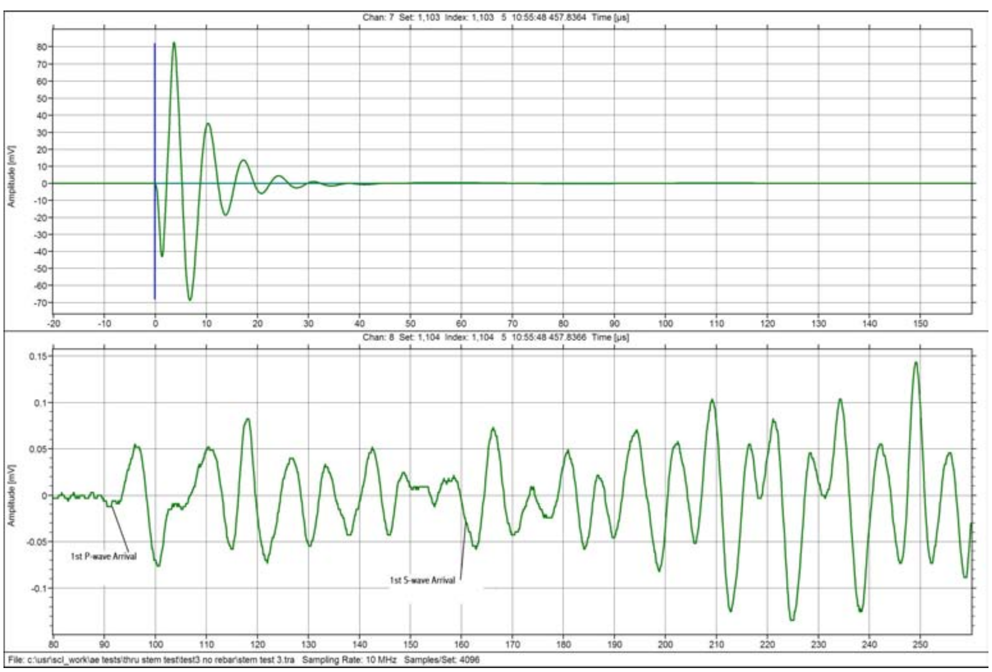

Figure E9 Wave forms of calibration pulse sent to AE pulser (upper plot) and response on opposite side of un-reinforced concrete test block at receiver position 1 (lower plot).

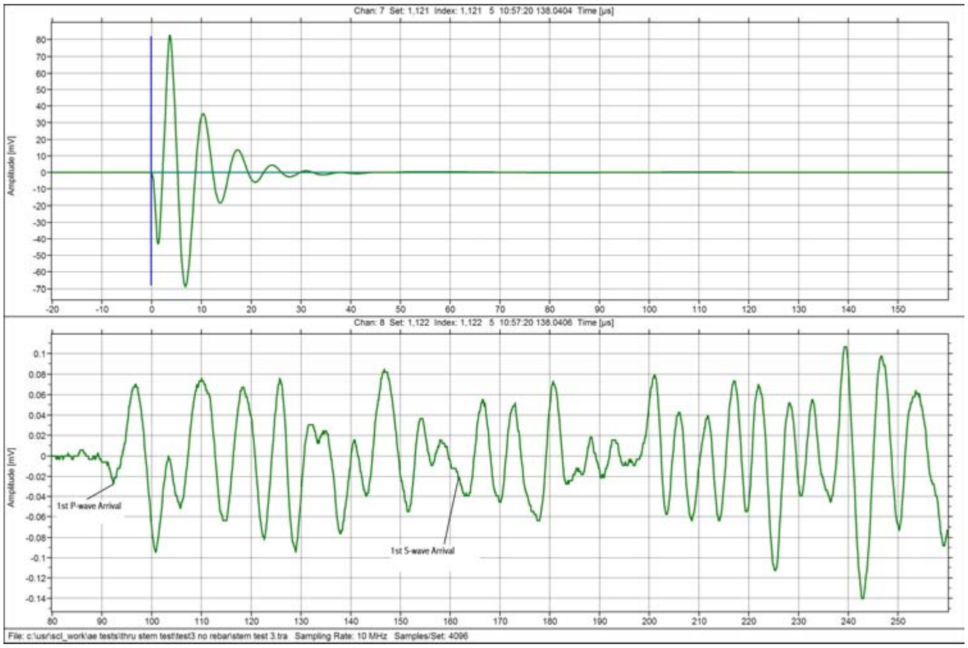

Figure E10 Wave forms of calibration pulse sent to AE pulser (upper plot) and response on opposite side of un-reinforced concrete test block at receiver position 2 (lower plot).

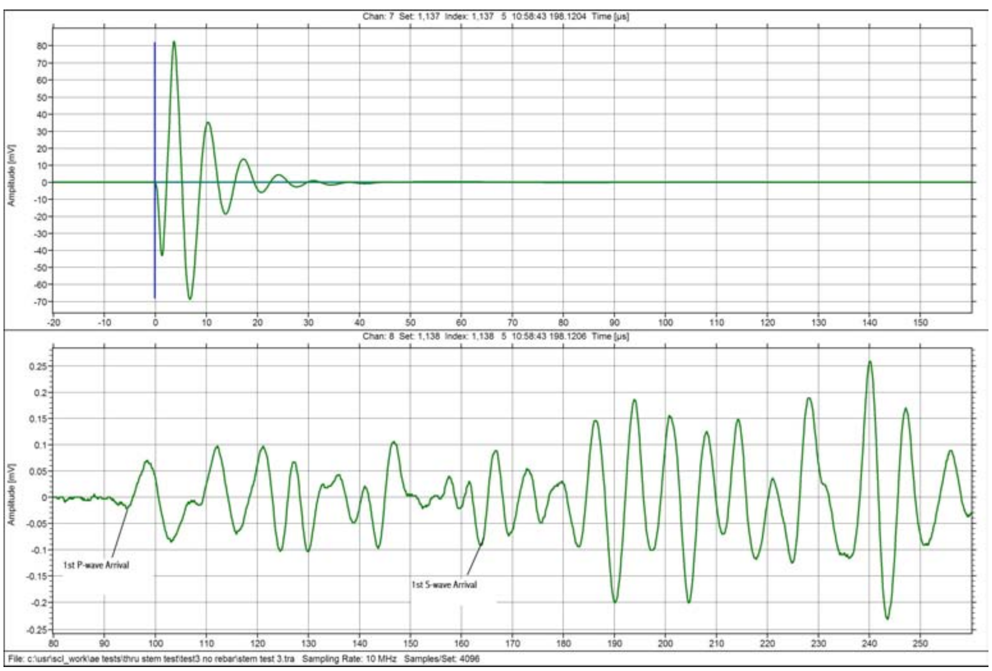

Figure E11 Wave forms of calibration pulse sent to AE pulser (upper plot) and response on opposite side of un-reinforced concrete test block at receiver position 3 (lower plot).

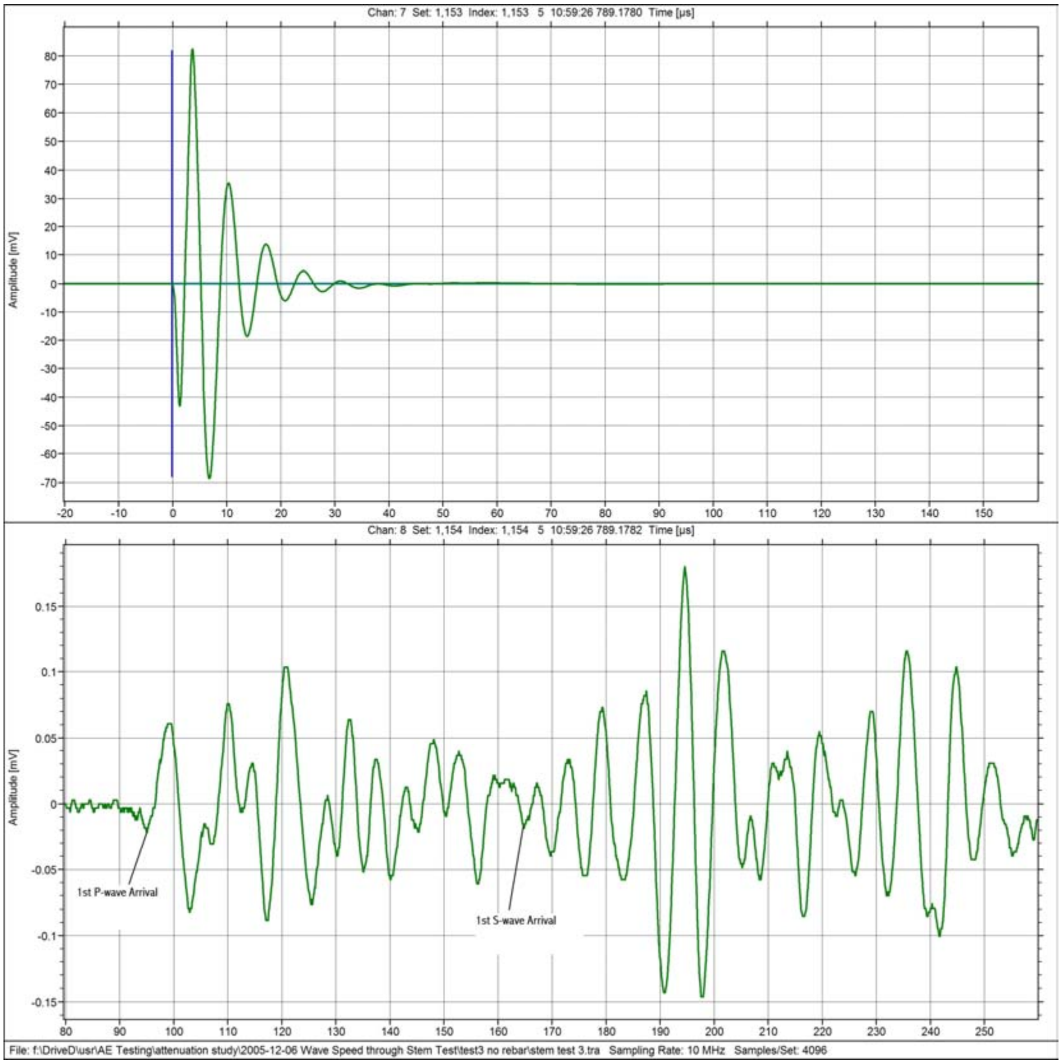

Figure E12 Wave forms of calibration pulse sent to AE pulser (upper plot) and response on opposite side of un-reinforced concrete test block at receiver position 3.5 (lower plot).

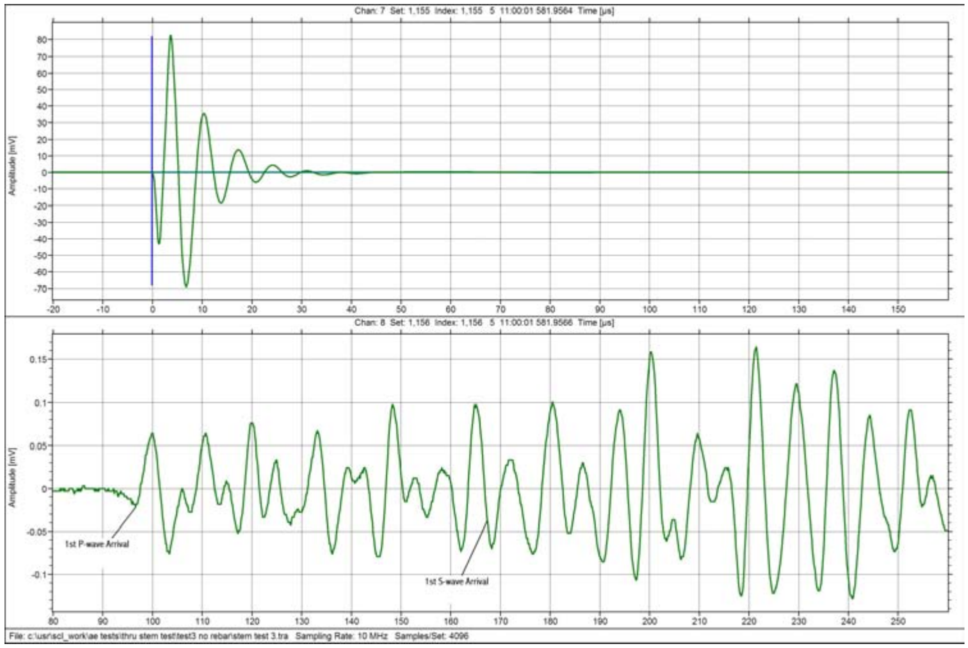

Figure E13 Wave forms of calibration pulse sent to AE pulser (upper plot) and response on opposite side of un-reinforced concrete test block at receiver position 4 (lower plot).

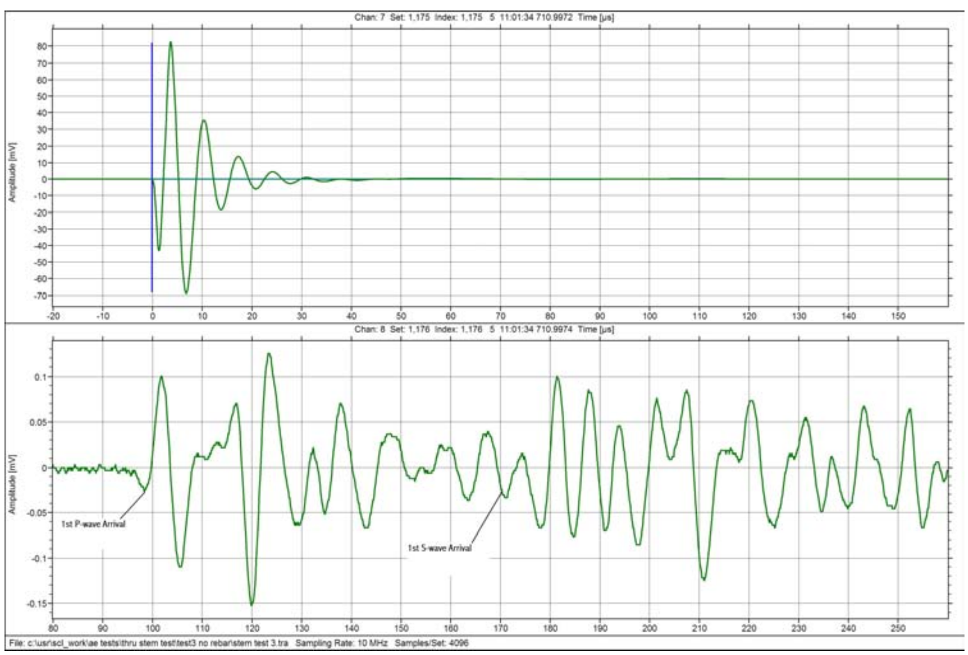

Figure E14 Wave forms of calibration pulse sent to AE pulser (upper plot) and response on opposite side of un-reinforced concrete test block at receiver position 5 (lower plot).

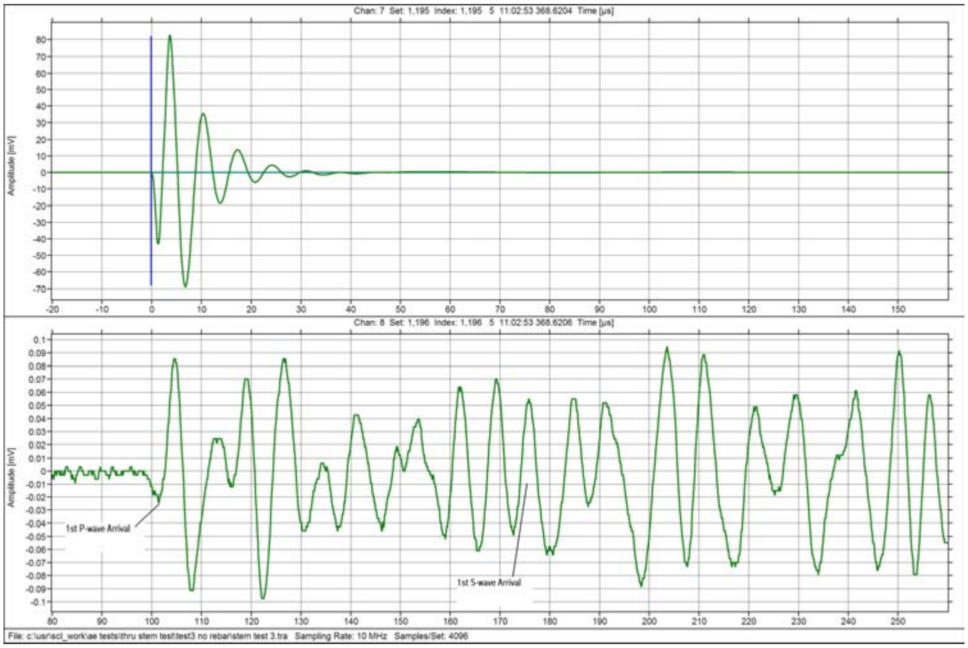

Figure E15 Wave forms of calibration pulse sent to AE pulser (upper plot) and response on opposite side of un-reinforced concrete test block at receiver position 6 (lower plot).

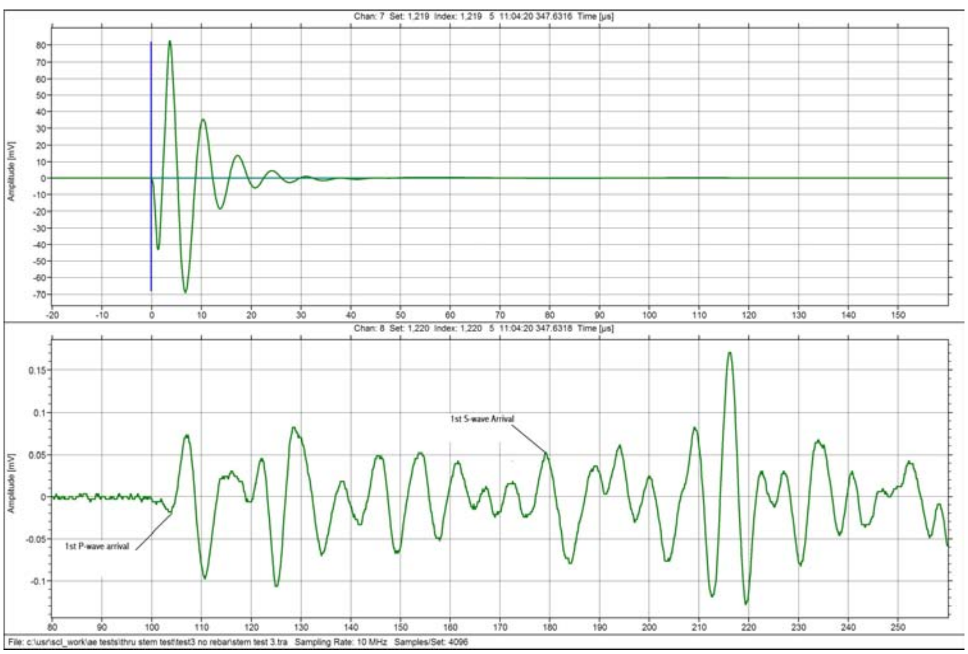

Figure E16 Wave forms of calibration pulse sent to AE pulser (upper plot) and response on opposite side of un-reinforced concrete test block at receiver position 7 (lower plot).

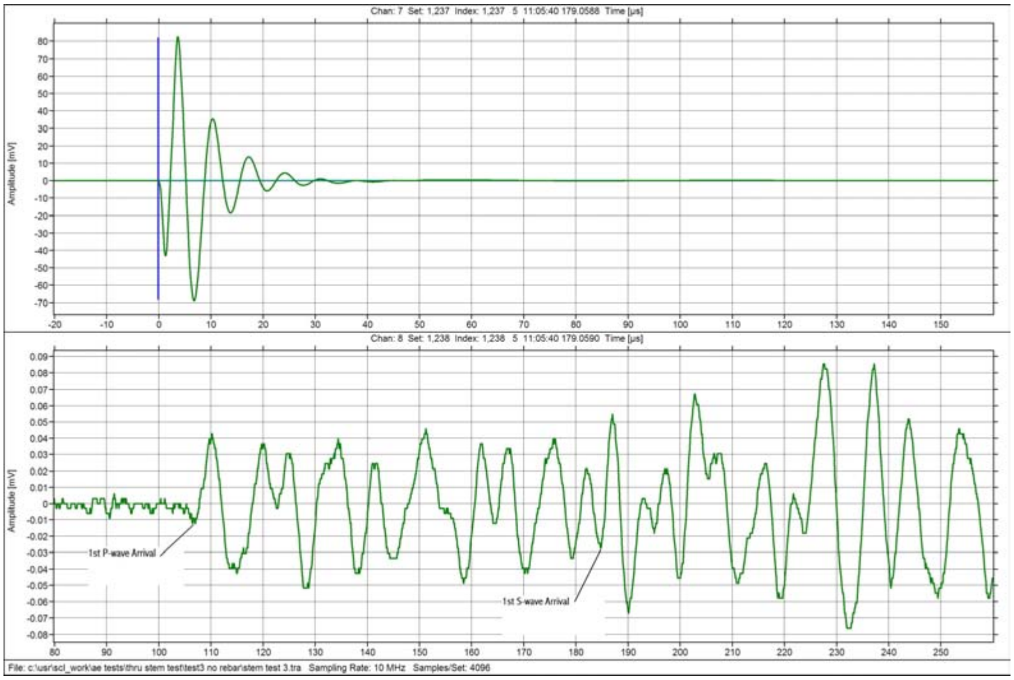

Figure E17 Wave forms of calibration pulse sent to AE pulser (upper plot) and response on opposite side of un-reinforced concrete test block at receiver position 8 (lower plot).

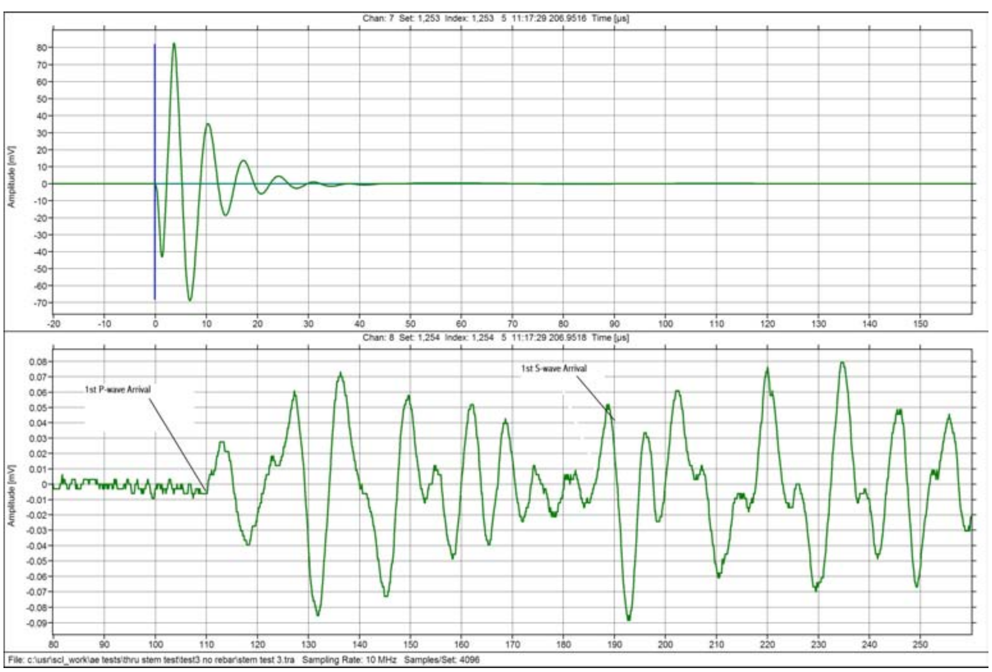

Figure E18 Wave forms of calibration pulse sent to AE pulser (upper plot) and response on opposite side of un-reinforced concrete test block at receiver position 9 (lower plot).

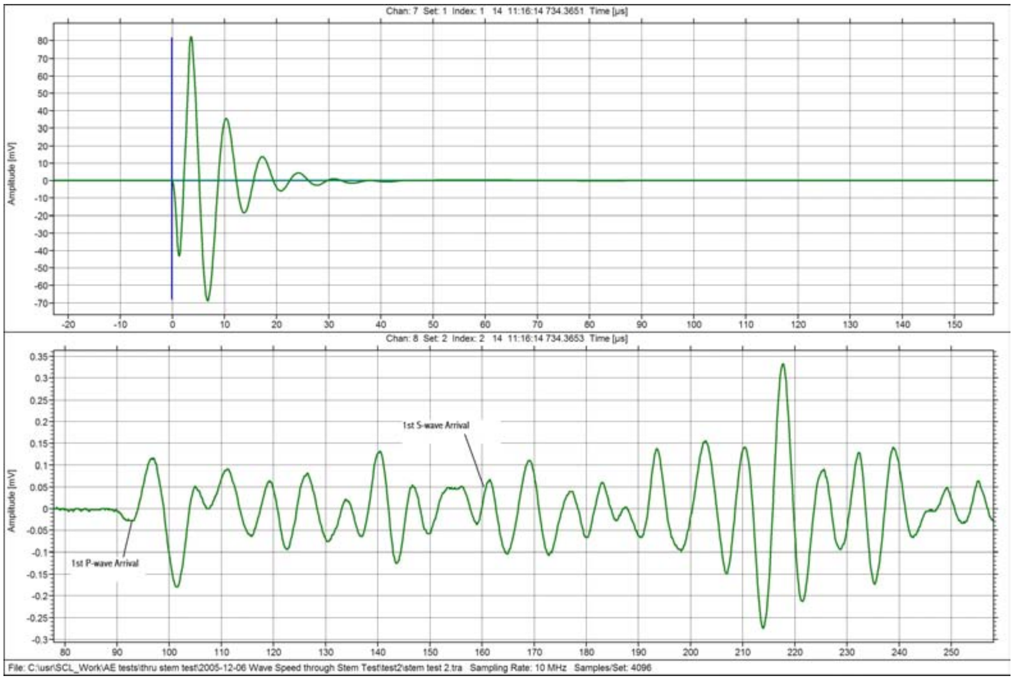

Figure E19 Wave forms of calibration pulse sent to AE pulser (upper plot) and response on opposite side of steel-reinforced concrete test block at receiver position 0 (lower plot).

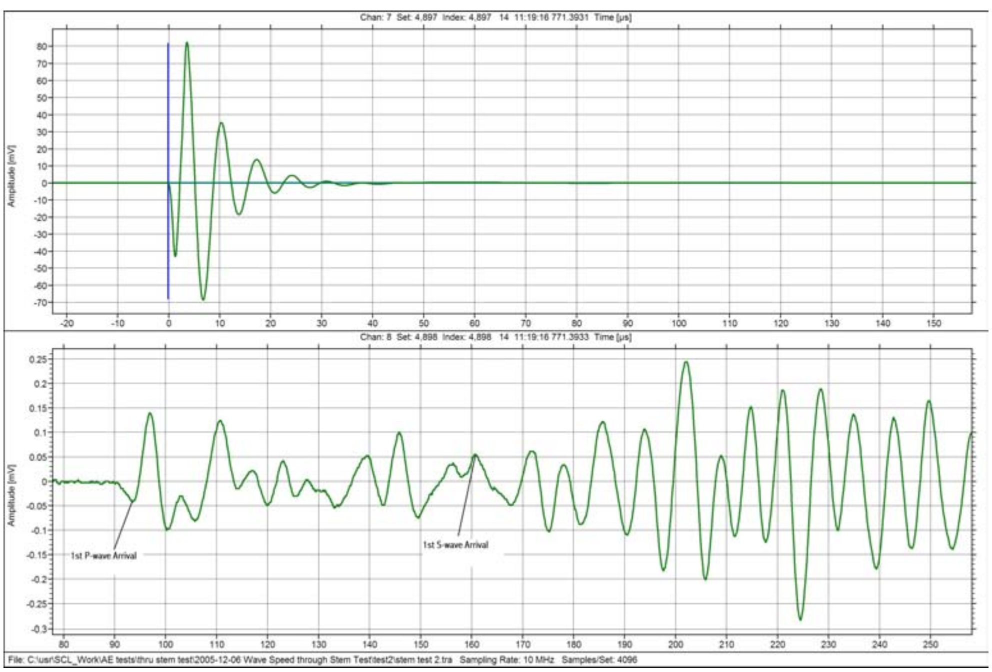

Figure E20 Wave forms of calibration pulse sent to AE pulser (upper plot) and response on opposite side of steel-reinforced concrete test block at receiver position 1 (lower plot).

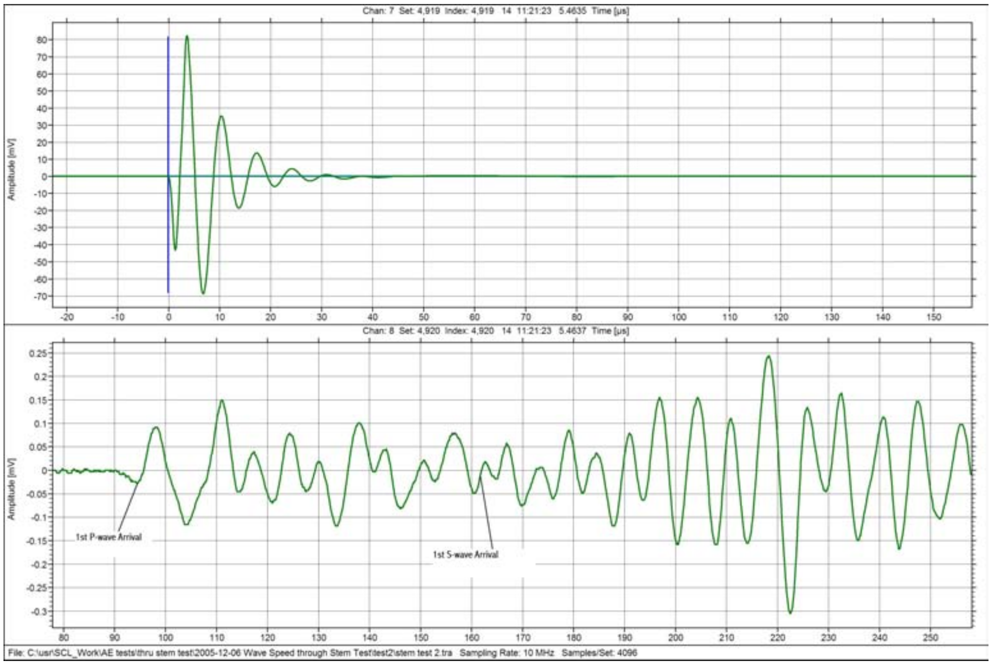

Figure E21 Wave forms of calibration pulse sent to AE pulser (upper plot) and response on opposite side of steel-reinforced concrete test block at receiver position 2 (lower plot).

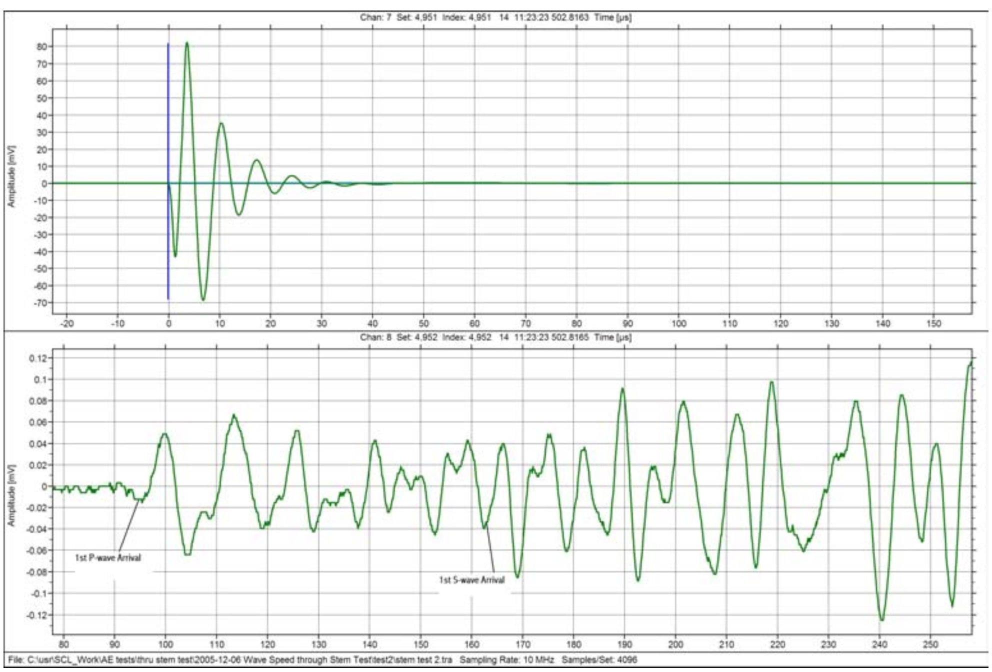

Figure E22 Wave forms of calibration pulse sent to AE pulser (upper plot) and response on opposite side of steel-reinforced concrete test block at receiver position 3 (lower plot).

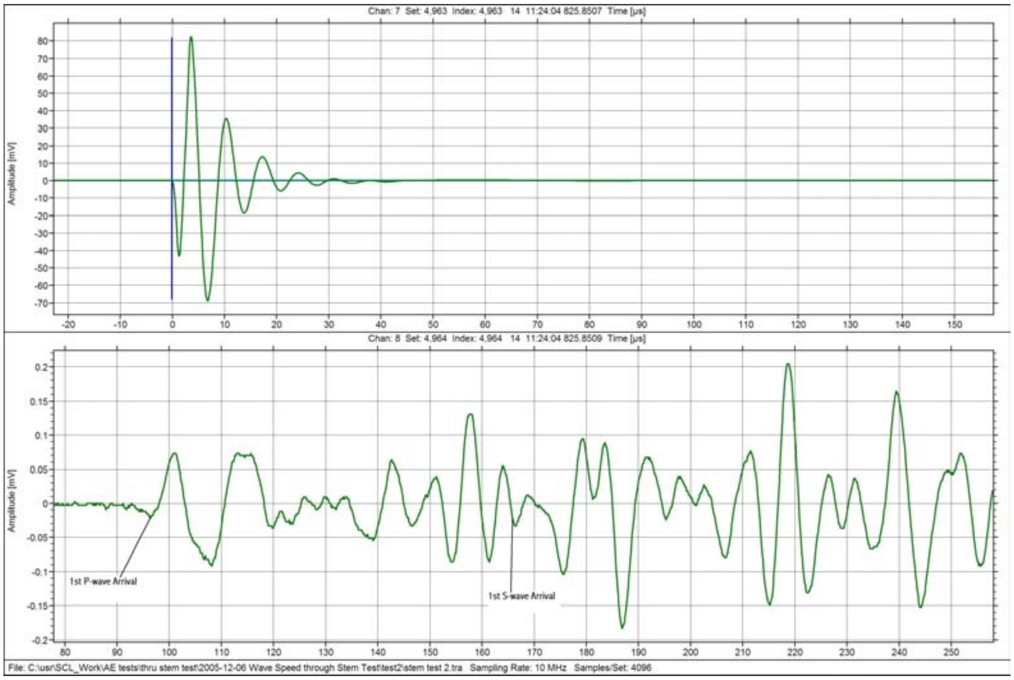

Figure E23 Wave forms of calibration pulse sent to AE pulser (upper plot) and response on opposite side of steel-reinforced concrete test block at receiver position 3.5 (lower plot).

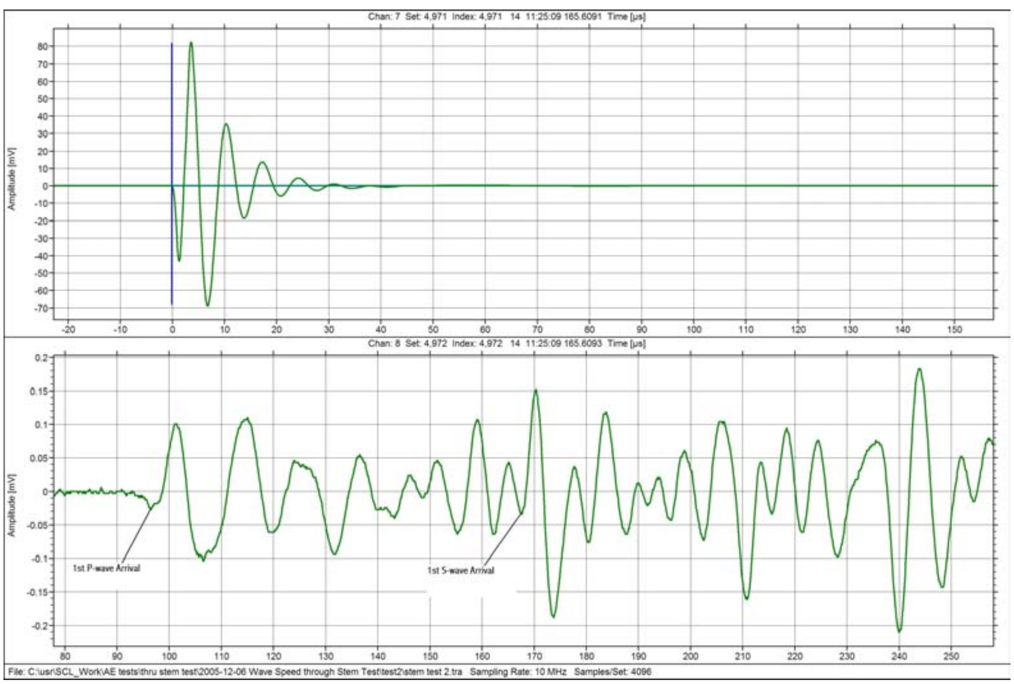

Figure E24 Wave forms of calibration pulse sent to AE pulser (upper plot) and response on opposite side of steel-reinforced concrete test block at receiver position 4 (lower plot).

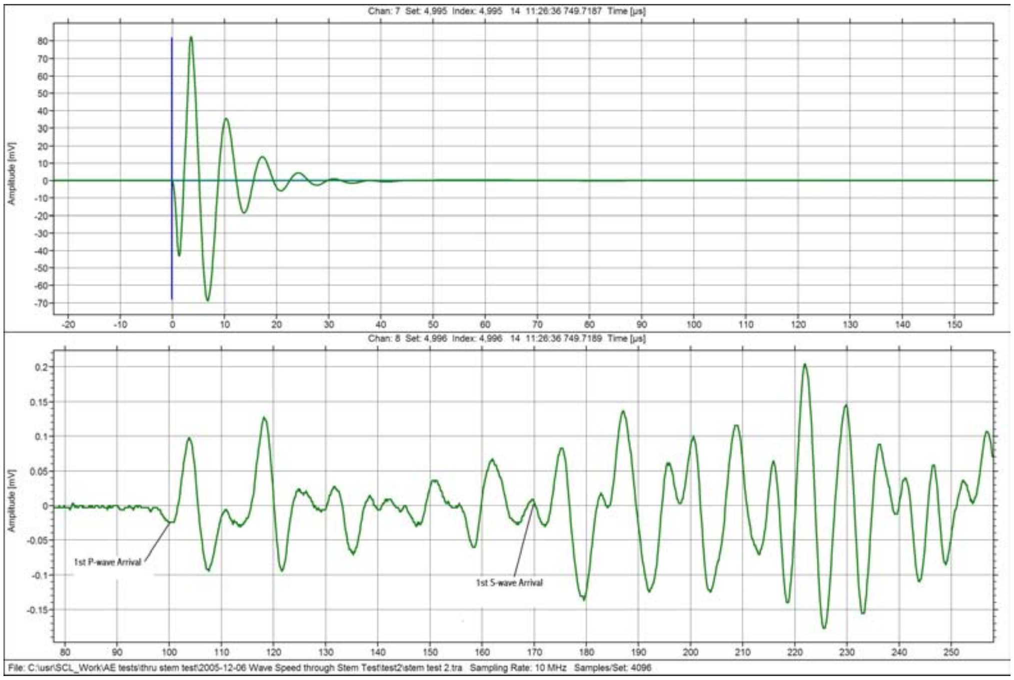

Figure E25 Wave forms of calibration pulse sent to AE pulser (upper plot) and response on opposite side of steel-reinforced concrete test block at receiver position 5 (lower plot).

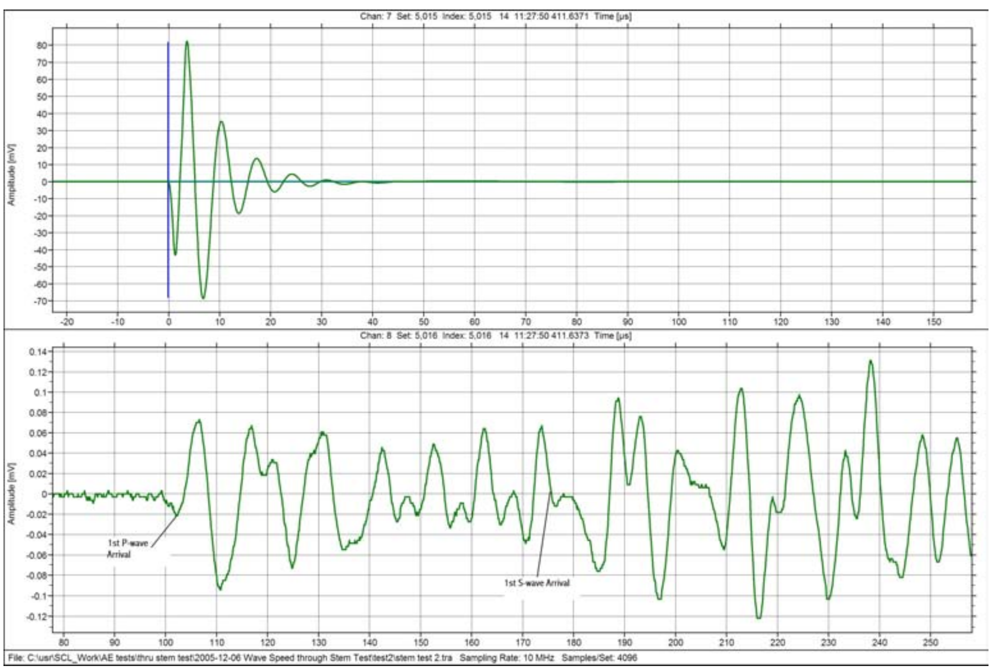

Figure E26 Wave forms of calibration pulse sent to AE pulser (upper plot) and response on opposite side of steel-reinforced concrete test block at receiver position 6 (lower plot).

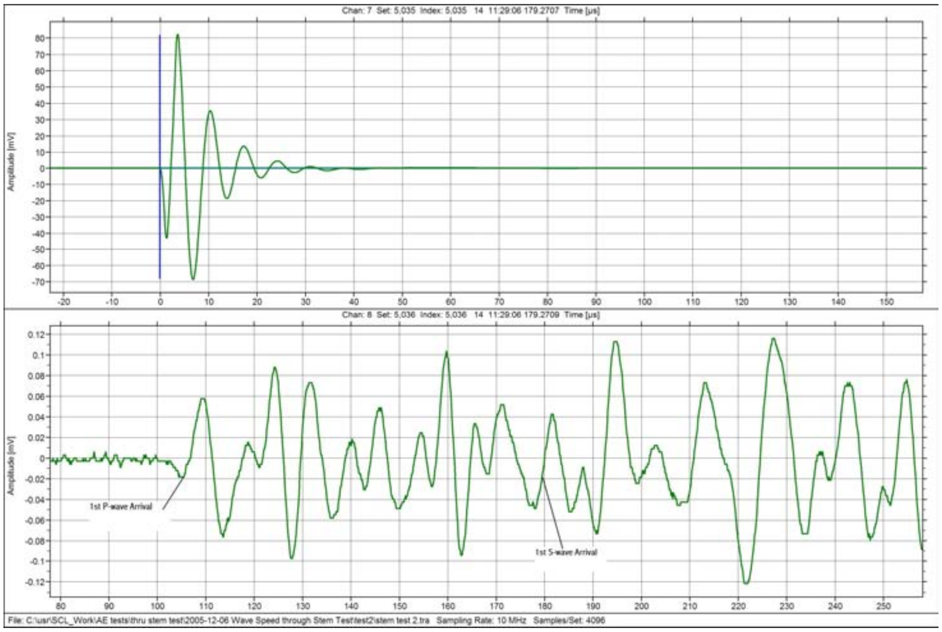

Figure E27 Wave forms of calibration pulse sent to AE pulser (upper plot) and response on opposite side of steel-reinforced concrete test block at receiver position 7 (lower plot).

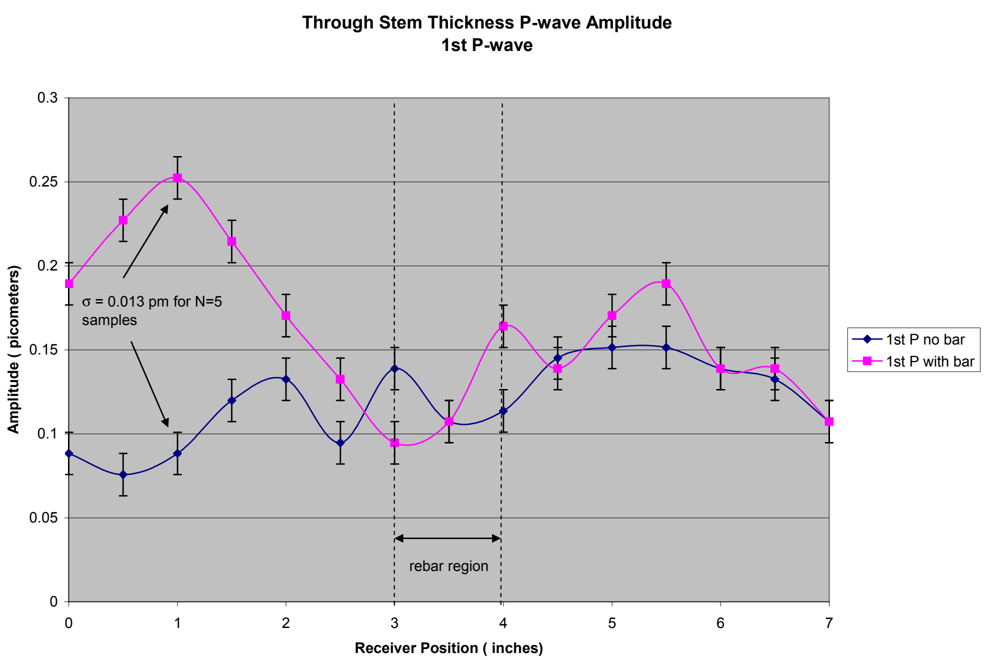

Figure E28 Comparison of 1st P-wave oscillation amplitudes at the various receiver positions for both un-reinforced and steel-reinforced concrete test blocks.

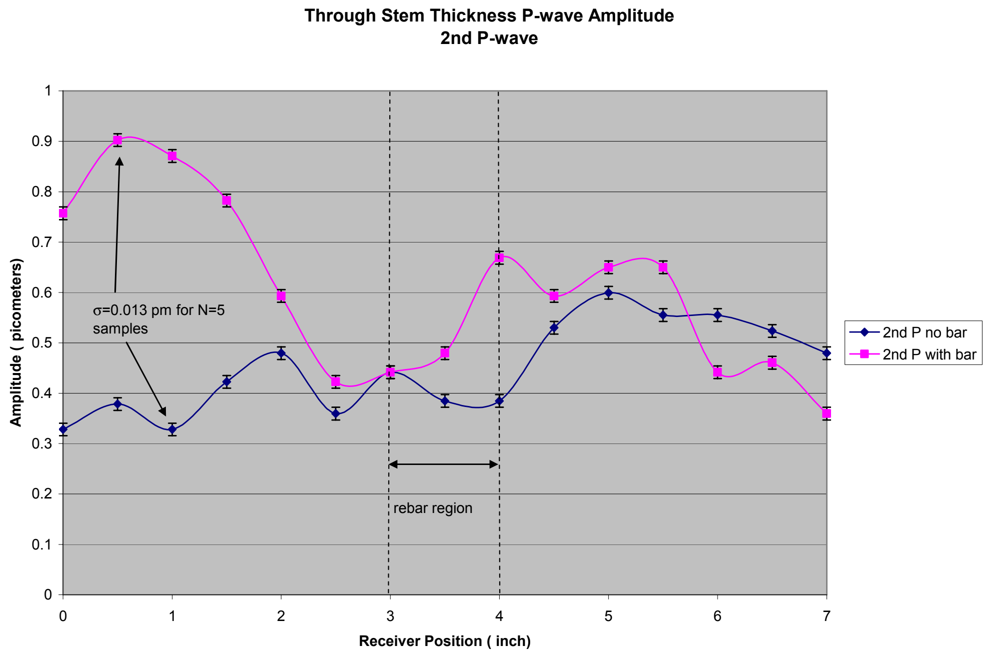

Figure E29 Comparison of 2nd P-wave oscillation amplitudes at the various receiver positions for both un-reinforced and steel-reinforced concrete test blocks.

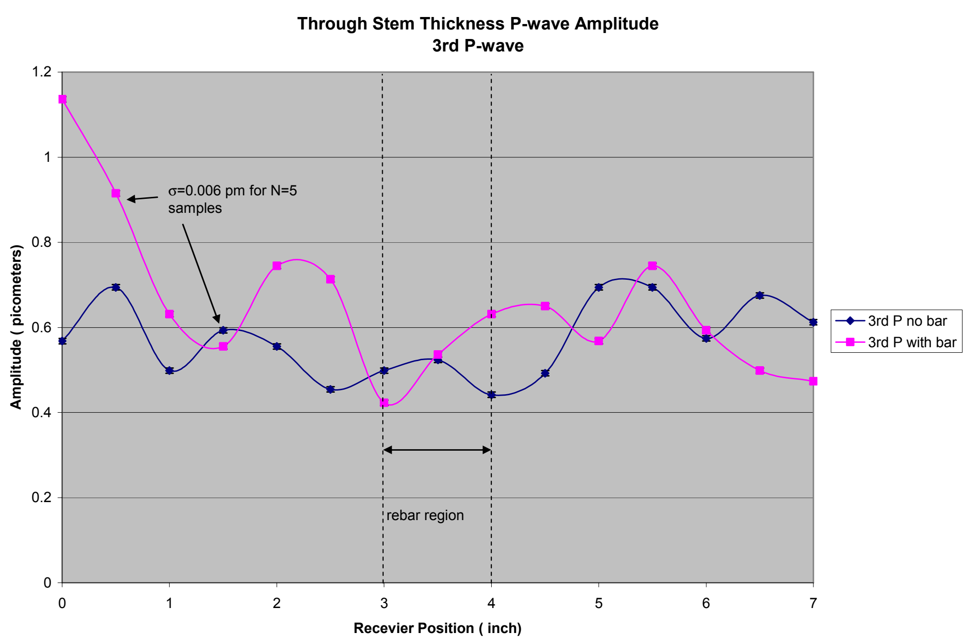

Figure E30 Comparison of 3rd P-wave oscillation amplitudes at the various receiver positions for both un-reinforced and steel-reinforced concrete test blocks.